Phase Behavior and Viscosity Modeling of Refrigerant-Lubricant Mixtures

Monsalvo, Matias Alfonso

Publication date:
2006

Document Version
Publisher's PDF, also known as Version of record

Citation (APA):
Monsalvo, M. A. (2006). *Phase Behavior and Viscosity Modeling of Refrigerant-Lubricant Mixtures*. Technical University of Denmark.

Phase Behavior and Viscosity Modeling of Refrigerant-Lubricant Mixtures

Matías A. Monsalvo

2006

Ph.D. Thesis

DTU

TECHNICAL UNIVERSITY OF DENMARK
DEPARTMENT OF CHEMICAL ENGINEERING
CENTER FOR PHASE EQUILIBRIA AND SEPARATION PROCESSES (IVC-SEP)

Phase Behavior and Viscosity Modeling of Refrigerant – Lubricant Mixtures

Matias A. Monsalvo

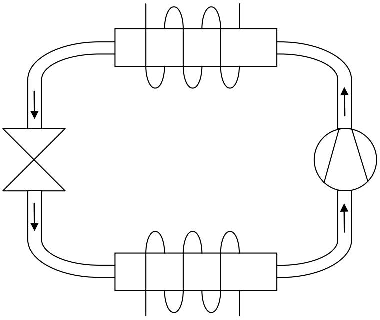

Ph. D. Thesis

Center for Phase Equilibria and Separation Processes (IVC-SEP)
Department of Chemical Engineering
Technical University of Denmark
DK-2800 Lyngby, Denmark

ISBN 87-91435-38-2

Printed by Book Partner, Nordhaven Digital

Copenhagen, Denmark.

With regard to Chapter 5 the author acknowledges the paper S. E. Quiñones-Cisneros, *Phys. Chem. Chem. Phys.*, 2004, **6**, 2307-2313.

Preface

This thesis is submitted as partial fulfillment of the requirements for obtaining the Ph.D. degree in chemical engineering at the Technical University of Denmark, Lyngby, Denmark. The project has been financially supported by the Danish Technical Research Council (STVF). The work presented in this thesis has been carried out from November 2002 to December 2005 in the research group Center for Phase Equilibria and Separation Processes (IVC-SEP) at the Department of Chemical Engineering. The work has been supervised in a first stage by Associate Professor Sergio E. Quiñones-Cisneros and Associate Professor Alexander Shapiro, and in a second stage by Associate Professor Alexander Shapiro and Associate Professor Kaj Thomsen. I would like to express my gratitude and thank my supervisors for their inspiration and fruitful discussions of topics related to this thesis, resulting in a very successful and productive collaboration. In particular to Associate Professor Sergio E. Quiñones-Cisneros for the knowledge he has shared and for giving me the chance to work at IVC-SEP. I would also like to thank Associate Professor Alexander Shapiro for his help and guidance, especially during the second part of this thesis.

I am very grateful to Professor Christian Boned and Associate Professor Antoine Baylaucq, both at the research group "Propiétés de Transport" at the Université de Pau, France, for giving me the opportunity to work in their group for six months. I would like to thank them for a very good collaboration. In particular, I would like to thank Associate Professor Antoine Baylaucq together with Dr. Patrick Reghem for valuable assistance and help in the laboratory.

To the colleagues that I have worked with at IVC-SEP, thanks for your help and sometimes your questions. Particularly, I would like to express my gratitude to Professor Erling H. Stenby for his support and to Annelise Lerche Kofod for taking care of a lot of administrative problems and her priceless help. Also, thanks to Amra Tihic for her help with the abstract in Danish.

To my friends in Argentina, Denmark and wherever else I have been in the last three years, thanks for their conscious or unconscious help. Especially, for many reasons, thanks to Mariana Gonzalez Bagnoli and Sylvain Verdier.

Finally, to my family for their help and for always supporting me in all the decisions I have made.

Abstract

Restrictions in the use of environmentally damaging compounds in refrigeration systems have led to important changes in the chemical design of refrigerants. In many cases new environmentally friendly refrigerants must be combined with lubricants in order to provide an adequate pressure-viscosity-temperature (p-η-T) relationship in a refrigeration cycle. This brings into consideration a multidisciplinary problem involving phase and dynamic behavior of refrigerant-lubricant mixtures. Since refrigerant-lubricant mixtures are likely to be highly asymmetric, another important phenomenon is involved: barotropic behavior (density inversions).

The aim of the project is accurate modeling and prediction of the phase, volumetric and dynamic properties that are required in the design of cooling cycles based on environmentally friendly refrigerant-lubricant mixtures. The work has been carried out with mixtures containing hydrofluorocarbon (HFC) and carbon dioxide as alternative refrigerants combined with polyalkylene glycols (PAG), polyol esters (POE), and alkyl benzenes (AB) as alternative synthetic lubricants. The description of the volumetric behavior (p-v-T) is studied based on different equations of state (EoS), ranging from simple cubic equations, through empirical approaches, to statistical mechanics based models. The evaluation of the p-η-T properties is carried out by means of several viscosity models, covering wide ranges of pressure and temperature for both pure compounds and mixtures. Special attention is paid to the recently developed friction theory (*f-theory*) viscosity model, which is used in combination with different equations of state (EoS). It has been shown that the *f-theory* in combination with simple cubic EoS can accurately reproduce the viscosity behavior of many compounds. Extension of the *f-theory* approach to other kinds of EoS has been partly investigated, in order to establish the lines along which the friction theory can be extended to non-cubic EoS.

The importance of studying phase behavior is also emphasized in this work. Refrigerant-lubricant mixtures, which are likely to be strongly asymmetric, may show complex phase behavior. The barotropic behavior is studied in greater detail. The origin of this phenomenon is studied, as well as the implications that the barotropic behavior has on both phase and viscosity behavior.

There is a lack of experimental data on viscosities of refrigerant-lubricant mixtures, especially, of well defined components. In order to evaluate and test the viscosity models, a comprehensive experimental study has been carried out for six binary mixtures composed of 1,1,1,2-

tetrafluoroethane (HFC-134a) + triethylene glycol dimethylether (TriEGDME) and HFC-134a + tetraethylene glycol dimethylether (TEGDME) in the temperature range 293.15 K to 373.15 K and pressures up to 100 MPa. The measurements have been carried out using a falling body viscometer with an experimental uncertainty of the order of ±2.5%. The data obtained have been used to evaluate the performance of several viscosity models. The analysis shows that the mixing rules proposed for the calculation of the viscosity of the mixtures are not adapted for these kinds of systems.

Résumé på dansk

Begrænsninger i brugen af miljøbelastende komponenter i kølesystemer har medført en væsentlig ændring i det kemiske design af kølemidler. I mange sammenhænge må nye miljøvenlige kølemidler kombineres med smøremidler for at opnå et tilstrækkelig tryk-viskositet-temperatur (p-η-T) forhold i en kølecyklus. Dette giver et multidisciplinær problem, herunder fase- og dynamiske opførsler af køle-smøremiddelblandinger. Da køle-smøremiddelblandinger er meget asymmetriske opstår et andet betydningsfuldt fænomen: barotropisk opførsel (omvending af densitet).

Formålet med projektet er på en præcis måde at modelere og forudsige fase, volumetriske og dynamiske egenskaber der er nødvendige i designet af kølecykluser baseret på miljøvenlige køle-smøremiddelblandinger. Studiet blev gennemført ved brug af blandinger indeholdende hydrofluorocarbon (HFC) og carbondioxid som alternative kølemidler kombineret med polyalkyne glykoler (PAG), polyol estere (POE) og alkyl benzoner (AB) som alternative smøremidler. Beskrivelsen af den volumetriske opførsel (p-ρ-T) bygger på forskellige tilstandsligninger (EoS), herunder simple kubiske ligninger over empiriske tilgange til statistiske mekanisk baserede modeller. Evalueringen af p-η-T egenskaber er gennemført ved brug af adskillige viskositets modeller bredt dækkende for tryk og temperatur for både rene komponenter og blandinger. Fokus har især været på anvendelsen af den nylig udviklede friktionsteori (f-teori) viskositetsmodel i kombination med forskellige tilstandslingninger (EoS). Det er endvidere blevet vist at f-teorien i kombination med simple kubiske EoS kan reproducere viskositetopførslen af mange blandinger. F-teorien er delvist blevet undersøgt og udvidet til andre typer af EoS, for bestemme retningslinierne for hvilke friktionsteorien kan udvides til ikke-kubiske EoS.

Vigtigheden af studie af faseopførsler er også indeholdt i dette studium. Køle-smøremiddelblandinger som har tendens til at være (sandsynligvis) høj-assymetriske kan vise kompleks faseopførsel. Barotropisk opførsel er nærmere undersøgt. Undgangspunktet for dette fænomen er blevet undersøgt samt påvirkningen som barotropisk opførsel har på både fase og viskositetsopførsler.

Der er mangel på eksperimentelle data af viskositet for køle-smøremiddelblandinger af veldefinerede komponenter. For at kunne evaluere og teste viskositetsmodellerne blev et omfattende eksperimentelt studium udført på seks binære blandinger sammensat af 1,1,1,2-tetrafluoroethane

(HFC-134a) + triethylene glycol dimethylether (TriEGDME) og HFC-134a + tetraethylene glycol dimethylether (TEGDME) i temperaturintervallet fra 293.15 K til 373.15 K og tryk op til 100 MPa. Målingerne blev udført ved brug af kuglefaldsviscosimeter med en nøjagtighed på ±2.5%. De opnåede data er blevet brugt til at evaluere anvendeligheden af flere viskositets-modellerne. Analyserne viser at reglerne for blandinger, foreslået til beregning af viskositeten af blandingerne, ikke er anvendelige for disse typer af systemer.

Contents

Refrigerant – Lubricant Mixtures 129

I – Introduction: Refrigerants and Lubricants

1.1 – Introduction: the beginning of commercial refrigeration

The beginning of refrigeration as an industry can be traced back to the mid-nineteenth century when Jacob Perkins built the first practical refrigeration machine in 1834 (Paul, 2003). This machine had all the elements of a modern vapor-compression system: a compressor, a condenser, an expansion device, and an evaporator. Perkins used ethyl ether in his early experiments. Ethyl ether was not a good refrigerant because it was both flammable and toxic. By the time of Perkins, refrigerants such as ammonia (NH_3), sulphur dioxide (SO_2) and carbon dioxide (CO_2) were available for use but complex compressors were required to use them. Before the end of the nineteenth century a forth practical refrigerant, methyl chloride (CH_3Cl), had appeared in France. Methyl chloride was the forerunner of the vast family of halocarbons. Nearly all of the early refrigerants were flammable, toxic or both and some were highly reactive. The task of finding a nonflammable refrigerant with good stability was given to Thomas Midgley in 1926 (Midgley, 1937). Midgley selected dichlorofluoromethane (CCl_2F_2) as a possible refrigerant. This chlorofluorocarbon refrigerant had advantageous properties such as non-flammability, low toxicity and showed a good performance in refrigeration cycles in terms of efficiency. Commercial chlorofluorocarbon (CFC) production began with CCl_2F_2 in early 1931, CCl_3F in 1932, $CClF_2CClF_2$ in 1933, and CCl_2FCClF_2 in 1934. The first hydrochlorofluorocarbon (HCFC) refrigerant, $CHClF_2$, was produced in 1936. By the 1950s, the complete range of domestic, commercial, industrial and air conditioning applications could be covered by the versatile range of halocarbon refrigerants. It appeared that there would be no room for any refrigerants other than halocarbons. CFCs were also used in other areas of society, as aerosol propellants, electronic cleaning solvents, and foam-blowing agents.

In 1974, the researchers Molina and Rowland (1974) produced the startling hypothesis that emissions of chlorinated halocarbons could damage the earth's atmosphere by the catalytic destruction of ozone in the stratosphere. By the mid-1980s, it was confirmed that the ozone layer over Antarctica was being progressively destroyed as Molina and Rowland had predicted. In 1987 most industrialized countries signed the Montreal Protocol calling for a 50% reduction of chlorofluorocarbons (CFCs) production by 1998; in a later review the total phasing out of CFCs by 1995, and of hydrochlorofluorocarbons (HCFCs) by 2030, was agreed.

Hydrofluorocarbons (HFCs) are being manufactured as ozone friendly replacements, although mixtures of HFCs, rather than pure substances, have proven to be more suitable. HFCs were initially promoted when the Montreal Protocol set the phase-out dates for CFCs and HCFCs. Hydrofluorocarbons are, however, not completely environmentally safe since their global warming potentials (GWP) are 100-5000 times higher than carbon dioxide. This implies that they can make a higher contribution to the Green House Effect but, on the other hand, their emission from heat pumps can be limited. At the present time there are no legal regulations against HFCs since they are considered a much better alternative than CFCs and HCFCs.

At the Kyoto meeting on Global Climate Change (Fletcher, 1999), the United States agreed to reduce emissions of six greenhouse gases by 7% bellow 1990 levels during a "commitment period" between 2008 and 2012, HFCs being among those gases. The Danish Government is the only government to plan the phasing out of HFCs. It proposes to eliminate HFCs with a phase-out date of 2006 and has introduced Europe's first tax on HFCs. The majority of EU countries have restrictions on some of the F-gases, but few except Denmark have real phase-out dates. Denmark is the first country in the world with such a radical move away from HFCs.

Attention has returned to some of the natural refrigerants (water, air, hydrocarbons, ammonia, and carbon dioxide) which were, to a large extent, replaced by the halocarbon refrigerants.

1.2 – Refrigeration process

In a continuous refrigeration process, heat is transferred from a low temperature level to a higher one. Heat pumps, refrigeration systems and air conditioners all work with a similar technique and have four main components: evaporator, condenser, compressor and expansion device. The evaporator and condenser are heat exchangers that are similar in their construction and purpose: heat is transferred from one fluid to another fluid. These four components are connected to each other with pipes in which a specific fluid (the refrigerant) is circulating. Figure 1.1 shows how the working fluid (refrigerant) is circulating in a refrigeration cycle. In the evaporator, heat is absorbed at low pressure and temperature, which leads to evaporation of the refrigerant. The vapor is then compressed by a compressor to a superheated vapor at high pressure. In the condenser, heat is removed at high pressure, causing the superheated vapor first to cool and then to condense. Then, the liquefied working fluid returns to the evaporator through a pressure-reducing expansion valve.

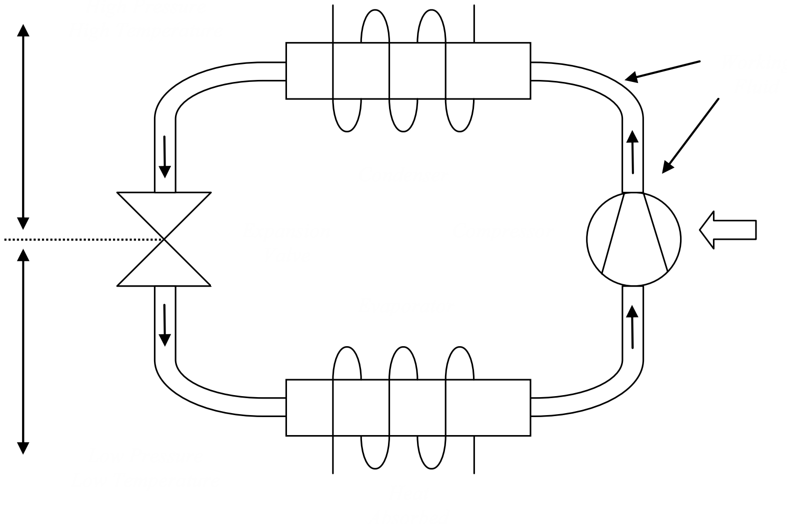

Figure 1.1 – Principle of the compression heat pump cycle.

In refrigeration equipment, the compressor is literally the heart of the system. There are three common types of compressors: piston compressors, screw compressors, and turbo compressors. These kinds of compressors have a certain amount of compressor oil (lubricant). The role of the lubricant is to reduce friction, prevent wear, and act as a seal between the high and the low pressure sides of the compressor. Thus, the refrigerant and the lubricant will come into contact and a mixture of refrigerant and lubricant will circulate through the compressor and the system. Due to the refrigerant's solubility in the compressor oil, the viscosity of the oil-rich phase may be substantially lowered giving rise to a potential breakdown of the compressor mechanical parts. Moreover, depending on the oil miscibility within the refrigerant-rich phase, even with an efficient oil separator installed after the compressor, part of the lubricant may migrate from the compressor to other parts of the system such as the evaporator, condenser, expansion device and piping. This will reduce system efficiency, since heat transfer may be reduced in the evaporator and condenser (Kruse and Schroeder, 1985). Thus, good knowledge of both viscosity and phase behavior of refrigerant + lubricant mixtures is of fundamental importance.

1.3 – Requirements of working fluids

Refrigerants are the working fluids in a refrigeration cycle. Their main duty is to evaporate and by this to extract heat from a heat source. There are many requirements when choosing refrigerants for refrigeration plants and air conditioners (Vamling *et al.* 1990). Some of these requirements are:

- Suitable pressures.
- High evaporating enthalpy.
- Low toxicity.
- Non-flammability.
- Compatibility with construction materials and lubricants.
- High COP.

COP stands for the coefficient of performance, a relationship between heat received in the condenser and work put into the compressor. The first requirement is illustrated in Figure 1.2, where the possible working temperature ranges for different operating pressures are given. Evaporation pressures are preferably above atmospheric pressure, since this will avoid air intake in case of a leak. The upper limit varies with compressor type but is usually between 2.5 MPa and 3 MPa.

1.3.1 – Environmental aspect of refrigerants

Besides the normal restrictions on chemicals concerning pollution, two global environmental demands have to be made on a refrigerant, namely:

- Low ozone depletion potential (ODP).
- Low global warming potential (GWP).

The ozone depletion potential (ODP) is defined as the integrated change in total ozone per unit mass emission of a specific compound, relative to the integrated change in the total ozone per unit mass of CFC-11 (trichlorofluoromethane). CFCs have a long lifetime and most of them reach the stratosphere. At this level, the ultraviolet radiation from the sun can easily decompose CFC molecules. Chlorine radicals act as a catalytic agent in ozone destruction. HCFCs still contain chlorine atoms, but the presence of hydrogen makes them reactive with chemical species in the troposphere. HFCs have no chlorine content and therefore no ODP.

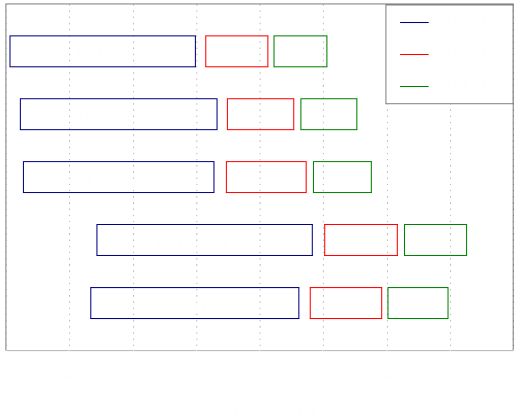

Figure 1.2 – Temperature ranges for some HFC working fluids

The global warming potential (GWP) represents an index determining the relative warming of a unit mass of a particular gas in comparison to the same mass of carbon dioxide. ODP and GWP values are presented in Table 1.1 for CFC, HCFC, HFC and natural refrigerants along with their critical parameters and molecular weights.

In the search for the optimal environmental working fluid, it is easy to draw misleading conclusions by paying attention only to the direct impact of different working fluids on the GWP. Heat pumps, air conditioners and refrigeration plants are normally driven by electricity, which will have an indirect impact. Depending on how the electricity is produced (by burning fossils, by nuclear power, by water power etc.) the indirect GWP for such a plant will vary. To be able to compare different plants, Fischer et al. (1991) described a concept called total equivalent global warming impact (TEWI). TEWI combines the direct and indirect global warming effects.

1.3.2 – Nomenclature

All refrigerants use an *R* in the first place followed by a three-digit number. The numbering system is defined in the following way:

- First digit: number of carbon atoms minus one.
- Second digit: number of hydrogen atoms plus one.

Name	*Formula*	*M* (g/mol)	T_c (K)	P_c (MPa)	v_c (cm³/mol)	*ω* (–)	*ODP* (–)	*GWP* (–)
Amonia	NH_3	17.031	405.4	11.353	72.47	0.257	0	0
Butane	C_4H_{10}	58.123	425.12	3.796	255	0.2	0	3
C. Diox.	CO_2	44.01	304.12	7.374	94.07	0.225	0	1
Ethane	C_2H_6	30.07	305.32	4.872	145.5	0.099	0	3
Isobutane	C_4H_{10}	58.123	407.85	3.64	262.7	0.186	0	3
Propane	C_3H_8	44.097	369.83	4.248	200	0.152	0	3
Propylene	C_3H_6	42.081	364.9	4.6	184.6	0.142	0	3
R11	CCl_3F	137.368	471.1	4.472	248	0.195	1	4000
R12	CCl_2F_2	120.913	385.1	4.13	217	0.179	1	8500
R13	$CClF_3$	104.459	301.84	3.873	180.3	0.175	1	11700
R14	CF_4	88.005	227.51	3.745	140.7	0.177	0	6500
R22	$CHClF_2$	86.468	369.28	4.986	166	0.221	0.055	1700
R23	CHF_3	70.014	298.97	4.836	133	0.267	0	12100
R32	CH_2F_2	52.024	351.26	5.805	121	0.278	0	580
R41	CH_3F	34.033	315	5.548	113.3	0.204	0	97
R113	CCl_2FCClF_2	187.375	487.4	3.378	325	0.249	0.8	5000
R114	$CClF_2CClF_2$	170.921	418.9	3.237	294	0.246	1	9300
R115	$CClF_2CF_3$	154.467	353.1	3.129	256	0.251	0.6	9300
R116	C_2F_6	138.012	293.04	3.039	221.9	0.257	0	9200
R123	$CHCl_2CF_3$	152.931	456.9	3.674	278.05	0.282	0.02	93
R123a	$CHClFCClF_2$	152.931	461.7		278		0.02	
R124	$CHClFCF_3$	136.476	395.6	3.634	243.8	0.288	0.022	480
R125	CHF_2CF_3	120.022	339.17	3.615	211.3	0.305	0	3200
R134	CHF_2CHF_2	102.032	391.74	4.64	190.4	0.293	0	1100
R134a	CF_3CH_2F	102.032	374.26	4.059	200.8	0.326	0	1300
R141b	$CHCl_2CH_2F$	116.95	477.35	4.25	254	0.225	0.11	630
R142b	CH_2ClCHF_2	100.495	410.3	4.048	231	0.231	0.065	2000
R143	CHF_2CH_2F	84.041	429.8	5.241	179.2	0.315	0	300
R143a	CF_3CH_3	84.041	346.3	3.792	193.6	0.259	0	4300
R152a	CH_2FCH_2F	66.051	386.41	4.516	181	0.276	0	140
R218	C_3F_8	188.2	345.1	2.68	299.82	0.325	0	8600
R227ea	CF_3CHFCF_3	170.03	376	2.98	293.15	0.3632	0	3500
R236ea	$CF_3CHFCHF_2$	152.05	412.5	3.502	268.88	0.382	0	1200
R236fa	$CF_3CH_2CF_3$	152.05	398.1	3.2	277.21	0.377	0	9400
R245ca	$CHF_2CF_2CH_2F$	134.05	447.6	3.925	256.02	0.355	0	640
R245fa	$CF_3CH_2CHF_2$	134.05	427	3.64	259.28	0.355	0	950
R245cb	$CF_3CF_2CH_3$	134.05	380.4	3.148	268.74	0.297	0	

Table 1.1 – Critical properties, molecular weight, ODP and GWP for CFC, HCFC, HFC and natural refrigerants. Critical properties and molecular weights were taken from (Poling *et al.* 2000) except underlined values that were obtained from (McLinden *et al.* 1998). ODP and GWP values from (Peal, 2003).

- Third digit: number of fluor atoms.

For example, the refrigerant R125 contains 2 carbon atoms, one hydrogen atom and five fluor atoms, the chemical formula is therefore C_2HF_5. Some refrigerants contain a small letter after such as "a", "b" or the like. This small letter indicates a certain structure of the refrigerant molecule which makes it more stable. Mixtures of HFCs are numbered with a "400" or a "500" plus a running number. In the case of organic compounds, such as ammonia, water or carbon dioxide, the three digit number starts with "700" to which the molecular weight of the molecule is added. Hydrocarbons are numbered in a similar way as HFCs. In this thesis the nomenclature R or HFC will be used indiscriminately.

1.3.3 – Refrigerants present

In some applications pure HFCs can be used, but in many applications mixtures of different HFCs will be preferable. The only two single-components in common use as a refrigerant are R23 (which has a very high GWP) and R134a, while the flammable substances R32, R152a and R143a can be added to the list of possible blend components.

R134a is extensively used in domestic refrigerators and in vehicle and residential air-conditioning. In the field of commercial refrigeration blends of several HFCs including R32, R125, R143a, R152a and R134a have been proposed to replace the CFCs used in the past. The derivatives of propane (R227, R236 and R245) are apparently suitable in small heat pumps; however none of those substances has a normal boiling point which makes it very suitable for commercial refrigeration. Mixtures of different refrigerants have been created by blending components to produce the required properties (Forbes, 2003).

Natural refrigerants, which have come back into use, include water, air, hydrocarbons, ammonia, and carbon dioxide. Hydrocarbon refrigerants such as propane, butane, isobutene have become dominant for domestic refrigeration in Northern Europe. The only serious disadvantage of the hydrocarbon refrigerants is their extreme flammability in air (Paul, 2003). Ammonia, which had never completely fallen out of use, came back into more common use. Carbon dioxide has a long history as a benign refrigerant but it completely fell out of use by the 1950s because of the advent of non-toxic halocarbon refrigerants, which were more efficient. Carbon dioxide has made a successful return to refrigeration. It will be increasingly used in a variety of ways. Most common applications of CO_2 at present are as an environmentally benign, as a low-temperature refrigerant, as refrigerant in supermarkets and as the low-temperature stage of large industrial freezing and cold storage systems (Coronas, 2003).

This thesis will focus on the HFC's as alternative refrigerants, which contain fluorine but not chlorine and therefore have no effect on the ozone layer. Yet, some refrigerants that are no longer in production or are banned (CFCs and HCFCs), but that might prove useful in future, will also be studied. Since refrigeration processes using CO_2 as refrigerant are of increasing interest lately, the study of carbon dioxide as "natural" refrigerant will also be carried out in this thesis. Besides, CO_2 + lubricant mixtures offer an excellent opportunity to show and discuss the complex phase behavior patterns that are likely to be found in asymmetric mixtures.

1.4 - Lubricants

Mineral oils have been used for decades with chlorinated refrigerants because they form highly miscible combinations. The mineral oils are generally blends of linear and branched alkanes (paraffins), and cyclic alkanes (naphthenes). Their typical chemical structures are shown in Figure 1.3. The mixtures are formulated with the purpose of having the desired viscosity – temperature - pressure relationship. The new HFC refrigerants show limited miscibility and have a low solubility in mineral oils. They generally have a higher solubility in a range of synthetic lubricants and show less tendency to phase separation.

(a) Paraffins (b) Naphthenes (c) Aromatics

Figure 1.3 - Chemical structure of mineral oils

Several properties are relevant when choosing a suitable lubricant for the compressor. Some of those are listed below (Fahl, 1998):

- Compatibility with construction materials and working fluid.
- High thermal and chemical stability.
- Good temperature-viscosity behavior.
- High boiling point and low solidifying point.

In addition, in interaction with the refrigerant, the lubricant has to guarantee a sufficient lubrication of the compressor at high temperatures and a low viscosity of the oil is needed at low temperatures for its reflux from the cold parts of the cycle into the compressor. The lubricant also has to reduce the temperature in the hot parts of the compressor, i.e., shaft and bearings. A lubricant that combines all the desirable properties and has no undesirable properties does not exist.

There are four main synthetic oil types used in replacement refrigerant systems. Their chemical structures are shown in Figure 1.4.

$$\mathrm{RO-[CH_2\overset{\displaystyle CH_3}{\overset{|}{C}}HO]_n[CH_2CH_2O]_m-OH}\qquad\mathrm{RO-[CH_2\overset{\displaystyle CH_3}{\overset{|}{C}}HO]_n-OH}$$

Polyalkylene glycol generalized

Polypropylene glycol mono-ol

(a) PAG synthetic oils

Diester

Polyol ester

(b) POE synthetic oils

(c) Alkyl benzene

(d) Poly-alpha-olefin

Figure 1.4 - Chemical structures for synthetic oil lubricants used in refrigeration systems.

- Polyalkylene glycols (PAGs): these lubricants offer advantages over mineral oils when used with HFCs. At high pressures and temperatures, they have low solubility in the gaseous refrigerants and they provide excellent lubricity. They are used mainly in automotive air-conditioning systems. PAGs are very hygroscopic and the other groups of PAGs are susceptible to oxidation, resulting in poor stability (Fukui *et al.*, 2000). These lubricants show poor miscibility/solubility with mineral oils.

- Polyol esters (POEs): they can be synthesized from renewable resources and are biodegradable. The POE lubricants have favorable properties as refrigeration oils compared to PAGs. They are less hygroscopic, have higher miscibility with HFCs and CO$_2$ refrigerants, and are miscible with mineral oils (Wahlström and Vamling, 2000). They are used mainly in domestic and commercial refrigeration systems.

- Alkyl benzenes (ABs): these lubricants cannot compete effectively with the POEs or the PAGs because of their limited miscibility with the HFCs. However, ABs show excellent chemical stability, high lubricity, and low hygroscopicity (Sunami *et al.*, 1995). They have been adopted for household refrigerators and dehumidifiers with appropriate modifications of the refrigeration cycle (Takigawa *et al.*, 2002).

- Poly-alfa olefin (PAOs): PAO lubricants are unsaturated hydrocarbon synthetic oils. These are used mainly in aerospace and military applications, due to their superior performance and stability. They are non hygroscopic. These lubricants are commonly used in ammonia systems because of their high fluidity at very low operating temperatures. Hauk and Weidner (2000) have reported that refrigerant + PAO systems may show barotropic behavior, which means that the refrigerant-rich phase has a higher density than the lubricant-rich phase. Oils that show density inversions are not recommended as lubricants.

In addition to the above four types of lubricants, new-lubricant oils based on ethers, such as polyvinylether (PVE) have recently been formulated (Cintar *et al.*, 2000). These lubricants have been confirmed to have superior performance over the POEs. Since PVE is a polymer, its chemical structure can be easily modified and, hence, miscibility can be adjusted by changing the mole ratio of the chemical structure shown in Figure 1.5.

Figure 1.5 – Chemical structures of PVE lubricant oil.

Commercial lubricant oils are mixtures of various classes of lubricants. These oils show superior performance such as improved lubricity, wear protection, chemical stability and hygroscopicity. However, a major problem in developing predictive methods is the identification of the components that are included in commercial lubricant blends. Refrigeration oils can vary very widely in composition and type depending on their source.

1.5 – Outline of the thesis

The thesis is divided into two parts; the first part consists of three chapters (Chapter II, III and IV) and will center on pure refrigerants and pure lubricants separately. In addition, a few refrigerant mixtures will also be included in this part. In Chapter II, some equations of state (EoS) are presented and an extensive comparative study of the performance of the different EoS is carried out. The approaches used range from simple models such as cubic equations of state, through empirical models, to statistical mechanics-based models.

Chapter III presents a review of various methods for estimating transport properties (especially viscosity) of gases and liquids for pure compounds and mixtures. Most of the viscosity models developed have been derived for hydrocarbons fluids due to their importance in the petroleum industry. The applicability of these models to pure refrigerants and pure lubricants will be studied and discussed. It is in this chapter that a few refrigerant mixtures will be studied.

Chapter IV pays attention to one viscosity model: the friction theory (*f*-theory). This model, which is used in combination with equations of state, appears to be particularly successful for estimating viscosities in wide temperature and pressure ranges. It has been shown that the *f*-theory in combination with a simple cubic EoS can accurately reproduce the viscosity behavior of many compounds. However, the extension of the *f*-theory approach to other kinds of models besides cubic

EoS has not been fully investigated. The main task of Chapter IV is to establish the lines along which the friction theory can be extended to a noncubic EoS.

The second part of the thesis (Chapter V, VI and VII) will focus on refrigerant + lubricant mixtures. Chapter V deals with barotropic behavior. This phenomenon, which has been left largely untouched in both experimental and theoretical research experience, seems to be associated to asymmetric mixtures. The focus of Chapter V will be on a better understanding of how such phenomenon originates and the implications that barotropic phenomena have on both phase and viscosity behavior.

Throughout Chapter VI the phase behavior, as well as the *p-v-T-x* behavior of refrigerant + lubricant mixtures will be studied. The phase and *p-v-T-x* modeling will be carried out based on experimental information found in the literature. This modeling part is mainly focused on mixtures containing PAGs, POEs, and APs as alternative compressor oils. Unfortunately, most publications on thermophysical properties of mixtures containing PAOs, PVE, or commercial lubricants do not include information about the oil composition. For that reason the modeling of mixtures containing those lubricants will not be discussed in this thesis.

In Chapter VII the experimental study and modeling of refrigerant + PAG systems is described. The experimental part of the thesis aims at covering a larger research project on thermophysical properties of the HFC + PAG systems started some years ago by the research group "Propriétés de Transport" (Laboratoire des Fluides Complexes) at the Université de Pau, France (Comuñas, 2002). Finally, the conclusions and further work are drawn in Chapter VIII.

Nomenclature

AB = Alkyl benzene

CFC = Chlorofluorocarbon

COP = Coefficient of performance

EoS = Equation of State

GWP = Global warming potential

HCFC = Hydrochlorofluorocarbon

HFC = Hydrofluorocarbon

M = Molecular weight

ODP = Ozone depletion potential

p = Pressure

PAG = Polyalkylene glycol

PAO = Poly-alfa olefin

POE = Polyol ester

PVE = Polyvinylether

T = Temperature

TEWI = Total equivalent global warming impact

v = Molar volume

Greek letters

ω = Acentric factor

Subscripts/superscripts

c = Critical

References

1. Cinar, C., Hadfield, M., Swallow, A., Smith, A. The influence of POE and PVE lubricant blends within hermetic refrigerating compressors operating with HFC-134a refrigerant. *Wear*. 2000, 241, 53-64.
2. Comuñas, M.J.P. Densidades y Viscosidades a Alta Presión de Nuevos Lubricantes Sintéticos y de las Mezclas Lubricante + HFC-134a. Medidas y Modelización. Ph.D. Thesis, Física Aplicada, Universidad de Santiago de Compostela, Santiago de Compostela, Spain, 2002.
3. Coronas, A. Private Communication. 2003.
4. Fahl, J. Lubricants for use with carbon dioxide as refrigerant. *KI Luft-Kältetechnik*. 1998, 8, 375-379.
5. Fletcher, S. Global Climate Change Treaty: The Kyoto Protocol. *Report for Congressional Research Service*. The Committee for the National Institute for the Environment, Washington D.C., 1999.
6. Fischer, S.K., Hughes, P.J., Fairchild, P.D., Kusik, C.L., Dieckmann, J.T., McMahon, E.M., Hobady, N. Energy and Global Warming Impacts of CFC Alternative Technologies: *Executive Summary. Report to AFEAS and U.S. Department of Energy*, Dec. 1991.
7. Forbes, P.S. Refrigerants: Past, Present and Future. *21st IIR International Congress of Refrigeration*. *Washington D.C.*, 2003.
8. Fukui, H., Sanechika, K-I., Ikeda, M. Novel refrigeration lubricants for use with HFC refrigerants. *Tribology International*. 2000, 33, 707-713.
9. Hauk, A., Weidner, E. Thermodynamic and Fluid-Dynamic Properties of Carbon Dioxide with different Lubricants in Cooling Circuits for Automobile Application. *Ind. Eng. Chem. Res.* 2000, 39, 4646-4651.
10. Kruse, H., Schroeder, M. Fundamentals of Lubrication in Refrigerating Systems and Heat Pumps. *ASHRAE Trans.* 1984, 90, 2.
11. McLinden, M.O., Klein, S.A., Lemmon, E.W., Peskin, A.P. NIST Thermodynamic and Transport Properties of Refrigerants and Refrigerant Mixtures – REFPROP, 6.01 ed., National Institute of Standards and Technology, Boulder, Colorado, USA, 1998.
12. Midgley, T. From the periodic table to production. *Ind. Eng. Chem.* 1937, 29, 239-244.
13. Molina, M.J., Rowland, F.S. Stratospheric sink for chlorofluoromethanes: chlorine atom-catalysed destruction of ozone. *Nature*. 1974, 249, 810-814.
14. Paul, J. Private Communication. 2003.

15. Poling, B.E., Prausnitz, J.M., O'Connell, J.P. The Properties of Gases and Liquids. Fifth Edition. Mc Graw Hill, New York, 2000.
16. Sunami, M., Takigawa, K., Suda, S., Sasaki, U. New immiscible refrigeration lubricant for HFCs. *ASHRAE Trans.* 1995, 101, 97-103.
17. Takigawa, K., Sandler, S.I., Yokozeki, A. Solubility and viscosity of refrigerant/lubricant mixtures: hydrofluorocarbon/ alkylbenzene systems. *Int. J. Ref.* 2002, 25, 1014-1024.
18. Vamling, L., Högberg, M., Berntsson, T. CFC Alternatives for High-temperature Heat Pumps Applications. *Proc. Of the 4th International Conference organized by BHR Group Limited – Applications and efficiency of heat pump systems*, STT/Springer-Verlag, Berlin, Munich, 1999, p 347.
19. Wahlström, Å., Lennart, V. Development of models for prediction of solubility for HFC working fluids in pentaerythritol ester compressor oils. *Int. J. Ref.* 2000, 23, 597-608.

Pure Refrigerants and Pure Lubricants

This part consists of three chapters:

- *Chapter II: Equations of State (EoS)*
- *Chapter III: Evaluation of Existing Viscosity Models*
- *Chapter IV: The Friction Theory*

II – Equations of State (EoS)

2.1 – Introduction

In this chapter, some *p-v-T* models are presented for estimating thermodynamic properties and phase equilibria. These models, commonly written as a function of *T* and *v*, are referred to as equations of sate (EoS). The *p-v-T* behavior of a pure fluid is illustrated in Figure 2.1, which shows different isotherms in a pressure-density diagram. At the critical point the critical isotherm exhibits a horizontal inflection, resulting in the following mathematical conditions:

$$\left(\frac{\partial p}{\partial v}\right)_{T_c}=0 \qquad \left(\frac{\partial^2 p}{\partial v^2}\right)_{T_c}=0 \tag{2.1}$$

In Figure 2.1, the full line to the left of the critical point represents saturated vapor, whereas the full line to the right of the critical point represents saturated liquid. The area lying inside the full lines is the two phase region, whereas only one phase, liquid or gas, exists outside for a given temperature and pressure. As the pressure goes to infinity the isotherms approach an asymptotic value, which can be interpreted as the hard-core volume. It can be seen from Figure 2.1 that liquids are almost incompressible for temperatures below the critical temperature. The ideal gas state is approached for temperatures significantly higher than the critical temperature and at low pressures.

Equations of state can be applied to pure substances as well as to mixtures for the correlation and prediction of thermodynamic properties. Therefore, a very large number of publications deal with the development or improvement of EoS. According to Deiters (1999) the number of EoS that has been published exceeds 2000. To illustrate the immense amount of work that has been done in this area, in this thesis different EoS have been chosen to describe the behavior of refrigerants, lubricants and their mixtures. The EoS chosen can be divided into three different classes:

- Cubic EoS.
- Non-Cubic EoS of the Benedict-Webb-Rubin (BWR) family.
- SAFT family.

Cubic EoS are chosen because of their common use in industry and their simplicity. Available literature shows that even for complex systems these equations are reasonably good. Non-cubic EoS of the BWR family have been developed to deliver more accurate density estimations than cubic EoS. For that reason they have also been included in this study. Finally, EoS of the SAFT family are chosen because of their molecular basis, their widespread use among researchers, and their growing use by practicing engineers.

Figure 2.1 – Pressure versus density of a pure fluid at different temperatures.

The goal of this chapter is to determine how well different EoS predict the pvT behavior of pure refrigerants and pure lubricants. In addition, most viscosity models that will be studied in the next chapter require temperature and density as the input variables; thus, an equation of state would normally be required to obtain the necessary volumetric data if not directly available. The modeling will be based on experimental information found in the literature containing vapor pressures and densities. First, the EoS will be introduced and briefly discussed. Although the modeling of mixtures will not be discussed until Chapter V, the extension of the different EoS to mixtures is introduced in this Chapter. In a second part, the obtained results for refrigerants and lubricants are presented and discussed.

2.2 - Cubic EoS

More than a thousand different equations of state (EoS) have been published since J.D. van der Waals proposed his equation of state in 1873. The van der Waals equation consists of a repulsive and a single attractive term

$$P=\frac{RT}{v-b}-\frac{a}{v^2} \qquad (2.2)$$

where v is the molar volume, b the covolume or the hard core volume, and a the intermolecular attraction parameter. The first term in Equation 2.2 is defined as the repulsive pressure, while the last term is the attractive pressure term also referred to as the internal pressure. The first accepted modification of the van der Waals EoS for engineering applications was the Redlich-Kwong (RK) EoS by Redlich and Kwong (1949), who multiplied the attractive part by $v(v+b)^{-1}T^{-0.5}$, but still kept the b parameter constant. Since the RK EoS was introduced, numerous modifications have been proposed and every year new cubic EoS or modifications of existing ones are proposed.

For most of the derived cubic EoS the main modifications have been performed on the attractive pressure contribution. In spite of their simplicity, cubic EoS such as the well-known Soave-Redlich-Kwong (SRK) EoS (Soave, 1972) or the Peng-Robinson (PR) EoS (Peng and Robinson, 1976) are still widely used within the chemical and petroleum industry. The cubic EoS used in this thesis are the Soave-Redlich-Wong (SRK) EoS, the Peng-Robinson (PR) EoS and the Stryjek and Vera (Stryjek and Vera, 1986) modification of the Peng-Robinson (PRSV) EoS. Also, the recently RK-PR EoS develop by Cismondi and Mollerup (2005) has been included.

2.2.1 - *The SRK, PR and PRSV EoS*

The SRK and PR EoS are referred to as two-parametric cubic EoS and the general expression for both EoS can be written as

$$P=\frac{RT}{v-b}-\frac{a(T)}{v^2+u\,b\,v+w\,b^2} \qquad (2.3)$$

where u and w are integers dependent on the cubic EoS, see Table 2.1. The b and $a(T)$ are obtained by solving Equations 2.1

$$b=\frac{\Omega_b\,RT_c}{P_c} \qquad (2.4)$$

$$a(T)=a_c\,\alpha(T) \qquad (2.5)$$

$$a_c=\Omega_a\frac{(RT_c)^2}{P_c} \qquad (2.6)$$

with

$$\alpha(T)=\left(1+m\left(1-\sqrt{T_r}\right)\right)^2 \qquad (2.7)$$

where T_r is the reduced temperature defined as T/T_c. This alpha function was proposed by Soave (1972) for the SRK EoS in order to improve the vapor-liquid equilibrium pressure compared to the original RK EoS (Redlich and Kwong, 1949). Soave correlated m against ω in the interval of ω from 0 to 0.5 obtaining

$$m=0.480+1.574\,\omega-0.176\,\omega^2 \qquad (2.8)$$

Peng and Robinson (1976) adapted the structure of the Soave alpha function for the PR EoS. The resulting equation is

$$m = 0.37464 + 1.54226\,\omega - 0.26992\,\omega^2 \qquad (2.9)$$

where ω is the acentric factor. Further improvements of the alpha function have extended the application of cubic EoS to many polar and nonpolar fluids, as it is the case with the Stryjek and Vera (1986) modification of the PR EoS (PRSV). For the PRSV EoS

$$\begin{aligned} m &= k_0 + k_1\left(1+\sqrt{T_r}\right)\left(0.7 - T_r\right) && T_r < 1 \\ m &= k_0 && T_r \geq 1 \end{aligned} \qquad (2.10)$$

with

$$k_0 = 0.378893 + 1.4897153\,\omega - 0.17131848\,\omega^2 + 0.0196554\,\omega^3 \qquad (2.11)$$

and k_1 is an adjustable parameter characteristic of each pure compound.

EoS	*u*	*w*	Ω_a	Ω_b	Z_c
SRK	1	0	0.427480	0.086640	0.300
PR	2	-1	0.457236	0.077796	0.307

Table 2.1 – Parameters for the SRK and PR EoS.

In order to apply the cubic EoS described in this section the van der Waals mixing rules are used. These mixing rules are given by

$$a_{mix} = \sum_{i=1}^{n}\sum_{j=1}^{n} x_i\, x_j \sqrt{a_i\, a_j}\left(1 - k_{ij}\right) \qquad (2.12)$$

$$b_{mix} = \sum_{i=1}^{n} x_i\, b_i \qquad (2.13)$$

where k_{ij} is a binary interaction parameter.

2.2.2 – The RK-PR EoS

An accurate three parameter EoS (RK-PR EoS) has been recently developed by Cismondi and Mollerup (2005). This new equation which connects the density dependence of the RK and PR EoS through a third parameter has shown to deliver very good results for alkanes from n-C_1 to n-C_8, CO_2 and NH_3. Some preliminary results on mixtures have shown that this new EoS predicts accurately the phase equilibria of asymmetric mixtures.

Any cubic EoS can be written in a general form as

$$P=\frac{RT}{v-b}-\frac{a(T)}{(v+\delta_1 b)(v+\delta_2 b)} \qquad (2.14)$$

Michelsen and Mollerup (2004) have shown that in the Redlich-Kwong-Peng-Robinson family the constants δ_1 and δ_2 can be replaced by a single parameter c

$$\begin{aligned}\delta_1+\delta_2&=c+1\\ \delta_1\delta_2&=-c\end{aligned} \qquad (2.15)$$

yielding $c = 0$ the RK EoS and $c = 1$ the PR EoS. By use of Equations 2.15, the RK-PR EoS is conveniently written as

$$P=\frac{RT}{v-b}-\frac{a(T)}{(v+\delta_1 b)\left(v+\frac{1-\delta_1}{1+\delta_1}b\right)} \qquad (2.16)$$

where $a(T)$ is defined by Equation 2.5. Instead of using the quadratic form proposed for $\alpha(T)$ (Soave, 1972) which does not decrease to zero at high temperatures and shows some drawbacks (Segura et al. 2003), Cismondi and Mollerup (2005) use the following form

$$\alpha(T)=\left(\frac{3}{2+T_r}\right)^k \qquad (2.17)$$

The recommendations for a straightforward implementation of the EoS is to set $Z_{c,\,EoS} = 1.168\ Z_{c,\,exp}$ (for non-associating fluids). This condition determines the third parameter δ_1, while b and a_c are obtained from solving the critical conditions and fixing T_c and P_c to their experimental values. In the RK-PR EoS the predicted Z_c (i.e. $Z_{c,\,EoS}$) is related to δ_1 by the following equation (Michelsen and Mollerup, 2004)

$$Z_c=\frac{y}{3y+d_1-1} \qquad (2.18)$$

with

$$d_1=\frac{1+\delta_1^2}{1+\delta_1} \qquad (2.19)$$

$$y=1+\sqrt[3]{2(1+\delta_1)}+\sqrt[3]{\frac{4}{1+\delta_1}} \qquad (2.20)$$

Equation 2.18 cannot be solved analytically for δ_1. For that reason Cismondi and Mollerup (2005) proposed the use of the following correlation to be employed safely in the range $0.20 < Z_c < 0.3383$

$$\delta_1=d_1+d_2\left(d_3-Z_c\right)^{d_4}+d_5\left(d_6-Z_c\right)^{d_7} \qquad (2.21)$$

The covolume and the critical value of the attractive parameter are calculated from Equations 2.4 and [illegible]

$$\Omega_a = \frac{3y^2 + 3yd_1 + d_1^2 + d_1 - 1}{\left(3y + d_1 - 1\right)^2} \qquad (2.22)$$

$$\Omega_b = \frac{1}{\left(3y + d_1 - 1\right)} \qquad (2.23)$$

Finally, the *k* constant for the temperature dependence of the attractive parameter in Equation 2.17 is obtained from the relation

$$k = \frac{Ln\left(a_{0.7}/a_c\right)}{Ln\left(3/2.7\right)} \qquad (2.24)$$

where $a_{0.7}$ is the value required to match the experimental vapor pressure at $T_r = 0.7$. The constants d_{ij} in Equation (2.21) are given in the appendix B in (Cismondi and Mollerup, 2005).

Extension to mixtures is straightforwardly performed by use of Equations 2.12 and 2.13 for *a(T)* and *b*. For the third parameter a linear mixing rule is proposed:

$$\delta_{1,mix} = \sum_{i=1}^{n} x_i \delta_{1,i} \qquad (2.25)$$

2.3 – Non-Cubic EoS

Among the numerous attempts that have been made to improve the inherent deficiencies in the cubic EoS, the BWR expressions based on the pioneering work of Benedict, Webb and Rubin (1940) are among the ones which have gained more acceptance. Benedict, Webb and Rubin combined polynomials in temperature with power series and exponentials of density into an eight-parameter form. Additional terms and parameters were later introduced by others to formulate modified Benedict-Webb-Rubin (mBWR) EoS. These types of highly accurate EoS are implemented in the National Institute of Standards and Technology (NIST) software package (*REFrigerant PROPerties*, REFPROP) for the correlation of thermodynamics and transport properties of selected pure and mixed, mainly refrigerants, compounds (McLinden et al. 1998).

Based on the BWR EoS, Soave (1995, 1999) derived a new general model (SBWR) for the accurate estimation of the densities of pure non-polar fluids, primarily hydrocarbons, and their mixtures. In addition, the SBWR EoS has been shown to accurately describe vapor-liquid equilibrium (VLE) data. In this work the applicability of the SBWR to refrigerants and lubricants is studied.

The general expression for the SBWR EoS in its first version (Soave, 1995) is written as

$$Z=\frac{P}{\rho RT}=1+B\rho+C\rho^{2}+D\rho^{4}+E\rho^{2}\left(1+F\rho^{2}\right)Exp\left(-F\rho^{2}\right) \qquad (2.26)$$

Later, Soave (1999) found that the term $C\rho^2$ has a negligible effect on the performance of the equation of state. In this way, Equation 2.26 can be written in terms of adimensional quantities as

$$Z=\frac{P_r}{T_r\psi}=1+\beta\psi+\delta\psi^{4}+\varepsilon\psi^{2}\left(1+\phi\psi^{2}\right)Exp\left(-\phi\psi^{2}\right) \qquad (2.27)$$

with

$$\psi=\frac{RT_c\rho}{P_c} \qquad (2.28)$$

The parameters in Equation 2.27 are defined as

$$\beta=B\left(\frac{P_c}{RT_c}\right)=\beta_c+b_1\left(1-\frac{1}{T_r^{1.6}}\right)+b_2\left(1-\frac{1}{T_r^{3.2}}\right)\omega$$

$$\delta=D\left(\frac{P_c}{RT_c}\right)^{4}=\delta_c\left(1+d_1\left(\frac{1}{T_r}-1\right)+d_2\left(\frac{1}{T_r}-1\right)^{2}\right) \qquad (2.29)$$

$$\varepsilon=E\left(\frac{P_c}{RT_c}\right)^{2}=\varepsilon_c+e_1\left(\frac{1}{T_r}-1\right)+e_2\left(\frac{1}{T_r}-1\right)^{2}+e_3\left(\frac{1}{T_r}-1\right)^{3}$$

$$\phi=F\left(\frac{P_c}{RT_c}\right)^{2}=fZ_c^{2}$$

where the subscript c refers to the critical point. Generally, the b_i, d_i, and e_i parameters in Equation 2.29 can be expressed by the following equation

$$G_i=G_{i1}+G_{i2}\,\omega+G_{i3}\,\omega^{2} \qquad (2.30)$$

the G_{ij} constants used to obtain the b_i, d_i, and e_i parameters are given in Table 2.2.

The critical parameters have been determined using the critical constraints (forcing the critical isotherm trough the critical point with zero slope and zero curvature; see Figure 2.1). The critical parameters are given by

$$\beta_c=b_0Z_c$$

$$\delta_c=d_0Z_c^{4} \qquad (2.31)$$

$$\varepsilon_c=e_0Z_c^{2}$$

where b_0, d_0 and e_0 are obtained from Equations 2.3 and $P_c/(RT_c\rho_c)=Z_c$.

$$e_0 = \frac{2-5Z_c}{\left(1+f+3f^2-2f^3\right)Exp\left(-f\right)}$$

$$d_0 = \frac{1-2Z_c-e_0\left(1+f-2f^2\right)Exp\left(-f\right)}{3} \qquad (2.32)$$

$$b_0 = Z_c - 1 - d_0 - e_0\left(1+f\right)Exp\left(-f\right)$$

Soave (1999) also found that it was appropriate to set $f = 0.77$.

i,j	b_{ij}	d_{ij}	e_{ij}
1,1	0.4220	0.4912	0.0841
1,2	0	0.6478	0.1318
1,3	0	0	0.0018
2,1	0.2340	0.3000	0.0750
2,2	0	0.3619	0.2408
2,3	0	0	-0.0140
3,1	0	0	-0.0065
3,2	0	0	0.1798
3,3	0	0	-0.0078

Table 2.2 – Constants for estimating b_i, d_i and e_i

In the first version of the SBWR, the critical compressibility factor is related to the acentric factor in the following way

$$Z_c = 0.2908 - 0.099\,\omega + 0.04\,\omega^2 \qquad (2.33)$$

in its second version, for optimal performance of the EoS, Soave (1999) suggested to adjust simultaneously Z_c and ω using vapor pressures and liquid density data.

When the SBWR is applied to mixtures, the critical temperature, the critical pressure, and the acentric factor are required. In order to determine these mixture properties, Soave (1995 and 1999) proposed the following mixing rules based on an analogy with the van der Waals mixing rules. In cubic EoS a quadratic mixing rule is generally applied to $a(T)$ (Equation 2.12). By combining Equations 2.5, 2.6, 2.7 and 2.12 leads to:

$$\begin{aligned} \frac{T_{c,mix}^2}{P_{c,mix}}\left(1+m_{mix}\right)^2 &= \sum_{i=1}^{n}\sum_{j=1}^{n} x_i x_j \left(1-k_{ij}\right)\frac{T_{c,i}T_{c,j}}{\sqrt{P_{c,i}P_{c,j}}}\left(1+m_i\right)\left(1+m_j\right) = S_1 \\ \frac{T_{c,mix}}{P_{c,mix}} m_{mix}^2 &= \sum_{i=1}^{n}\sum_{j=1}^{n} x_i x_j \left(1-k_{ij}\right)\sqrt{\frac{T_{c,i}T_{c,j}}{P_{c,i}P_{c,j}}}\, m_i m_j = S_2 \end{aligned} \tag{2.34}$$

Further for cubic EoS a linear mixing rule is applied to *b* (Equation 2.13). By combining Equations 2.4 and 2.13 leads to

$$\frac{T_{c,mix}}{P_{c,mix}} = \sum_{i=1}^{n} x_i \frac{T_{c,i}}{P_{c,i}} = S_3 \tag{2.35}$$

Finally, from Equations 2.34 and 2.35

$$\begin{aligned} T_{c,mix} &= \frac{S_1}{\left(\sqrt{S_2}+\sqrt{S_3}\right)^2} \\ P_{c,mix} &= \frac{T_{c,mix}}{S_3} \\ m_{mix} &= \sqrt{\frac{S_2}{S_3}} \end{aligned} \tag{2.36}$$

These mixing rules do not lead to the acentric factor of the mixture, but to m_{mix}, which is a function of the acentric factor. Based on VLE data for alkane systems Soave (1999) obtained the following relationship between *m* and *ω*

$$m = 1.25\,\omega \tag{2.37}$$

which is valid for both pure compounds and mixtures. This leads to

$$\omega_{mix} = \frac{m_{mix}}{1.25} \tag{2.38}$$

If Z_c is not calculated by means of Equation (2.33), the following mixing rule is applied

$$Z_{c,mix} = \frac{\displaystyle\sum_{i=1}^{n} \frac{x_i Z_{c,i} T_{c,i}}{P_{c,i}}}{\displaystyle\sum_{i=1}^{n} \frac{x_i T_{c,i}}{P_{c,i}}} \tag{2.39}$$

2.4 – The PC-SAFT EoS

SAFT (Statistical Associating Fluid Theory) is a statistical mechanics-based EoS (Chapman et al. 1988, 1989, and 1990) developed from Wertheim's first-order perturbation theory (Wertheim 1984a, 1984b, 1986a, and 1986b). SAFT equation, which seems to have done an admirable job in bridging the gap between molecular theories and engineering applications, initially considers the fluid of interest to be a mixture of independent segments. The theory predicts the change in free energy both upon bonding these segments to form chains and on the further association on the chain-like molecules. SAFT and its various modifications and extensions such SAFT hard sphere (SAFT-HS), SAFT Lennard-Jones (SAFT-LJ), soft-SAFT, perturbed-chain SAFT (PC-SAFT), polar SAFT, SAFT with variable range (SAFT-VR), SAFT with variable range for electrolytes (SAFT-VRE) have demonstrated the ability to accurately predict the thermodynamic properties and phase behavior of simple, hydrogen bonding, polar and polymeric mixtures (Müller and Gubbins, 2001).

In the case of refrigerants and lubricants very few works have been done so far with EoS of the SAFT family. For example, Galindo *et al.* (1997) have used the SAFT-HS approach to describe the phase equilibria of mixtures containing HF (hydrogen fluoride) + HFC-134a and HFC-32. In 1998, Galindo *et al.* (1998) modeled HFCs and their mixtures using SAFT-VR. Kiselev and Ely (2000) have used a simplified crossover SAFT EoS to describe thermodynamics properties of pure HFCs and their binary mixtures. The model used by these authors gives an accurate prediction of the critical parameters for pure fluids and a good representation of the *p-v-T* and VLE properties. In recent publications, Swaminathan and Visco (2005a, 2005b) applied the SAFT-VR to describe pure components properties of HFCs, HCFCs, CFCs and the VLE of their mixtures. For lubricants the simplified SAFT of Fu and Sandler (1995) for the modeling of POEs was used by Huber *et al.* (2002).

Refrigerant are polar molecules, but it is not clear whether or not they exhibit hydrogen bonding. Recent experimental neutron scattering data for HFC-124 suggest that these molecules do not form hydrogen bonds (Mort *et al.* 1997). Galindo *et al.* (1997, 1998) and Swaminathan and Visco (2005a, 2005b) used models that do not include an explicit contribution for the polar interactions, but include bonding sites in order to model the dipolar anisotropy of the systems. In other words, they treat the attractive interactions due to the dipoles, or weak hydrogen bonds, as a type of association. On the other hand, Kiselev and Ely (2000) and Huber *et al.* (2002) do not consider any explicit contribution for polar effects.

In this work the EoS of the SAFT family chosen is that due to Gross and Sadowski (2001), PC-SAFT. This EoS, which is reasonably simple to implement (compared with many versions of SAFT) and it is relatively undemanding computationally, has proved successful in predicting and correlating thermodynamic properties and phase equilibria in many systems. In PC-SAFT the reference fluid is given by the hard-chain fluid with an effective collision diameter of the chain segments, $d(T)$, obtained with the potential proposed by Chen and Kreglewski (1977). For a component i, this temperature-dependent hard segment diameter is given by

$$d_i(T)=\sigma_i\left(1-0.12\,Exp\left(-\frac{3\varepsilon_i}{kT}\right)\right) \qquad (2.40)$$

where σ_i is the temperature-independent segment diameter, ε_i denotes the depth of the potential well and k is the Boltzmann constant.

The PC-SAFT equation of state is given as a hard-chain contribution (*hc*), a perturbation contribution which accounts of the attractive interactions (*disp*) of chains, and the association contribution (*assoc*), which is zero in fluids where no associative interactions are considered. Taking these terms into account, the compressibility factor can be expressed as

$$Z=1+Z^{hc}+Z^{disp}+Z^{assoc} \qquad (2.41)$$

The hard-chain contribution (Z^{hc}) is identical to the SAFT reference fluid taken from Chapman et al. (1988, 1989, and 1990) and depends on the number of segments, m in the molecular chain. This term is given by

$$Z^{hc}=\overline{m}\,Z^{hs}-\sum_{i=1}^{n}x_i\left(m_i-1\right)\rho_s\frac{\partial\ln\left(g_{ii}^{hs}\right)}{\partial\rho_s} \qquad (2.42)$$

$$\overline{m}=\sum_{i=1}^{n}x_i m_i \qquad (2.43)$$

where ρ_s ($1/\text{Å}^3$) is the total number density of molecules, Z^{hs} is the hard sphere reference contribution, and g_{ii}^{hs} is the radial pair distribution function for segments in a hard-sphere system. Terms Z^{hs} and g_{ii}^{hs} in Equation 2.42 are given by

$$Z^{hs}=\frac{\zeta_3}{1-\zeta_3}+\frac{3\zeta_1\zeta_2}{\zeta_0\left(1-\zeta_3\right)^2}+\frac{3\zeta_2^3-\zeta_3\zeta_2^3}{\zeta_0\left(1-\zeta_3\right)^3} \qquad (2.44)$$

$$g_{ii}^{hs}=\frac{1}{1-\zeta_3}+\left(\frac{d_i d_j}{d_i+d_j}\right)\frac{3\zeta_2}{\left(1-\zeta_3\right)^2}+\left(\frac{d_i d_j}{d_i+d_j}\right)^2\frac{2\zeta_2^2}{\left(1-\zeta_3\right)^3} \qquad (2.45)$$

where

$$\zeta_n=\frac{\pi}{6}\rho_s\sum_{i=1}^{n}x_i m_i d_i^n \qquad (2.46)$$

for n from 1 to 3. The perturbation contribution (Z^{disp}) is taken from the perturbation theory of Barker and Henderson (1967) which is derived for spherical molecules and extended for chain molecules composed of spherical segments. In this theory, the Helmholtz free energy is given as a sum of first and second order contributions by

$$\frac{A^{disp}}{kTN}=\frac{A_1}{kTN}+\frac{A_2}{kTN} \qquad (2.47)$$

Both terms in Equation 2.47 can be written for any potential function, and for square-well chains were simplified by Gross and Sadowski (2001) to

$$\frac{A_1}{kTN}=-2\pi\rho_s I_1(\eta,\bar{m})\sum_i\sum_j x_i x_j m_i m_j\left(\frac{\varepsilon_{ij}}{kT}\right)\sigma_{ij}^3 \qquad (2.48)$$

$$\frac{A_2}{kTN}=-\pi\rho_s\bar{m}\left(1+Z^{hc}+\rho_s\frac{\partial Z^{hc}}{\partial\rho_s}\right)^{-1} I_2(\eta,\bar{m})\sum_i\sum_j x_i x_j m_i m_j\left(\frac{\varepsilon_{ij}}{kT}\right)^2\sigma_{ij}^3 \qquad (2.49)$$

Where the following compressibility term can be obtained from Equation 2.42

$$\left(1+Z^{hc}+\rho_s\frac{\partial Z^{hc}}{\partial\rho_s}\right)=\left(1+\bar{m}\frac{8\eta-2\eta^2}{(1-\eta)^4}+(1-\bar{m})\frac{20\eta-27\eta^2+12\eta^3-2\eta^4}{[(1-\eta)(2-\eta)]^2}\right) \qquad (2.50)$$

being η the packing fraction which is equal to ζ_3 and represents a reduced segment density. In Equations 2.48 and 2.49, the terms $I_1(\eta,m)$ and $I_2(\eta,m)$ can be expressed as power series in density η, where the coefficients are functions of the chain length

$$I_1(\eta,\bar{m})=\sum_{i=0}^{6}a_i(\bar{m})\eta^i \qquad (2.51)$$

$$I_2(\eta,\bar{m})=\sum_{i=0}^{6}b_i(\bar{m})\eta^i \qquad (2.52)$$

The dependence of the coefficients $a_i(m)$ and $b_i(m)$ with the segment number is the following

$$a_i(\bar{m})=a_{0i}+\frac{\bar{m}-1}{\bar{m}}a_{1i}+\frac{(\bar{m}-1)(\bar{m}-2)}{\bar{m}^2}a_{2i} \qquad (2.53)$$

$$b_i(\bar{m})=b_{0i}+\frac{\bar{m}-1}{\bar{m}}b_{1i}+\frac{(\bar{m}-1)(\bar{m}-2)}{\bar{m}^2}b_{2i} \qquad (2.54)$$

the coefficients a_{0i}, a_{1i}, a_{2i}, b_{0i}, b_{1i} and b_{2i} in Equations 2.53 and 2.54 are universal constants and were determined by Gross and Sadowski (2001). The parameters for a pair of unlike segments are obtained by conventional Berthelot-Lorentz combining rules:

$$\sigma_{ij}=\frac{1}{2}\left(\sigma_i+\sigma_j\right) \qquad (2.55)$$

$$\varepsilon_{ij}=\sqrt{\varepsilon_i\varepsilon_j}\left(1-k_{ij}\right) \qquad (2.56)$$

In this work, taking into account the good results obtained by Kiselev and Ely (2000) and Huber *et al.* (2002) (who did not include an explicit contribution for the polar interactions) and in order to gain simplicity the considered compounds are treated as nonassociating, i.e. Z^{assoc} is set equal to zero. In this way, three parameters are required for each pure compound: m_i (segment number), σ_i (segment diameter) and ε_i (depth of pair potential). These parameters are simultaneously adjusted to liquid density and vapor pressure data.

2.5 – Results and discussions: refrigerants

The performance of the different EoS is evaluated on four refrigerants for which sufficient experimental data exist over wide ranges of temperature and pressure. The studied refrigerants are:

- R32 (difluoromethane).
- R125 (pentafluoroethane).
- R134a (1,1,1,2-tetrafluoroethane).
- R152a (1,1-difluoroethane).

The experimental database used for refrigerants includes density and vapor pressure data. For each refrigerant the references are given in Appendix A along with the number of points (NP), and the temperature and pressure ranges. In order to analyse and evaluate the performance of the considered EoS, the following quantities defined below are used:

$$AAD=\frac{100}{NP}\sum_{i=1}^{NP}\left|\frac{\rho_{i,cal}-\rho_{i,exp}}{\rho_{i,exp}}\right| \qquad (2.57)$$

$$Bias=\frac{100}{NP}\sum_{i=1}^{NP}\frac{\rho_{i,cal}-\rho_{i,exp}}{\rho_{i,exp}} \qquad (2.58)$$

$$MDev=\max\left|\frac{\rho_{cal}-\rho_{exp}}{\rho_{exp}}\right| \qquad (2.59)$$

where ρ_{exp} is the experimental density, and ρ_{cal} is the value calculated using a given model. The AAD (absolute average deviation) and MDev (maximum deviation) indicate how close the calculated values are to the experimental values, while the quantity Bias is an indication of how well the calculated values are distributed around the experimental values.

2.5.7 – Results cubic EoS comparisons

The pure component parameters needed in cubic EoS are taken from Table 1.1 in Chapter 1. The k_1 value necessary for calculating α in Equation 2.10 for the PRSV EoS is adjusted against vapor pressure data. In Table 2.3 the AAD and MDev obtained in vapor pressure with the four cubic EoS are presented. The range of reduced temperatures where experimental vapor pressures are available corresponds to $T_r = 0.5$–1. It can be seen that the experimental vapor pressures are reproduced accurately up to the critical point for all four models. Especially, for PR, PRSV, and RK-PR, the agreement with experimental data is found to be excellent. In Figure 2.2 the vapor pressure curves obtained for R125 and R152a with the SRK, PR, PRSV, and RK-PR approaches are compared with experimental data. The vapor pressure curves are shown in the Clausius-Clapeyron representation. In this way, the low-temperature region is better observed.

EoS		R32	R125	R134a	R152a
	T-range (K)	204–351	180–339	214–373	205–386
	NP	269	213	256	313
SRK	AAD (%)	1.56	0.70	1.27	1.64
	MDev (%)	5.29	4.21	4.85	6.10
PR	AAD (%)	0.70	0.38	0.44	0.60
	MDev (%)	2.46	2.77	1.78	2.57
PRSV [(a)]	AAD (%)	0.33	0.27	0.31	0.55
	MDev (%)	1.77	1.91	0.84	2.07
RK-PR [(b)]	AAD (%)	0.29	0.71	0.79	0.41
	MDev (%)	1.92	3.06	2.58	1.82

Table 2.3 – Performance of the cubic EoS to reproducing vapor pressures. (a) The k_1 values presented in Equation 2.10 were adjusted against vapor pressure and their values are {-0.058, 0.020, 0.001, and -0.015} for R32, R125, R134a, and R152a respectively. (b) The k values necessary in Equation 2.17 is the value required to match the experimental vapor pressure at $T_r = 0.7$. Their values are {1.967, 2.498, 2.464, and 2.137} for R32, R125, R134a, and R152a, respectively.

The AAD and MDev [illegible] results are given in Table 2.4. In comparison [illegible] between SRK and PR (or PRSV) is that the latter, in general, gives slightly better correlations for the volumetric properties.

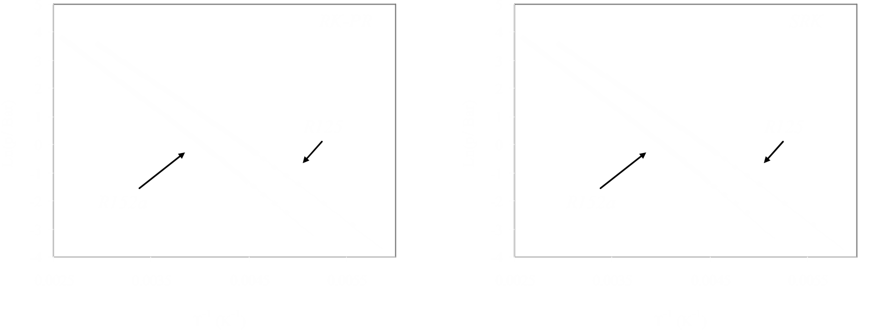

Figure 2.2 – Vapor pressure as Clausius-Clapeyron representation for HFC-125 and HFC-152a compared with the RK-PR and SRK predictions.

		R32	*R125*	*R134a*	*R152a*
EoS	*T-range* (K)	142-473	178-400	200-423	158-453
	p-range (Bar)	0.7-350	1.2-679	1-1400	1-352
	NP	903	655	474	514
SRK	AAD (%)	14.58	6.43	8.61	13.81
	MDev (%)	33.52	23.87	18.91	25.60
PR	AAD (%)	8.42	3.26	1.33	5.71
	MDev (%)	26.40	18.63	9.88	16.47
PRSV	AAD (%)	8.39	3.25	1.34	5.73
	MDev (%)	26.27	18.62	9.85	16.41
RK-PR	AAD (%)	2.44	2.89	1.26	2.07
	MDev (%)	18.67	20.84	8.90	12.52

Table 2.4 – Performance of the cubic EoS in reproducing densities. The k_i and k values are the same ones reported in Table 2.3.

A closer look at the large MDev obtained with all the models (especially for R32 and R125) shows that they are coming from the area close to the critical region. It has also been observed that the gas density is predicted better than the liquid density. In order to improve the density predictions the

Péneloux volume translation (Péneloux *et al.* 1982) can be introduced. This approach consists of a simple translation of the frame of reference so that the volume (or density) representation may better be overlapped to the experimental data. However, in spite of its popularity, this volume translation approach has no effect in the compressibility performance of the EoS. It should be taken into account that if a temperature dependent Péneloux translation is applied, this may induce the very serious pathological problem of isotherm crossing or violation of the condition of thermal stability (Salim and Trebble, 1991).

2.5.2 – Results SBWR EoS: refrigerants

Two approaches are used to determine the critical compressibility factor. In the first approach, Z_c is calculated by means of Equation 2.34. In the second approach, as recommended by Soave (1999) for a better performance of the SBWR EoS, the Z_c and ω parameters are simultaneously adjusted to vapor pressures and liquid density data by minimizing the objective function

$$\min_{(Z_c,\omega)} f = \sum_{i=1}^{NP}\left(\frac{\rho_{i,cal}^{liq}-\rho_{i,exp}^{liq}}{\rho_{i,exp}^{liq}}\right)^2 + \sum_{i=1}^{NP}\left(\frac{P_{i,cal}^{sat}-P_{i,exp}^{sat}}{P_{i,exp}^{sat}}\right)^2 \qquad (2.60)$$

For that purpose, the experimental vapor pressures and liquid densities reported in Appendix A have been used. Hereafter, this version of SBWR will be called "SBWR-reg". The ω and Z_c values using both approaches (SBWR or SBWR-reg) are given, along with AAD and MDev in vapor pressures and densities in Table 2.5. It can be seen that the vapor pressure is represented very accurately using either SBWR or SBWR-reg version. Very good description of the vapor pressure can be seen in Figure 2.3. The volumetric predictions are improved when regressing ω and Z_c, especially for R125 and R134a where SBWR-reg does a very good job. It is interesting to notice that for R32 and R152a, the simple RK-PR model gives better results than SBWR-reg model (compare Tables 2.4 and 2.5).

2.5.3 – Results PC-SAFT EoS: refrigerants

The parameters of PC-SAFT (m, σ, and ε) are adjusted, as for the SBWR-reg EoS, using vapor pressure and liquid density data by minimizing the following objective function

$$\min_{(m,\sigma,\varepsilon)} f = \sum_{i=1}^{NP}\left(\frac{\rho_{i,cal}^{liq}-\rho_{i,exp}^{liq}}{\rho_{i,exp}^{liq}}\right)^2 + \sum_{i=1}^{NP}\left(\frac{P_{i,cal}^{sat}-P_{i,exp}^{sat}}{P_{i,exp}^{sat}}\right)^2 \qquad (2.61)$$

Component	ω	Z_c	Densities		Vapor Pressures	
			AAD (%)	MDev (%)	AAD (%)	MDev (%)
SBWR [1]						
R32	0.2768	0.2665	8.36	18.45	0.49	3.47
R125	0.3050	0.2643	1.44	15.97	0.36	1.97
R134a	0.3268	0.2627	1.48	9.23	0.42	2.79
R152a	0.2760	0.2665	6.78	8.23	0.54	3.72
SBWR-reg [2]						
R32	0.2617	0.2590	6.95	15.88	0.31	2.00
R125	0.3153	0.2695	0.70	16.00	0.24	3.10
R134a	0.3154	0.2585	0.50	9.23	0.26	0.92
R152a	0.2581	0.2583	4.59	7.90	0.23	1.62

Table 2.5 – Performance of the SBWR and SBWR-reg EoS in reproducing vapor pressures and densities. [1] Z_c is calculated by means of Equation 2.33 using tabulated ω values. [2] Z_c and ω are simultaneously adjusted to vapor pressures and liquid densities.

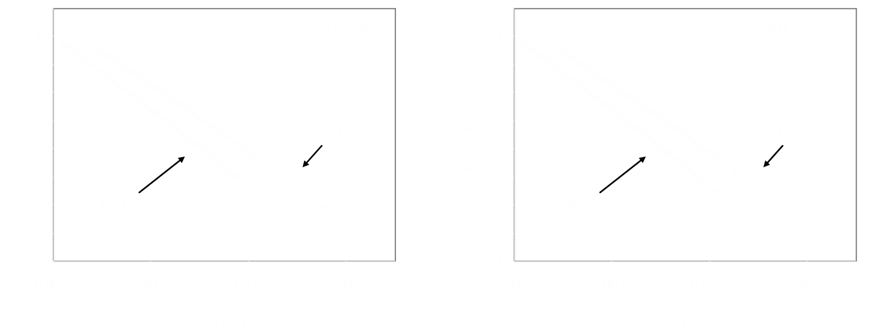

Figure 2.3 – Vapor pressure as Clausius-Clapeyron representation for HFC-125 and HFC-152a compared with the SBWR and SBWR-reg predictions.

Liquid densities at saturation have not been used (contrary to usual practice when adjusting the parameters in the EoS of the SAFT family). The ability of PC-SAFT to predict densities at saturation will be shown in the next section.

The optimized parameters along with AAD and MDev in densities and vapor pressures are given in Table 2.6. The description of the vapor pressure up to the critical point can be seen in Figure 2.4, with a slight overprediction of the experimental critical point. A good description of the [illegible] properties is obtained with the PC-SAFT EoS; however, as for the SBWR-ag model, the RK-PR EoS delivers in some cases better results than the PC-SAFT EoS (compare Tables 2.4 and 2.6).

Component	σ (Å)	ε/k (K)	*m*	Densities		Vapor Pressures	
				AAD (%)	MDev (%)	AAD (%)	MDev (%)
R32	2.754	173.158	2.764	3.85	20.70	0.54	3.63
R125	3.127	156.891	3.100	0.98	20.36	0.59	1.97
R134a	2.935	164.265	3.491	1.00	22.92	0.81	3.53
R152a	3.101	192.117	2.718	2.29	19.89	0.97	2.02

Table 2.6 – Performance of the PC-SAFT EoS in reproducing vapor pressures and densities.

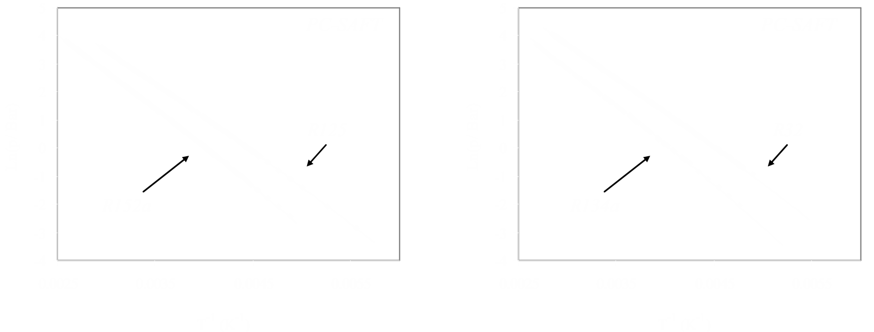

Figure 2.4 – Vapor pressure as Clausius-Clapeyron representation for HFC-125, HFC-152a, HFC-32, and HFC-134a compared with the PC-SAFT predictions.

Finally, care should be taken in interpreting the values of *m* in Table 2.6. The *m* parameter essentially describes the asymmetry in the molecular shape. Since refrigerant molecules are mainly derived from methane and ethane molecules one may expect the *m* values to be between one and two in order to retain a physically reasonable molecular shape. In fact, Galindo *et al.* (1997, and 1998) adopted values of *m* close to one in their works on refrigerants and SAFT EoS, adjusting the five left parameters against experimental data. Although, the *m* values reported in Table 2.6 may not be entirely satisfactory, the fitting of the segment parameter rather than imposed it was found to provide better results. On the other hand, in terms of thermophysical properties HFC molecules behave differently from methane or ethane. Consequently, there should be no reasons why HFC molecules must adopt *m* values similar to the *m* values of methane or ethane.

2.5.4 – Discussions: refrigerants

In terms of vapor pressures all the models have shown to deliver satisfactory results. In terms of densities, the capabilities of the six EoS are shown in Figures 2.5 and 2.6 where density deviations are plotted as function of temperature and pressure. In the case of SRK, RK-PR, and SBWR-reg models it can be seen that most of the points are placed above the zero axis, which means that these models overpredict the densities (AAD ≈ Bias). On the other hand, for the PR, PRSV, and PC-SAFT EoS the calculated values are better distributed around the experimental values since no bias trend is to be seen. The best results are found with RK-PR, SBWR-reg and PC-SAFT models. The RK-PR EoS, which requires neither vapor pressures nor experimental densities for the adjustment of its parameters, provides similar or sometimes even better results than SBWR-reg and PC-SAFT. In the case of PC-SAFT, although the results obtained are satisfactory, a better agreement with experimental data might be found by use of more sophisticated versions. An improvement is expected in the results by inclusion of bonding sites in the model with the aim to take into account polarity of the molecules. The inclusion of polar effects in order to improve the results can serve as a rigorous test of the EoS itself and further studies in that direction may prove useful. However, as stated before, in order to gain simplicity and in view of the good results obtained, no explicit contribution for polar interactions is accounted.

Another important aspect in refrigeration cycles is the correct description of the critical region, since refrigeration cycles may operate around critical conditions. To better illustrate this, Figure 2.7 shows the critical isotherms for R32 and R125 along with the coexisting densities. The cubic EoS give similar results (classical critical behavior). Slightly better results are obtained with the RK-PR EoS. It is well-known that the two-parameter EoS (i.e. SRK, PR, or PRSV in this case) are unable to represent the critical point exactly, since at least three parameters are necessary for exact representation of the critical point (Michelsen and Mollerup, 2004). In the case of the PR-RK EoS, which is a three-parameter EoS, underestimation of the critical density was found to be necessary in order to better reproduce the whole critical isotherm (Cismondi and Mollerup, 2005). SBWR-reg EoS can represent the flatness of the critical isotherm very well, and the coexisting densities are also represented accurately. PC-SAFT describes saturated densities correctly, but fails at reproducing the

Figure 2.5 – HFC-32 (♦), HFC-125 (▲), HFC-134a (■), and HFC-152a (●) density deviations, $100\times(\rho_{exp} - \rho_{cal})/\rho_{exp}$, as a function of temperature with the SRK, PR, PRSV, RK-PR, SBWR-reg, and PC-SAFT EoS.

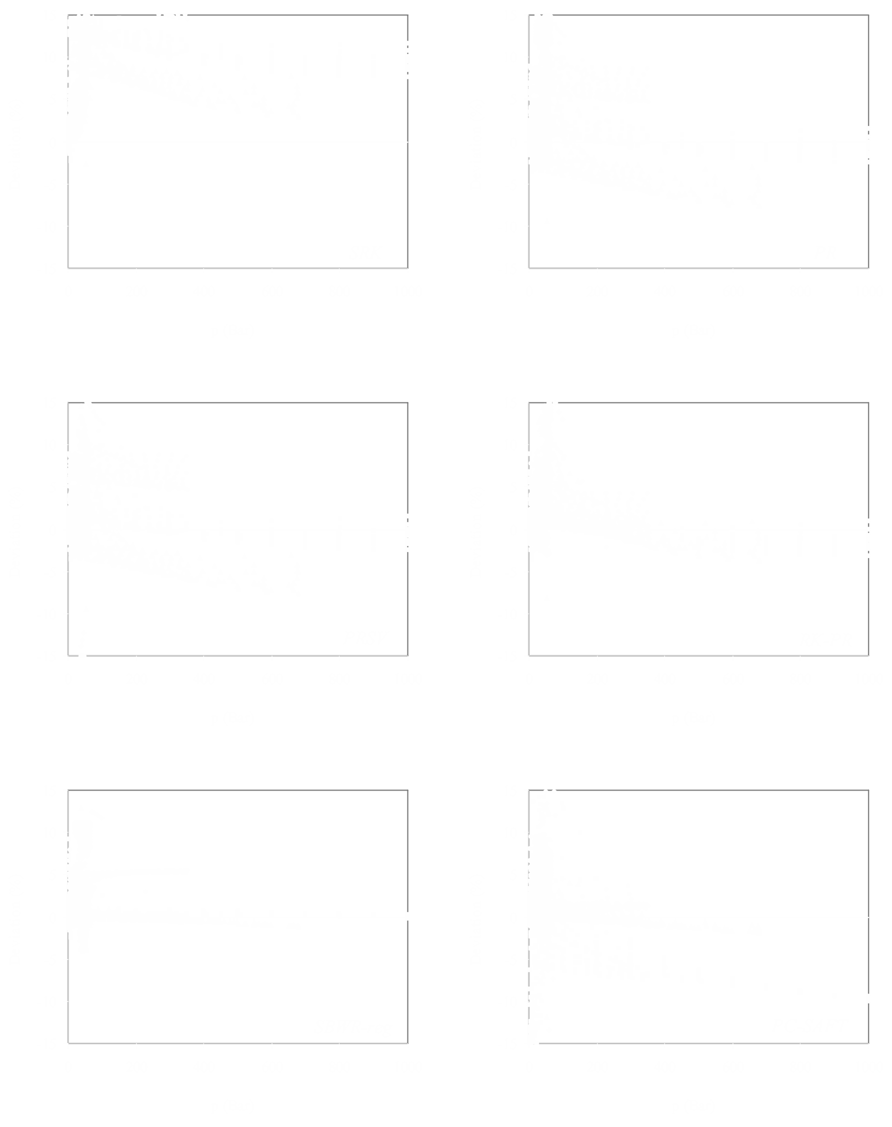

Figure 2.6 – HFC-32 (♦), HFC-125 (▲), HFC-134a (■), and HFC-152a (●) density deviations, $100\times(\rho_{exp}-\rho_{cal})/\rho_{exp}$, as a function of pressure with the SRK, PR, PRSV, RK-PR, SBWR-reg, and PC-SAFT EoS.

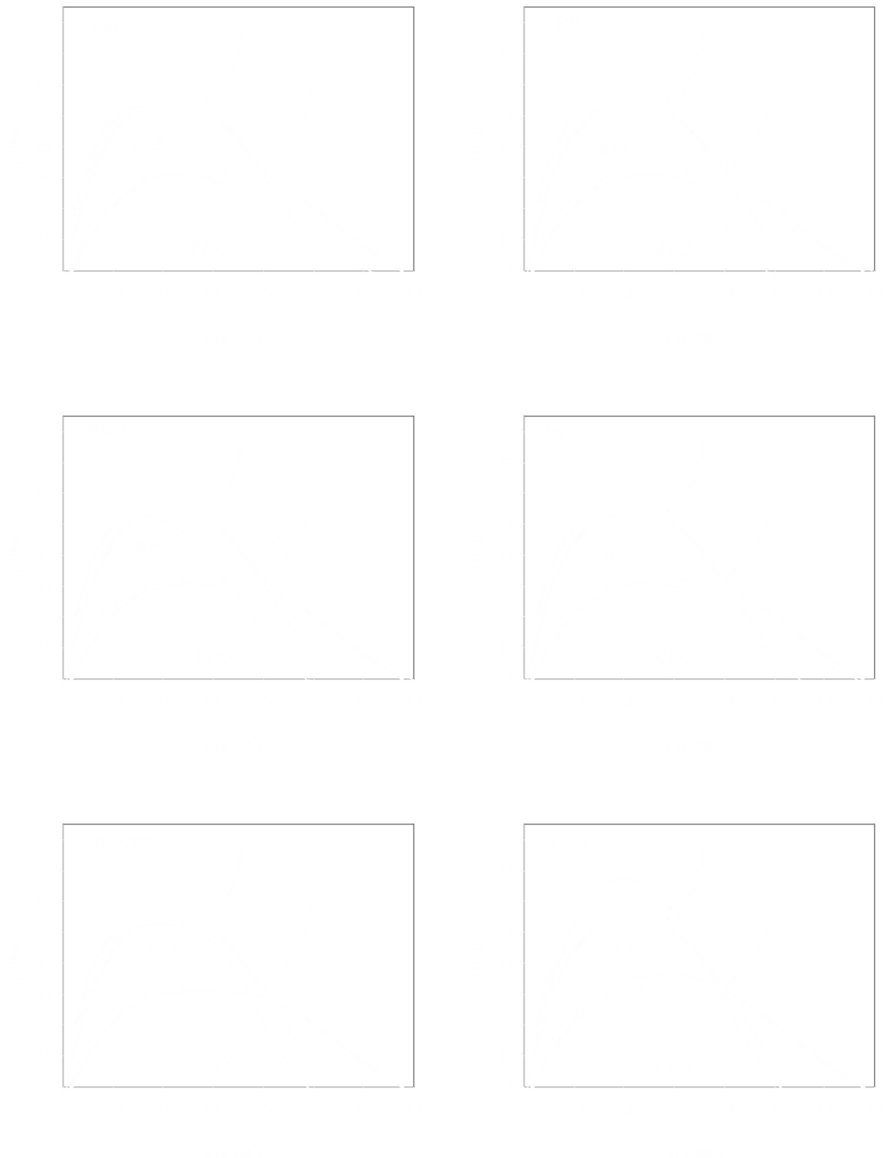

Figure 2.7 – Vapor – liquid coexistence densities (—) for HFC-32 and HFC-125 and densities at the critical isotherm (---) using six EoS. Experimental values: critical isotherm (●): HFC-32 by Defibaugh *et al.* (1994), and HFC-125 by Defibaugh and Morrison (1992); saturated densities (♦): HFC-32 by Holcomb *et al.* (1993), and HFC-125 by Defibaugh and Morrison (1992).

critical isotherm. This is a well-known fact, since EoS of the SAFT family, in general, underestimate the critical properties. Different attempts have been made in order to improve the critical description of the PC-SAFT EoS, but this seems to be at the expense of the liquid densities (Cismondi *et al.* 2005).

2.6 – Results and discussions: lubricants

The performance of the EoS is also evaluated on the three lubricants, for which experimental density data exist over wide ranges of temperature and pressure. The studied lubricants consist of two PAGs (Comuñas, 2002) and one POE (Wahlstrom and Vamling, 1999, and Fandiño *et al.* 2005). The chemical names of the lubricants are:

- TEGDME (tetraethylene glycol dimethylether).
- TriEGDME (triethylene glycol dimethylether).
- PEB8 (Pentaerythritol tetra 2-ethylhexanoate).

One of the most difficult problems for lubricant oils is that no values for the scaling parameters (T_c, P_c and ω) have been determined for many of these compounds. Furthermore, experimental data on vapor pressures are usually not available in the literature. In addition, actual lubricant oils are mixtures of various compounds with very high boiling points. In order to solve these problems several authors have proposed different methods. For example, when cubic EoS are used to fit solubility data, Yokozeki (2001) has proposed to treat the lubricants naphtenic mineral (MO), alkylbenzene (AB), and polyol ester (POE) oils as an hypothetical oil named "UniOIL". Critical properties of this hypothetic oil are: T_c = 800 K, and P_c = 950 kPa. Elvassore *et al.* (1999) have developed a group contribution method for determining the three parameters *a*, *b*, and *c* of the cubic Sako *et al.* (1989) EoS. Baylaucq *et al.* (2002), Garcia *et al.* (2003), and Teodorescu *et al.* (2003) have used group contribution methods for the estimation of T_c, P_c, and ω. In this direction, Zhelezny *et al.* (2003), and Medvedev *et al.* (2004) have proposed different methods for estimating pseudocritical properties for these compounds.

2.6.1 – Results cubic EoS: lubricants

Two approaches are used to determine the $a(T)$ and b parameters in the SRK and PR EoS. First, the scaling parameters reported by Baylaucq *et al.* (2002) for TriEGDME and TEGDME and by Cisneros *et al.* (2003) for PEB-8 are employed. The parameters are shown in Table 2.7. In the second approach, the three PR pure component parameters are simultaneously fit to experimental liquid densities by minimizing the objective function:

$$\min_{(T_c, P_c, \omega)} f = \sum_{i=1}^{NP} \left(\frac{\rho_{i,cal}^{liq} - \rho_{i,exp}^{liq}}{\rho_{i,exp}^{liq}} \right)^2 \qquad (2.62)$$

Note that this fitting is essentially the same as that used to obtain pure component parameters for the modern EoS such as SAFT. Hereafter, this version of PR will be referred as "PR-regressed" or "PR-reg" for short. The idea of fitting the pure component parameters of a cubic equation to liquid density data is well-known and has been applied by Ting *et al.* (2003) among others. Since experimental vapor pressures are not available for the lubricants studied, PRSV is not included in this section.

Component	*M* (g/mol)	T_c (K)	P_c (Bar)	ω
TriEGDME	178.23	663.85	23.3	0.713
TEGDME	222.28	703.52	19.1	0.882
PEB-8	640.94	745.59	7.00	1.254

Table 2.7 – Molar mass, critical temperature, critical pressure and acentric factor for PAGs (Baylauq *et al.* 2002) and POE (Garcia *et al.* 2003).

For the RK-PR EoS the T_c and P_c reported in Table 2.7 are considered. To calculate k and Z_c the following procedure is applied. Since:

$$P_r\left(T_r = 0.7\right) = 10^{-1-\omega} \qquad (2.63)$$

the k constant necessary to match the experimental vapor pressure at $T_r = 0.7$ is adjusted using Equation 2.63 and the ω values of Table 2.7. Unfortunately, the available predictive methods for estimating v_c (or Z_c which is necessary to calculate the third parameter δ_1) seem to cover too limited ranges of the acentric factor. For this reason, and following the proposal of Soave (Soave 1995), the well-known Rackett equation is used:

$$v_L^{sat} = \frac{RT_c}{P_c} Z_{Ra}^{1+(1-T_r)^{2/7}} \qquad (2.64)$$

where Z_{Ra} can be used as a substitute for the critical compressibility factor Z_c. In fact, Z_{Ra} should coincide with Z_c since the liquid volume at the critical temperature:

$$v_{L,c}^{sat} = \frac{RT_c}{P_c} Z_{Ra} \qquad (2.65)$$

should be equal to the critical volume $v_c = Z_cRT_c/P_c$. Soave (1995) correlated $Z_c = Z_{cc}$ as a function of ω in a broad range of ω obtaining Equation 2.33. To estimate the critical compressibility factor the empirical correlation suggested by Soave (1995) has been used.

The AAD and MDev in densities for the three lubricants are shown in Table 2.8 along with temperature and pressure ranges. It can be seen that for both PAGs the RK-PR model does a better job compared to SRK and PR, confirming the very good performance of this new EoS. The performance of the three cubic EoS is similar for PEB8.

EoS		*TriEGDME*	*TEGDME*	*PEB-8*
	T-range (K)	293-373	293-373	268-367
	p-range (Bar)	1-600	1-600	1-450
	NP	117	117	114
SRK	AAD (%)	17.88	21.46	16.28
	MDev (%)	19.62	23.33	17.84
PR	AAD (%)	8.23	12.33	12.74
	MDev (%)	10.38	14.57	15.07
RK-PR	AAD (%)	3.78	2.60	12.47
	MDev (%)	6.37	5.58	14.95

Table 2.8 – Performance of the PR, SRK and RK-PR EoS in reproducing densities.

In Table 2.9 the PR-reg new parameters along with the AAD and MDev in densities are presented. As observed, the density predictions can be notably improved by simultaneously regressing T_c, P_c, and ω. Of course, the same procedure could be applied to SRK or RK-PR EoS improving significantly the results.

Parameter	*TriEGDME*	*TEGDME*	*PEB-8*
T_c (K)	664.56	719.80	664.30
P_c (Bar)	26.2	22.8	6.90
ω	0.416	0.395	0.812
	Deviations		
AAD (%)	1.47	1.01	1.08
MDev (%)	3.13	2.28	3.23

Table 2.9 – Performance of the PR-reg EoS in reproducing densities.

2.6.2 – Results SBWR EoS: lubricants

As for pure refrigerants two approaches are used to estimate the pure component parameters required by the EoS. In the first approach, critical temperatures, critical pressures and acentric factors reported in Table 2.7 are used and the critical compressibility factor is calculated by means of Equation 2.33 (SBWR). In the second approach Z_c and ω are simultaneously fit to liquid densities (SBWR-reg). The results obtained with SBWR and SBWR-reg are presented in Table 2.10, showing that the results obtained for TriEGDME and TEGDME are better that the ones obtained for PEB-8. Again, the representation of the *p–v–T* properties is improved when adjusting Z_c and ω.

Component	ω	Z_c	Densities AAD (%)	 MDev (%)
SBWR				
TriEGDME	0.713	0.241	5.45	5.88
TEGDME	0.882	0.235	5.53	6.11
PEB-8	1.254	0.230	19.72	21.13
SBWR-reg				
TriEGDME	0.430	0.244	0.59	1.47
TEGDME	0.460	0.236	0.64	1.55
PEB-8	0.155	0.235	3.98	10.11

Table 2.10 - Performance of the SBWR and SBWR-reg EoS in reproducing densities.

2.6.3 – Results PC-SAFT EoS: lubricants

The adjustable parameters of PC-SAFT (σ, ε, *m*) for lubricants are listed in Table 2.11 along with the AAD in densities. The agreement between experimental and calculated values is excellent. In case of TriEGDME and TEGDME the maximum deviation has the same order of magnitude as the reported experimental uncertainty (Comuñas, 2002).

Component	σ (Å)	ε/k (K)	m	Densities	
				AAD (%)	MDev (%)
TrEGDME	3.137	236.384	8.082	0.06	0.24
TEGDME	3.132	242.714	10.024	0.04	0.26
PEB-8	4.653	397.041	10.546	0.46	1.67

Table 2.11 – Performance of the PC-SAFT EoS in reproducing densities.

2.6.4 – Discussions: lubricants

The aim of this section is to compare the different EoS used. Figures 2.8 and 2.9 show density deviations as function of temperature and pressure for the three lubricants. It can be seen that "PR-reg" and PC-SAFT models do not show any bias trend, neither with temperature nor with pressure. This is not the case for the rest of the models, since they under or over predict the density. The new RK-PR EoS has shown to do a good job describing *p-v-T* properties, if one takes into account that no experimental densities has been used in the adjustment of its parameters. Peng-Robinson is a surprisingly accurate EoS, but only if its pure component parameters are regressed to liquid densities. In fact, in spite of its simplicity "PR-reg" delivers better results than "SBWR-reg". Even though no explicit contribution is taken into account for the different interactions that lubricant molecules may show (permanent or induced multipolar interactions, weak hydrogen bonds, etc), PC-SAFT has shown to excellently describe the *p-v-T* properties of these compounds.

2.7 – Conclusions

In this Chapter several EoS for estimating thermophysical properties were introduced. The ability of these models in predicting vapor pressures and densities was tested on pure refrigerants and pure lubricants. It can be concluded that the best results are obtained with RK-PR, SBWR-reg, and PC-SAFT EoS. It is also important to remark that simple models such as PR-reg can represent the *p-v-T* behavior very accurately, as it has been seen in the case of pure lubricants. This procedure could have been applied to pure refrigerants as well, improving the density representation. However, this would be at the expense of the critical area. Since the correct description of the critical region is very important, the adjustment of T_c, P_c and ω was not carried out for refrigerants.

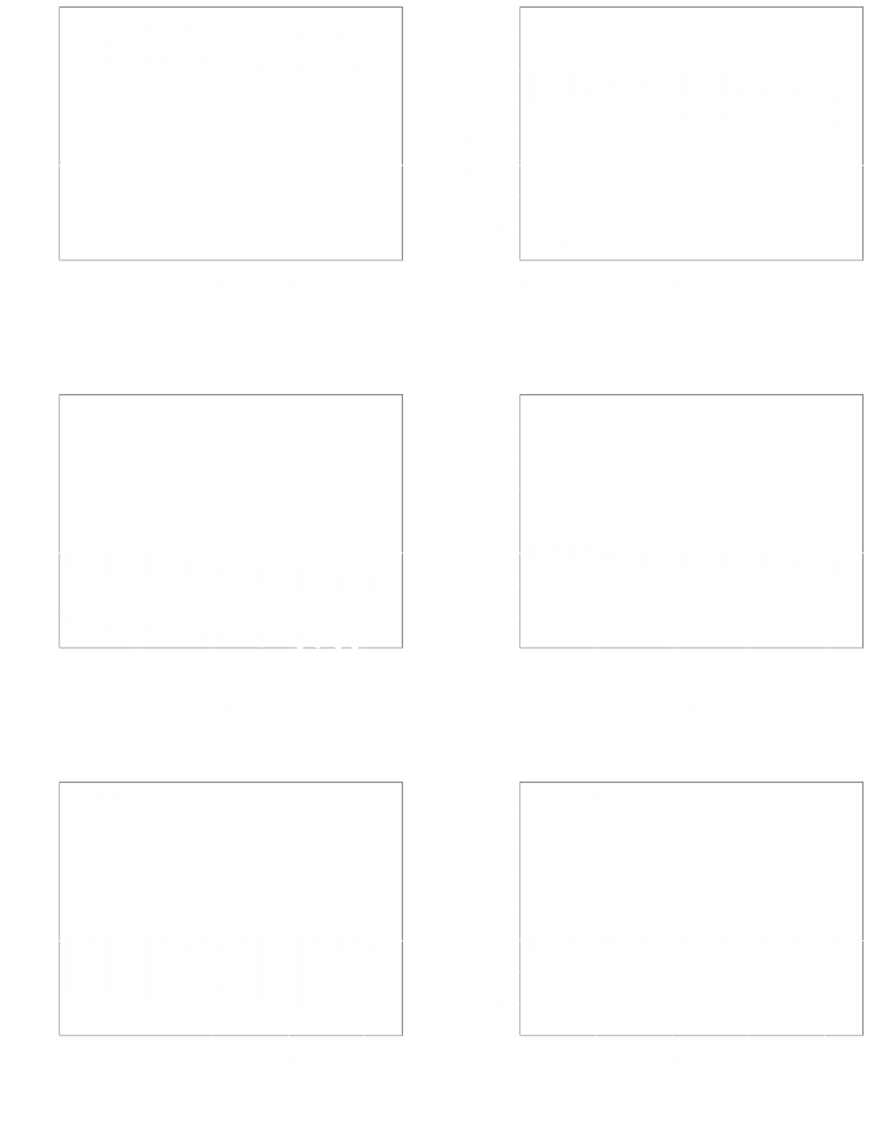

Figure 2.8 – TriEGDME (♦), TEGDME (▲), and PEB8 (●) density deviations, 100×(ρ_{exp}−ρ_{cal})/ρ_{exp}, as a function of temperature with the RK-PR, PR-reg, SBWR-reg, and PC-SAFT EoS.

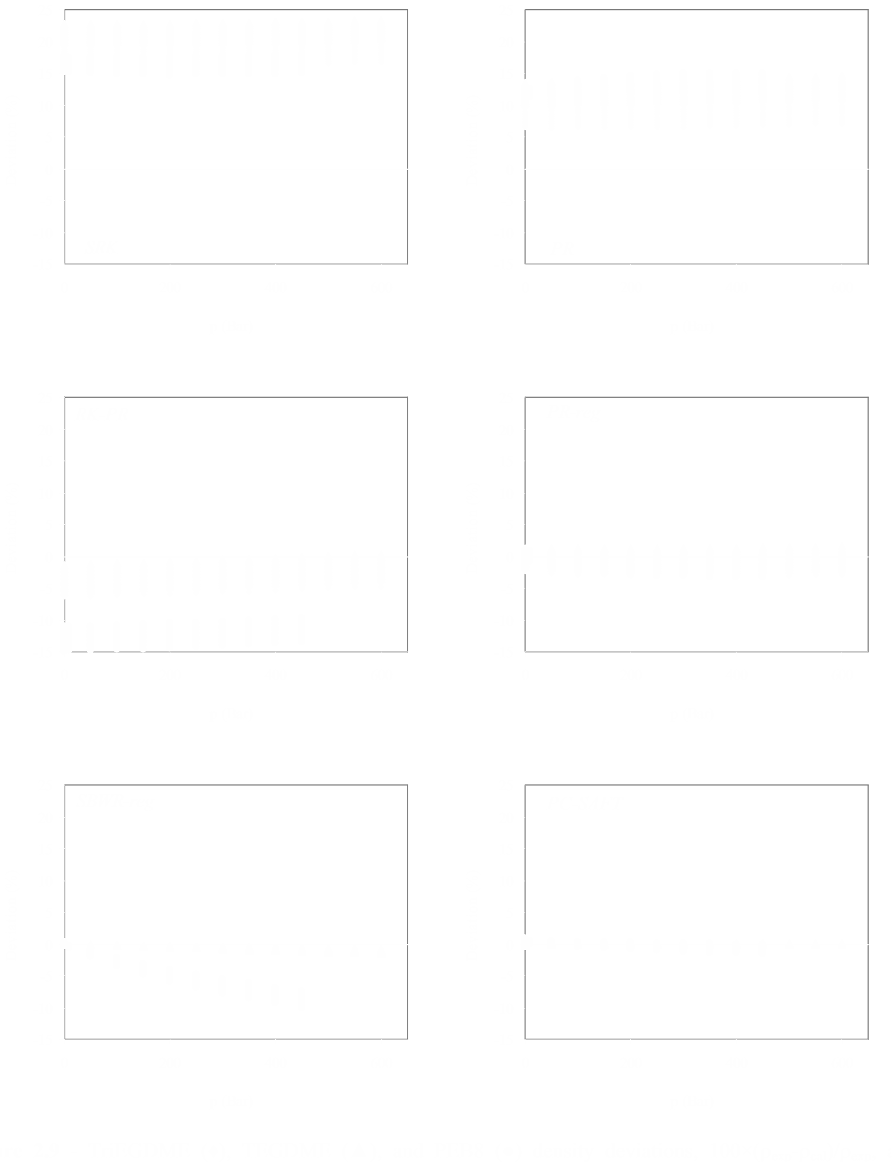

Figure 2.9 – TriEGDME (♦), TEGDME (▲), and PEB8 (●) density deviations, 100×(ρ$_{exp}$-ρ$_{cal}$)/ρ$_{exp}$ as a function of pressure with the RK-PR, PR-reg, SRWR-reg, and PC-SAFT EoS.

Nomenclature

a = Attractive energy parameter

AAD = Average absolute deviation

b = van der Waals covolume

Bias = Bias

BWR = Benedict-Webb-Rubin

EoS = Equation of state

k = Boltzmann constant

k_{ij} = Binary interaction parameter

m = Number of segments per chain

M = Molecular weight

MDev = Maximum deviation

n = Number of components

N = Total number of molecules

NP = Number of points

p = Pressure

PAG = Polyalkylene glycols

PC-SAFT = Perturbed-chain statistical associating fluid theory

POE = Polyol ester

PR = Peng-Robinson

PRSV = Peng-Robinson-Stryjek-Vera

R = Gas constant

RK-PR = Redlich-Kwong-Peng-Robinson

SBWR = Soave-Benedict-Webb-Rubin

SRK = Soave-Redlich-Kwong

T = Temperature

v = Molar volume

VLE = Vapor-liquid equilibrium

x = Mole fraction

Z = Compressibility factor

Greek letters

δ_1 = Third parameter in RK-PR EoS

ε = Depth of pair potential

ρ = Density

ρ_s = Total number density of molecules

σ = Segment diameter

ω = Acentric factor

Subscripts/superscripts

assoc = Association

c = Critical

cal = Calculated property

disp = Contribution due to dispersive attractions

exp = Experimental property

hc = Contribution of hard-chain system

hs = Contribution of hard-sphere system

i = Component "i"

j = Component "j"

L = Liquid

mix = Mixture

r = Reduce property

Ra = Rackett

sat = Property at saturation condition

References

1. Barker, J.A., Henderson, D. Perturbation Theory and Equation of State for Fluids. II. A Successful Theory of Liquids. *J. Chem. Phys.* 1967, 47, 4714-4721.
2. Baylaucq, A., Comuñas, M.J.P., Boned, C., Allal, A., Fernández, J. High-pressure viscosity and density modeling of two polyethers and two dialkyl carbonates. *Fluid Phase Equilib.* 2002, 192, 249-263.
3. Benedict, M., Webb, G.B., Rubin, L.C. An empirical equation for thermodynamics properties of light hydrocarbons and their mixtures. *J. Chem. Phys.* 1940, 334-345.
4. Chapman, W.G., Jackson, G., Gubbins, K.E. Phase Equilibria of Associating Fluids: Chain Molecules with Multiple Bonding Sites. *Mol. Phys.* 1988, 65, 1057-1067.
5. Chapman, W.G., Gubbins, K.E., Jackson, G. SAFT: Equation of State Solution Model for Associating Liquids. *Fluid Phase Equilib.* 1989, 52, 31-38.
6. Chapman, W.G., Gubbins, K.E., Jackson, G., Radosz, M. New Reference Equation of State for Associating Liquids. *Ind. Eng. Chem. Res.* 1990, 29, 1709-1721.
7. Chen, S.S., Kreglewski, A. Applications of the augmented van der Waals theory of fluids. I. Pure fluids. *Ber. Bunsen-Ges. Phys. Chem.* 1977, 81, 1048-1052.
8. Cismondi, M., Mollerup, J. Development and application of a three-parameter RK-PR equation of state. *Fluid Phase Equilib.* 2005a, 232, 74-89.
9. Cismondi, M., Brignole, E.A., Mollerup, J. Rescaling of three-parameter equations of state: PC-SAFT and SPHCT. *Fluid Phase Equilib.* 2005b, 234, 108-121.
10. Comuñas, M.J.P. Densidades y Viscosidades a Alta Presión de Nuevos Lubricantes Sintéticos y de las Mezclas Lubricante + HFC-134a. Medidas y Modelización. Ph.D. Thesis, Física Aplicada, Universidad de Santiago de Compostela, Santiago de Compostela, Spain, 2002.
11. Defibaugh, D., Morrison, G. Compressed Liquid Densities and Saturation Densities of Pentafluoroethane (R125). *Fluid Phase Equilib.* 1992, 80, 157-166.
12. Defibaugh, D., Morrison, G., Weber, L. Thermodynamic Properties of difluoromethane. *J. Chem. Eng. Data* 1994, 39, 333-340.
13. Deiters, U.K. Remarks on publications dealing with equations of state. *Fluid Phase Equilib.* 1999, 161, 205-219.
14. Elvassore, N., Bertucco, A. A Cubic Equation of State with Group Contributions for the Calculation of Vapor-Liquid Equilibria of Mixtures of Hydrofluorocarbons and Lubricant Oils. *Ind. Eng. Chem. Res.* 1999, 38, 2110-2118.

15. Fandiño, O., Pensado, A.S., Lugo, L., Comuñas, M.J.P., Fernández, J. Compressed Liquid Densities of Squalane and (Pentaerythritol tetra 2-ethylhexanoate) *J. Chem. Eng. Data* 2005, 50, 939-946.
16. Fu, Y.-H., Sandler, S.I. A simplified SAFT Equation of State for Associating Compounds and Blends. *Ind. Eng. Chem. Res.* 1995, 34, 1897-1909.
17. Galindo, A., Whitehead, P.J., Jackson, G. predicting the Phase Equilibria of Mixtures of Hydrogen Fluoride with Water, Difluoroethane (HFC-152a), and 1,1,1,2-Tetrafluoroethane (HCF-134a) Using a Simplified SAFT approach. *J. Phys. Chem. B* 1997, 101, 2082-2091.
18. Galindo, A., Gil-Villegas, A., Whitehead, P.J., Jackson, G., Burgess, A.N. Prediction of Phase Equilibria for Refrigerant Mixtures of Difluoroethane (HFC-32), 1,1,1,2-Tetrafluoroethane (HCF-134a), and Pentafluoroethane (HFC-125a) Using SAFT-VR. *J. Phys. Chem. B* 1998, 102, 7632-7639.
19. García, J., Monsalvo, M.A., Quiñones-Cisneros, S.E., Fernández, J. Modelling Phase Equilibria and Viscosity for Refrigerant-Lubricant Oil Systems. *21st IIR International Congress of Refrigeration*, *Washington D. C.*, 2003.
20. Gross, J., Sadowski, G. Perturbed-Chain SAFT: An Equation of State Based on a Perturbation Theory for Chain Molecules. *Ind. Eng. Chem. Res.* 2001, 40, 1244-1260.
21. Holcomb, C., Niesen, V., Van Poolen, L., Outcalt, S. Coexisting densities, vapor pressures and critical densities of refrigerants R32 and R152a at 300-385 K. *Fluid Phase Equilib.* 1993, 91, 145-157.
22. Huber, M.L., Lemmon, E.W., Friend, D.G. Modeling bubble points of mixtures of hydrocarbon refrigerants and polyol ester lubricants. *Fluid Phase Equilib.* 2002, 194-197, 511-519.
23. Kiselev, S.B., Ely, J.F. Simplified crossover SAFT equation of state for pure fluids and fluid mixtures. *Fluid Phase Equilib.* 2000, 174, 93-113.
24. McLinden, M.O., Klein, S.A., Lemmon, E.W., Peskin, A.P. NIST Thermodynamic and Transport Properties of Refrigerants and Refrigerant Mixtures - REFPROP, 6.01 ed., National Institute of Standards and Technology, Boulder, Colorado, USA, 1998.
25. Medvedev, O.O., Zhelezny, P.V., Zhelezny, V.P. Prediction of phase equilibria and thermodynamic properties of refrigerant/oil solutions. *Fluid Phase Equilib.* 2004, 215, 29-38.
26. Michelsen, M.L., Mollerup, J.M. Thermodynamic Models: Fundamental and Computational Aspects. Tie-Line publications, Denmark, 2004.
27. Mort, K.A., Johnson, K.A., Cooper, D.L., Burgess, A.N., Howells, W.S. The liquid structure of trifluoromethane. *Mol. Phys.* 1997, 90, 415-424.

28. Müller, E.A., Gubbins, K.E. Molecular-Based Equations of Sate for Associating Models. *Ind. Eng. Chem. Res.* 2001, 40, 2193.
29. Péneloux, A., Rauzy, E., Fréze, R. A Consistent Correction for Redlich-Kwong-Soave Volumes. *Fluid Phase Equilib.* 1982, 8, 7-23.
30. Peng, D.-Y., Robinson, D.B. A New Two-Constant Equation of State. *Ind. Eng. Chem. Fundam.* 1976, 15, 59–64.
31. Redlich, O., Kwong, J.N.S. On the Thermodynamic of Solutions. V An Equation of State. Fugacities of Gaseous Solutions. *Chemical Rev.* 1949, 44, 233 – 244.
32. Sako, T., Wu, A.H., Prausnitz, J.M. A Cubic Equation of State for High-Pressure Phase Equilibria of Mixtures Containing Polymers and Volatile Fluids. *J. Appl. Polym. Sci.* 1989, 38, 1839-1858.
33. Salim, P.H., Trebble, M.A. A modified Trebble-Bishnoi equation of state: thermodynamic consistency revisited. *Fluid Phase Equilib.* 1991, 65, 59-71.
34. Segura, H., Kraska, T., Mejía, A., Wisniak, J., Polishuk, I. Unnoticed Pitfalls of Soave-Type Alpha Functions in Cubic Equations of State. *Ind. Eng. Chem. Res.* 2003, 42, 5662-5673.
35. Soave, G.S. Equilibrium Constants from a Modified Redlich-Kwong Equation of State. *Chem. Eng. Sci.* 1972, 27, 1197-1203.
36. Soave, G.S. A Noncubic Equation of State for the Treatment of Hydrocarbon Fluids at Reservoir Conditions. *Ind. Eng. Chem. Res.* 1995, 34, 3981–3994.
37. Soave, G.S. An effective modification of the Benedict-Webb-Rubin equation of sate. *Fluid Phase Equilib.* 1999, 164, 157-172.
38. Stryjek, R., Vera, J.H. Vapor-Liquid Equilibrium of Hydrochloric Acid Solutions with the PRSV Equation of State. *Fluid Phase Equilib.* 1986, 25, 279-290.
39. Swaminathan, S., Visco, D.P. Thermodynamic Modeling of Refrigerants Using the Statistical Associating Fluid Theory with Variable Range. 1. Pure Components. *Ind. Eng. Chem. Res.* 2005a, 44, 4798-4805.
40. Swaminathan, S., Visco, D.P. Thermodynamic Modeling of Refrigerants Using the Statistical Associating Fluid Theory with Variable Range. 2. Applications to binary Mixtures. *Ind. Eng. Chem. Res.* 2005a, 44, 4806-4814.
41. Ting, P.D., Joyce, P.C., Jog, P.K., Chapman, W.G., Thies, M.C. Phase equilibrium modeling of mixtures of long-chain and short-chain alkanes using Peng-Robinson and SAFT. *Fluid Phase Equilib.* 2003, 206, 267-286.

42. Teodorescu, M., Lugo, L., Fernández, J. Modeling of Gas Solubility Data for HFCs–Lubricant Oil Binary Systems by Means of the SRK Equation of State. *Int. J. Thermophys.* 2003, 24, 1043-1060.
43. Wahlstrom, Å., Vamling, L. Solubility of HFC32, HFC125, HFC125, HFC134a, HFC143a and HFC152a in a Pentaerythritol Tetrapentanoate Ester. *J. Chem. Eng. Data* 1999, 44, 823-828.
44. Wertheim, M.S. Fluids with Highly Directional Attractive Forces. I. Statistical Thermodynamics. *J. Stat. Phys.* 1984a, 35, 19.
45. Wertheim, M.S. Fluids with Highly Directional Attractive Forces. II. Thermodynamic Perturbation Theory and Integral Equations. *J. Stat. Phys.* 1984b, 35, 35.
46. Wertheim, M.S. Fluids with Highly Directional Attractive Forces. III. Multiple Attraction Sites. *J. Stat. Phys.* 1986a, 42, 459.
47. Wertheim, M.S. Fluids with Highly Directional Attractive Forces. IV. Equilibrium Polymerization. *J. Stat. Phys.* 1986b, 42, 477.
48. Yokozeki, A. Solubility of Refrigerants in Various Lubricants. *Int. J. Thermophys.* 2001, 22, 1057-1071.
49. Zhelezny, P.V., Zhelezny, V.P., Scripov, V.P. Determination of the pseudocritical parameters for refrigerant/oil solutions. *Fluid Phase Equilib.* 2003, 212, 285-302.

III – Evaluation of Existing Viscosity Models

3.1 – Introduction: viscosity

If a shearing stress is applied to any portion of a confined fluid, the fluid will move with a velocity gradient with its maximum velocity at the point where the stress is applied. If the local shear stress at any point is divided by the velocity gradient, the radio obtained is defined as the viscosity of the medium. Viscosity is a measured of the internal fluid friction, which tends to oppose any dynamic change in the fluid motion. In an explicit way the shear stress is defined as:

$$\tau = \eta \frac{\partial u}{\partial h} \qquad (3.1)$$

which is Newton's Law of viscosity, where $\partial u/\partial h$ is the velocity gradient or the shear rate. Fluids following Newton's Law are called Newtonian fluids. The viscosity of these fluids is independent of the shear stress and the velocity gradient, but depends on conditions of state (pressure p, volume v, and temperature T). Some fluids called non-Newtonian, do not follow Newton's law, and the viscosity depends on the shear stress and the shear rate. Non-Newtonian fluids may be classified as Bingham plastic, dilatant, and pseudoplastic fluids. Bingham plastic fluids such as drilling mud and tooth paste require a punch in order to move, because the shear stress needs to exceed a certain minimum value. Pseudo-plastic fluids such as polymer melts, gelatine, and mayonnaise become less viscous with increasing shear rate. The reason is that long molecules become better oriented at high shear rates, resulting in a reduction of the viscosity (higher mobility). For dilatant fluids the opposite happens – the fluid becomes more viscous with increasing shear rate. Slurries and suspensions with a high concentration of particles belong to the dilatant fluids. The behavior of the shear stress as a function of the shear rate (velocity gradient) is shown in Figure 3.1. Non-Newtonian fluids, in spite of being of great interest for many industrial applications, will not be considered further since the fluids considered in this work are assumed to behave as Newtonian fluids.

Since viscosity is defined as a shearing stress divided by a velocity gradient, it should have the dimensions of mass/ (length) (time). Viscosities are expressed in poises, centipoises, micropoises, etc. A poise (P) denotes a viscosity of 0.1 N.s/m². The following conversion factors apply to viscosity units:

1 P = 100 cP = 1×10⁶ μP = 0.1 N.s/m² = 1 g/(cm.s) = 0.1 Pa.s = 100 mPa.s

The kinematic viscosity is the ratio of the viscosity to the density. With viscosity in Pa.s and the density of kg/m³, the unit of kinematic viscosity is the stokes, with the units m²/s.

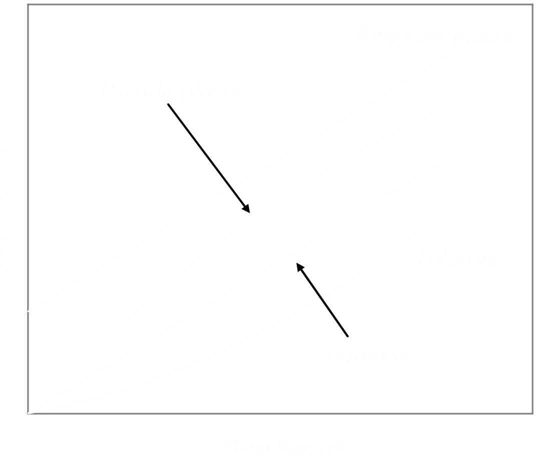

Figure 3.1 – Shear stress versus shear rate (velocity gradient) for Newtonian and non-Newtonian fluids.

In this Chapter, some existing viscosity models are presented and compared. Several models for predicting the viscosity of pure components and mixtures are available in abundance in the literature with excellent reviews available by Poling *et al.* (2000), Monnery *et al.* (1995), and Mehrotra *et al.* (1996). These models describe the viscosity of a fluid as a function of temperature, volume and composition, and every year new models or modifications of existing ones are derived and proposed. The available viscosity models range from highly theoretical models to simple empirical correlations. Many of these models are only suitable for predicting either the liquid or the gas phase viscosity. In addition, most of the viscosity models have been derived for hydrocarbons and their mixtures. The extension of these studies to refrigerants, lubricants and their mixtures is not so prolific. For this reason the aim of this chapter is to study the applicability of existing viscosity models to pure refrigerants and pure lubricants. Some refrigerant mixtures will also be included in this chapter.

3.2 – Viscosity behavior versus temperature, pressure and composition

The viscosity of a fluid changes with temperature, pressure and composition. In the gaseous state the viscosity is much lower than in the liquid state. The reason is that the distance between the molecules in the gas phase is greater than in the liquid phase. In the liquid phase, the transfer of momentum is mainly due to intermolecular effects between the dense packed molecules, whereas in the gaseous phase the momentum is transferred by collisions of the freely moving molecules.

Figure 3.2 shows a qualitative representation of the viscosity behavior of pure fluids as a function of the reduced pressure for various isotherms. At the saturation pressure, a jump in the viscosity is observed for reduced temperatures below 1.0, when going from the vapor phase to the liquid phase. When the pressure approaches zero for a given temperature, the viscosity approaches the dilute gas limit. In general, the viscosity of a fluid in the gaseous phase increases with increasing temperature, whereas the viscosity of liquids decreases with increasing temperature. In all cases, the viscosity increases with increasing pressure. However, for dense supercritical fluids at a constant reduced pressure above 1.0, the viscosity decreases with increasing temperature down to a minimum and then increases with the temperature, see Figure 3.2. As the pressure is increased this minimum is shifted towards higher temperatures. At very high temperatures, the viscosity of dense supercritical fluids will only be slightly higher than the value at the dilute gas limit.

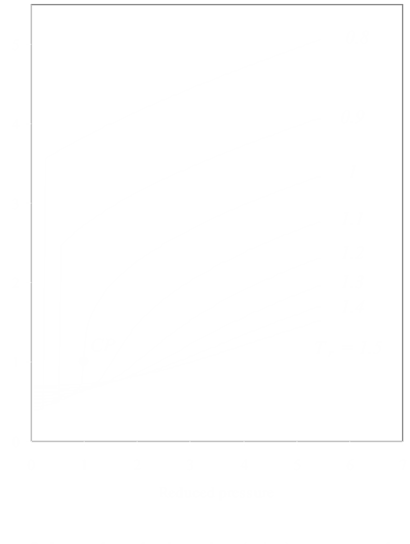

Figure 3.2 General illustration of the reduced viscosity (η/η_c) versus reduced pressure (P/P_c) for various reduced temperatures (T/T_c). CP is the critical point.

When the critical point is approached the derivative of the viscosity with respect to the pressure tends to infinite. In addition, in the vicinity of the critical point an abnormal viscosity behavior is observed, when the viscosity is plotted against the density for different isotherms very close to the critical temperature. The viscosity tends to infinite so that its value is larger than would otherwise be expected. This is illustrated in Figure 3.3 for CHF_3 (Yokoyama and Takahashi, 1997) and the similar behavior has been found and observed for nitrous oxide (Yokoyama *et al.* 1996), carbon dioxide (Iwasaki and Takahashi, 1981), nitrogen (Zozulya and Blagoi, 1975) and xenon (Strumpf *et al.* 1974). The abnormal viscosity behavior disappears with increasing temperature and it is only important very close to the critical isotherm. For thermal conductivity, this abnormal critical behavior is much more pronounced than for the viscosity.

For mixtures the viscosity behavior versus temperature, pressure, and composition is more complex than for pure fluids. The viscosity of mixtures can vary in different ways with composition at constant temperature and pressure. For example, for gaseous mixtures of refrigerants either a minimum (Yokoyama *et al.* 2004) or a maximum (Yokoyama *et al.* 2001) can be found when plotting viscosity versus temperature at constant pressure. Monotonical viscosity behavior can be also observed, and an as example of refrigerant mixtures showing this behavior the paper by Yokoyama *et al.* 2000 can be mentioned.

Figure 3.3 – Viscosity behavior of CHF_3 in the vicinity of the critical point for two isotherms close to the critical one (T_c = 298.97 K). Experimental points are taken from Yokoyama and Takahashi (1997).

3.3 - Estimation of gas viscosities

Gas phase viscosity is primarily a function of momentum transfer by translation of the molecules with relatively few collisions as has been described by kinetic theory of gases. Essentially all gas viscosity estimation techniques are based on either the Chapman-Enskog theory or the law of corresponding states. Both approaches are discussed below. However, before proceeding the theory of Chapman and Enskog will be briefly discussed.

3.3.1 – The dilute gas viscosity: theoretical approach

The dilute gas viscosity is defined as the viscosity at the zero density limit and is based on the kinetic theory of gases. This is described in detail in many references, of which two of the most well known are Hirschfelder *et al.* (1954) and Chapman and Cowling (1939). The simplest kinetic model for gases assumes all molecules to be noninteracting rigid spheres of diameter σ and mass *m* moving at some mean velocity and colliding with other such molecules after moving a "mean free path" distance. Simple kinetic theory gives the following expression for dilute gas viscosity:

$$\eta_0 = \frac{2}{3\pi^{3/2}} \frac{\sqrt{(mkT)}}{\sigma^2} \tag{3.2}$$

If the molecules attract or repel one another due to intermolecular forces, the Chapman-Enskog theory is typically applied. The Chapman-Enskog theory treats the interactions between colliding molecules in detail. In general terms, the solution for the viscosity is written:

$$\eta_0 = \frac{5}{16\pi^{1/2}} \frac{\sqrt{(mkT)}}{\sigma^2 \Omega^*} \tag{3.3}$$

which is very similar to the simplified treatment except for the constant and the inclusion of the collision integral Ω^*. The collision integral has been determined for the Lennard-Jones intermolecular potential and empirically correlated by Neufeld *et al.* (1972):

$$\Omega^* = \frac{1.16145}{T^{*0.14874}} + \frac{0.52487}{Exp\left(0.77320\,T^*\right)} + \frac{2.16178}{Exp\left(2.43787\,T^*\right)} \\ -6.435\times10^{-4}\,T^{*0.14874}\,Sin\left(18.0323\,T^{*-0.76830} - 7.27371\right) \tag{3.4}$$

with

$$T^* = \frac{kT}{\varepsilon} \tag{3.5}$$

where ε is the minimum of the pair potential energy. In units of μP, Equation 3.3 may be written as:

$$\eta_0 = 26.693\,\frac{\sqrt{(MT)}}{\sigma^2 \Omega^*} \tag{3.6}$$

with *M* in g/mol, *T* in K, and σ in Å. To calculate viscosity from Equations 3.5 or 3.6, parameters σ and ε/*k* are required; these must be obtained from the same compilation data because both parameters are regressed from viscosity data simultaneously.

3.3.2 – Method of Chung et al.: semi-theoretical approach

The kinetic theory of gases and the Chapman-Enskog theory have formed the basis of achieving accurate semi-theoretical models for predicting the viscosity of gases at low pressure. Based on the this theory and the empirical expression for the reduced collision integral (Neufeld *et al.*, 1972), Chung *et al.* (1988) derived an empirical dilute gas viscosity model incorporating structural effects in order to apply the model in polyatomic, polar, and hydrogen bonding fluids over wide ranges of temperature. This model is able of predicting the dilute gas viscosity of several polar and non-polar fluids within an uncertainty of 1.5%. Chung *et al.* (1988) employed Equation 3.6 with:

$$\sigma = 0.809\, v_c^{1/3} \qquad (3.7)$$

$$\frac{\varepsilon}{k} = \frac{T_c}{1.2593} \qquad (3.8)$$

Thus, combining Equations 3.6, 3.7, and 3.8 after simplification and multiplication by F_c result in:

$$\eta_0 = 40.785\, \frac{\sqrt{MT}}{v_c^{2/3}\, \Omega^*} F_c \qquad (3.9)$$

To calculate the collision integral, the correlation of Neufeld *et al.* (1972) is used. The dilute gas viscosity obtained by Equation 3.9 has units of microPoise (μP), when the temperature *T* is in K and the critical volume v_c in cm³/mol, *M* is the molecular weight and T_c the critical temperature. The empirical expression for the F_c factor is defined as

$$F_c = 1 - 0.2756\,\omega + 0.059035\,\mu_r^4 + \chi \qquad (3.10)$$

where ω is the acentric factor, μ_r a dimensionless dipole moment ($\mu_r = 131.3\mu/(v_c T_c)^{0.5}$, with μ in debyes, T_c in K, and v_c in cm³/mol), and χ a correction factor for the hydrogen bonding effects in associating substances, such as alcohols.

3.3.3 – Corresponding states method: empirical approach

From an Equation such as 3.6, if one associates σ³ with v_c which is subsequently proportional to RT_c/P_c a reduced viscosity can be defined and a corresponding states relationship is established.

$$\eta_r = \xi\eta = f(T_r) \tag{3.11}$$

$$\xi = 0.176\left(\frac{T_c}{M^3 P_c^4}\right)^{1/6} \tag{3.12}$$

where ξ = viscosity reduction parameter $(\mu P)^{-1}$ when T_c is in Kelvin, M is in g/mol and P_c is in bar.

By dimensional analysis, Stiel and Thodos (1961, 1962) developed empirical corresponding states equations for nonpolar and polar gases. Although various empirical versions of Equation 3.11 have been proposed, Poling *et al.* (2000) recommended the method of Lucas (1980) which includes a correction factor for polar fluids based on reduced dipole moment, μ_r.

$$\eta_0\xi = \left[0.807 T_r^{0.618} - 0.357\exp(-0.449T_r) + 0.340\exp(-4.058T_r) + 0.018\right] F_P^0 F_Q^0 \tag{3.13}$$

where F_P^0 and F_Q^0 are correction factors to account for polarity or quantum effects. To obtain F_P^0 a reduced dipole moment is required. Lucas (1980) defines this quantity as:

$$\mu_r = 52.46\frac{\mu^2 P_c}{T_c^2} \tag{3.14}$$

where μ is in debyes, P_c is in bars, and T_c is in Kelvin. Then F_P^0 values are found as:

$$\begin{aligned} F_P^0 &= 1 && 0.000 \le \mu_r < 0.022 \\ F_P^0 &= 1 + 30.55(0.292 - Z_c)^{1.72} && 0.022 \le \mu_r < 0.075 \\ F_P^0 &= 1 + 30.55(0.292 - Z_c)^{1.72}\left|0.96 + 0.1(T_r - 0.7)\right| && 0.075 \le \mu_r \end{aligned} \tag{3.15}$$

The factor F_Q^0 is used only for the quantum gases He, H_2, and D_2.

3.3.4 – Methods for mixtures

The rigorous kinetic theory of Chapman and Enskog can be extended to determine the viscosity of low-pressure multicomponent mixtures. The final expressions are quite complicated and rarely used to estimate mixture viscosities. Two well-known simplifications of the rigorous theoretical expressions are shown below. Wilke (1950) derived the following mixing rule based on the kinetic gas theory with several simplifications in order to estimate the dilute gas viscosity of a mixture.

$$\eta_{mix} = \sum_{i=1}^{n}\frac{y_i\eta_i}{\sum_{j=1}^{n} y_j\phi_{ij}} \tag{3.16}$$

with

$$\phi_{ij}=\frac{\left[1+\left(\frac{\eta_{0,i}}{\eta_{0,j}}\right)^{0.5}\left(\frac{M_j}{M_i}\right)^{0.25}\right]^2}{\frac{4}{\sqrt{2}}\left(1+\frac{M_i}{M_j}\right)^{0.5}} \quad (3.17)$$

Another simple mixing rule is the calculation procedure proposed by Herning and Zipperer (1936)

$$\eta_{0,mix}=\frac{\sum_{i=1}^{n}x_i\,\eta_{0,i}\sqrt{M_i}}{\sum_{i=1}^{n}x_i\sqrt{M_i}} \quad (3.18)$$

These mixing rules are totally predictive in the sense that they only require the molecular weight, the dilute gas viscosity, and the mole fraction of the pure compounds. Wilke mixing rule is capable of describing the right viscosity behavior of gas mixtures showing a nonlinear and non-monotonical behavior or attaining a maximum, when the viscosity is plotted versus the composition at constant temperature. The mixing rule by Herning and Zipperer has been found suitable for estimating the dilute gas viscosity of hydrocarbon mixtures.

3.4 - Estimation of dense fluid viscosities

In dense phases, the momentum transfer is dominated by collisions and interacting force fields between the densely packed molecules. The theoretical description of liquids is difficult due to these intermolecular forces, which consist of short range effects such as repulsions and hydrogen bonding, and long range effects such as attractions. Inclusion of these effects in models is typically through a simplified treatment. Most theoretical models of dense gas or liquid phase are based on statistical mechanics. A further complication is the structure and degree of disorder between the molecules. There is no widely accepted simple theoretical method to calculate viscosity of liquids. The two models described in this section are: the hard-sphere approach, which has a semi-theoretical background, and the self-referencing method, which is entirely empirical.

3.4.1 – The hard-sphere viscosity scheme: semi-theoretical approach

This model has been developed by Dymond and Awan (1989) and Assael *et al.* (1990), (1992a) and (1992b) for the simultaneous correlation of self-diffusion, viscosity and thermal conductivity of dense fluids over wide ranges of pressure and temperature. The transport coefficients of real dense fluids expressed in terms of $v_r = v/v_0$ with v the molar volume and v_0 the close-packed volume defined as $v_0 = N_A\sigma^3/2^{1/2}$ where N_A is Avogadro's constant and σ the hard-core diameter, are assumed to be directly proportional to the values given by the exact hard-sphere theory.

For rough spherical molecules at high densities, Chandler (1975) showed that the self-diffusion coefficient and the viscosity were directly proportional to the smooth hard sphere values. This idea has been extended by Dymond and Awan (1989) and Assael *et al.* (1990), (1992a) and (1992b) by assuming that a corresponding states relationship exists between the experimental transport properties of rough non-spherical molecules and the smooth hard-sphere values (subscript shs). Thus, the experimental viscosity can be defined as:

$$\eta_{exp} = R_\eta\,\eta_{shs} \qquad (3.19)$$

where the proportionality factor R_η, described as the roughness factor, accounts for molecular roughness and departure from molecular sphericity. The roughness factor is assumed to be independent of both temperature and density. The exact smooth hard-sphere transport coefficient for viscosity is given by the product of the value from Enskog's theory η_E (Enskog, 1922) and the computed correction from molecular dynamic simulations to Enskog's theory $(\eta/\eta_E)_{MD}$:

$$\eta_{shs} = \eta_E\left(\eta/\eta_E\right)_{MD} \qquad (3.20)$$

Instead of calculating the transport coefficients directly, which requires knowledge of the core size σ as well of the roughness factor, Dymond (1973) has shown that it is convenient to express the viscosity as reduced quantities:

$$\eta^*_{exp} = R_\eta\,\eta^*_{shs} = R_\eta\left[\frac{\eta_{shs}}{\eta_0}\right]\left[\frac{v}{v_0}\right]^{2/3} \qquad (3.21)$$

where subscript zero refers to the low-density hard-sphere coefficient in the first-order approximation. The expression for the low-density viscosity is given by Equation 3.5. The reduced smooth hard-sphere viscosity can be obtained from experimental values after substitution of the hard-sphere expressions, which gives:

$$\eta^*_{exp} = \frac{\eta^*_{exp}}{R_\eta} = \frac{16\sqrt{\pi}}{5}(2N_A)^{1/3}\left[\frac{1}{MRT}\right]^{1/2}\frac{\eta_{exp}V^{2/3}}{R_\eta} \qquad (3.22)$$

In order to determine R_η and v_0 for a given temperature a plot of $\mathrm{Log}_{10}(\eta^*_{exp})$ versus $\mathrm{Log}_{10}(v)$ from experiment is superimposed on the theoretical plot of $\mathrm{Log}_{10}(\eta^*_{exp})$ versus $\mathrm{Log}_{10}(v/v_0)$, by vertical and horizontal adjustment. The universal curve for viscosity was originally developed for n-alkanes (Assael *et al.* 1992a), but it has also been applied to aromatic hydrocarbons (Assael *et al.* 1992d), alcohols (Assael *et al.* 1994) and a few refrigerants (Assael *et al.* 1995). The universal curves were expressed in terms of the reduced volume $v_r = v/v_0$:

$$\mathrm{Log}_{10}\left[\frac{\eta^*_{exp}}{R_\eta}\right] = \sum_{i=0}^{7} a_{\eta i}\left(\frac{1}{v_r}\right)^i \qquad (3.23)$$

where

$$\begin{aligned} a_{\eta 0} &= 1.0945 & a_{\eta 4} &= 797.6900 \\ a_{\eta 1} &= -9.26324 & a_{\eta 5} &= -1221.9770 \\ a_{\eta 2} &= 71.0385 & a_{\eta 6} &= 987.5574 \\ a_{\eta 3} &= -301.9012 & a_{\eta 7} &= -319.4636 \end{aligned} \qquad (3.24)$$

The $a_{\eta i}$ coefficients are universal, independent of the chemical structure of the compound. For various pure compounds it has been observed that v_0 is temperature dependent, whereas R_η is temperature independent for pseudo-spherical molecules. For molecules that either depart too much from sphericity or have hydrogen bonds, such as alcohols (Assael *et al.* 1994), R_η shows a temperature dependency.

In order to apply the hard-sphere scheme to mixtures, Assael *et al.* (1992c) introduced the following linear mixing rules:

$$V_{0,mix} = \sum_{i=1}^{N} x_i V_{0,i} \qquad R_{\eta,mix} = \sum_{i=1}^{N} x_i R_{\eta,i} \qquad M_{mix} = \sum_{i=1}^{N} x_i M_i \qquad (3.25)$$

3.4.2 - The self-referencing model: empirical approach

Kanti *et al.* (1989) derived a self-reference model in order to calculate the viscosity of liquid petroleum fluids. For this kind of fluids, it is difficult to use equations based on physical properties such as molar mass, critical pressure, and temperature or acentric factor since, for mixtures, they have to be known for each one of the components. The method does not involve molar mass or any other physical properties or critical parameters. It can be applied without restriction to pure substances or to chemically very rich systems such as petroleum cuts. The model is based on the approach derived by Kashiwagi and Makita (1982). In this approach the liquid viscosity of a fluid versus pressure for a given temperature is related to the measured viscosity at atmospheric pressure and the corresponding temperature. In this way, it is assumed that the measured viscosity value contains within itself sufficient information about the studied fluid. The proposed model of Kashiwagi and Makita (1982) is presented below:

$$Ln\left(\frac{\eta(p,T)}{\eta(p_0,T)}\right) = E\,Ln\left(\frac{D+p}{D+p_0}\right) \qquad (3.26)$$

where D and E are adjustable parameters dependent on the temperature and the fluid and $p_0 = 0.1$ MPa. Consequently, measurements of the viscosity at atmospheric pressure are required for each temperature. In order to avoid measuring the viscosity at atmospheric pressure for every selected temperature Kanti *et al.* (1989) introduced the following expression adapting the relationship by van Velzen *et al.* (1972):

$$\eta(p_0,T) = \eta(p_0,T_0)\,Exp\left[\alpha\left(\frac{1}{T}-\frac{1}{T_0}\right)\right] \qquad (3.27)$$

with

$$\alpha = g\,y_0^2 + h\,y_0 + i \qquad (3.28)$$

and $y_0 = \ln[\,\eta(p_0,T_0)]$ where T_0 and p_0 are the chosen reference temperature and pressure respectively. In addition, Kanti *et al.* (1989) also derived expressions for the temperature dependent D and E parameters:

$$D + p_0 = d\,y^2 + e\,y + f \qquad (3.29)$$

$$E = a\,y^2 + b\,y + c \qquad (3.30)$$

where $y = \ln[\,\eta(p_0,T)]$. By substituting Equations 3.27, 3.28, 3.29 and 3.30 into Equation 3.26 the approach by Kanti *et al.* (1989) is obtained:

$$Ln\left(\frac{\eta(p,T)}{\eta(p_0,T_0)}\right) = \left(a\,y^2 + b\,y + c\right)Ln\left(1+\frac{(p-p_0)}{d\,y^2 + e\,y + f}\right) + \left(g\,y_0^2 + h\,y_0 + i\right)\left(\frac{1}{T}-\frac{1}{T_0}\right) \qquad (3.31)$$

This equation is used with p in MPa, T_0 and T in K and $\eta(p_0,T_0)$ in mPa.s and $y = y_0 + (g\,y_0^2 + h\,y_0 + i)(1/T - 1/T_0)$.

The original parameters in the model (a, b, c, d, e, f, g, h, i) were determined by an analysis based on n-alkanes (C_7, C_{10}, C_{12}, C_{14}, C_{15}, C_{16}, C_{18}) and alkyl benzenes (butyl, hexyl, octyl). The only external property required in this viscosity approach is the measured viscosity at T_0 and p_0. Afterwards, Canet *et al.* (2002) and Comuñas *et al.* (2004) have shown that in order to use this method with synthetic mixtures of known composition, the nine parameters should be adjusted for each pure compound. It must be noticed that when a value for $\eta(p_0,T_0)$ is chosen, this value must be kept constant.

Extension to mixtures is performed by use of the following mixing rules

$$\delta_{mix} = \sum_{i=1}^{n} x_i\,\delta_i \qquad (3.32)$$

where δ_{mix} represents each one of the parameters (a, b, c, d, e, f, g, h, i), and x_i is the mole fraction of compound i. This model has the disadvantage that is not totally predictive for mixtures since it requires the knowledge of one experimental viscosity value, $\eta(p_0,T_0)$, for the studied composition.

3.5 - Models applicable to both liquids and gases

The models described in this section can be applied to both liquid and gas phases and have been developed to predict the viscosity of mainly hydrocarbons and their mixtures. The studied models are: the free-volume, and the TRC model, and a viscosity model based on a cubic EoS. These approaches have different background ranging from semitheoretical to entirely empirical.

3.5.1 - The free-volume viscosity model: semi-theoretical approach

Recently an approach in order to model the viscosity of Newtonian fluids (in the condensed phase) with small molecules has been proposed by Allal *et al.* (2001a and 2001b). This approach connects viscosity to molecular structure via a representation of the free volume fraction. In its first version the model could be only applied to dense fluids but a version valid for low density states has also been developed (Allal *et al.* 2001c). In this last version the dynamic viscosity has the following form:

$$\eta = \eta_0 + \Delta\eta \qquad (3.33)$$

where the first term η_0 is a dilute gas contribution and the second one $\Delta\eta$ is the dense gas contribution. The dilute gas viscosity η_0 is defined as the viscosity at the dilute gas limit and, for several fluids can be accurately represented by the Chung *et al.* (1988) model. It has been demonstrated (Allal *et al* 2001c) that the viscosity in the dense state can be written as:

$$\Delta\eta = \frac{\rho N_A L^2 \zeta}{M} \qquad (3.34)$$

where ρ is the density, M is the molar mass, N_A is Avogadro's constant, L an average characteristic molecular quadratic length, and ζ the friction coefficient of a molecule. The free-volume model of Doolittle (1951) is defined as

$$\Delta\eta = A\,Exp\left(\frac{B}{f_v}\right) \qquad (3.35)$$

where the free-volume fraction can be defined as $f_v = (v - v_0)/v_0$ with v the molecular volume and v_0 the hard-core volume. Allal *et al.* (2001c) defined the free-volume fraction by

$$f_v = \left(\frac{RT}{E}\right)^{\frac{3}{2}} \qquad (3.36)$$

To establish this relation it is assumed that the molecule moves in a potential field controlled by the intermolecular energy E due to the neighboring molecules. This intermolecular energy can be approximated (Allal *et al.* 2001c) by $E = E_0 + PM/\rho$ where the term PM/ρ is connected to the energy necessary to form the vacant vacuums available for the diffusion of the molecules and the term $E_0 = \alpha\rho$ is connected to the energy barrier that the molecule has to exceed in order to diffuse. With these hypotheses and using the Doolittle result (1951), Allal *et al.* (2001c) have proposed the following expression for the friction coefficient:

$$\zeta = \zeta_0\,Exp\left(\frac{B}{f_v}\right) \qquad (3.37)$$

where B characterizes the free-volume overlap and

$$\zeta_0 = \frac{E}{N_A l_f}\left(\frac{M}{3RT}\right)^{\frac{1}{2}} \qquad (3.38)$$

where l_f is the dissipation length of the energy E. Finally, the general expression of the free-volume viscosity model is obtained by combining Equations 3.34, 3.36, 3.37, and 3.38 and shown below

$$\eta = \eta_0 + \frac{\rho l_f\left(\alpha\rho + \frac{PM}{\rho}\right)}{(3RTM)^{\frac{1}{2}}}\,Exp\left[B\left(\frac{\alpha\rho + \frac{PM}{\rho}}{RT}\right)^{\frac{3}{2}}\right] \qquad (3.39)$$

where the coefficient α, the coefficient B and the length (L^2/l_f) are three adjustable parameters of each fluid. The unit of the viscosity is Pa.s, when all other units are kept in SI units. This model has been shown to deliver accurate viscosity estimations from very low to high pressures (Allal *et al.* 2001c) for pure fluids. For mixtures, the model can be also applied using the following mixing rules:

$$\frac{1}{B_{mix}}=\sum_{i=1}^{n}\frac{x_i}{B_i} \qquad l_{mix}=\sum_{i=1}^{n}x_i l_i \tag{3.40}$$

$$\alpha_{mix}=\sum_{i=1}^{n}\sum_{j=1}^{n}x_i x_j\left(\alpha_i \alpha_j\right)^{\frac{1}{2}} \qquad M_{mix}=\sum_{i=1}^{n}x_i M_i \tag{3.41}$$

Equations 3.16 or 3.18 can be used for the dilute gas viscosity term.

3.5.2 – LBC model: empirical approach

In petroleum engineering a commonly used empirical correlation based on the residual viscosity concept is the correlation by Jossi *et al.* (1962), because it can be applied to both gases and liquids. However, this approach is generally referred to as the Lohrence-Bray-Clark (LBC) correlation (1964), because Lohrenz *et al.* introduced a procedure for calculating the viscosity of hydrocarbon mixtures and reservoir fluids using the same equation and coefficients originally derived by Jossi *et al.* (1962) for pure fluids. The residual viscosity concept is based on the empirical observation that the difference between the viscosity of a dense gas or a liquid and that of the dilute gas is approximately independent of temperature and primary a function of density.

Based on a dimensional analysis, Jossi *et al.* (1962) derived the following equation:

$$(\eta-\eta_0)\xi=f(\rho_r) \tag{3.42}$$

Where ρr the reduced density (ρ/ρc) and ξ is given by

$$\xi=T_c^{1/6}\,M^{-1/2}\,P_c^{-2/3} \tag{3.43}$$

Jossi *et al.* (1962) established that experimental data from gas to liquid phases for 11 relatively non-polar substances fell equally on a single curve which was fitted to the following equation ($0.02 < \rho_r < 3.0$)

$$\left[(\eta-\eta_0)\xi+10^{-4}\right]^{\frac{1}{4}}=a_0+a_1\rho_r+a_2\rho_r^2+a_3\rho_r^3+a_4\rho_r^4 \tag{3.44}$$

where η is the fluid viscosity in mPa.s when the units of T_c and P_c are K and atm respectively, along with original coefficients a_i given by Jossi *et al* (1962). Recently, a modification of the LBC model (Al-Syabi *et al.* 2001) has been proposed in which structural and thermal effects are incorporated. The modified LBC model is given below

$$\left[(\eta-\eta_0)\xi+10^{-4}\right]^{\frac{1}{4}}=h_0+h_1\rho_r+h_2T_r^{g_1}M^{g_2}\rho_r^2+h_3T_r^{g_3}M^{g_4}\rho_r^3+h_4T_r^{g_5}M^{g_6}\rho_r^4 \tag{3.45}$$

where the b_i, $q_{i,}$ and s_i coefficients are given in Al-Syabi *et al.* (2001). These coefficients are adjusted for light compounds and n-alkanes up to n-octadecane. Hereafter this version of the LBC model will be referred as "LBC-mod".

In order to apply these methods to mixtures, the mixing rules introduced by Lohrenz *et al.* (1964) to estimate the dilute gas viscosity and the viscosity reducing parameter are used

$$\xi_{mix} = \left(\sum_{i=1}^{n} x_i T_{ci}\right)^{1/6} \left(\sum_{i=1}^{n} x_i M_i\right)^{-1/2} \left(\sum_{i=1}^{n} x_i P_{ci}\right)^{-2/3} \qquad (3.46)$$

$$\eta_{0,mix} = \frac{\sum_{i=1}^{n} x_i \eta_{0,i} M_i^{1/2}}{\sum_{i=1}^{n} x_i M_i^{1/2}} \qquad (3.47)$$

$$\rho_{c,mix} = \left(\sum_{i=1}^{n} \frac{x_i V_{ci}}{M_i}\right)^{-1} \qquad (3.48)$$

The mixing rule for the dilute gas viscosity is the mixing rule proposed by Herning and Zipperer (1936), Equation 3.18. The dilute gas viscosity of the pure components is obtained with the following expressions proposed by Stiel and Thodos (1961) and adapted by Jossi *et al.* (1962)

$$\eta_{0,i} = \frac{34\times10^{-5}\, T_{r,i}^{0.94}}{\xi_i} \qquad T_{r,i} \le 1.5$$
$$\eta_{0,i} = \frac{17.78\times10^{-5}\left(4.58\, T_{r,i}^{0.94} - 1.67\right)^{5/8}}{\xi_i} \qquad T_{r,i} > 1.5 \qquad (3.49)$$

3.5.3 – Viscosity equations of state: empirical approach

This concept is based on the phenomenological similarity observed between *p-v-T* and *p-η-T* surfaces resulting in a viscosity correlation which is an explicit function of temperature and pressure. This similarity was pointed out by Phillips early in 1912 (Phillips, 1912). The method can be applicable both for the gas and the liquid phase. Little and Kennedy (1968) derived the first EoS based viscosity model from the van der Waals EoS by interchanging *p* and *T*, replacing *v* with *η*. Additionally, the gas constant *R* and the *a* and *b* parameters were replaced by empirical functions for each pure compound. Recently, Guo *et al.* (1997) used the same procedure in order to derive two new viscosity models based on cubic EoS, the first model is based on the Patel-Teja EoS (Patel and Teja, 1982) and the second on the Peng-Robinson EoS (Peng and Robinson, 1976). In this work the modified PR viscosity model by Guo (1998) is presented and will be referred as the PRVIS model. The mathematical formulation of the model is given below:

$$T=\frac{rP}{\eta-b^{*}}-\frac{a}{\eta(\eta+b)+b(\eta-b)} \qquad (3.50)$$

$$a=0.45724\frac{r_c^2P_c^2}{T_c} \qquad (3.51)$$

$$b=0.07780\frac{r_cP_c}{T_c} \qquad (3.52)$$

$$r=r_c\,\tau(T_r,P_r) \qquad (3.53)$$

$$r_c=\frac{\eta_cT_c}{P_cZ_c} \qquad (3.54)$$

$$b^{*}=b\varphi(T_r,P_r) \qquad (3.55)$$

where T_c, P_c, and Z_c are the critical pressure, critical temperature and critical compressibility factor, respectively. The critical viscosity η_c is obtained by the Uyehara and Watson (1944) equation

$$\eta_c=7.7\times10^{-4}\frac{M^{1/2}P_c^{2/3}}{T_c^{1/6}} \qquad (3.56)$$

The unit of η_c is mPa.s when the temperature is in K and the pressure in atm. The τ and φ parameters are estimated using the following expressions:

$$\tau(T_r,P_r)=\frac{1}{\left(1+Q_1\left(\sqrt{P_rT_r}-1\right)\right)^2} \qquad (3.57)$$

$$\varphi(T_r,P_r)=Exp\left[Q_2\left(\sqrt{T_r}-1\right)\right]+Q_3\left(\sqrt{P_r}-1\right)^2 \qquad (3.58)$$

and the Q parameters are determined in the following way

For ω < 0.3

$$Q_1=0.829599+0.350857\,\omega-0.747680\,\omega^2$$

$$Q_2=1.94546-3.19777\,\omega+2.80193\,\omega^2 \qquad (3.59)$$

$$Q_3=0.299757+2.20855\,\omega-6.64959\,\omega^2$$

For ω > 0.3

$$Q_1=0.956763+0.192829\,\omega-0.303189\,\omega^2$$

$$Q_2=-0.258789-37.1071\,\omega+20.5510\,\omega^2 \qquad (3.60)$$

$$Q_3=5.16307-12.8207\,\omega+11.0109\,\omega^2$$

where ω is the acentric factor. To apply this method to mixtures the following mixing rules are used:

$$a_{mix} = \sum_{i=1}^{n} x_i \, a_i \tag{3.61}$$

$$b_{mix} = \sum_{i=1}^{n} x_i \, b_i \tag{3.62}$$

$$b^*_{mix} = \sum_{i=1}^{n} \sum_{j=1}^{n} x_i \, x_j \sqrt{b^*_i b^*_j} \tag{3.63}$$

$$r_{mix} = \sum_{i=1}^{n} x_i \, r_i \tag{3.64}$$

The calculated viscosity by the PRVIS model has units of mPa.s when the pressure and critical pressure are in atm. An advantage of the PRVIS model is that the density of the considered fluid is not required as an input. The only required parameters are the critical constants along with the mole fractions in the case of mixtures.

3.6 - The dilute gas viscosity: results

The performance of the dilute gas viscosity models by Chung *et al.* (1988), Equation 3.9, and by Lucas (1980), Equation 3.13, has been evaluated by comparing the calculated dilute gas viscosities with the values reported in the literature for pure refrigerants and refrigerant mixtures. The Chung *et al.* method requires as input data T_c, v_c, M and ω, whereas the Lucas model requires the knowledge of T_c, P_c, Z_c and M. Both models also require the value of μ for polar compounds. It should be noticed that none of the models needs adjustable parameters. The list of refrigerants consists of R12, R13, R14, R32, R124, R125, R134a, and R152a. For each refrigerant the references are given in the Appendix B. The required properties have been taken from Table 1.3 in Chapter 1, and the μ-values from Poling *et al.* (2001). As in the previous chapter, the quantities AAD, Bias, and MDev are used to compare the performance of the models. The obtained AAD and MDev for both models, together with the temperature range, are given in Table 3.1.

Overall, the obtained results for both models are satisfactory. Better results are observed with the Chung *et al.* model, except for R32 and R152a. In Figure 3.4 the viscosity deviations are plotted as function of temperature. It can be seen that almost all the points lay below the zero axis which means that in general both models over predict the viscosity.

Compound	*NP*	*T-range (K)*	*Chung et al.*		*Lucas*	
			AAD (%)	MDev (%)	AAD (%)	MDev (%)
R12	18	303-363	2.19	11.72	3.22	9.62
R13	16	303-363	2.81	7.66	3.68	6.81
R14	77	150-873	6.63	12.02	8.82	14.61
R32	24	225-340	14.65	15.32	11.69	12.61
R124	14	273-333	3.82	5.21	11.23	12.23
R125	24	273-333	3.22	5.58	9.75	12.26
R134a	22	273-333	7.08	9.91	11.18	13.94
R152a	21	273-333	18.68	20.06	9.80	11.48

Table 3.1 – Performance of the Chung *et al.* (1988) and Lucas (1980) models in the low-pressure range. References reported in the Appendix B.

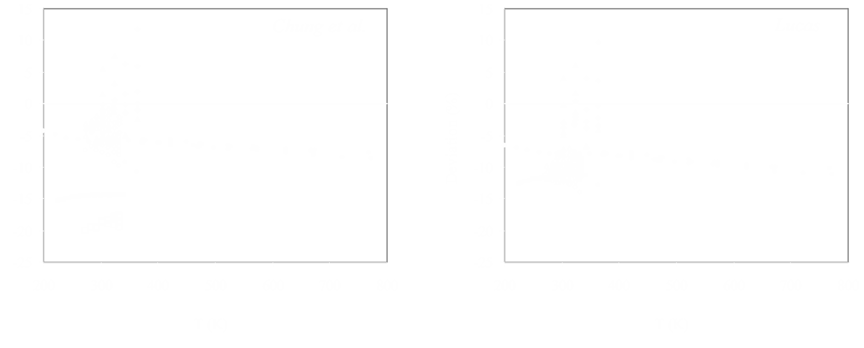

Figure 3.4 – R12 (♦), R13 (▲), R14 (●), R32 (■), R124 (◊), R125 (Δ), R134a (○), and R152a (□) viscosity deviations, $100\times(\eta_{exp}-\eta_{cal})/\eta_{exp}$ as a function of temperature with the Chung *et al.* and Lucas models.

The ability of the two mixing rules introduced in section 3.3.4 (Equations 3.16 and 3.18) has also been tested on 7 refrigerant mixtures at low pressures. The experimental points are taken from the literature (Nabizadeh and Mayinger, 1999, and Bivens *et al.*, 1993) and consist of either binary or ternary mixtures candidates to replace the refrigerant R22. The performance of both mixing rules is combination with the Chung *et al.* model is presented in Table 3.2. A good description of the mixtures is observed with both mixing rules.

Mixture	*NP*	*T-range (K)*	*Wilke*		*Herning et al.*	
			AAD (%)	MDev (%)	AAD (%)	MDev (%)
R-143a/125/134a⁽¹⁾ (52/44/4%)	7	305-392	2.19	2.22	1.40	1.43
R-32/125/143a⁽¹⁾ (23/25/52%)	7	298-398	0.90	1.90	1.68	1.75
R-32/125⁽¹⁾ (50/50%)	9	298-398	0.83	1.54	0.53	1.20
R-143a/125⁽¹⁾ (50/50%)	8	299-401	2.01	2.48	1.17	1.64
R-22/125/290⁽²⁾ (38/60/2%)	7	253-373	0.88	1.81	1.01	2.41
R-22/125/290⁽²⁾ (60/38/2%)	7	253-373	0.93	1.81	0.89	2.41
R-125/143a/134a⁽²⁾ (44/52/4%)	7	253-373	0.99	1.60	0.51	0.81

Table 3.2 – Performance of the Wilke (1950) and Herning and Zipperer (1936) mixing rules in combination with the Chung *et al.* (1988) model at low pressures. References: ⁽¹⁾ Nabizadeh and Mayinger (1999) and ⁽²⁾ Bivens *et al.* (1993). Note: the percentages are given in mass fractions.

3.7 – Dense fluids: results

A few compounds were chosen to test the ability of the hard-sphere viscosity scheme and the self-referencing model. These two models are only applicable to dense phases. The studied compounds consist of four refrigerants: R32, R125, R134a, and R152a, and two lubricants: TriEGDME, and TEGDME (a total of 668 experimental points). For each fluid the references are given in the Appendix B, along with the temperature, pressure, and density ranges, reported accuracy, and the experimental technique used. It should be mentioned that the experimental viscosities reported in Appendix B cover the liquid and the gas phases. In this section only the liquid viscosities have been taken into account.

3.7.1 – The hard-sphere scheme: results and discussions

The hard-sphere model requires as inputs the temperature and molar volumes. For consistency purposes it was decided to employ the experimental densities also reported in the Appendix B. In a recent publication of Assael *et al.* (2000) a value of $R_\eta = 1$ is recommended for all halogenated methane and ethane refrigerants, and the following expression for the close-packed volume:

$$v_0 = \sum_{i=1}^{4} \varphi_i \left(\frac{T}{T_C} \right)^{i-1} \qquad (3.65)$$

For molecules that depart too much from sphericity Assael *et al.* (1994) recommended adjusting R_η against experimental data. For that reason the coefficients R_η and v_0 have been adjusted for pure lubricants, using an expression similar to Equation 3.65 for v_0. The results are presented in Table 3.5. It can be seen that the model gives satisfactory results for refrigerants and lubricants up to high pressures. The percentage of points whose experimental viscosity deviates by more than 2 % correspond to 24 %, being the remaining points inside the range ± 2 % deviation. In the case of refrigerants it was found that the coefficient φ_4 has a negligible effect on the performance of the model. Thus this parameter was set to zero.

Parameter	*R32*	*R125*	*R134a*	*R152a*	*TriEGDME*	*TEGDME*
R_η	1	1	1	1	1.93	2.30
φ_1	32.966	55.239	50.411	47.630	235.32	405.76
φ_2	-18.567	-8.642	-7.290	-16.910	-524.38	-1384.32
φ_3	9.309	-0.441	0.228	5.670	907.45	2690.73
φ_4	0	0	0	0	-591.02	-1846.52

Component	*NP – T and p ranges – Deviations*				
	NP	*T* (K)	*p* (Bar)	AAD (%)	MDev (%)
R32	48	241-343	2-156	1.18	13.54
R125	127	200-420	25-530	2.57	17.27
R134a	326	200-423	1-1400	2.64	14.19
R152a	41	200-333	1-177	1.19	9.85
TriEGDME	63	293-373	1-1400	1.13	2.93
TEGDME	63	293-373	1-1400	1.41	3.46

Table 3.5 – Comparison of calculated viscosities with experimental values, temperature and pressure ranges, and R_η and φ_i (cm³/mol) coefficients. Note: critical temperatures necessary to Equation 3.65 are taken from Table 3.1 for refrigerants and Table 3.3 for lubricants.

3.7.2 The self-referencing model: results and discussions

Comuñas *et al.* (2004) have shown that in order to apply this method to refrigerants and lubricants, the *a*, *b*, *c*, *d*, *e*, *f*, *g*, *h* and *i* parameters should be adjusted for each compound. This method does not require densities as input or knowledge of the critical parameters. It requires, however, one experimental viscosity value for the pressure and temperature of reference. The temperature and pressure of reference is generally chosen to be T_0 = 293.15 K and p_0 = 1 bar (Kanti *et al.* 1989). In the case of refrigerants p_0 is chosen to be higher due to the fact that refrigerants may be at gas state under mentioned conditions (Comuñas *et al.* 2004). The parameters for each component, along with the AAD and MDev are presented in Table 3.4. The temperature, pressure and viscosity of reference are also shown in Table 3.4. Viscosities calculated with the self-reference method agree well with the experimental data, as shown in Table 3.4. In the case of the self-referencing method 87.2 % of all points deviate less than ± 2 % from experimental data.

Parameter	*R32*	*R125*	*R134a*	*R152a*	*TrEGDME*	*TEGDME*
a	3.182	3.328	-0.314	0.427	0.520	0.609
b	19.594	-1.934	-0.644	11.842	-0.414	-0.943
c	47.849	5.219	0.483	77.421	1.475	1.759
d	-779.727	347.732	-4.795	664.932	10.515	10.539
e	-583.510	509.388	47.885	-741.652	-11.807	-11.785
f	3175.239	692.325	136.441	1916.704	191.112	191.126
g	129.645	209.678	71.549	172.549	-17.954	-17.825
h	497.086	481.572	396.013	452.350	446.240	116.326
i	1269.687	1278.456	1348.074	1250.450	1244.919	1244.976

Component	*Reference conditions and deviations*				
	η_0 (mPa.s)	T_0 (K)	p_0 (Bar)	AAD (%)	MDev (%)
R32	0.14	293.20	106	2.35	7.92
R125	0.20	293.20	124	2.17	5.48
R134a	0.30	293.15	200	0.75	3.14
R152a	0.20	293.15	108	1.85	7.07
TrEGDME	2.57	293.15	200	1.38	4.86
TEGDME	4.46	293.15	200	2.15	8.57

Table 3.4 – Comparison of calculated viscosities with experimental values, viscosity, temperature, and pressure of reference, and *a*, *b*, *c*, *d*, *e*, *f*, *g*, *h* and *i* coefficients. Note: temperature and pressure ranges are the same ones as in Table 3.3.

Finally, the good capabilities of hard-sphere and self-referencing models are shown in Figure 3.5, where viscosity deviations are plotted as function of temperature.

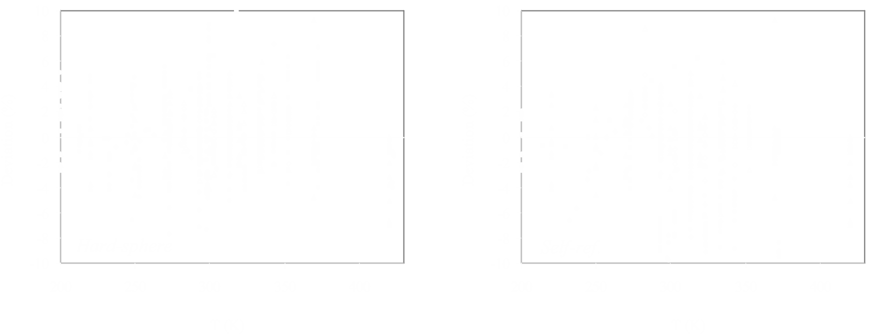

Figure 3.5 – R32 (♦), R125 (▲), R134a (●), R152a (■), TriEGDME (◊), TEGDME (△), viscosity deviations, 100×(η_{exp} - η_{cal})/ η_{exp} as a function of temperature with the hard-sphere and self-referencing models.

3.8 – Liquids and gases

In this section, the performance of the free-volume, LBC, LBC-mod, and PRVIS model is evaluated. Given that these models are applicable to both liquids and gases, all the experimental points reported in Appendix B are used to study and compare the ability of these methods in describing the *p*-*T*-*η* properties. The database contains viscosity data for 17 refrigerants and 2 lubricants over wide ranges of pressure and temperature (a total of 3287 experimental points). In addition, 7 well-defined refrigerant mixtures have been included in this analysis. Again, all the parameters required by the models are obtained from Table 1.1 in Chapter 1 for refrigerants and Table 2.7 in Chapter 2 for lubricants. Further, experimental densities have been used in the free-volume, LBC, and LBC-mod models. Although the parameters in the LBC and LBC-mod models were adjusted to compounds different than refrigerants and lubricants, the original parameters were kept with the aim of studying the predictive capabilities of the models. In the same way, the original parameters in the PRVIS model have been used. In the free-volume model three parameters are needed for each pure compound α, *B*, and *l*. The α, *B*, and *l* parameters obtained by a least squares fit of the experimental data to the model are presented in Table 3.5.

Compound	*NP*	*T-range* (K)	*p-range* (MPa)	*Free-volume* AAD (%)	MDev (%)	*LBC* AAD (%)	MDev (%)
R11	133	242–453	0.1–59	4.83	15.23	23.78	42.06
R12	166	202–433	0.1–59	4.00	25.94	16.82	31.62
R13	475	89–413	0.1–59	5.62	55.00	16.76	119.00
R14	168	150–873	0.1–59	5.00	12.03	7.55	14.18
R22	126	150–383	0.1–30.5	1.97	7.05	10.92	20.70
R32	241	223–423	0.1–15.6	2.15	12.55	3.98	26.98
R113	18	273–353	0.1–2.1	0.30	0.72	44.90	50.89
R114	130	183–363	0.1–59	1.57	8.74	41.85	61.61
R115	102	173–333	0.1–59	6.14	35.94	24.19	54.51
R123	138	288–423	0.1–33	2.75	9.65	18.92	55.41
R124	149	150–420	0.1–56	2.60	16.38	34.61	84.41
R125	294	176–423	0.1–53	2.05	24.25	14.72	39.36
R134a	536	200–423	0.1–140	2.66	8.78	17.37	31.45
R141b	57	200–333	0.95–30	1.91	4.04	32.99	64.86
R142b	134	273–423	0.1–5	1.16	6.68	6.93	10.00
R143a	119	256–423	0.1–9	3.08	11.86	6.72	28.14
R152a	175	200–423	0.1–17.7	1.09	8.22	3.21	19.23
TriEGDME	63	283–423	0.1–100	1.46	4.43	56.96	73.50
TEGDME	63	283–423	0.1–100	1.54	3.70	70.63	84.62

Compound	*LBC-mod* AAD (%)	MDev (%)	*PRVIS* AAD (%)	MDev (%)
R11	15.09	41.09	29.55	99.70
R12	8.85	24.61	17.40	97.90
R13	9.42	128.42	21.87	118.20
R14	4.79	9.04	5.19	32.67
R22	5.36	14.89	19.50	82.54
R32	7.36	21.09	33.98	94.50
R113	32.56	36.47	97.10	98.61
R114	31.60	46.32	94.81	99.25
R115	17.17	47.24	49.11	98.32
R123	7.38	27.79	40.21	72.12
R124	23.37	72.60	35.22	86.05
R125	8.03	35.43	201.22	543.80
R134a	10.03	22.34	170.18	645.89
R141b	23.98	50.80	37.88	71.98
R142b	3.02	8.26	30.30	55.32
R143a	3.82	21.53	35.56	92.65
R152a	4.51	9.59	28.85	98.10
TriEGDME	26.76	40.12	17.64	55.47
TEGDME	38.78	52.59	18.03	91.28

Table 3.6 – Performance of viscosity models for pure compounds

Mixture	*Ref*	*NP*	*T-range* (K)	*p-range* (MPa)	*Free-volume* AAD (%)		*LBC* AAD (%)	
					AAD (%)	MDev (%)	AAD (%)	MDev (%)
R-125/134a	1	340	298-423	0.1-6.6	2.16	5.61	6.26	11.71
R-125/32	2,3	392	298-423	0.1-7.7	4.78	28.59	8.00	35.92
R-134a/32	4	329	298-423	0.1-7.6	4.88	9.49	3.94	10.06
R-143a/125/134a	3	40	303-392	0.1-3	3.07	12.16	3.51	5.01
R-32/125/143a	3	33	297-333	0.1-2.5	2.23	7.18	1.10	4.10
R-143a/125	3	35	299-324	0.1-3.1	3.17	10.16	4.41	17.95

Mixture	*LBC-mod*		*PRVIS*	
	AAD (%)	MDev (%)	AAD (%)	MDev (%)
R-125/134a	4.21	9.95	324.14	987.68
R-125/32	6.39	30.53	333.28	789.98
R-134a/32	4.41	8.55	223.72	879.98
R-143a/125/134a	3.29	4.26	298.42	611.71
R-32/125/143a	1.67	3.49	145.78	342.78
R-143a/125	3.79	15.26	344.93	665.87

Table 3.7 – Performance of viscosity models for mixtures. References: (1) Yokoyama *et al.* 2000, (2) Yokoyama *et al.* 2001, (3) Nabizadeh and Mayinger 1999, and (4) Yokoyama *et al.* 2004.

good results for refrigerant mixtures, as shown in Table 3.7 and Figure 3.8. However, in the case of mixtures large deviations are found in the whole range of viscosities studied (see Figure 3.9).

As mentioned previously, the reported experimental densities were used with the LBC and LBC-mod models, since these two models strongly depend on the density (sixteenth degree polynomials in the reduced density). In Tables 3.6 and 3.7 it can be seen by comparing the LBC and LBC-mod results that better predictions are obtained with the LBC-mod model. The only exception is R32 for which the LBC performs better than the LBC-mod. The performance of the LBC model for viscosity estimation of pure refrigerants and lubricants is only satisfactory for a few fluids. The LBC model predicts the viscosity with an AAD less than 5% only for R32 and R152a. The model describes viscosities of refrigerants better than viscosities of lubricants. This is expected, given that the LBC model was adjusted to only light compounds. However, in spite of the fact that refrigerants are such components, their viscosity is not described satisfactorily in most of the cases. For mixtures (see Table 3.7) the results obtained with the LBC model can be considered as satisfactory. However,

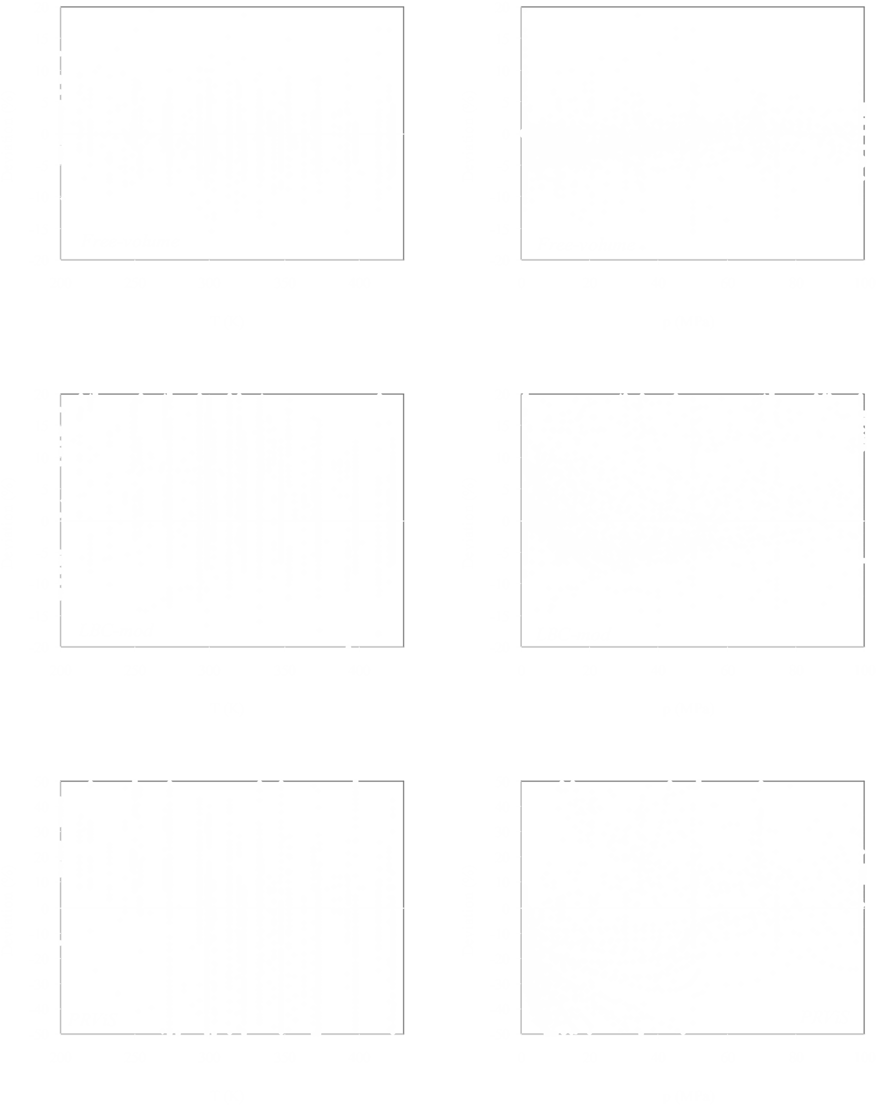

Figure 3.6 – Viscosity deviations, $100 \times (\eta_{exp} - \eta_{cal}) / \eta_{exp}$ as a function of temperature and pressure with the free-volume, LBC-mod, and PRVIS models for pure refrigerants and pure lubricants (a total of 3287 experimental points).

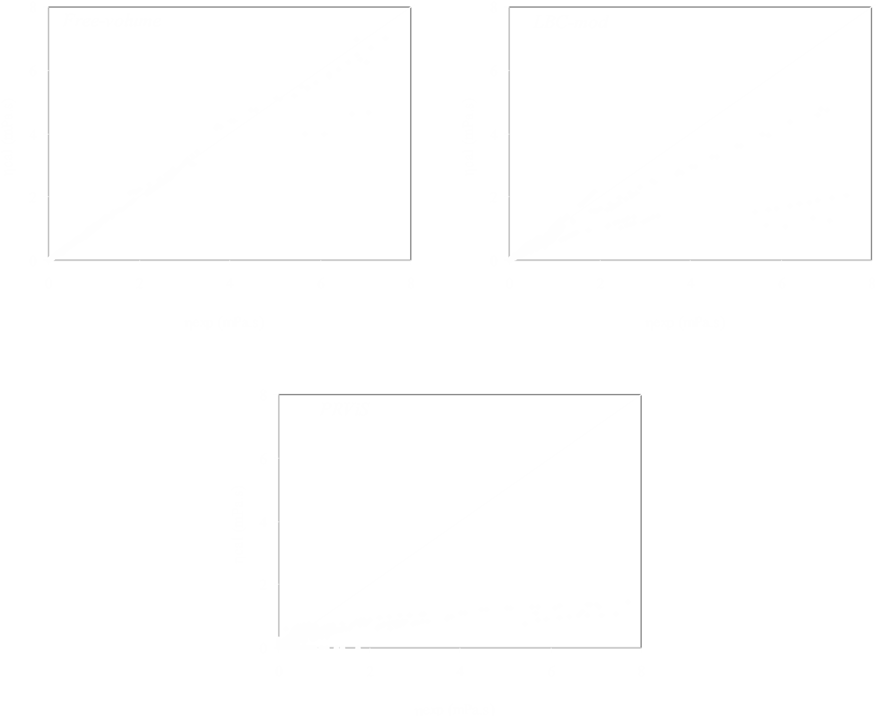

Figure 3.7 – Comparison of experimental viscosities for pure fluids with viscosities calculated by different models.

and structural effects are added (LBC-mod model), the results are improved, but still the viscosity predictions are not entirely satisfactory. Now, only three compounds are described with an AAD less than 5 % (R142b, R143a, and R152a). The capabilities of the LBC-mod model are illustrated in Figure 3.6 where the viscosity deviations are plotted as functions of temperature and pressure. For the LBC-mod only 41.8 % of all points fall within ± 5 % deviation, while the rest of the points are placed outside this range. In Figure 3.7 a plot experimental versus calculated viscosities is displayed. From this last figure it can be seen that, as the viscosity exceeds a value of approximately 1.5 mPa.s, the LBC-mod model starts underestimating the viscosity and the deviations increase with increasing viscosity. As the LBC model, the LBC-mod model predicts much better the viscosity of the mixtures than the viscosity of pure fluids, as shown in Table 3.7 and Figure 3.8.

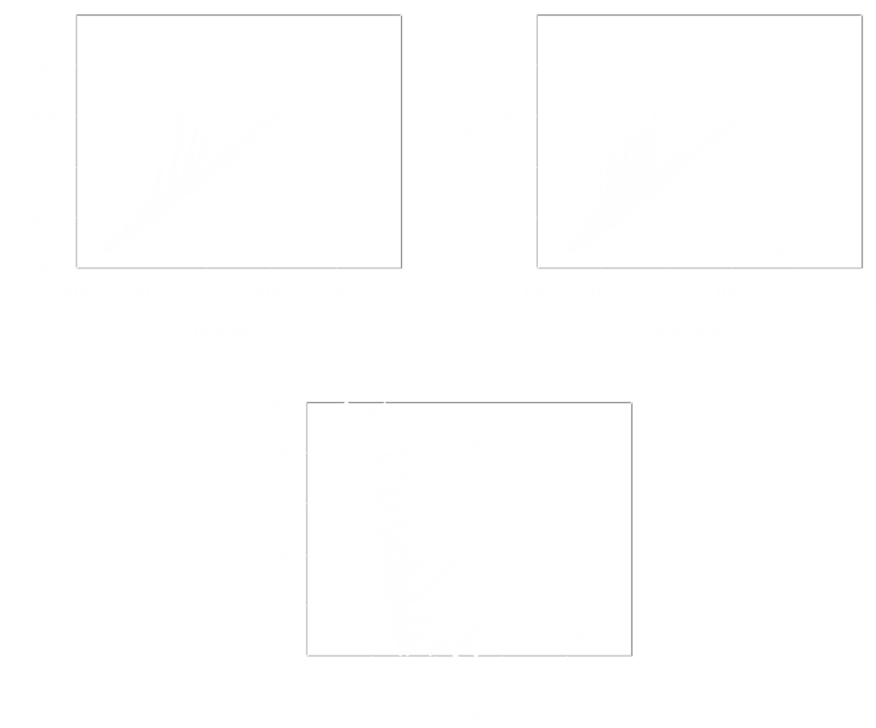

Figure 3.8 – Comparison of experimental viscosities for mixtures with viscosities calculated by different models.

The PRVIS model is the viscosity model giving the worst results, as shown in Tables 3.6 and 3.7 and Figures 3.6 to 3.8. For pure fluids, the model is able to predict the viscosity with an AAD less than 10 % only for one refrigerant (R141), and in some cases the AAD is extremely large (see R125 and R134a in Table 3.6, for example). In fact, only 13.05 % of all points are within the deviation of ± 5 %. From Figure 3.7, it can be appreciated that the model under predicts the data almost in the whole range of the viscosities analyzed. For mixtures the results are even worse than for pure fluids reaching very high average absolute deviations in all cases (Table 3.7 and Figure 3.8).

3.9 – Conclusions

An extensive evaluation of several existing viscosity models derived mainly for hydrocarbon fluids, has been performed for refrigerants, lubricants, and refrigerant mixtures over wide ranges of temperature and pressure. In order to carry out this evaluation, a database containing 17 pure refrigerants, 2 lubricants, and 7 well-defined refrigerant mixtures have been created. The evaluated models are the hard-sphere model and the self-referencing method, which are only applicable to dense phases, the free-volume model, and the well-known LBC model, along with a modification of the original LBC version. In addition, a viscosity model based on the PR EoS (the PRVIS model) has been evaluated.

From this evaluation it has been observed that the free-volume model is the one giving the best results in wide ranges of temperature and pressure. The model is applicable to both liquid and gas phases. Since in refrigeration cycles, the refrigerants work both in gas and in liquid conditions, the use of models such as the free-volume model provides a powerful tool for description of the viscosity. The results obtained with the hard-sphere model and the self-referencing method are very satisfactory, too. However, these two models are only valid for liquid states, making the choice of these models not very attractive for refrigerant related applications. In the case of lubricants, which are consistently found in the liquid phase, the applicability of these two models may be of value. For example, the self-referencing method, which does not require knowledge of critical parameters or molar mass, can be used to describe the viscosity of commercial lubricants, since for these compounds the critical parameters are not always known, or these fluids consist of mixtures of various components with unknown chemical compositions. The LBC model and its modification by Al-Syabi *et al.* (2001) have shown to be not appropriate for describing the viscosity of these compounds. It is important to keep in mind that these two models were originally developed for light compounds different than the substances studied here. Better results should be expected if the original parameters of the model will be re-adjusted. The LBC and LBC-mod models are, on the other hand, surprisingly accurate in describing the viscosity of the refrigerant mixtures. However, care should be taken when interpreting the results obtained with these two models for pure compounds and mixtures. For pure compounds, the LBC and LBC-mod model are being evaluated up to high pressures in almost all cases (see Table 3.5). For mixtures, on the contrary, the pressure does not reach very high values (see Table 3.7). Consequently, the dilute gas term has an important contribution in all cases. In this way, what is principally being evaluated for mixtures is the performance of the dilute gas term rather than the performance viscosity model. Unfortunately, there seems to be no viscosity data for refrigerant mixtures at higher pressures. In Chapter VII the performance of the models will be tested on refrigerant + lubricant mixtures up to very high pressures, making possible to study the performance of the different viscosity models. Finally, the PRVIS model has completely failed in describing the viscosity of both pure compounds and mixtures.

Nomenclature

AAD = Average absolute deviation
b_f = Dissipation length of energy E
B = Free-volume overlap, adjustable parameter in the free-volume model
$Bias$ = Bias
$E=E_0+pM/\rho$ = Intermolecular energy
EoS = Equation of state
k = Boltzmann's constant
k_{ij} = Binary interaction parameter
$l=L^2/b_f$ = Adjustable parameter in the free-volume model
L = Average characteristic molecular quadratic length
m = Mass of one molecule
M = Molecular weight
$MDev$ = Maximum deviation
n = Number of components
NP = Number of points
N_A = Avogadro's number
p = Pressure
p_0 = Reference pressure
PR = Peng-Robinson
$PRVIS$ = Peng-Robinson viscosity model
R = Gas constant
R_η = Roughness factor, adjustable parameter in the friction theory model
T = Temperature
T_0 = Reference temperature
v = Molar volume
v_0 = Close-packed volume
x = Mole fraction
Z = Compressibility factor

Greek letters

α = Adjustable parameter in the free-volume model

$\partial u/\partial h$ = Shear rate

σ = Hard-core diameter

ε = Intermolecular potential attractive energy well depth

ω = Acentric factor

ρ = Density

μ = Dipole moment

μ_r = Dimensionless dipole moment

ξ = Viscosity reduction parameter

χ = Correction factor for hydrogen bonding effects in the Chung et al. model

ζ = Friction coefficient of a molecule

η = Viscosity

η_0 = Dilute gas viscosity

η_E = Viscosity Enskog's theory

η_{exp}^* = Viscosity in the hard-sphere scheme expressed as reduced quantity

η_{shs}^* = Smooth hard-sphere viscosity expressed as reduced quantity

Ω^* = Collision integral

$\Delta\eta$ = Viscosity dense gas contribution in the free-volume model

τ = Shear stress

Subscripts/superscripts

c = Critical

cal = Calculated property

exp = Experimental property

i = Component "i"

j = Component "j"

MD = Molecular dynamics

mix = Mixture

r = Reduce property

shs — Smooth hard-sphere

References

1. Allal, A., Moha-Ouchane, M., Boned, C. A New Free Volume Model for Dynamic Viscosity and Density of Dense Fluids Versus Pressure and Temperature. *Phys. Chem. Liq.* 2001a, 39, 1–30.
2. Allal, A., Boned, C., Dauge, P. A New Free Volume Model for Dynamic Viscosity of Dense Fluids Versus Pressure and Temperature. Extension to a Predictive Model for Not Very Associative Mixtures. *Phys. Chem. Liq.* 2001b, 39, 607–624.
3. Allal, A., Boned, C., Baylaucq, A. Free-volume viscosity model for fluids in the dense and gaseous states. *Phys. R. E* 2001c, 64, 011203/1 – 10.
4. Al-Syabi, Z., Danesh, A., Tohidi, B., Todd, A.C., Tehrani, D.H. A residual viscosity correlation for predicting the viscosity of petroleum reservoir fluids over wide ranges of pressure and temperature. *Chem. Eng. Sci.* 2004, 222–223, 135–148.
5. Assael, M.J., Dymond, J.H., Tselekidou, V. Correlation of High-Pressure Thermal Conductivity, Viscosity, and Diffusion Coefficients for n-Alkanes. *Int. J. Thermophys.* 1990, 11, 863–873.
6. Assael, M.J., Dymond, J.H., Papadaki, M., Patterson, P.M. Correlation and Prediction of Dense Fluid Transport Coefficients. I. n-Alkanes. *Int. J. Thermophys.* 1992a, 13, 269–281.
7. Assael, M.J., Dymond, J.H., Papadaki, M., Patterson, P.M. Correlation and Prediction of Dense Fluid Transport Coefficients. II. Simple Molecular Fluids. *Fluid Phase Equilib.* 1992b, 75, 245–255.
8. Assael, M.J., Dymond, J.H., Papadaki, M., Patterson, P.M. Correlation and Prediction of Dense Fluid Transport Coefficients. III. n-Alkanes Mixtures. *Int. J. Thermophys.* 1992c, 13, 659–669.
9. Assael, M.J., Dymond, J.H., Patterson, P.M. Correlation and Prediction of Dense Fluid Transport Coefficients. V. Aromatic Hydrocarbons. *Int. J. Thermophys.* 1992d, 13, 895–905.
10. Assael, M.J., Dymond, J.H., Polimatidou, S.K. Correlation and Prediction of Dense Fluid Transport Coefficients. VI. n-Alcohols. *Int. J. Thermophys.* 1994, 15, 189–201.
11. Assael, M.J., Dymond, J.H., Polimatidou, S.K. Correlation and Prediction of Dense Fluid Transport Coefficients. VII. Refrigerants. *Int. J. Thermophys.* 1995, 16, 761–772.
12. Assael, M.J., Dalaouti, N.K., Dymond, J.H., Feleki, E.P. Correlation for Viscosity and Thermal Conductivity of Liquid Halogenated Ethane Refrigerants. *Int. J. Thermophys.* 2000, 21, 367–375.

13. Bivens, D.B., Yokozeki, A., Geller, V.Z., Paulaitis, M.E. Transport Properties and Heat Transfer of Alternatives for R502 and R22. In ASHRAE/NIST Refrigerants Conference: Refrigerants for the 21st Century. National Institute of Standards and Technology, Gaithersburg, MD, 1993, Vol. 1, 73–84.
14. Canet, X., Baylaucq, A., Boned, C. High-pressure (up to 140 MPa) dynamic viscosity of the methane+decane system. *Int. J. of Thermophys.* 2002, 23, 1469–1486.
15. Chandler D. Rough Hard Sphere Theory of the Self-Diffusion Constant for Molecular Liquids. *J. Chem. Phys.* 1975, 62, 1358–1363.
16. Chapman, S., Cowling, T.G., Burnett, D. The Mathematical Theory of Non-Uniform Gases. Third Edition, Cambridge University Press, UK. 1939.
17. Chung, T.-H., Ajlan, M., Lee, L.L., Starling, K.E. Generalized Multiparameter Correlation for Nonpolar and Polar Fluid Transport Properties. *Ind. Eng. Chem. Res.* 1988, 27, 671–679.
18. Comuñas, M.J.P., Baylaucq, A., Boned, C., Fernández, J. High-Pressure Measurements of the Viscosity and Density of two Polyethers and Two Dialkyl Carbonates. *Int. J. Thermophys.* 2001, 22, 749–767.
19. Dymond, J.H. Transport Properties in Dense Fluids. Proc. 6th Symposium Thermophysical Properties. *ASME*, New York. 1973 143–157.
20. Dymond, J.H. Awan, M.A. Correlation of High-Pressure Diffusion and Viscosity Coefficients for n-Alkanes. *Int. J. Thermophys.* 1989, 10, 941–951.
21. Enskog D. Kinetische Theorie – Der Wärmeleitung, Reibung und Selbstdiffusion in Gewissen Verdichteten Gasen und Flüssigkeiten. Kungliga Svenska Vetenskapsakademiens Handlingar, Stockholm, Sweden. 1922, 63(4), 1–44.
22. Guo, X.-Q., Wang, L.-S., Rong, S.-X. Guo, T.-M. Viscosity Model Based on Equations of State for Hydrocarbon Liquids and Gases. *Fluid Phase Equilib.* 1997, 139 405–421.
23. Guo -T.-M. *Private Communication.* 1998
24. Herning, F., Zipperer, L. Beitrag zur Berechnung der Zähigkeit Technischer Gasgemische aus den Zähigkeitswerten der Einzelbestandteile. *Das Gas- und Wasserfach.* 1936, 79, 49–54 and 69–73.
25. Hirschfelder, J.O., Curtiss, C.F., Bird, R.B. Molecular Theory of Gases and Liquids. Fourth Edition. John Wiley & Sons. New York, USA. 1954.
26. Iwasaki, H., Takahashi, M. Viscosity of Carbon Dioxide and Ethane. *J. Chem. Phys.* 1981, 74, 1930–943.
27. Jossi, J.A., Stiel, L.I., Thodos, G. The Viscosity of Pure Substances in the Dense Gaseous and Liquid Phases. *AIChE J.* 1962, 8, 59-63.

28. Kanti, M., Zhou, H., Ye, S., Boned, C., Lagourette, B., Saint-Guirons, H., Xans, P., Montel, F. Viscosity of Liquid Hydrocarbons, Mixtures, and Petroleum Cuts, as a Function of Pressure and Temperature. *J. Phys. Chem.* 1989, 93, 3860–3864.
29. Kashiwagi, H., Makita, T. Viscosity of 12 Hydrocarbon Liquids in the Temperature Range 298 – 348 K at Pressures up to 110 MPa. *Int. J. Thermophys.* 1982, 3, 289-305.
30. Little, J.E., Kennedy, H.T. A Correlation of the Viscosity of Hydrocarbon Systems with Pressure, Temperature and Composition. *Soc. Petr. Eng. J.* June, 1968, 157-162.
31. Lohrenz, J., Bray, B.G., Clark, C.R. Calculating Viscosities of Reservoir Fluids From Their Compositions. *J. Pet. Tech.* 1964, 16, 1171-1176.
32. Lucas, K. Review of Present Status of Transport Properties Predictions. Phase Equilibria and Fluid Properties in the Chemical Industry, DECHEMA, 1980.
33. Mehrotra, A.K., Monnery, W.D., Svrcek, W.Y. A Review of Practical Calculation Methods for the Viscosity of Liquid Hydrocarbons and Their Mixtures. *Fluid Phase Equilib.* 1996, 117, 344–355.
34. Monnery, W.D., Svrcek, W.Y., Mehrotra, A.K. Viscosity: A Critical Review of Practical Predictive and Correlative Methods. *Can. J. Chem. Eng.* 1995, 73, 3–40.
35. Nabizadeh, H., Mayinger, F. Viscosity of R404A, R407C, R410A and R507. *Int. J. Thermophys.* 1999, 20, 777-790.
36. Neufeld, P.D., Janzen, A.R., Aziz, R.A. Empirical Equations to Calculate 16 of the Transport Collision Integrals Ω * for the Lennard-Jones (12-6) Potential. *J. Chem. Phys.* 1972, 57, 1100-1102.
37. Patel, N.C., Teja, A.S. A New Cubic Equation of State for Fluids and Fluid Mixtures. *Chem. Eng. Sci.* 1982, 37, 463-473.
38. Peng, D.-Y., Robinson, D.B. A New Two-Constant Equation of State. *Ind. Eng. Chem. Fundam.* 1976, 15, 59–64.
39. Phillips, P. The Viscosity of Carbon Dioxide. *Proceedings of the Royal Society of London* 1912, 87A, 48-61.
40. Poling, B.E., Prausnitz, J.M., O'Connell, J.P. The Properties of Gases and Liquids, Fifth Edition. Mc Graw Hill, New York, 2000.
41. Stiel, L.I., Thodos, G. The Viscosity of Nonpolar Gases at Normal Pressure. *AIChE J.* 1961, 7, 611–615.
42. Stiel, L.I., Thodos, G. The Viscosity of Polar Gases at Normal Pressure. *AIChE J.* 1962, 8, 229–232.

43. Strumpf, H.J., Collings, A.F., Pings, C.J. Viscosity of Xenon and Ethane in the Critical Region. *J. Chem. Phys.* 1974, 60, 3109–3123.

44. Uyehara, O.A., Watson, K.M. A Universal Viscosity Correlation. *Nat. Petroleum News.* 1944, 36, R714-722.

45. van Velzen, D., Cardozo, R.L., Langenkamp, H. A Liquid Viscosity-Temperature-Chemical Constitution Relation for Organic Compounds. *Ind. Eng. Chem. Fundam.* 1972, 11, 20–25.

46. Wilke, C.R. A Viscosity Equation for Gas Mixtures. *J. Chem. Phys.* 1950, 18, 517–519.

47. Yokoyama C., Takahashi M., and Takahashi, S. Viscosity of Nitrous Oxide in the Critical Region. *Int. J. Thermophys.* 1994, 15 603–626.

48. Yokoyama, C., Takahashi, M. Viscosity of CHF$_3$ in the Critical Region. *Int. J. Thermophys.* 1997, 18, 1369–1385.

49. Yokoyama, C., Nishino, T., Takahashi, M. Viscosity of gaseous mixtures of HFC-125 (pentafluoroethane) + HFC-134a (1,1,1,2-tetrafluoroethane) under pressure. *Fluid Phase Equilib.* 2000, 174, 231–240.

50. Yokoyama, C., Nishino, T., Takahashi, M. Viscosity of Gaseous Mixtures of HFC125+HFC32. *Int. J. Thermophys.* 2001, 22, 1329.

51. Yokoyama, C., Nishino, T., Takahashi, M. Viscosity of Gaseous Mixtures of HFC-134a+HFC-32. *Int. J. Thermophys.* 2004, 25, 71-88.

52. Zozulya, V.N., Blagoi, Y.P. Viscosity of Nitrogen Near the Liquid-Vapor Critical Point. *Soviet Physics JETP.* 1974, 39 99–105.

IV – The Friction Theory

4.1 – Introduction

Recently, the friction theory (*f-theory*), a theory for viscosity modeling based on friction concepts of classical mechanics, has been introduced by Quiñones-Cisneros *et al.* (2000). This new theory, which was developed at the IVC-SEP group as one of the main contributions to the Extended Viscosity and Density Technology (EVIDENT) project, makes it possible accurate viscosity–pressure–temperature (η–p–T) modeling based on the van der Waals types equation of state. Popular cubic equations of state, such as the SRK (Soave, 1972) and the PR (Peng and Robinson, 1976), have been successfully applied to obtain accurate η–p–T models (even close to the critical region) of fluids such as *n*-alkanes (Quiñones-Cisneros *et al.* 2000, and 2001a, and Zéberg-Mikkelsen *et al.* 2001c), hydrogen plus natural gas (hythane) mixtures (Zéberg-Mikkelsen *et al.* 2001a), light gases (Zéberg-Mikkelsen *et al.* 2001b), pure alcohols (Zéberg-Mikkelsen *et al.* 2002a), natural gas (Zéberg-Mikkelsen *et al.* 2002b), carbon dioxide plus hydrocarbon mixtures (Zéberg-Mikkelsen *et al.* 2002c) or more complex fluids such as dense reservoir fluids (Quiñones-Cisneros *et al.* 2001b, 2003, 2004a, 2004b, and 2005, and Schmidt *et al.* 2005).

Even though it has been shown that cubic EoS *f-theory*-based models can accurately reproduce the viscosity behavior of different fluids, the accuracy of the density predictions is still limited by the algebraic structure of the cubic EoS. Until now, the viscosity modeling with the *f-theory* model in combination with noncubic EoS has been carried out only for a few hydrocarbons (Quiñones-Cisneros *et al.* 2002) and one refrigerant (Comuñas *et al.* 2003). Therefore, it is of theoretical as well as of industrial interest to explore the extension of the *f-theory* approach to other kinds of models besides the cubic EoS. Of practical interest are models capable of a better density description, as well as models that can be applied to associating fluids. On the other hand, the *f-theory* has mainly been applied to model and predict the viscosity of fluids related to the petroleum industry. Therefore, application of the friction theory to the new class of fluids, as studied in the present thesis, is of industrial and theoretical value.

In a first part of this chapter the friction theory is introduced and briefly discussed. The modeling of pure refrigerants, pure lubricants, and some refrigerant mixtures is carried out with the aid of two cubic EoS presented and discussed in Chapter II, the PR EoS (Peng and Robinson, 1976) and the RK-PR EoS (Cismondi and Mollerup, 2005). In the second part, the extension of the *f-theory* to EoS besides cubic is investigated. The aim is to discuss the basis along which the friction theory can be extended to the noncubic EoS. The noncubic EoS studied are the SBWR EoS (Soave 1995, and 1999) and the PC-SAFT EoS (Gross *et al.* 2001). Finally, a comparison among the different *f-theory* models is carried out in the last part of this chapter.

4.2 – The friction theory

The friction theory for viscosity modeling has been introduced by Quiñones-Cisneros *et al.* (2000) on the basis of the principles of classical mechanics and thermodynamics. A fundamental difference between the *f-theory* and other available approaches for viscosity modeling is that the viscosity in excess of the dilute gas viscosity is approached as a mechanical property. In the *f-theory*, the viscosity is linked to the pressure, which is the main mechanical variable. By use of a simple cubic equation of state (EoS) highly accurate viscosity estimations can be obtained, from low to extremely high pressures. The cubic EoS are optimized for good pressure-temperature performance, and, therefore, good viscosity-pressure performance can also be obtained, as illustrated by Quiñones-Cisneros *et al.* (2000). This is achieved regardless of the accuracy of the estimated density.

In the *f-theory* the total viscosity, η, is separated into a dilute gas viscosity term η_0 and a residual friction term η_f.

$$\eta = \eta_0 + \eta_f \qquad (4.1)$$

The dilute gas viscosity η_0 is defined as the viscosity at the zero density limit, while the residual friction term η_f is related to a connection between the van der Waals repulsive and attractive pressure terms via the Amonton-Coulomb friction law. The residual friction term may be expressed by the following quadratic model

$$\eta_f = \kappa_r p_r + \kappa_a p_a + \kappa_{rr} p_r^2 \qquad (4.2)$$

where κ_r, κ_a and κ_{rr} are temperature dependent friction coefficients, and p_r and p_a are the van der Waals repulsive and attractive pressure contributions, respectively. These contributions may be obtained with the aid of simple cubic EoS, such as the SRK (Soave, 1972) or the PR (Peng and Robinson, 1976) EoS. In the following sections the basic ideas behind the *f-theory* are described along with the main *f-theory* models developed.

4.2.1 - Basic ideas of the friction theory

From classical mechanics it is known that when two bodies in contact are moving relative to each other, the contact forces act between them. In order to maintain the motion, a force F parallel to the contact surface has to be applied. This force is opposite to the kinetic friction F_k as illustrated in Figure 4.1. Experimentally, the kinetic friction has been found to be constant for wide ranges of speed. Further, the two bodies will be pressed together by the normal force N acting perpendicular to the contact surface. According to the classical mechanical Amonton-Coulomb friction law, the ratio between the kinetic friction and the normal force is given by

$$\mu_k = \frac{F_k}{N} = \frac{A\tau}{A\sigma} = \frac{\tau}{\sigma} \tag{4.3}$$

where μ_k is known as the kinetic friction coefficient, which is assumed to depend only on the smoothness of the surfaces of the materials and not on the surface area A. The kinetic friction F_k in Equation 4.3 can be expressed in terms of the shear stress τ, and the normal force N in terms of the pressure or normal stress σ acting on the contact surface area A.

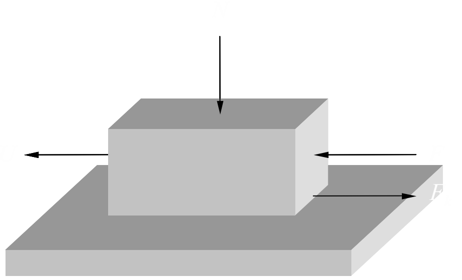

Figure 4.1 – Basic forces acting in the case of a block moving during friction contact. N is the pressure normal force, F the pushing force responsible for the movement, F_k the opposite friction force, and U the resulting velocity.

For a fluid made up of many parallel layers of thickness ∂h (Figure 4.2), the normal force N keeps the layers together. The friction force F_k resists to displacement of the layers. The flow may be described in terms of the rate of shear $\partial u/\partial h$, i.e. the change of rate at which one layer moves relative to an adjacent layer. For a fluid at rest, the normal stress N can be related to the isotropic total pressure p, which, according to the van der Waals theory of fluids, can be separated into a repulsive and an attractive pressure term as follows:

$$p = p_r + p_a \qquad (4.4)$$

where p_r and p_a are the contributions to the pressure coming from the short-range repulsive intermolecular forces and the long-range attractive intermolecular forces, respectively. In the case of a fluid under shear motion, the shear stress τ (i.e. the dragging force) acting between the moving layers can be separated into a dilute gas collision term τ_0 and a residual friction term τ_f.

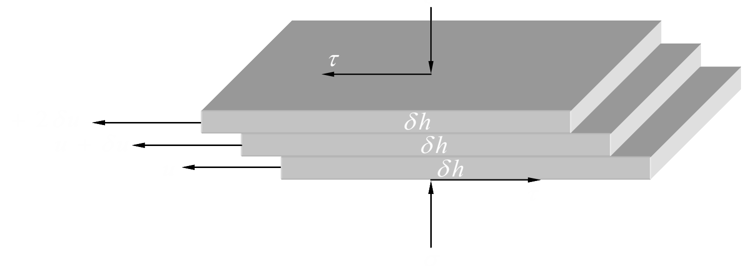

Figure 4.2 – Multilayer model for laminar shear flow. σ (or P) is the pressure normal force, τ (or F) the opposite friction force, u the reference velocity, δu the relative velocity difference, and δh the distance of the lawyers.

$$\tau = \tau_0 + \tau_f \qquad (4.5)$$

Here, the dilute gas term is only important at the ideal gas limit where the friction term vanishes. Thus, when a fluid is brought under shear motion, the attractive and repulsive intermolecular forces both contribute to friction. Thus, the residual friction shear stress term τ_f may be considered to consist of attractive friction shear contribution τ_a and repulsive contribution τ_r.

$$\tau_f = \tau_a + \tau_r \qquad (4.6)$$

By analogy with the Amonton-Coulomb friction law, Quiñones-Cisneros et al. (2000) assumed that the attractive dragging force τ_a and the repulsive dragging force τ_r are analytical functions of the attractive pressure term p_a and the repulsive pressure term p_r, respectively. Expansion of τ_a and τ_r in an n-th order Taylor series from the origin (i.e. the dilute gas limit where $p = p_r = p_a = 0$) results in:

$$\tau_a = \sum_{i=1}^{n} \tau_{a,i}\, p_a^i \qquad (4.7)$$

and

$$\tau_r = \sum_{i=1}^{n} \tau_{r,i}\, p_r^i \qquad (4.8)$$

The zero order terms in Equations 4.7 and 4.8 have been eliminated under the assumption that at the dilute gas limit the fluid layers are so far apart that they do not feel any kind of frictional dragging force. When Equations 4.7 and 4.8 are truncated after the first order, they become equivalent to the Amonton-Coulomb friction law:

$$\tau_a = \mu_a P_a \qquad (4.9)$$

and

$$\tau_r = \mu_r P_r \qquad (4.10)$$

The coefficients $\mu_a = \tau_{a,1}$ and $\mu_r = \tau_{r,1}$ are analogous to the Amonton-Coulomb coefficients of kinetic friction. The repulsive contribution to the shear stress is of a short-range nature and it becomes dominant term for dense fluids. The attractive forces are more long-range, and the corresponding contribution to viscosity are likely to prevail in light fluids. When a fluid is brought under high pressure, the intermolecular distance between the moving layers reduces. Therefore, under high pressures the short-range repulsive forces prevail over the long-range attractive forces. Due to this, Quiñones-Cisneros *et al.* (2000) suggested a second order truncation of the repulsive shear stress term, Equation 4.8, for fluids under high pressures, whereas the higher order contributions to the attractive term are neglected. This leads to the following expression for the friction shear stress term τ_f:

$$\tau_f = \mu_r P_r + \mu_a P_a + \mu_{rr} P_r^2 \qquad (4.11)$$

From the definition of viscosity $\eta = \tau/(\delta u/\delta h)$ (Section 3.1 in Chapter 3), the friction viscosity contribution η_f can be written as

$$\eta_f = \frac{\mu_r P_r + \mu_a P_a + \mu_{rr} P_r^2}{\delta u / \delta h} \qquad (4.12)$$

resulting in

$$\eta_f = \kappa_r P_r + \kappa_a P_a + \kappa_{rr} P_r^2 \qquad (4.13)$$

where η_f may be given by Equation 4.13 and η_0 is the dilute gas viscosity. The dilute gas viscosity can be obtained by the Chung *et al.* (1988) model. In Chapter 3, this model was shown to satisfactorily predict the dilute gas viscosity of various refrigerant fluids over wide range of temperatures. If the second-order repulsive pressure term is neglected, Equation 4.13 reduces to the equation

$$\eta_f = \kappa_r p_r + \kappa_a p_a \qquad (4.16)$$

which is analogous to the Amonton-Coulomb friction law. This model for viscosity is referred to as the linear *f-theory* model.

4.2.2 – Illustration and discussion of the f-theory

In order to illustrate the application of the *f-theory* to real fluids Quiñones-Cisneros *et al.* (2000) used the SRK EoS (Soave, 1972) and the PRSV EoS (Stryjek and Vera, 1986), which are the two of the widely used cubic EoS of the van der Waals family, containing a repulsive pressure term p_r and an attractive pressure term p_a.

The performance of the linear and quadratic *f-theory* models with the SRK EoS is studied from low to very high pressures using isothermal viscosity data of methane at 273.1 K (van der Gulik *et al.* 1992). Methane is only considered for the purpose of demonstrating the capabilities of the linear and quadratic friction theory models. The application of the linear *f-theory* with the SRK EoS is shown in Figure 4.3 for the 273.1 K isotherm of methane for pressures up to 10000 bar. From the results presented in this figure it can be seen that when the linear *f-theory* model is only suitable for pressures up to 1000 bar. Monotonically increasing deviations are obtained as the model is extrapolated to higher pressures. By using all of the data for the fitting of the linear *f-theory* model a significant improvement is obtained compared with the results obtained using only data up to 1000 bar. However, although the results are improved, it can be seen from Figure 4.3 that there are regions where clear deviations are encountered. On the other hand, by fitting the quadratic *f-theory* model to the entire pressure range very accurate matching results are obtained, see Figure 4.4. In this case the deviations are within the experimental uncertainty.

Figure 4.3 – Results for modeling the 273.1 K methane isotherm (van der Gulik *et al.* 1992, ◊) by use of the linear *f-theory* with the SRK EoS for pressures up to 10000 Bar. Note: (—) shows the results of fitting the model to the data up to 1000 Bar, (- - -) shows the results when all the data have been used for fitting the model.

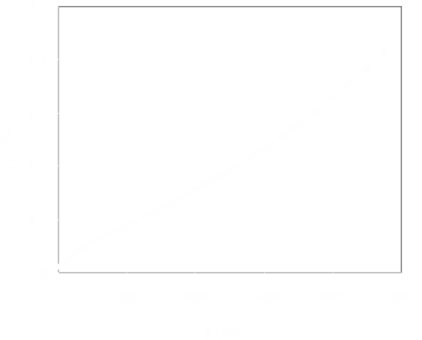

Figure 4.4 – Results for modeling the 273.1 K methane isotherm (van der Gulik *et al.* 1992, ◊) by use of the quadratic *f-theory* with the SRK EoS for pressures up to 10000 Bar.

The different friction contributions in the quadratic *f-theory* model have been analyzed in order to get an understanding of the high-pressure viscosity results. Figure 4.5 shows the friction contributions to the viscosity given by the linear repulsive term ($\eta_{fr} = \kappa_r p_r$), the linear attractive term ($\eta_{fa} = \kappa_a p_a$), and the quadratic repulsive term ($\eta_{frr} = \kappa_{rr} p_r^2$) for methane at 273.1 K. These results clearly show that from low pressure to pressures up to 1000 bar, both of the linear terms are the dominating terms, whereas the quadratic term may be neglected. However, as the pressure increases, far beyond 1000 bar, the attractive term appears to converge to a constant while the linear and the quadratic repulsive terms become the dominating terms.

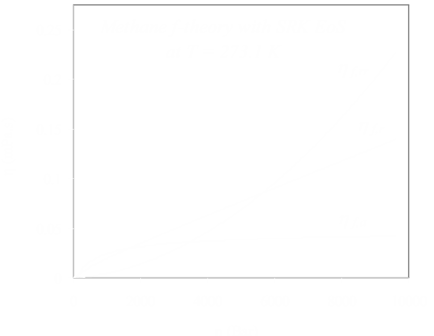

Figure 4.5 – Contribution of the different friction terms in the case of modeling methane at *T* = 273.1 K using the quadratic *f*-theory with the SRK EoS for pressures up to 10000 Bar.

The temperature dependency of κ_r, κ_a, κ_{rr} with temperature has been extensively studied by Quiñones-Cisneros *et al.* (2000) based on accurate modeling of single isotherms using the quadratic *f*-theory model. Quiñones-Cisneros *et al.* (2000) established, among many other mathematical models that the following exponential series performs satisfactorily

$$\kappa_r = a_0 + \sum_{i=1}^{2} a_i \left(Exp\left[i\left(T_r^{-1} - 1 \right) \right] - 1 \right) \tag{4.17}$$

$$\kappa_a = b_0 + \sum_{i=1}^{2} b_i \left(Exp\left[i\left(T_r^{-1} - 1 \right) \right] - 1 \right) \tag{4.18}$$

$$\kappa_{rr} = \sum_{i=2}^{2} c_i \left(Exp\left[i\left(T_r^{-1} - 1 \right) \right] - 1 \right) \tag{4.19}$$

In Equations 4.17 and 4.18, Quiñones-Cisneros *et al.* (2000) have shown that the low order a_0 and b_0 constants are important for the modeling of the high-temperature region, while the high-order exponential terms become relevant at low temperatures. In the case of the quadratic term (Equation 4.19), the series starts with the second-order term, since the addition of low-order terms appears not to be required, and it is forced to vanish as the temperature goes to infinity. Also, for mathematical convenience, the origin of the series for κ_r and κ_a has been shifted to the critical point.

4.3 – Friction theory + cubic EoS

As shown by Quiñones-Cisneros *et al.* (2000, and 2001a) good viscosity-pressure performance is usually achieved by use of cubic EoS regardless of how accurate the density performance may be. Similar results are expected by use of the *f*-theory in combination with the EoS such as SRK, PR, PRSV or RK-PR. In Chapter II it was shown that among the different cubic EoS studied, PR and RK-PR show the best performance. Since the main objective of this chapter is to develop accurate *f*-theory viscosity models to be coupled with the EoS capable of delivering a good *p*–*v*–*T* description, the two cubic EoS chosen with the *f*-theory are PR and RK-PR. Similar viscosity results may be expected with other cubic EoS, such as SRK or PRSV.

The references to the data used in the derivation of the results, as well as relevant information, are listed in Appendix B. All of the parameters required by the equations of state for pure refrigerants are listed in Table 1.1, Chapter 1. In the case of lubricants and the PR EoS, in Chapter II it was shown that the density predictions can be notably improved by simultaneous adjustment of the equation parameters: T_c, P_c, and ω. The adjusted values of T_c, P_c, and ω from Table 2.4 in Chapter II have been used.

4.3.1 – Five parameter model: pure compounds

For pure fluids, the temperature dependency of the friction parameters was presented in the previous section. Although best results are expected when Equations 4.17 to 4.19 are reduced to a seven-constant parametric model, a lower number of fitted constants may suffice. As stated above, the low-order terms in Equations 4.17 and 4.18 are important for modeling the high-temperature region, while the higher-order exponential terms are important at low temperatures. Therefore, one way to obtain a five-parameter model, while satisfying these conditions at the same time, is to eliminate the zero-order term in the κ_r- and κ_a-expressions, while switching the origin of the first-order terms in the series, so that they do not converge to zero at the critical point. This results in the following equations:

$$\kappa_r = a_1\, Exp\left[T_r^{-1} - 1\right] + a_2\left(Exp\left[2\left(T_r^{-1} - 1\right)\right] - 1\right) \qquad (4.20)$$

$$\kappa_a = b_1\, Exp\left[T_r^{-1} - 1\right] + b_2\left(Exp\left[2\left(T_r^{-1} - 1\right)\right] - 1\right) \qquad (4.21)$$

$$\kappa_{rr} = c_2\left(Exp\left[2\,T_r^{-1}\right] - 1\right) \qquad (4.22)$$

With these expressions, the accuracy of the model greatly depends on the quality of the experimental data. For many particular compounds under study, significant differences were found between experimental data reported by different researchers. However, since the aim of this work is not a critical review of the data, all the available data points were used. The parameters in Equations 4.20 to 4.22 were obtained in the following way, as recommended by Quiñones-Cisneros *et al.* (2000). As a first step, the residual friction viscosity $\eta_f = \eta - \eta_0(T)$ is obtained by calculating the dilute gas term using the Chung *et al.* model. Then, since a pure substance always exists as one phase, the EoS is solved in order to obtain the repulsive and the attractive pressure terms that correspond to the analyzed phase. Finally, using the least squares method, the friction coefficient can be obtained by fitting the T-p_r-p_a-η_f data to the five-constant model (or any other appropriate parametric law). For lubricants, which are consistently found in the liquid phase state, the dilute gas term may always be neglected. In general, the dilute-gas term may be neglected if a fluid to be modeled is a high-pressure dense fluid or a subcritical liquid phase at a reduced temperature lower than 0.8.

The parameters obtained for the studied refrigerants and lubricants are shown in Table 4.1 for the PR EoS and in Table 4.2 for the RK-PR EoS. The corresponding AAD comparisons between the PR and RK-PR based *f-theory* models are shown in Table 4.3. Also, for comparison purposes the free-volume results already presented in Chapter III are shown. For all the studied cases, the results obtained by the parameterized *f-theory* models exhibit the AAD less than 5 %. The results obtained by use of the PR or RK-PR *f-theory* models are very similar, which confirms the fact that the accuracy of the *f-theory* does not depend of the accuracy of the chosen cubic EoS. Overall, the friction theory models perform better than the free-volume model (Allal *et al.* 2001a and 2001b). From a total of 3287 experimental points the PR *f-theory* model predicts the viscosity of the studied fluids with an AAD within ± 5 % for 87% of all points. The remaining 13 % of the points lie outside this range. For the RK-PR *f-theory* model these percentages are 85.5 % and 14.5 %, respectively.

Figure 4.6 shows the modeling results with the PR *f-theory* model for R134a and R125. Several viscosity versus pressure isotherms are compared to representative experimental data, both for the gas and the liquid phase. Clearly, the performance of the friction theory is satisfactory over the entire temperature and pressures range. In order to show stability of the model, the isotherms in Figure 4.6 have been extrapolated outside the experimental pressure range. However, regardless of the stable behavior of the models, application of the *f-theory* outside the fitted temperature and pressure range needs care.

Compound	*f-theory with the PR EoS*				
	a_1 (μP/Bar)	a_2 (μP/Bar)	b_1 (μP/Bar)	b_2 (μP/Bar)	c_2 (μP/Bar^2)×10^{-5}
R11	-0.1961	-1.1401	-1.6786	-0.3468	6.0168
R12	0.2445	-0.3236	-1.2318	0.0892	3.1533
R13	-0.4868	-0.7610	-2.0020	-0.0983	5.0192
R14	-0.6627	-0.6479	-1.8890	0.1328	4.9164
R22	0.2551	-1.1208	-0.8869	-0.5167	3.6436
R32	-0.1757	-0.3430	-1.0172	0.2349	2.4605
R113	-0.1318	-0.2572	-0.7629	0.1762	1.3121
R114	-0.1516	-0.2953	-0.8773	0.2026	3.4779
R115	-1.3873	3.4868	-3.8495	10.1082	4.0154
R123	0.2267	-1.7168	-1.4099	-0.8985	9.1636
R124	-0.7053	-1.8010	-2.3523	-0.7357	11.3075
R125	-0.5730	-0.9870	-2.2843	0.0419	10.8231
R134a	-0.4358	-0.9315	-1.9555	-0.1813	7.2593
R141b	-0.4543	-1.8177	-1.8111	-0.7396	8.7814
R142b	0.1023	-0.5071	-0.0858	1.0352	72.3911
R143a	-0.6608	-1.2834	-2.1321	-0.3875	1.6289
R152a	-0.1825	-0.0967	-1.2203	0.2916	2.8298
TriEGDME	-2.5609	1.1612	-3.4037	0.6276	4.3407
TEGDME	-5.1985	1.9019	-5.1733	0.8411	5.3985

Table 4.1 – Parameters for the *f-theory* with the PR EoS (five-constant parametric model).

Compound	*f-theory with the RK-PR EoS*				
	a_1 (μP/Bar)	a_2 (μP/Bar)	b_1 (μP/Bar)	b_2 (μP/Bar)	c_2 (μP/Bar^2)×10^{-5}
R11	-0.1181	-1.1537	-1.8256	-0.3994	7.0444
R12	0.0773	-0.1109	-1.5787	0.3846	4.4093
R13	-0.5450	-0.7845	-2.2287	-0.1128	5.8674
R14	-0.5353	-0.5024	-1.7888	1.1949	7.1526
R22	0.3557	-1.0039	-0.8279	-0.4757	3.4665
R32	-0.1666	-0.2541	-0.9023	0.3075	1.7792
R113	-0.1250	-0.1905	-0.6767	0.2306	9.7044
R114	-1.6591	4.2201	-4.6524	12.0032	7.3904
R115	-1.4814	3.7080	-4.1539	10.7171	2.6584
R123	0.0336	-0.9557	-1.7007	-0.3169	8.0491
R124	-1.0389	-1.5880	-2.8207	-0.3777	12.8409
R125	-0.6194	-0.9005	-2.4148	0.1300	11.9076
R134a	-0.4522	-0.8736	-1.9530	-0.0268	7.1477
R141b	-0.4266	-2.0530	-1.8777	-0.9047	10.1029
R142b	0.1086	-0.5225	-0.0698	1.4190	75.8755
R143a	-0.6851	-1.2459	-2.0943	-0.2903	1.6179
R152a	-0.1676	-0.1025	-1.1498	0.2841	2.5137
TriEGDME	-1.4433	-0.1972	-2.2900	0.0739	5.7449
TEGDME	-2.8058	-0.8739	-3.5976	-0.3427	9.7477

Table 4.2 – Parameters for the *f-theory* with the RK-PR EoS (five-constant parametric model).

Compound	NP	f - PR AAD (%)	f - PR MDev (%)	f - RK-PR AAD (%)	f - RK-PR MDev (%)	Free-volume AAD (%)	Free-volume MDev (%)
R11	133	1.13	7.31	0.99	7.67	4.83	15.23
R12	166	2.46	21.13	2.70	21.89	4.00	25.94
R13	475	3.44	35.40	3.79	36.45	5.62	55.00
R14	168	4.52	12.06	4.53	12.05	5.00	12.03
R22	126	1.46	5.93	1.44	7.03	1.97	7.05
R32	241	2.50	18.08	2.47	18.71	2.15	12.55
R113	18	0.26	0.71	0.26	0.71	0.30	0.72
R114	130	1.40	5.90	1.39	5.75	1.57	8.74
R115	102	3.47	26.27	3.43	25.95	6.14	35.94
R123	138	1.99	5.42	1.76	5.13	2.75	9.65
R124	149	3.28	17.16	3.34	18.00	2.60	16.38
R125	294	2.01	12.04	2.28	11.30	2.05	24.25
R134a	536	2.56	10.36	2.57	10.81	2.66	8.78
R141b	57	0.84	2.86	0.83	2.75	1.91	4.04
R142b	134	0.85	6.17	0.86	6.11	1.16	6.68
R143a	119	2.02	15.80	2.09	15.62	3.08	11.86
R152a	175	1.72	12.00	1.67	11.88	1.09	8.22
THEGDME	63	3.40	6.91	2.18	6.98	1.46	4.43
TEGDME	63	3.42	9.22	2.87	9.41	1.34	3.70
Overall		2.48		2.51		3.11	

Table 4.3 – Comparison of viscosity models for pure compounds. NP: number of points.

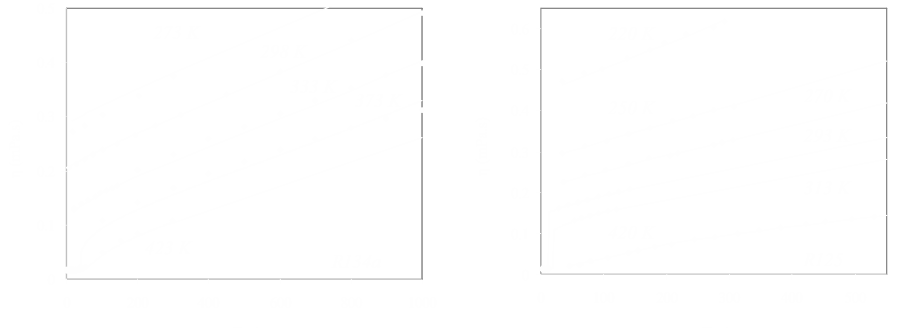

Figure 4.6 – Calculated viscosity for R134a and R125 using the PR f-theory model (—) compared with experimental values (♦). Note: all experimental points are reported in Appendix B.

4.3.2 – Five parameter model – mixtures

In order to apply the *f-theory* to mixtures, Quiñones-Cisneros *et al.* (2000), preserving the basic *f-theory* structure, derived simple mixing rules for the κ_r, κ_a, and κ_{rr} friction coefficients. The mixture viscosity η_{mix} is given by

$$\eta_{mix}=\eta_{0,mix}+\eta_{f,mix} \tag{4.23}$$

The dilute gas viscosity of the mixture $\eta_{0,mix}$ is calculated as

$$\eta_{0,mix}=Exp\left[\sum_{i=1}^{n}x_i\,Ln\left(\eta_{0,i}\right)\right] \tag{4.24}$$

In all cases, subscript "*i*" refers to the corresponding pure component of the *n*-component mixture. The dilute gas viscosity of the pure compounds can be estimated by the correlation of Chung *et al.* (1988). The mixture friction contribution term is given by

$$\eta_{f,mix}=\kappa_{r,mix}\,p_{r,mix}+\kappa_{a,mix}\,p_{a,mix}+\kappa_{rr,mix}\,p_{r,mix}^{2} \tag{4.25}$$

where $p_{a,mix}$ and $p_{r,mix}$ are the attractive and repulsive pressure contributions of the mixture and the $\kappa_{r,mix}$, $\kappa_{a,mix}$ and $\kappa_{rr,mix}$ are the corresponding viscous friction coefficients for the mixture. For the last coefficients, the following mixing rules have been suggested by Quiñones-Cisneros *et al.* (2000)

$$\kappa_{r,mix}=\sum_{i=1}^{n}z_i\,\kappa_{r,i} \tag{4.26}$$

$$\kappa_{a,mix}=\sum_{i=1}^{n}z_i\,\kappa_{a,i} \tag{4.27}$$

$$\kappa_{rr,mix}=\sum_{i=1}^{n}z_i\,\kappa_{rr,i} \tag{4.28}$$

where a weighted fraction exponential rule for z_i has been proposed

$$z_i=\frac{x_i}{M_i^{\varepsilon}\,MM} \tag{4.29}$$

$$MM=\sum_{i=1}^{n}\frac{x_i}{M_i^{\varepsilon}} \tag{4.30}$$

For mixtures of components of close molecular weights (i.e., such as mixtures refrigerant + refrigerant), good results are obtained just by setting $z_i = x_i$ (or $\varepsilon = 0$). However, as the difference in molecular weights increases (for mixtures such as refrigerant + lubricant), better results are obtained by setting ε to a value different than zero. For the SRK EoS, the best results were found with $\varepsilon = 0.15$, while for the PRSV EoS better results correspond to $\varepsilon = 0.075$ (Quiñones-Cisneros *et al.* 2000). In a later publication, a universal value of $\varepsilon = 0.30$ was proposed (Quiñones-Cisneros *et al.* 2001a). However, these values of ε were obtained based on the information on hydrocarbon mixtures, but not refrigerant-lubricant mixtures.

As in Chapter III, the experimental database for mixtures consists of seven well defined refrigerant mixtures. For the PR and the RK-PR EoS, the customary linear and quadratic van der Waals mixing rules are used, and the binary interaction parameter (k_{ij}) is set to be equal to zero. The use of binary interaction parameters is strongly recommended when the EoS used is unable to describe the correct phase behavior (see for example Zéberg-Mikkelsen *et al.* 2002c). In this thesis, it was found that for the refrigerant + refrigerant mixtures to be studied the cubic EoS can represent the right phase behavior with $k_{ij} = 0$. The ε-value in Equations 4.29 and 4.30 was also set to zero for refrigerant-refrigerant mixtures.

Table 4.4 shows the values of AAD and MDev for some binary and ternary mixtures obtained with the PR and RK-PR *f-theory* models, in comparison with the results obtained by the free-volume model. In most cases, the values of AAD are within the experimental uncertainty. A comparison with the free-volume results shows, again, better performance of the friction theory. Performance of the *f-PR* viscosity predictions for the binary system R125 + R32 and R134a + R32 is shown in Figure 4.7 in comparison with the experimental data available.

Mixture	*Ref*	*NP*	*f-PR*		*f-RK-PR*		*Free-volume*	
			AAD (%)	MDev (%)	AAD (%)	MDev (%)	AAD (%)	MDev (%)
R-125/134a	1	340	1.63	10.09	1.55	10.85	2.16	5.61
R-125/32	2,3	392	3.09	8.78	3.24	8.56	4.78	28.59
R-134a/32	4	329	1.49	12.75	1.86	11.25	4.88	9.49
R-143a/125/134a	3	40	2.84	10.40	2.41	9.56	3.07	12.16
R-32/125/143a	3	33	2.03	9.85	1.52	9.85	2.23	7.18
R-143a/125	3	35	1.89	8.89	1.42	9.23	3.17	10.16
Overall			2.14		2.23		3.87	

Table 4.4 – Performance of the *f-theory* viscosity models and free-volume approach for mixtures. References: (1) Yokoyama *et al.* 2000, (2) Yokoyama *et al.* 2001, (3) Nabizadeh and Mayinger 1999, and (4) Yokoyama *et al.* 2004. *NP*: number of points.

Figure 4.7 – Calculated viscosity for refrigerant mixtures using the PR *f-theory* model (—) compared with experimental values (♦). Experimental data: R125 + R32 by Yokoyama *et al.* (2001) and R134a + R32 by Yokoyama *et al.* (2004).

4.3.3 – General friction theory models: pure compounds

The friction term (η$_f$) in the friction theory can be expressed in a reduced form defined as (Quiñones-Cisneros *et al.* 2001)

$$\hat{\eta}_f = \frac{\eta_f}{\eta_c} \quad (4.31)$$

where η$_c$ is the effective critical viscosity. It follows from the basic definition of the friction theory that the reduced friction viscosity term consists of reduced attractive and reduced repulsive contributions:

$$\hat{\eta}_f = \hat{\eta}_{f,r} + \hat{\eta}_{f,a} \quad (4.32)$$

The attractive term is given by

$$\hat{\eta}_{f,a} = \hat{\kappa}_a \left(\frac{p_a}{p_c}\right) \quad (4.33)$$

and the repulsive contribution by

$$\hat{\eta}_{f,r} = \hat{\kappa}_r \left(\frac{p_r}{p_c}\right) + \hat{\kappa}_{rr} \left(\frac{p_r}{p_c}\right)^2 \quad (4.34)$$

The temperature-dependent reduced friction coefficients are separated into the critical contribution, describing the reduced critical isotherm, and the residual contribution. This results in the following expressions for the reduced friction coefficients in Equations 4.33 and 4.34:

$$\hat{\kappa}_a = \hat{\kappa}_a^c + \Delta\hat{\kappa}_a; \quad (4.35)$$

$$\hat{\kappa}_r = \hat{\kappa}_r^c + \Delta\hat{\kappa}_r; \quad (4.36)$$

$$\hat{\kappa}_{rr} = \hat{\kappa}_{rr}^c + \Delta\hat{\kappa}_{rr} \quad (4.37)$$

The critical friction coefficients are constants. The residual friction coefficients must vanish as the critical isotherm is approached. For these coefficients Quiñones-Cisneros *et al.* (2001a) proposed the following empirical expressions with a simple dependency on T_c and P_c:

$$\begin{aligned}\Delta\hat{\kappa}_a &= \kappa_{a,0,0}(\Gamma-1) + \left(\kappa_{a,1,0} + \kappa_{a,1,1}\psi\right)\left(Exp(\Gamma-1)-1\right) \\ &+ \left(\kappa_{a,2,0} + \kappa_{a,2,1}\psi + \kappa_{a,2,2}\psi^2\right)\left(Exp(2\Gamma-2)-1\right);\end{aligned} \quad (4.38)$$

$$\begin{aligned}\Delta\hat{\kappa}_r &= \kappa_{r,0,0}(\Gamma-1) + \left(\kappa_{r,1,0} + \kappa_{r,1,1}\psi\right)\left(Exp(\Gamma-1)-1\right) \\ &+ \left(\kappa_{r,2,0} + \kappa_{r,2,1}\psi + \kappa_{r,2,2}\psi^2\right)\left(Exp(2\Gamma-2)-1\right);\end{aligned} \quad (4.39)$$

$$\Delta\hat{\kappa}_{rr} = \kappa_{rr,2,1}\psi\left(Exp(2\Gamma)-1\right)(\Gamma-1)^2, \quad (4.40)$$

where

$$\Gamma = \frac{T_c}{T}, \quad (4.41)$$

and

$$\psi = \frac{RT_c}{P_c}. \quad (4.42)$$

The constants contained in the parametric model for the residual friction coefficients, Equations 4.35 through 4.40, were fitted to the recommended viscosity data by Zéberg-Mikkelsen (2001a). This fitting was carried out using an iterative optimization procedure for the critical viscosities. The estimated universal parameters are reported in Table 4.5 for the SRK, PR and PRSV *f-theory* models.

For the n-alkanes, a simple correlation between the ratio η_c/p_c and the molecular weight was established by Quiñones-Cisneros *et al.* (2001a). An empirical equation is given by

$$\eta_c = 0.597556\, p_c M^{0.601652} \quad (4.43)$$

Finally, although the general friction theory models have shown to accurately represent the viscosities of hydrocarbons with simple molecular structure, in order to account for the viscosity effect of different molecular structures such as refrigerants or lubricants, a third-order p_r corrective term may be required (Zéberg-Mikkelsen *et al.* 2004). In this case, the friction viscosity is as follows:

$$\eta_f = \eta_c\hat{\eta}_f + \kappa_{rrr}\left(\frac{p_r}{p_c}\right)^3 \quad (4.44)$$

with

$$\kappa_{rr} = \kappa_{rr,2,1}\left[\exp(2\Gamma)-1\right](\Gamma-1)^2 \qquad (4.29)$$

	SRK	*PR*	*PRSV*
$\kappa_{a,0,0}$	−0.114804	0.048917	0.0261033
$\kappa_{a,1,0}$	0.246622	0.270572	0.194487
$\kappa_{a,1,1}$	-1.15648×10^{-4}	1.10473×10^{-4}	1.00432×10^{-4}
$\kappa_{a,2,0}$	−0.0394638	0.0448111	0.0401761
$\kappa_{a,2,1}$	4.18863×10^{-5}	4.08972×10^{-5}	3.94113×10^{-5}
$\kappa_{a,2,2}$	-5.91999×10^{-9}	5.79765×10^{-9}	5.91258×10^{-9}
$\kappa_{r,0,0}$	−0.315903	0.357875	0.325026
$\kappa_{r,1,0}$	0.566713	0.637572	0.586974
$\kappa_{r,1,1}$	-1.00860×10^{-4}	6.02128×10^{-5}	3.70512×10^{-5}
$\kappa_{r,2,0}$	−0.0729995	0.079024	0.0764776
$\kappa_{r,2,1}$	5.17459×10^{-5}	3.72408×10^{-5}	3.38714×10^{-5}
$\kappa_{r,2,2}$	-5.68708×10^{-9}	5.65610×10^{-9}	6.32233×10^{-9}
$\kappa_{rr,2,1}$	1.35994×10^{-8}	1.37290×10^{-8}	1.43698×10^{-8}
κ_{a}^{c}	-0.165302	-0.140464	-0.140464
κ_{r}^{c}	0.00699574	0.0119902	0.0119902
κ_{rr}^{c}	0.00126358	0.00085115	0.00085115

Table 4.5 – Residual friction and reduced critical parameters for the SRK, PR and PRSV *f*-theory models.

Further on, three versions of the general *f*-theory model will be studied. First, the critical viscosity will be calculated by means of Equation 4.41, and the general friction theory model will be used in conjunction with the PR EoS. In this way, the model is totally predictive, since it is based on standard tabulated constants. This version of the model will be referred to as "general *f*-PR-0". In the second approach, the critical viscosity η_c will be fitted for each pure compound, following the same fitting procedure as described in section 4.3.1, with the difference of fitting one instead of five parameters. This version will be referred to as "general *f*-PR-1". Finally, two parameters will be adjusted per a pure compound: the critical viscosity η_c and the constant ε in Equation 4.41. This last version of the model will be called "general *f*-PR-2". The critical viscosities and the ε parameter for the general *f*-PR-1 and general *f*-PR-2 models are reported in Table 4.6.

Compound	*general f-PR-1*	*general f-PR-2*	
	η_c (μP)	η_c (μP)	d_2 (μP) ×10^7
R11	502.007	492.769	3.289
R12	425.721	423.468	5.653
R13	405.659	383.868	0.253
R14	361.496	350.904	395.012
R22	431.937	416.406	0.856
R32	325.303	333.08	0.024
R113	663.542	616.236	21.646
R114	705.638	575.285	8.712
R115	600.630	580.654	13.012
R123	587.567	545.22	2.538
R124	515.641	490.451	2.419
R125	461.785	448.935	33.695
R134a	474.671	463.766	12.629
R141b	507.403	477.457	2.112
R142b	285.957	227.264	31.211
R143a	353.105	323.622	327.136
R152a	336.901	332.74	4.904
TriEGDME	427.458	392.744	0.466
TEGDME	416.266	397.152	0.159

Table 4.6 – Critical viscosities and d_2 constants for refrigerants and lubricants.

In Table 4.7 the AAD and MDev obtained with the different general models are presented. The general *f-PR-0* model performs satisfactorily only for few pure compounds. In many cases this version of the model produces large AAD. The viscosity predictions can be improved by adjustment of η_c as it can be seen for the general *f-PR-1* model. Improvement of the AAD is observed in many cases. The results can be further improved by inclusion of a second adjustable parameter (general *f-PR-2*). In some cases the general *f-PR-2* model delivers better results than the free volume model (compare Tables 4.8 and 4.5). The results obtained with this last version of the model can be considered very satisfactory, if one takes into account that only two adjustable parameters are used for each pure compound and that the general friction theory models were originally developed for other kinds of fluids. Figure 4.8 shows the general *f-PR-2* model results for R134a and R125. The model shows good and stable performance. However, there are some regions where the model clearly deviates (see for example the high-pressure region for R134a or the low-temperature region for R125).

Compound	NP	general f-PR-0		general f-PR-1		general f-PR-2	
		AAD (%)	MDev (%)	AAD (%)	MDev (%)	AAD (%)	MDev (%)
R11	133	5.01	19.38	4.25	21.64	2.74	13.75
R12	166	4.73	20.47	3.41	21.44	3.11	21.58
R13	475	10.62	59.02	11.19	56.20	6.95	38.00
R14	168	5.56	12.03	5.14	12.03	5.09	12.03
R22	126	7.08	25.55	6.62	26.23	2.57	7.86
R32	241	7.02	23.20	4.00	18.90	4.00	18.90
R113	18	28.84	37.98	6.19	12.92	1.60	3.72
R114	130	27.74	50.62	7.29	31.50	4.38	9.23
R115	102	16.77	42.20	6.95	34.68	6.14	34.55
R123	138	13.09	44.06	7.03	27.48	3.75	14.88
R124	149	20.57	67.51	14.71	59.95	7.83	26.21
R125	294	10.27	39.33	6.60	27.43	5.71	22.76
R134a	536	14.02	40.80	6.23	28.67	4.91	27.30
R141b	57	13.66	42.88	10.33	35.00	2.90	9.04
R142b	134	4.59	17.52	2.53	12.27	1.17	10.57
R143a	119	6.70	20.29	6.61	18.84	6.34	20.75
R152a	175	3.80	17.97	3.78	17.70	3.67	13.35
TriEGDME	63	17.81	35.66	7.42	22.35	6.14	20.63
TEGDME	63	16.35	39.07	8.24	27.93	8.25	27.46
Overall		11.03		6.92		4.95	

Table 4.7 – Comparison of general viscosity models for pure compounds. NP: number of points.

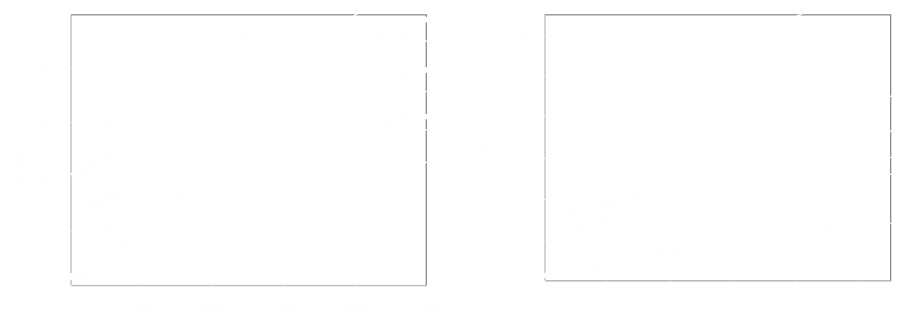

Figure 4.8 – Calculated viscosity for R134a and R125 using the general f-PR-2 model (—) compared with experimental values (•). Note: all experimental points are reported in Appendix B.

4.3.4 – General friction theory models: mixtures

In order to apply the general *f-theory* models to an *n*-component mixture, the mixture friction coefficients required for the *f-theory* can be obtained from the pure-compound reduced friction coefficients defined in Equations 4.35 through 4.42. This leads to the following expressions:

$$\kappa_{r,mix}=\sum_{i=1}^{n} z_i\frac{\eta_{c,i}\,\kappa_{r,i}}{P_{c,i}} \qquad (4.46)$$

$$\kappa_{a,mix}=\sum_{i=1}^{n} z_i\frac{\eta_{c,i}\,\kappa_{a,i}}{P_{c,i}} \qquad (4.47)$$

$$\kappa_{rr,mix}=\sum_{i=1}^{n} z_i\frac{\eta_{c,i}\,\kappa_{rr,i}}{P_{c,i}^{2}} \qquad (4.48)$$

Here the values of z_i are defined by Equations 4.29 and 4.30. The dilute and the friction terms of the mixture are calculated by means of Equations 4.24 and 4.31 respectively. If the third-order friction coefficient is used in conjunction with the general model, an exponential mixing rule can be employed (Zéberg-Mikkelsen *et al.* 2004)

$$Ln\left(\kappa_{rrr,mix}\right)=\sum_{i=1}^{n} x_i\,Ln\left(\kappa_{rrr,i}\right) \qquad (4.49)$$

Mixture	*Ref*	*NP*	*general f-PR-0*		*general f-PR-1*		*general f-PR-2*	
			AAD (%)	MDev (%)	AAD (%)	MDev (%)	AAD (%)	MDev (%)
R-125/134a	1	340	6.42	24.26	3.99	14.22	3.25	18.56
R-125/32	2,3	392	3.74	22.79	3.56	20.85	3.69	17.25
R-134a/32	4	329	5.93	26.92	5.27	22.09	4.85	21.96
R-143a/125/134a	3	40	5.12	25.60	4.25	17.56	3.89	22.30
R-32/125/143a	3	33	4.25	21.20	3.25	23.25	3.50	20.59
R-143a/125	3	35	6.56	22.35	4.12	18.96	3.89	22.10
Overall			5.28		4.20		3.90	

Table 4.8 – Performance of the general models for mixtures. References: (1) Yokoyama *et al.* 2000, (2) Yokoyama *et al.* 2001, (3) Nabizadeh and Mayinger 1999, and (4) Yokoyama *et al.* 2004. *NP*: number of points.

Table 4.8 shows the values of AAD obtained for viscosity predictions with the general *f-theory* models for different kinds of the refrigerant mixtures. The characteristic viscosities and coefficient d_2 given in Table 4.6 have been used. In general, a good agreement is found with the different versions of the model.

4.4 – Friction theory + the SBWR EoS

This section approaches the issue of accurate simultaneous viscosity and density modeling, by extending the *f-theory* approach to the SWBR equation of state (Soave, 1995 and 1999). As shown in Chapter II, the SBWR EoS is capable of accurate density predictions for refrigerants and lubricants. The SBWR EoS + *f-theory* model is applied to the accurate viscosity modeling for almost all the compounds as studied in Chapter II. These compounds are: R32, R125, R134a, R152a, and the two lubricants: TriEGDME and TEGDME.

The *f-theory* is based on the van der Waals concept of a balance between the repulsive and the attractive pressure terms, while a BWR type of the EoS is not structured in this way. However, there are alternative ways by which the *f-theory* can be adapted to an EoS that is not of the van der Waals type. For example, if the total pressure in a given EoS is written as a sum of *n* terms:

$$p = \sum_{i=1}^{n} p_i \, , \tag{4.50}$$

a straightforward extension of the *f-theory* is to express the viscosity as follows:

$$\eta_f = \sum_{i=1}^{n} \left(\kappa_{i,1}\, p_i + \kappa_{i,2}\, p_i^2 \right) \tag{4.51}$$

A term-by-term analysis may show that some of the second-order terms may be neglected if they do not provide important contributions at high pressures. This approach has been tested for the SBWR EoS for pure n-alkanes (Quiñones-Cisneros *et al.* 2002), and accurate modeling results have been obtained for pure components. However, if the viscosity of mixtures is predicted using the same simple mixing rules as with other *f-theory* models, the results may not be as good, due to large discrepancies in the magnitudes of the different SBWR EoS terms for different substances. Therefore, if a model such as the one given in Equation 4.51 is used for the prediction of mixture viscosities, adequate mixing rules have to be developed. A straightforward extension of the *f-theory* may result in an unnecessarily large number of friction parameters. An alternative approach to accurately model the viscosity of pure fluids and satisfactory mixture viscosity predictions is to group the terms of the non-van der Waals EoS into attractive-like and repulsive-like pressure terms, to obtain a model more consistent with the *f-theory* (Quiñones-Cisneros *et al.* 2002). In the case of the SBWR EoS, this can be achieved by splitting the equation into the following attractive-like and repulsive-like pressure terms:

$$p_a = B\,R\,T\,\rho^2, \qquad (4.52)$$

and

$$p_r = \left(1 + D\,\rho^4 + E\,\rho^2\left(1 + F\,\rho^2\right)Exp\left(-F\,\rho^2\right)\right)R\,T\,\rho \qquad (4.53)$$

Figure 4.9 shows the p/p_c, p_a/p_c and p_r/p_c isotherms predicted by the SBWR and the PR EoS for R134a at a reduced temperature of 0.5. It can be seen that Equations 4.52 and 4.53 have a correct qualitative attractive and repulsive performance. Therefore, the extension of the *f-theory* to the SBWR EoS may be carried out by use of Equations 4.52 and 4.53 in combination with the viscosity friction term given by Equation 4.13.

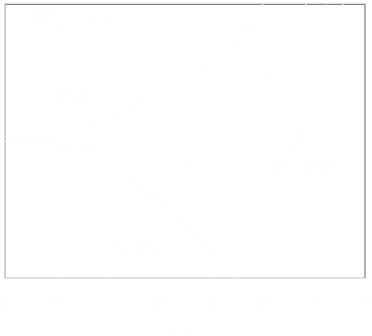

Figure 4.9 – The SBWR (—) and PR (– –) R134a reduced pressure, reduced attractive pressure term, and reduced repulsive pressure term as function of reduced density at $T/T_c = 0.5$.

For the temperature dependence of the friction parameters, it has been found that the five-constant model (Equations 4.20 to 4.22) gives accurate results. To derive models for refrigerants and lubricants, an overall least-square fitting to the data of Appendix E has been carried out. The SBWR EoS has been used as described in Chapter II, with adjustment of Z_c and ω for each compound, i.e., the version of EoS used is "SBWR-zeg". The ASBWR friction constants required in Equations 4.20-4.22 are listed in Table 4.9. Table 4.10 has the number of points of the modeled data together with the average absolute deviation and the maximum deviation. The results reported in Table 4.10 show very accurate model performance in all cases. In almost all cases the average absolute deviation is of the order of the experimental uncertainty.

Compound	*f-theory* with the SBWR-reg EoS				
	a_1 (μP/Bar)	a_2 (μP/Bar)	b_1 (μP/Bar)	b_2 (μP/Bar)	c_2 (μP/Bar^2) ×10^4
R32	0.0795	-0.4012	-0.4507	0.2427	0.1375
R125	-0.0971	-0.8868	-1.4472	0.6328	0.5311
R134a	0.2610	-0.1157	-0.8345	0.8669	0.2460
R152a	0.0923	0.1895	-0.6399	0.6310	0.0882
TrIEGDME	0.4306	-0.9277	-1.3440	-0.0092	0.2224
TEGDME	0.6010	-1.7912	-1.9970	-0.3542	0.3544

Table 4.9 – Parameters for the *f-theory* with the SBWR EoS (five-constant parametric model).

Compound	*NP*	*f – SBWR-reg*	
		AAD (%)	MDev (%)
R32	241	1.97	11.58
R125	294	2.32	11.16
R134a	536	2.61	13.72
R152a	175	1.50	7.50
TrIEGDME	63	0.84	3.90
TEGDME	63	1.24	5.29

Table 4.10 – Performance of the *f-theory* SBWR-reg model for pure compounds. *NP*: number of points.

An advantage of combining a friction theory model with a BWR type of EoS is the improved predictive capability for the densities. This is depicted in Figure 4.10, where some representative viscosity–versus–density isotherms are compared to experimental data for different compounds. Figure 4.10 also includes a comparison with the viscosity predictions obtained for the five-parameter PR *f-theory* model. The best performance of the new model is observed for R134a (in the low-temperature region), TrIEGDME and TEGDME. The results obtained for R32 are similar for both models. This is not surprising, since, as shown in Chapter II, the PR and the SBWR-reg EoS describe the p–v–T properties of this compound in a similar way.

Figure 4.10 – Selected experimental dense phase viscosity (♦) of HFC-32, HFC-134a, TriEGDME, and TEGDME in comparison with the *f-theory* SRK (—) and the *f-theory* PR (---) predictions for various temperatures. Note: experimental values reported in Appendix B.

4.5 – Friction theory + the PC-SAFT EoS

The PC-SAFT EoS can be conveniently grouped in an attraction-dominant and a repulsive-dominant pressure contributions:

$$p_a = Z^{disp} RT\rho \qquad (4.54)$$

and

$$p_r = \left(1 + Z^{hc}\right)RT\rho \qquad (4.55)$$

where Z is the compressibility factor. Subscript disp accounts for attractive interactions, and hc is the hard-chain contribution. The expressions for these may be found in Gross and Sadowski (2001), as plot of the repulsive and attractive PC-SAFT contributions is similar to Figure 4.8. For the friction coefficients Equations 4.20 to 4.22 have been used. The coefficients are reported in Table 4.11.

Compound	*f-theory* with the PC-SAFT EoS				
	a_1 (μP/Bar)	a_2 (μP/Bar)	b_1 (μP/Bar)	b_2 (μP/Bar)	c_2 (μP/Bar^2) ×10^4
R32	0.3303	-0.2801	0.1086	-0.1134	0.0464
R125	0.5487	0.4869	-0.0092	0.6116	0.1176
R134a	-0.2660	-0.4271	-0.6049	-0.0570	0.1704
R152a	0.3851	-0.6948	0.1090	-0.5326	0.0744
TriEGDME	-3.5103	-2.0537	-3.9139	-0.7942	0.3094
TEGDME	-5.5341	-3.6590	-6.1968	-1.6421	0.4513

Table 4.11 – Parameters for the *f-theory* with the PC-SAFT EoS (five-constant parameters model).

Table 4.12 shows the average absolute deviation and the maximum deviation for the studied compounds. As for the *f-theory* + SBWR EoS, a good viscosity description is obtained. Overall, *f*-SBWR-reg delivers better results than *f*-PC-SAFT (compare Table 4.10 and 4.12). Moreover, although the general accuracy of the viscosity predictions is satisfactory, the results obtained with the *f-theory* PC-SAFT appear to be less accurate than the results obtained with the *f-theory* models based on the cubic EoS. Performance of the PC-SAFT *f-theory* model is shown for R32, R134a, TriEGDME, and TEGDME in a viscosity versus density plot for various isotherms in Figure 4.11.

Compound	*NP*	*f – PC-SAFT*	
		AAD (%)	MDev (%)
R32	241	2.61	12.39
R125	294	3.05	18.59
R134a	536	2.55	19.89
R152a	175	1.55	12.82
TriEGDME	63	2.01	4.47
TEGDME	63	2.86	6.94

Table 4.12 – Performance of the *f-theory* PC-SAFT model for pure compounds. NP: number of points.

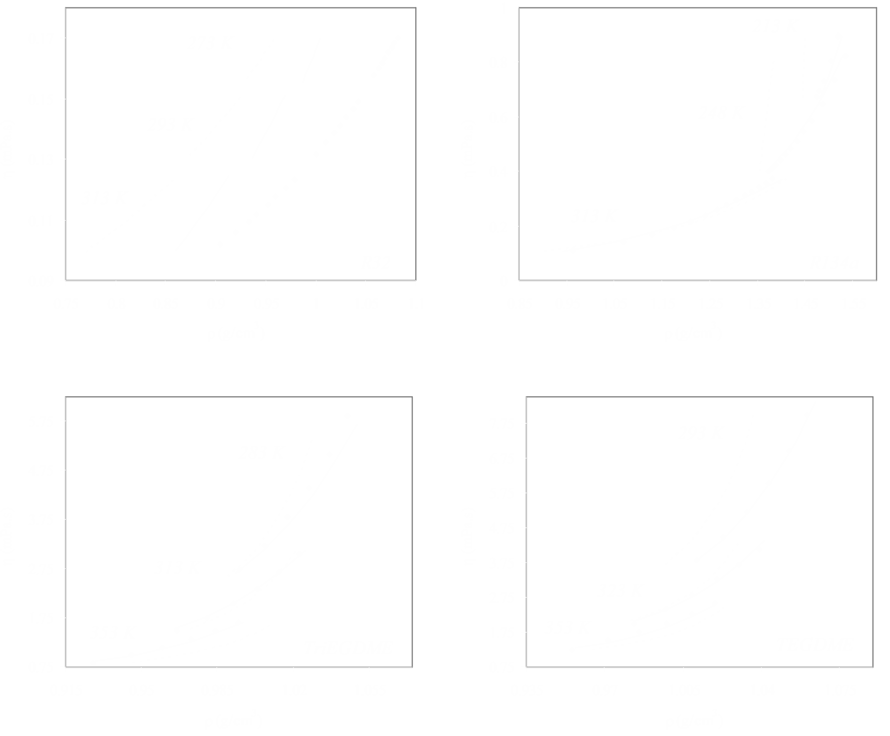

Figure 4.11 – Selected experimental dense phase viscosity (●) of HFC-32, HFC-134a, TrEGDME, and TEGDME in comparison with the *f-theory* PC-SAFT (—) and the *f-theory* PR (---) predictions for various temperatures. Note: experimental values reported in Appendix B.

4.6 – Comparison among the models

For comparison, calculated versus experimental viscosities are plotted in Figure 4.12 for the different models considered throughout this Chapter for R32, R125, R134a, R152a TrEGDME, and TEGDME. Overall, a good performance can be observed, except for the *general f-PR-1* and the *general f-PR-2*. These models show large deviations, especially in the high-viscosity range.

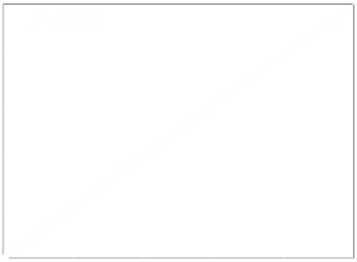

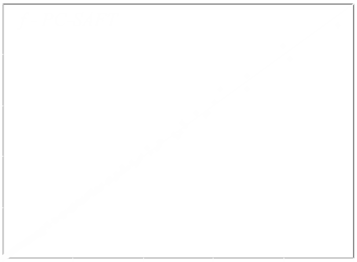

4.7 - Conclusions

Starting from basic principles of classical mechanics and thermodynamics Quiñones-Cisneros *et al.* (2000) introduced the *f-theory* for viscosity modeling. In the *f-theory* the viscosity in excess of the dilute gas limit is approached as a mechanical rather than a transport property. By linking the Amonton-Coulomb friction law with the van der Waals repulsive and attractive pressure terms of a simple cubic EoS, it has been shown that highly accurate viscosity modeling can be achieved. In this work, the *f-theory* has been applied in conjunction with the cubic EoS to predict the viscosity of pure refrigerants, pure lubricants and few refrigerant mixtures over wide ranges of temperature and pressure. The results obtained with the *f-theory* are very satisfactory in the most cases. Compared with the free-volume model (which was studied in Chapter III and showed the best performance among the existing viscosity models), better results are obtained on the basis of the *f-theory*.

Based on recommended viscosities for *n*-alkanes Quiñones-Cisneros *et al.* (2001a) developed general *f-theory* models in conjunction with the SRK, the PR, and the PRSV EoS. The general *f-theory* models depend only on one adjustable property: effective critical viscosity. These general one-parameter *f-theory* models have shown to deliver good results only for few compounds. However, the results can be improved by inclusion of a second adjustable parameter. The results obtained with the general *f-PR-2* are surprisingly good in some cases.

An extension of the *f-theory* to models besides cubic EoS has also been carried out in this chapter. The equations used were the SBWR EoS and the PC-SAFT EoS. Originally, these two EoS are not divided into repulsive-like and attractive-like pressure terms. They were regrouped into the two terms, so that correct qualitative performance could be obtained. Although the *f*-SBWR and the *f*-PC-SAFT have shown a satisfactory agreement with experimental data, the results seem to be less accurate than the results obtained with the *f-theory* + cubic EoS. This may be due to a better repulsive and attractive structure of the cubic EoS compared to the SBWR or PC-SAFT EoS. Nonetheless, the results obtained may be considered to be satisfactory. This shows that, for pure compounds, the *f-theory* can be extended to noncubic EoS as it has been carried out in this work.

Since for mixtures the *f-theory* is totally predictive, comparison of the *f-theory* based models with experimental data for mixtures may serve as a real test for the theory. Unfortunately, as mentioned in Chapter III, the experimental data for refrigerant mixtures reported in the literature do not cover wide pressure ranges. In Chapter VII, a first attempt at predicting the viscosity of refrigerant + lubricant mixtures up to very high pressures with these models will be considered.

Nomenclature

A = Nominal area of the surfaces between two bodies under friction contact

AAD = Average absolute deviation

EoS = Equation of state

F = Shear force

F_k = kinetic friction force

h = Fluid thickness

k_{ij} = Binary interaction parameter

M = Molecular weight

MM = Weighted molecular weight average

$MDev$ = Maximum deviation

n = Number of components

N = Normal force

NP = Number of points

p = Pressure

$PC\text{-}SAFT$ = Perturbed-chain statistical associating fluid theory

PR = Peng-Robinson

$PRSV$ = Peng-Robinson-Stryjek-Vera

R = Gas constant

$RK\text{-}PR$ = Redlich-Kwong-Peng-Robinson

$SBWR$ = Soave-Benedict-Webb-Rubin

SRK = Soave-Redlich-Kwong

T = Temperature

u = Velocity of displacing layers

U = Displacement velocity

v = Molar volume

x = Mole fraction

z = mass weighted fraction

Z = Compressibility factor

Greek letters

δh = Thickness of displacing layers
$\partial u/\partial h$ = Shear rate
η = Total viscosity
η_0 = Dilute gas viscosity
η_f = Friction viscosity
κ_a = Linear attractive viscous friction coefficient
κ_r = Linear repulsive viscous friction coefficient
κ_{rr} = Quadratic repulsive viscous friction coefficient
μ_k = Coefficient of kinetic friction
μ_a = Linear attractive Amontons-Coulomb coefficient of kinetic friction
μ_r = Linear repulsive Amontons-Coulomb coefficient of kinetic friction
μ_{rr} = Quadratic repulsive Amontons-Coulomb coefficient of kinetic friction
ρ = Density
σ = Normal stress
τ = Total shear stress
τ_0 = Dilute gas collision shear stress
τ_a = Attractive friction shear stress
τ_f = Friction shear stress
τ_r = Repulsive friction shear stress
ω = Acentric factor

Subscripts/superscripts

a = Attractive
c = Critical
cal = Calculated property
disp = Contribution due to dispersive attraction
exp = Experimental property
hc = Residual contribution of hard-chain system
i = Component "i"

i = Component "i"

mix = Mixture

r = Reduce property, repulsive

References

1. Allal, A., Moha-Ouchane, M., Boned, C. A New Free Volume Model for Dynamic Viscosity and Density of Dense Fluids Versus Pressure and Temperature. *Phys. Chem. Liq.* 2001a, 39, 1–30.
2. Allal, A., Boned, C., Daugé, P. A New Free Volume Model for Dynamic Viscosity of Dense Fluids Versus Pressure and Temperature. Extension to a Predictive Model for Not Very Associative Mixtures. *Phys. Chem. Liq.* 2001b, 39, 607–624.
3. Cismondi, M., Mollerup, J. Development and application of a three-parameter RK-PR equation of state. *Fluid Phase Equilib.* 2005, 232, 74-89.
4. Chung, T.-H., Ajlan, M., Lee, L.L., Starling, K.E. Generalized Multiparameter Correlations for Nonpolar and Polar Fluid Transport Properties. *Ind. Eng. Chem. Res.* 1988, 27, 671–679.
5. Comuñas, M.J.P., Baylaucq, A., Quiñones-Cisneros, S.E., Zéberg-Mikkelsen, C.K., Boned, C., Fernández, J. Viscosity measurements and correlations for 1,1,1,2-tetrafluoroethane (HFC-134a) up to 140 MPa. *Fluid Phase Equilib.* 2003, 210, 21–32.
6. Gross, J., Sadowski, G. Perturbed-Chain SAFT: An Equation of State Based on a Perturbation Theory for Chain Molecules. *Ind. Eng. Chem. Res.* 2001, 40, 1244-1260.
7. Nabizadeh, H., Mayinger, F. Viscosity of R404A, R407C, R410A and R507. *Int. J. Thermophys.* 1999, 20, 777-790.
8. Peng, D.-Y., Robinson, D.B. A New Two-Constant Equation of State. *Ind. Eng. Chem. Fundam.* 1976, 15, 59–64.
9. Quiñones-Cisneros, S.E., Zéberg-Mikkelsen, C.K., Stenby, E.H. The Friction Theory (f-theory) for Viscosity Modeling. *Fluid Phase Equilib.* 2000, 169, 249-276.
10. Quiñones-Cisneros, S.E., Zéberg-Mikkelsen, C.K., Stenby, E.H. One Parameter Friction Theory Models for Viscosity. *Fluid Phase Equilib.* 2001a, 178, 1-16.
11. Quiñones-Cisneros, S.E., Zéberg-Mikkelsen, C.K., Stenby, E.H. the friction theory for viscosity modelling: extension to crude oil systems. *Chem. Eng. Sci.* 2001b, 56, 7007 – 7015.
12. Quiñones-Cisneros, S.E., Zéberg-Mikkelsen, C.K., Stenby, E.H. Accurate Density and Viscosity Modeling of Nonpolar Fluids Based on the "f-Theory" and a Noncubic Equation of State. *Int. J. Thermophys.* 2002, 23, 41 – 55.
13. Quiñones-Cisneros, S.E., Zéberg-Mikkelsen, C.K., Stenby, E.H. Friction theory of crude oil viscosity at reservoir based on dead oil properties. *Fluid Phase Equilib.* 2003, 212, 233 – 243.

14. Quiñones-Cisneros, S.E., Zéberg-Mikkelsen, C.K., Baylaucq, A., Boned, C. Viscosity Modeling and Prediction of Reservoir Fluids: From Natural Gas to Heavy Oils. *Int. J. Thermophys.* 2004a, 25, 1353-1366.
15. Quiñones-Cisneros, S.E., Dalberg, A., Stenby, E.H. PVT Characterization and Viscosity Modeling and Prediction of Crude Oils. *Pet. Sci. Tech.* 2004b, 22, 1309-1326.
16. Quiñones-Cisneros, S.E., Andersen, S.I. Density and Viscosity Modeling and Characterization of Heavy Oils. *Energy and Fuels.* 2005, 19, 1314-1318.
17. Schmidt, K.A.G., Quiñones-Cisneros, S.E., Kvamme, B. Density and Viscosity Behavior of a North Sea Crude Oil, Natural Gas Liquid, and Their Mixtures. *Energy and Fuels.* 2005, 19, 1303-1313.
18. Soave, G.S. Equilibrium Constants from a Modified Redlich-Kwong Equation of State. *Chem. Eng. Sci.* 1972, 27, 1197-1203.
19. Soave, G.S. A Noncubic Equation of State for the Treatment of Hydrocarbon Fluids at Reservoir Conditions. *Ind. Eng. Chem. Res.* 1995, 34, 3981-3994.
20. Soave, G.S. An effective modification of the Benedict-Webb-Rubin equation of state. *Fluid Phase Equilib.* 1999, 164, 157-172.
21. Stryjek, R., Vera, J.H. Vapor-Liquid Equilibrium of Hydrochloric Acid Solutions with the PRSV Equation of State. *Fluid Phase Equilib.* 1986, 25, 279-290.
22. van der Gulik, P.S., Mostert, R., van den Berg, H.R. The Viscosity of Methane at 273 K up to 1 GPa. *Fluid Phase Equil.* 1992, 79, 301 – 311.
23. Yokoyama, C., Nishino, T., Takahashi, M. Viscosity of gaseous mixtures of HFC-125 (pentafluoroethane) + HFC-134a (1,1,1,2-tetrafluoroethane) under pressure. *Fluid Phase Equilib.* 2000, 174, 231-240.
24. Yokoyama, C., Nishino, T., Takahashi, M. Viscosity of Gaseous Mixtures of HFC125+HFC32. *Int. J. Thermophys.* 2001, 22, 1329.
25. Yokoyama, C., Nishino, T., Takahashi, M. Viscosity of Gaseous Mixtures of HFC134a+HFC-32. *Int. J. Thermophys.* 2004, 25, 71-88.
26. Zéberg-Mikkelsen, C.K., Quiñones-Cisneros, S.E., Stenby, E.H. Viscosity Prediction of Hydrogen + Natural Gas Mixtures (Hythane). *Ind. Eng. Chem. Res* 2001a, 40, 2966-2970.
27. Zéberg-Mikkelsen, C.K., Quiñones-Cisneros, S.E., Stenby, E.H. Viscosity Modeling of Light Gases at Supercritical Conditions Using the Friction Theory. *Ind. Eng. Chem. Res* 2001b, 40, 3848-3854.
28. Zéberg-Mikkelsen, C.K., Quiñones-Cisneros, S.E., Stenby, E.H. Viscosity Prediction of Hydrocarbon Mixtures Based on the Friction Theory. *Pet. Sci. Tech.* 2001c, 19, 893-910.

29. Zéberg-Mikkelsen, C.K. Viscosity study of hydrocarbon fluids at reservoir conditions, modeling and measurements. Ph.D Thesis, Technical University of Denmark, Lyngby, Denmark, 2001d.
30. Zéberg-Mikkelsen, C.K., Quiñones-Cisneros, S.E., Stenby, E.H. Viscosity modeling of associating fluids based on the friction theory: pure alcohol. *Fluid Phase Equilib.* 2002a, 194-197, 1191-1203.
31. Zéberg-Mikkelsen, C.K., Quiñones-Cisneros, S.E., Stenby, E.H. Viscosity Prediction of Natural Gases Using the Friction Theory. *Int. J. Thermophys.* 2002b, 23, 437-454.
32. Zéberg-Mikkelsen, C.K., Quiñones-Cisneros, S.E., Stenby, E.H. Viscosity Prediction of Carbon Dioxide + Hydrocarbon Mixtures Using the Friction Theory. *Pet. Sci. Tech.* 2002c, 20, 27-42.
33. Zéberg-Mikkelsen, C.K., Baylaucq, A., Barrouhou, M., Quiñones-Cisneros, S.E., Boned, C. Comparative study of viscosity models on the ternary system methylcyclohexane + cis-decalin + 2,2,4,4,6,8,8-heptamethylnonane up to 100 MPa. *Fluid Phase Equilib.* 2004, 222-223, 135-148.

Refrigerant + Lubricant Mixtures

This part consists of three chapters:

- *Chapter V: Analysis of Phase Behavior*
- *Chapter VI: Modeling Phase Equilibria and p–v–T–x Behavior*
- *Chapter VII: Viscosity Measurements and Modeling*

V – Analysis of Phase Behavior

5.1 – Introduction

The complexity and variety of the phase behavior patterns found in mixtures has been a subject of research and discussion for many scientists, at least, since the time of van der Waals. Such research has gradually intensified during the last few decades owing to the great diversity of new applications that phase behavior finds in various areas of physical sciences. In relation to this, van Konynenburg and Scott (1980) first introduced a classification for the main types of phase behavior patterns that binary mixtures may develop. Furthermore, based on the van der Waals equation of state, van Konynenburg and Scott (1980) also located the different types of phase behavior patterns that they found in parameter space diagrams; thus, also introducing the concept of a global phase diagram.

Phase behavior of asymmetric and associating mixtures can be complex, exhibiting closed miscibility gaps, open miscibility gaps, liquid-liquid-vapor equilibrium, and even barotropic phenomena. When variables such as temperature and/or pressure are varied, normally not only the compositions but also other properties of the coexisting phases change. It can happen that, during such a variation, the density difference between the coexisting phases decreases and even changes sign. This behavior is called "barotropy" and the point where the barotropy occurs is an "isopycnic point" (Schneider *et. al.* 2000).

After the initial work of van Konynenburg and Scott (1980) a great deal of progress in understanding the complex phase behavior, some of which may follow from more elaborated theoretical models, has been further achieved (Deiters and Pegg 1989, van Pelt *et al.* 1995, and Galindo and Blas 2002 among many others). However, from the beginning, there is one area that appears to have been neglected: barotropic behavior. The study and understanding of barotropic phenomenon and its relation to phase behavior has largely been neglected both in the laboratory as well as in theoretical research. In fact, in the literature a large number of theoretical and experimental works showing solubility and compositional phase diagrams, but leaving density largely untouched, can be found. Nevertheless, as pointed out by Quiñones-Cisneros (1996 and 2004) full understanding of global phase behavior may not be possible without also taking into account barotropic phenomena.

From both experimental and theoretical research experience, it can be asserted that the type of phase behavior to be discussed in this chapter may develop from two main kinds of contributions: asymmetry and/or association. In refrigerant + lubricant applications, the complex phase behavior that those mixtures may show is mainly due to asymmetry (Hauk and Weidner, 2000). In fact, Hauk and Weidner (2000) have studied the properties of CO_2 with different lubricants for automobile cooling circuit applications finding complex phase behavior along with barotropic phenomena. Therefore, due to its industrial importance and relevance, throughout this work barotropic behavior will be studied exclusively due to asymmetry. However, this phenomenon might also take place in the presence of association and as an example of binary mixtures of industrial interest with at least one associating compound showing complex phase behavior, the work of Bruner (1985) can be mentioned.

This chapter will first be focused on a better understanding of how such phenomenon originates, as it appears to be intrinsically linked to the transition between type II and III phase behavior. After that, the relation between phase and viscosity behavior will be discussed throughout a series of examples, since viscosity seems to follow the complex phase behavior that these mixtures develop.

5.1.1 – Importance of studying phase and viscosity behavior in refrigerant – lubricant systems

In the case of refrigeration cycles, the circulating fluid comes into contact with the lubricant used in the compressors. Some of the refrigerant may dissolve into the oil phase giving rise to the development of complex phase behavior. The dissolved refrigerant may substantially lower the viscosity of the oil-rich phase resulting in lower lubrication properties and giving rise to a potential breakdown of the compressor mechanical parts. Thus, good knowledge of both viscosity and phase behavior is of a fundamental importance. Moreover, depending on the oil miscibility within the refrigerant-rich phase, even with an efficient oil separator installed, part of the lubricant oil may migrate from the compressor to other parts of the system such as the evaporator, condenser, expansion device and piping. Therefore, some related problems might also develop as a consequence of the occurring of phase separation at unforeseen places of a refrigeration cycle. For example, oil accumulation may take place inside the heat exchanger tubes, reducing heat transfer capabilities and resulting in the overall decrement of the refrigeration cycle performance. In fact, because at the evaporator the temperature and the pressure are the lowest in a refrigeration cycle, this is the place where most probably phase separation may occur. Thus, as the refrigerant evaporates, it leaves a liquid oil film on the internal cold surface of the evaporator tubing. Hence, for an optimal performance design the phase and transport properties of the coexisting phases must be understood.

and the viscosity has to be adequate in order for the oil with condensed refrigerant to be fed back into the compressor.

5.2 – Classification of fluid phase behavior

On the basis of the projection of the critical lines in the p–T plane, van Konynenburg and Scott (1980) classified the different types of phase behavior patterns that binary mixtures may develop. Their classification is based on the presence or absence of critical lines and on the way three-phase lines, when present, are connected to them. The phase diagrams can be divided into subclasses by considering additional characteristics such as the existence of azeotropy (positive or negative) or heteroazeotropy (indicated by adding "A" or "HA"). Further subdivision is due to the occasional temperature or pressure minima along critical lines. The critical lines may end in various ways: the pure one-component gas-liquid critical points (C_1 and C_2), or at a critical point located at very high pressures (C_m). Van Konynenburg and Scott (1980) introduced this critical point at high pressure to describe the course of some critical lines. In addition, critical lines may terminate at the end of three-phase lines, at upper or lower critical end points (UCEP or LCEP). It should be noticed that azeotropic phenomena play an important role in this classification.

Figure 5.1 shows a schematic representation of the six types of phase diagrams. In type I mixtures, only vapor-liquid separation occurs, whereas in type II to type VI mixtures liquid-liquid immiscibility also takes place in some regions of the diagram. Types I and II have a continuous critical curve from one pure critical point to the other, whereas types III, IV and V are distinguished by the absence of a continuous gas-liquid critical curve. Mixtures conforming to type VI are invariably composed of complex molecules, in the sense that hydrogen bonding or other strong intermolecular forces are present. This type was introduced by Rowlinson and Swinton (1982) and the van der Waals EoS cannot describe this kind of behavior.

The main characteristics of the different phase diagrams are as follow:

- *Type I*: the usual conditions under which a binary mixture will conform to type I behavior are that the two substances should be of similar chemical types and/or their critical properties should be comparable. These mixtures can be conveniently distinguished first by the shape of the continuous critical curve and, further, by noting the presence or absence of azeotropy.

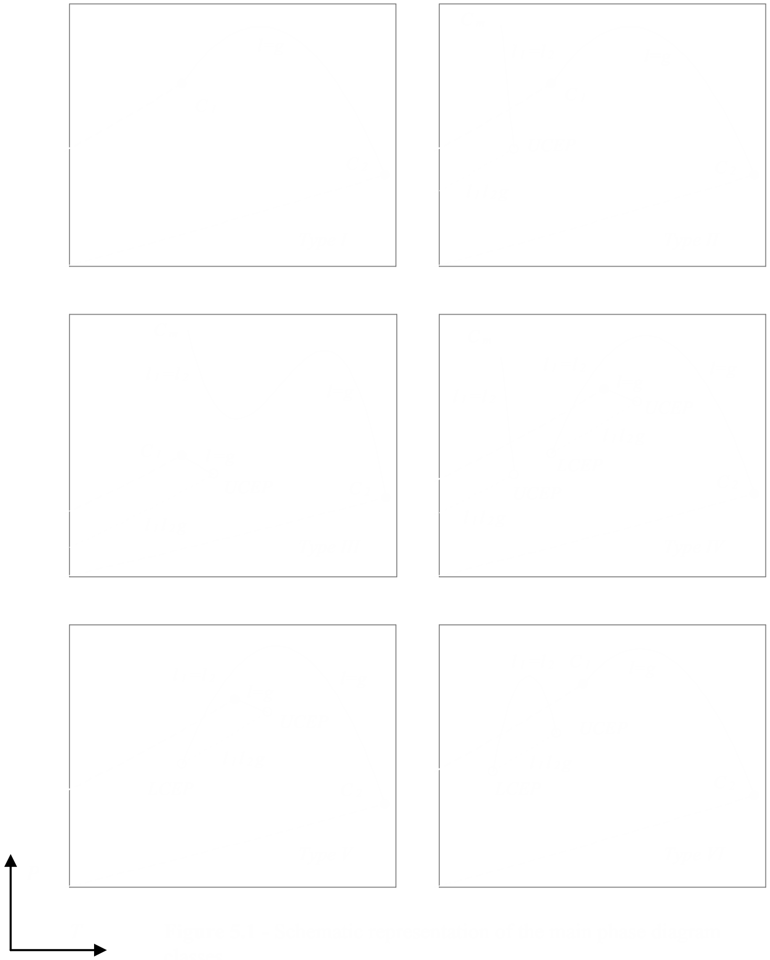

Figure 5.1 – Schematic representation of the main phase diagram classes.

- *Type II:* type II is characterized by the presence of liquid-liquid immiscibility at low temperatures. There is thus one additional critical line that extends down (with either negative or positive slope) from a C_m to low pressures where it terminates at the upper critical end point (UCEP) and the third, gaseous, phase is formed. A three phase line (L_1L_2g) extends from the UCEP to lower pressures and temperatures. If the three-phase line is above the vapor pressure curve of the most volatile component, a heterogeneous azeotrope, or heteroazeotrope, is formed.

- *Type III:* type III mixtures have two critical curves, one starting at the C_2 that goes to infinite pressure C_m. The other one starts at C_1 and meets a three-phase line at an UCEP (this UCEP is sometimes referred as a K-point). The branch of critical line starting at C_m cannot be clearly identified as being vapor-liquid or liquid-liquid. In addition, the shape of this branch can be different to the one shown in Figure 5.1 (see Rowlinson and Swinton, 1982 for examples). As in the case of type II if the three-phase curve lies everywhere above the vapor-pressure curve of the more volatile component, these systems will show heteroazeotropy (Type III-HA).

- *Type IV:* in type IV phase behavior three critical curves exist, as shown in Figure 5.1. One of them is a liquid-liquid critical curve that stars at C_m and goes down to the UCEP of the first three-phase line. The second one starts at C_1 and ends in an UCEP of a second three-phase line (K point). The third critical curve starts at C_2 and ends at a LCEP of the latter three-phase line. This last critical curve changes its character. Near the C_2 has a vapor-liquid character, whereas near the LCEP the curve has a liquid-liquid character.

- *Type V:* Type V mixtures, see Figure 5.1, have two critical curves and correspond to type IV mixtures without the steep liquid-liquid critical curve.

- *Type VI:* binary mixtures showing type VI phase behavior have a continuous vapor-liquid critical curve between C_1 and C_2. In addition, these mixtures have a liquid-liquid critical curve that starts at a LCEP of a three-phase line and ends at an UCEP on the same three-phase line. The liquid-liquid critical curve can be extended below both end-points showing a closed critical curve (with stable, metastable and unstable parts).

It is important to notice that type III, IV and V contain critical lines, which cannot be clearly identified as liquid-liquid or liquid-vapor. Quiñones-Cisneros (1997) has extensively studied type III phase diagrams, showing the importance of studying molar density phase diagrams alongside the compositional phase diagrams in order to define new criteria for delimiting the regions of liquid-vapor and liquid-liquid equilibria. In addition, Quiñones-Cisneros (1997) has clearly identified the liquid-liquid and liquid-vapor parts of the critical lines as well as the point of transition from liquid-liquid into liquid-vapor.

In the next section type II, III and IV phase diagrams will be discussed. It will be shown that, as a result of asymmetry, binary mixtures can display phase behavior transition from type II to type III trough an intermediate type IV. It is during the type IV transition that barotropic phenomenon is likely to develop. Type V diagrams are probably type IV with the liquid-liquid critical curve hidden below the melting curve (van Konynenburg and Scott, 1980). For that reason, type V phase diagrams are not considered in this chapter, since in terms of barotropic phenomena the features found in type IV diagrams would be the same as in type V diagrams. However, before proceeding, given the importance that critical phenomena play in this discussion, the mathematical conditions of a critical point in a binary mixture will be briefly formulated.

5.2.1 Critical phenomena: theory

The critical point of a fluid is a point in pressure-temperature-composition space at which the coexisting liquid and vapor phases become indistinguishable. The density, refractive index, and all the other properties of the two phases approach the same value. For a pure component, this occurs for a fixed temperature and pressure. For a binary system, critical points may exist over a range of pressure, temperature and compositions, resulting in a critical line. The classical prescription of critical points in a binary mixture in terms of the molar Gibbs energy *G* can be found in many textbooks on thermodynamics, e.g. Rowlinson and Swinton (1982).

$$\left(\frac{\partial^2 G}{\partial x^2}\right)_{p,T}=0 \qquad \left(\frac{\partial^3 G}{\partial x^3}\right)_{p,T}=0 \tag{5.1}$$

In the following the abbreviated notation for multiple differentiations of Rowlinson and Swinton (1982) is used:

$$G_{ix}=\left(\frac{\partial^i G}{\partial x^i}\right)_{p,T} \tag{5.2}$$

According to this notation, the critical conditions can be written as $G_{2x}=0$ and $G_{3x}=0$. In Equation 5.1 the partial derivatives of *G* are used to define the criteria for the critical state in a binary mixture. However, *G* has pressure, temperature and composition (*p*, *T*, *x*) as independent variables. Since most equations of state contain the molar volume *v*, *T*, and *x* as independent variables, a Helmholtz energy formulation of the critical conditions is to be preferred. The molar Helmholtz energy *A* has *v*, *T* and *x* as independent variables. The molar Gibbs energy is related to the molar Helmholtz energy: $dG = dA + d(pv)$. The critical conditions can now be written down in terms of the molar Helmholtz energy derivatives. To perform the transformations from the molar Gibbs energy criteria to the molar Helmholtz energy criteria the Jacobian transformation procedure (Shaw, 1935) is used:

$$G_{2x} = A_{2x} - \left(\frac{A_{vx}^2}{A_{2v}}\right) \tag{5.3}$$

$$G_{3x} = A_{3x} - 3\,A_{v2x}\left(\frac{A_{vx}}{A_{2v}}\right) + 3\,A_{2vx}\left(\frac{A_{vx}}{A_{2v}}\right)^2 - A_{3v}\left(\frac{A_{vx}}{A_{2v}}\right)^3 \tag{5.4}$$

To determine the critical points an expression for A in terms of v, T and x is necessary.

5.2.2 - Stability tests

All the calculated critical points should be subjected to three stability tests. These stability tests distinguish between thermodynamically stable, metastable and unstable critical points. The stability tests can be subdivided into local stability tests (i.e. tests on mechanical and material instability) and global stability tests.

The mechanical stability test: If $(\partial p/\partial v)_{Tx} > 0$ or $A_{2v} < 0$, then the critical phase is said to be "mechanically unstable". A small density fluctuation will cause the critical phase to split into a liquid and a vapor phase. Mechanical instability can only occur in azeotropic mixtures if the liquid and the coexisting vapor, both with the azeotropic composition, become critical.

The material stability test: If $G_{4x} < 0$ the critical phase is unstable with respect to separation into two phases with different compositions, i.e. the critical phase is materially unstable. These two local stability tests are extensively discussed by Rowlinson and Swinton (1982). The material stability test can be expressed in terms of the molar Helmholtz energy:

$$G_{4x} = A_{4x} - 4\,A_{v3x}\left(\frac{A_{vx}}{A_{2v}}\right) + 6\,A_{2v2x}\left(\frac{A_{vx}}{A_{2v}}\right)^2 - 4\,A_{3vx}\left(\frac{A_{vx}}{A_{2v}}\right)^3 + A_{4v}\left(\frac{A_{vx}}{A_{2v}}\right)^4$$
$$- \frac{3}{A_{2v}}\left(A_{v2x} - 2\,A_{2vx}\left(\frac{A_{vx}}{A_{2v}}\right) + A_{3v}\left(\frac{A_{vx}}{A_{2v}}\right)^2\right)^2 < 0 \tag{5.5}$$

Global stability test: When a critical phase has passed both local stability tests, it may still be possible that it is thermodynamically metastable. This happens if a phase separation that would lower the molar Gibbs energy of the system at the same pressure and temperature is possible. To ensure that a critical phase is locally stable, only the signs of two derivatives (A_{2V} and C_{3V}) have to be evaluated at the critical pressure, temperature and composition. The global stability criterion requires a full investigation of the molar Gibbs energy plane at the pressure and temperature of the critical phase, i.e., it is necessary to check that at the critical temperature and pressure, no auxiliary phases with concentration $0 < x^a < 1$ will have a molar Gibbs energy lower than that of the tested critical phase with concentration x^c. Michelsen (1982a, and 1982b) presented the following mathematical formulation

$$\left(\mu_1^a - \mu_1^c\right)x^a + \left(\mu_2^a - \mu_2^c\right)\left(1 - x^a\right) > 0 \qquad (5.6)$$

where the subscript "c" stands for critical and "a" for auxiliary. Importance of the global stability test is expressed by the fact that the LCEP and UCEP are defined as the last stable points of the critical lines that connect equilibrium of immiscible phases.

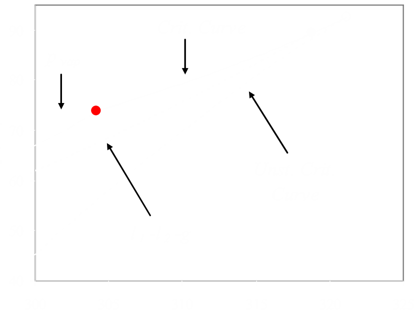

Figure 5.2 – Pressure – temperature projection of the full critical curve, including the metastable, and unstable sections as well as the three phase and vapor pressure curve for the CO$_2$ + n-C$_{16}$ mixture. Points: critical point of pure CO$_2$ (●) critical end point (∗) and high order spinodal point (○).

Many of the following diagrams contain states that are unstable or metastable, and these are marked as such. Mechanically unstable states are always discarded. An example of the unstable and metastable parts of the critical lines is shown in Figure 5.2. Although not relevant for the discussion the binary system corresponds to a mixture of CO$_2$ + n-decane calculated with the PR (Peng and Robinson, 1976) EoS (with $k_{ij} = 0.11$) showing Type III phase behavior. It can be seen that if the critical line is calculated using only Equations 5.3–5.4, it will extend to regions of high pressures and, after passing through a high order spinodal point, turns unstable and diverges to the low pressure region. A high order spinodal point (located at the cusp of the critical line) represents a point of limit of stability for which $G_{2x} = 0$. Clearly, the section of the critical curve between the solid point that corresponds to the critical end point of the l_1–l_2–g curve and the high order spinodal point relates to a metastable critical state.

5.3 – Type II to type III phase behavior transition

The use of a cubic equation of state as simple as the van der Waals equation, or one of its derivations such as the Soave-Redlich-Kwong EoS (Soave, 1972) or the Peng-Robinson EoS (Peng and Robinson, 1976), represents a powerful tool for a better understanding of the complex phase behavior found in mixtures. Since cubic EoS are extremely useful and well-established models, not only for a qualitative description but also for the quantitative modeling of actual applications, the equation used in this section in the calculation of the phase diagrams is the PR EoS. However, it is important to mention that this chapter is not intended for the accurate numerical modeling of any particular system. The main objective of this chapter is the theoretical understanding of barotropic behavior and its connection to viscosity.

The asymmetric systems to be studied here correspond to binary mixtures of CO_2 with n-alkylbenzenes (ABs, $C_6H_5C_nH_{2n+1}$). This binary system is chosen since refrigeration processes using CO_2 as refrigerant are of increasing interest. They are involved in many applications like vehicle air conditioning, residential air conditional or heat pump systems (Skaugen, 2002). In addition, some of the synthetic lubricant candidates for CO_2 refrigeration systems are the AB types (Quiñones-Cisneros *et al.* 2005).

For CO_2 the critical parameters and acentric factor are taken from Poling *et al.* (2000). Critical temperatures and critical pressures for the series of n-alkylbenzenes have been measured by Nikitin *et al.* (2002). For the purposes of this chapter, the individual parameters have not been used. Rather, it is better to use the carbon number dependent predictive correlations suggested by Nikitin *et al.* (2002) for the n-alkylbenzenes series. Nikitin *et al.* (2002) also provide correlations for the calculation of the acentric factor as a function of critical properties. Furthermore, in all cases to be illustrated throughout this chapter, the molar mass of an n-AB compound is calculated with the following formula:

$$M_{n-AB} = (77.1039 + 12.0107\,n + 1.00794(2n+1)) \qquad (5.7)$$

For mixtures, the PR EoS has been employed in combination with the quadratic mixing rule for a and linear rule for b. In addition, for a more realistic representation, the universal binary parameter $k_{ij} = 0.076$ has been applied (this value of k_{ij} will be commented in Chapter VI). In this way, a general PR model for the CO_2 + AB series is obtained, for which transitional phase behavior can be studied as a sole function of the carbon number (n) of the n-alkylbenzene molecule and, of course, the natural variables: temperature (T), molar volume (v), and mole fraction of CO_2 (x).

For description of the phase behavior patterns relevant to this chapter the basic nomenclature introduced in section 5.2 will be followed. In particular, the CO_2 critical point will be denoted as C_1, the n-AB critical point as C_2, and a hypothetical high pressure critical point as C_m.

5.3.1 - From type II to type III

The PR model used in this chapter predicts a transition from type II phase diagrams to type III for CO_2 + n-alkylbenzene mixtures between n-butylbenzene ($C_{10}H_{14}$) and n-octylbenzene ($C_{14}H_{22}$). Figure 5.3 shows the two limiting cases for this transition. In the case of the type III phase diagram in Figure 5.3 the molar isopycnic curve, defined as the point at which two coexisting phases have the same molar density, is also shown. The metastable and the unstable parts of the critical curves are also plotted. The metastable part corresponds to the solid section of the critical curve between the UCEP and the high order spinodal point, and the unstable part corresponds to the dashed section of the critical curve. Also, due to projection overlapping, the customary pure component vapor pressure curves have been omitted.

Figure 5.4 shows a detailed depiction of the different phase behavior features that develop in the neighborhood of the pure CO_2 critical point. The molar isopycnic curve starts almost at the point where the liquid-vapor critical curve coming from C_1 joins the L_2-L_1-g coexisting curve. For type III phase diagrams showing a minimum in the pressure-temperature projection (as the one in Figure 5.3), the isopycnic curve is likely to start along the three-phase curve (Quiñones-Cisneros, 1997), but this might not be the case for other variations of type III or other types of phase diagrams. This fact can be appreciated in Figure 5.5, where pressure-molar density diagrams at three different temperatures are depicted. By comparing the temperatures T = 310.55 K and T = 310.75 K, it can be observed that the L_2 coexisting phase in the L_1-L_2-g equilibria has moved from a higher than L_1 molar density to a lower than L_1 molar density. Clearly, the intermediate temperature shown in Figure 5.5, i.e. T = 310.60 K, represents the point where the isopycnic curve starts. The molar isopycnic curve will continue until it joins the critical curve that starts at C_2 and goes to C_n (see Figure 5.3). This last joining point represents the separation between the liquid-liquid and liquid-vapor critical curve.

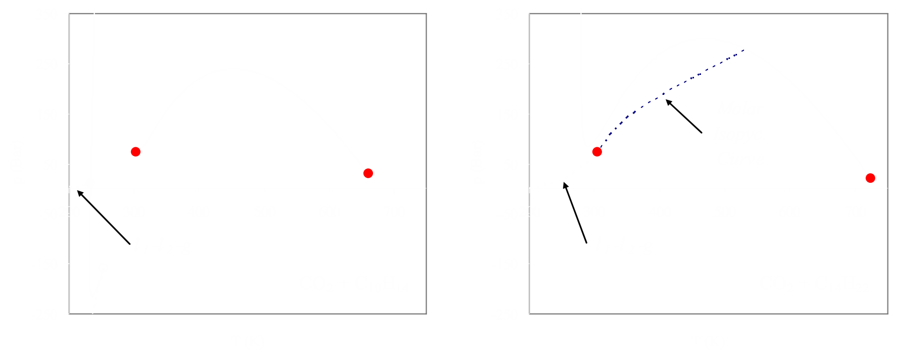

Figure 5.3 – Last type II and first type III phase diagram for the CO_2 + alkylbenzene series. Lines: stable and metastable critical curves (—), unstable critical curve (—), l_1-l_2-g curve (—), and isopycnic curve (---). Points: pure component critical point (●), critical end point (●) and high order spinodal point (○).

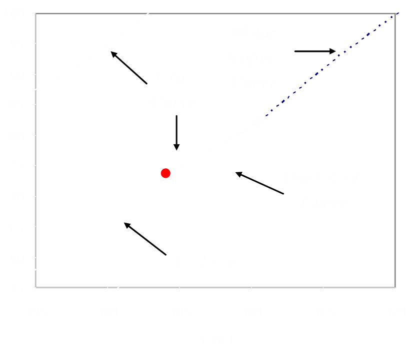

Figure 5.4 - Pressure – temperature detailed depiction for the CO_2 + octylbenzene mixture of the phase diagram area in the neighborhood of the pure CO_2 critical point. Points: critical point of pure CO_2 (●), critical end point (●) and high order spinodal point (○).

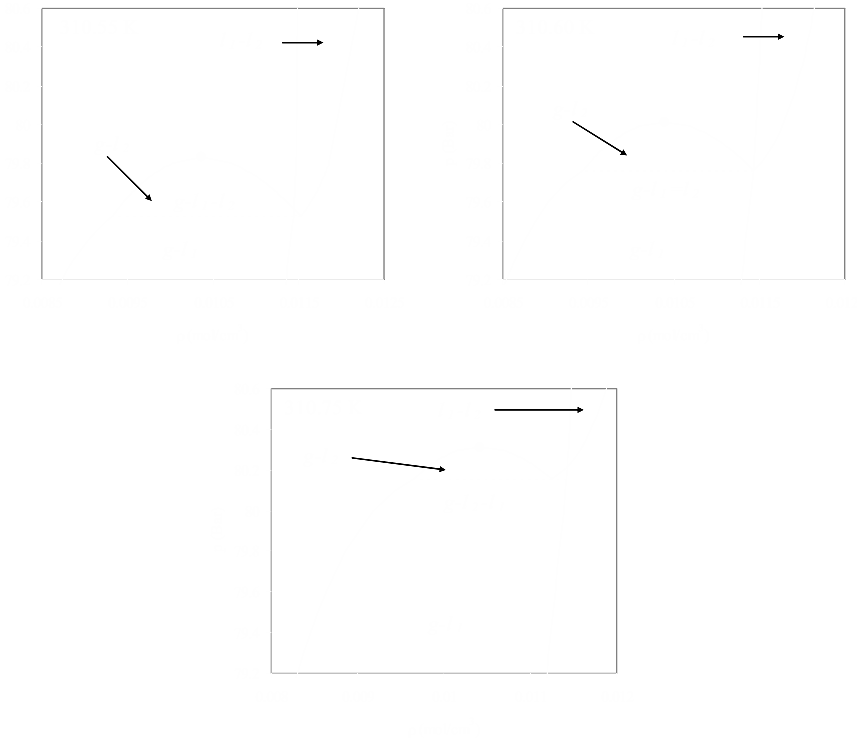

Figure 5.5 – Pressure – molar density phase diagrams for the CO_2 + octylbenzene mixture at different temperatures. Gas phase (*g*), liquid phase rich in AB (*l*$_1$), and liquid phase rich in CO_2 (*l*$_2$). The points (●) denote *l*$_1$-*l*$_2$ critical points and the dashed curve (---) denotes the three phase curve.

The physical meaning and importance of the molar isopycnic curve can be better appreciated by analyzing higher temperatures than the ones shown in Figure 5.5. For example, at temperatures above the *l*$_1$-*l*$_2$-*g* curve, the density of the coexisting phases can develop a density loop (see Figure 5.6). An important implication of this density loop is that the liquid-liquid immiscibility region (*l*$_1$-*l*$_2$) does not disappear, but continues after the *l*$_1$-*l*$_2$-*g* coexistence curve has come to an end. This phenomenon can only be seen in those pressure–molar density diagrams where a molar density inversion between the liquid and vapor phases occurs at the molar isopycnic point. In the pressure-mole fraction diagram shown in Figure 5.6 the region below the isopycnic point corresponds to *l*$_1$-*g* phase equilibria while the region above the isopycnic point corresponds to *l*$_1$-*l*$_2$ phase equilibria.

Clearly, the molar isopycnic curve can be defined as an equilibrium curve along which the following equation is satisfied

$$\rho_{l_1} - \rho_{l_2} = 0 \qquad (5.8)$$

This condition is illustrated in Figure 5.6. Similarly to the three-phase curve, the molar isopycnic curve can have a critical ending point. In Figure 5.6, the molar isopycnic critical ending point is found at *T* = 533K. At this point the molar isopycnic and the critical curves meet.

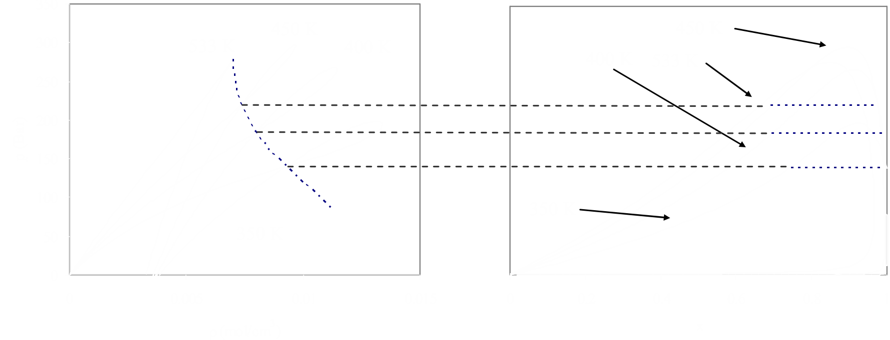

Figure 5.6 – Pressure – molar density and pressure – mole fraction of CO₂ phase diagrams for the CO₂ + octylbenzene mixture at different temperatures. Below the isopycnic point a gas phase (*g*) is found in equilibrium with a liquid phase rich in AB (*l*₁), whereas above the isopycnic point a liquid phase rich in AB (*l*₁) is found in equilibrium with a liquid phase rich in CO₂ (*l*₂). The dashed curve on the right (---) denotes the molar isopycnic point.

As pointed out by Deiters and Pegg (1989), the first step in the transition away from type II phase behavior is the appearance of the type IV phase behavior as a consequence of the developing, along the critical curve that joins C_1 with C_2, of a tricritical point as the transition point (three phases become identical). This transition state is represented by a phase diagram where the three-phase line connecting the two critical lines shrinks to zero (Figure 5.7). A mathematical criterion for the tricritical point is $G_{2x} = G_{3x} = G_{4x} = G_{5x} = 0$. In addition, for a tricritical point to be locally stable, the sixth derivative of the molar Gibbs energy with respect to the composition at constant *p* and *T* should be positive ($G_{6x} > 0$).

Figure 5.7 – Tricritical point as transitional state between type I and IV

In the case of the PR model used in this chapter, the transitional tricritical point is found at $T_{tcr} = 321.282$ K, $v_{tcr} = 73.645$ cm^3 mol^{-1} and $x_{tcr} = 0.9584$ for a mixture of CO_2 plus a hypothetical n-alkylbenzene with a molar mass of 141.764 g mol^{-1} ($n = 4.538$ with $C_6H_5C_nH_{2n+1}$). Such a hypothetical transitional tricritical point appears at a molar mass slightly below the molar mass of pentylbenzene ($C_{11}H_{16}$), with a molar mass 148.245 g mol^{-1}. Thus, as shown in Figure 5.8, the CO_2 + $C_{11}H_{16}$ mixture shows type IV phase behavior that includes a small three phase region (l_1-l_2-g), which bifurcates away from the tricritical point. This regular type IV phase behavior can be defined as distorted type II (Quiñones-Cisneros, 2004).

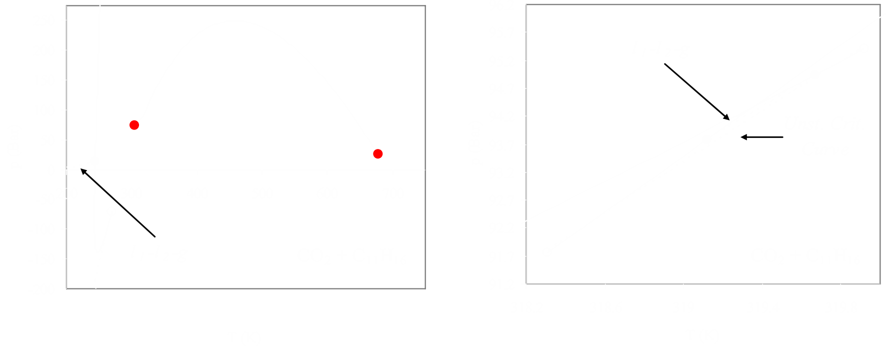

Figure 5.8 – Pressure – temperature projection of the full critical curves, including the metastable and unstable sections as well as the three phase coexisting curve, for the CO_2 + $C_{11}H_{16}$ mixture. The detailed magnification on the right shows type IV phase behavior. Lines: stable and metastable critical curves (—), unstable critical curve (---), and l_1-l_2-g curve (—). Points: pure component critical point (●), critical end point (○) and high order spinodal point (◇).

As asymmetry increases, another important transition takes place. The transition is illustrated in Figure 5.9, where it can be seen that two of the high order spinodal points approach a double high order spinodal, so that the critical curves converge to a transition point (Quiñones-Cisneros, 2004). Figure 5.9 shows the phase diagram for the mixture of CO_2 + hypothetical alkylbenzene with a molar mass of 157.5 g.mol^{-1} (n = 5.6598 with $C_6H_5C_nH_{2n+1}$).

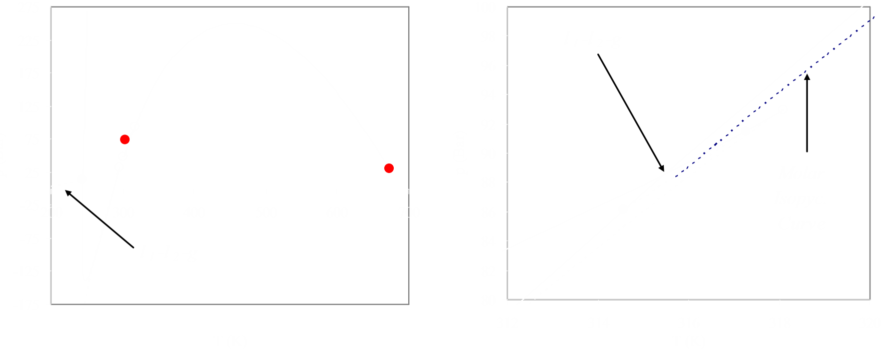

Figure 5.9 – Pressure – temperature projection for the CO_2 + AB hypothetical mixture (M_{AB} = 157.50 g.mol^{-1}, n = 5.6598). The detailed magnification on the right also shows type IV phase behavior including molar density inversion. Lines: stable and metastable critical curves (—), unstable critical curve (—), l_1-l_2-g curve (—), and isopycnic curve (---). Points: pure component critical point (●), critical end point (■) and high order spinodal point (○).

The double high order spinodal transition point is found at T_{tra} = 298.878 K, v_{tra} = 66.687 cm^3.mol^{-1}, and x_{tra} = 0.9372 for a CO_2 mixture with a hypothetical n-alkylbenzene of molar mass 157.805 g.mol^{-1} (n = 5.6816 with $C_6H_5C_nH_{2n+1}$). The main feature here is that at this transitional point the critical curve coming from C_1 loses its unstable section and becomes continuously connected to C_2. This fact can be observed in Figure 5.10, which shows the pressure-temperature projection for a mixture of CO_2 + heptylbenzene ($C_{13}H_{20}$). The section of the critical line between the UCEP of the first branch of the l_1-l_2-g line and the LCEP of second branch of the l_1-l_2-g line corresponds to metastable states. The critical curve that originates at C_2 after passing through a high order spinodal point, turns unstable and diverges to the low pressure region. This last type of phase diagram was defined as type IVb by Quiñones-Cisneros (2004) (the designation used in this work), or distorted type III by Deiters and Pegg (1989). A temperature-pressure projection for CO_2 + hexylbenzene ($C_{12}H_{18}$) shows the type IVb phase behavior as well. Yet, for the system CO_2 + heptylbenzene depicted in Figure 5.10 another important feature can be noticed more clearly; the minimum of the critical curve joining C_A with C_B has moved upwards from negative to positive pressures. Clearly, further increment in the asymmetry of the system will result in a transition from type IVb to type III through a double critical end point.

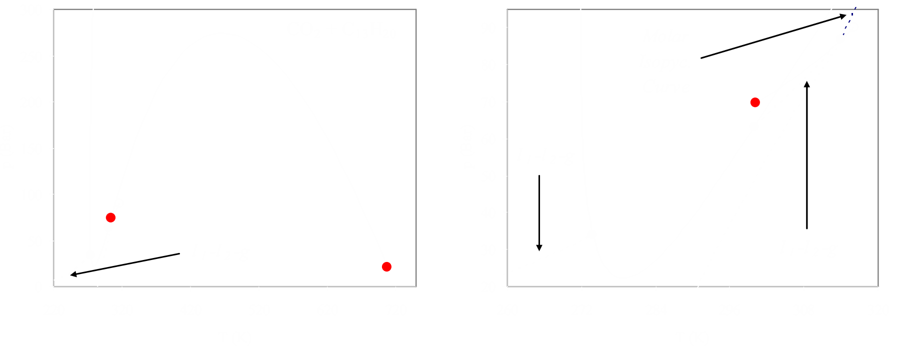

Figure 5.10 – Pressure – temperature projection for the CO$_2$ + heptylbenzene mixture. The detailed magnification on the right also shows type IVb phase behavior including molar density inversion. Lines: stable and metastable critical curves (—), unstable critical curve (---), L_1L_2g curve (—), and isopycnic curve (---). Points: pure component critical point (●), critical end point (▼) and high order spinodal point (○).

Deiters and Pegg (1989) established that the double critical end point (DCEP) takes place where the critical line just touches the three-phase line. The mathematical conditions for the DCEP have been derived by Deiters and Pegg (1989):

$$G_{2x}^{c} = G_{3x}^{c} = 0 \quad \text{(criticality)} \tag{5.9}$$

$$\mu_i^{c} = \mu_i^{\alpha} \quad \text{(phase equilibrium with } i = 1,2) \tag{5.10}$$

$$\frac{S_{2x}^{c}}{V_{2x}^{c}} = \frac{S^{c} - S^{\alpha} - \left(x^{c} - x^{\alpha}\right) S_x^{c}}{V^{c} - V^{\alpha} - \left(x^{c} - x^{\alpha}\right) V_x^{c}} \quad \text{(slope criterion)} \tag{5.11}$$

The notation for the derivatives S_x, S_{2x}, V_x and V_{2x} is analogous to that for G_{2x}. These values can be expressed in terms of derivatives of the Helmholtz energy (Deiters and Pegg, 1989). Such a transitional point (Figure 5.11) is found at T_{DCEP} = 284.77 K, v_{DCEP} = 66.2378 cm^3.mol^{-1} and x_{DCEP} = 0.9107 for the CO$_2$ mixture with a hypothetical n-alkylbenzene with a molar mass of 182.039 g.mol^{-1} (n = 7.4093 with C$_6$H$_5$C$_n$H$_{2n+1}$).

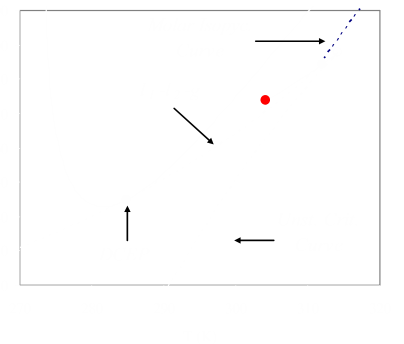

Figure 5.11 - Double critical end point (DCEP) as transition state between type IVb and III. Lines: stable and metastable critical curves (—), unstable critical curve (---), L-L-g curve (—), and isopycnic curve (---). Points: pure component critical point (●), critical end point and DCEP (indicated) (■) and high order spinodal point (◆).

Finally, before proceeding with the analysis of the barotropy-related implications of this type of phase behavior, it is interesting to point out that the conventional pressure-temperature projections may not be the best way to analyze these types of transitions. A better representation is obtained when other types of projections are analyzed, such as the fundamental volume-composition projections shown in Figure 5.12. Here the phase behavior transition for $CO_2 + C_6H_5C_nH_{2n+1}$ mixtures is shown from pentylbenzene ($n = 5$) to octylbenzene ($n = 8$) through two intermediates, a hypothetical alkylbenzene (with $n = 5.35$) and hexylbenzene ($n = 6$). For $n = 5$ the molar isopycnic curve is not found. Also, for $n = 5$ it can be better appreciated that the critical curve starting at C_2 continues to C_1 (through meta- and unstable states). For the mixture containing the hypothetical alkylbenzene with $n =$ 5.35 (before the double high order spinodal point is reached) the molar isopycnic curve starts and ends at two different points of the critical curve showing a closed loop. Similarly to the three phase line, a molar isopycnic line can have critical ending points. This isopycnic curve does not intersect the L-L-g curve. This confirms the fact that isopycnic curves do not necessarily have to meet the L-L-g curves (Quiñones-Cisneros, 1997). After crossing the double high order spinodal point (CO_2 + hexyl and octylbenzene) the molar isopycnic curve reaches the L-L-g curve, making the L-L region not disappearing but continuing after the three phase curve comes to the end point. For $n = 6$ the three phase and the molar isopycnic curves meet almost at the critical end point (x close to 1), whereas this is not the case for $n = 8$. In the last two examples shown in Figure 5.12 ($n = 6$ and 8), if the molar isopycnic curve is extended below the three phase curve, the closed loop is again found. The parts of the curve below the L-L-g curve correspond to unstable or metastable states. Figure 5.12 also illustrates clearly the way the critical lines are connected to C_1, C_2 and C_m. For example, for $n = 5.35$ it can be seen how the two high order spinodal points approach each other. A similar feature can be observed for $n = 6$ showing the lower and upper critical three phase end point approaching each other (before the DCEP is reached).

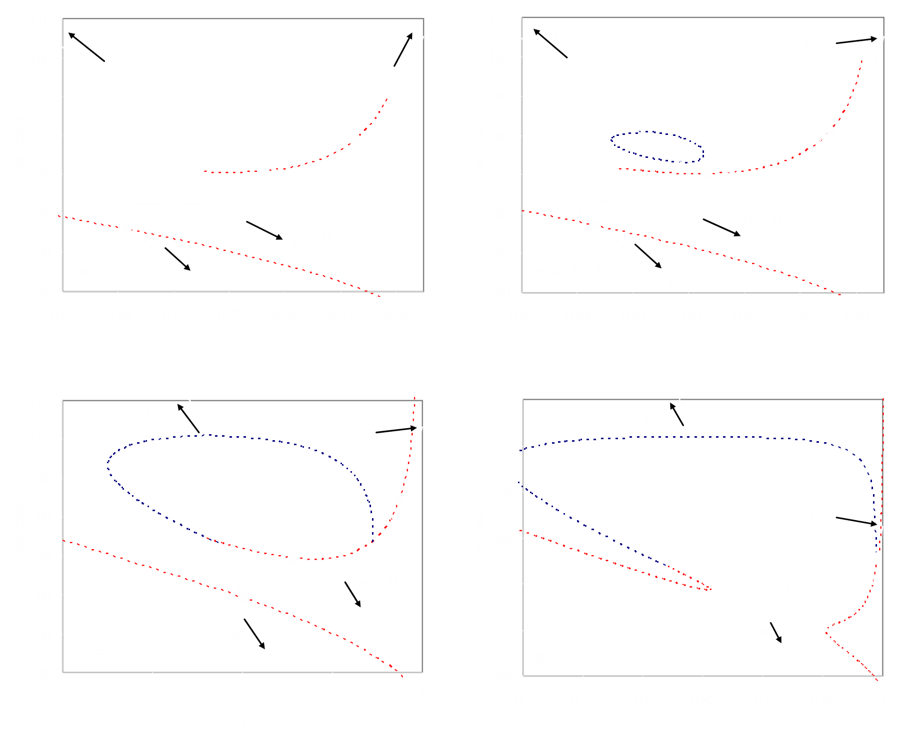

Figure 5.12 - Volume – composition projections showing different characteristics. Lines: stable and metastable critical curve (—), unstable critical curve (—), l_1-l_2-g curve (---), and isopycnic curve (---). Points: critical end point (●) and high order spinodal point (○). Note: in this figure due to projection overlapping the l_1-l_2-g curve is plotted in red.

5. 4 – Barotropic phenomena

In this work barotropic phenomena refer to molar density or volume inversions under pressure, but not necessarily mass density inversion under gravitational field. Nevertheless, the fact that a molar isopycnic curve is found suggests that it is quite possible that, for the right combination of molecular weights and compositions, mass density inversion can be observed. Certainly, other phenomena such as association may develop similar patterns. However, as discussed in the Introduction, the asymmetry-induced barotropicity is of high industrial importance and in such a case, once a molar density inversion occurs, the subsequent mass density inversion will depend on the ratio between the molar masses of the compounds.

To better illustrate the relation between asymmetry and barotropic phenomena, let us consider the phase behavior transition in the type II system shown in Figure 5.13. For this example, Figures 5.13 and 5.14 show pressure–composition and composition–molar volume phase diagrams at $T = 230$ K and $T = 240$ K, before and after the curve of the three coexisting phases ends. A specific volumetric behavior of the condensed phases can be noticed in the composition–molar volume phase diagrams. In general, when at subcritical conditions only liquid–vapor phase equilibria are present, the liquid and vapor binodal curves simply connect the saturation liquid and vapor molar volumes of the pure components, as in the 240 K phase diagram in Figure 5.14. In addition, in the case of asymmetric mixtures with large M_r, the difference in the coexisting molar volumes can be substantial and the tie-lines may have a rather low, most likely positive, slope, as shown in Figure 5.14. However, as an incipient third liquid phase develops, the three-phase triangle appears with an L_1–L_2 tie-line tangential to the liquid binodal curve. Consequently, the L_1–L_2 curve is almost normal to the L_1–g tie-lines. In other words, transition from a L_1–g tie-line to a L_1–L_2 tie-line will require rotation of around 90°.

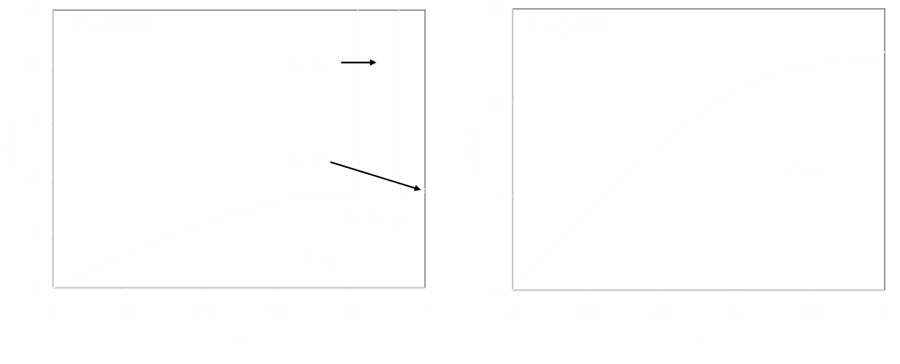

Figure 5.13 – Pressure – composition phase diagrams for the CO$_2$ + butlybenzene mixtures before and after the three phase critical end point in type II phase behavior system.

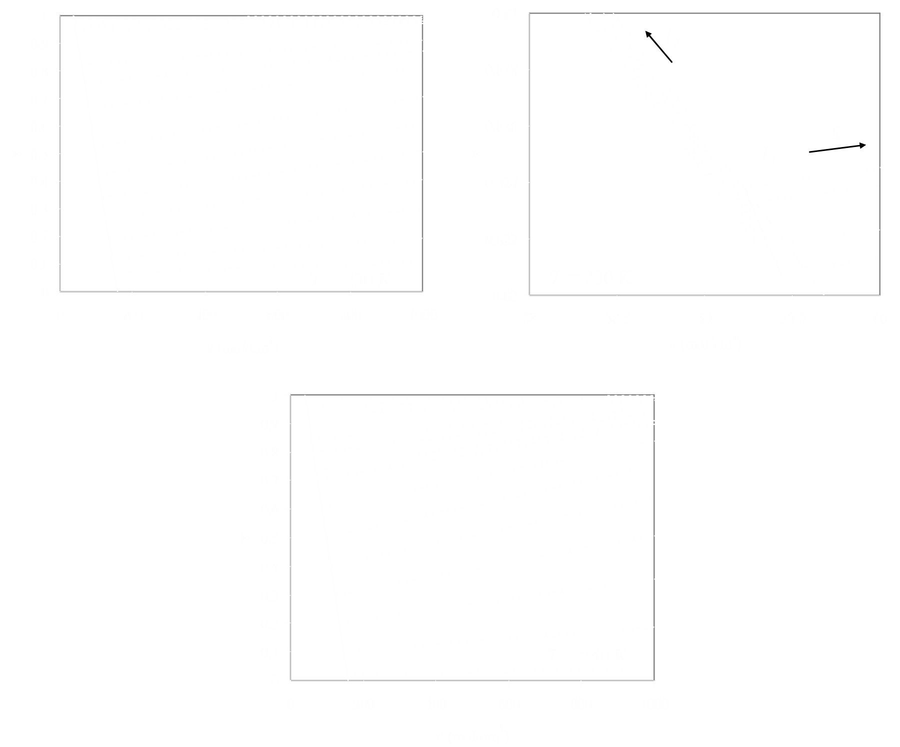

Figure 5.14 - Composition – molar volume phase diagrams for the CO$_2$ + butylbenzene mixtures before and after the three phase critical end point in type II phase behavior system.

Let us now consider the upper branch of the three phase curve for the CO$_2$ + hexylbenzene type IV system shown in Figure 5.15. This figure shows the three conventional pressure-composition phase diagrams: the two critical limiting temperatures of the three-phase curve, diagrams (*a*) and (*c*), and the point where the molar isopycnic curve initiates, i.e. where the coexisting liquid phases have same molar volume, diagram (*b*). From these diagrams it is clear that no information can be inferred regarding the barotropic behavior of the system.

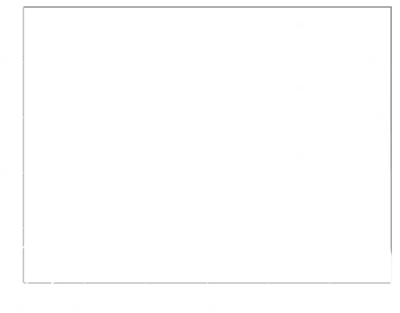

Figure 5.15 – Pressure – composition phase diagrams for the CO$_2$ + hexylbenzene mixture. Diagram (*a*) corresponds to the lower critical end point and diagram (*c*) to the upper critical end point of the l_1-l_2-g curve. Diagram (*b*) corresponds to the lower end point of the molar isopycnic curve, i.e. the point at which the l_1 and the l_2 coexisting phases have the same molar density.

Let us compare these diagrams with their equivalent composition-volume phase diagrams, Figure 5.16. In the case of example (*b*) it can be seen that the tie-lines in the l_1–l_2 immiscible region detach from the three phase triangle with a negative slope, while the tie-lines in the l_1–g and l_2–g immiscible regions all have positive slopes. At the l_1–l_2 phase of the l_1–l_2–g triangle in Figure 5.16, Equation 5.8 is satisfied. Quiñones-Cisneros (2004) has defined a vector *r*

$r=(r_v,r_x)=(v_b-v_a,x_b-x_a)$, (5.12)

where v_a and x_a are the molar volume and mole fraction of a coexisting phase "*a*". Clearly, the condition $r_v = 0$ is equivalent to Equation 5.8. As an ordinary critical point is approached, it can be shown that

$r \rightarrow u_1$, (5.13)

where u_1 is the eigenvector associated with the critical smallest eigenvalue of the Helmholtz free energy Hessian *H* (*v*, *x*, *T**) corresponding to the constant temperature *T** (Quiñones-Cisneros, *et al.* 2002). Consequently, for a given vector

$u_1=(u_v,u_x)$ (5.14)

an isopycnic critical ending point is defined as a point where, in addition to Equation 5.1, the following equation is also satisfied:

$u_v=0$ (5.15)

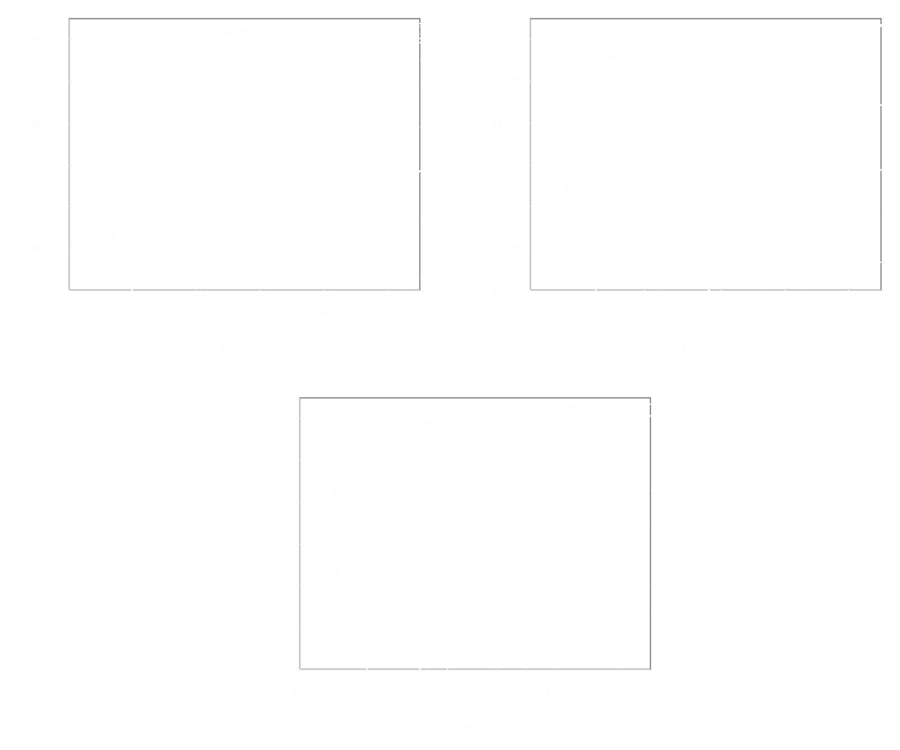

Figure 5.16 - Composition – molar volume phase diagrams for the CO$_2$ + hexylbenzene mixture. Diagram (*a*) corresponds to the lower critical end point and diagram (*c*) to the upper critical end point of the l_1-l_2-g curve. Diagram (*b*) corresponds to the lower end point of the isopycnic curve, i.e. the point at which l_1 and l_2 coexisting phases have the molar volume. Diagrams (*a*) and (*c*) show the upper and lower critical tie lines toward which the three phase triangle collapse.

Clearly, u_r is the volume-direction projection of the tie-lines at the limit where the ordinary critical point is approached. Therefore, global barotropic behavior can also be mapped onto the u_r based diagrams, such as the u_r–temperature diagram of Figure 5.17, which is produced for the mixture of CO$_2$ + alkylbenzene on the basis of the PR EoS used in this work. The examples shown in Figure 5.17 correspond to CO$_2$ + pentylbenzene, of the hypothetical substance AB of Figure 5.9, and of the octylbenzene. Since at the pure component critical points $u_r = 1$, a joined u_r–T critical curve passes through a minimum, which would not be too deep for mixtures of similar components. On the other hand, as asymmetry develops and a transition from type II to type III phase behavior takes place, the u_r–T critical curve stretches and eventually bifurcates at the transitional double high order spinodal point. After that, the u_v–T critical curve that originates from C_2 may not come back; it may continue downwards as the critical curve diverges at high pressures. At a moment where either of these curves crosses the zero axis the barotropy occurs. Therefore, as indicated by the u_v–T critical curve projections in Figure 5.17, once the transitional high order double spinodal is crossed, i.e. type IVb and III phase behavior develops, the critical curves that join C_2 with C_m have a strong tendency to move and stay at the negative u_v region. This is the reason why in asymmetric systems, barotropic phenomenon is strongly linked to the type III phase behavior, as well as to all types of phase behavior that may be related to this type of transitional behavior.

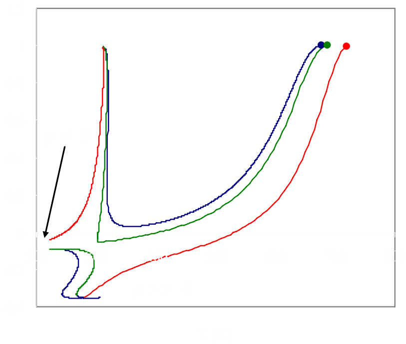

Figure 5.17 – Critical eigenvector volume projection for the CO_2 + pentylbenzene (–), CO_2 + hypothetical alkylbenzene (–), and CO_2 + octylbenzene (–) mixtures. p < 0 indicates the negative pressure unstable region divergence area of the full critical curves and p >> 0 the high-pressure divergence area. (Note: no stability classification has been included in this figure).

5.5 – Viscosity behavior in refrigerant + lubricant systems

In this section the general aspects of viscosity behavior linked to the type of asymmetric mixtures such as refrigerant + lubricant mixtures are discussed. For illustration, the friction theory (Quiñones-Cisneros *et al.* 2000) in combination with the PR EoS has been used for the viscosity behavior modeling. The importance of studying the viscosity behavior in refrigerant + lubricant systems is illustrated in the work of Hauk and Weidner (2000). They concluded that knowledge of the viscosity behavior is essential to evaluate the applicability of new lubricants as well as in the design of the refrigeration cycles.

The transport properties are not equilibrium properties. Viscosity can only be measured in a nonequilibrium experiment. This is contrary to density, which can be found in a static apparatus and, thus, is an equilibrium property. However, both properties reflect the effects of the molecular motion and interaction. Even though viscosity is a nonequilibrium property, it, like density, is a function of the thermodynamic state of the fluid. The scope of this section is to show the profound effect that phase behavior will have in the mixture transport properties such as the fluid viscosity.

To illustrate the relation between viscosity and the type of phase behavior that refrigerant-lubricant mixtures may develop, the *f-theory* (Quiñones-Cisneros et al. 2001) has been applied. For the purpose of this work the PR one-parameter general model given in Quiñones-Cisneros et al. (2001) has been used. With this *f-theory* approach, as studied in Chapter IV, the modeling of the viscosity of pure compounds requires fitting of one parameter per compound: the characteristic critical viscosity η_c. Unfortunately, it appears not to be any viscosity data for alkylbenzenes, making it impossible to fit parameters for the mixtures studied in this section. Then, the η_c value is calculated by means of the empirical equation given by Quiñones-Cisneros et al. (2001):

$$\eta_c = 0.597556\, p_c\, M^{0.601652} \qquad (5.10)$$

As in section 5.3, the critical parameters for AB are calculated using the correlations given by Nikitin et al. (2002). For mixtures, the mixing rules proposed in Quiñones-Cisneros et al. (2001) are used, with the regular van der Waals mixing rules with the same binary interaction parameter employed in Section 5.3 (k_{ij} = 0.076). Finally, before proceeding, it is important to remark again that the calculations in this section are purely qualitative, focusing on the relation between phase and viscosity behavior. The accuracy of a particular viscosity model is beyond the scope of this work. The phase diagrams to be shown in this section will be referred as type I, II or III.

5.5.1 - Relation between phase and viscosity behavior

In the previous section it was shown how rather small changes in the size of a molecule may completely change the phase behavior. In this section, it will be shown that the viscosity behavior closely follows this behavior. The types of phase behavior relevant to refrigerant + lubricant mixtures are of the basic type I, types II, III as well as transitional type IV. Let us start the analysis of viscosity behavior in asymmetric mixtures from the basic type I phase behavior. Figure 5.18 shows how the viscosity of the liquid phase evolves as temperature increases from totally subcritical conditions to the temperature above the pure refrigerant critical temperature. At subcritical conditions the curve falling liquid viscosity varies from the pure lubricant viscosity (the highest viscosity point in the curve) to the pure liquid refrigerant viscosity (the lowest point), and a low viscosity vapor phase coexists with a higher viscosity liquid phase. If the operating temperature is below the refrigerant critical temperature, then as the pressure increases, most of the lubricant stays in a single condensed phase with the viscosity depending on the composition of the mixture.

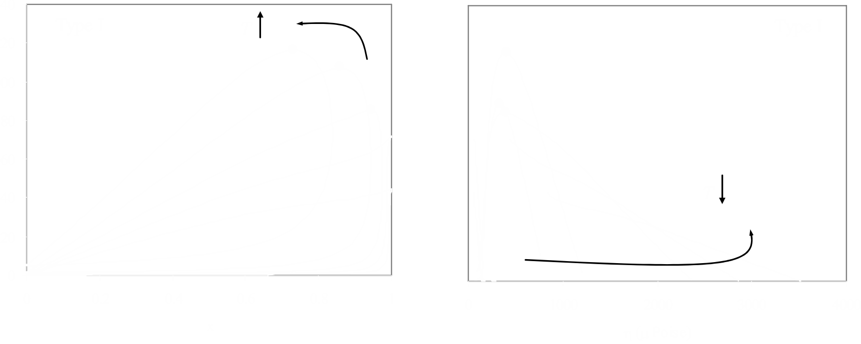

Figure 5.18 – Pressure – composition and pressure – viscosity diagrams for type I (or not intercepting type III) phase behavior at several temperatures. Vapor-liquid critical points (●).

For the Type III phase behavior, a low-temperature region may be considered first (T = 275 K, Figure 5.3). This temperature is low with respect to the lubricant critical temperature, but it may be within operating conditions for a cooling circuit, Figure 5.19. In this initial region multiple phase equilibria may be found, including unbounded liquid-liquid immiscibility. Figure 5.19 shows the strong relation between the phase and viscosity behavior, as essentially the same patterns are observed in the corresponding pressure-viscosity diagram. In the intermediate-temperature region (between T = 300 – 315 K, Figure 5.3) complex phase behavior along with barotropic behavior is found (see Figure 5.20). The immiscible region is bounded in this example. However, in principle, it may extend to high pressures, or even become unbounded. As illustrated in Figure 5.20, in the intermediate-temperature region the viscosity also reflects the complexity of the phase behavior. The low-viscosity fluid rich in refrigerant phase may exist even at high pressures.

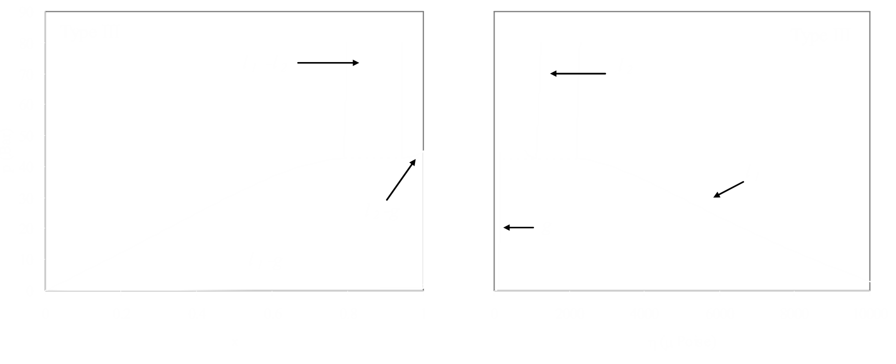

Figure 5.19 - Pressure – composition and pressure – viscosity diagrams for type III phase behavior.

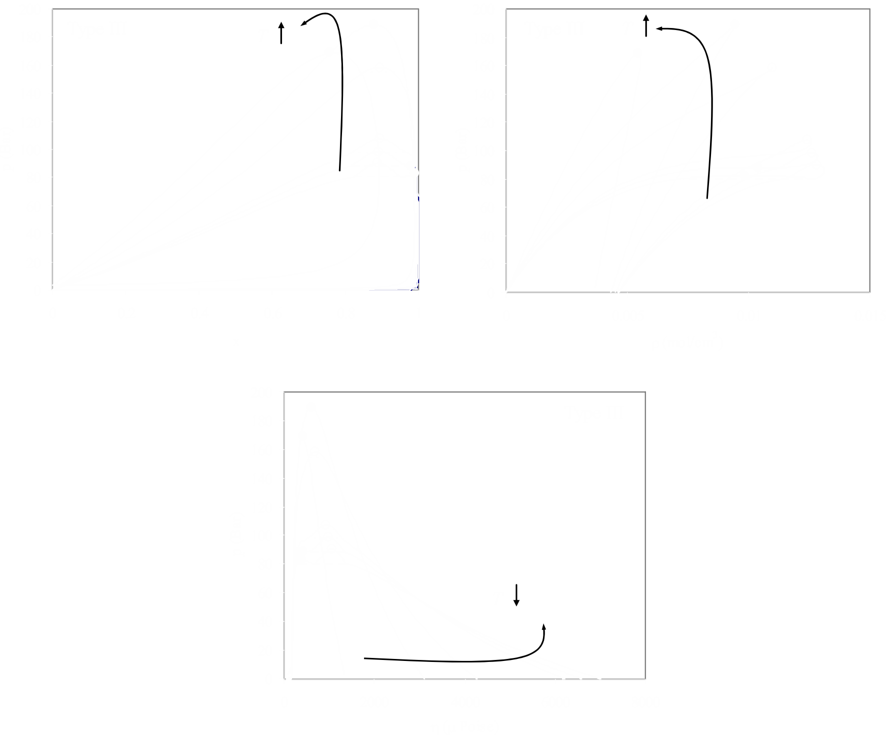

Figure 5.20 – Pressure – composition, pressure – molar density, and pressure – viscosity diagrams for type III phase behavior at *T* in the intermediate-temperature region. The two lower dashed lines in the diagram denote the L_1-L_2-g equilibria while the upper two dotted lines the molar density inversion points. Points: liquid-liquid critical points, (●) and liquid-vapor critical point (○).

As a last example, Figure 5.21 shows the pressure-mass density and pressure-viscosity phase diagrams for a refrigerant + lubricant system of industrial interest at $T = 353.15$ K (García *et al.* 2003). On the pressure-mass density diagram the density inversion can be observed. The viscosity behavior also reflects the complexity of the phase behavior. However, the high viscosity associated with the L_2 phase exceeds the viscosity of the L_1 phase in spite of the density inversion between them.

Appearance of a heavy phase with a low viscosity may cause undesirable effects in the cooling circuit. For example, as explained in Chapter I, the refrigeration cycles can operate with an oil separator installed after the compressor. The function of the oil separator is to collect the lubricant oil, which may migrate from the compressor, and to re-circulate it into the compressor. If the mass density inversion takes place, it may happen that the collected heavy phase, which is returned to the compressor, will not have the desired viscosity.

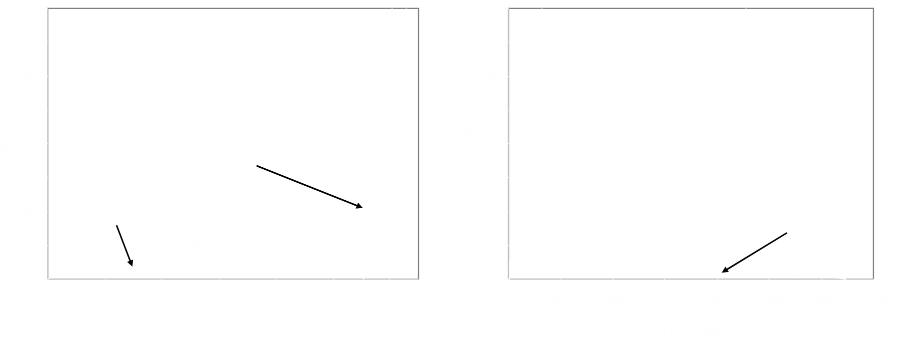

Figure 5.21 - Pressure – mass density and pressure – viscosity diagrams for type III phase behavior for HFC-134a + triethylene glycol at $T = 353.15$ **K showing mass density inversion.**

5.6 - Conclusions

In this chapter the barotropic behavior of refrigerant + lubricant mixtures has been discussed. Very few studies carried out so far show the importance of this phenomenon. In the work by Quiñones-Cisneros (1997) on the type III phase behavior, it is shown how the liquid-vapor critical curve detaching from the less volatile component has a transition toward a liquid-liquid curve at the point where the molar isopycnic curve joins the critical curve. Actually, the liquid-vapor critical curve that originates in the critical point of the less volatile component bifurcates into a liquid-liquid critical curve and a molar isopycnic curve. In this work, by taking advantage of simple models such as the PR equation of state, it is shown how barotropic behavior is linked to the transition from type II to type III phase behavior in asymmetric systems.

The development of the tricritical point represents the first step in the transition away from the type II to the regular type IV phase behavior. As asymmetry increases, transition from the regular type IV to the type IVb phase behavior takes place through the double high order spinodal point, and transition from the type IVb to the type III phase behavior through the double critical end point. To recapitulate, the transition from type II to type III due to increasing dissimilarities between the compounds takes place through two intermediates: the regular type IV and the type IVb. It appears that the molar isopycnic curve originates after the tricritical point and before the double high order spinodal point. The first appearance of barotropic behavior takes place when the minimum of the curve u_r-T just touches the zero axis (see Figure 5.17). This is represented by a point along the critical curve in Figure 5.12, instead of a closed loop. For strong barotropic behavior it is required that the critical curves originating at the pure component critical points are disjoined, after the double high order spinodal point is crossed. The first appearance of barotropic criticality, i.e. u_r vanishing and becoming negative, may also be used as a weak condition for phase behavior transition between type II and type III as a function of increasing asymmetry in binary asymmetric mixtures. Furthermore, it may also be of value exploring the extension of this study to other kind of type III phase diagrams. For other kind of type III phase diagrams see Rowlinson and Swinton (1982) and Deiters and Pegg (1989) for instance.

In the second part of this chapter, the connection between phase and viscosity behavior was studied. It was shown that phase behavior strongly affects the viscosity. Throughout a series of examples it was shown that there is a strong relation between phase and viscosity behavior. Moreover, within operating conditions (see Figure 5.21) it is possible to find the mass density inversions. As a result of these inversions, a heavy low-viscous phase may sometimes coexist with a light phase possessing a high viscosity. In particular, a light high-viscous phase may be found in the refrigeration cycle. This high-viscosity phase can be trapped in unwanted places of the cooling circuit having a significant impact on the heat transfer characteristics.

[illegible]

viscosity study based on correctly tuned EoS, with the corresponding coupled f-theory viscosity model, can also be used to prevent technical problems such as the compressor problems that may follow from diminished lubrication properties as it may be caused by an inappropriate chemical selection of the refrigerant or lubricant.

Nomenclature

A	=	Molar Helmholtz free energy
AB	=	Alkylbenzene
C_1	=	CO$_2$ critical point
C_2	=	AB critical point
C_∞	=	Infinity pressure critical point
$DCEP$	=	Double critical end point
G	=	Molar Gibbs energy
G_x	=	Derivative of the G with respect to composition at T and p
H	=	Helmholtz free energy Hessian matrix
$LCEP$	=	Lower critical end point
M	=	Molecular weight
p	=	Pressure
S	=	Entropy
T	=	Temperature
t	=	Vector
$UCEP$	=	Upper critical end point
u_1	=	Eigenvector associated with the critical smallest eigenvalue of H
V	=	Molar volume
x	=	CO$_2$ mole fraction

Greek letters

μ	=	Chemical potential

Subscripts/superscripts

a	=	Auxiliary
c	=	Critical

References

1. Brunner, E. Fluid mixtures at high pressures. III. Isothermal phase equilibria of (ethene+methanol) at 284.15 and 298.15K. *J. Chem. Thermodyn.* 1985, 17, 671-685.
2. Deiters, U.K., Pegg, I.L. Systematic investigation of the phase behavior in binary fluid mixtures. I Calculations based on the Redlich-Kwong equation of state. *J. Chem. Phys.* 1989, 90, 6632–6641.
3. Galindo, A., Blas, F.J. Theoretical Examination of the Global Fluid Phase Behavior and Critical Phenomena in Carbon Dioxide + *n*-Alkane Binary Mixtures. *J. Phys. Chem. B* 2002, 106, 4503–4515.
4. García, J., Monsalvo, M.A., Quiñones-Cisneros, S.E., Fernández, J. Modelling Phase Equilibria and Viscosity for Refrigerant-Lubricant Oil Systems. *21st IIR International Congress of Refrigeration, Washington D. C.*, 2003.
5. Hauk, A., Weidner, E. Thermodynamic and Fluid-Dynamic Properties of Carbon Dioxide with different Lubricants in Cooling Circuits for Automobile Application. *Ind. Eng. Chem. Res.* 2000, 39, 4646-4651.
6. Michelsen, M.L. The isothermal flash problem. Part I. Stability. *Fluid Phase Equilib.* 1982, 9, 1-19.
7. Michelsen, M.L. The isothermal flash problem. Part I. Stability. *Fluid Phase Equilib.* 1982, 9, 21-40.
8. Nikitin, E.D., Popov, A.P., Bogatishcheva, N.S. Vapor-Liquid Critical Properties of n-Alkylbenzenes from Toluene to 1-Phenyltridecane. *J. Chem. Eng. Data* 2002, 47, 1012-1016.
9. Peng, D.-Y., Robinson, D.B. A New Two-Constant Equation of State. *Ind. Eng. Chem. Fundam.* 1976, 15, 59–64.
10. Poling, B.E., Prausnitz, J.M., O'Connell, J.P. The Properties of Gases and Liquids. Fifth Edition. Mc Graw Hill, New York. 2000.
11. Quiñones-Cisneros, S.E. Phase and critical behavior in type III phase diagrams. *Fluid Phase Equilib.* 1997, 134, 103-112.
12. Quiñones-Cisneros, S.E., Zéberg-Mikkelsen, C.K., Stenby, E.H. The Friction Theory (f-theory) for Viscosity Modeling. *Fluid Phase Equilib.* 2000, 169, 249-276.
13. Quiñones-Cisneros, S.E., Zéberg-Mikkelsen, C.K., Stenby, E.H. One Parameter Friction Theory Models for Viscosity. *Fluid Phase Equilib.* 2001, 178, 1-16.

14. Quiñones-Cisneros, S.E., Valle-Arizmendi, L., Barragán-Aroche, F., Bazúa-Rueda, E. Sequential Algorithm for calculating ordinary critical points. 2002.
15. Quiñones-Cisneros, S.E. Barotropic phenomena in complex phase behavior. *Phys. Chem. Chem. Phys.* 2004, 6, 2307-2313.
16. Quiñones-Cisneros, S.E., García, J., Fernández, J., Monsalvo, M.A. Phase and viscosity behavior of refrigerant-lubricant mixtures. *Int. J. Ref.* 2005, 28, 714-724.
17. Rowlinson, J.S., Swinton, F.L. Liquids and Liquid Mixtures. Butterworths Monographs in Chemistry, London, 1982.
18. Schneider, G.M., Scheidgen, A.L., Klante D. Complex Phase Equilibrium Phenomena in Fluid Mixtures up to 2 GPa-Cosolvency, Holes, Windows, Closed Loops, High-Pressure Immiscibility, Barotropy, and Related Effects. *Ind. Eng. Chem. Res.* 2000, 39, 4476-4480.
19. Shaw, A.N. The derivation of Thermodynamical Relations for a Simple System. *Phil. Trans. Roy. Soc. London A.* 1935, 234, 299-328.
20. Skaugen, G. The effects of active and passive control in a transcritical CO_2 vapor compression cycle. *Proceedings of the Eurotherm Seminar No. 72*, Valencia, Spain 2003, 339-348.
21. Soave, G.S. Equilibrium Constants from a Modified Redlich-Kwong Equation of State. *Chem. Eng. Sci.* 1972, 27, 1197-1203.
22. van Konynenburg, P.H., Scott, R.L. Critical Lines and Phase Equilibria in Binary Van Der Waals Mixtures. *Philos. Trans. R. Soc. London, Ser. A* 1980, 298, 495–540.
23. van Pelt, A., Peters, C.J., de Swaan Arons, J., Deiters, U.K. Global phase behavior based on the simplified-perturbed hard-chain equation of state. *J. Chem. Phys.* 1995, 102, 8361–8375.

VI – Modeling Phase Equilibria and *p-v-T-x* Behavior

6.1 – Introduction

The ability to model the thermodynamic phase behavior and thermophysical properties of refrigerant + lubricant mixtures is of considerable industrial and academic interest. From an industrial point of view, the study (measurements and modeling) of thermophysical properties of such mixtures is necessary for the successful transition to new environmentally alternative refrigerants. Information on solubilities, densities and viscosities for these systems is extremely important for optimal design of refrigeration and air-conditioning systems. The solubility is also required when dimensioning an oil separation system. Moreover, good description of the thermophysical properties and phase equilibria is invaluable in choosing a proper lubricant for a particular compressor (Yokozeki, 2001). From an academic perspective, the ability to predict phase equilibria and p–v–T–x behavior of asymmetric mixtures (as in the case of refrigerant + lubricant systems) can serve as a rigorous test of the EoS itself.

In spite of their importance, experimental and theoretical studies involving refrigerant + lubricant oils of known composition and structure and which may also include density are still scarce and further studies are necessary. For example, only some phase equilibria experimental data of hydrofluorocarbons (HFCs) refrigerants with n-alkanes (Wahlstrom and Vamling 1996, and 1997) and HFCs with synthetic lubricant oils of known structure such as polyalkylene glycols (PAGs) (Coronas *et al.* 2002, López *et al.* 2004, and Tseregounis and Riley 1994), polyol ester (POEs) (Wahlstrom and Vamling 1999, and 2000) and alkyl benzenes (ABs) (Poot and de Loos 2002 and 2004, and Takigawa, 2002) are published in the literature. In the case of CO$_2$ refrigerant + ABs the works by Fall and Luks (1985, and 1986), Lansangan *et al.* (1987), and Tiffin *et al.* (1978) can be mentioned. Certainly, due to unquestionable importance in the petroleum industry, as well as other subsequent relevant applications such as supercritical extraction, the phase behavior of natural gas components, paraffins and their mixtures with CO$_2$ is extensively studied and, putting aside the barotropic aspects of phase behavior, quite well-understood (Schneider 1968 and 1972, between many others references). All of these studies are also of relevance for refrigeration since many of these components, such as propane, butane and CO$_2$ are also used as refrigerants and long chain paraffines can also be used as lubricants. Regarding densities, the experimental studies are even scarcer: to the best of our knowledge, only works by Comuñas *et al.* (2002a, 2002b, and 2002c) and Kumagai *et al.* (1993, and 1994) can be found in the literature for HFCs + PAGs.

Different approaches have been used to model phase behavior of refrigerant + lubricant mixtures. A perturbed-hard-sphere-chain EoS (Bertucco *et al.* 1999 and Huber *et al.* 2002), a cubic EoS alone (Yokozeki 2001), or combined with a group contribution model for the lubricant oil (Elvassore and Bertucco, 1999), among others, have been used to describe these mixtures. In this chapter the equations of state already presented and discussed in Chapter II are used. Special attention is paid to the PR EoS and the PC-SAFT EoS. The aim is to determine how well cubic and modern equations of state predict the phase and the p-ρ-T behavior.

In the first part of this chapter the cubic EoS by Peng and Robinson (1976) is used to predict phase equilibria. It has long been recognized that the main advantage of the cubic EoS is the potential reliability for describing different kinds of systems in wide ranges of pressures and temperatures. Nevertheless, the underlying theories for these equations, which do not account for the geometry and structure of molecular species, may not be satisfactory for modeling asymmetric mixtures. For that reason, the PC-SAFT EoS by Gross and Sadowski (2001) is also used. Particular attention is paid to the ability of these two models in describing phase behavior transitions for mixtures containing CO_2 as a refrigerant. In the second part, the p-ρ-T-x modeling is carried out with the aid of the following EoS: PR, RK-PR (Cismondi and Mollerup, 2005), SBWR (Soave, 1995, and 1999), and PC-SAFT. The results obtained in this chapter will be coupled with the friction theory in Chapter VII to predict the viscosity of these mixtures.

6.2 – Experimental database

The experimental database used in this chapter contains p-T-x and p-ρ-T-x data found in the literature. The studied refrigerant are: R32, R125, R134a, and R152a. The list of lubricants consists of:

- PAGs: Hexylene glycol (HEXG), triethylene glycol (TRIG), tetraethylene glycol (TETG), triethylene glycol dimethylether (TriEGDME), and tetraethylene glycol dimethylether (TEGDME).
- POEs: Pentaerythritol tetrapentanoate (PEC5), and pentaerythritol tetra-2-ethylhexanoate (PEB8).
- ABs: n-butylbenzene (AB4), n-hexylbenzene (AB6), n-heptylbenzene (AB7), and n-octylbenzene (AB8).

All these lubricants are compounds with known chemical structure. The designations used for PAGs, POEs, and ABs are listed in Table 6.1, along with chemical formulas and molecular weights.

	Compound	Formula	M (g.mol^{-1})
PAGs	HEXG	$C_6H_{14}O_2$	118.20
	TRIG	$C_6H_{14}O_4$	150.20
	TriEGDME	$C_8H_{18}O_4$	178.23
	TETG	$C_8H_{18}O_5$	194.20
	TEGDME	$C_{10}H_{22}O_5$	222.30
POEs	PEC-5	$C_{25}H_{44}O_8$	472.62
	PEB-8	$C_{37}H_{68}O_8$	640.94
ABs	AB4	$C_{10}H_{14}$	134.22
	AB6	$C_{12}H_{18}$	162.27
	AB7	$C_{13}H_{20}$	176.30
	AB8	$C_{14}H_{22}$	190.32

Table 6.1 – Designation, chemical formulae and molecular weight for PAGs, POEs, and ABs.

The scaling parameters (T_c, P_c, and ω) have been taken from Table 1.1 (Chapter I) for refrigerants, and from the DIPPR database (1998) for HEXG, TRIG, and TETG. For the lubricant PEC-5 the scaling parameters reported by Garcia et al. (2008) are used, while for TriEGDME, TEGDME and PEB-8 the values reported in Table 2.9 (Chapter II) have been employed. For alkylbenzenes the parameters and correlations by Nikitin et al. (2002) are used (see details in Chapter V).

6.3 – Modeling phase equilibria and coexisting densities

The two models used in this section, the PR EoS and the PC-SAFT EoS, have been discussed and applied to pure compounds in Chapter II. Extension to mixtures has also been introduced in the mentioned chapter. In all examples of this section, it has been found to be necessary to adjust binary interaction parameters. This adjustment is carried out by minimizing the objective function:

$$\min_{k_{ij}} f = \frac{1}{NP}\sum_{i=1}^{NP}\left|x_{i,\exp} - x_{i,cal}\right| \qquad (6.1)$$

where NP is the number of experimental points, and x is the mole fraction of refrigerant in the liquid phase. No significant improvement has been observed, by considering the temperature-dependent binary interaction parameter. Thus, no temperature dependence of the [illegible] is considered. The vapor phase of these mixtures is always considered to be [illegible] pure [illegible] assumption made for these systems ([illegible] et al. [illegible]).

6.3.1 – HFC refrigerants + PAGs systems

The experimental database includes solubilities of HFC-134a + TriEGDME ([illegible]) and HFC-134a + HEXG, TRIG, TETG, and TEGDME (Tseregounis and Riley [illegible]). [illegible] absolute percent deviations (AAD) between experimental and calculated phase compositions [illegible] in Table 6.2 for five binary systems containing HFC-134a + PAGs for the PR EoS [illegible] binary interaction parameters (k_{ij}), the numbers of points, and the temperature ranges are also shown.

Ref	PAG	NP	T range (K)	k_{ij}	AAD %
HFC-134a	HEXG	81	[illegible]	[illegible]	[illegible]
	TRIG	49	[illegible]	[illegible]	[illegible]
	TriEGDME	80	[illegible]	[illegible]	[illegible]
	TETG	77	[illegible]	[illegible]	[illegible]
	TEGDME	64	[illegible]	[illegible]	[illegible]

Table 6.2 – Deviation between calculated and experimental compositions in the liquid phase for HFC-134a + PAGs with the PR EoS. NP is the number of experimental points.

An example of the accuracy of the gas solubility correlation and the phase diagram prediction is shown in Figure 6.1 for HFC-134a + HEXG and HFC-134a + TRIG systems. For the HFC-134a + TRIG mixture it can be observed that the lubricant TRIG is partially miscible [illegible]. The mixture with lubricant TETG also exhibits liquid-liquid immiscibility. Tseregounis and Riley have measured the maximum amount of the HFC-134a that can be dissolved in [illegible] mole fraction of HFC-134a is, approximately, from [illegible] mole fraction [illegible] temperatures [illegible] K and [illegible] K. The PR EoS with the [illegible] amount of HFC-134a that can be dissolved in TRIG and TETG [illegible] fraction, respectively. It can be observed that the PR EoS [illegible] TETG, in agreement with the experimental results. Furthermore, [illegible] predicts complete miscibility for the systems containing HEXG and TEGDME [illegible] studied temperatures, which is also in agreement with experimental results. The k_{ij} parameters obtained for the HFC-134a + TRIG and + TETG binary systems have also been used to predict the coexisting densities taken from the literature (Kumagai *et al.* 1993, and 1994). The AAD calculated are on average 2.2% for TRIG and 3.1% for TETG mixtures.

Figure 6.1 – Example of solubility data and L_1-L_2-g prediction for HFC-134a + HEXG and HFC-134a + TRIG (Tseregounis and Riley 1994). Experimental data: 273.15 K (●), 283.15 K (■), 293.15 K (▲), 303.15 K (◆), 313.15 K (○), 323.15 K (□), 333.15 K (△), and 353.15 K (◇). Solid lines denote the calculated data by the PR EoS. Horizontal lines represent the predicted L_1-L_2-g region.

The PC-SAFT EoS has been applied to correlate phase equilibria of the binary mixtures HFC-134a + TriEGDME and HFC-134a + TEGDME. The results are presented in Table 6.3. It can be observed that the PC-SAFT EoS gives better results than the PR EoS. It is also noteworthy that the k_{ij} parameters for the PR and the PC-SAFT EoS are of the same order of magnitude. In Figure 6.2 the PR and the PC-SAFT predictions are shown for HFC-134a + TriEGDME and TEGDME.

Ref	*PAG*	*NP*	*T-range* (K)	k_{ij}	*AAD* (%)
HFC-134a	*TriEGDME*	80	283–353	−0.0287	1.97
	TEGDME	84	283–353	−0.0387	2.22

Table 6.3 – Deviation between calculated and experimental compositions in the liquid phase for HFC-134a + PAGs with the PC-SAFT EoS. *NP* is the number of experimental points. The *m*, σ, and ε parameters for these compounds are reported in Chapter II.

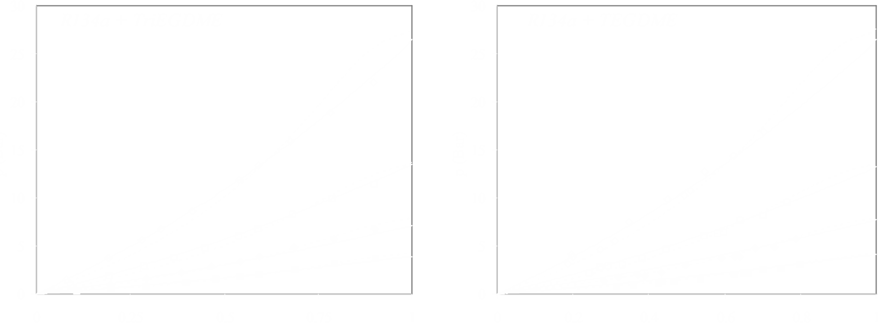

Figure 6.2 – Example of solubility predictions for HFC-134a + TriEGDME (Coronas *et al.* 2002) and HFC-134a + TEGDME (Tseregounis and Riley 1994). Experimental data: 283.15 K (■), 303.15 K (◆), 323.15 K (□), and 353.15 K (◇). Lines denote calculated data by the PR EoS (—) and the PC-SAFT EoS (—). Note: for clarity not all the experimental points are shown on this figure.

6.3.2 – HFC refrigerants + POEs: results

The experimental database consists of 10 binary systems containing HFCs (HFC-32, HFC-125, HFC-134a, and HFC-152a) + POEs (PEC-5 and PEB-8). Tables 6.4 and 6.5 present the results for these systems. Overall, good fit to experimental data can be seen for both models at all the investigated temperatures. The results for the PC-SAFT model are, again, slightly better than those for the PR model. However, the binary interaction parameters needed for the PC-SAFT EoS are higher than the interaction parameters for the PR EoS.

Figure 6.3 shows the *p-x* diagrams for the mixtures of HFC-32, HFC-125, HFC-134a, and HFC-152a with the PEB-8 at various temperatures. The PC-SAFT equation of state predicts liquid-liquid immiscibility for some temperatures and for some of the mixtures, whereas the PR EoS predicts complete miscibility at all of the studied temperatures in all cases. For these systems no liquid-liquid split has been reported by Wahlström and Vamling (1999, and 2000). However, this behavior has been observed for systems containing the POEs, such as HFC-32 + a commercial POE (Takaishi and

Ref	*POE*	*NP*	*T-range (K)*	k_{ij}	*AAD (%)*
HFC-32	*PEC5*	28	303-363	-0.0450	4.35
HFC-125		30	303-363	0.0158	0.90
HFC-134a		28	303-363	-0.0125	1.20
HFC-152a		24	303-363	-0.0220	2.20
HFC-32	*PEB8*	28	303-363	-0.0550	4.25
HFC-125		24	303-363	0.0567	3.60
HFC-134a		23	303-363	-0.0210	1.70
HFC-152a		20	303-363	-0.0477	2.20

Table 6.4 – Deviation between calculated and experimental compositions in the liquid phase for HFCs + POEs with the PR EoS. *NP* is the number of experimental points.

Ref	*POE*	*NP*	*T-range (K)*	k_{ij}	*AAD (%)*
HFC-32	*PEB8*	28	303-363	0.1273	4.12
HFC-125		24	303-363	0.0550	3.95
HFC-134a		23	303-363	0.0984	1.42
HFC-152a		20	303-363	0.0785	1.85

Table 6.5 – Deviation between calculated and experimental compositions in the liquid phase for HFCs + POEs with the PC-SAFT EoS. *NP* is the number of experimental points. The *m*, σ, and ε parameters for these compounds are reported in Chapter II.

6.3.3 – CO₂ and HFC refrigerants + ABs: results

Alkylbenzenes can be used as synthetic aromatic hydrocarbon lubricants in the refrigeration cycles. Although these lubricants cannot compete effectively with the POEs or the PAGs, they show excellent stability and low hygroscopicity. Besides, from a theoretical point of view, the homologous series CO_2 + n-AB provides an excellent opportunity to confirm the continuity of the fluid phase behavior in binary mixtures. As stated in Chapter V, in the scheme of van Konynenburg and Scott (1980), four of the six types of known binary phase behavior are relevant to refrigerant + lubricant mixtures. There is

Figure 6.3 – Example of solubility predictions for HFCs + POEs (Wahlström and Vamling, 2000). Experimental data: 303.15 K (■), 323.15 K (♦), 343.15 K (□), and 363.15 K (◊). Lines denote the calculated data by the PR EoS (—) and the PC-SAFT EoS (– –).

a good amount of reliable experimental phase equilibria and critical data for mixtures of carbon dioxide + n-alkylbenzenes, which confirms that type II, III and IV phase behavior are displayed by these mixtures.

For the homologous series CO_2 + ABs, the following topographical transitions were found in the behavior of the *l*₁–*l*₂–*g* loci (Fall and Luks 1985, and 1986):

- A locus extending from a quadruple point (*s*–*l*₁–*l*₂–*g*) to an UCEP (*l*₁=*l*₂–*g*). This behavior is displayed by CO_2 + AB4 mixtures (Tiffin *et al.* 1978).
- A locus with two branches: one like the *l*₁–*l*₂–*g* locus previously described, referred to as the lower branch, and an upper branch that extends from a LCEP (*l*₁=*l*₂–*g*) up to an UCEP (*l*₁–

$l_2 = g$). This UCEP is sometimes called "K-point". This behavior is displayed by CO₂ + AB7 mixtures (Fall and Luks 1986, and Lansangan *et al.* 1987).

- A locus which topographically is the result of a merger of the two branches previously described, extending from a quadruple point to a K-point. The octylbenzene to pentadecylbenzene mixtures with carbon dioxide exhibit such a behavior.

The system CO_2 + AB6 does not clearly belong to the type II or type IV phase behavior. In the earlier study of Fall and Luks 1986, it was established that this mixture has no upper branch to its l_1-l_2-g locus. Later, Lansangan *et al.* (1987) established that this system is extremely close to forming such a branch, although they did not report experimental values for the second branch. According to these authors, this mixture is very close to exhibiting a K-point superimposed upon the LCEP, that is, it has a state which is coincidentally close to a tricritical point. To recapitulate, the mixtures of CO_2 + n-AB4 show the type II behavior, the mixtures of CO_2 + n-AB6 belong to either type II or IV, the mixtures of CO_2 + n-AB7 belong to type IV, and the mixtures of CO_2 + n-AB8 or longer n-AB compounds belong to type III.

The critical points, critical end points, and l_1-l_2-g loci, which determine the type of phase behavior, are computed with the PR and the PC-SAFT EoS. To perform calculations with the PR EoS, as in the previous chapter, the critical parameters are taken from Poling *et al.* (2000) and Nikitin *et al.* (2002) for CO_2 and ABs respectively. However, in this chapter the individual parameters for ABs have been used. To be able to compare the calculation obtained from the PC-SAFT EoS with experimental data, the m, σ, and ε parameters for CO_2 reported by Gross and Sadowski (2001) are used. These authors have also reported values for n-AB from n = 0 to 4. It has been observed for a version of SAFT known as SAFT-VR (Jiang and Prausnitz, 2000) that certain groups of parameters vary linearly with the carbon number. Figure 6.4 shows that the combinations m, $m\varepsilon/k$, and $m\sigma^3$ vary linearly with molecular weight. This linear extrapolation has been used to obtain PC-SAFT parameters for the n-AB compounds beyond butylbenzene. The equations for the lines in Figure 6.4 are:

$$m = 0.7244 + 0.022\,M_{n-AB} \qquad (6.2)$$

$$m\varepsilon/k = 223.4120 + 6.2356\,M_{n-AB} \qquad (6.3)$$

$$m\sigma^3 = -16.0188 + 1.7361\,M_{n-AB} \qquad (6.4)$$

Figure 6.4 – Groups *m*, *m*ε/*k*, and *m*σ³ versus molecular weight for linear alkylbenzenes up to butylbenzene. Points are PC-SAFT parameters reported by Gross and Sadowski (2001), and lines are linear fits to these points. The lines are described by Equations 6.2 – 6.4.

The calculation of phase equilibria requires determination of the binary interaction parameters. They have been obtained by simultaneously adjustment of the l-g and l-l-g experimental data. In doing so, for the PR EoS, it was possible to ensure that the mixture CO₂ + ABP corresponds to the intermediate type IV phase behavior. The optimized value is k_{ij} = 0.076. This value has then been used in order to predict the phase behavior of CO₂ + ABM, ABE, and ABB mixtures. This procedure has also been applied to CO₂ + n-alkane mixtures with the SAFT-VR EoS by Galindo and Blas (2002). For the PC-SAFT EoS it was found that better agreement with experimental results is achieved by adjusting binary interaction parameters for each system. Using the optimized parameters, the *p*-*T*-*x* diagram of CO₂ + *n*-ABP is calculated (Figure 6.5). As can be seen, the PR and the PC-SAFT EoS describe this system in a similar manner. The percent AAD between experimental and calculated phase compositions are 5.3 % and 5.4 % for the PR EoS (k_{ij} = 0.076) and for the PC-SAFT EoS (k_{ij} = 0.12), respectively. The *l*-*l*-*g* locus is reproduced by the PR EoS with AAD = 7.2 % and by the PC-SAFT EoS with AAD = 6.6 %. Both equations predict type IV phase behavior, in agreement with experimental results.

As stated above, it is not clear whether the CO₂ + ABB system belongs to type II or type IV. With the same binary interaction parameter (k_{ij} = 0.076) the PR EoS predicts the type IV phase behavior, while the PC-SAFT EoS with the k_{ij} = 0.127 predicts the type III phase behavior. This is displayed in Figure 6.6. As a consequence of predicting the phase behavior erroneously, the PC-SAFT EoS predicts the liquid-liquid immiscibility in the regions where the *l*-*g* equilibrium has been experimentally observed (see for example *T* = 288.15 K to 318.15 K in Figure 6.6). For this system the AAD in compositions are 5 % and 4.6 % for PR and PC-SAFT respectively. The mole fractions along the l_1-l_2-g locus are described with an AAD of 9 % and 4.7 % for the PR EoS and the PC-SAFT EoS, correspondingly.

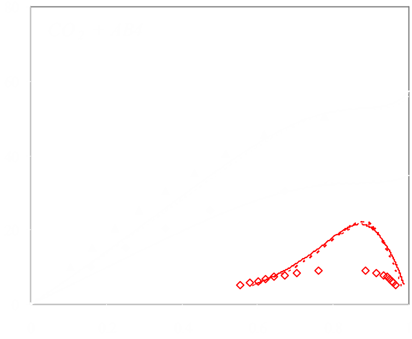

Figure 6.5 – Compositions as function of pressure for the *l*-*g* locus at T = 273.15 K (◆), and 293.15 K (▲) (Tiffin *et al.* 1978) compared with the PR (—) and PC-SAFT (---) predictions. PR predictions with k_{ij} = 0.076, and PC-SAFT predictions with k_{ij} = 0.12. The red open triangles (◊) correspond to the l_1-l_2-*g* locus at different temperatures (Tiffin *et al.* 1978).

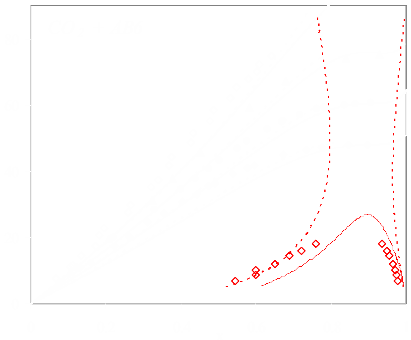

Figure 6.6 – Compositions as function of pressure for the *l*-*g* locus at T = 288.15 K (●), 298.15 K (◆), 308.15 K (▲), and 318.15 K (▼) (Lansangan *et al.* 1987) compared with the PR (—) and PC-SAFT (---) predictions. PR predictions with k_{ij} = 0.076, and PC-SAFT predictions with k_{ij} = 0.127. The red open triangles (◊) correspond to the l_1-l_2-*g* locus at different temperatures (Fall and Luks 1986).

The results for the system CO$_2$ + AB7 are shown in Figure 6.7. The PR EoS can correctly reproduce the experimental phase behavior found for this system (type IV), whereas the PC-SAFT EoS with k_{ij} = 0.13 predicts the type III phase behavior. Again, the PC-SAFT EoS predicts liquid-liquid immiscibility in the regions where complete miscibility has been reported. The AAD in solubilities are 4.9 % and 4.6 % and the AAD in mole fractions along the three-phase line are 9 % and 4.7 %, for the PR and the PC-SAFT EoS, in that order.

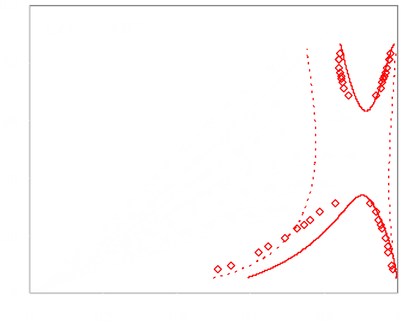

Figure 6.7 – Compositions as function of pressure for the *l-g* locus at T = 268.15 K (♦), 278.15 K (●), 288.15 K (▲), 298.15 K (◊), 308.15 (○), and 318.15 K (Δ) (Lansangan *et al.* 1987) compared with the PR (- -) and PC-SAFT (—) predictions. PR predictions with k_{ij} = 0.076, and PC-SAFT predictions with k_{ij} = 0.13. The red open triangles (◊) correspond to the l_1-l_2-g locus at different temperatures (Fall and Luks 1986).

The binary system CO$_2$ + AB8, which is depicted in Figure 6.8, exhibits the type III phase behavior. This is correctly represented by both PR EoS and PC-SAFT EoS with the k_{ij} = 0.132. The solubilities are described with an AAD of 3.5% and 4.7% for the PR and the PC-SAFT EoS, whereas the coexisting mole fractions upon the l_1-l_2-g locus are described with an AAD of 3.5% and 4.6%. In Table 6.6 the experimental and calculated UCEP and LCEP points are shown. It is clear that the PR EoS gives a good description of the phase behavior of the mixture, whereas the PC-SAFT EoS fails at predicting the transitions in the type of phase behavior observed when the molecular weight varies. The k_{ij} parameters required by the PC-SAFT EoS are always higher than the k_{ij} parameters required by the PR EoS.

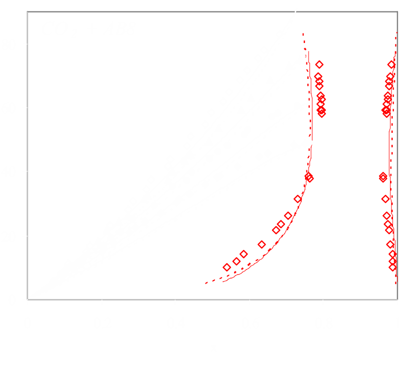

Figure 6.8 – Compositions as function of pressure for the *l*-*g* locus at *T* = 288.15 K (●), 298.15 K (■), 308.15 K (▲), and 318.15 K (◇) (Lansangan *et al.* 1987) compared with the PR (—) and PC-SAFT (---) predictions. PR predictions with k_{ij} = 0.076, and PC-SAFT predictions with k_{ij} = 0.132. The red open triangles ◊ correspond to the l_1-l_2-*g* locus at different temperatures (Fall and Luks 1986).

n-AB	Type of CEP	Experimental		PR		PC-SAFT	
		T (K)	*P* (Bar)	*T* (K)	*P* (Bar)	*T* (K)	*P* (Bar)
n-AB4	UCEP^a	231.98	9.54	257.93	21.55	258.50	22.46
n-AB6	UCEP^a	251.40	20.19	262.27	26.88	–	–
n-AB7	UCEP^a	270.24	33.10	273.90	34.03	–	–
n-AB7	LCEP	301.68	66.57	299.98	63.24	–	–
n-AB7	UCEP^b	312.67	84.99	314.01	86.71	313.80	88.07
n-AB8	UCEP^b	310.27	81.67	307.75	77.73	312.75	83.69

Table 6.6 – Critical end-point (CEP) temperatures and pressures for CO_2 + n-AB mixtures. Experimental (Fall and Luks 1986) and calculated values using the PR and the PC-SAFT models. ^{a} An upper critical end point at low temperatures (l_1=l_2-*g*). ^{b} An upper critical end point at high temperatures (l_1-l_2=*g*).

The k_{ij} parameters for the CO_2 + *n*-AB binary systems have also been used to predict coexisting densities (Tiffin *et al.* 1978, and Lansangan *et al.* 1987). The PR EoS predicts the densities with an AAD of 7.5%, 6.3%, 7.2%, and 8.1% for mixtures of CO_2 + AB4, AB6, AB7, and AB8, respectively. The PC-SAFT EoS delivers better results, the being AAD equal to 3.2%, 4.3%, 4.8%, and 4.5% for the same mixtures. As an example, Figure 6.9 shows the results for CO_2 + AB7 and CO_2 + AB8, where better performance of the PC-SAFT EoS can be observed, especially in the low-pressure and low-temperature region. Fall and Luks (1985, and 1986) also reported mass density inversions for these systems. Inversion was found upon the three-phase curve for CO_2 + AB6 and CO_2 + AB8. For CO_2 + AB8 inversion is observed at T near 280 K. These inversions can be correctly described by the PR and the PC-SAFT EoS, as illustrated in Figure 6.10. However, as a consequence of the incorrect phase behavior description, the PC-SAFT approach predicts mass density inversions for the system CO_2 + AB7, which is not in agreement with the experimental results.

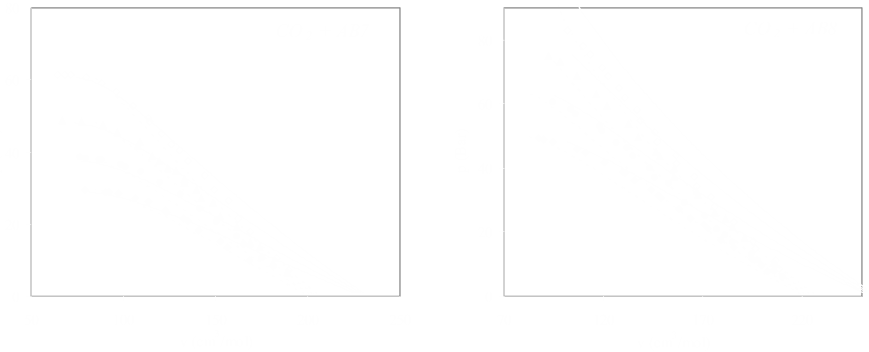

Figure 6.9 – Coexisting molar volumes for CO_2 + AB7 and CO_2 + AB8 at T = 288.15 K (◆), 298.15 K (●), 308.15 K (▲), and 318.15 K (○) (Lansangan *et al.* 1987) compared with the PR (—) and PC-SAFT (- -) predictions.

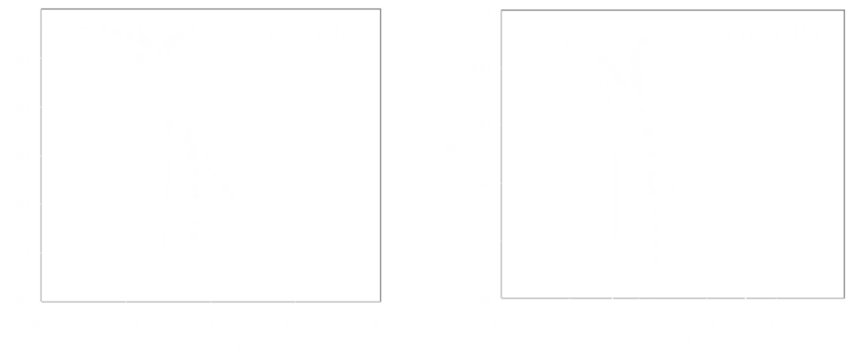

Figure 6.10 – Coexisting mass densities along the L_1–L_2–g locus (Fall and Luks 1985, and 1986). Predictions with PR (—) and PC-SAFT (- -). Points: density associated with L_1 phase (◆), density phase associated with L_2 phase (○), and UCEP and LCEP predicted by the PR EoS (●).

As an example of liquid-liquid equilibrium correlation, Figure 6.11 shows the T-x representations at p = 50 and 100 Bar for the system HFC-134a + AB8 (Pool and de Loos, 2003, 2004). The system, which is not very pressure dependent, can be correlated correctly with the PR and the PC-SAFT EoS, except for the critical region, where both models seem to extend the L-curves up to very high temperatures.

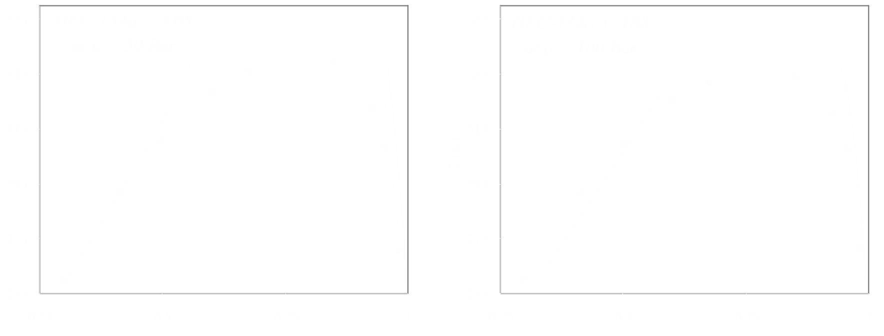

Figure 6.11 – Liquid-liquid equilibria in the system HFC-134a + AB8 at p = 50 and 100 Bar. Predictions with PR (—) k_{ij} = 0.120 and PC-SAFT (—) k_{ij} = 0.135. The m, σ, and ε parameters for HFC-134a are reported in Chapter II.

6.4 – Modeling p-v-T-x behavior up to high pressures

Liquid densities for HFC-134a + TriEGDME and HFC-134a + TEGDME have been measured by Comuñas *et al.* (2002b, and 2002c) from atmospheric pressures up to 60 MPa, in the range T = 293.15 K to 373.15 K. These authors studied a total of six mole fractions for the first system and eight for the latter. This represents a good database to test the ability of the PR, RK-PR, SWDR, and PC-SAFT EoS. Table 6.7 shows the average percent deviations and the maximum deviations of the densities for the different models. Good agreement with experimental data is observed in all cases. In Chapter II it was shown that the PR, RK-PR, SBWR-rep, and PC-SAFT EoS predict the densities of pure HFC-134a, TriEGDME, and TEGDME satisfactorily. This may explain the good results for mixtures of these substances obtained with all the models. The Peng-Robinson EoS is surprisingly accurate, yet it is important to remark again that the pure component parameters (T_c, P_c, and ω) for lubricants have been adjusted to reproduce experimental densities. The RK-PR EoS shows again good capabilities in description of the volumetric properties.

EoS	*Mixture*	*R134a + TriEGDME*	*R134a + TEGDME*
	NP	594	792
PR	AAD (%) MDev (%)	1.23 3.81	1.25 3.96
RK-PR	AAD (%) MDev (%)	1.21 4.37	1.38 4.04
SBWR-reg	AAD (%) MDev (%)	1.09 2.88	1.83 4.35
PC-SAFT	AAD (%) MDev (%)	1.01 3.21	1.20 3.98

Table 6.7 – Average absolute deviation and maximum deviation for HFC-134a + PAGs obtained with the PR, RK-PR, SWBR-reg, PC-SAFT EoS. *NP* denotes number of points.

Figure 6.12 displays the variations of density versus *x* for the system HFC-134a + TEGDME at $T = 373.15$ K for different isobars. It can be appreciated that at low pressures the density shows a maximum at mole fractions close to 0.9. This maximum is predicted by the PR and the PC-SAFT models. Although not shown in Figure 6.12, the RK-PR and the SBWR-reg EoS are also able to predict this phenomenon. Similar behavior is characteristic of the system HFC-134a + TriEGDME at low pressures and high temperatures, and at mole fractions close to 0.9, the density of the mixture has a larger value than the density of pure HFC-134a. This phenomenon has also been observed by Cavestri and Schafer (2000) for the HFC-410A + POEs mixtures.

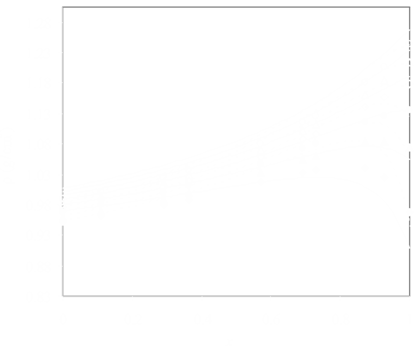

Figure 6.12 – Densities for HFC-134a + TEGDME using the PR (—) and PC-SAFT (—) EoS compared with experimental values at *p* = 100 bar (♦), 200 Bar (▲), 300 Bar (●), 400 Bar (◊), 500 (Δ) Bar, and 600 (○) Bar.

For comparison, the calculated versus experimental densities are plotted in Figure 6.13, where the good performance of the four EoS can be appreciated. The PR and RK-PR EoS show larger deviations in the low-density range. It can also be observed that the SWBR-reg and the PC-SAFT models overestimate the densities in the high density region.

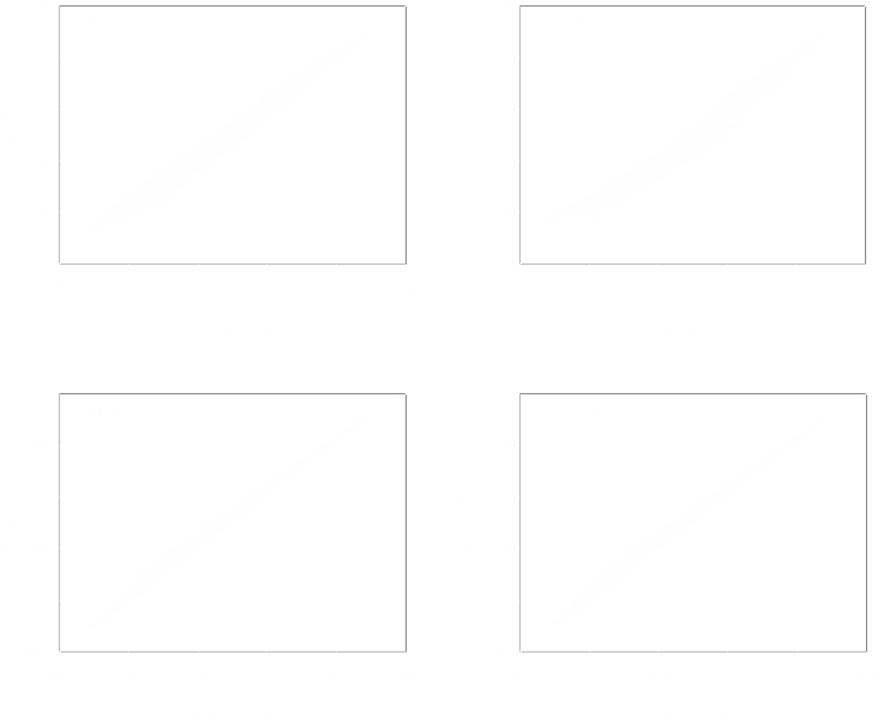

Figure 6.13 – Comparisons of experimental densities for R134a + TriEGDME (♦), and R134a + TEGDME (▲) with densities calculated by different EoS.

6.5 – Conclusions

Modeling of phase equilibria and volumetric properties has been carried out based on experimental information found in the literature. Extensive comparison has been carried out between the cubic equations of state, such the PR EoS, and the statistical models such as the PC-SAFT. Both models have shown similar performance in predicting phase equilibria of HFC + PAG, POE or AB systems, in most of the cases requiring small values for the binary interaction parameters. In many cases the k_{ij} parameters for the PR EoS are smaller than the parameters for the PC-SAFT EoS, which might indicate a higher prediction capability of the PR EoS for the systems under study. However, care should be taken when interpreting these results, since in the PC-SAFT EoS several interactions that these mixtures may present (polar interactions, weak hydrogen bonds, etc) have not been taken into account. Nonetheless, the predictions with the PC-SAFT EoS may be considered as satisfactory.

A global phase behavior of carbon dioxide mixtures with *n*-alkylbenzenes is also studied with application of the PR and the PC-SAFT EoS. The PR EoS has shown to predict the continuity in fluid phase behavior observed experimentally, by use of the same interaction parameter for all the mixtures. This binary interaction parameter is obtained from a single mixture (CO_2 + AB7) and then transferred to other systems. Experimental solubilities are also described accurately by the PR EoS. The PC-SAFT approach also shows good agreement between experimental and calculated solubilities. However, this model does not always reproduce global phase behavior. This may be due to different reasons. First, carbon dioxide has no dipole moment because of its molecular symmetry, but it possesses a significant quadrupole moment, which may cause electrostatic interactions. These interactions are not accounted for in the PC-SAFT approach, as the CO_2 is assumed to exhibit dispersion interactions only. Another important reason for the discrepancies can be the values of the *m*, *σ*, and *ε* parameters used for CO_2, as they were optimized for a good description of the vapor pressure and coexisting densities. A better description may probably be obtained by use of the rescaled parameters. The densities along the *l-g* locus have also been calculated using the optimized values k_{ij}. In spite the qualitative discrepancies, the results obtained on the basis of the PC-SAFT EoS are generally better than those produced by the PR model.

The models have also been tested with regard to their ability to reproduce liquid densities up to high pressures. For comparison, the RK-PR and the SBWR-reg models were also included. In general, the four models represent the *p-v-T-x* properties satisfactorily. Quantitatively, slightly better results are obtained on the basis of the PC-SAFT EoS. The Peng-Robinson EoS can be used to describe accurately these asymmetric mixtures, but only if the pure-component parameters and the interaction coefficient are regressed.

Nomenclature

AAD = Average absolute deviation

EoS = Equation of state

k_{ij} = Binary interaction parameter

m = Number of segments per chain

LCEP = Lower critical end point

M = Molecular weight

NP = Number of points

p = Pressure

PAG = Polyalkylene glycols

PC-SAFT = Perturbed-chain statistical associating fluid theory

POE = Polyol ester

PR = Peng-Robinson

RK-PR = Redlich-Kwong-Peng-Robinson

SBWR = Soave-Benedict-Webb-Rubin

T = Temperature

UCEP = Upper critical end point

v = Molar volume

x = Mole fraction of refrigerant

Greek letters

ε = Depth of pair potential

ρ = Density

σ = Segment diameter

ω = Acentric factor

Subscripts/superscripts

cal = Calculated property

exp = Experimental property

i = Component "i"

j = Component "j"

References

1. Bertucco, A., Elvassore, N., Fermeglia, M., Prausnitz, J.M. Perturbed-hard-sphere-chain equation of state for phase equilibria of mixtures containing a refrigerant and a lubricant oil. *Fluid Phase Equilib.* 1999, 158-159, 183-191.
2. Bobbo, S., Scattolini, M., Camporese, R., Fedele, L., Stryjek, R. Solubility of Carbon Dioxide in Pentaerythritol Esters. *7th International Conference, Thermophysical Properties and Transfer Processes of Refrigerants*. Vicenza, Italy, 2005, 193-200.
3. Cavestri, R.C., Schafer, W.R. Measurement of Solubility, Viscosity, and Density of R410A Refrigerant/Lubricant Mixtures. *ASHRAE Trans.* 2000, 106, 277-283.
4. Cismondi, M., Mollerup, J. Development and application of a three-parameter RK-PR equation of state. *Fluid Phase Equilib.* 2005, 232, 74-89.
5. Comuñas, M.J.P. Densidades y Viscosidades a Alta Presión de Nuevos Lubricantes Sintéticos y de las Mezclas Lubricante + HFC-134a. Medidas y Modelización. Ph.D. Thesis, Física Aplicada, Universidad de Santiago de Compostela, Santiago de Compostela, Spain, 2002a.
6. Comuñas, M.J.P., Fernández, J., Baylaucq, A., Canet, X., Boned, C. PρTx measurements for HFC-134a + triethylene glycol dimethylether. *Fluid Phase Equilib.* 2002b, 199, 185-195.
7. Comuñas, M.J.P., Baylaucq, A., Boned, C., Canet, X., Fernández, J. High-Pressure Volumetric Behavior of x 1,1,1,2-tetrafluoroethane + (1 − x) 2,5,8,11,14-Pentaoxapentadecane (TEGDME) Mixtures. *J. Chem. Eng. Data.* 2002c, 47, 233-238.
8. Coronas, A., Mainar, A.M., Kashinath, R.P., Conesa, A., Shibao, S., Sherlock, S. Solubility of 1,1,1,2-tetrafluoroethane in Triethylene Glycol Dimethyl Ether. *J. Chem. Eng. Data.* 2002, 47, 56-58.
9. DIPPR. Tables of Physical and Thermodynamics Properties of Pure Compounds. AIChE: New York, 1998.
10. Elvassore, N., Bertucco, A. A Cubic Equation of State with Group Contributions for the Calculation of Vapor-Liquid Equilibria of Mixtures of Hydrofluorocarbons and Lubricant Oils. *Ind. Eng. Chem. Res* 1999, 38, 2110-2118.
11. Fall, D.J., Luks, K.D. Liquid-liquid-vapor equilibria of the binary mixtures carbon dioxide + n-pentadecylbenzene and carbon dioxide + n-nonylbenzene. *Fluid Phase Equilib.* 1985, 23, 259-267.
12. Fall, J.L., Luks, K.D. Liquid-liquid-vapor phase equilibria behavior of certain binary carbon dioxide + n-alkylbenzene mixtures. *Fluid Phase Equilib.* 1986, 28, 87-96.

13. Galindo, A.; Blas, F.J. Theoretical Examination of the Global Fluid Phase Behavior and Critical Phenomena in Carbon Dioxide + *n*-Alkane Binary Mixtures. *J. Phys. Chem. B* 2002, 106, 4503–4515.
14. García, J.; Monsalvo, M.A.; Quiñones-Cisneros, S.E.; Fernández, J. Modeling Phase Equilibria and Viscosity for Refrigerant-Lubricant Oil Systems. *21st IIR International Congress of Refrigeration*, Washington D.C., 2003.
15. Gross, J.; Sadowski, G. Perturbed-Chain SAFT: An Equation of State Based on a Perturbation Theory for Chain Molecules. *Ind. Eng. Chem. Res.* 2001, 40, 1244-1260.
16. Huber, M.L.; Lemmon, E.W.; Friend, D.G. Modeling bubble points of mixtures of hydrocarbon refrigerants and polyol ester lubricants. *Fluid Phase Equilib.* 2002, 194-197, 511-519.
17. Jiang, J.W.; Prausnitz, J.M. Phase Equilibria for Chain-Fluid Mixtures near to and far from the critical region. *AIChE J.* 2000, 46, 2525-2535.
18. Kumagai, K.; Mochida, H.; Takahashi, S. Liquid viscosities and densities of HFC134a + glycol mixtures. *Int. J. Thermophys.* 1993, 14, 45-53.
19. Kumagai, K.; Miura-Mochida, H.; Takahashi, S. Revised Viscosities for HFC-134a + Glycol Mixtures from 273 to 333 K. *Int. J. Thermophys.* 1994, 15, 109-115.
20. Lansangan, R.M.; Jangkamolkulchai, A.; Luks, K.D. Binary Vapor-Liquid Equilibria Behavior in the vicinity of Liquid-Liquid-Vapor Loci. *Fluid Phase Equilib.* 1987, 36, 49-66.
21. López, E.R.; Mainar, A.M.; García, J.; Urieta, J.S.; Fernández, J. Experimental and predicted solubilities of HFC134a (1,1,1,2-tetrafluoroethane) in polyethers. *Ind. Eng. Chem. Res.* 2004, 43, 1523-1529.
22. Nikitin, E.D.; Popov, A.P.; Bogatishcheva, N.S. Vapor-Liquid Critical Properties of n-Alkylbenzenes from Toluene to 1-Phenyltridecane. *J. Chem. Eng. Data* 2002, 47, 1012-1016.
23. Peng, D.-Y.; Robinson, D.B. A New Two-Constant Equation of State. *Ind. Eng. Chem. Fundam.* 1976, 15, 59–64.
24. Poling, B.E.; Prausnitz, J.M.; O'Connell, J.P. The Properties of Gases and Liquids. Fifth Edition. McGraw-Hill, New York. 2000.
25. Poot, W.; de Loos, T.W. High pressure phase equilibria in the system 1,1,1,2-tetrafluoroethane + heptylbenzene. *Fluid Phase Equilib.* 2005, 230, 69-75.
26. Poot, W.; de Loos T.W. High pressure phase behaviour of binary systems of refrigerants and phenylalkanes: the system 1,1,1,2-tetrafluoroethane+phenyloctane. *Fluid Phase Equilib.* 2004, 222-223, 255-259.

27. Schneider, G. Phase Equilibria in Binary Fluid Systems of Hydrocarbons with Carbon Dioxide, Water, and Methane. *Chem. Eng. Prog. Symp. Ser.* 1968, 64, 9-15.
28. Schneider, G.M. Phase Behavior and Critical Phenomena in Fluid Mixtures under Pressure. *Ber. Bunsenges. Phys. Chem.* 1972, 76, 325-331.
29. Soave, G.S. A Noncubic Equation of State for the Treatment of Hydrocarbon Fluids at Reservoir Conditions. *Ind. Eng. Chem. Res.* 1995, 34, 3981-3994.
30. Soave, G.S. An effective modification of the Benedict-Webb-Rubin equation of state. *Fluid Phase Equilib.* 1999, 164, 157-172.
31. Takaishi, Y., Oguchi, K. Solubility of R-32 and Polyester Lubricant Mixtures. Proc. 19th Int. Congress of Refrigeration, The Hague, The Netherlands, 1995; 564-574.
32. Takigawa, K., Sandler, S.I., Yokozeki, A. Solubility and viscosity of refrigerant/lubricant mixtures: hydrofluorocarbon/ alkylbenzene systems. *Int. J. Refrig.* 2002, 25, 1014-1024.
33. Tiffin, D.L., DeVera, A.L., Luks, K.D., Kohn, J.P. Phase-equilibria behavior of the binary systems carbon dioxide-n-butylbenzene and carbon dioxide-trans-decalin. *J. Chem. Eng. Data.* 1978, 23, 45-47.
34. Tseregounis, S.I., Riley, M.J. Solubility of HFC-134a refrigerant in glycol-type compounds: effects of glycol structure. *AIChE Journal.* 1994, 40, 726-737.
35. van Konynenburg, P.H., Scott, R.L. Critical Lines and Phase Equilibria in Binary Van Der Waals Mixtures. *Philos. Trans. R. Soc. London, Ser. A.* 1980, 298, 495-540.
36. Wahlstrom, A., Vamling, L. Solubility of HCFC22, CFC114 and HFC152a in n-Hexadecane. *Can. J. Chem. Eng.* 1996, 74, 426-428.
37. Wahlstrom, A., Vamling, L. The Solubility of HFC125, HFC134a, HFC143a and HFC152a in n-Eicosane, n-Hexadecane, n-Tridecane and 2, 6, 10, 14-Tetramethylpentadecane. *Can. J. Chem. Eng.* 1997, 75, 544-550.
38. Wahlstrom, A., Vamling, L. Solubility of HFC32, HFC125, HFC134a, HFC143a and HFC152a in a Pentaerythritol Tetrapentanoate Ester. *J. Chem. Eng. Data.* 1999, 44, 823-828.
39. Wahlstrom, A., Vamling, L. Solubility of HFCs in Pentaerythritol tetraalkyl Esters. *J. Chem. Eng. Data.* 2000, 45, 97-103.
40. Yokozeki, A. Solubility of Refrigerants in Various Lubricants. *Int. J. Thermophys.* 2001, 22, 1057-1071.

VII – Viscosity Measurements and Modeling

7.1 – Introduction: viscosity of refrigerant + lubricant mixtures

The literature contains a large number of experimental studies dedicated to the variation of viscosity η versus temperature and composition. However, many of these viscosity measurements are carried out only at atmospheric pressure. The experimental studies of viscosity as a function of pressure are less frequent, particularly for mixtures. In the case of refrigerant + lubricant mixtures, the number of publications concerning the systematic studies of viscosity versus temperature, pressure and composition has increased in the past few years. For instance, Geller *et al.* (1995 and 1996) and Geller (1998) have reported experimental viscosities of binary HFCs (hydrofluorocarbons) + commercial POEs (polyol esters) mixtures in the temperature interval 253.15 K to 393.15 K for saturation pressures up to 5 MPa, for lubricant mass concentrations between 0.25% and 1%. The same systems have been studied by Jonsson and Lilje (1998) at temperatures between 313.15 K and 353.15 K and pressures up to 34 MPa, for the complete composition range. Cavestri and Schafer (2000) have determined the viscosity for HFC-410A + commercial POE mixtures, at temperatures between 258.15 K and 378.15 K at saturation pressures. However, these authors do not provide detailed information about structure and composition of the lubricants. It is therefore difficult to use these experimental data in the development of predictive models. The dynamic viscosity of HFCs + pentaerythritol ester (lubricants of known structure) systems has been measured by Wahlström and Vamling (1999) and by Thébault and Vamling (1999) at saturation pressures in the temperature range 300 K to 350 K over the refrigerant mass concentration range 0% to 30%.

Experimental studies analyzing the viscosity of HFCs + ABs (Alkylbenzenes) or HFCs + PAGs (polyalkylene glycols) systems are less frequent. To the best of our knowledge, there are only two papers reporting experimental data on HFCs + ABs (Sunami *et al.* 1997 and Takigawa *et al.* 2002). In the first of these papers, the viscosity is studied in the temperature range 273.15 K – 353.15 K and pressures up to 1 MPa for refrigerant mass concentrations between 0.05% and 0.22%. In the second paper, the viscosities are reported in the temperature interval 313.15 K to 353.15 K and pressures up to 3 MPa, covering a wide composition range, but the chemical structures of the lubricants, again, are not reported. In contrast, it is possible to find publications reporting experimental viscosity data for HFC-134a + PAGs, where information on the chemical structure of the lubricants is given. Kumagai *et al.* (1993 and 1994) reported experimental viscosities for HFC-134a with ethylene glycol, diethylene glycol, triethylene glycol, tetraethylene glycol, and two polyethylene glycols from 273.15 K to 333.15 K at saturation pressures. Comuñas *et al.* (2004)

studied the *p-T-η-x* behavior of HFC-134a + triethylene glycol dymethyl ether and tetraethylene glycol dymethyl ether in the temperature range 293.15 K to 373.15 K and pressures up to 140 MPa. These authors studied only one composition for each system at low lubricant concentrations.

Recently, the research group "Propriétés de Transport" (Laboratoire des Fluides Complexes) at the Université de Pau, France has decided to undertake an extensive experimental study of the densities and the viscosities of the pure refrigerants (Comuñas *et al.*, 2003), pure lubricants (Comuñas *et al.*, 2001) and their mixtures (Comuñas *et al.* 2002a, 2002b, and 2004). In order to complete this study on refrigerant + lubricant mixtures and to provide data on these asymmetric binary systems, in the present investigation, it has been decided to study the *p-T-η-x* behavior of 1,1,1,2-tetrafluoroethane, HFC-134a + triethylene glycol dimethylether, TriEGDME (system 1) and HFC-134a + tetrathylene glycol dymethyl ether, TEGDME (system 2). A total of 6 binary mixtures have been analyzed.

The viscosity and the density of the three pure compounds have been measured in the temperature range 283.15 K – 373.15 K and up to 60 MPa for densities and up to 200 MPa for viscosities (Comuñas *et al.* 2001 and 2003). For these three pure compounds, the viscosity and the density at 293.15 K and 353.15 K are shown in Figure 7.1 as functions of the pressure. The fastest increase of the viscosity with pressure occurs for the lubricant TEGDME. This can be related to the molecular structure of the compounds. When a fluid is compressed, the mobility of the molecules is reduced, resulting in increase of the viscosity. This effect is stronger for more complex molecules. It can also be observed that the viscosity of a refrigerant is in general various orders of magnitude lower than the viscosity of a lubricant. The shape of the density versus pressure curves is similar for both lubricants. The density of TriEGDME and TEGDME increases gradually with pressure, whereas for HFC-134a the increase is more abrupt. The densities of the compressed HFC-134a are higher than those of TriEGDME and TEGDME.

Figure 7.1 – Viscosity and density versus pressure for TriEGDME (x), TEGDME (∆), and PEG 250 (◊) at *T* = 293.15 K (—) and *T* = 353.15 K (---). Experimental points: Comuñas *et al.* 2002.

7.2 – Experimental techniques and procedures

The equipment used to measure the viscosity of the binary mixtures is described below along with the operating procedure. The measurements were carried out at the Université de Pau, France (Laboratoire des Fluides Complexes) using an especially designed isobaric-transfer falling-body viscometer (Daugé *et al.* 2001). This viscometer can be filled at high pressure following an isobaric procedure. Consequently, the study of the dynamic viscosity of heavy compounds as well as mixtures containing light compounds is possible.

7.2.1 – The falling body viscometer

The principle of the falling body viscometer is that a solid body (sinker) with hemispherical ends falls vertically under gravitational influence through a fluid. The fluid is forced to flow through the annulus between the sinker and the measuring tube. During the free fall, the sinker accelerates until the viscous force becomes equal to the gravitational force, where the maximal velocity of the sinker is reached. In this way, the viscosity of the fluid can be related to the velocity of the sinker. The velocity of the sinker can be obtained by measuring the time Δt that takes the sinker to fall the distance between two fixed reference points, see Bonisov (1998). For this procedure, the following working equation is applied:

$$\eta = K\left(\rho_S - \rho_L\right)\Delta t \qquad (7.1)$$

where ρ_S and ρ_L are the densities of the sinker and the fluid, respectively, and K is a coefficient characteristic of the viscometer and of the falling body. Falling body viscometers are commonly used to measure viscosities at high pressures, and they can be applied to very viscous fluids. For fluids with a low viscosity, the calibration constant (K) may become a function of the falling time. Various authors (Daugé *et al.* 2001, Papaioannou *et al.* 1993, Sen *et al.* 1990 and Tilly *et al.* 1994) have suggested another form of the governing equation, $\eta = f(\Delta t\Delta\rho)$, with $\Delta\rho = \rho_S - \rho_L$. The following form can be used:

$$\eta = a(\Delta t\,\Delta\rho)^2 + b\,\Delta t\,\Delta\rho + c \qquad (7.2)$$

in which the parameters a, b and c are determined by calibration with well-known fluids in the pressure and temperature ranges studied.

Figure 7.2 - Description of the measuring cell.

The measuring cell is represented schematically in Figure 7.2. It is made up of a cylindrical tube *b* (internal diameter 8 mm, external diameter 14.3 mm, length 600 mm, maximum pressure allowed 200 MPa), which contains an inner cylindrical tube *a* (internal diameter 6.47 mm, external diameter 7.94 mm, length 600 mm) ended up with two HP connectors *c* and *d*. The sample is filled in both tubes. Four holes are drilled on the inner tube in order to have the same pressure inside and outside this tube and thus avoid its deformation. Four electrical coils *e* are used on the outer tube to detect the passage of the falling body; a variation of the magnetic flux is detected through the coils. The space allowed between the HP tube *a* and the aluminum cylinder *f* contains a heat-carrying liquid which is used to thermoregulate the whole system. The temperature in the viscometer is controlled by an AOIP (always on IP) system in which the MESUREX probe is placed inside the cell through the aperture *g*. The heat-carrying circuit is connected to a thermostat (HUBER brand, UNISTAT model) whose thermostatic bath temperature can be regulated to within 0.05 °C in the temperature range -30 °C to +200 °C. The pressure in the measuring cell is increased by means of a supplementary cell, built in with a piston and filled with the compression liquid. The compression liquid is kept on the other side of the piston, which avoids its direct contact with the fluid studied. Both measuring and piston cells are placed in an automated air-pulsed thermal regulator in order to provide a homogeneous temperature in the equipment.

The sinker is a solid stainless steel cylinder with hemispherical ends. It has a diameter of 6.35 mm ±0.01 mm and a length of 20 mm, whereas its density, ρ_S, is 8.7 g/cm^3. The sinker is designed so that laminar conditions are obtained in the annulus during the fall of the sinker. Further, the ratio of the sinker to tube radii is 0.98, which is greater than the value of 0.93 suggested by Kiran and Sen (1992) to minimize eccentricity effects.

The detection of the sinker is based on the electromagnetic effect induced by the sinker when passing through the coils located on the measuring tube. Each pair of coils consists of a "primary" and a "secondary" coil; the four secondary coils are connected in a series, while the four primary ones are connected in parallel to a variable-frequency generator, providing an input signal on the order of 10 V and 1000 Hz. In the absence of the sinker, the induced signal is produced by the metallic tube and the studied fluid. When the sinker passes through the first pair of coils, the signal induced on the second coil reaches a maximum and the secondary circuit is unbalanced and used to operate a trigger which starts an electronic timer (chronometer). In the electronic system used to detect the maximum of the sinker, the sinusoidal signal is respectively amplified, filtered and converted into a continuous signal. This system contains a circuit, which detects any small change in the variation of the tension. The next three pairs of coils switch off the timer in a similar manner so that three fall times for the same temperature and pressure conditions are measured. The comparison of these three fall times shows that the maximum fall velocity is reached before the very first coil. The length of the tube (600 mm) ensures that the distance ran by the sinker before it reaches the first coils is long enough to have ended the acceleration motion of the fall. The variation in the signal is illustrated in Figure 7.3 as the sinker passes through the measuring tube. The value of Δt represents the time it takes to the sinker to fall from the upper coil to the lower coil, and $V_S(t)$ the variation of the tension as function of time.

The system with four coils is an important caution because this system aims at measuring low dynamic viscosity and thus shorter fall times. Since the viscometer is able to rotate 180° about the horizontal axis, a continuous series of measurements can be carried out over wide ranges of temperature and pressure without disturbing the sample. After each measure the viscometer is turned in order to bring the sinker back to its starting position. The viscometer is rotated by an engine, which also ensures that the viscometer is vertically placed.

Figure 7.3 – Variation of the tension for the detection of the falling body

7.2.2 – Isobaric transfer

Due to the fact that lubricants and refrigerants are in two different thermodynamic states at atmospheric pressure and ambient temperature, accurate measurements of their mixtures require specific procedures for the preparation of the samples and proper filling of different equipment used in this work. The filling technique of the viscometer is based on the isobaric transfer procedure at high pressure. To ensure correct transfer, the temperature and pressure conditions have to be chosen so that the fluid is in a monophasic liquid state. This is compulsory in order to have the same fluid in the apparatus as in the pressurized reservoir cell containing the sample. According to the volume of the measurement cell (about 20 cm³), a volume of 120 cm³ of sample is necessary for the complete procedure described hereafter. The system, which is shown in Figure 7.4, is composed of two high-pressure piston cells called "cell 1" and "cell 2" having a volume of 120 cm³, a gas compressor (NOVA Swiss brand), the reservoir cell which contains the pressurized sample, a vacuum pump (LEYBOLD brand, TRIVAC Type), and an electrically controlled double-chamber displacement pump (TOP brand). Both chambers of this pump contain compression oil. The valves are of AUTOCLAVE and SITEC types.

The mixtures are prepared in a high-pressure variable-volume cell (reservoir), containing a stainless steel ball (to agitate and homogenize the mixture) and equipped with a piston to isolate the mixture from the pressurizing fluid. This high pressure cell is pressurized to a pressure higher than the bubble pressure (for the T considered) to ensure that the mixture is in a single phase and is homogeneous. To increase the pressure of the mixture, the reservoir is filled with compression oil (pump chamber 2). Cells 1 and 2 have then to be fully filled with compression oil and have the same pressure as the reservoir. The transfer is processed following two steps: first, the transfer from the reservoir to cell 1, and then, the transfer from cell 1 to the measuring cell. To perform these two transfers, the double-chamber pump is used. The electric control of the pump makes it possible to use chambers 1 and 2 either independently or simultaneously.

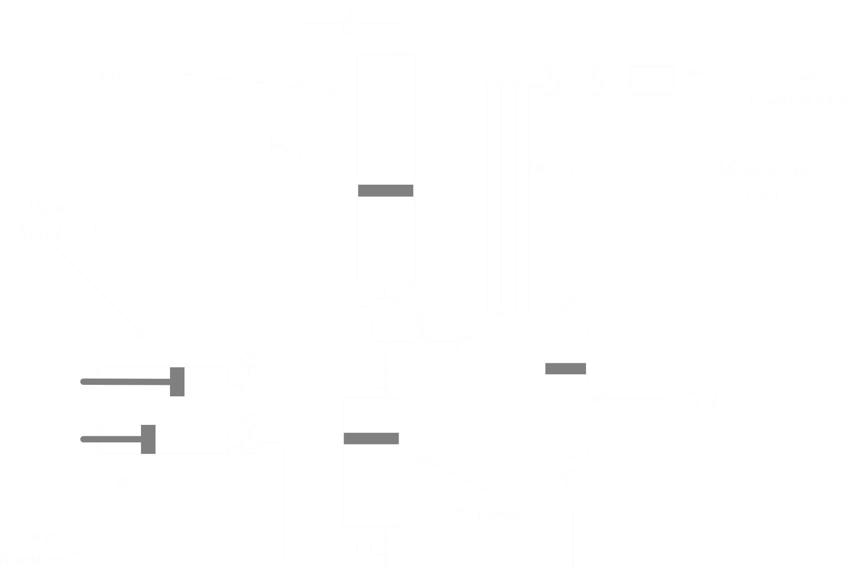

Figure 7.4 - Description of the device.

This first part of the transfer consists of moving 120 cm^3 of the sample from the reservoir to cell 1 at constant pressure *p*. The reservoir and cell 1 are isolated from the rest of the equipment, and compression oil is introduced in the reservoir with the pump chamber 2. Transfer is stopped when a volume of approximately 120 cm^3 has been pumped into cell 1. At this stage, the reservoir is removed and the measuring cell is brought to high pressure using the gas compressor (with nitrogen for example).

The second part of transfer consists in filling the measuring cell. Cell 1 is connected to the measuring cell (full of compressed gas). The sample fluid contained in cell 1 and the gas are evacuated as rapidly as possible toward cell 2 (full of compression oil) by means of the double-chamber pump. Cell 2 recovers the gas and a part of the sample fluid which may have been polluted during the transfer. The equivalent of 3 times the volume of the measuring cell is transferred (i.e. 60 cm^3) in order to ensure that the sample within it (20 cm^3) is unpolluted. Cell 2, the double-chamber pump, and the gas compressor are removed.

In order to regulate the pressure in the viscometer, the double-chamber pump is removed and replaced by a NOVA-brand pneumatic pump, with a maximum pressure of 160 MPa, which is connected to cell 1. It is thus possible to perform investigations up to 150 MPa with no difficulty. The experiments are performed within the temperature interval 0 °C to 120 °C. The latter limit value is a constraint imposed by the specifications of the various elements used in the assembly, in particular the pressure gauge connections, whose capabilities are not guaranteed at temperatures higher than 120 °C. The pressure is governed by simply adding or removing compression oil from cell 1. The pressure is monitored by means of a pressure gauge (HBM-P3M type), which can measure pressures up to 200 MPa, connected directly to the capillary tube between the measuring cell and cell 1. The accuracy has been estimated to be ±0.1 MPa for pressure and ±0.5 K for temperature.

7.2.3 - Mixtures preparation

The mixtures are prepared in the high-pressure variable-volume cell (reservoir) as described by Canet, 2001. First, vacuum is made in the reservoir and the first compound (the lubricant which is a liquid at atmospheric pressure) is introduced. The loaded volume is exactly controlled by a burette with an uncertainty of 0.05 cm^3. Secondly, with the aim of controlling the amount of HFC-134a, a bottle (of 400 cm^3 capacity) is filled and connected to the reservoir after being weighted so as to introduce the second compound. After the equilibrium pressure is reached between both cells, they are disconnected and the bottle containing the remaining HFC-134a is weighed. The exact amount of HFC-134a introduced for the mixture is then determined. Finally, the reservoir containing the two compounds of the mixture is pressurized as described in the previous section.

7.2.4 - Calibration procedure

[illegible]

a reproducibility of better than 1%. The final values are the averages of these measurements. For this purpose, toluene, decane and tetraethylene glycol dymethyl ether (TEGDME) were chosen. The falling time was measured for these three compounds between T = 293.15 K and 373.15 K in steps of 20 K and from 10 MPa to 100 MPa in 10 MPa intervals.

In order to determine the constants in Equation 7.2 the density and viscosity values were interpolated from published experimental data for toluene (Kashiwagi and Makita 1982, Assael *et al.* 1991, Dymond *et al.* 1991, Krall *et al.* 1992, Oliveira and Wakeham 1992, Vieira dos Santos and Nieto de Castro 1997, and Harris 2000), decane (Kashiwagi and Makita 1982, Knapstad *et al.* 1990, and Oliveira and Wakeham 1992) and TEGDME (Comuñas *et al.* 2001). The apparatus parameters (a, b and c) were determined by plotting the viscosity values η versus $\Delta\rho/\Delta t$ for each temperature. For example, Figure 7.5 shows the curve at T = 333.15 K where slight curvature can be observed. However, actual viscosity measurements are not available for all of the reference fluids in the entire ranges of temperature and pressure studied in this work. Therefore, to minimize the uncertainty in the viscosity estimations, in addition to the previous interpolated viscosity values, the viscosities of the reference fluids were calculated using the hard-sphere model of Assael *et al.* (1980, 1992a and 1992b) and the friction theory model of Quiñones-Cisneros *et al.* (2000, 2001). As a result, up to three different viscosity estimations, for each one of the reference sets of viscosities, are derived for each measured temperature and pressure. The final experimental values for viscosity are the averages of the values obtained with the three methods. The deviations between the viscosity values predicted using the different calibration curves (experimental data, hard sphere and friction theory) are in most cases of the order of 1–2 %. However, for the 373.15 K isotherm and pressures above 60 MPa, due to the lack of reference data, the deviations between the calibration methods may reach higher values (of the order of 10 %).

The calibration curve has then been used to determine the viscosity of triethylene glycol dymethyl ether (TriEGDME), which has been tested against literature data (Comuñas *et al.* 2001). The viscosity of pure TriEGDME has been measured for temperatures between 293.15 K and 353.15 K and pressures from 0.1 MPa to 100 MPa and an average absolute deviation (AAD) of 0.97 % obtained. The viscosity values obtained using the different calibration curves (experimental data, friction theory and hard sphere model) are presented in Table 7.1. As stated above, the differences between the different viscosity estimations are of the order of 1–2%. Table 7.1 also contains the final viscosity values (the averages of the values obtained with the three methods) and the literature data. This calibration method described above has been applied in recent publications concerning the dynamic viscosity of pure HFC-134a (Comuñas *et al.* 2003) and mixtures of HFC-134a + lubricants at high concentrations of HFC-134a (Comuñas *et al.* 2004).

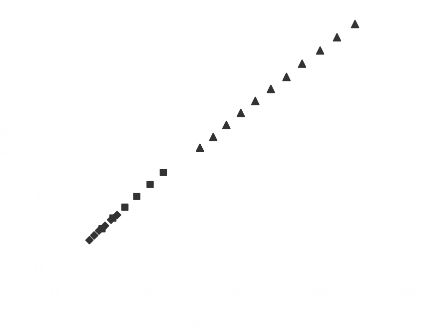

Figure 7.5 - Calibration curve at T = 333.15 K. Toluene (♦), decane (■), and TEGDME (▲).

7.2.5 - Characteristics of the samples

The three substances used to prepare the binary mixtures are commercially available chemicals with the following purity levels: 1,1,1,2-tetrafluoroethane (CF_3CH_2F, HFC-134a: Gazechim Froid with a purity better than 99.94%, a water content of no more than 24 ppm and a molar mass of 102.03 g/mol), triethylene glycol dimethylether (CH_3O-$((CH_2)_2O)_3$-CH_3, TriEGDME: Aldrich with a purity better than 99% and a molar mass of 178.23 g/mol), and tetraethylene glycol dimethylether (CH_3O-$((CH_2)_2O)_4$-CH_3, TEGDME: Aldrich with a purity better than 99% and a molar mass of 222.28 g/mol). The binary mixtures have been prepared by very careful weighing in a high pressure reservoir cell, following the procedure described in Canet (2001), to obtain HFC-134a mole fractions x = 0.3427 and 0.5940 for the system 1 (HFC-134 + TriEGDME) and x = 0.2769, 0.4433, 0.6858 and 0.8797 for the system 2 (HFC-134a + TEGDME).

T (K)	P (MPa)	η_{ex} (mPa.s)	η_{FT} (mPa.s)	η_{HS} (mPa.s)	η_{av} (mPa.s)	η_{lit} (mPa.s)	$\Delta\eta/\eta$ (%)
293.15	0.1	2.128	2.153	2.125	2.135	2.185	2.27
293.15	20	2.527	2.562	2.520	2.536	2.570	1.31
293.15	40	2.957	3.004	2.950	2.970	3.005	1.15
293.15	60	3.416	3.475	3.410	3.434	3.450	0.48
293.15	80	3.901	3.974	3.905	3.926	3.930	0.09
293.15	100	4.411	4.498	4.405	4.438	4.435	-0.06
313.15	0.1	1.478	1.508	1.480	1.489	1.485	-0.25
313.15	20	1.744	1.776	1.745	1.755	1.755	-0.01
313.15	40	2.034	2.066	2.034	2.044	2.040	-0.22
313.15	60	2.346	2.375	2.344	2.355	2.350	-0.21
313.15	80	2.680	2.703	2.677	2.687	2.680	-0.25
313.15	100	3.037	3.049	3.033	3.040	3.045	0.18
333.15	0.1	1.129	1.120	1.112	1.120	1.080	-3.74
333.15	20	1.319	1.308	1.299	1.308	1.300	-0.64
333.15	40	1.513	1.500	1.491	1.501	1.505	0.24
333.15	60	1.707	1.694	1.685	1.695	1.715	1.16
333.15	80	1.900	1.887	1.879	1.889	1.925	1.89
333.15	100	2.092	2.080	2.073	2.082	2.130	2.27
353.15	0.1	0.852	0.844	0.846	0.847	0.835	-1.48
353.15	20	0.993	0.986	0.986	0.988	1.000	1.16
353.15	40	1.142	1.138	1.134	1.138	1.150	1.04
353.15	60	1.300	1.299	1.289	1.296	1.310	1.07
353.15	80	1.465	1.472	1.451	1.463	1.480	1.16
353.15	100	1.639	1.656	1.621	1.639	1.655	0.98

Table 7.1 – Measured dynamic viscosity values, η_{exp} (mPa.s), for TriEGDME compared with literature values (Comuñas *et al.* 2001). η_{ex} = viscosity values obtained using experimental data, η_{FT} = viscosity values obtained using the friction theory model, η_{HS} = viscosity values obtained using the hard sphere model, and η_{av} = final viscosity values, obtained as the average of the three viscosity estimations.

7.3 – Experimental results

Measurements of the dynamic viscosity η have been carried out in the homogeneous liquid state at 5 temperatures 293.15 K, 313.15 K, 333.15 K, 353.15 K and 373.15 K and pressures from 10 MPa to 100 MPa in 10 MPa steps for the six compositions mentioned before. For the system 1 a total of 100 experimental points were obtained (x = 0.3427 and 0.5940) and for the system 2 a total of 200 experimental points were obtained (x = 0.2369, 0.4415, 0.6135 and 0.8045). For convenience, viscosity data previously obtained at the laboratory (Comuñas *et al.* 2004) are also included (x = 0.9295 for the system 1 and x = 0.9290 for the system 2) in this study.

The experimental densities for the two systems were previously measured by Comuñas *et al.* (2002a, 2002b) from 10 MPa to 60 MPa and at the same temperatures. However, the mole fractions studied in this work (for both systems) are not the same as reported by Comuñas *et al.* (2002a and 2002b). Therefore, it was necessary to perform some interpolations and extrapolations. First, since the densities of the studied samples have only been determined up to 60 MPa, several extrapolations were performed for each one of the mole fractions studied by Comuñas *et al.* The extrapolations have been performed using a Tait-type equation as described by El-Tahir *et al.* (1995):

$$\rho(p,T)=\frac{A_0+A_1T+A_2T^2+A_3T^3}{1-C\ln\left(\dfrac{B_0+B_1T+B_2T^2+p}{B_0+B_1T+B_2T^2+p_{ref}}\right)}\quad \text{(at a given mole fraction)}\qquad (7.3)$$

The AAD obtained for both systems by use of the Equation 7.3 is less than 0.01%. Second, density values were generated up to 100 MPa by means of Equation 7.3 for each mole fraction. Finally, at a given temperature, densities were obtained by means of the following equation:

$$\rho(p,x)=\frac{C_0+C_1p+C_2p^2+C_3x+C_4x^2+C_5x^3}{1+C_6p+C_7x+C_8x^2+C_9x^3}\quad \text{(at a given }T\text{)}\qquad (7.4)$$

The AAD obtained by use of the Equation 7.4 is less than 0.02% (for both systems). The validity of this method is discussed by Canet (2001) and Daugé *et al.* (2001). These authors show that an error of 1% in the density of the fluids leads to a relative error of 0.2% in viscosity.

The dynamic viscosity and density values are listed in Appendix C as a function of temperature T, pressure p, and mole fraction of HCF-134a x. The uncertainty on the viscosity estimations is ±2 % for 293.15 K, 313.15 K and 333.15 K and up to 100 MPa, ±3 % for 353.15 K, up to 100 MPa and ±4 % for 373.15 K and up to 60 MPa. As stated above, for the last isotherm, due to the lack of experimental values, the differences between the viscosity values predicted using the different calibration methods (hard-sphere and friction theory) may be higher (of the order of 10%).

Figures 7.6 and 7.7 show the variation of viscosity with pressure for different temperatures and with temperature for different pressures. A general pattern is consistent with previous results on either pure compounds, or binary mixtures (Canet *et al.* 2001, and Zéberg-Mikkelsen *et al.* 2001). The variations of viscosity versus pressure and temperature are smooth for each composition. Viscosity increases with pressure and decreases with temperature.

Figure 7.6 – Viscosity values for *x* HFC-134a + (1-*x*) TriEGDME at *x* = 0.5940 and for *x* HFC-134a + (1-*x*) TEGDME at *x* = 0.4433. Temperatures: 293.15 K (◆), 313.15 K, (▲), 333.15 K (●), 353.15 K (◇), and 373.15 K (△).

Figure 7.7 – Viscosity values for *x* HFC-134a + (1-*x*) TriEGDME at *x* = 0.3427 and for *x* HFC-134a + (1-*x*) TEGDME at *x* = 0.6633. Pressures: 20 MPa (◆), 40 MPa (▲), 60 MPa (●), 80 MPa (◇), and 100 MPa (△).

Figure 7.8 displays the variations of viscosity versus mole fraction at *T* = 333.15 K and at *p* = 60 MPa for HFC-134a + TEGDME. In order to complete Figure 7.8, the reported data for the pure compounds and for the binaries given by Comuñas *et al.* (2001, 2003, and 2004) have been used. The figure shows monotonic decrease of viscosity with increasing composition of refrigerant at constant temperature and pressure. Similar plots may be obtained for other temperatures and pressures. The system HFC-134a + TriEGDME shows similar behavior.

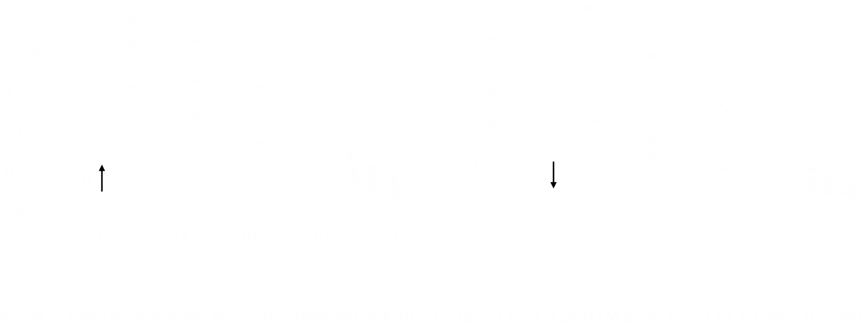

Figure 7.8 – Viscosity versus mole fraction for *x* HFC-134a + (1-*x*) TEGDME at *T* = 333.15 and *p* = 60 MPa. Pressures: 20 MPa (♦), 40 MPa (◊), 60 MPa (▲), 80 MPa (Δ), and 100 MPa (●). Temperatures: 293.15 K (♦), 313.15 K, (◊), 333.15 K (▲), 353.15 K (Δ).

7.4 – Viscosity modeling

The viscosity data obtained for the two binary systems composed of HFC-134a + TriEGDME and HFC-134a + TEGDME in the course of this investigation, combined with those previously obtained by Comuñas *et al.* (2001, 2003, and 2004) on the three pure compounds and the two binaries, represent the most comprehensive experimental study of these systems up to 100 MPa in the temperature range 293.15 K to 373.15 K at 8 different compositions (a total of 400 experimental points). These data can be used to carry out an extensive comparative study and evaluation of the performance of different viscosity models incorporating the effects of temperature, pressure, and composition. Most compositional dependent viscosity models have been derived based on viscosity measurements of pure compounds. The models studied are: classical mixing rules, the hard-sphere scheme, the self-referencing model, the free-volume model, the LBC and the LBC-mod models, and the friction theory. The two first models are applicable only to dense states, while the rest of the models are applicable to both gases and liquid. In the free-volume, LBC, and friction models, the dilute gas term η_0 is always neglected, since the mixtures to be modeled are high-pressure dense fluids.

7.4.1 – Classical mixing rules

Several mixing laws have been developed for calculating the viscosity of liquid mixtures. The objective of these mixing laws is to predict the viscosity of liquid mixtures using only the viscosity and density of the pure components along with the composition. Two of the most well-known mixing laws derived for binary mixtures are the Grunberg-Nissan mixing law (Grunberg and Nissan 1949) and the Kato-Chaudhri mixing law (Kato and Chaudhri 1984). For a multicomponent mixture, the ideal Grunberg-Nissan mixing law can be written as follows:

$$\ln\left(\eta_{mix}\right)=\sum_{i=1}^{n} x_i \ln\left(\eta_i\right) \qquad (7.5)$$

where η_i and x_i represent the viscosity and mole fraction of component "i" respectively. The model is very simple since no adjustable parameters are required, only the viscosity of the pure compounds and the composition. The Kato-Chaudhri mixing law can be expressed as:

$$\ln\left(v_{mix}\,\eta_{mix}\right)=\sum_{i=1}^{n} x_i \ln\left(v_i\,\eta_i\right) \qquad (7.6)$$

where v_{mix} and v_i are respectively the molar volumes of the mixture and of the pure compounds. Both mixing laws are totally predictive in the sense that only properties of the pure compounds are required. The deviations obtained for the two mixing laws by comparing the predicted viscosities with the experimental values are given in Table 7.2 for each of the binary systems. Both mixing laws underestimate the viscosity, since the Bias is negative and has the numerical absolute value as the AAD.

Mixture	NP	AAD (%)	Bias (%)	MDev (%)
Grunberg-Nissan				
HFC-134a + TriEGDME	150	28.94	-28.94	48.78
HFC-134a + TEGDME	250	32.91	-32.91	55.62
Kato-Chaudhri				
HFC-134a + TriEGDME	150	32.55	-32.55	53.22
HFC-134a + TEGDME	250	38.04	-38.04	61.60

Table 7.2 – Results for viscosity predictions with the classical ideal mixing laws Equations 7.5 and 7.6.

The Grunberg-Nissan mixing law can be modified by introducing adjustable parameters believed to be representative in some way of the interactions within the considered system. Irving (1977) has evaluated 25 of the more promising equations with experimental data from the literature recommending the modified Grunberg-Nissan equation. Adjustable parameters can be introduced in different ways. The following expression, which is written for binary mixtures, shows how the Grunberg-Nissan mixing law can be modified in a simple way

$$\ln(\eta_{mix}) = \sum_{i=1}^{2} x_i \ln(\eta_i) + x_1 x_2 d_{12} \qquad (7.7)$$

The d_{12} parameter is a quantity characteristic of the intermolecular interactions between components 1 and 2. By minimizing the average absolute deviation between the calculated and experimental data d_{12} = 1.33 for HCF134a + TrIEGDME and d_{12} = 1.68 for HFC134a + TEGDME have been obtained. As it can be seen from Table 7.3, when adjustable parameters are introduced, a significant improvement is achieved. The obtained results for both binary systems are better than the results obtained with the ideal Grunberg-Nissan mixing law. However, when adjustable parameters are introduced, the model is not longer totally predictive.

Mixture	NP	AAD (%)	Bias (%)	MDev (%)
HFC-134a + TrIEGDME	150	11.04	-5.15	36.01
HFC-134a + TEGDME	250	15.53	-6.79	43.69

Table 7.3 - Results for viscosity predictions with the modified Grunberg-Nissan mixing law Equation 7.7

7.4.2 – The hard-sphere viscosity scheme

This model has been described in detail in Chapter III, section 3.3.1. The performance of the model has been evaluated for R32, R125, R134a, R152a, TrIEGDME and TEGDME. The viscosity calculations for HFC-134a + TrIEGDME and TEGDME have been performed using the pure compounds parameter reported in Table 3.3 and the mixing rules described in section 3.4.1. The results are presented in Table 7.4 where it can be seen that the average absolute deviation is several times the experimental uncertainty. As indicated by the Bias, the model always under predicts the viscosity.

Mixture	*NP*	AAD (%)	Bias (%)	MDev (%)
HFC-134a + TrEGDME	150	16.66	−16.66	31.97
HFC-134a + TEGDME	250	14.34	−14.34	29.66

Table 7.4 - Results for viscosity predictions with the hard-sphere scheme.

7.4.3 – The self-referencing model

The self-referencing model has been also described and applied to the same number of compounds as the hard-sphere scheme in Chapter III. For mixtures (see section 3.4.2) the model cannot be considered as totally predictive, as it requires knowledge of the viscosity of reference for each composition. Using the measured viscosity at 200 bar and 293.15 K as the reference point for each composition and the pure compound parameters reported in Table 3.4 the viscosities of mixtures have been estimated. The results are shown in Table 7.5. By comparing the self-referencing model with the hard-sphere scheme, a better agreement with experimental data can be observed. Also, better distribution of calculated points around experimental data is observed, as indicated by the Bias.

Mixture	*NP*	AAD (%)	Bias (%)	MDev (%)
HFC-134a + TrEGDME	150	5.80	−4.26	27.97
HFC-134a + TEGDME	250	7.08	−3.67	36.11

Table 7.5 - Results for viscosity predictions with the self-referencing method using $T_0 = 293.15$ K and $p_0 = 200$ Bar as the reference conditions.

7.4.4 – The free-volume model

The free-volume model, also studied in Chapter III, has shown to describe satisfactorily the viscosity of refrigerants and lubricants. Good results were also found when the model was applied to refrigerant mixtures up to pressures of the order of 10 MPa. The free-volume approach was applied to refrigerant + lubricant mixtures using the mixing rules described in section 3.5.3. The results are presented in Table 7.6. The model does not deliver good results. The AAD is found to be several times the experimental uncertainty. It can be concluded that the mixing rules, generally empirical, proposed for the calculation of the viscosity mixtures are probably not adapted to such asymmetric systems as mixtures of refrigerants and lubricants. Further studies on this matter are required.

Mixture	*NP*	AAD (%)	Bias (%)	MDev (%)
HFC-134a + TriEGDME	150	19.82	-19.82	51.71
HFC-134a + TEGDME	250	31.28	-31.28	56.99

Table 7.6 – Results for viscosity predictions with the free-volume model.

7.4.5 – The LBC and LBC-mod models

The LBC and LBC-mod models were introduced and applied to predict the viscosity of refrigerants and lubricants in Chapter III. Although it was found that these models do not describe the viscosity of refrigerants and lubricants in a satisfactory manner, computation of the viscosity of the studied binary systems has also been carried out. The results are presented in Table 7.7. The LBC model fails in predicting the viscosity of these mixtures. Improved results are obtained if thermal and structural effects are added, LBC-mod, but still there are large discrepancies between experimental and calculated values.

Mixture	*NP*	AAD (%)	Bias (%)	MDev (%)
LBC				
HFC-134a + TriEGDME	150	44.04	-44.04	62.95
HFC-134a + TEGDME	250	48.14	-48.14	77.01
LBC-mod				
HFC-134a + TriEGDME	150	30.78	-30.78	54.90
HFC-134a + TEGDME	250	34.92	-34.92	56.11

Table 7.7 – Results for viscosity predictions with the LBC and LBC-mod model.

7.4.6 – The friction theory

In Chapter IV different versions of the *f-theory* have been studied and applied to model the p-η-T behavior of pure compounds and few refrigerant mixtures. Good agreement between experimental and calculated values has been found for pure compounds. In this section the *f-theory* in conjunction with the PR, the RK-PR, the SBWR-reg and the PC-SAFT EoS is applied to the refrigerant + lubricant mixtures. The pure compound parameters for each version of the *f-theory* models to be used are reported in Chapter IV. Viscosity mixture calculations have been carried out in the following way: for the PR and the RK-PR EoS Equations 4.29 and 4.30 have been used with ε = 0.3, as recommended by Quiñones-Cisneros *et al.* (2001) when modeling asymmetric mixtures. The noncubic equations of state, SBWR-reg and PC-SAFT, however, cannot be used with ε = 0.3, since this value has only been adjusted for cubic EoS. In their work on *f-theory* + the SWBR EoS, Quiñones-Cisneros *et al.* (2002) used linear mixing rules to calculate the viscosity of hydrocarbon mixtures, with satisfactory results. Thus, in this thesis similar mixing rules have been employed for the *f*-SBWR-reg and *f*-PC-SAFT, i.e. Equations 4.29 and 4.30 are used with ε = 0.

The results of applying the *f-theory* to mixtures are presented in Table 7.8. In general, large AAD are produced by the *f-theory* models. The best results are obtained with the *f-theory* in combination with the cubic EoS. In all the cases the AAD can be lowered by 2 or 3 % for the *f-theory* + the PR and the RK-PR EoS, just by setting ε = 0, i.e. by use of the linear mixing rules. This ε parameter has been adjusted to correctly describe the viscosity of asymmetric hydrocarbon mixtures. However, in spite of the fact that refrigerants + lubricants are such mixtures, their viscosity is not described satisfactorily. This might suggest that ε is not a transferable parameter. The results with the *f-theory* + the SBWR-reg and the PC-SAFT EoS are entirely not satisfactory. In fact, the LBC-model approach originally developed for compounds different than refrigerants and lubricants, delivers better results than *f*-SBWR-reg and *f*-PC-SAFT (compare Tables 7.7 and 7.8). With the hope of improving the results, the value of ε has been adjusted by minimizing the difference between experimental and calculated values, however no significant improvement has been observed. For the *f*-SBWR-reg model the AAD can only be lowered by 1-2 % with ε = 0.15, and in the case of *f*-PC-SAFT the AAD can be lowered by 2-4 % with ε = 0.23. This is an indication of the limitations of the mixing rules used. It appears that adequate mixing rules have to be developed for the prediction of mixture viscosities when the friction theory is used with noncubic EoS. It is noteworthy that in spite of being a cubic EoS, the deviations obtained with the *f-theory* + the RK-PR EoS are much higher than those obtained with the *f*-PR model. It seems that the mixing rules proposed in the friction theory are in fact only appropriate for the cubic EoS originally used: PR, SRK, and PRSV EoS.

Mixture	NP	AAD (%)	Bias (%)	MDev (%)
<u>*f-theory + PR*</u>				
HFC-134a + TrIEGDME	150	12.29	-12.29	21.23
HFC-134a + TEGDME	250	11.19	-8.18	26.44
<u>*f-theory + RK-PR*</u>				
HFC-134a + TrIEGDME	150	22.42	-22.42	35.67
HFC-134a + TEGDME	250	24.76	-24.76	42.10
<u>*f-theory + SBWR-reg*</u>				
HFC-134a + TrIEGDME	150	34.16	-34.16	58.59
HFC-134a + TEGDME	250	43.81	-43.81	76.62
<u>*f-theory + PC-SAFT*</u>				
HFC-134a + TrIEGDME	150	48.38	-48.38	74.38
HFC-134a + TEGDME	250	85.18	-85.18	161.02

Table 7.8 - Results for viscosity predictions with the *f-theory* models

7.4.7 – Comparison among the models

The performance of the mixing-rule scheme (Equation 7.5), the hard-sphere scheme, the self-referencing method, the free-volume model, the LBC model, and the *f-theory* in conjunction with the PR EoS is shown in Figure 7.9 where experimental viscosities are plotted versus calculated values. The best results are obtained with the self-referencing method. Among the three models with physical background the best results are seen with the *f*-PR model. The *f*-PR model also shows the best performance in the high-viscosity range (or low-temperature and high-pressure range) where the self-referencing method shows larger deviations.

Figure 7.9 – Comparison of experimental viscosities for HFC-134a + TriEGDME and HFC-134a + TEGDME with viscosities calculated by different models.

7.5 – Conclusions

Using a falling body viscometer the dynamic viscosity of 6 binary mixtures composed of refrigerants + lubricants has been measured up to 100 MPa in the monophasic liquid state from 293.15 K to 353.15 K. The systems studied correspond to HFC-134a + TriEGDME and HFC-134a + TEGDME. In order to obtain the dynamic viscosity, the density has been obtained from previous investigation carried out at the laboratory at the same temperature conditions and up to 60 MPa. A Tait-type equation has been used to extrapolate the densities up to 100 MPa. The uncertainty in the measured values is of the order of ±2.5%, some additional uncertainty is found for the high-pressure measurements at 373.15 K due to the lack of reference experimental data for the calibration of the apparatus. The viscosity measurements reported in this work together with the viscosity measurements for the pure and binary systems reported by Comuñas *et al.* (2001, 2003, and 2004), represent the most comprehensive study for binary refrigerant-lubricant mixtures.

The experimental viscosity data have been used in order to evaluate the performance of five different viscosity models and simple mixing rules. The evaluated models range from recently derived models, such as the free-volume model, the hard-sphere scheme, or the friction theory, trough widely used models within the oil industry, such as the well-known LBC model, to empirical correlations such as the self-referencing method. The conclusion of this evaluation and comparison of the different models is that the best results are obtained with the self-referencing method, which needs one experimental viscosity value for the pressure and temperature of reference, follow by the friction theory in combination with the PR EoS. In most cases the viscosity predictions are under predicted, since the Bias is negative and has the same numerical absolute value as the AAD (except for the self-referencing method and *f*-PR model). Although the self-referencing method gives the overall best performance for the considered binary systems, it can only be applied to liquid and dense fluids, but not gases, which may be a requirement within the refrigeration industry. This is also the case for the mixing laws and the hard-sphere scheme. It is interesting to notice that the three methods with physical background (hard-sphere, free volume, and friction theory) can describe the viscosity of the pure compounds satisfactorily, whereas for their mixtures, the average absolute deviation is several times the experimental uncertainty. This may be an indication for the limitation of the used mixing rules in correctly reproducing the viscosity of these kinds of systems.

A study of the friction theory model in combination with equations of state besides PR, SRK, or PRSV has also been carried out. The evaluated EoS were: the recently developed RK-PR cubic EoS, the SWBR EoS and the based-statistical mechanics equation, the PC-SAFT EoS. These equations have shown to describe the p-v-T-x behavior of these systems with similar or lower accuracy (Chapter VI). These models have shown to deliver similar results in describing the viscosities of pure compounds (Chapter IV). However, for the mixtures studied in this chapter the results with the different *f*-theory models vary widely depending on the EoS used. Apparently adequate mixing rules need to be developed when the *f*-theory is used in combination with EoS different than PR, SRK, and PRSV.

Nomenclature

AAD = Average absolute deviation

$Bias$ = Bias

d_{12} = Empirical parameter in Equation 7.7

M = Molecular weight

$MDev$ = Maximum deviation

n = Number of components

NP = Number of points

p = Pressure

$PC\text{-}SAFT$ = Perturbed-chain statistical associating fluid theory

PR = Peng-Robinson

$PRSV$ = Peng-Robinson-Stryjek-Vera

$RK\text{-}PR$ = Redlich-Kwong-Peng-Robinson

$SBWR$ = Soave-Benedict-Webb-Rubin

T = Temperature

v = Molar volume

$V_s(t)$ = Variation of the tension as function of time

x = Mole fraction of refrigerant

Greek letters

Δt = Time

ε = Empirical parameter used in the *f-theory* mixing rules (Equations 4.29 and 4.30)

η = Viscosity

ρ = Density

Subscripts/superscripts

cal = Calculated property

exp = Experimental property

i = Component "i"

j = Component "j"

L = Liquid

ref = Reference

S = Solid

References

1. Assael, M.J., Dymond, J.H., Tselekidou, V. Correlation of High-Pressure Thermal Conductivity, Viscosity, and Diffusion Coefficients for n-Alkanes. *Int. J. Thermophys.* 1990, 11, 863–873.
2. Assael, M.J., Papadaki, M., Wakeham, W.A. Measurements of the Viscosity of Benzene, Toluene, and m-Xylene at Pressure up to 80 MPa. *Int. J. Thermophys.* 1991, 12, 449-457.
3. Assael, M.J., Dymond, J.H., Papadaki, M., Patterson, P.M. Correlation and Prediction of Dense Fluid Transport Coefficients. I. n-Alkanes. *Int. J. Thermophys.* 1992a, 13, 269-281.
4. Assael, M.J., Dymond, J.H., Papadaki, M., Patterson, P.M. Correlation and Prediction of Dense Fluid Transport Coefficients. II. Simple Molecular Fluids. *Fluid Phase Equilib.* 1992b, 75, 245-255.
5. Borisov, V.B. The Equation for a Falling-Cylinder Viscometer. *High Temp.* 1998, 36, 293-378.
6. Barrouhou, M., Zéberg-Mikkelsen, C.K., Baylaucq, A., Boned, C. High-Pressure Viscosity and Density Measurements for the Asymmetric Binary System cis-Decalin + 2,2,4,4,6,8,8-Heptamethylnonane. *Int. J. Thermophysics* 2003, 24, 937-952.
7. Canet, X. Viscosité Dynamique et Masse Volumique sous Hautes Pressions de Mélanges Binaires et Ternaires d'Hydrocarbures Lourds et Légers. Thèse de Doctorant, Université de Pau, Pau, France. 2001.
8. Canet, X., Daugé, P., Baylaucq, A., Boned, C., Zéberg-Mikkelsen, C.K., Quiñones-Cisneros, S.E., Stenby, E.H. Density and Viscosity of the 1-Methylphthalene + 2,2,4,4,6,8,8-Heptamethylnoname System from 293.15 to 353.15 K at Pressures up to 100 MPa. *Int. J. Thermophys.* 2001, 22, 1669-1689.
9. Cavestri, R.C., Schafer, W.R. Measurement of Solubility, Viscosity, and Density of R410A Refrigerant/Lubricant Mixtures. *ASHRAE Trans.* 2000, 106, 277-285.
10. Comuñas, M.J.P., Baylaucq, A., Boned, C., Fernández, J. High-Pressure Measurements of the Viscosity and Density of two Polyethers and Two Dialkyl Carbonates. *Int. J. Thermophys.* 2001, 22, 749–767.
11. Comuñas, M.J.P., Fernández, J., Baylaucq, A., Canet, X., Boned, C. PρTx measurements for HFC-134a + triethylene glycol dimethylether. *Fluid Phase Equilib.* 2002a, 199, 185-195.

12. Comuñas, M.J.P., Baylaucq, A., Boned, C., Canet, X., Fernández, J. High-Pressure Volumetric Behavior of x 1,1,1,2-tetrafluoroethane+(1-x) 2,5,8,11,14-Pentaoxapentadecane (TEGDME) Mixtures. *J. Chem. Eng. Data* 2002b, 47, 233-238.
13. Comuñas, M.J.P., Baylaucq, A., Quiñones-Cisneros, S.E., Zéberg-Mikkelsen, C.K., Boned, C., Fernández, J. Viscosity measurements and correlations for 1,1,1,2-tetrafluoroethane (HFC-134a) up to 140 MPa. *Fluid Phase Equilib.* 2003, 210, 21–32.
14. Comuñas, M.J.P., Baylaucq, A., Boned, C., Fernández, J. Dynamic Viscosity for HFC-134a + Polyether Mixtures up to 373.15 K and 140 MPa at Low Polyether Concentration. Measurements and Modeling. *Ind. Eng. Chem. Res.* 2004, 43, 804−814.
15. Daugé, P., Baylaucq, A., Marlin, L., Boned, C. Development of an Isobaric Transfer Viscometer Operating up to 140 MPa. Application to a Methane + Decane System. *J. Chem. Eng. Data* 2001, 46, 823-830.
16. Dymond, J.H., Awan, M.A., Glen, N.F., Isdale J.D. Transport Properties of Nonelectrolyte Liquid Mixtures. VIII. Viscosity Coefficients for Toluene and for Three Mixtures of Toluene + Hexane from 25 to 100°C at Pressures up to 500 MPa. *Int. J. Thermophys.* 1991, 12, 275-287.
17. El-Tahir, A., Boned, C., Lagourette, B., Xans, P. Determination of the Viscosity of Various Hydrocarbons and Mixtures of Hydrocarbons Versus Temperature and Pressure. *Int. J. Thermophys.* 1995, 16, 1309-1334.
18. Glasstone S., Laidler K.J., Eyring H. The Theory of Rate Processes, the Kinetics of Chemical Reactions, Viscosity, Diffusion, and Electrochemical Phenomena. McGraw- Hill, New York, 1941.
19. Geller, V.Z., Davis, K.E. Solubility and Viscosity of Refrigerant/POE Lubricant Mixtures. *19th International Congress of Refrigeration.* 1995; IVa, p223.
20. Geller, V.Z., Paulaitis, M.E., Bivens, D.B., Yokozeki, A. Viscosities of HFC-32 and HFC-32/Lubricant Mixtures. *Int. J. Thermophys.* 1996, 17, 75-83.
21. Geller, V. Thermophysical Properties of Alternative Refrigerant/ Lubricant Mixtures. *Refrigeration Science and Technology*, IIR Proceedings Series; International Institute of Refrigeration (IIR), Paris, France, 1998, 49-56.
22. Grunberg L., Nissan A.H. Mixture Law for Viscosity. Nature 1949, 164, 799 – 800.
23. Harris, K.R. Temperature and Density Dependence of the Viscosity of Toluene. *J. Chem. Eng. Data* 2000, 45, 893-897.
24. Irving, J.B. Viscosity of Binary Liquid Mixtures: The effectiveness of Mixtures Equations. Natl. Eng. Lab. Rept. 631, 1977, Glasgow, Scotland.

25. Jonsson, U.J., Lilje, K.C. Elastohydrodynamic Lubrication Properties of Polyol Ester Lubricants-R134a Mixtures. *Proceedings of the 1998 International Compressor Engineering Conference at Purdue*, Purdue University, West Lafayette, IN, 1998, 1, p123.
26. Kashiwagi, H., Makita, T. Viscosity of 12 Hydrocarbon Liquids in the Temperature Range 298 – 348 K at Pressures up to 110 MPa. *Int. J. Thermophys.* 1982, 3, 289-305.
27. Katti, P.K., Chaudhri M.M. Viscosities of Binary Mixtures of Benzyl Acetate with Dioxane, Aniline, and m-Cresol. *J. Chem. Eng. Data* 1964, 9, 442-443.
28. Kiran, E., Sen, Y.L. High-Pressure Viscosity and Density of n-Alkanes. *Int. J. Thermophys.* 1992, 13, 411-442.
29. Knapstad, B., Skjolsvik, P.A., Oye, H.A. Viscosity of n-Decane - Methane System in the Liquid Phase. *Ber. Bunsen-Ges. Phys. Chem.* 1990, 94, 1156-1165.
30. Krall, A.H., Sengers, J.V., Kestin, J. Viscosity of Liquid Toluene at Temperatures from 25 to 100°C and at Pressures up to 30 MPa. *J. Chem. Eng. Data* 1992, 37, 349-355.
31. Kumagai, K., Mochida, H., Takahashi, S. Liquid viscosities and densities of HFC-134a + glycol mixtures. *Int. J. Thermophys* 1993, 14, 45 – 53.
32. Kumagai, K., Miura-Mochida, H., Takahashi, S. Revised Viscosities for HFC-134a + Glycol Mixtures from 273 to 333 K. *Int. J. Thermophys.* 1994, 15, 109-115.
33. Oliveira, C.M.B.P., Wakeham W.A. The Viscosity of Five Liquid Hydrocarbons at Pressures up to 250 MPa. *Int. J. Thermophys.* 1992, 13, 773-790.
34. Papaioannou, D., Bridakis, M., Panayiotou, C. Excess Dynamic Viscosity and Excess Volume of N-Butylamine + 1-Alkanol Mixtures at Moderately High Pressure. *J. Chem. Eng. Data* 1993, 38, 370-378.
35. Quiñones-Cisneros, S.E., Zéberg-Mikkelsen, C.K., Stenby, E.H. The Friction Theory (f-theory) for Viscosity Modeling. *Fluid Phase Equilib.* 2000, 169, 249-276.
36. Quiñones-Cisneros, S.E., Zéberg-Mikkelsen, C.K., Stenby, E.H. One Parameter Friction Theory Models for Viscosity. *Fluid Phase Equilib.* 2001, 178, 1-16.
37. Sen, Y.L., Kiran, E.A. New Experimental System to Study the Temperature and Pressure Dependence of Viscosity, Density, and Phase Behavior of Pure Fluids and Solutions. *J. Supercrit. Fluids* 1990, 3, 91-99.
38. Sunami, M., Takigawa, K., Suda, S., Sasaki, U. New Immiscible Refrigeration Lubricant for HFCs. *ASHRAE Trans.* 1997, 95, 980-986.
39. Takigawa, K., Sandler, S.I., Yokozeki, A. Solubility and viscosity of refrigerant-lubricant mixtures: hydrofluorocarbon/ alkylbenzene systems. *Int. J. Refrig.* 2002, 25, 1014-1024.

40. Thébault, C., Vamling, L.A. New Correlation for Viscosity of Oil/Refrigerant Mixtures. *Int. Congr. Refrig. Third Millennium, 20th*, 1999, p707.

41. Tilly, K.A., Foster, N.R., Macnaughton, S.J., Tomasko, D.L. Viscosity Correlations for Binary Supercritical Fluids. *Ind. Eng.Chem. Res.* 1994, 33, 681-688.

42. Vieira dos Santos F.J., Nieto de Castro C.A. Viscosity of Toluene and Benzene under High Pressure. *Int. J. Thermophys.* 1997, 18, 367-378.

43. Wahlström, Å., Vamling, L. Viscosity for Mixtures of HFCs and Pentaerythritol Esters. *Int. Congr. Refrig. Third Millennium, 20th*, 1999, p348.

44. Zéberg-Mikkelsen, C.K., Canet, X., Baylaucq, A., Quiñones-Cisneros, S.E., Boned, C., Stenby, E.H. High Pressure Viscosity and Density Behavior of Ternary Mixtures: 1-Methylnaphthalene + n-Tridecane + 2,2,4,4,6,8,8-Heptamethylnonane. *Int. J. Thermophys.* 2001, 22, 1691-1725.

Concluding Remarks

The main conclusions drawn are listed in Chapter VIII.

VIII – Conclusions

8.1 – Concluding overview

The main research objective of this project has been the accurate modelling and prediction of the phase, volumetric and dynamic properties that are required in the design of cooling cycles based on environmentally friendly refrigerant-lubricant mixtures. The thesis has been divided into two parts. The first part, containing three chapters, covers pure refrigerants and pure lubricants separately. The second part, also containing three chapters, focuses on the refrigerant + lubricant mixtures. The main conclusions may be summarized as follows:

- *Chapter I:* The history of refrigeration is discussed. The new environmentally friendly refrigerants are introduced. The requirements for refrigerants as working fluids in refrigeration cycles and the environmental requirements are discussed. The importance of carbon dioxide as benign refrigerant is also discussed. It is also explained why refrigerants must be combined with lubricants. The main synthetic oil lubricants proposed for refrigeration applications are presented, along with their desirable properties.

- *Chapter II:* different equations of state (EoS) are studied with the aim to determine how well they predict the *p–v–T* behavior of pure refrigerants and pure lubricants. The EoS chosen can be divided into three classes: cubic EoS, non-cubic EoS of the BWR family, and the PC-SAFT EoS. The equations are tested for their ability to reproduce vapor pressures and densities for a number of compounds, for which sufficient experimental data exists over wide ranges of pressures and temperatures. The results of this evaluation show that cubic equations of state such as the RK-PR are appropriate for the description of the thermophysical properties of these compounds. The RK-PR EoS, which requires neither vapor pressure nor experimental densities for the adjustment of its parameters, provides in some cases better results than more sophisticated models such as the SBWR or the PC-SAFT EoS. Also, the well-known PR EoS has shown good performance, but only if its pure-compound parameters are adjusted against experimental data. Non-cubic equations of state such as the SBWR also provide good results, but, as for the PR EoS, the adjustment of the pure-compound parameters is required. The results obtained on the basis of the PC-SAFT EoS can also be considered as satisfactory, although the applied version of this equation of state does not involve all the possible interactions that the molecules may exhibit.

- *Chapter III.* An evaluation of the performance of five viscosity models was carried out over wide ranges of pressure and temperature. Most of the evaluated models are widely used within the oil and gas industry. The evaluated models are: the hard-sphere, the self-referencing method, the free-volume model, the original LBC model along with its modification (LBC-mod), and the PRVIS model (a model based on the PR EoS and exploiting similarity between the p-v-T and the p-η-T relationships). These five models have been tested on the experimental data for 17 pure refrigerants and 2 pure lubricants, up to high pressures. In addition, 7 well-defined refrigerant mixtures at moderate pressures have been included in this analysis. The hard-sphere scheme, the self-referencing method and the free-volume model have shown to describe the p-η-T behavior satisfactorily. Among these three models, the free-volume approach is very attractive for refrigeration related applications, since it can be applied to both liquids and gases. The hard-sphere, self-referencing and free-volume models require adjustment of the pure-compound parameters. The LBC and LBC-mod models, on the other hand, produce good results only for few compounds. Better results with these models are expected if the original parameters of the LBC and LBC-mod models are re-adjusted. The PRVIS model has been one of the worst, and it should not be recommended for refrigerant applications. An analysis of the performance of models applicable to gases in the low-pressure range has also been carried out.

- *Chapter IV.* This chapter discusses the friction theory. This approach to viscosity modeling is used in combination with the PR, the RK-PR, the SBWR and the PC-SAFT equations of state. The database of experimental points used to test this set of models is the same as in previous chapters. Overall, the results obtained with applications of the five-parameter *f*-theory models are very satisfactory. Compared with the free-volume approach, which shows the best results among the viscosity models studied in Chapter III, the *f*-theory provides generally better results. Further, the SBWR and the PC-SAFT EoS have been regrouped into a repulsive-like and attractive-like pressure terms in order to be combined with the *f*-theory. A satisfactory agreement with experimental data is found for the *f*-theory combined with such equations of state. However, the viscosity predictions with these EoS are found to be less accurate than the predictions obtained with the *f*-theory + cubic EoS.

- *Chapter V.* The study of refrigerant + lubricant mixtures begins in this chapter, directed into the theoretical understanding of the complex phase behavior that asymmetric mixtures develop. Particular attention is given to barotropic behavior, since this phenomenon has been left largely untouched in both experimental and theoretical research. The chapter aims at clarifying, in terms of the global phase diagram approach, the origin of this phenomenon. For CO_2 + alkylbenzene mixtures it is shown that there is a continuous transition from type II to type III phase behavior, through an intermediate type IV. It is during the type IV transition that the barotropic phenomenon is likely to develop in asymmetric mixtures. The connection between phase and viscosity behavior was studied by with application of the f-theory. It was shown that phase behavior strongly affects viscosity. The combination of phase and viscosity modeling techniques discussed in this chapter provides a powerful tool for the design of refrigeration cycles and the prevention of some problems intrinsic to this type of systems, such as density inversions.

- *Chapter VI:* In this chapter the phase and *p*-*v*-*T*-*x* behavior of the mixtures containing HFC or CO_2 refrigerants + PAGs, POEs, and ABs as lubricants is studied based on experimental information found in the literature. The PR and the PC-SAFT EoS are tested for their capabilities to predict solubilities and densities of the coexisting phases. Global phase behavior of the carbon dioxide mixtures with n-alkylbenzenes is also studied with application of the PR and the PC-SAFT EoS. The PR EoS has shown to predict the continuity in fluid phase behavior observed experimentally. It requires the only interaction parameter for all the mixtures. The PC-SAFT EoS, on the other hand, is not always able to reproduce correct phase behavior. The PR, and the PC-SAFT EoS have also been tested with regard to their ability to reproduce liquid densities at high pressures. In this analysis the RK-PR, and the SBWR EoSs are also included. Overall, good results are obtained for all the models.

- *Chapter VII:* The experimental study and modeling of HFC-134a + TriEGDME, and HFC-134a + TEGDME mixtures has been carried out. 300 experimental points have been obtained at various pressures between 10 MPa and 100 MPa in the monophasic liquid state from T = 293.15 K to 373.15 K. The measurements have been carried out using a falling body viscometer. The general uncertainty is of the order of ±2.5%. The data have been correlated using seven viscosity models (a mixing rule based model, self-referencing method, hard-sphere model, free volume model, friction theory and the LBC model). All the considered models utilize characteristic parameters and properties of the pure compounds. They are totally predictive with regard to mixture viscosities, except for the self-referencing method, which requires one experimental value at each composition for the reference pressure and temperature. In general, all the studied models show large average absolute deviations. As shown in Chapters III and IV, these models can describe the p-η-T properties of pure compounds satisfactorily. Thus, this may be an indication for the limitation of the used mixing rules for correct viscosity reproduction for this kind of systems. Extension of the *f-theory* model to equations besides PR, SRK, and PRSV has also been studied in comparison to the new experimental data. This analysis reveals that adequate mixing rules need to be developed when the *f-theory* is used in combination with the RK-PR, the SBWR, and the PC-SAFT EoS.

8.2 – Future challenges

The new challenges open for investigation and the ideas worth to be tested are listed below:

- As mentioned in Chapter II, the application of equations of the SAFT family to refrigerant + lubricant mixtures has not been fully investigated. The fluids studied in this thesis are assumed to exhibit dispersion interactions only. Thus, inclusion of the polar effects or weak hydrogen bonds, among other kinds of interactions, may serve as a real test for the PC-SAFT EoS itself or other kinds of EoS.

- It is possible to find in the literature the data on phase equilibria for refrigerant + refrigerant mixtures. Extension of the SAFT family EoS to these mixtures may prove useful.

- The new RK-PR EoS has shown to provide very good results describing vapor pressures and volumetric behavior of pure compounds. Some preliminary results show that this EoS can also reproduce correctly the p-v-T-x behavior of HFC-134a + PAGs mixtures (Chapter VI). Therefore, it would be useful to extend the study of the performance of the RK-PR EoS and its capability to predict phase equilibria of asymmetric mixtures similar to those studied in this thesis.

- Experimental viscosity measurements on pure lubricants and refrigerant + lubricant mixtures up to high pressures are still scarce. Further studies in this direction are necessary. These data can aid at developing new or improved mixing rules for the viscosity models.

Appendix A

Appendix A: Selected References for Refrigerants

A.1 – Vapor pressure references for R32, R125, R134a and R152a

The vapor pressure data given in Tables A.1 – A.4 are based on experimental values for the given temperature range. NP is the number of data points.

R32

Reference	*NP*	*T-range* (K)
Defibaugh (1994)	18	268-348
Fu (1995)	60	233-351
Holcomb (1993)	25	295-348
Magee (1996)	7	270-330
Malbrunot (1968)	28	204-348
Qian (1993)	9	280-350
Sato (1994)	21	320-351
de Vries (1997)	32	223-295
Weber (1993)	27	208-237
Weber (1994)	17	235-266
Widiatmo (1994)	25	204-351

Table A.1 – Selected references for R32.

R125

Reference	*NP*	*T-range* (K)
Boyes (1995)	29	273-335
Duarte-G. (1997)	15	220-338
Magee (1996)	33	180-335
Ye (1995)	12	290-339
Weber (1994)	104	219-285
Widiatmo (1994)	20	220-338

Table A.2 – Selected references for R125.

R134a

Reference	*NP*	*T-range* (K)
Baehr (1991)	37	303-374
Goodwin (1993)	57	214-313
Oliveira (1993)	17	238-343
Zhu (1992)	45	210-340

Table A.3 – Selected references for R134a

R152a

Reference	*NP*	*T-range* (K)
Blanke (1992)	36	312-384
Holcomb (1993)	33	311-384
Silva (1993)	38	220-273
Tamatsu (1992)	46	320-386
Zhao (1992)	166	237-365

Table A.4 – Selected references for R152a

A.2 – Density references for R32, R125, R134a and R152a

The density data given in Tables A.5 – A.8 are based on experimental values for the given temperature and pressures ranges. NP is the number of data points.

R32

Reference	*NP*	*Phase*	*T-range* (K)	*p-range* (MPa)
Defibaugh (1994)	382	*l-g*	242-373	0.2-10
Fu (1995)	121	*g*	243-373	0.1-6
Luddecke (1996)	73	*l*	153-348	3.2-32
Magee (1996)	133	*l*	142-395	4.2-35
Malbrunot (1968)	139	*l-g*	248-473	0.5-20
Sato (1994)	55	*g*	330-420	3.5-10

Table A.5 - Summary of the data sets selected for R32

R125

Reference	*NP*	*Phase*	*T-range* (K)	*p-range* (MPa)
Defibaugh (1992)	162	*l*	275-369	1.6-6.3
Duarte-G. (1997)	230	*l-g*	180-400	0.1-68
Magee (1996)	77	*l*	178-298	3.6-36
Ye (1995)	93	*g*	290-390	0.1-3.6
Zhang (1996)	47	*g*	290-390	0.1-3.2

Table A.6 - Summary of the data sets selected for R125

R134a

Reference	*NP*	*Phase*	*T-range* (K)	*p-range* (MPa)
Assael (1997)	59	*l-g*	273-333	0.1-15
Comuñas (2002)	70	*l*	293-373	0.1-60
Diller (1993)	63	*l*	200-300	0.6-37
Okubo (1992)	81	*l*	213-423	1.5-30
Oliveira (1993)	43	*l*	293-343	0.6-51
Padua (1997)	37	*l*	248-298	0.8-100
Shibasaki (1998)	126	*g*	298-423	0.1-5.7

Table A.7 - Summary of the data sets selected for R134a

R152a

Reference	*NP*	*Phase*	*T-range* (K)	*p-range* (MPa)
Blanke (1992)	208	*l*	160-453	0.6-30.5
Magee (1998)	134	*l*	158-400	2-35.2
Takahashi (1987)	112	*g*	296-423	0.1-5
Tamatsu (1992)	60	*l-g*	330-440	1.6-10

Table A.8 - Summary of the data sets selected for R152a.

A.3 – References in Appendix A

1. Assael, M.J.; Polimatidou, S.K. Measurements of the Viscosity of Refrigerants in the Vapour Phase. *Int. J. Thermophys.* 1997, 18, 353-366.
2. Baehr, H.D.; Tillner-Roth, R. Measurements and correlation of the vapour pressures of 1,1,1,2-tetrafluoroethane (R134a) and R152a. *J. Chem. Thermodyn.* 1991, 23, 1063-1068.
3. Blanke, W.; Weiß, R. Isochoric (p,v,T) Measurements on CH3CHF2 (R152a) in the Liquid State from the Triple Point to 450 K and at Pressures up to 30 MPa. *Fluid Phase Equilib.* 1992, 80, 179-190.
4. Boyes, S.J.; Weber, L.A. Vapour pressures and gas-phase (p, ρn, T) values for CF3CHF2 (R125). *J. Chem. Thermodynamics* 1995, 27, 163-174.
5. Comuñas, M.J.P. Densidades y Viscosidades a Alta Presión de Nuevos Lubricantes Sintéticos y de las Mezclas Lubricante + HFC-134a. Medida y Modelización. Ph.D. Thesis, Física Aplicada, Universidad de Santiago de Compostela, Santiago de Compostela, Spain, 2002.
6. Defibaugh, D.R.; Morrison, G. Compressed Liquid Densities and Saturation Densities of Pentafluoroethane (R125). *Fluid Phase Equilib.* 1992, 80, 157-166.
7. Defibaugh, D.; Morrison, G.; Weber, L. Thermodynamic Properties of Difluoromethane. *J. Chem. Eng. Data* 1994, 39, 333-340.
8. Diller, D.E.; Aragon, A.S.; Laesecke, A. Measurements of the Viscosities of Saturated and Compressed Liquid 1,1,1,2-tetrafluoroethane (HFC-134a), 2,2-dichloro-1,1,1-trifluoroethane (R123) and 1,1-dichloro-1-fluoroethane (R141b). *Fluid Phase Equilib.* 1993, 88, 251-262.
9. Duarte-Garza, H.A.; Stouffer, C.E.; Hall, K.R.; Holste, J.C.; Marsh, K.N.; Gammon, B.E. Experimental Critical Constants, Vapor Pressures, and Vapor and Liquid Densities for Pentafluoroethane (R-125). *J. Chem. Eng. Data* 1997, 42, 745-753.
10. Fu, Y.; Han, L.; Zhu, M. PVT properties, vapor pressures and critical parameters of HFC-32. *Fluid Phase Equilib.* 1995, 111, 273-286.
11. Goodwin, A.R.H.; Defibaugh, D.R.; Weber, L.A. Vapor pressure of 1,1-difluoroethane (R152a). *Int. J. Thermophys.* 1992, 13, 837-847.
12. Holcomb, C.; Niesen, V.; Van Poolen, L.; Outcalt, S. Coexisting densities, vapor pressures and critical densities of refrigerants R-32 and R-152a, at 300-385 K. *Fluid Phase Equilib.* 1993, 91, 145-157.

13. Luddecke T.O., Magee, J.W. Molar Heta capacity at Constant Volume of Difluoromethane (R32) and Pentafluoroethane (R125) from the Triple-Point Temperature to 345 K at Pressures to 35 MPa. *Int. J. Thermophys.* 1996, 17, 823-849.
14. Magee, J. Isochoric p-ρ-T measurements on difluoromethane (R32) from 142 to 396 K and pentafluoroethane (R125) from 178 to 398 at pressures to 35 MPa. *Int. J. Thermophys.* 1996, 17, 803-822.
15. Magee, J. Isochoric p-ρ-T measurements on 1,1-Difluoroethane (R152a) from 158 to 400 K and 1,1,1-Trifluoroethane (R143a) from 166 to 400 K at Pressures to 35 MPa. *Int. J. Thermophys.* 1998, 19, 1381-1395.
16. Malbrunot, P., Meunier, P., Scatena, G. Pressure-volume-temperature behavior of difluoromethane. *J. Chem. Eng. Data* 1968, 13, 16-21.
17. Okubo, T., Nagashima, A. Measurements of the Viscosity of HCFC-123 in the Temperature Range 233-418 K and at Pressures up to 20 MPa. *Int. J. Thermophys.* 1992, 13, 401-410.
18. Oliveira, C.M.B.P., Wakeham, W.A. The Viscosity of Liquid R134a. *Int. J. Thermophys.* 1993, 14, 33-44.
19. Pádua, A.A.H., Fareleira, J.M.N.A., Calado, J.C.G., Wakeham, W.A. Viscosity of Compressed Liquid 1,1,1,2-tetrafluoroethane (R134a) *J. Chem. Eng. Data.* 1996, 41, 731-735.
20. Qian, Y., Nishimura, A., Sato, H., Watanabe, K. Compressibility factors and virial coefficients of difluoromethane (HFC-32) determined by Burnett Method. *JSME Int. Journal* 1993, 36, 665-670.
21. Sato, T., Sato, H., Watanabe, K. *PVT* properties measurements for difluoromethane. *J. Chem. Eng. Data* 1994, 39, 851-854.
22. Shibasaki-Kitawa, N., Takahashi, M., Yokoyama, C. Viscosity of Gaseous HFC-134a (1,1,1,2-Tetrafluorethane) Under High Pressures. *Int. J. Thermophys.* 1998, 19, 1285-1295.
23. Silva, A.M., Weber, L.A. Ebulliometric Measurement of the Vapor Pressure of 1-Chloro-1,1-Difluoroethane and 1,1 -Difluoroethane. *J. Chem. Eng. Data* 1993, 38, 644-646.
24. Takahashi, M., Yokoyama, C., Takahashi, S. Viscosities of gaseous R13B1, R142b, and R152a. *J. Chem. Eng. Data* 1987, 32, 98-103.
25. Tamatsu, T., Sato, T., Sato, H., Watanabe, K. An Experimental Study of the Thermodynamics Properties of 1,1-Difluoroethane. *Int. J. Thermophys.* 1992 13, 985-997.
26. de Vries, B. Thermodynamische Eingenschaften der alternativen Kältemittel R-32, R-125, R143a. DKV-Forsch.-Ber. Nr.59 (DKV, Stuttgart, 1997) (in German).

27. Ye, F., Sato, H., Watanabe K., Gas-Phase *PVT* Properties and Vapor Pressures of Pentafluoroethane (HFC-125) Determined According to the Burnett Method. *J. Chem. Eng. Data* 1995, 40, 148-152.
28. Weber, L., Goodwin, A. Ebulliometric Measurement of the vapor pressure of difluoromethane. *J. Chem. Eng. Data* 1993, 38, 254-256.
29. Weber, L., Silva, M. Measurements of the vapor pressures of difluoromethane, 1-chloro-1,2,2,2-tetrafluoroethane, and pentafluroethane. *J. Chem. Eng. Data* 1994, 39, 808-812.
30. Widiatmo, J., Sato, H., Watanabe, K. Saturated-liquid densities and vapor pressures of 1,1,1-trifluoroethane, difluoromethane and pentafluoroethane. *J. Chem. Eng. Data* 1994, 39, 304-308.
31. Zhang, H.-L., Sato, H., Watanabe, K. Gas Phase *PVT* Properties for the Difluoromethane +Pentafluoroethane (R-32 + 125) System. *J. Chem. Eng. Data* 1996, 41, 1401-1408.
32. Zhao Z.Y., Yin J.M., Tan L.C. Measurements of PVT properties and vapor pressures for HCF152a. *Fluid Phase Equilib.* 1992, 80, 191-202.
33. Zhu, M.-S., Wu, J., Fu, Y.-D. New experimental vapor pressure data and a new vapor pressure equation for HFC134a. *Fluid Phase Equilib.* 1992, 80, 99-105.

Appendix B

Appendix B: Viscosity References for Pure Refrigerants and Pure Lubricants

B.1 – Viscosity references for refrigerants

In Tables B.1 to B.17 the references for the experimental refrigerant viscosities along with the experimental temperature, pressure and density ranges are shown. In addition the experimental technique used and the reported accuracy are given. When values for the experimental densities were not available, they were generated by an equation of state.

R11

Reference	*NP*	*Phase*	*T-range* (K)	*p-range* (MPa)	*ρ-range* (Kg/m^3)	*Method*	*Accur.* (%)
Assael (1994a)	32	*l*	273-333	1.4-19	1392-1565	Vibrating	0.50
Geller (1975)	92	*l-g*	242-453	0.1-59	854-1624 (1)	Capillary	-
Phillips (1970)	9	*l*	209-352	0.1	1339-1673	Capillary	-

Table B.1 – Selected references and data for R11. Reference for EoS: (1) Span and Wagner, 2003.

R12

Reference	*NP*	*Phase*	*T-range* (K)	*p-range* (MPa)	*ρ-range* (Kg/m^3)	*Method*	*Accur.* (%)
Assael (1994a)	32	*l*	273-333	1.2-15.1	1186-1441	Vibrating	0.50
Geller (1975)	107	*l-g*	244-433	1.1-59	39-1494 (1)	Capillary	-
Kamien (1959)	18	*g*	303-363	0.1-2	4-110 (1)	Capillary	-
Phillips (1970)	9	*l*	202-312	0.1	1256-1600	Capillary	-

Table B.2 – Selected references and data for R12. Reference for EoS: (1) Span and Wagner, 2003.

R13

Reference	*NP*	*Phase*	*T-range* (K)	*p-range* (MPa)	*ρ-range* (Kg/m^3)	*Method*	*Accur.* (%)
Diller (1989)	55	*l*	150-320	1.1-35	207-1728	Torsional	2.00
Geller (1975)	108	*l-g*	244-413	0.1-39	5-1456 $^{(1)}$	Capillary	-
Geller (1980)	118	*l*	89-299	3.5-39	959-2034 $^{(1)}$	Capillary	-
Kamien (1959)	16	*g*	303-363	0.1-2	3.5-105 $^{(1)}$	Capillary	-
Phillips (1970)	8	*l*	192-273	0.1	1129-1520	Capillary	-
Takahashi (1985)	170	*g*	273-373	0.1-10.4	4.4-607	Osc-Disk	1.00

Table B.3 – Selected references and data for R13.Reference for EoS: $^{(1)}$ Magee *et al.* 2000.

R14

Reference	*NP*	*Phase*	*T-range* (K)	*p-range* (MPa)	*ρ-range* (Kg/m^3)	*Method*	*Accur.* (%)
Abe (1979)	9	*g*	333-468	0.1	2.3-3.1 $^{(1)}$	Osc-Disk	0.30
Dawe (1970)	20	*g*	293-873	0.1	1.2-3.7 $^{(1)}$	Capillary	1.00
Geller (1975)	75	*l-g*	293-433	0.1-39	3-1172 $^{(1)}$	Capillary	-
Gough (1976)	10	*g*	150-320	0.1	3.3-7.4 $^{(1)}$	Capillary	1.00
Hellemans (1973)	9	*g*	298-873	0.1	1.2-3.6 $^{(1)}$	Osc-Disk	0.30
Kamien (1959)	24	*g*	303-363	0.1-2	3-76.2 $^{(1)}$	Capillary	-
Kestin (1971)	2	*g*	296-303	0.1	3 $^{(1)}$	Osc-Disk	0.10
Kestin (1976)	3	*g*	296-477	0.1	2.2-3.6 $^{(1)}$	Osc-Disk	0.20
Kestin (1977a)	16	*g*	296-673	0.1	1.6-3.6 $^{(1)}$	Osc-Disk	0.20
Kestin (1977b)	5	*g*	298-668	0.1	1.6-3.6 $^{(1)}$	Osc-Disk	0.30

Table B.4 – Selected references and data for R14. Reference for EoS: $^{(1)}$ Platzer and Maurer, 1989

R22

Reference	*NP*	*Phase*	*T-range* (K)	*p-range* (MPa)	*ρ-range* (Kg/m³)	*Method*	*Accur.* (%)
Assael (1994c)	32	*l*	273-333	1.3-15	1042-1320	Vibrating	0.50
Diller (1993a)	77	*l*	150-320	1-30.5	1100-1675	Torsional	3.00
Kamien (1959)	17	*g*	303-363	0.1-2	3-76.2 ⁽¹⁾	Capillary	-

Table B.5 - Selected references and data for R22. Reference for EoS: ⁽¹⁾ Span and Wagner, 2003

R32

Reference	*NP*	*Phase*	*T-range* (K)	*p-range* (MPa)	*ρ-range* (Kg/m³)	*Method*	*Accur.* (%)
Assael (1994b)	26	*l*	273-313	1.6-15.6	905-1082	Vibrating	0.50
Assael (1995)	3	*l*	273-313	0.8-2.5	893-1056	Vibrating	-
Dunlop (1993)	1	*g*	298	0.10	2 ⁽¹⁾	Capillary	0.30
Geller (1996)	51	*l-g*	253-363	0.1-5.3	2-1114	Capillary	1.20
Oliveira (1993b)	33	*l-g*	252-343	0.1-5	4-1181	Vibrating	3.00
Oliveira (1999)	13	*g*	223-343	0.1-5	4-194	Vibrating	0.80
Takahashi (1995)	114	*g*	298-423	0.1-10	1.5-556	Osc-Disk	0.30

Table B.6 - Selected references and data for R32. Reference for EoS: ⁽¹⁾ Span and Wagner, 2003

R113

Reference	*NP*	*Phase*	*T-range* (K)	*p-range* (MPa)	*ρ-range* (Kg/m³)	*Method*	*Accur.* (%)
Kumagai (1991)	9	*l*	273-353	0.2-2	1334-1534	Capillary	-
Kumagai (2000)	9	*l*	273-353	0.1-2.1	1334-1534	Capillary	-

Table B.7 - Selected references and data for R113.

R114

Reference	*NP*	*Phase*	T-range (K)	p-range (MPa)	ρ-range (Kg/m^3)	*Method*	*Accur.* (%)
Geller (1975)	90	*l*	183-273	1.1-59	1636-1736 (1)	Capillary	-
Kamien (1959)	12	*g*	303-363	0.1-2	3-76.2 (1)	Capillary	-
Kumagai (1991)	9	*l*	273-353	0.2-2	1334-1534	Capillary	-
Kumagai (2000)	9	*l*	273-353	0.1-2.1	1334-1534	Capillary	-
Phillips (1970)	10	*l*	273-353	0.1	1220-1530	Capillary	-

Table B.8 – Selected references and data for R114. Reference for EoS: (1) Defibaugh and Moldover, 1997.

R115

Reference	*NP*	*Phase*	T-range (K)	p-range (MPa)	ρ-range (Kg/m^3)	*Method*	*Accur.* (%)
Geller (1975)	79	*l*	177-333	1.1-59	1582-1756 (1)	Capillary	-
Kamien (1959)	15	*g*	303-363	0.1-2	6-162 (1)	Capillary	-
Phillips (1970)	8	*l*	198-303	0.1	1200-1660	Capillary	-

Table B.9 – Selected references and data for R115. Reference for EoS: (1) Defibaugh and Moldover, 1997.

R123

Reference	*NP*	*Phase*	T-range (K)	p-range (MPa)	ρ-range (Kg/m^3)	*Method*	*Accur.* (%)
Diller (1993b)	29	*l*	200-300	3.2-33	1470-1731	Torsional	-
Nabizadeh (1992)	31	*g*	302-423	0.1-2	4-134	Osc-Disk	0.30
Okubo (1992)	36	*l*	233-298	1.1-20	1462-1680	Capillary	0.10
Yokoyama (2000)	42	*g*	323-423	0.1-2	4-126	Osc-Disk	0.30

Table B.10 – Selected references and data for R123.

R124

Reference	*NP*	*Phase*	*T-range* (K)	*p-range* (MPa)	*ρ-range* (Kg/m^3)	*Method*	*Accur.* (%)
Assael (1994c)	32	*l*	273-313	1.5-17	1237-1465	Vibrating	0.50
Assael (1997)	14	*g*	273-333	0.1-1	7.2-56	Vibrating	1.00
Diller (1993c)	103	*l*	150-420	3.3-56	206-1755	Torsional	3.00

Table B.11 – Selected references and data for R124.

R125

Reference	*NP*	*Phase*	*T-range* (K)	*p-range* (MPa)	*ρ-range* (Kg/m^3)	*Method*	*Accur.* (%)
Assael (1994c)	22	*l*	273-313	2.5-12.1	1158-1402	Vibrating	0.50
Assael (1997)	24	*g*	273-333	0.1-2	7-141.3	Vibrating	1.00
Diller (1993c)	105	*l*	176-420	3.3-53	179.6-1667	Torsional	3.00
Dunlop (1993)	1	*g*	298	0.1	4.9 (1)	Capillary	0.30
Takahashi (1999b)	131	*g*	298-423	0.1-9	3.5-533	Osc-Disk	0.30
Wilson (1992)	11	*l-g*	216-422	0.1-3.4	3-1538 (1)	Capillary	2.00

Table B.12 – Selected references and data for R125. Reference for EoS: (1) Span and Wagner, 2003

R134a

Reference	*NP*	*Phase*	*T-range* (K)	*p-range* (MPa)	*ρ-range* (Kg/m^3)	*Method*	*Accur.* (%)
Assael (1994b)	32	*l*	273-333	0.9-15	1059-1326	Vibrating	0.50
Assael (1997)	22	*g*	273-333	0.1-1.5	5.4-72	Vibrating	1.00
Comuñas (2003)	70	*l*	293-373	10-140	964-1503	Falling	2.00
Diller (1993b)	63	*l*	200-300	0.6-37	1200-1545	Torsional	2.00
Okubo (1993)	81	*l*	213-423	1.5-30	645-1519	Capillary	1.30
Oliveira (1993a)	43	*l*	293-343	0.6-51	999-1375	Vibrating	0.60
Padua (1996)	37	*l*	248-298	0.8-100	1208-1535	Vibrating	2.50
Shibasaki (1998)	126	*g*	298-423	0.1-5.7	3-396	Osc-Disk	0.30
Wilhelm (2001)	62	*l*	300-340	0.8-100	1000-1443 (1)	Vibrating	0.50

Table B.13 – Selected references and data for R134a. Reference for EoS: (1) Span and Wagner, 2003

R141b

Reference	*NP*	*Phase*	*T-range* (K)	*p-range* (MPa)	*ρ-range* (Kg/m^3)	*Method*	*Error* (%)
Assael (1994a)	32	*l*	273-333	0.95-19	1167-1303	Vibrating	0.50
Diller (1993b)	25	*l*	200-300	5.1-30	1235-1418	Torsional	–

Table B.14 – Selected references and data for R141b.

R142b

Reference	*NP*	*Phase*	*T-range* (K)	*p-range* (MPa)	*ρ-range* (Kg/m^3)	*Method*	*Error* (%)
Kumagai (2000)	9	*l*	273-333	0.1-2.1	1330-1410	Capillary	–
Nabizadeh (1992)	29	*g*	304-372	0.1-2	3.1-94	Osc-Disk	0.30
Takahashi (1987)	96	*g*	298-423	0.1-5	1.7-511	Osc-Disk	–

Table B.15 – Selected references and data for R142b.

R143a

Reference	*NP*	*Phase*	*T-range* (K)	*p-range* (MPa)	*ρ-range* (Kg/m^3)	*Method*	*Error* (%)
Dunlop (1993)	1	*g*	298	0.1	2.75 (1)	Capillary	0.30
Kumagai (1991)	6	*l*	273-323	0.6-2.5	800-1022	Capillary	–
Kumagai (2000)	6	*l*	273-323	0.3-2	875-1011	Capillary	–
Ripple (1997)	9	*l*	256-308	0.3-1.6	845-1100	Capillary	–
Takahashi (1999a)	97	*g*	298-423	0.1-9	1.5-360	Osc-Disk	–

Table B.16 – Selected references and data for R143a.

R152a

Reference	*NP*	*Phase*	*T-range* (K)	*p-range* (MPa)	*ρ-range* (Kg/m³)	*Method*	*Accur.* (%)
Assael (1994a)	32	*l*	273-333	1.5-17.7	806-988	Vibrating	0.50
Assael (1997)	21	*g*	273-333	0.2-1.2	5.2-37.2	Vibrating	1.00
Dunlop (1993)	1	*g*	298.15	0.10	2.7 (1)	Capillary	0.30
Phillips (1970)	9	*l*	200-318	0.10	845-1100	Capillary	-
Takahashi (1987)	112	*g*	298-423	0.1-5.3	2-261.5	Osc-Disk	-

Table B.17 – Selected references and data for R152a. Reference for EoS: (1) Span and Wagner, 2003.

B.2 – Viscosity references for lubricants

In Tables B.18 and B.19 the references for the experimental lubricant viscosities along with the experimental temperature, pressure and density ranges are shown. In addition the experimental technique used and the reported accuracy are given.

TriEGDME

Reference	*NP*	*Phase*	*T-range* (K)	*p-range* (MPa)	*ρ-range* (Kg/m³)	*Method*	*Accur.* (%)
Comuñas (2001)	48	*l*	283-353	0.1-100	928-1045	Falling	2.00
Conesa (1998)	15	*l*	283-423	0.10	860-994	Capillary	1.00

Table B.18 – Selected references and data for TriEGDME.

TEGDME

Reference	*NP*	*Phase*	*T-range* (K)	*p-range* (MPa)	*ρ-range* (Kg/m³)	*Method*	*Accur.* (%)
Comuñas (2001)	48	*l*	283-353	0.1-100	956-1069	Falling	2.00
Conesa (1998)	15	*l*	283-423	0.10	891-1020	Capillary	1.00

Table B.19 – Selected references and data for TEGDME.

B.3 – References in Appendix B

1. Abe, Y., Kestin, J., Khalifa, H.E., Wakeham, W.A. The Viscosity and Diffusion Coefficients of the Mixtures of Light Hydrocarbons with Other Polyatomic Gases. *Ber. Bunsen-Ges. Phys. Chem.* 1979, 83, 271-276.
2. Assael, M.J., Polimatidou, S.K., Vogel, E., Wakeham, W.A. Measurements of the Viscosity of R11, R12, R141b and R152a in the Temperature Range 270-340K at Pressures up to 20 MPa. *Int. J. Thermophys.* 1994a, 15, 575-589.
3. Assael, M.J., Dymond, J.H., Polimatidou, S.K. Measurements of R134a and R32 in the Temperature Range 270-340 K at Pressures up to 20 MPa. *Int. J. Thermophys.* 1994b, 15, 591-601.
4. Assael, M.J., Polimatidou, S.K. Measurements of the Viscosity of Liquid R22, R124, and R125 in the Temperature Range 273-333 K at Pressures up to 17 MPa. *Int. J. Thermophys.* 1994c, 15, 779-790.
5. Assael, M.J., Karagiannidis, L., Polimatidou, S.K. Measurements of the Viscosity of New Refrigerants in the Temperature Range 270-340 K at Pressures up to 20 MPa. *Int. J. Thermophys.* 1995, 16, 133-143.
6. Assael, M.J., Polimatidou, S.K. Measurements of the Viscosity of Refrigerants in the Vapour Phase. *Int. J. Thermophys.* 1997, 18, 353-366.
7. Comuñas, M.J.P., Baylaucq, A., Boned, C., Fernández, J. High-Pressure Measurements of the Viscosity and Density of Two Polyethers and Two Dialkyl Carbonates. *Int. J. Thermophys.* 2001, 22, 749-768.
8. Conesa, A., Shen, S., Coronas, A. Liquid Densities, Kinematic Viscosities, and Heat Capacities of Some Ethylene Glycol Dimethyl Ethers at Temperatures from 283.15 to 423.15 K. *Int. J. Thermophys.* 1998, 19, 1343-1358.
9. Comuñas, M.J.P., Baylaucq, A., Quiñones-Cisneros, S.E., Zéberg-Mikkelsen, C.K., Boned, C., Fernández, J. Viscosity measurements and correlations for 1,1,1,2-tetrafluoroethane (HFC-134a) up to 140 MPa. *Fluid Phase Equilib.* 2003, 210, 21–32.
10. Dawe, R.A., Maitland, G.C., Rigby, M., Smith, E. B. High-Temperature Viscosities and Intermolecular Forces of Quasi-Spherical Molecules. *J. Chem. Soc. Faraday Trans.* 1970, 66, 1955-1965.
11. Defibaugh, D., Moldover, M.R. Compressed and Saturated Liquid Densities for 18 Halogenated Organic Compounds. *J. Chem. Eng. Data* 1997, 42, 160-168.

12. Diller, D.E., Aragon, A.S., Laesecke, A. Measurements of the Viscosity of Saturated and Compressed Liquid Chlorodifluoromethane (R22). *Int. J. Refrig.* 1993a, 16, 19-22.
13. Diller, D.E., Aragon, A.S., Laesecke, A. Measurements of the Viscosity of Saturated and Compressed Liquid 1,1,1,2-tetrafluoethane (R134a), 2,2-dichloro-1,1,1-trifluoroethane (R123) and 1,1-dichloro-1-fluoroethane (R141b). *Fluid Phase Equilib.* 1993b, 88, 251-262.
14. Diller, D.E., Peterson, S.M. Measurements of the Viscosities of Saturated and Compressed Fluid 1-Chloro-1,2,2,2-tetrafluoroethane (R124) and Pentafluoroethane (R125) at Temperatures between 120 and 420 K. *Int. J. Thermophys.* 1993c, 14, 55-66.
15. Dunlop, P.J. Viscosities of a Series of Gaseous Fluorocarbons at 25 °C. *J. Chem. Phys.* 1994, 100, 3149-3151.
16. Geller, V.Z., Ivanchenko, S.I., Kronberg, A.V. Investigation of Viscosity of Freons of the Methane Series. *Teplofiz. Svoistva Veshchestv Mater.* 1975, 8, 148-161 *(in Russian)*.
17. Geller, V.Z. Viscosity of Freons of the Methane, Ethane, and Propane Series. Generalizations of Experimental Data. *Teplofiz. Svoistva Veshchestv Mater.* 1980, 15, 89-115*(in Russian)*.
18. Geller, V.Z., Paulaitis, M.E., Bivens, D.B., Yokozeki, A. Viscosity of HFC-32 and HFC-32/Lubricant Mixtures. *Int. J. Thermophys.* 1996, 17, 75-83.
19. Gough, D.W., Matthews, G.P., Smith, E.B. Viscosity of Nitrogen and Certain Gaseous Mixtures at Low Temperatures. *J. Chem. Soc., Faraday Trans. I* 1976, 72, 645-653.
20. Hellemans, J.M., Kestin, J., Ro, S.T. The Viscosity of CH_4, CF_4 and SF_6 over a Range of Temperatures. *Physica (Amsterdam)* 1973, 65, 376-380.
21. Kamien, C.Z., Witzell, O.W. Effect of Pressure and Temperature on the Viscosity of Refrigerants in the Vapor Phase. *ASHRAE J.* 1959, 65, 663-674.
22. Kestin, J., Ro, S.T., Wakeham, W.A. Reference Values of the Viscosity of Twelve Gases at 25 °C. *J. Chem. Soc., Faraday Trans.* 1971, 67, 2308-2313.
23. Kestin, J., Khalifa, H.E., Wakeham, W.A. Viscosity of Multicomponent Mixtures of Four Complex Gases. *J. Chem. Phys.* 1976, 65, 5186-5188.
24. Kestin, J., Khalifa, H.E., Wakeham, W.A. The Viscosity of Gaseous Mixtures Containing Krypton. *J. Chem. Phys.* 1977a, 67, 4254-4259.
25. Kestin, J., Khalifa, H.E., Ro, S.T., Wakeham, W.A. The Viscosity and Diffusion Coefficients of Eighteen Binary Gaseous Systems. *Physica A* 1977b, 88, 242-260.
26. Kumagai, A., Takahashi, S., Viscosity of Saturated Liquid Fluorocarbon Refrigerants from 273 to 353 K, *Int. J. Thermophys.* 1991, 12, 105-117.
27. Kumagai A., Yokoyama, C., Revised Viscosity of Saturated Liquid Halocarbon Refrigerants from 273 to 353 K, *Int. J. Thermophys.* 2000, 21, 909-912.

28. Magee, J.W., Outcalt, S.L., Ely, J.F. Molar Heat Capacity C_v, Vapor Pressure, and (p, ρ, T) Measurements to 35 MPa and a New Equation of State for Chlorotrifluoroetahen (R13). *Int. J. Thermophys.* 2000, 21, 1097-1121.

29. Nabizadeh, H., Mayinger, F. Viscosity of Gaseous R123, R134a, and R142b. *High Temp.-High Pressures* 1992, 24, 221-230.

30. Okubo, T., Nagashima, A. Measurements of the Viscosity of HCFC 123 in the Temperature Range 233-418 K and at Pressures up to 20 MPa. *Int. J. Thermophys.* 1992, 13, 401-410.

31. Okubo T., Hasuo, T., Nagashima, A. Viscosity of Liquid R134a. *Int. J. Thermophys.* 1992, 13, 931–942.

32. Oliveira, C.M.B.P., Wakeham, W.A. The Viscosity of Liquid R134a. *Int. J. Thermophys.* 1993a, 14, 33-44.

33. Oliveira, C.M.B.P., Wakeham, W.A. The Viscosity of R32 and R125 at Saturation. *Int. J. Thermophys.* 1993b, 14, 1131-1143.

34. Oliveira, C.M.B.P., Wakeham, W.A., Viscosity of R134a, R32 and R125 at Saturation. *Int. J. Thermophys.* 1999, 20, 365-373.

35. Padua, A.A.H., Fareleira, J.M.N.A., Calado, J.C.G., Wakeham, W.A. Viscosity of Compressed Liquid 1,1,1,2-tetrafluoethane (R134a) *J. Chem. Eng. Data.* 1996, 41, 731–735.

36. Phillips, T.W., Murphy, K.P. Liquid Viscosity of Halocarbons. *J. Chem. Eng. Data.* 1970, 15, 304-307.

37. Platzer, B., Maurer, G. A generalized Equation of State for Pure Polar and Nonpolar Fluids. *Fluid Phase Equilib.* 1989, 51, 223-236.

38. Ripple, D., Defibaugh, D. Viscosity of the Saturated Liquid Phase of Three Fluorinated Ethanes: R152a, R143a, and R125. *J. Chem. Eng. Data* 1997, 42, 360-364.

39. Shibasaki-Kitawa, N., Takahashi, M., Yokoyama, C. Viscosity of Gaseous HFC 134a (1,1,1,2-Tetrafluoroethane) Under High Pressures. *Int. J. Thermophys.* 1998, 19, 1285-1295.

40. Spam, R., Wagner, W. Equations of State for Technical Applications. III. Results for polar Fluids. *Int. J. Thermophys.* 2003, 24, 111-162.

41. Takahashi, M., Yokoyama, C., Takahashi, S. Viscosities of gaseous R13B1, R142b, and R152a. *J. Chem. Eng. Data* 1987, 32, 98-103.

42. Takahashi, M., Shibasaki-Kitakawa, N., Yokoyama, C., Takahashi, S. Gas Viscosity of Difluoromethane from 298.15 to 423.15 K and up to 10 MPa. *J. Chem. Eng. Data* 1995, 40, 900-902.

43. Takahashi, M., Shibasaki-Kitakawa, N., Yokoyama, C. Viscosity of Gaseous HFC-143a (1,1,1-Trifluoroethane) under High Pressures. *Int. J. Thermophys.* 1999a, 20, 435-443.

44. Takahashi, M., Shibasaki-Kitakawa, N., Yokoyama, C. Viscosity of Gaseous HFC-125 (Pentafluoroethane) under High Pressures. *Int. J. Thermophys.* 1999b, 20, 445-453.
45. Wilhelm, J. IUPAC Round Robin Project on Transport Properties of R134a, *Private Communication*, 2001.
46. Wilson, L.C., Wilding, W.V., Wilson, G.M., Rowley, R.L., Felix, V.M., Chisolm-Carter, T. Thermophysical Properties of HFC-125. *Fluid Phase Equilib.* 1992, 80, 167-177.
47. Yokoyama, C., Takahashi, M. Viscosity of Gaseous HCFC-123 (2,2-Dichloro-1,1,1-Trifluoroethane) in the Temperature Range from 323.15 to 423.15 K and at Pressures up to 2 MPa, *Int. J. Thermophys.* 2000, 21, 695-240.

Appendix C

Appendix C: Measured Viscosities of Refrigerant + Lubricant Mixtures

C.1 HFC-134a + TriEGDME

p (MPa)	T (K)	$\rho^{(1)}$ (g/cm^3)	η (mPa.s)	x (-)
10	293.15	1.053	1.588	0.3427
20	293.15	1.061	1.740	0.3427
30	293.15	1.069	1.908	0.3427
40	293.15	1.076	2.088	0.3427
50	293.15	1.082	2.276	0.3427
60	293.15	1.089	2.472	0.3427
70	293.15	1.095	2.672	0.3427
80	293.15	1.100	2.878	0.3427
90	293.15	1.106	3.087	0.3427
100	293.15	1.111	3.301	0.3427
10	313.15	1.030	1.158	0.3427
20	313.15	1.039	1.262	0.3427
30	313.15	1.048	1.372	0.3427
40	313.15	1.055	1.486	0.3427
50	313.15	1.063	1.605	0.3427
60	313.15	1.070	1.730	0.3427
70	313.15	1.076	1.860	0.3427
80	313.15	1.082	1.997	0.3427
90	313.15	1.088	2.140	0.3427
100	313.15	1.094	2.289	0.3427
10	333.15	1.008	0.863	0.3427
20	333.15	1.018	0.936	0.3427
30	333.15	1.027	1.011	0.3427
40	333.15	1.036	1.086	0.3427
50	333.15	1.044	1.167	0.3427
60	333.15	1.051	1.249	0.3427
70	333.15	1.058	1.334	0.3427
80	333.15	1.065	1.421	0.3427

Table C.1 – Experimental viscosity values for x HFC-134a + (1-x) TriEGDME. $^{(1)}$ Densities have been estimated not measured.

p (MPa)	T (K)	$\rho^{(1)}$ (g/cm^3)	η (mPa.s)	x (-)
90	333.15	1.071	1.511	0.3427
100	333.15	1.077	1.603	0.3427
10	353.15	0.985	0.656	0.3427
20	353.15	0.997	0.715	0.3427
30	353.15	1.007	0.774	0.3427
40	353.15	1.016	0.835	0.3427
50	353.15	1.025	0.897	0.3427
60	353.15	1.033	0.960	0.3427
70	353.15	1.041	1.025	0.3427
80	353.15	1.048	1.091	0.3427
90	353.15	1.055	1.159	0.3427
100	353.15	1.061	1.228	0.3427
10	373.15	0.962	0.521	0.3427
20	373.15	0.975	0.570	0.3427
30	373.15	0.987	0.619	0.3427
40	373.15	0.997	0.670	0.3427
50	373.15	1.007	0.722	0.3427
60	373.15	1.016	0.775	0.3427
70	373.15	1.024	0.830	0.3427
80	373.15	1.032	0.886	0.3427
90	373.15	1.039	0.944	0.3427
100	373.15	1.046	1.003	0.3427
10	293.15	1.053	1.588	0.5940
20	293.15	1.061	1.740	0.5940
30	293.15	1.069	1.908	0.5940
40	293.15	1.076	2.088	0.5940
50	293.15	1.082	2.276	0.5940
60	293.15	1.089	2.472	0.5940
70	293.15	1.095	2.672	0.5940
80	293.15	1.100	2.878	0.5940
90	293.15	1.106	3.087	0.5940
100	293.15	1.111	3.301	0.5940
10	313.15	1.030	1.158	0.5940

Table C.1 – *Continued*

p (MPa)	T (K)	$\rho^{(1)}$ (g/cm^3)	η (mPa.s)	x (-)
20	313.15	1.039	1.262	0.5940
30	313.15	1.048	1.372	0.5940
40	313.15	1.055	1.486	0.5940
50	313.15	1.063	1.605	0.5940
60	313.15	1.070	1.730	0.5940
70	313.15	1.076	1.860	0.5940
80	313.15	1.082	1.997	0.5940
90	313.15	1.088	2.140	0.5940
100	313.15	1.094	2.289	0.5940
10	333.15	1.008	0.863	0.5940
20	333.15	1.018	0.936	0.5940
30	333.15	1.027	1.011	0.5940
40	333.15	1.036	1.088	0.5940
50	333.15	1.044	1.167	0.5940
60	333.15	1.051	1.249	0.5940
70	333.15	1.058	1.334	0.5940
80	333.15	1.065	1.421	0.5940
90	333.15	1.071	1.511	0.5940
100	333.15	1.077	1.603	0.5940
10	353.15	0.985	0.656	0.5940
20	353.15	0.997	0.715	0.5940
30	353.15	1.007	0.774	0.5940
40	353.15	1.016	0.835	0.5940
50	353.15	1.025	0.897	0.5940
60	353.15	1.033	0.960	0.5940
70	353.15	1.041	1.025	0.5940
80	353.15	1.048	1.091	0.5940
90	353.15	1.055	1.159	0.5940
100	353.15	1.061	1.228	0.5940
10	373.15	0.962	0.521	0.5940
20	373.15	0.975	0.570	0.5940
30	373.15	0.987	0.619	0.5940
40	373.15	0.997	0.670	0.5940

Table C.1 *Continued*

p (MPa)	T (K)	$\rho^{(1)}$ (g/cm^3)	η (mPa.s)	x (-)
50	373.15	1.007	0.722	0.5940
60	373.15	1.016	0.775	0.5940
70	373.15	1.024	0.830	0.5940
80	373.15	1.032	0.886	0.5940
90	373.15	1.039	0.944	0.5940
100	373.15	1.046	1.003	0.5940

Table C.1 – *Continued.*

C.2 – HFC-134a + TEGDME

p (MPa)	T (K)	$\rho^{(1)}$ (g/cm^3)	η (mPa.s)	x (-)
10	293.15	1.054	3.132	0.2769
20	293.15	1.061	3.378	0.2769
30	293.15	1.067	3.669	0.2769
40	293.15	1.074	3.992	0.2769
50	293.15	1.079	4.341	0.2769
60	293.15	1.085	4.710	0.2769
70	293.15	1.090	5.095	0.2769
80	293.15	1.095	5.495	0.2769
90	293.15	1.100	5.907	0.2769
100	293.15	1.105	6.329	0.2769
10	313.15	1.034	2.001	0.2769
20	313.15	1.041	2.197	0.2769
30	313.15	1.048	2.395	0.2769
40	313.15	1.055	2.601	0.2769
50	313.15	1.062	2.816	0.2769
60	313.15	1.068	3.043	0.2769
70	313.15	1.073	3.282	0.2769

Table C.2 – Experimental viscosity values for *x* HFC-134a + (1-*x*) TEGDME. (1) Densities have been estimated not measured.

p (MPa)	T (K)	$\rho^{(1)}$ (g/cm^3)	η (mPa.s)	x (-)
80	313.15	1.079	3.535	0.2769
90	313.15	1.084	3.803	0.2769
100	313.15	1.089	4.088	0.2769
10	333.15	1.013	1.406	0.2769
20	333.15	1.022	1.533	0.2769
30	333.15	1.030	1.664	0.2769
40	333.15	1.037	1.800	0.2769
50	333.15	1.044	1.941	0.2769
60	333.15	1.051	2.086	0.2769
70	333.15	1.057	2.236	0.2769
80	333.15	1.063	2.391	0.2769
90	333.15	1.068	2.549	0.2769
100	333.15	1.073	2.712	0.2769
10	353.15	0.993	1.038	0.2769
20	353.15	1.003	1.133	0.2769
30	353.15	1.011	1.229	0.2769
40	353.15	1.019	1.328	0.2769
50	353.15	1.027	1.431	0.2769
60	353.15	1.034	1.536	0.2769
70	353.15	1.041	1.653	0.2769
80	353.15	1.047	1.773	0.2769
90	353.15	1.053	1.900	0.2769
100	353.15	1.058	2.035	0.2769
10	373.15	0.973	0.832	0.2769
20	373.15	0.983	0.907	0.2769
30	373.15	0.993	0.986	0.2769
40	373.15	1.002	1.069	0.2769
50	373.15	1.010	1.156	0.2769
60	373.15	1.018	1.247	0.2769
70	373.15	1.025	1.342	0.2769
80	373.15	1.031	1.441	0.2769
90	373.15	1.037	1.545	0.2769
100	373.15	1.043	1.654	0.2769

Table C.2 *Continued*

p (MPa)	T (K)	$\rho^{(1)}$ (g/cm^3)	η (mPa.s)	x (-)
10	293.15	1.086	2.335	0.4433
20	293.15	1.095	2.537	0.4433
30	293.15	1.102	2.765	0.4433
40	293.15	1.109	3.014	0.4433
50	293.15	1.116	3.282	0.4433
60	293.15	1.122	3.568	0.4433
70	293.15	1.128	3.871	0.4433
80	293.15	1.134	4.191	0.4433
90	293.15	1.140	4.527	0.4433
100	293.15	1.145	4.877	0.4433
10	313.15	1.063	1.527	0.4433
20	313.15	1.072	1.674	0.4433
30	313.15	1.081	1.824	0.4433
40	313.15	1.089	1.978	0.4433
50	313.15	1.096	2.140	0.4433
60	313.15	1.103	2.310	0.4433
70	313.15	1.109	2.490	0.4433
80	313.15	1.116	2.680	0.4433
90	313.15	1.121	2.881	0.4433
100	313.15	1.127	3.094	0.4433
10	333.15	1.040	1.097	0.4433
20	333.15	1.050	1.195	0.4433
30	333.15	1.060	1.297	0.4433
40	333.15	1.068	1.402	0.4433
50	333.15	1.076	1.512	0.4433
60	333.15	1.084	1.624	0.4433
70	333.15	1.091	1.741	0.4433
80	333.15	1.098	1.861	0.4433
90	333.15	1.104	1.984	0.4433
100	333.15	1.110	2.111	0.4433
10	353.15	1.018	0.824	0.4433
20	353.15	1.029	0.908	0.4433
30	353.15	1.039	0.984	0.4433

Table C.2 Continued

p (MPa)	T (K)	$\rho^{(a)}$ (g/cm^3)	η (mPa.s)	x (-)
40	353.15	1.049	1.064	0.4433
50	353.15	1.057	1.147	0.4433
60	353.15	1.066	1.233	0.4433
70	353.15	1.073	1.323	0.4433
80	353.15	1.080	1.415	0.4433
90	353.15	1.087	1.510	0.4433
100	353.15	1.094	1.609	0.4433
10	373.15	0.994	0.662	0.4433
20	373.15	1.007	0.720	0.4433
30	373.15	1.018	0.783	0.4433
40	373.15	1.029	0.850	0.4433
50	373.15	1.038	0.921	0.4433
60	373.15	1.047	0.994	0.4433
70	373.15	1.055	1.069	0.4433
80	373.15	1.063	1.147	0.4433
90	373.15	1.070	1.226	0.4433
100	373.15	1.077	1.307	0.4433
10	293.15	1.135	1.514	0.6333
20	293.15	1.145	1.679	0.6333
30	293.15	1.155	1.851	0.6333
40	293.15	1.164	2.031	0.6333
50	293.15	1.172	2.219	0.6333
60	293.15	1.180	2.414	0.6333
70	293.15	1.188	2.617	0.6333
80	293.15	1.195	2.827	0.6333
90	293.15	1.201	3.045	0.6333
100	293.15	1.208	3.269	0.6333
10	313.15	1.107	1.046	0.6333
20	313.15	1.119	1.151	0.6333
30	313.15	1.130	1.260	0.6333
40	313.15	1.140	1.374	0.6333
50	313.15	1.149	1.493	0.6333
60	313.15	1.158	1.616	0.6333

Table C.2 – *Continued*

p (MPa)	T (K)	$\rho^{(1)}$ (g/cm^3)	η (mPa.s)	x (-)
70	313.15	1.166	1.745	0.6333
80	313.15	1.173	1.878	0.6333
90	313.15	1.181	2.016	0.6333
100	313.15	1.187	2.159	0.6333
10	333.15	1.078	0.724	0.6333
20	333.15	1.092	0.845	0.6333
30	333.15	1.105	0.922	0.6333
40	333.15	1.116	1.003	0.6333
50	333.15	1.126	1.087	0.6333
60	333.15	1.136	1.173	0.6333
70	333.15	1.144	1.260	0.6333
80	333.15	1.153	1.349	0.6333
90	333.15	1.160	1.438	0.6333
100	333.15	1.168	1.529	0.6333
10	353.15	1.050	0.609	0.6333
20	353.15	1.066	0.665	0.6333
30	353.15	1.080	0.725	0.6333
40	353.15	1.092	0.788	0.6333
50	353.15	1.103	0.854	0.6333
60	353.15	1.114	0.921	0.6333
70	353.15	1.123	0.990	0.6333
80	353.15	1.132	1.061	0.6333
90	353.15	1.141	1.132	0.6333
100	353.15	1.149	1.205	0.6333
10	373.15	1.020	0.471	0.6333
20	373.15	1.039	0.524	0.6333
30	373.15	1.055	0.577	0.6333
40	373.15	1.069	0.631	0.6333
50	373.15	1.081	0.685	0.6333
60	373.15	1.092	0.739	0.6333
70	373.15	1.103	0.794	0.6333
80	373.15	1.112	0.849	0.6333
90	373.15	1.121	0.904	0.6333

Table C.2 – Continued

p (MPa)	T (K)	$\rho^{(1)}$ (g/cm³)	η (mPa.s)	x (–)
100	373.15	1.130	0.960	0.6333
10	293.15	1.221	0.557	0.8797
20	293.15	1.241	0.613	0.8797
30	293.15	1.258	0.671	0.8797
40	293.15	1.274	0.733	0.8797
50	293.15	1.287	0.796	0.8797
60	293.15	1.300	0.863	0.8797
70	293.15	1.312	0.932	0.8797
80	293.15	1.323	1.003	0.8797
90	293.15	1.334	1.077	0.8797
100	293.15	1.343	1.154	0.8797
10	313.15	1.178	0.412	0.8797
20	313.15	1.202	0.460	0.8797
30	313.15	1.222	0.506	0.8797
40	313.15	1.240	0.553	0.8797
50	313.15	1.255	0.600	0.8797
60	313.15	1.269	0.647	0.8797
70	313.15	1.282	0.695	0.8797
80	313.15	1.294	0.744	0.8797
90	313.15	1.306	0.794	0.8797
100	313.15	1.316	0.845	0.8797
10	333.15	1.133	0.321	0.8797
20	333.15	1.162	0.364	0.8797
30	333.15	1.186	0.405	0.8797
40	333.15	1.206	0.444	0.8797
50	333.15	1.223	0.483	0.8797
60	333.15	1.239	0.522	0.8797
70	333.15	1.253	0.561	0.8797
80	333.15	1.266	0.600	0.8797
90	333.15	1.278	0.640	0.8797
100	333.15	1.290	0.681	0.8797
10	353.15	1.086	0.256	0.8797
20	353.15	1.121	0.299	0.8797

Table C.2 – *Continued*

p (MPa)	T (K)	$\rho^{(1)}$ (g/cm^3)	η (mPa.s)	x (-)
30	353.15	1.149	0.336	0.8797
40	353.15	1.172	0.370	0.8797
50	353.15	1.191	0.404	0.8797
60	353.15	1.209	0.436	0.8797
70	353.15	1.225	0.469	0.8797
80	353.15	1.239	0.501	0.8797
90	353.15	1.252	0.533	0.8797
100	353.15	1.264	0.565	0.8797
10	373.15	1.035	0.195	0.8797
20	373.15	1.079	0.234	0.8797
30	373.15	1.111	0.268	0.8797
40	373.15	1.138	0.300	0.8797
50	373.15	1.160	0.330	0.8797
60	373.15	1.179	0.360	0.8797
70	373.15	1.196	0.390	0.8797
80	373.15	1.211	0.419	0.8797
90	373.15	1.225	0.449	0.8797
100	373.15	1.238	0.478	0.8797

Table C.2 – *Continued*

Ada Villafáfila García

Measurement and Modeling of Scaling Minerals

ISBN: 87-91435-30-7

Measurement and Modelling of Scaling Minerals

Ada Villafáfila García

Ph.D. Thesis

31 August 2005

Department of Chemical Engineering
IVC-SEP
Technical University of Denmark
DK-2800 Kgs. Lyngby
Denmark

ISBN 87-91435-30-7

Printed by Book Partner,
Nørhaven Digital,
Copenhagen, Denmark

Preface

This thesis is submitted as partial fulfilment of the requirements for the Ph.D. degree at the Technical University of Denmark.

This work, granted by the IVC-SEP, has been carried out at the Department of Chemical Engineering at the Technical University of Denmark, from October 2002 to September 2005. Associated Professor Kaj Thomsen and Professor Erling H. Stenby have supervised the development of this Ph.D. study. I wish to express my sincere gratitude to my supervisors for their interest, support, quality advice and constructive reviews during these 3 years.

I would like to thank DONGs Jubilæumslegat for financial support for the experimental part of this Ph.D. project. I wish to express my sincere gratitude to Dr. Simon I. Andersen and to technician Povl V. Andersen for their constant help and support during the development of the experimental setup, and for their valuable ideas and challenges.

Special mention has to be made to the students Valerie Montel, who searched for some of the information about magnesite, and to Charlotte Coudert and Eduardo Ribeiro, who conducted many of the solubility measurements.

At the Technical University of Denmark, I need to thank all the staff working at IVC-SEP for creating such a nice environment, and especially to the Ph.D. students for their friendship.

I want to show a special mention to my parents, Gonzalo and Mercedes, for their love and support in all the moments of my life. Gracias por todo lo que habéis hecho por mí y por ser como sois. Os quiero.

And last, but not least, I would like to thank Diego for his love, patience, support and friendship during all these years in Denmark, and for making the most out of this experience. Gracias por compartir los mejores años de mi vida, por crear aquellas manos suaves como las uvas. Todo lo llenas tú, todo lo llenas.

Lyngby, September 2005

Ada
Villafáfila

Ada Villafáfila García

Summary

This Ph.D. project can be divided into two main sections. The first one, covering chapters 2 to 7, deals with the calculation of vapour-liquid, solid-liquid, and speciation equilibria for sparingly soluble salts found in natural waters, under hydrothermal conditions (up to 300ºC and 1000 bar). Chapters 8 and 9 focus on the experimental part of this dissertation, analyzing different experimental procedures to determine salt solubility at high temperature and pressure, and developing a setup to perform those measurements.

The motivation behind both parts of the Ph.D. project is the problem of scale formation found in many industrial processes, and especially in oilfield and geothermal operations. We want to contribute to the study of this problem by releasing a simple and accurate thermodynamic model capable of calculating the behaviour of scaling minerals, covering a wide range of temperature and pressure. Reliable experimental solubility measurements under conditions similar to those found in reality will help the development of strong and consistent models.

Chapter 1 is a short introduction to the problem of scale formation, the model chosen to study it, and the experiments performed.

Chapter 2 is focused on thermodynamics of the systems studied and on the calculation of vapour-liquid, solid-liquid, and speciation equilibria. The effects of both temperature and pressure on the solubility are addressed, and explanation of the model calculations is also given.

Chapter 3 presents the thermodynamic model used in this Ph.D. project. A review of alternative activity coefficient models an earlier work on scale formation is provided. A guideline to the parameter estimation procedure and the number of parameters estimated in the present work are also described.

The prediction of solid-liquid equilibrium of sulphate scaling minerals ($SrSO_4$, $BaSO_4$, $CaSO_4$ and $CaSO_4{\cdot}2H_2O$) at temperatures up to 300ºC and pressures up to 1000 bar is described in chapter 4. Results for the binary systems (M^{2+}, SO_4^{2-})-H_2O; the ternary systems (Na^+, M^{2+}, SO_4^{2-})-H_2O, and (Na^+, M^{2+}, Cl^-)-H_2O; and the quaternary systems (Na^+, M^{2+})(Cl^-, SO_4^{2-})-H_2O, are presented. M^{2+} stands for Ba^{2+}, Ca^{2+}, or Sr^{2+}.

Chapter 5 is devoted to the correlation and prediction of vapour-liquid-solid equilibria for different carbonate systems causing scale problems ($CaCO_3$, $BaCO_3$, $SrCO_3$, and $MgCO_3$), covering the temperature range from 0 to 250ºC and pressures up to 1000 bar. The solubility of CO_2 in pure water, and the solubility of CO_2 in solutions of different salts (NaCl and

Na_2SO_4) have also been correlated. Results for the binary systems MCO_3-H_2O, and CO_2-H_2O; the ternary systems MCO_3-CO_2-H_2O, CO_2-NaCl-H_2O, and CO_2-Na_2SO_4-H_2O; and the quaternary system CO_2-NaCl-Na_2SO_4-H_2O are given. M^{2+} stands for Ca^{2+}, Mg^{2+}, Ba^{2+}, and Sr^{2+}. This chapter also includes an analysis of the $CaCO_3$-$MgCO_3$-CO_2-H_2O system.

Chapter 6 deals with the system NaCl-H_2O. Available data for that system at high temperatures and/or pressures are addressed, and sodium chloride solubility calculations are performed up to 2000 bar.

Chapter 7 includes a validation of the model by comparing our predictions to data for real natural waters not used during the parameterization. A very good agreement between our predictions and the field observations is obtained, making us confident about the validity of the model, despite the high temperature, pressure and ionic strength of the tested systems.

In chapter 8, alternative experimental procedures to determine solubility at high temperature and pressure are introduced: Synthetic fluid inclusion technique, electrochemical technique, quartz crystal microbalances, and conductivity measurements.

Chapter 9 describes the experimental procedure followed and the setup employed to determine barite solubility in NaCl solutions at high temperature and pressure. The analytical technique chosen to determine Ba^{2+} concentrations (inductively coupled plasma mass spectrometry) is explained. Few experimental results for the systems NaCl-H_2O (used for validation) and $BaSO_4$-NaCl-H_2O are reported and analyzed.

Chapter 10 contains the conclusions of the Ph.D. project.

Resume på Dansk

Dette Ph.D. projekt kan inddeles i to hovedsektioner. Den første hovedsektion dækker kapitlerne 2 til 7 og handler om beregning af damp - væske, fast stof – væske og specieringsligevægte for tungt opløselige salte som findes i naturligt forekommende vand under hydrotermiske betingelser (op til 300ºC og 1000 bar). I kapitlerne 8 og 9 fokuseres der på den eksperimentelle del af denne afhandling. Her analyseres forskellige eksperimentelle metoder til bestemmelse af saltopløselighed ved høje temperaturer og tryk. Desuden beskrives udviklingen af en eksperimentel opstilling til at foretage disse målinger.

Motivationen bag begge dele af dette Ph.D. projekt er problemet med aflejring af mineraler fra vandige opløsninger. Det er et problem man møder i mange industrielle processer og ganske særligt inden for olieindvinding og indvinding af geotermisk energi. Vi ønsker at bidrage til studiet af dette problem ved at offentliggøre en simpel, men nøjagtig termodynamisk model der er i stand til at gengive faseforholdene for disse tungt opløselige salte i et bredt temperatur- og trykinterval. Gode eksperimentelle målinger under betingelser, der svarer til de naturlige hydrotermiske betingelser bidrager til at udvikle gode modeller.

Kapitel 1 er en kort introduktion til problemet med aflejring af mineraler samt modellen, der er valgt til at beskrive fænomenet og de eksperimenter, der er blevet udført.

Kapitel 2 fokuserer på den termodynamiske beskrivelse af de pågældende systemer, og på beregning af damp – væske, fast stof – væske og specieringsligevægte. Opløselighedens temperatur- og trykafhængighed beskrives og der gives forklaringer om modelberegningerne.

I kapitel 3 præsenteres den termodynamiske model, der bruges i dette Ph.D. projekt. Der gives et resume af alternative aktivitetskoefficientmodeller og tidligere arbejder om saltaflejringer. Metoden til at bestemme modelparametre beskrives og antallet af parametre diskuteres.

Forudsigelse af fast stof – væske ligevægt for tungt opløselige sulfatmineraler ($SrSO_4$, $BaSO_4$, $CaSO_4$ and $CaSO_4{\cdot}2H_2O$) ved temperaturer op til 300ºC and tryk op til 1000 bar beskrives i kapitel 4. Resultater for de binære systemer (M^{2+}, SO_4^{2-})-H_2O; de ternære systemer (Na^+, M^{2+}, SO_4^{2-})-H_2O, og (Na^+, M^{2+}, Cl^-)-H_2O; samt de kvaternære systemer (Na^+, M^{2+})(Cl^-, SO_4^{2-})-H_2O præsenteres. M^{2+} står for Ba^{2+}, Ca^{2+}, eller Sr^{2+}.

Kapitel 5 indeholder hovedsageligt beskrivelsen af arbejdet med at korrelere og forudsige damp – væske ligevægte for forskellige karbonat systemer, der forårsager problemer med mineraludfældning ($CaCO_3$, $BaCO_3$, $SrCO_3$, og $MgCO_3$). Korrelationen gælder temperaturintervallet fra 0 til 250ºC and tryk op til 1000 bar. Opløseligheden af CO_2 i rent vand og opløseligheden af CO_2 i forskellige saltopløsninger (NaCl and Na_2SO_4) er også omfattet af denne korrelation. Resultater for de binære systemer MCO_3-H_2O, og CO_2-H_2O; de ternære systemer MCO_3-CO_2-H_2O, CO_2-NaCl-H_2O, og CO_2-Na_2SO_4-H_2O; og det kvaternære system CO_2-NaCl-Na_2SO_4-H_2O rapporteres. M^{2+} står for Ca^{2+}, Mg^{2+}, Ba^{2+}, og Sr^{2+}. Dette kapitel omfatter også en analyse af $CaCO_3$-$MgCO_3$-CO_2-H_2O systemet.

Kapitel 6 drejer sig om NaCl-H_2O systemet. Data for dette system ved høje temperaturer og tryk rapporteres og natriumklorid opløseligheder beregnes op til 2000 bar.

I kapitel 7 valideres den udviklede model ved at sammenligne modelberegninger med data for naturligt forekommende vand, der ikke blev brugt til parameterbestemmelsen. Overensstemmelsen mellem vore forudsigelser og feltobservationerne er udmærket. Da opløsningerne fra disse feltobservationer har høj temperatur, højt tryk og høj ionstyrke styrker disse beregninger vor overbevisning om modellens gyldighed.

I kapitel 8 introduceres alternative eksperimentelle metoder til bestemmelse af opløseligheder ved høj temperatur og tryk: Synthetic fluid inclusion teknikken, den elektrokemiske teknik, metoder med anvendelse af quartz krystal microvægte og ledningsevnemålinger.

Kapitel 9 omhandler den eksperimentelle metode og opstilling der blev anvendt i dette projekt til bestemmelse af barit opløselighed i NaCl opløsninger ved høj temperatur og højt tryk. Den analytiske teknik der blev valgt til bestemmelse af Ba^{2+} koncentrationer (ICP-MS, Inductively Coupled Plasma Mass Spectrometry) forklares. Nogle få eksperimentelle resultater for systemerne NaCl-H_2O og $BaSO_4$-NaCl-H_2O rapporteres og analyseres.

Kapitel 10 indeholder konklusionerne, der kan drages af Ph.D. projektet.

Symbols

Symbol	
α	pressure parameter 1
β	pressure parameter 2
γ	activity coefficient
Δ_r^0	standard change in a chemical reaction
μ	chemical potential
ν	stoichiometric coefficient / kinematic viscosity
ϕ	fugacity coefficient / volume fraction
κ	partial molal compressibility
κ	isothermal compressibility
Φ	osmotic coefficient
Θ	constant (200 K) in equation 2-33 / constant (228 K) in equation aI-2
θ	surface area fraction
Ψ	fraction given in equation 3-6 / constant (2600 bar) in equation aI-2
ω	rotational speed
r	volume parameter
q	surface area parameter
u	interaction energy parameter
a	activity
f	fugacity
A	Debye-Hückel parameter / area
b	Debye-Hückel constant
F	Faraday's constant / frequency
N_A	Avogadro's number
N	harmonic
ε_0	vacuum permitivity
d / ρ	density
D	dielectric constant / diffusion coefficient
i_L	limiting current
C	concentration in mol dm^{-3}
	constant (41.84 bar cm3 cal^{-1}) in equation aI-2
c	stiffness
I	ionic stregth
G	Gibbs free energy
H	enthalpy
S	entropy
$H_{i,j}$	Henry's constant of species i in solvent j
C_p	heat capacity
K_e	equilibrium constant
P	pressure
P_0	reference pressure

Symbol	
R	gas constant
s	solubility
T	temperature
T_0	reference temperature
V	partial molar volume
V	volume
x	mole fraction in the liquid phase
y	mole fraction in the vapour phase
M	molar mass / molarity
m	molality
z	coordination number / ionic charge
w	Born coefficient
$\mathring{a}$	ion size parameter in Helgeson's approach
a, b, c, d, e	used in equation 2-42, explained in equation 2-43
$a_{1,j}, a_{2,j}, a_{3,j}, a_{4,j}$	Helgeson's coefficients (equation aI-2)
$c_{1,j}, c_{2,j}$	Helgeson's coefficients (equation aI-2)
b_{il}, b_{ni}, b_{nl}	short-range interaction parameters in Helgeson's approach
Z, Q, Y	solvent Born functions in Helgeson's approach
Γ_γ	mole fraction-molality conversion factor
M^{2+}	Ba^{2+}, Ca^{2+}, Sr^{2+}, Mg^{2+}
F	objective function
SD	standard deviation
ASD	average standard deviation
AAD	average absolute deviation
$MAAD$	mean average absolute deviation
RD	residual deviation
CV	variation coefficient
$ndata$	number of data
n	number of moles
l	liquid phase
g	vapor phase
C_{p1}, C_{p2}, C_{p3}	heat capacity coefficients
superscripts	
0	pure component standard state
$*$	solute standard state (mole fraction)
E	excess
IG	ideal gas
∞	infinite dilution
sat	saturation
m	molality scale
subscripts	
w	water
l	liquid phase
c	crystalline

subscripts	
g	vapour phase
dis	disolution reaction
m	molality scale
$calc$	calculated
exp	experimental
f	formation
r	reaction
q	quartz crystal

1. Introduction

The present Ph.D. project covers both modelling and experimental determinations of the solubility of scaling minerals in natural waters under hydrothermal conditions, in connection with the problem of scale formation. This chapter gives a general introduction to the problem of scale formation, to the model used to estimate the solubility behaviour of scaling minerals, and to the experimental setup developed to determine salt solubility at high temperature and pressure.

1.1 Scale Formation

Scale formation is a common problem in many industrial processes, such as the production of oil (Shams El Din and Mohammed, 1989, Yuan et al., 1994, 1997, Sorbie and Mackay, 2000, Dyer and Graham, 2002) and the production of geothermal energy (Arnorsson, 1989, Gill, 1998, Potapov et al., 2001). It can be defined as hard adherent mineral deposits that precipitate from brine solution. The amount and location of scale depends on different factors, such as the degree of supersaturation, kinetics, solution pH and composition, CO_2 content, temperature and pressure.

In the reservoir, the natural water is in equilibrium with its surroundings at ambient temperature and pressure. As the brine flows up through the well, both temperature and pressure decrease considerably and the equilibrium is disturbed. This will generally lead to solid-phase deposition (Atkinson et al., 1991). The formation of carbonate scale is mainly associated with the pressure and pH changes of the production fluid, while the occurrence of sulphate scale is mainly due to the mixing of incompatible brines.

Carbon dioxide is generally present in large amounts in geothermal and oilfield fluids at reservoir temperature and pressure conditions. The decrease of pressure during the flow path reduces considerably the solubility of carbonate minerals, leading in some cases to the deposit of solid minerals ($CaCO_3$, $MgCO_3$, $BaCO_3$, $SrCO_3$) in the inner wall of the pipe. From all the carbonate minerals, calcite ($CaCO_3$) seems to be the most likely to precipitate (Wat et al., 1992). The most commonly found carbonate scales in the oil industry are the salts of calcium, barium, and strontium (Li et al., 1995). Dyer and Graham (2002) also added magnesium carbonates to that list.

In offshore oilfield developments, mixing of incompatible waters due to water flooding is the main cause of sulphate scale formation. Two waters are incompatible if they interact chemically and precipitate minerals when mixed. When sulphate-rich injection water (often seawater) is mixed with the Ba^{2+}, Ca^{2+} and Sr^{2+}- rich formation water, it is very likely that barite ($BaSO_4$), celestite ($SrSO_4$), gypsum ($CaSO_4{\cdot}2H_2O$) and/or anhydrite ($CaSO_4$) precipitation takes place (Sorbie and Mackay, 2000).

Mineral scale deposition causes serious damage in utilization systems and reduces the flow area. Therefore, the production rate (and the re-injection capacity) drops down, with the consequent economical loss: BP looses around 4 million bbls per year in the North Sea (Graham and Mackay, 2003). The cross section decrease caused by solid deposition onto the inner wall of a pipe is shown in figure 1-1. In some cases, the choke of the flow line is so large that the well needs to be closed (Zhang et al., 2001). Scaling can also cause safety problems due to blockage and failure of valves (Graham and Mackay, 2003). According to Dyer and Graham (2002), the future expectations in the oil field in the North Sea are even more alarming, due to the recent development of reservoirs with a very large salinity (total dissolved solids around 300000 ppm), high temperature (more than 175°C) and high pressure (800-1000 bar) (Eastern Trough Area Project, ETAP).

Figure 1-1. Scale formation in a pipe.

In the geothermal field, mineral deposition limits the degree of utilization of geothermal energy. Geothermal energy has many advantages (it is renewable, clean, safe and flexible) but it is necessary to minimize operation costs in order to make its production competitive with other energy resources.

1.2 Thermodynamic Model

Scale prevention is technically and economically more effective than redissolution once scale has formed. One essential step in scale prevention is scale prediction. Unfortunately, that is a difficult task because the thermodynamics of brines is a sensitive function of their composition, temperature and pressure. These variables change considerably during the flow path of the fluid and can also vary significantly from well to well (even within the same resource area). Moreover, they can change in a single well over the lifetime of the resource. Therefore, effective prediction of the scaling tendency requires a reliable thermodynamic model. In this Ph.D. project we have focused on the prediction of mineral solubility in natural waters under conditions of varying brine composition, temperature and pressure.

The majority of the programs (He and Morse, 1992, Møller et al., 1998, Zhenhao et al., 1996) employed to predict scale tendency use the framework provided by Pitzer (1991). For multicomponent solutions, Pitzer's approach requires both binary and ternary parameters and thus both binary and ternary experimental data for all the species in the mixture. Unfortunately, such data are not available for some systems of importance in natural waters, and are especially scarce at the high temperature and pressure conditions we are dealing with. In many cases the quantity and quality of experimental data do not justify the use of many parameters. Clearly, a method requiring limited amount of data but leading to accurate predictions for the solid-liquid-vapour equilibrium and crystallization processes for electrolyte solutions would be of great use. This is the case of the extended UNIQUAC model, which is the thermodynamic model selected in the present work to determine the aqueous-phase activity coefficients, while the vapour-phase fugacities are determined by the Soave-Redlich-Kwong (SRK) cubic equation of state.

The extended UNIQUAC model is capable of accurately representing multicomponent systems with common ions, covering a range of temperature and ionic strength large enough to represent the conditions found in geothermal and oil production wells. Using this approach, the number of parameters is considerably lower than the number of parameters required by Pitzer's model (only two parameters per species plus two parameters per species pair are required by the extended UNIQUAC model). At the same time, the temperature dependency is accounted for in the model equations, avoiding the introduction of a new set of parameters. Two additional parameters have been added to the model presented by Thomsen and Rasmussen (1999), in order to account for the pressure dependency. The results obtained through this modification are very satisfactory in the pressure range investigated (1 to 1000 bar).

This work presents the results obtained for some of the major species present in natural waters and some of the most problematic scaling minerals found in oilfield and geothermal operations ($BaSO_4$, $SrSO_4$, $CaSO_4$, $CaSO_4 \cdot 2H_2O$, $CaCO_3$, $BaCO_3$, $SrCO_3$, $MgCO_3$). Parameters for the system CO_2-Na-H-Ca-Mg-Ba-Sr-OH-Cl-SO_4-CO_3-HCO_3 have been estimated on the basis of available experimental SLE data.

1.3 Experimental Determination of Solubilities

There is a general lack of data on the solubility of most of the scaling minerals in water and in NaCl solutions, especially at high temperatures and pressures. Some of the available data are inconsistent, and most of the published data only cover a narrow range of low temperature (around 25ºC) and NaCl concentration, and are measured at atmospheric pressure. The use of such data can lead to weak models and inaccurate predictions. The few sources dealing with high temperature and pressure cannot be cross-checked due to the different conditions measured. Therefore, a larger databank is necessary to understand and predict the causes of precipitation and dissolution of scaling minerals in nature.

During this Ph.D. project, an experimental setup has been developed in order to determine barite solubility in the ternary system NaCl-$BaSO_4$-H_2O from very diluted solutions to the saturation point. The setup can cover the temperature range from room conditions up to 300ºC, and pressures up to 10000 psi.

1.4 References in Chapter 1

Arnorsson, E., 1989. Deposition of calcium carbonate minerals from geothermal waters. Theoretical considerations. Geothermics 18, 33-39.

Atkinson, G., Oklahoma, U., Raju, K., Aramco, S., Howell R.D., 1991. The thermodynamics of scale prediction. SPE 21021, 209-215.

Dyer, S.J., Graham, G.M., 2002. The effect of temperature and pressure on oilfield scale formation. Journal of Petroleum Science and Engineering 35, 95-107.

Gill, J.S., 1998. Silica scale control. Chemical Treatment, 41-45.

Graham, G.M., Mackay, E.J., 2003. A background to inorganic scaling-mechanisms, formation and control. 5th Intl. SPE Oilfield Scale Symposium. Aberdeen, UK.

He, S., Morse, J.W., 1992. Prediction of halite, gypsum, and anhydrite solubility in natural brines under subsurface conditions. Computer & Geosciences 19, 1-22.

Li, Y.H., Crane, S.D., Coleman, J. R., 1995. Novel approach to predict the co-precipitation of $BaSO_4$ and $SrSO_4$. SPE 29489, 447-461.

Møller, N., Greenberg, J.P., Weare, J.H., 1998. Computer modelling for geothermal systems: Predicting carbonate and silica scale formation, CO_2 breakout and H_2S exchange. Transport in Porous Media 33, 173-204.

Pitzer, K.S., 1991. Activity coefficients in electrolyte solutions, 2nd edition. CRC Press, Boca Raton, pp. 293-422.

Potapov, V.V., Kashpura, V.N., Alekseev, V.I., 2001. A study of the growth of deposits in geothermal power systems. Thermal Engineering 48 (5), 395-400.

Shams El Din, A.M., Mohammed, R.A., 1989. The problem of alkaline scale formation from a study on Arabian Gulf water. Desalination 71, 313-324.

Sorbie, K.S., Mackay, E.J., 2000. Mixing of injected, connate and aquifer brines in water flooding and its relevance to oilfield scaling. Journal of Petroleum Science and Engineering 27, 85-106.

Thomsen, K., Rasmussen, P., 1999. Modeling of vapor-liquid-solid equilibrium in gas-aqueous electrolyte systems. Chemical Engineering Science 54, 1787-1802.

Wat, R.M.S., Sorbie, K.S., Todd, A.C., Chen, P., Jiang, P., 1992. Kinetics of $BaSO_4$ crystal growth and effect in formation damage. SPE 23814, 429-437.

Yuan, M., Todd, A.C., Sorbie, K.S., 1994. Sulfate scale precipitation arising from seawater injection: a prediction study. Marine and Petroleum Geology 11(1), 24-30.

Yuan, M.D., Anderson, M., Jamieson, E., 1997. Investigation and improvement of $BaSO_4$ scale inhibition tests. Society of Petroleum Engineers 37304, 765-768.

Zhang, Y., Shaw, H., Farquhar, R., Dawe, R., 2001. The kinetics of carbonate scaling-application for the prediction of downhole carbonate scaling. Journal of Petroleum Science and Engineering 29, 85-95.

Zhenhao, D., Møller, N., DeRocher, T., Weare, J.H., 1996. Prediction of boiling, scaling and formation conditions in geothermal reservoirs using computer programs. Geothermics 25 (6), 663-678.

2. Thermodynamics

This chapter is intended to explain the thermodynamic basis needed to describe solubility phenomena and calculate solid-liquid, vapour-liquid, and speciation equilibria at various temperatures and pressures.

The condition for chemical equilibrium for a species B at a given temperature T and pressure P in the phases α and β is that the chemical potential of B be equal in the two phases:

$$\mu_B^\alpha(T,P,\mathbf{n}^\alpha) = \mu_B^\beta(T,P,\mathbf{n}^\beta) \tag{2-1}$$

where **n** represents the concentrations of the different components in the system and μ_B the chemical potential of B. If more than two phases are present, equation 2-1 is extended to all of them. The chemical potential of component B is the sum of the standard state chemical potential and a concentration dependent term which is calculated in this work by means of the extended UNIQUAC model.

2.1 Standard States

The standard state for solid phases is the pure crystalline component at the system temperature and pressure.

The standard state for vapour species is the pure ideal gas at the reference pressure P_0 (chosen to be 1 bar) and the temperature of the system.

For the liquid phase, two different standard states are used, one for the solvent and another for the ions and molecules. The symmetric convention is used for water, while the unsymmetric convention based on mole fraction is used for all other species.

The chemical potential of water can be written as

$$\mu_w = \mu_w^0 + RT\ln a_w = \mu_w^0 + RT\ln(\gamma_w x_w) \tag{2-2}$$

In equation 2-2, μ_w^0 is the standard state chemical potential of water, which is the chemical potential of pure liquid water at the system temperature and pressure, a_w is the water activity, R is the gas constant (8.314 J mol^{-1} K^{-1}), T is the system temperature in Kelvin, x_w is the mole fraction of water, and γ_w is the symmetric water activity coefficient. According to the symmetric convention, the activity coefficient of water is unity in the pure component state at all temperatures ($\gamma_w \to 1$ as $x_w \to 1$).

For aqueous solutions, the osmotic coefficient (Φ) is usually used as a measure for the activity of water.

$$\Phi = -\frac{\ln a_w}{M_w \sum_j \nu_{Bj} m_{Bj}} \qquad \textbf{(2-3)}$$

where M_w is the molar mass of water in kg mol^{-1}, m_B is the molality of salt B, which dissociates into ν_{Bj} moles of ions per mol of salt.

The chemical potential of ion *i* (or any solute *i*) can be written as

$$\mu_i = \mu_i^* + RT\ln(\gamma_i^* x_i) \qquad \textbf{(2-4)}$$

where μ_i^* is the standard state chemical potential of ion *i* based on the unsymmetrical convention and mole fraction scale, at the system temperature and pressure. γ_i^* is the rational unsymmetric activity coefficient for ion *i*, where $\gamma_i^* \rightarrow 1$ as $\sum x_i \rightarrow 0$. The standard state is the pure component standard state normalized so that solute activity coefficients are equal to unity at infinite dilution.

The unsymmetric activity coefficient can be calculated from the symmetric activity coefficient and the symmetric activity coefficient at infinite dilution (γ^∞):

$$\gamma_i^* = \frac{\gamma_i}{\gamma_i^\infty} \qquad \textbf{(2-5)}$$

2.2 Vapour-Liquid Equilibrium

Equilibrium is reached when equation 2-1 is fulfilled for all the components and phases of a system. For a volatile component as H_2O, the vapour-liquid equilibrium (VLE) is represented as

$$H_2O\ (l) \leftrightarrow H_2O\ (g) \qquad \textbf{(2-6)}$$

And equation 2-1 becomes

$$\mu_{w,l} = \mu_{w,g} \qquad \textbf{(2-7)}$$

where the subscripts *l* and *g* refer to liquid and vapour phases, respectively.

For the liquid phase, the chemical potentials of water and CO_2 are given by equations 2-2 and 2-4, respectively.

The chemical potential of the volatile component *i* (water, carbon dioxide) in the vapour phase can be calculated as

$$\mu_{i,g} = \mu_i^{IG} + RT \ln \frac{\hat{f}_{i,g}}{P_0} \tag{2-8}$$

where μ_i^{IG} is the chemical potential of component *i* in the standard state, P_0 is the reference pressure (1 bar), and $\hat{f}_{i,g}$ is the fugacity of component *i* in the gas phase at the temperature and pressure of the system, which can be written as

$$\hat{f}_{i,g} = y_i \hat{\phi}_{i,g} P \tag{2-9}$$

where y_i refers to the mole fraction of component *i* in the gas phase, *P* is the total pressure, and $\hat{\phi}_{i,g}$ is the fugacity coefficient for component *i* in the gas phase, calculated in this work from the Soave-Redlich-Kwong (SRK) cubic equation of state. For sufficiently low pressures, the fugacity coefficient is close to unity, and the fugacity of species *i* can be assimilated to the partial pressure of that component.

By combining equations 2-2, 2-7, 2-8 and 2-9, the condition 2-1 for equilibrium between vapour and liquid can be written:

$$\mu_w^0 + RT \ln x_w \gamma_w = \mu_w^{IG} + RT \ln \frac{y_w \hat{\phi}_{w,g} P}{P_0} \tag{2-10}$$

and the vapour-liquid equilibrium equation for water can be expressed as:

$$\ln \frac{y_w \hat{\phi}_{w,g} P}{x_w \gamma_w P_0} = \frac{\mu_w^0 - \mu_w^{IG}}{RT} \tag{2-11}$$

The approach used in equation 2-11 requires the chemical potentials of liquid (μ_w^0) and vapour (μ_w^{IG}). These potentials are not available at temperatures above the critical. For this reason, a different approach using the Henry's constant and a Poynting correction is chosen for CO_2.

The fugacity of a component *i* in the liquid phase can be calculated as

$$\hat{f}_{i,l} = H_{i,j} \gamma_i^* x_i \tag{2-12}$$

where $H_{i,j}$ is the Henry's law constant of component *i* in solvent *j*. It is defined as

$$H_{i,j} = \lim_{x_i \to 0} \left(\frac{\hat{f}_{i,l}}{\gamma_i^* x_i} \right)_{T,P,n_{j \neq i}} \tag{2-13}$$

The dependency of fugacity with pressure is given from classical thermodynamics as

$$\left(\frac{\partial \ln \hat{f}_i}{\partial P}\right)_{T,n} = \frac{\overline{V}_i}{RT} \qquad \textbf{(2-14)}$$

where $\overline{V}_i$ is the partial molar volume of component *i*. Integrating equation 2-14 from a reference pressure P_0 to pressure *P*:

$$\hat{f}_{i,l,P} = \hat{f}_{i,l,P_0} \cdot \exp\left(\frac{\overline{V}_i (P - P_0)}{RT}\right) \qquad \textbf{(2-15)}$$

Inserting the definition of fugacity given by equation 2-12 into equation 2-15:

$$\hat{f}_{i,l,P} = H_{i,j,P_0} \gamma_i^* x_i \cdot \exp\left(\frac{\overline{V}_i (P - P_0)}{RT}\right) \qquad \textbf{(2-16)}$$

Inserting equation 2-16 in the definition of the Henry's law constant (equation 2-13), the dependency with pressure is obtained:

$$H_{i,j} = \lim_{x_i \to 0}\left[\frac{\hat{f}_{i,l,P_0}}{x_i} \exp\left(\frac{\overline{V}_i (P - P_0)}{RT}\right)\right]_{P,T,n_{i \neq j}} \qquad \textbf{(2-17)}$$

At infinite dilution ($x_i \to 0$), the total pressure is the saturation pressure of the solvent, and equation 2-17 may be rewritten as

$$H_{i,j} = H_{i,j,P_j^{sat}} \cdot \exp\left(\frac{\overline{V}_i^* (P - P_j^{sat})}{RT}\right) \qquad \textbf{(2-18)}$$

and the Krichevsky-Ilinskaya equation is obtained

$$\hat{f}_{i,l} = H_{i,j,P_j^{sat}} \gamma_i^* x_i \cdot \exp\left(\frac{\overline{V}_i^* (P - P_j^{sat})}{RT}\right) \qquad \textbf{(2-19)}$$

At equilibrium, the isofugacity criteria must be fulfilled, and

$$\ln(y_i \hat{\phi}_i P) = \ln\left[H_{i,j,P_j^{sat}} \gamma_i^* x_i \cdot \exp\left(\frac{\overline{V}_i^* (P - P_j^{sat})}{RT}\right)\right] \qquad \textbf{(2-20)}$$

Rearranging equation 2-20, the vapour-liquid equilibrium equation for CO_2 can therefore be written as:

$$\ln \frac{y_{CO_2} \hat{\phi}_{CO_2,g} P}{x_{CO_2} \gamma_{CO_2}^*} = \frac{\overline{V}_{CO_2}^* (P - P_w^{sat})}{RT} + \ln H_{CO_2} \qquad \textbf{(2-21)}$$

The fugacity coefficients for both H_2O (g) and CO_2 (g) are calculated by the cubic SRK equation of state using classical mixing rules. The Henry's constant for carbon dioxide in water (H_{CO_2}) is calculated according to Rumpf and Maurer (1993):

$$\ln H_{CO_2} = 192.876 - \frac{9624.4}{T} + 1.441 \cdot 10^{-2} T - 28.749 \ln T \qquad \textbf{(2-22)}$$

where T is the temperature in Kelvin and H_{CO_2} is given in MPa·mol^{-1}·kg. Equation 2-22 is based on molality scale, so the Henry's law constant value is converted to mole fraction scale before using it. The empirical correlation 2-22 was based on selected literature data for the solubility of carbon dioxide in pure water. The temperature range of applicability of equation 2-22 is from 0 to 200°C. Nevertheless, we applied equation 2-22 up to 250°C obtaining very satisfactory results. The standard state partial molar volume used for calculating the Poynting correction follows a temperature dependency as indicated in equation 2-23 (Rumpf and Maurer, 1993)

$$\overline{V}^*_{CO_2} = 77.83350021 - 327.8959231 \cdot 10^{-3} T + 594.8558514 \cdot 10^{-6} T^2 \qquad \textbf{(2-23)}$$

In equation 2-23 T is the temperature in Kelvin and $\overline{V}^*_{CO_2}$ is given in cm^3·mol^{-1}.

2.3 Solid-Liquid Equilibrium

For a mineral $M_{\nu_M} X_{\nu_X} nH_2O$ consisting of ν_M cations M, ν_X anions X and n molecules of H_2O, the solid-liquid equilibrium can be expressed as

$$M_{\nu_M} X_{\nu_X} nH_2O\,(c) \Leftrightarrow \nu_M M^{zM+}\,(aq) + \nu_X X^{zX-}\,(aq) + nH_2O\,(l) \qquad \textbf{. (2-24)}$$

The condition for equilibrium, corresponding to equation 2-1, is:

$$\mu_{M_{\nu M} X_{\nu X} nH_2O(c)} = \nu_M \mu_{M^{ZM+}(aq)} + \nu_X \mu_{X^{ZX-}(aq)} + n\mu_w \qquad \textbf{(2-25)}$$

Using the previous definitions for the chemical potentials (equations 2-2 and 2-4), equation 2-25 can be rewritten as

$$(\gamma^*_{M^{ZM+}} x_{M^{ZM+}})^{\nu_M} (\gamma^*_{X^{ZX-}} x_{X^{ZX-}})^{\nu_X} a_w^n = \exp\left(- \frac{\nu_M \mu^*_{M^{ZM+}} + \nu_X \mu^*_{X^{ZX-}} + n\mu^0_w - \mu^0_{M_{\nu M} X_{\nu X} \cdot nH_2O}}{RT} \right) \qquad \textbf{(2-26)}$$

The chemical potential of the salt $M_{\nu_M} X_{\nu_X} nH_2O$ is equal to its standard state chemical potential since the solid salt is in its standard state: Pure crystalline component at the system temperature and pressure.

The left hand side of equation 2-26 is the solubility product (K_e) of the salt $M_{\nu_M} X_{\nu_X} nH_2O$. The numerical value of K_e can be calculated from the right hand side of equation 2-26 Solid-liquid equilibrium calculation reduces to the solution of equation 2-26 to obtain the composition of the liquid phase in equilibrium with the solid phase(s). The concentrations on the left-hand side of equation 2-26 can then be adjusted by iteration until the activity product yields the desired value. Therefore, to predict solid-liquid equilibrium, a model for activity coefficients in mixed electrolyte solutions is needed, together with the knowledge of the thermodynamic solubility products of all the possible solid phases formed in the system under consideration, at the system temperature and pressure.

2.4 Speciation Equilibrium

Dissociation equilibrium can be derived in an analogous manner as described for solid-liquid equilibrium. The hydrogen carbonate ion dissociates following reaction 2-27.

$$HCO_3^- \ (aq) \leftrightarrow CO_3^{2-} \ (aq) + H^+ \ (aq) \tag{2-27}$$

Applying the definition of the chemical potential for ions given in equation 2-4 a similar expression to equation 2-26 is obtained:

$$\frac{x_{CO_3^{2-}} \cdot \gamma^*_{CO_3^{2-}} \cdot x_{H^+} \cdot \gamma^*_{H^+}}{x_{HCO_3^-} \cdot \gamma^*_{HCO_3^-}} = \exp\left(-\frac{\mu^*_{CO_3^{2-}} + \mu^*_{H^+} - \mu^*_{HCO_3^-}}{RT} \right) \tag{2-28}$$

Equations 2-26 and 2-28 can be written in a more general way as

$$K_{e,j} = \exp\left(-\frac{\Delta_r G_j^0}{RT} \right) = \prod_i (x_i \gamma_i)^{\nu_{i,j}} \tag{2-29}$$

where $\Delta_r G_j^0$ is the change in standard state Gibbs free energy for equilibrium j at the temperature T and pressure P, and $\nu_{i,j}$ is the stoichiometric coefficient of species i in equilibrium j.

2.5 Standard State Chemical Potentials

Standard state chemical potentials are required by the extended UNIQUAC model in order to perform calculations. These properties can be found at 25ºC and 1 bar in different data compilations (i.e., NIST, 1990). The standard state for solutes reported in thermodynamic tables is based on the hypothetical ideal unit mean molal solution ($\mu_i^{*,m}$). These values in the molality scale are converted by equation 2-30 to the mole fraction scale prior to their use by the model.

$$\mu_i^* = \mu_i^{*,m} - RT \ln M_w \quad \textbf{(2-30)}$$

When the standard state chemical potentials are not available in literature (as it is the case for $Na_2SO_4 \cdot CaSO_4$ or $BaSO_4 \cdot SrSO_4$, among others) they can be fitted to experimental solubility data.

2.6 Temperature Effect on Solubility

Values for the standard state Gibbs free energy at temperatures other than 25ºC can be calculated using the Gibbs-Helmholtz equation

$$\left[\frac{\partial\left(\Delta_r G^0 / RT\right)}{\partial T}\right]_P = -\frac{\Delta_r H^0}{RT^2} \quad \textbf{(2-31)}$$

The change in standard state enthalpy ($\Delta_r H^0$) by the equilibrium is temperature dependent:

$$\left[\frac{\partial \Delta_r H^0}{\partial T}\right]_P = \Delta_r C_p^0 \quad \textbf{(2-32)}$$

where $\Delta_r C_p^0$ is the variation in standard state heat capacity due to the reaction. For pure crystalline salts, the standard state heat capacity is often nearly constant in a wide temperature range. For ions, on the other hand, the standard state heat capacity cannot be considered temperature independent. It can be eventually calculated by the correlation (Thomsen et al., 1996):

$$C_{pi}^* = C_{p1,i} + C_{p2,i} T + \frac{C_{p3,i}}{T - \Theta} \quad \textbf{(2-33)}$$

where Θ is a constant equal to 200 K. The parameters $C_{p1,i}$, $C_{p2,i}$, and $C_{p3,i}$ can be fitted to experimental heat capacity data or can be taken from data compilations (Kelley, 1960). The standard state heat capacity at 25°C can also be found in data compilations.

2.7 Pressure Effect on Solid-Liquid Equilibrium

The saturation concentration of a salt can be calculated from equation 2-29. According to equation 2-29, this saturation concentration is a function of the solubility product and the activity coefficients of the ions of the salt. The solubility product and the activity coefficients are temperature and pressure dependent (the activity coefficients are composition dependent as well). Therefore, in order to estimate scale formation in a well (where pressure changes with depth) the pressure effect on solubility (and thus on the solubility product and activity coefficients) must be taken into consideration.

2.7.1 Pressure Dependence of the Solubility Product

The derivative of K_e with respect to pressure at constant temperature is expressed as

$$\left(\frac{\partial \ln K_e}{\partial P}\right)_T = -\frac{\Delta \overline{V}_{dis}}{RT} \qquad \textbf{(2-34)}$$

where $\Delta \overline{V}_{dis}$ is the increment in standard partial molar volume for a mineral dissolution reaction. For example, for the dissolution reaction $\mathrm{BaSO_4(c)} \Leftrightarrow \mathrm{Ba^{2+}} + \mathrm{SO_4^{2-}}$:

$$\Delta \overline{V}_{dis} = \overline{V}^{*}_{Ba^{2+}} + \overline{V}^{*}_{SO_4^{2-}} - V^{0}_{BaSO_4} \qquad \textbf{(2-35)}$$

The isothermal compressibility is defined as

$$\kappa = -\frac{1}{V}\left(\frac{\partial V}{\partial P}\right)_T \qquad \textbf{(2-36)}$$

The partial molar compressibility of component *i* is defined as

$$\overline{\kappa}_i = -\left(\frac{\partial \overline{V}_i}{\partial P}\right)_T \qquad \textbf{(2-37)}$$

and for the dissolution reaction 2-35:

$$\left(\frac{\partial \Delta \overline{V}_{dis}}{\partial P}\right)_T = -\Delta \overline{\kappa}_{dis} \qquad \textbf{(2-38)}$$

where $\Delta \overline{V}_{dis}$ is defined in equation 2-35 and $\Delta \overline{\kappa}_{dis}$ is the corresponding change in standard partial molar compressibility.

The change in standard partial molar compressibility is considered pressure independent in this work.

Integrating equation 2-34, the correction required to account for the pressure dependency of the solubility product (and therefore, of the standard state chemical potentials of the different species taking place in the dissolution reaction) is obtained:

$$\ln K_{e,P} = \ln K_{e,P_0} - \frac{\Delta \overline{V}_{dis,P_0}}{RT}(P-P_0) + \frac{\Delta \overline{\kappa}_{dis}}{2RT}(P-P_0)^2 \qquad \textbf{(2-39)}$$

2.7.2 Pressure Dependence of Activity Coefficients

The pressure effect on the activity coefficient of species *i* at constant temperature *T* is described by the thermodynamic relation

$$\left(\frac{\partial \ln \gamma_i}{\partial P}\right)_{T,\mathrm{n}} = \frac{\overline{V}_i^E}{RT} \tag{2-40}$$

where $\overline{V}_i^E$ is the excess partial molar volume of component *i*.

Equation 2-40 is valid for water and ions (symmetric and unsymmetric standard states). Integrating equation 2-40, the pressure effect on the activity coefficient is obtained as

$$\ln \gamma_{i,P} = \ln \gamma_{i,P_0} + \frac{\overline{V}_{i,P_0}^E}{RT}(P-P_0) - \frac{\overline{\kappa}_i^E}{2RT}(P-P_0)^2 \tag{2-41}$$

By substituting equation 2-39 and equation 2-41 into equation 2-29 the following relation is obtained:

$$\ln K_{e,P} = \ln K_{e,P_0} - a(P-P_0) + b(P-P_0)^2 = c + \sum_{i=1}^{m} \nu_i \left[\ln \gamma_{i,P_0} + d(P-P_0) - e(P-P_0)^2\right] \tag{2-42}$$

where

$$a = \frac{\Delta \overline{V}_{dis,P_0}}{RT}$$
$$b = \frac{\Delta \overline{\kappa}_{dis}}{2RT}$$
$$c = \sum_{i=1}^{m} \nu_i \ln x_i \tag{2-43}$$
$$d = \frac{\overline{V}_{i,P_0}^E}{RT}$$
$$e = \frac{\overline{\kappa}_i^E}{2RT}$$

In equations 2-42 and 2-43, *m* is the number of species (ions and water) that constitute the mineral $M_{\nu_M} X_{\nu_X} nH_2O$ and ν refers to the stoichiometric coefficient of the SLE reaction.

Equations 2-42 and 2-43 show the corrections that must be applied to both the solubility product and the residual and combinatorial terms of the activity coefficients to introduce the pressure effect in the solubility calculations. The Debye-Hückel term for the activity coefficient is calculated at the system pressure, and therefore, correction 2-41 is not required for this term. The Debye-Hückel parameter *A* given by equation 3-10 is a function of the density and dielectric constant, both of them evaluated at the system temperature and pressure.

In the present work, we have included two additional parameters (α and β) to the extended UNIQUAC thermodynamic model presented by Thomsen and Rasmussen (1999) to account for pressure dependence:

$$\ln K_{e,P} = \ln K_{e,P_0} + \alpha(P-P_0) + \beta(P-P_0)^2 \tag{2-44}$$

No further corrections to account for pressure are applied, apart from α and β (except for the calculation of the A Debye-Hückel parameter). Thus, the residual and combinatorial terms of the activity coefficients are calculated at the reference pressure, so that equation 2-42 becomes:

$$\ln K_{e,P_0} + \alpha(P-P_0) + \beta(P-P_0)^2 = c + \sum_{i=1}^{m} \nu_i \left[\ln \gamma_{i,P_0}\right] \tag{2-45}$$

For equation 2-45 to be consistent with equation 2-42, it is necessary that

$$\alpha = -\frac{\Delta \overline{V}_{dis,P_0}}{RT} - \sum_{i=1}^{m} \nu_i \frac{\overline{V}_{i,P_0}^{E}}{RT} = -a - \sum_{i=1}^{m} \nu_i d \tag{2-46}$$

$$\beta = \frac{\Delta \overline{\kappa}_{dis}}{2RT} + \sum_{i=1}^{m} \nu_i \frac{\overline{\kappa}_{i}^{E}}{2RT} = b + \sum_{i=1}^{m} \nu_i e \tag{2-47}$$

Using two fitting parameters to correct for the pressure effect is preferred over evaluating α and β from the physical properties (equations 2-46 and 2-47), because of the lack of accurate experimental data for both the partial molar volume and compressibility.

Most of the experimental measurements of partial molar volumes are limited to simple ions and are reliable at low temperatures only. The interpolations performed in some cases to calculate $\overline{V}_i$ at temperatures different from the experimental values, show differences as large as 0.3 cm^3 mol^{-1} (Millero, 1981). Yousef et al. (2001) demonstrated that an accurate value for the standard partial molar volume is critical for a reliable prediction of solubility at high pressures. Such values are generally overestimated by the equations of state (Millero, 1981).

In the case of compressibility, the situation is even worse and reliable data are very difficult to find. The derivation of $\overline{\kappa}_i$ from compressibility studies is experimentally difficult (Lown et al., 1968). The number of ions studied is also small, especially in the marine environment, and a large divergence can be found among the various authors. There are no compressibility data for mixed electrolyte solutions and it is impossible nowadays to make a precise calculation of the change in standard partial molar compressibility for natural highly concentrated brines (Krumgalz et al., 1999). Even the error introduced by neglecting this term cannot be defined with any precision. Very limited data are available for the effect of temperature on $\overline{\kappa}_i$ and the effect of pressure is neglected. The effect of pressure has nevertheless not been studied in detail and seems to be more important for low temperatures. Lown et al. (1968) demonstrated that the molar compressibility for different acid-base equilibria could be assumed pressure independent in the range 1-2000 bar. According to Millero (1981), such a dependence should be accounted for above 700 bar (the error introduced at 1000 bar is around 4%). For $SrSO_4$ at 1000 bar, neglecting the change in partial molar compressibility with pressure leads to an overestimation of the ratio $K_{e,T,P} / K_{e,T,P_0}$ by as much as 39% (Millero, 1981). The error caused by uncertainties in both molar volume and compressibility should also be added to the latter percentage (around 6% for seawater, according to Millero, 1981). By estimating the values of the pressure parameters α and β from experimental solubility data we will avoid these inaccuracies.

2.8 Model Calculations

The calculations performed to achieve the final solution are explained based on the specific system $CaCO_3$-CO_2-H_2O. The following equilibrium processes are taken into account for that system:

Vapour-liquid equilibria:

$$\mathrm{CO_2(g) \Leftrightarrow CO_2(aq)} \quad \textbf{(2-48)}$$

$$\mathrm{H_2O(g) \Leftrightarrow H_2O(l)} \quad \textbf{(2-49)}$$

Speciation equilibria:

$$\mathrm{CO_2(aq) + H_2O(l) \Leftrightarrow HCO_3^- + H^+} \quad \textbf{(2-50)}$$

$$\mathrm{HCO_3^- \Leftrightarrow CO_3^{2-} + H^+} \quad \textbf{(2-51)}$$

$$\mathrm{H_2O(l) \Leftrightarrow H^+ + OH^-} \quad \textbf{(2-52)}$$

Except for the carbonate/bicarbonate system, all the other electrolytes are considered strong electrolytes and therefore completely dissociated. The formation of association products such as $\mathrm{CaCO_3^0}$ or $\mathrm{CaHCO_3^+}$ is not considered (the same criteria is applied to all the systems studied in the present work).

Liquid-solid equilibrium:

$$\mathrm{Ca^{2+} + CO_3^{2-} \Leftrightarrow CaCO_3(c)} \quad \textbf{(2-53)}$$

Each of the equilibrium processes 2-48 to 2-53 can be expressed in a form similar to equation 2-29. To calculate the equilibrium phase compositions of a mixture of CO_2, $CaCO_3$ and H_2O, equations 2-48 to 2-53, together with the electroneutrallity condition and the condition that the sum of the mole fractions in the gas phase and the sum of the mole fractions in the liquid phase is equal to unity, is solved with respect to the mole fractions of the *n* components in the liquid phase (H_2O, Ca^{2+}, CO_3^{2-}, HCO_3^-, H^+, OH^-, $CO_2(aq)$), the mole fractions of the *n'* components in the gas phase (H_2O (g) and CO_2 (g)) and the bubble point pressure, by adjusting the amounts of the *n''* solid phases ($CaCO_3$ (c)). At equilibrium, equation 2-54 must be fulfilled

$$K_{CaCO_3} = a_{Ca^{2+}} a_{CO_3^{2-}} \tag{2-54}$$

In general, a *s*-salt saturation point has to fulfil equation 2-55 for all *s* salts:

$$K_k = \prod_i a_i^{v_{k,i}} \quad k = 1 \ldots s \tag{2-55}$$

while for the rest of the salts potentially formed by the system

$$K_k > \prod_i a_i^{v_{k,i}} \quad k > s \tag{2-56}$$

Equation 2-55 is solved by a Newton-Raphson method using analytical composition derivatives of the activity coefficients.

For the calculation of the bubble point pressure of the solution, an initial guess of both pressure and composition is introduced in the program. Then, all the speciation equilibria equations are solved simultaneously. The fugacities of the vapour phase components appear in the equations for the vapour-liquid equilibria 2-48 and 2-49, which can be expressed as in equation 2-29. From those equations the mole fractions of the components forming the vapour phase can be calculated. If the sum of those mol fractions is different from unity, a new pressure is guessed. The procedure is repeated until a final solution is found.

2.9 References in Chapter 2

Kelley, K.K., 1960. High-temperature heat-content, heat-capacity, and entropy data for the elements and inorganic compounds. Bulletin/Bureau of Mines 584, 1-211.

Krumgalz, B.S., Starinsky, A., Pitzer, K.S., 1999. Ion-interaction approach: pressure effect on the solubility of some minerals in submarine brines and seawater. Journal of Solution Chemistry 28 (6), 667-692.

Lown, D.A., Thirsk, H.R., Lord W.J., 1968. Effect of pressure on ionization equilibria in water at 25°C. Trans. Faraday Soc. 64, 2073-2080.

Millero, F.J., 1981. The effect of pressure on the solubility of minerals in water and seawater. Geochimica et Cosmochimica Acta 46, 11-22.

NIST Chemical Thermodynamics Database Version 1.1, 1990. U.S. Department of Commerce, National Institute of Standards and Technology, Gaithesburg MD 20899.

Rumpf B., Maurer G., 1993. An experimental and theoretical investigation on the solubility of carbon dioxide in aqueous solutions of strong electrolytes. Ber. Bunsenges. Phys. Chem. 97(1), 85-97.

Thomsen, K., Rasmussen, P., Gani, R., 1996. Correlation and prediction of thermal properties and phase behaviour for a class of electrolyte systems. J. Chem. Eng. Science 51, 3675-3683.

Thomsen, K., Rasmussen, P., 1999. Modeling of vapor-liquid-solid equilibrium in gas-aqueous electrolyte systems. Chemical Engineering Science 54, 1787-1802.

Yousef, A.M., Elkanzi, E.M., Singh, H., 2001. Prediction of supercritical CO_2 solubility using the Krichevsky-Ilinskaya equation with v2 as an Adjustable Parameter. J. of Supercritical Fluids 20, 105-112.

3. Extended UNIQUAC Model

In the present work, aqueous phase activity coefficients are calculated by means of the extended UNIQUAC model, improved with the addition of two pressure parameters to account for the pressure dependency of solubility. The gas phase fugacity for volatile components in the system is calculated by the Soave-Redlich-Kwong (SRK) cubic equation of state, using classical mixing rules.

The extended UNIQUAC model was chosen due to its simplicity and at the same time good accuracy to represent solid-liquid-vapour equilibria for multicomponent electrolyte solutions up to high ionic strengths and temperatures. The model only requires two parameters per species, plus two parameters per pair of interacting species, reducing the amount of experimental data required (scarce for the systems of interest in the present work, especially for multicomponent solutions at high temperature and pressure). Bromley's and Helgeson's models were also studied, but the extended UNIQUAC model was preferred due to its higher capability to perform calculations in multicomponent electrolyte solutions with common ions. A closer view to Bromley's and Helgeson's model is included in Appendix I.

3.1 Activity Coefficient Models

One of the first studies devoted to describe the thermodynamic behaviour of electrolyte solutions was performed by Lewis and Randall in 1921. Their motivation was the inaccuracy obtained for strong electrolytes when applying models derived from Arrhenius' theory of electric dissociation. Such models were adequate for weak electrolytes, but not for strong electrolytes. They proposed several methods to determine activity coefficients from measurements of the electromotive force, the freezing point, and the vapour pressure. One year later (in 1922), Brønsted postulated that there would only be specific interactions between ions of the opposite sign, while interactions between ions of the same sign would only depend on the electrical charges. In 1923, Debye and Hückel developed the first successful model (the Debye-Hückel limiting law) for the activity coefficients of dilute aqueous electrolytes. They considered the solvent to be a continuous dielectric. The ions interact following Coulomb's law, and the effect of all other ions on a given ion is calculated by the Poisson-Boltzmann equation. The Debye-Hückel (D-H) limiting law is a simplification of the Debye-Hückel equation where ions are considered to be point charges. The limiting law is reliable up to ionic strengths of 0.001 m. When ions are considered as hard spheres instead, the limiting law is transformed into the extended Debye-Hückel law, reliable for ionic strengths up to 0.1 m.

Since the Debye-Hückel limiting law, many authors have proposed modifications to that model in order to extend its range of applicability. Bjerrum (1926) attributed the differences between experimental data and the Debye-Hückel theory to ionic association of ions of opposite charge. Guggenheim (1935) combined the extended D-H law with the principles of Brønsted (1922) and suggested an expression for the mean activity coefficient with one solute-specific parameter. The expression is valid up to ionic strengths of 0.1 m. Stokes and Robinson (1948) modified the D-H model introducing the ion-solvent interactions in terms of hydration, obtaining a two parameters equation to calculate the activity coefficients in electrolyte solutions. They assumed that ions were surrounded by solvent molecules and their ionic character was shielded. The behaviour of the solution is then determined by the free solvent molecules. Their model was applicable to 1:1 and 1:2 electrolyte solutions up to 4 m. In 1962, Davies added the term "aI" (I being the ionic strength and a a constant) to the original Debye-Hückel expression. His equation was frequently used in geochemical modelling, but only for temperatures close to 25°C and ionic strengths of a few tenths molal (Sahai et al., 1998). Hamer and Wu (1972) added to the D-H equation a serial function of the ionic strength, improving the correlation results due to the additional parameters.

Bromley (1973) modified the D-H model introducing an additional term that was dependent on the ionic strength. His one-parameter equation was found empirically from fitting experimental data. Bromley's model only uses one interaction parameter for each salt, which can be calculated as the sum of contributions from cation and anion. Many of those parameters are reported in literature (Zemaitis et al., 1986, Iliuta et al., 1999, Borge et al., 1996, Raposo et al., 1998, Belaustegi et al., 1999). According to Chen et al. (1998), the model had an accuracy of 5% for 1:1 electrolytes up to 6 m, but was limited to only 1 m solutions for other types of electrolytes. The properties of multicomponent electrolyte solutions are very often determined within the framework provided by Pitzer (1973, 1975, 1991), who developed one of the most popular virial expansion models. Using the pressure equation of statistical thermodynamics, Pitzer pointed out that the interaction coefficient is a function of the ionic strength. The general formulation of Pitzer's model is principally made up of two parts in terms of excess Gibbs energy. The first corresponds to the Debye-Hückel model, and the second is an empirical expression for the second and third virial coefficients that takes into account the binary and ternary interactions neglected in the first part. Third virial coefficients for three ions of the same charge have been neglected as they are assumed to be very small. According to Pérez-Villaseñor and Iglesias-Silva (2002), the main disadvantage when using Pitzer's equations is that the concentration range normally cannot exceed a molality of 6. Other authors have also realized the same problem (Pitzer and Mayorga, 1973, Chen et al., 1982, Haghtalab and Vera, 1988, Marshall et al., 1995, Renon, 1996). Pitzer's formalism requires both binary and ternary experimental data for all components in the mixture. Some attempts to reduce the number of parameters used in Pitzer's model have also been made. Krop (1999) used a modified Pitzer's excess Gibbs free energy in which binary and ternary interaction parameters relate to the interactions of electrolytes in a solution rather than to the interactions of real species in a solution (i.e., cations, anions and non dissociated molecules). This approach reduces the number of parameters significantly. Pérez-Villaseñor and Iglesias-Silva (2002) assumed the double ion interactions to be independent of the ionic strength, therefore reducing the number of parameters. To achieve a similar accuracy, they also optimized the value of the b Debye-Hückel parameter for each electrolyte solution. Lietzke et al. (1975) presented a two-structure model to predict activity coefficients of each component in a mixed electrolyte solution. The model incorporated the ion atmosphere description of Debye-Hückel at low concentrations, and a function of ionic stregth at high concentrations. The contribution of each term was weighted by a partition function. The model needs three parameters for each electrolyte. Helgeson (Helgeson and Kirkham, 1974a, b, 1976, Helgeson et al., 1981, Shock and Helgeson, 1988, Johnson et al., 1992) developed equations to calculate the standard molal thermodynamic properties of minerals, gases, aqueous species, and reactions as a function of temperature and pressure. He proposed an equation to calculate activity coefficients for electrolyte solutions which is a simple extension by a term dependent on the ionic strength of the D-H model. Helgeson calculated successfully thermodynamic and transport properties of aqueous species at temperatures up to 1000^{o}C and pressures up to 5 kbar (Shock and Helgeson, 1988). He studied a huge amount of binary systems at different temperature and pressure conditions, and their results were in agreement with the experimental data (Helgeson et al., 1981). Lin et al. (1998) developed a characteristic-parameter correlation model for the aqueous strong electrolyte solutions. The model consists of the long range ion-ion interaction described by Pitzer-Debye-Hückel and short range ion-solvent molecule interaction attributed to solvation effect. This model contains three parameters of physical significance.

The Debye-Hückel model has also been combined with different local-composition models, such as UNIQUAC or NRTL. For instance, Cruz and Renon (1978) combined the Debye-Hückel expression with the NRTL model and a Born model contribution. They considered the changes in the dielectric constant with the salt concentration. To describe a system formed by one salt and one solvent, four adjustable parameters are needed. A similar approach is followed by Ball et al. (1985), who used a different Born contribution, resulting in a reduced number of adjustable parameters (two for a binary system). Chen et al. (1982) and Chen and Evans (1986) used the electrostatic function of the Pitzer's model with a local composition term, which is an extension of the NRTL equation for electrolyte solutions. With this model, the number of interaction parameters to describe a binary system is reduced to two. They obtained good results for mixtures below concentrations of 6 m. Their model requires pair interaction parameters for each binary mixture. A very similar approach to Chen's et al. (1982) is followed by Haghtalab and Vera (1988), using the original expression given by D-H to account for the long range interactions. Sander (1984) added the Debye-Hückel equation to the UNIQUAC model (extended UNIQUAC), allowing the latter to be used for electrolyte solutions. Nicolaisen et al. (1993) simplified Sander's version of the extended UNIQUAC model in order to contain only binary parameters with no concentration dependency. This latter model is the one used in this work, with a different procedure to estimate parameters to that followed by Nicolaisen et al. (1993). The temperature dependency of the parameters is included in the model equations. Also, the model can be applied for mixed solvents. Liu et al. (1989) used an approach including the D-H term and a three-parameter Wilson equation derived by Renon and Prausnitz (1969). The D-H term only accounts for the long range interactions between the central ion and all ions outside the first coordination shell. The Wilson term accounts for the short range interactions, where the interactions between the ions within the first coordination shell are included. The model parameters are ion specific. Polka et al. (1994) proposed a new expression for the excess Gibbs energy formed by three contributions: A Debye-Hückel term to account for long range electrostatic interactions, the UNIQUAC equation for the description of short range interactions between all particles, and a middle range contribution to include all indirect effects of the charge interactions. The model needs four parameters for each electrolyte present in the solution. According to Polka et al. (1994), their results are comparable to the models of Sander et al. (1986a, b, c), Macedo et al. (1990), Pitzer and Mayorga (1973), Bromley (1973) and Chen et al. (1982) for the 362 binary and 185 ternary (two solvents and one salt) systems studied. A very similar model to extended UNIQUAC is the one used by Lu et al. (1996), where physical interactions between all species are taken into account combining the D-H law and the UNIQUAC model. The expression employed for the D-H law and the value of the *b* Debye-Hückel parameter differs from the ones in the extended UNIQUAC model.

Apart from modifications to the D-H law, many other activity coefficient models not including the D-H term have also been developed (Rasaiah and Friedman, 1968, Meissner et al., 1972, Tan, 1987, 1990, Pal et al., 1991, Kolker and De Pablo, 1995, Zuo and Fürst, 1998, Vanderbeken et al., 1999, Clegg and Simonson, 2001).

3.2 Previous Work on Scale Formation

Scale formation has been a problem for the development of the geothermal power and for the oil industry for a long time. The prediction of salt deposition during production is an important tool to fight against scale formation, and has been widely investigated during the last decades. Numerous saturation indexes and computer algorithms have been developed to determine when and where scale will occur.

Some of the first models predicting scale formation have important shortcomings, and as a result large errors in scale prediction may occur. This is the case of Helgeson (1970) and Miller et al. (1977), who did not consider the pressure effect on scaling. The effect of pressure on solubility is relatively small compared to that of temperature. In geothermal energy and oil production, however, the pressure change is of the order of hundreds of bars through the injection, reservoir, and production system, and the effect on solubility change may be significant.

Some models assume the solubility in natural waters is comparable to that in sodium chloride solutions of the same total ionic strength, neglecting the effect of all other ions present in the system. (Millero, 1979, Jacques and Bourland, 1983, Raju and Atkinson, 1988, 1989, Battistelli et al., 1997). In many cases, the possibility of co-precipitation of different scaling minerals is not taken into account, and simple empirical predictions (generally limited to pure water, CO_2-water, or NaCl solutions) for the formation of a particular precipitate as a function of temperature, pressure and ionic strength are used. Jacobson and Langmuir (1974) reported temperature dependent dissociation constants of calcite ($CaCO_3$) from 0 to 50ºC at 1 atm, based on conductance measurements and using the extended Debye-Hückel equation. Millero (1979) developed an empirical temperature, salinity, and pressure dependent equation to determine the solubility product of calcite in seawater. The equation includes two adjustable parameters, and the pressure dependency is taken into account by the partial molar volume and compressibility changes. Plummer and Busenberg (1982) reported empirical temperature dependent equations to calculate the solubility product of calcite, aragonite and varetite in CO_2-H_2O solutions, based on their 350 experimental measurements from 0 to 90ºC at 1 atm. Individual ion activity coefficients were determined from the equations of Truesdell and Jones (1974), which are modifications from the Debye-Hückel equations. A similar approach is followed by Jacques and Bourland (1983) based on their own experimental results. They presented a predictive equation for the solubility of celestite ($SrSO_4$) in water containing up to 200 g L^{-1} NaCl, at temperatures from 38 to 149ºC and pressures from 7 to 207 bar. Reardon and Armstrong (1986) reported a temperature dependent equation to calculate celestite solubility product, and used Pitzer's formalism to calculate the activity coefficient and fit their experimental results. No pressure correction is included since the experimental data used were all measured at atmospheric pressure. Raju and Atkinson (1988, 1989) developed equations to calculate thermodynamic properties and equilibrium constants as a function of temperature and ionic strength, based on their experimental data for $SrSO_4$ and $BaSO_4$. The activity coefficients were calculated from Pitzer's equations. The heat capacity value reported for Sr^{2+} at 25ºC is -7.4 J K^{-1} mol^{-1}, extremely different from the value of -106 J K^{-1} mol^{-1} reported by Marcus (1997), and used as initial guess in this work. Howell et al. (1992) derived an equation to calculate the solubility product of $SrSO_4$ in NaCl solutions as a function of temperature and pressure, based on their experimental results. Also, an equation to determine the mean activity coefficient as a function of temperature, pressure and ionic strength is reported. Duan et al. (1996) used Pitzer's approach to calculate the liquid phase activity coefficients, while an EOS developed by Duan et al. (1992a, b) was used to represent the vapour phase. Their model was implemented only for $CaCO_3$ solubility in NaCl solutions, and gases CO_2 and CH_4. Battistelli et al. (1997) modelled mixtures of water, sodium chloride, and a slightly soluble non condensable gas (air, CO_2, CH_4, H_2, or N_2) in connection to geothermal reservoirs. The system is modelled by an equation of state developed by Battistelli et al. (1993) and includes precipitation and dissolution of solid salt. The concentration of solutions that are both vapour and halite (NaCl) saturated was calculated using an equation by Potter quoted in Chou (1987). The applicability of the model ranges from 100 to 350ºC and up to a partial CO_2 pressure of 100 bar. Satman et al. (1999) studied the effect of calcite deposition in geothermal wells performance. The solubility of calcite in CO_2-H_2O solutions up to high temperature and pressure was obtained through a simple correlation derived from experimental data.

Some investigators prefer the use of solubility indices to determine whether or not precipitation of a certain mineral will take place at given conditions of temperature and pressure. Oddo and Tomson (1994) compared the Langelier (1936), and Oddo and Tomson (1994) saturation indices relative to calcium carbonate scale. They also introduced a new saturation index for barium, strontium, and calcium sulphate scale formation. The equilibrium constants required to obtain the saturation index were derived from literature data as a function of temperature, pressure, and ionic strength, by performing a non-linear least-squares fit of the data sets. For $CaCO_3$, the saturation index was improved by the addition of the CO_2 fugacity, calculated by the Peng-Robinson equation of state. Marshall (1989) calculated the saturation index for calcite from the reconstructed reservoir water composition at Dixie Valley (Nevada, EEUU) geothermal field. The ion-association type model EQ3NR developed by Wolery (1983) and the specific-interaction model EQUIL developed by Weare (1987) were used to determine activity coefficients in the Na-Ca-Cl-CO_2-H_2O system and to calculate the distribution of elements in the reservoir and production water.

All the previous models are focused on a single mineral or couple of minerals, and therefore cannot be applied to determine real concentrations in natural waters, where many different species coexist and interact with each other. Models accounting for all the possible reactions taking place simultaneously are scarcer. Among them, we can mention Harvie and Weare (1980), who used Pitzer's formalism to study the solubility of solid phases in the system Na-K-Ca-Mg-Cl-SO_4-H_2O at 25ºC and 1 atm. This study has been later extended by different authors to cover wider ranges of temperature, pressure, and to include additional species present in connate and injection waters. In general, to determine salt solubility at high temperature and pressure, the dissociation constants are described as a function of temperature and pressure. Then, the saturated concentration is calculated by the use of Pitzer's activity coefficient model. However, the studies disagree about the temperature dependency of Pitzer parameters. Harvie et al. (1984) considered new carbonate species, modelling the system Na-K-Ca-Mg-Cl-SO_4-HCO_3-CO_3-CO_2-H_2O at 25ºC and 1 atm. Møller (1988) constructed a variable temperature model for the Na-Ca-Cl-SO_4-H_2O system from 25 to 250ºC. Greenberg and Møller (1989) extended the seven component seawater model developed by Harvie and Weare (1980) from 0 to 250ºC and from zero to high ionic strength (around 18 m). The pressure is considered to be 1 atm up to 100ºC and the saturation pressure of water above 100ºC. Spencer et al. (1990) parameterized the same system as Greenberg and Møller (1989) at low temperatures (from -60 to 25ºC). Spencer et al. (1990) had some problems when predictions were carried in sulphate-dominated systems, and a new re-parameterization of those systems was performed by Marion and Farren (1999). Additionally, they consider five new sulphate minerals (gypsum – $CaSO_4 \cdot 2H_2O$- among them) allowing a more complete treatment of the system. He and Morse (1993) predicted the solubility of halite, gypsum and anhydrite ($CaSO_4$) in Na-K-H-Ca-Mg-Cl-OH-SO_4-H_2O solutions of varying composition as a function of temperature (from 0 to 200ºC) and pressure (from 1 to 1000 bar). In 1998, Møller et al. predicted carbonate scale formation in the Na-K-H-Ca-Cl-SO_4-H_2O system up to 250ºC, and silica scale formation in the Na-Mg-Cl-SO_4-SiO_2-H_2O system up to 320ºC. The gas phase is modelled by using an equation of state (Duan et al., 1992a).

Pitzer's approach has also been used by many investigators to include new species of great importance in connection to scale formation in the oil and geothermal industry (as Ba^{2+} and Sr^{2+}). Monnin and Galinier (1988) proposed a predictive model for the solubility of barite ($BaSO_4$) and celestite in the Na-H-K-Ca-Mg-Ba-Sr-Cl-OH-SO_4-H_2O system at 25ºC based on Pitzer's ion interaction model, and in the parameterization performed by Harvie et al. (1984). The model fails for highly concentrated waters, but the accuracy for barite and celestite solubility calculations in the low to moderate concentration region is better than ±10%. The previous model was later extended by Monnin (1999), covering temperatures from 0 to 200ºC, and pressures up to 1 kbar. Pressure correlations are evaluated through partial molar volume calculations within Pitzer's formalism. The compressibility effects have been neglected due to the lack of experimental data. Haarberg (1989) developed a scale prediction model for the minerals $CaCO_3$, $BaSO_4$, $CaSO_4$ and $CaSO_4 \cdot 2H_2O$. He compared some of the results obtained using Pitzer's formalism whit results from Sander's (1984) model, and concluded the former model gives the best description of experimental data. Gas phase fugacities for carbon dioxide were calculated according to Houghton et al. (1957). Activity coefficients for aqueous CO_2 were determined from the equations of Weiss (1974) or Naumov et al. (1974), depending on the temperature of the system. The model predictions are reliable up to 175ºC and 400 bar. Yuan and Todd (1991) developed a model to predict sulphate scaling tendency in oilfield operations, taking into account the possible co-precipitation of $BaSO_4$, $SrSO_4$ and $CaSO_4$. The model is based on Pitzer's formalism to calculate activity coefficients, but does not use the parameterization reported by Harvie et al. (1984). Instead, they determined new parameters and thermodynamic solubility products based on solubility data. According to Yuan and Todd (1991), the limited number of published data makes Pitzer's approach to take into account the pressure effect impractical. Instead, they developed empirical equations from the correlation of solubility with pressure. The model was used to predict sulphate scaling potential of mixing injection water and formation water in the North Sea, and the predictions were substantiated by field observations. Nonetheless, some of the predictions by Yuan and Todd (1991) and Yuan et al. (1994) do not agree with those by Vetter et al. (1982) and Atkinson et al. (1991). Kaasa (1998) presented a model than can predict pH and mineral solubility ($CaSO_4$, $CaSO_4 \cdot 2H_2O$, $BaSO_4$, $SrSO_4$, $CaCO_3$, $FeCO_3$, FeS and NaCl) together with multiphase equilibria and the phase distribution for CO_2, H_2S and hydrocarbon components. The equation of state given by Vonka et al. (1995) is used to describe the volumetric behaviour of the gas phase and the phase equilibrium between gas and oil. That equation is linked to the Pitzer's model and solved simultaneously. Carrier et al. (1998) combined two thermodynamic models to describe salt solubility in the system Na-K-Ca-Ba-Sr-Cl-SO_4-H_2O. Helgeson, Kirkman and Flowers (HKF) modified equations of state (Helgeson et al., 1981) are used to calculate the dissociation constants of mineral species, while Pitzer ionic interaction model is used to calculate activity coefficients for the ions. The model was applied in the temperature range from 25 to 350ºC, and pressures from 1 to 160 bar. Pátzay et al. (1997) developed an equilibrium simulation algorithm to represent $CaCO_3$, $CaSO_4$, $BaSO_4$, and SrSO4 scale formation in a Na-K-Mg-Ca-H-Ba-Sr-Cl-Br-SO_4-OH-HCO_3-CO_3-CO_2-H_2O system using Davies and Pitzer models. The predicted results using Pitzer's activity coefficients fitted the literature data well.

Pitzer's framework is probably the most widely used to determine solubility of scaling minerals in natural waters at high temperature and pressure. Nevertheless, some investigators opted for other approaches. Arnórsson et al. (1982) calculated the composition and aqueous speciation of geothermal reservoir waters from 0 to 370ºC. The species considered were SiO_2, B, Na, K, Ca, Mg, Fe, Al, NH_3, CO_2, SO_4, H_2S, Cl, F, N_2, O_2, H_2, and CH_4. The equilibrium constants for the different reactions taking place were calculated as a function of temperature from experimental data on thermodynamic properties, following the methods described by Helgeson (1967, 1969), and Helgeson et al. (1978). Individual activity coefficients for ions were also calculated following Helgeson's framework, with the required parameters taken from Helgeson and Kirkhan (1974a, b). Potapov et al. (2001) studied the possibility and efficiency of chemical treatment of the geothermal separate prior to reinjection under conditions of the Verkhne-Mutnovsk (Russia) geothermal power station. They simulated the chemical equilibrium in the multicomponent aqueous solution and calculated the activity coefficients from the semi-empirical formula of Helgeson quoted in Kaz'min (1983).

Some of the later models coupled thermodynamics and kinetics to obtain a more reliable prediction of scale formation (Wat et al., 1992, Zhang et al., 2001); and others consider fluid dynamics and flow in porous media (Bertero et al., 1988, Li et al., 1995). Wat et al. (1992) performed experiments on kinetics of $BaSO_4$ crystal growth and concluded the rate of growth of barite can be represented by a second order rate equation. Zhang et al. (2001) used a thermodynamic model (Kharaka et al., 1988) coupled to a kinetic model to predict $CaCO_3$ deposition downhole. The model has been applied to predict the scale formed on the internal surface of a tube, and the predicted results are in good agreement with the real scale profile. Bertero et al. (1988) presented a numerical model coupling a reservoir-fluid-flow/thermal-equilibrium simulator with a chemical-equilibrium computer code. The output of the model is the evolution with time of the amount of scale formed when changes in the injection water temperature occur or when there is mixing of incompatible waters. Li et al. (1995) developed a model to predict co-precipitation of $BaSO_4$ and $SrSO_4$ in oil fields. The computer model simulates reactive flow through porous media. Dissolved ions move in the aqueous phase by convection and diffusion, while the solid phase does not move with the fluid.

There are also several commercial programs to determine mineral scaling potential in oil and gas production. OLI (http://www.olisystems.com/oliscale.htm) is a software that computes gas-liquid-oil-solid equilibria up to 316ºC, 1517 bar and $7 \cdot 10^5$ TDS. The model uses a revised Helgeson’s equation of state to consider the temperature and pressure effects on the brine, while the SRK equation of state is used to account for the temperature and pressure effects both in the vapour and in the organic phase. Different activity coefficient models are implemented (Bromley, Zemaitis, Pitzer and Setschnow).

3.3 The Extended UNIQUAC Model

In this work, the extended universal quasichemical (extended UNIQUAC) model, as presented by Thomsen and Rasmussen (1999), is used to model solutions containing electrolytes, covering wide ranges of concentration, temperature, and pressure. The model was originally developed to represent vapour-liquid equilibrium in mixed solvents where salts were present. Since then, it has been applied to describe solid-liquid, liquid-liquid, and vapour-liquid equilibria in a wide range of system with good accuracy (Nicolaisen et al., 1993, Thomsen, 1997, Thomsen et al., 1996, 2004, Thomsen and Rasmussen, 1999).

The extended UNIQUAC model is a local composition model derived from the original UNIQUAC model (Abrams and Prausnitz, 1975, Maurer and Praustniz, 1978) by adding a Debye-Hückel term (Sander, 1984, Sander et al., 1986a, b) to take into account the presence of ionic species in the solution. The UNIQUAC term, which is subdivided into a combinatorial or entropic term and a residual or enthalpic term, takes into account the short range ion-ion, ion-solvent and solvent-solvent interactions. The Debye-Hückel term was originally derived for an ideal solution of charged particles, and takes into account long range, electrostatic ion-ion interactions. For salt-free solutions, the model reduces to the original UNIQUAC equation.

Hence, the excess Gibbs energy expression by the extended UNIQUAC model consists of three terms:

$$G^E = G^E_{Combinatorial} + G^E_{Residual} + G^E_{Debye-Hückel} \tag{3-1}$$

where G^E is the molar excess Gibbs energy. The combinatorial and residual terms are identical to the terms used in the original UNIQUAC equation. These terms are based on the rational, symmetric activity coefficient convention, while the Debye-Hückel term is based on the rational, symmetric convention for water, and the rational, unsymmetric convention for ions.

The combinatorial, entropic term takes into account the deviation from ideality due to differences in size and shape of the species forming the system. It is expressed as:

$$\frac{G^E_{Combinatorial}}{RT} = \sum_i x_i \ln\left(\frac{\phi_i}{x_i}\right) - \frac{z}{2}\sum_i q_i x_i \ln\left(\frac{\phi_i}{\theta_i}\right) \tag{3-2}$$

where R is the gas constant (8.314 J K^{-1} mol^{-1}), T is the temperature in Kelvin, x_i is the mole fraction of species i, z is the coordination number (the number of nearest neighbours, arbitrarily fixed at 10), ϕ_i is the volume fraction of species i, and θ_i is the surface area fraction of species i, expressed as:

$$\phi_i = \frac{x_i r_i}{\sum_l x_l r_l} \tag{3-3}$$

$$\theta_i = \frac{x_i q_i}{\sum_l x_l q_l} \tag{3-4}$$

where r_i and q_i are the volume and surface area parameters for species i.

The residual, enthalpic term takes into account the short-range molecular energetic interactions, and it is calculated as:

$$\frac{G^E_{Residual}}{RT} = -\sum_i x_i q_i \ln\left(\sum_k \theta_k \psi_{ki}\right) \tag{3-5}$$

where ψ_{ki} is given by

$$\psi_{ki} = \exp\left(-\frac{u_{ki} - u_{ii}}{T}\right) \tag{3-6}$$

In equation 3-6, u_{ki} (= u_{ik}) and u_{ii} are the interaction energy parameters. They are temperature dependent:

$$u_{ki} = u_{ki}^0 + u_{ki}^t (T - 298.15) \tag{3-7}$$

The Debye-Hückel contribution to the excess Gibbs energy of the extended UNIQUAC model is given by the expression:

$$\frac{G^E_{Debye-Hückel}}{RT} = -x_w M_w \frac{4A}{b^3}\left[\ln(1 + bI^{1/2}) - bI^{1/2} + \frac{b^2 I}{2}\right] \tag{3-8}$$

where M_w is the molar mass of water (0.01801534 kg mol^{-1}), x_w is the mole fraction of water, A is a temperature and pressure dependent Debye-Hückel parameter, b is a constant equal to 1.5 (kg $mol^{-1})^{½}$, and I is the ionic strength based on molality, calculated as:

$$I = 0.5\sum_i m_i z_i^2 = 0.5\frac{\sum_i x_i z_i^2}{x_w M_w} \tag{3-9}$$

In equation 3-9, z_i is the charge of ion i and m_i is the molality (mol (kg $H_2O)^{-1}$) of ion i.
Equation 3-8 is a simplification by Fowler and Guggenheim (1949) of the excess Gibbs energy given by Debye and Hückel (1923).
The parameter A is calculated as

$$A = \frac{F^3}{4\pi N_A}\left[\frac{d}{2(\varepsilon_0 DRT)^3}\right]^{½} \tag{3-10}$$

F is the Faradays constant (96484.6 C mol^{-1}), N_A is the Avogadro's number ($6.023 \cdot 10^{23}$ mol^{-1}), ε_0 is the vacuum permittivity ($8.8542 \cdot 10^{-12}$ $C^2J^{-1}m^{-1}$), d is the density of the solution (kg m^{-3}), and D is the dielectric constant (relative permittivity) of the solution (dimensionless). Both d and D are functions of temperature and pressure, and are calculated according to Wagner and Pruss (1993).
The extended Debye-Hückel law is based on the assumption of infinite dilution. Therefore, it can describe the non-ideal behaviour caused by electrostatic forces in very dilute electrolyte solutions. As the ionic strength increases, the accuracy of the extended Debye-Hückel law decreases, and it is not accurate for ionic strengths higher than 0.1 m. Therefore, the Debye-Hückel parameter A is only valid in very dilute solutions, where the density and relative permittivity of the solution are very close to the properties of pure water. For this reason, the parameter A for aqueous solutions is calculated according to the density and dielectric constant of pure water, instead of the properties of the real solution. According to Thomsen (1997), the value of the Debye-Hückel contribution to the activity coefficient is only changed a few percent when the density of pure water at 25°C is used instead of the density of a saturated solution of NaCl. Regarding the relative permittivity, the values for

pure water and real solutions may be rather different, especially in the high concentration region. Nevertheless, the ions only “see” pure water around them, and thus it is the property of water and not the solution the one needed in the *A* parameter.

The activity coefficient for species *i* is obtained by partial molar differentiation:

$$\ln \gamma_i = \left[\frac{\partial \left(\frac{nG^E}{RT} \right)}{\partial n_i} \right]_{P,T,n_{j \neq i}} \tag{3-11}$$

Using equation 3-11 and the correspondent excess Gibbs free energy equations (equations 3-2, 3-5 and 3-8), the different contributions to the activity coefficient can be obtained:

$$\ln \gamma = \ln \gamma^{Debye-Hückel} + \ln \gamma^{Combinatorial} + \ln \gamma^{Residual} \tag{3-12}$$

It is necessary at this point to take into account that the different terms in equation 3-1 are not based on the same conventions. The combinatorial and residual UNIQUAC terms are based on the rational, symmetrical activity coefficient convention, while the Debye-Hückel term is based on the rational, symmetric convention for water, and the rational, unsymmetric convention for ions. The unsymmetric activity coefficient for ion *i* (γ_i^*) ca be obtained from the symmetric activity coefficient using the relationship

$$\ln \gamma_i^* = \ln \gamma_i - \ln \gamma_i^\infty \tag{3-13}$$

Therefore, the equation for the unsymmetric activity coefficient of ion *i* is transformed into equation 3-14, while for water it is reduced to the form of equation 3-12.

$$\ln \gamma_i^* = \ln \gamma_i^{Combinatorial} - \ln \gamma_i^{\infty,Combinatorial} + \ln \gamma_i^{Residual} - \ln \gamma_i^{\infty,Residual} + \ln \gamma_i^{*,Debye-Hückel} \tag{3-14}$$

The combinatorial and residual parts of the rational, symmetric activity coefficients are

$$\ln \gamma_i^{Combinatorial} = \ln \left(\frac{\phi_i}{x_i} \right) + 1 - \frac{\phi_i}{x_i} - \frac{z}{2} q_i \left[\ln \left(\frac{\phi_i}{\theta_i} \right) + 1 - \frac{\phi_i}{\theta_i} \right] \tag{3-15}$$

$$\ln \gamma_i^{Residual} = q_i \left[1 - \ln \left(\sum_k \theta_k \psi_{ki} \right) - \sum_k \frac{\theta_k \psi_{ik}}{\sum_l \theta_l \psi_{lk}} \right] \tag{3-16}$$

where *i* can be applied to both water and ions.

The infinite dilution terms of the combinatorial and residual parts of the activity coefficient can be obtained by setting the mole fraction of water equal to one (infinite dilution for ion *i*)

$$\ln \gamma_i^{\infty,Combinatorial} = \ln\left(\frac{r_i}{r_w}\right) + 1 - \frac{r_i}{r_w} - \frac{z}{2} q_i \left[\ln\left(\frac{r_i q_w}{r_w q_i}\right) + 1 - \frac{r_i q_w}{r_w q_i}\right] \tag{3-17}$$

$$\ln \gamma_i^{\infty,\mathrm{R}esidual} = q_i \left[1 - \ln \psi_{wi} - \psi_{iw}\right] \tag{3-18}$$

Where γ_i^{∞} is the infinite dilution activity coefficient of ion *i* in pure water.

By partial molal differentiation of equation 3-8, the contribution to the activity coefficient by the Debye-Hückel term is obtained, both for water and for ions:

$$\ln \gamma_w^{Debye-Hückel} = M_w \frac{2A}{b^3}\left[1 + bI^{1/2} - \frac{1}{1+bI^{1/2}} - 2\ln(1+bI^{1/2})\right] \tag{3-19}$$

$$\ln \gamma_i^{*,Debye-Hückel} = -z_i^2 \frac{AI^{1/2}}{1+bI^{1/2}} \tag{3-20}$$

Finally, the symmetric, rational activity coefficient for water can be expressed as

$$\begin{aligned}\ln \gamma_w = {} & \ln\left(\frac{\phi_w}{x_w}\right) + 1 - \frac{\phi_w}{x_w} - \frac{z}{2} q_w \left[\ln\left(\frac{\phi_w}{\theta_w}\right) + 1 - \frac{\phi_w}{\theta_w}\right] + \\ & q_w \left[1 - \ln\left(\sum_k \theta_k \psi_{kw}\right) - \sum_k \frac{\theta_k \psi_{wk}}{\sum_l \theta_l \psi_{lk}}\right] + \\ & M_w \frac{2A}{b^3}\left[1 + bI^{1/2} - \frac{1}{1+bI^{1/2}} - 2\ln(1+bI^{1/2})\right]\end{aligned} \tag{3-21}$$

The unsymmetric, rational activity coefficient for ion *i* is:

$$\begin{aligned}\ln \gamma_i^* = {} & \ln\left(\frac{\phi_i}{x_i}\right) + 1 - \frac{\phi_i}{x_i} - \frac{z}{2} q_i \left[\ln\left(\frac{\phi_i}{\theta_i}\right) + 1 - \frac{\phi_i}{\theta_i}\right] \\ & - \ln\left(\frac{r_i}{r_w}\right) + 1 - \frac{r_i}{r_w} - \frac{z}{2} q_i \left[\ln\left(\frac{r_i q_w}{r_w q_i}\right) + 1 - \frac{r_i q_w}{r_w q_i}\right] \\ & + q_i \left[1 - \ln\left(\sum_k \theta_k \psi_{ki}\right) - \sum_k \frac{\theta_k \psi_{ik}}{\sum_l \theta_l \psi_{lk}}\right] \\ & - q_i \left[1 - \ln \psi_{wi} - \psi_{iw}\right] - z_i^2 \frac{AI^{1/2}}{1+bI^{1/2}}\end{aligned} \tag{3-22}$$

The activity coefficients for water and ion *i* as expressed in equations 3-21 and 3-22 are rational (mole fraction based) activity coefficients. They can be converted to molal activity coefficients ($\gamma_{i,m}^*$) using equation 3-23.

$$\gamma_{i,m}^{*} = \gamma_i^{*}\left(1 - \sum_j x_j\right) \tag{3-23}$$

where the summation is over all ionic species. In the case of water, $\gamma_{i,m}^{*}$ and γ_i^{*} are replaced by $\gamma_{w,m}$ and γ_w, respectively.

3.4 Gas Phase Fugacities

The only two volatile solutes considered in this work are water and carbon dioxide. Ions are considered non volatile species and kept in the aqueous solution in the whole range of temperature and pressure investigated. Therefore, only the fugacity of vapour water and gaseous carbon dioxide are required by the model.

At low pressure the vapour phase behaves almost like a perfect gas and the vapour phase fugacity coefficient is approximately one. Therefore, at low pressures, equation 2-9 for fugacity is simplified to:

$$\hat{f}_{i,g} = y_i P \tag{3-24}$$

The pressure range covered in the present work goes up to 1000 bar, and thus it is necessary to take into account the non-ideal behaviour of aqueous solutions of gases as CO_2 at high pressures. To do so, the gas phase fugacity coefficients are calculated by the Soave-Redlich-Kwong cubic equation of state, using classical mixing rules.

3.5 Model Parameters

The parameters required by the Debye-Hückel contribution to the extended UNIQUAC model are *A* and *b* in equation 3-8. The *A* parameter is calculated as a function of temperature and pressure as shown by equation 3-10. The *b* parameter can be explained in terms of specific short-range interactions between the ions and water or each other, but is best regarded as an empirical parameter. In this work, *b* is given the constant value 1.5 (kg $(\text{mol}^{-1}))^{½}$.

The parameters required by the SRK cubic equation of state are derived from the critical properties of the volatile species. The critical properties for water are taken from Wagner and Pruss (1993).

The UNIQUAC model requires the volume and surface area parameters for each species (r_i and q_i, respectively, in equations 3-3 and 3-4), and the interaction energy parameters for each pair of interacting species (u_{ki} and u_{ii} in equation 3-6). No ternary parameters are required.

In the UNIQUAC model presented by Abrams and Prausnitz (1975) the volume and surface area parameters for non-electrolytes (but for water) were calculated based on the geometry of the species. This calculation is not reliable for electrolyte systems, since the dimension of an ion in a crystal lattice differs from the real dimension in an aqueous solution as consequence of hydration. Therefore, both r_i and q_i are fitted to experimental data (Thomsen, 1997).

Due to the constraint of electroneutrality, the properties of ions must be measured relative to the properties of a "reference ion". The hydrogen ion was taken as that reference ion. Its thermodynamic properties (Gibbs free energy of formation, enthalpy of formation and heat capacity) in its standard state (hypothetical ideal one molal solution) are by convention all fixed at zero at all temperatures. If the standard chemical potential is given in a different standard state (and therefore not necessarily equal to zero), equation 3-25 can be applied:

$$\mu_i^{*,m} = \mu_i^0 + RT\ln(M_w\gamma_i^{\infty}) = \mu_i^* + RT\ln M_w \qquad \textbf{(3-25)}$$

The natural logarithm of the infinite dilution activity coefficient for the hydrogen ion ($\ln\gamma_{H^+}^{\infty}$) is taken to be zero at any temperature. Using this convention the infinite dilution activity coefficient of ion *i* can be calculated relative to H^+. The value for the volume parameter for the hydrogen ion is obtained from equation 3-17, fixing q_{H^+} at zero and using the *r* and *q* parameters for water given by Abrams and Prausnitz (1975) (Thomsen, 1997). The interaction energy parameters between the hydrogen ion and the rest of the species were fixed to 10^{10} K and 0, meaning no interaction between the hydrogen ion and the other components. With this convention, the contribution of the hydrogen ion to the residual excess Gibbs energy is null, and thus the activity coefficient for H^+ is mainly determined by the Debye-Hückel term at all concentrations and temperatures (Thomsen et al., 1996).

Some of the u_{ki}^0 and u_{ki}^t parameters have been assigned the values 2500 K and 0, respectively. This is the case for the interaction parameters between aqueous CO_2 and CO_3^{2-}. Solutions containing CO_3^{2-} are characterized by containing an insignificant amount of aqueous CO_2. Therefore, the interaction between those two species can be considered negligible. The same explanation is followed by the interaction parameter between Ba^{2+} and SO_4^{2-}. The solubility of $BaSO_4$ in all the systems studied is so low, that the interaction between those two ions may be considered negligible. In other cases, the lack of experimental data for certain salts makes it difficult to estimate some parameters. This is the case for the binary interaction energy parameters between Sr^{2+} or Ba^{2+} and OH^-. Moreover, those interactions are not considered relevant for the aim of the present work and are assumed to be low. As done by Thomsen et al. (1996), the water-water and the like cation interaction energy parameters have been fixed at zero to reduce the total number of parameters. This will influence the numerical value of the other parameters, but not the value of the binary interactions (ψ_{ki} in equation 3-6), which is calculated from the difference between interaction energy parameters.

Many of the UNIQUAC parameters required in the present work have already been estimated or given a fixed value and can be found in Thomsen (1997) or Thomsen et al. (1999). This is the case for volume and surface area parameters for H_2O, H^+, Na^+, Ca^{2+}, Mg^{2+}, Cl^-, SO_4^{2-}, OH^-, CO_3^{2-} and HCO_3^-. Table 3-1 shows all the possible binary interactions between the different species considered in the present work. Cells in light grey represent parameters that have already been determined or given a fixed value. Cells in blue represent parameters to be estimated (or fixed) in the present work.

The unknown r_i, q_i, u_{ki}^0 *and* u_{ki}^t parameters are determined on the basis of experimental data from the IVC-SEP databank for electrolyte solutions (http://www.ivc-sep.kt.dtu.dk/databank/databank.asp).

The low number of parameters required by the extended UNIQUAC model to perform solid-liquid, liquid-liquid, vapour-liquid and speciation equilibria calculations is one of the main advantages of the model. The total number of parameters needed by the extended UNIQUAC model is similar to that required by the NRTL model, but considerably lower than the number required by Pitzer's approach. According to Krop (1999), the complete thermodynamic description of the three component system NH_3-CO_2-H_2O using Pitzer's approach requires as many as 248 parameters (128 of them of binary and 120 of ternary interactions) assuming the symmetry of the ternary interaction parameters. Otherwise, the number of total parameters is furthermore increased. If the same system is described by the extended UNIQUAC model, the total number of parameters is decreased to 52: 16 volume and surface area parameters for the eight species considered by Krop (1999) (H^+, OH^-, $NH_3(aq)$, NH_4^+, $CO_2(aq)$, CO_3^{2-}, HCO_3^- and NH_2COO^-), and 36 binary interaction energy parameters. Of those, fixed values would be given to the interaction energy parameters between the hydrogen ion and any other species, and for the interaction NH_4^+-NH_4^+. Therefore, the number of unknown parameters is reduced to 43. If the temperature dependency needs to be included in the model, the number of parameters required by

Pitzer's approach would increase by a factor of 4-5, while only 120 parameters would be needed by the extended UNIQUAC model.

Table 3-1.
Binary interaction energy parameters for the multicomponent system considered in the present work

	CO_2	H_2O	H^+	Na^+	Ca^{2+}	Ba^{2+}	Sr^{2+}	Mg^{2+}	HCO_3^-	OH^-	Cl^-	CO_3^{2-}	SO_4^{2-}
CO_2	🟦												
H_2O	🟦	(1)											
H^+	🟦	(1)	(1)										
Na^+	🟦	(1)	(1)	(1)									
Ca^{2+}	🟦	(2)	(2)	🟦	(2)								
Ba^{2+}	🟦	🟦	🟦	🟦	🟦	🟦							
Sr^{2+}	🟦	🟦	🟦	🟦	🟦	🟦	🟦						
Mg^{2+}	🟦	(2)	(2)	(2)	(2)	🟦	🟦	(2)					
HCO_3^-	🟦	(1)	(1)	(1)	🟦	🟦	🟦	🟦	(1)				
OH^-	🟦	(1)	(1)	(1)	(2)	🟦	🟦	🟦	(1)	(1)			
Cl^-	🟦	(1)	(1)	(1)	(2)	🟦	🟦	(2)	(1)	(1)	(1)		
CO_3^{2-}	🟦	(1)	(1)	(1)	🟦	🟦	🟦	🟦	(1)	(1)	(1)	(1)	
SO_4^{2-}	🟦	(1)	(1)	(1)	(2)	🟦	🟦	(2)	(1)	(1)	(1)	(1)	(1)

(1) Parameters taken from Thomsen et al. (1999).
(2) Unpublished parameters

3.6 Parameter Estimation

All the parameters required are estimated on the basis of experimental data, mainly solid-liquid equilibrium data, in the temperature range from -10°C to 300°C , pressures up to 1000 bar and concentrations from infinite dilution to saturation. Binary, ternary and quaternary data sets for mixtures with solvent water; cations Na^+, Ca^{2+}, Mg^{2+}, Sr^{2+} and Ba^{2+}; and anions Cl^-, CO_3^{2-}, HCO_3^- and SO_4^{2-} were used. Also, VLE and SLE experimental data containing carbon dioxide were employed.

All data were analyzed before being used. The first data check is done within each source of data, analyzing the tendency followed by the solubility with increasing temperature, pressure and/or salt concentration. For all the salts analyzed at high pressure in the present work, solubility increases with increasing pressure. Regarding the temperature and salt concentration, the behaviour varies from one system to another (e.g., $CaSO_4$ solubility in pure water decreases with increasing temperature, while $BaSO_4$ solubility in pure water increases with temperature up to around 125°C, and behaves in the opposite way for higher temperatures). The trend followed by each system studied is generally well known and should be easily observed in the experimental data used. Also, the experimental procedure and device used to perform the measurements can be studied in order to find out methodological errors. Finally, data from different sources at the same conditions can be compared and those points considerably far away from the main tendency can be rejected. Note that for certain systems, the amount of data at high temperature and pressure are scarce and such comparison is difficult or even impossible. The problem is enhanced when the experiments are performed in solutions containing a second salt instead of pure water. The number of points that can be compared in this case is reduced drastically.

The parameter estimation procedure varied depending on the system and number of unknown parameters. For example, for the system NaCl-$SrSO_4$-H_2O, the unknown parameters were the volume and surface area parameters for Sr^{2+}, and the binary interaction energy parameters between Sr^{2+} and H_2O, H^+, Na^+, Sr^{2+}, Cl^-, SO_4^{2-}, and OH^-. As mentioned previously, some of these parameters are fixed due to the lack of available experimental data or to reduce the total number of parameters. Thus, $u^0_{Sr^{2+}-Sr^{2+}} = 0\,K$, $u^t_{Sr^{2+}-Sr^{2+}} = 0$, $u^0_{Sr^{2+}-H^+} = 10^{10}\,K$, $u^t_{Sr^{2+}-H^+} = 0$, $u^0_{Sr^{2+}-OH^-} = 2500\,K$ and $u^t_{Sr^{2+}-OH^-} = 0$. The final set of parameters to be estimated was $r_{Sr^{2+}}$, $q_{Sr^{2+}}$, $u^0_{Sr^{2+}-H_2O}$, $u^t_{Sr^{2+}-H_2O}$, $u^0_{Sr^{2+}-Na^+}$, $u^t_{Sr^{2+}-Na^+}$, $u^0_{Sr^{2+}-Cl^-}$, $u^t_{Sr^{2+}-Cl^-}$, $u^0_{Sr^{2+}-SO_4^{2-}}$, and $u^t_{Sr^{2+}-SO_4^{2-}}$. The volume and surface area parameter for Sr^{2+}, together with the interaction energy parameters between Sr^{2+}-H_2O, Sr^{2+}-Cl^- and Sr^{2+}-Na^+ were estimated on the basis of experimental data for the binary system $SrCl_2$-H_2O and for the ternary system $SrCl_2$-NaCl-H_2O. These parameters were determined simultaneously in order to differentiate between the interaction Sr^{2+}-H_2O and the other interactions. Once these parameters are estimated, the Sr^{2+}-SO_4^{2-} binary interaction energy is obtained from experimental solubility data for the binary system $SrSO_4$-H_2O at low pressure (atmospheric pressure or the saturation pressure of the solution at the given temperature) and the ternary system $SrSO_4$-Na_2SO_4-H_2O. The pressure parameters for the salt $SrSO_4$ were determined on the basis of experimental solubility data for celestite in pure water at high pressure. Finally, experimental data on the quaternary system NaCl-$SrSO_4$-H_2O are added to the database and all parameters are estimated simultaneously.

To estimate the parameters values, a non-linear, least squares minimization is performed in order to minimize the difference between calculated and experimental data. Such difference was calculated in different ways according to the type of data and the system being studied. For the majority of the systems, the objective function to minimize was:

$$F = \sum_{i=1}^{ndata} \left| \frac{\sum_{j=1}^{n} (s_{j,calc} - s_{j,\exp})}{\sum_{j=1}^{n-1} s_{j,\exp} + 0.04} \right| \cdot 100 \qquad \textbf{(3-26)}$$

where the summation is over the data points and *s* is the solubility in mass percentage. *Calc* and *exp* in equation 3-26 refer to calculated and experimental data, respectively. The summation in the numerator of equation 3-26 is over all the species present in the system (water, ions and molecules), while the summation in the denominator includes all the species but water. Most of the salts we are dealing with have a very low solubility in water and using solubility in the denominator of the objective function would magnify the error, even though the agreement between experimental points and the model is good. The problem was solved by introducing 0.04 in the denominator of equation 3-26. The constant 0.04 was found to give low deviations if the experimental points were well represented by the extended UNIQUAC model and vice versa.

When estimating parameters for the NaCl-H_2O system, the large solubility of sodium chloride in water allows the use of the residual deviation (equation 3-27) as the objective function:

$$F_{NaCl-H_2O} = \sum_{i=1}^{ndata} \left| \frac{\sum_{j=1}^{n} (s_{j,calc} - s_{j,\exp})}{\sum_{j=1}^{n} s_{j,\exp}} \right| \cdot 100 \qquad \textbf{(3-27)}$$

3.7 References in Chapter 3

Abrams, D.S., Prausnitz, J.M., 1975. Statistical thermodynamics of liquid mixtures: A new expression for the excess gibbs energy of partly or completely miscible systems. AIChE Journal 21, 116-128.

Arnórsson, S., Sigurdsson, S., Svavarsson, H., 1982. The chemistry of geothermal waters in Iceland. I. Calculation of aqueous speciation from 0° to 370°C. Geochimica et Cosmochimica Acta 46, 1513-1532.

Atkinson, G., Raju, K., Howell, R.D., 1991. The thermodynamics of scale prediction. Proceedings of the SPE Interantional Symposium on Oilfield Chemistry, 20-22, Anaheim, CA, USA, Society of Petroleum Engineers, Dallas, 209-215.

Ball, F.X., Planche, H., Fürst, W., Renon, H., 1985. Representation of deviation from ideality in concentrated aqueous solutions of electrolytes using a mean sperical approximation molecular model. AIChE Journal 31, 1233-1240.

Battistelli, A., Calore, C,. Pruess, K., 1993. A fluid property module for the TOUGH2 simulator for saline brines with non-condensible gas. Proceedings 18th Workshop on Geothermal Reservoir Engineering, Stanford, CA, pp. 249-259.

Battistelli, A., Calore, C., Pruess, K., 1997. The simulator TOUGH2/EWASG for modelling geothermal reservoirs with brines and non-condensible gas. Geothermics 26 (4), 437-464.

Belaustegi, Y., Olazabal, M. A., Madariaga, J. M., 1999. Development of a Modified Bromley's Methodology for the estimation of ionic media effects on solution equilibria. Part 4. The chemical model of Fe(III) with the halide ligands in aqueous solution at 25ºC Fluid Phase Equilibria 155, 21-31.

Bertero, L., Chierici, G.L., Gottardi, G., Mesini, E., Mormino, G., 1988. Chemical equilibrium models: Their use in simulating the injection of incompatible waters. SPE Reservoir Engineering 14126, 288-294.

Bjerrum, N., 1926. Untersuchungen über ionenassoziation. Mat. Fys. Medd., Kgl. Danske Videnskabernes Selskab 7 (9), 3-48.

Borge, G., Castaño, R., Carril, M. P., Corbillón, M. S., Madariaga, J. M., 1996. Development of a Modified Bromley's Methodology (MBM) for the estimation of ionic media effects on solution equilibria Part 1. Calculation of the interaction parameters in the molar and molal scales at 25ºC Fluid Phase Equilibria, 121, 85-98.

Bromley, L.A., 1973. Thermodynamic properties of strong electrolytes in aqueous solutions. AIChE Journal 19, 313-320.

Brønsted, J. N, 1922. Studies on solubility. IV. Principle of the specific interaction of ions. Journal of the Americal Chemical Society 44, 877-898.

Carrier, H., Ye, S., Vanderbeken, I., Li, J., Xans, P., 1998. Salt solubility under high pressure and high temperature. High Temperature-High Pressure 30, 629-634.

Chen, C., Britt, H., Boston, J., Evans, L., 1982. Local composition model for the excess Gibbs energy of aqueous electrolyte systems. AIChE. J. 28, 588.

Chen, C.C., Evans, L.B., 1986. A local composition model for the excess Gibbs energy of aqueous electrolyte systems. AIChE Journal 32, 444-454.

Chou, I.M., 1987. Phase relations in the system NaCl-KCl-H_2O. III. Solubilities of halite in vapor-saturated liquids above 445°C and redetermination of phase equilibrium properties in the system NaCl-H_2O. Geochimica et Cosmochimica Acta 51, 1965-1975.

Clegg, S.L., Simonson, J.M., 2001. A BET model of the thermodynamics of aqueous multicomponent solutions at extreme concentration. J. Chem. Thermodynamcis 33, 1457-1472.

Cruz, J.L., Renon, H., 1978. A new thermodynamic representation of binary electrolyte solutions nonideality in the whole range of concentrations. AIChE Journal 24, 817-830.

Davies, C.W., 1962. Ion association. Butterworths, London.

Debye, P., Hückel, E., 1923. Zur Theorie der Elektrolyte. I. Gefrierpunktserniedrigung und verwandte Erscheinungen. Physikalische Zeitschrift 24, 185-206.

Duan, Z., Møller, N, Weare, J.H., 1992a. An equation of state for the CH_4-CO_2-H_2O systems: I. Pure systems from 0 to 1000ºC and 0 to 8000 bar. Geochimica et Cosmochimica Acta 56, 2605-2617.

Duan, Z., Møller, N, Weare, J.H., 1992b. An equation of state for the CH_4-CO_2-H_2O systems: II. Mixtures from 50 to 1000ºC and 0 to 1000 bar. Geochimica et Cosmochimica Acta 56, 2619-2631.

Duan, Z., Møller, N., DeRocher, T., Weare, J.H., 1996. Prediction of boiling, scaling and formation conditions in geothermal reservoirs using computer programs TEQUIL and GEOFLUIDS. Geothermics 25 (6), 663-678.

Fowler, S.R., Guggenheim, E.A., 1949. Statistical thermodynamics. University Press, Cambridge, 1965

Greenberg, J.P., Møller, N., 1989. The prediction of mineral solubilities in natural waters: A chemical equilibrium model for the Na-K-Ca-Cl-SO_4-H_2O system to high concentration from 0 to 250ºC. Geochimica et Cosmochimica Acta 53, 2503-2518.

Guggenheim, E.A., 1935. The specific thermodynamic properties of aqueous solutions of strong electrolytes. Philosphical Magazine 19, 588-643.

Haarberg, T., 1989. Mineral deposition during oil recovery. An equilibrium model. Ph.D. Thesis. Instittut for Uorganisk Kjemi, Norges Tekniske Høgskole, Trondheim, Norway.

Haghtalab, A., Vera, J., 1988. A non-random factor model for the excess Gibbs energy of electrolyte solutions. AIChE J. 34, 803-813.

Hamer, W.J., Wu, Y.C., 1972. Osmotic coefficients and mean activity coefficients of uni-univalent electrolytes in water at 25ºC. J. Phys. Chem. Ref. Data 1, 1047-1099.

Harvie, C.E., Weare, J.H., 1980. The prediction of mineral solubilities in natural waters.. Geochim. et Cosmochim. Acta 44, 981-997.

Harvie, C.E., Möller, N., Weare, J.H., 1984. The prediction of mineral solubilities in natural waters: The Na-K-Mg-Ca-H-Cl-SO_4-OH-HCO_3-CO_3-CO_2-H_2O system. Geochimica et Cosmochimica Acta 48, 723-751.

He, S., Morse, J.W., 1993. Prediction of halite, gypsum, and anhydrite solubility in natural brines under subsurface conditions. Computer & Geosciences 19, 1-22.

Helgeson, H.C., 1967. Thermodynamics of complex dissociation in aqueous solutions at elevated temperatures. J. Phys. Chem. 71, 3121-3136.

Helgeson, H.C., 1969. Thermodynamics of hydrothermal systems at elevated temperatures and pressures. Amer. J. Sci. 267, 729-804.

Helgeson, H.C., 1970. Calculation of mass transfer in geochemical process involving aqueous solutions. Geochimica et Cosmochimica Acta 34, 569-592.

Helgeson, H.C., Kirkham, D.H., 1974 a. Theoretical prediction of the thermodynamic behaviour I. American Journal of Science 274, 1089-1198.

Helgeson, H.C., Kirkham, D., 1974 b. Theoretical prediction of the thermodynamic behaviour of aqueous electrolytes at high pressures and temperatures: II. Debye-Hückel parameters for activity coefficients and relative partial molal properties. Amer. J. Sci. 274, 1199-1261.

Helgeson, H.C., Kirkham, D.H., 1976. Theoretical prediction of the thermodynamic behaviour III American Journal of Science 276, 97-240.

Helgeson, H.C., Delany, J.M., Nesbitt, H., Wayne; B., Dennis, K., 1978. Summary and critique of the thermodynamic properties of rock-forming minerals. Pp 229

Helgeson H.C., Kirkham D.H., Flowers G.C., 1981. Theoretical prediction of the thermodynamic behaviour IV. American Journal of Science 281, 1249-1516.

Houghton, G., McLean, A.M., Ritchie, P.D., 1957. Compressibility, fugacity, and water-solubility of carbon dioxide in the region 0-36 atm. and 0-100ºC. Chemical Engineering Science 6, 132-137.

Howell, R.D., Raju, K., Atkinson, G., 1992. Thermodynamics of "Scale" mineral solubilities 4. $SrSO_4$. J. Chem. Eng.

Data 37, 464-469.

Iliuta, M., Rasmussen, P., Thomsen, K., 1999. Electrolyte solutions continuing education course, IVC-SEP, Technical University of Denmark, Lyngby, Denmark.

Jacques, D.C., Bourland, B.I., 1983. A study of solubility of strontium sulphate. SPEJ, 292-300.

Jacobson, R.L., Langmuir, D., 1974. Dissociation constants of calcite and $CaHCO_3^+$ from 0 to 50°C. Geochimica et

Cosmochimica Acta 33, 301-318.

Johnson, J.W., Oelkers, E.H., Helgeson, H.C., 1992. SUPCRT92: A software package for calculating the standard molal thermodynamic properties of minerals, gases, aqueous species, and reactions from 1 to 5000 bar and 0 to 1000ºC. Computers and Geosciences 18, 899-947.

Kaasa, B., 1998. Prediction of pH, mineral precipitation and multiphase equilibria during oil recovery. Ph.D. thesis. Institutt for Uorganisk Kjemi. Norges Teknisk-Naturvitenskapelige Universitet, Trondheim, pp. 5-272.

Kharaka, Y.K., Gunter, W.D., et al., 1988. Solmineq 88: A computer program for geochemical modelling of water-rock interactions. U.S. Geological Survey, Water-Resources Investigations Report, California, pp. 88-4221.

Kaz'min, L.A., 1983. Computer-based methods of physicochemical simulation of water-rock interaction in Geochemistry. Cand. Sci. (Geol.-Min.) Dissertation, Irkutsk.

Kolker, A., de Pablo, J.J., 1995. Thermodynamic modeling of concentrated aqueous electrolyte. AIChE Journal 41, 1563-1571.

Krop, J., 1999. New approach to simplify the equation for the excess Gibbs free energy of aqueous solutions of electrolytes applied to the modelling of the NH_3-CO_2-H_2O vapour-liquid equilibria. Fluid Phase Equilibria 163, 209-229.

Langelier, W.G., 1936. The analytical control of anti-corrosion water treatment. J. AWWA 25, 1500-1521.

Lewis, G.N., Randall, M., 1921. The activity coefficient of strong electrolytes. J. Am. Chem. Soc. 43, 1112-1154.

Li, Y-H., Crane, S. D., Coleman, J. R., 1995. Novel approach to predict the co-precipitation of $BaSO_4$ and $SrSO_4$. SPE 29489, 447-461.

Lietzke, M.H., Stoughton, R.W., 1975. Extension of a two-structure model for electrolyte solutions to aqueous mixed electrolyte systems. J. Inorg. Nucl. Chem. 37, 2503-2506.

Lin, C., Tseng, H., Lee, L., 1998. A three-characteristic-parameter model for strong electrolytes. Fluid Phase Equilibria 152, 169-185.

Liu, Y., Harvey, A.H., Prausnitz, J.M., 1989. Thermodynamics of concentrated electrolyte solutions. Chem. Eng. Comm. 77, 43-66.

Lu, X., Zhang, L., Wang, Y., Shi, J., 1996. Simultaneous prediction of activity coefficients and enthalpy for aqueous electrolyte solutions at high temperature Fluid Phase Equilibria 116, 201-208.

Macedo, E. A., Skovborg, P., Rasmussen, P., 1990. Calculation of phase equilibria for solutions of strong electrolytes in solvent-water mixtures. Chem. Eng. Sci. 45, 875-882.

Marcus, Y., 1997. Ion Properties. Marcel Dekker, Inc.

Marion, G.M., Farren, R.E., 1999. Mineral solubilities in the Na-K-Mg-Ca-Cl-SO_4-H_2O system: A re-evaluation of the sulphate chemistry in the Spencer-Møller-Weare model. Geochimica et Cosmochimica Acta 63 (9), 1305-1318.

Marshall J.R., 1989. Thermodynamic calculations of calcium carbonate scaling in geothermal wells, Dixie Valley geothermal field, U.S.A. Geothermics 18 (1-2), 269-277.

Marshall, S., May, P., Hefter, G., 1995. Least square analysis of osmotic coefficient data at 25ºC according to Pitzer's equation, 1:1 electrolytes. J. Chem. Eng. Data 40, 1041-1052.

Maurer, G., Prausnitz, J.M., 1978. On the derivation and extension of the UNIQUAC equation. Fluid Phase Equilibria 2, 91-99.

Meissner, H.P., Kusik, C.L., Tester, J.W., 1972. Activity coefficients of strong electrolytes in multicomponent aqueous solution. AIChE Journal 18, 294-298.

Miller, D.G., Piwinskii, A.J., Yamauchi, R., 1977. Geochemical equilibrium codes: A means of modelling precipitation and reinjection phenomena in the Salton Sea geothermal field. SPE 6604.

Millero, F.J., 1979. The thermodynamics of the carbonate system in seawater. Geochimica et Cosmochimica Acta 43 (10), 1651-1661.

Monnin, C., Galinier, C., 1988. The solubility of celestite and barite in electrolyte solutions and natural waters at 25ºC: A thermodynamic study. Chemical Geology 71, 283-296.

Monnin, C., 1999. A thermodynamic model for the solubility of barite and celestite in electrolyte solutions and seawater to 200ºC and to 1 kbar. Chemical Geology 153, 187-209.

Møller, N., 1988. The prediction of mineral solubilities in natural waters: A chemical equilibrium model for the system to high temperature and concentration. Geochimica et Cosmochimica Acta 52, 821-837.

Møller, N., Greenberg, J.P., Weare, J.H., 1998. Computer modelling for geothermal systems: Predicting carbonate and silica scale formation, CO_2 breakout and H_2S exchange. Transport in Porous Media 33, 173-204.

Naumov, V.B., Khakimov, A.K., Khodakovskiy, I.L., 1974. Solubility of carbon dioxide in concentrated chloride solutions at high temperatures and pressures. Geokhimiya 1, 45-55.

Nicolaisen, H., Rasmussen, P., Sørensen, J.M., 1993. Correlation and predicition of mineral solubilities in the reciprocal salt system (Na^+, K^+)(Cl^-, SO_4^{2-})-H_2O at 0-100ºC Chemical Engineering Science 48, 3149-3158.

Oddo, J.E., Tomson, M.B., 1994. Why scale forms and how to predict it. SPE Production and Facilities, 47-54.

Pal, K., Mahapatra, P., Sengupta, M., 1991. Activity measurements in aqueous mixed electrolyte solutions. 5. Ternary mixtures of (i) hydrochloric acid, (ii) mono-, di-, or trimethylammonium chloride, and (iii) water of constant total molality. J. Chem. Eng. Data 36, 440-446.

Pátzay, G., Stáhl, G., Kármán, F.H., Kálmán, E., 1997. Modeling of scale formation and corrosion from geothermal water. Electrochimica Acta 43 (1-2), 137-147.

Pérez-Villaseñor, F., Iglesias-Silva, G.A., 2002. Osmotic and activity coefficients using a modified Pitzer equation for strong electrolytes 1:1 and 1:2 at 298.15 K. I&EC Res. 41, 1031-1037.

Pitzer, K., 1973. Thermodynamics of electrolytes I. Theoretical basis and general equations. Journal of Physical Chemistry 77 (2), 268-277.

Pitzer, K.S., Mayorga, G., 1973. Thermodynamics of electrolytes II. J. Phys. Chem. 77, 2300.

Pitzer, K.S., 1975. Thermodynamics of electrolytes. V. Effects of higher-order electrostatic terms. Journal of Solution Chemistry 4 (3), 249-265.

Pitzer, K.S., Simonson, J.M., 1991. Thermodynamics of multicomponent, miscible, ionic systems: theory and equations. Journal of Physical Chemistry 95 (17), 6746.

Plummer, L.N., Busenberg, E., 1982. The solubilities of calcite, aragonite and vaterite in CO_2-H_2O solutions between 0 and 90ºC, and an evaluation of the aqueous model for the system $CaCO_3$-CO_2-H_2O. Geochimica et Cosmochimica Acta 46, 1011-1040.

Polka, H. M., Li, J., Gmehling, J., 1994. A g^E model for single and mixed solvent electrolyte systems. Fluid Phase Equilibria 94, 115-127.

Potapov, V.V., Kashpura, V.N., Alekseev, V.I., 2001. A study of the growth of deposits in geothermal power systems.

Thermal Engineering 48 (5), 395-400.

Raju, K.U.G., Atkinson, G., 1988. Thermodynamics of scale mineral solubilities. 1. $BaSO_4$ (s) in H_2O and aqueous NaCl. J. Chem. Eng. Data 33, 490-495.

Raju, K.U.G., Atkinson, G., 1989. Thermodynamics of scale mineral solubilities. 2. $SrSO_4$ (s) in aqueous NaCl. J. Chem. Eng. Data 34, 361-364.

Raposo, J. C., Sanz, J., Borge, G., Olazábal, M. A., Madariaga, J. M., 1998. Fluid Phase Equilibria 155, 1-19.

Rasaiah, J.C., Friedman, H.L., 1968. Charged square-well model for ionic solutions. J. Chem. Phys. 48, 2724-2749.

Reardon, E.J., Armstrong, D.K., 1987. Celestite (SrSO4(s)) solubility in water, seawater and NaCl solution.

Geochimica et Cosmochimica Acta 51, 63-72.

Renon, H., Prausnitz, J.M., 1969. Derivation of the three-parameter Wilson equation for the excess Gibbs energy of liquid mixtures. AIChE Journal 15 (5), 785.

Renon, H., 1996. Models for excess properties of electrolyte solutions: Molecular bases and classification, needs and trends for new developments. Fluid Phase Equilibria 116, 217.

Sahai, N., Sverjensky, D.A., 1998. GEOSURF: A computer program for modeling adsorption on mineral surfaces from aqueous solution. Computers and Geosciences 24 (9), 853-873.

Sander, B., 1984. Extended UNIFAC/UNIQUAC models for gas solubility calculations and electrolyte solutions. Ph.D. Thesis, Technical University of Denmark, Lyngby, Denamrk.

Sander, B. Fredenslund, Aa., Rasmussen, P., 1986a. Calculation of vapour-liquid equilibria in mixed solvent/salt systems using an extended UNIQUAC equation. Chemical Engineering Science 41, 1171-1183.

Sander, B., Rasmussen, P. Fredenslund, Aa., 1986b. Calculation of vapour-liquid equilibria in nitric acid-water-nitrate salt systems using an extended UNIQUAC equation. Chemical Engineering Science 41, 1185-1195.

Sander, B., Rasmussen, P., Fredenslund, Aa., 1986c. Calculation of solid-liquid equilibria in aqueous solutions of nitrate salts using an extended UNIQUAC equation. Chemical Engineering Science 41, 1197-1202.

Satman, A., Ugur, Z., Onur, M., 1999. The effect of calcite deposition on geothermal well inflow performance. Geothermics 28, 425-444.

Shock, E.L., Helgeson, H.C., 1988. Calculation of the thermodynamic and transport properties. Geochimica et Cosmochimica Acta 52, 2009-2036.

Spencer, R.J., Møller, N., Weare, J.H., 1990. The prediction of mineral solubilities in natural waters: A chemical equilibrium model for the Na-K-Ca-Mg-Cl-SO_4-H_2O system at temperatures below 25ºC. Geochimica et Cosmochimica Acta 54, 575-590.

Stokes, R.H., Robinson, R.A., 1948. Ionic hydration and activity in electrolyte solutions. J. Am. Chem. Soc. 70, 1870-1878.

Tan, T.C., 1987. Model for predicting the effect of dissolved salt on the vapour liquid equilibrium of solvent mixtures. Chem. Eng. Res. Des. 65, 355-365.

Tan, T.C., 1990. A modified NRTL model for predicting the effect of dissolved solute on the vapour-liquid equilibrium of solvent mixtures. Chem. Eng. Res. Des. 68, 93-103.

Thomsen, K., Rasmussen, P., Gani, R., 1996. Correlation and prediction of thermal properties and phase behaviour for a class of electrolyte systems. Chemical Engineering Science 51, 3675-3683.

Thomsen, K., 1997. Aqueous electrolytes: model parameters and process simulation. Ph.D. thesis. Technical University of Denmark, Denmark.

Thomsen, K., Rasmussen, P., 1999. Modeling of vapor-liquid-solid equilibrium in gas-aqueous electrolyte systems. Chemical Engineering Science 54, 1787-1802.

Thomsen, K., Iliuta, M., Rasmussen, P., 2004. Extended UNIQUAC model for correlation and prediction of vapor-liquid-liquid-solid equilibria in aqueous salt systems containing non-electrolytes. Part B. Alcohol (ethanol, propanols, butanols) - water - salt systems. Chemical Engineering Science 59, 3631-3647.

Truesdell, A.H., Jones, B.F., 1974. WATEQ, a computer program for calculating chemical equilibria of natural waters. U.S. Geol. Survey J. Res. 2, 233-248.

Vanderveken, I., Suyu, Y., Bouyssiere, B., Carrier, H., Xans, P., 1999. Ability of the MHV2 mixing rule to describe the effect of salt on gas solubility in brines at high temperature and high pressure. High Temperatures-High Pressures 31, 653-663.

Vetter, O.J., Kandarpa, V., Harouaka, A., 1982. Prediction of scale problems due to injection of incompatible waters. JPT, 273-284.

Vonka, P., Løvland, J., Prokes, T., 1995. Describing vapor-liquid equilibria in methanol $PLU n-alkane systems by means of an equation of state with association. Int. J. of Thermophysics 16 (1), 227-236.

Wagner, W., Pruss, A., 1993. International equations for the saturation properties of ordinary water substance. J. Phys. Chem. Ref. Data 22, 783-787.

Wat, R.M.S., Sorbie, K.S., Todd, A.C., Chen, P., Jiang, P., 1992. Kinetics of $BaSO_4$ crystal growth and effect in formation damage. SPE 23814, 429-437.

Weare, J.H., 1987. Models of mineral solubility in concentrated brines with application to field observations. Chap. 5. Rev. in Mineralogy 17. Mineral Soc. Of Amer., 143-176.

Weiss, R.F., 1974. Carbon dioxide in water and seawater: The solubility of a non-ideal gas. Marine Chemistry 2, 203-215.

Wolery, T.J., 1983. EQ3NR a computer program for geochemical aqueous speciation-solubility calculations: User's guide and documentation. Lawrence Livermore Nat. Lab. Rpt., pp. 191.

Yuan, M.D., Todd, A.C., 1991. Prediction of sulfate scaling tendency in oilfield operations. SPE 18484, 237-250.

Yuan, M., Todd, A.C., Sorbie, K.S., 1994. Sulfate scale precipitation arising from seawater injection: a prediction study. Marine and Petroleum Geology 11(1), 24-30.

Zemaitis, J. F. Jr., Clark, D. M., Rafal, M., Scrivner, N. C., 1986. Handbook of aqueous electrolyte thermodynamics, design institute for physical property data, New York.

Zhang, Y., Shaw, H., Farquhar, R., Dawe, R., 2001. The kinetics of carbonate scaling – application for the prediction of downhole carbonate scaling. Journal of Petroleum Science and Engineering 29, 85-95.

Zuo, Y.X., Fürst, W., 1998. Use of an electrolyte equation of state for the calculation of vapour-liquid equilibria and mean activity coefficients in mixed solvent electrolyte systems. Fluid Phase Equilibria 150-151, 267-275.

4. Sulphate Scaling Minerals

This chapter covers the modelling work performed on sulphate scaling minerals, and it has been published with the title “Prediction of mineral scale formation in geothermal and oilfield operations using the extended UNIQUAC model. Part I. Sulfate scaling minerals” in Geothermics 34 (2005), 61-97 (authors: Ada Villafáfila García, Kaj Thomsen and Erling H. Stenby).

The literature contains little information on most of the systems studied in this chapter at temperatures and pressures different from 25°C and 1 bar. Some of the data present in the literature are, moreover, highly suspected of being erroneous and comparisons among the results reported by different authors show an unacceptable variation in many cases. Reliable and accurate solubility measurements covering a wide range of thermodynamic conditions are necessary in order to accurately determine scale formation, otherwise, false predictions could be produced, such as over-or underestimates of scale formation or even negligence of the same (Vetter et al., 1983). So far the data on $BaSO_4$ and $SrSO_4$ solubilities in the high temperature and pressure range are somewhat incomplete.

Of special concern is any system containing barite, as the solubilities are extremely low and therefore difficult to measure accurately.

According to Vetter et al. (1983), the celestite solubilities determined by atomic absorption spectroscopy (which is a common experimental technique used for this purpose) can have a relative deviation as high as 16%. This value is expected to be even larger for barite.

In the following, it will be demonstrated that the extended UNIQUAC model is able to give a very good representation of the solid-liquid phase equilibria in the binary and ternary systems, over the entire temperature, pressure and concentration range investigated. It will be shown that the model correlates the appearance and disappearance of the different solids very nicely. In all cases, the absolute deviation between extended UNIQUAC calculations and the experimental data is within experimental accuracy. A more detailed explanation about the procedure for calculating the experimental standard deviation is given in section 4.1.

The high accuracy of the extended UNIQUAC model seems to decrease when four different ions are present in the solution, which may be explained in part by the very large scatter in data for these kinds of systems. In most of the cases, the lack of experimental measurements at the same conditions (especially at high temperatures and pressures) makes it impossible to detect inaccurate data by comparison. For example, figure 4-1 shows the inconsistencies between different data sets for the quaternary $SrSO_4$-NaCl-H_2O system at 25ºC and 1 bar. In this case, the fact that a large number of investigators have studied the same system makes it easy to identify the unreliable data sets. As temperature and pressure increase, however, the number of sources reporting measurements of this type of system at the same conditions generally drops to one or two and no comparison is possible.

This being the case, most of the data containing four ions and water were used for parameter regression, even though some data sets were in clear disagreement. We discarded only the data sets that followed a wrong tendency when varying temperature, pressure and salt concentration.

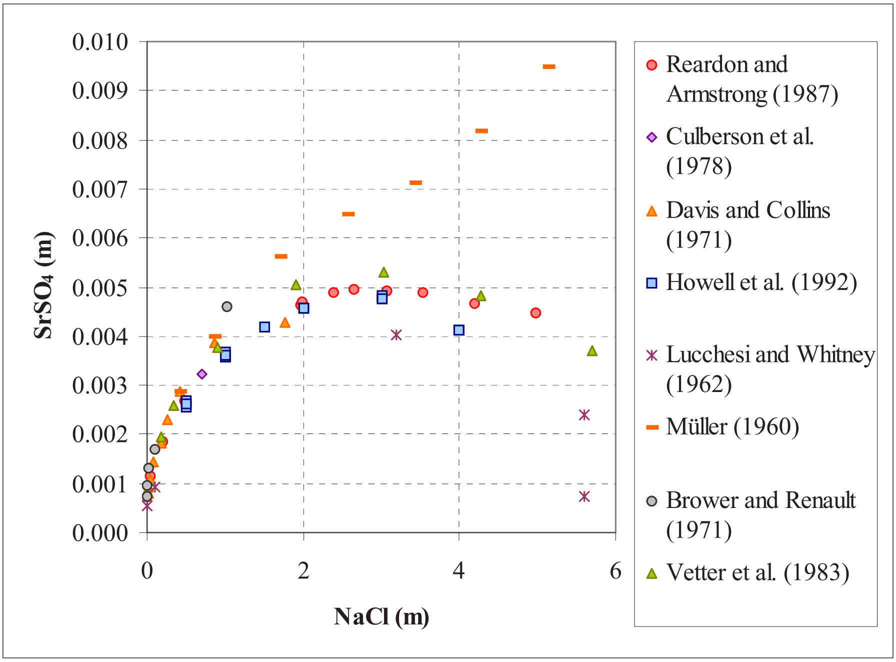

Figure 4-1. Experimental solid-liquid phase diagram for the $SrSO_4$-NaCl-H_2O system at 25ºC and 1 bar.

The surface area and volume parameters obtained from the present work, together with the values required for other species obtained by Thomsen and Rasmussen (1999) are given in table 5-15 in Chapter 5. The binary energy interaction parameters for the extended UNIQUAC model are shown in table 5-16 and table 5-17. Finally, the two new pressure parameters added to the extended UNIQUAC model to account for the pressure dependency are given in table 5-18. The parameters obtained from the present work are marked in bold.

The values for the standard state Gibbs free energy, enthalpy and heat capacity for the different crystalline phases analyzed are taken (whenever it was available) from the NIST Chemical Thermodynamics Database (1990). Those values are also reported in table 4-20.

4.1 Calculation of the Mean Absolute Deviation

Because of the different pressure and temperature conditions used by the different authors, it was not possible to include all the experimental measurements in the standard deviation (*SD*) calculation. In order to use as much information as possible, we calculated a weighted average standard deviation (*ASD*) from the *SD* of experiments carried out at the same conditions of temperature and pressure.

$$SD = \sqrt{\frac{\sum_{i=1}^{n}(m - m_{average})^2}{n-1}} \tag{4-1}$$

$$ASD = \frac{\sum_i n_i \cdot SD_i}{\sum n_i} \tag{4-2}$$

Thus, in equation 4-1, *n* represents the number of experimental data at the same *T* and *P* and the standard deviation is calculated for all the available experimental data sets at constant conditions. These *SD* values are introduced in equation 4-2, where the summation is over all the different data sets. All the calculations are performed in molality units (*m*).

For ternary systems, the standard deviation for each salt is assumed to be similar to the *SD* for the binary system salt-H_2O, as the real value could not be calculated because of a complete lack of data at the same conditions of temperature, pressure and salt concentration. This calculation was possible for the system $CaSO_4$-Na_2SO_4-H_2O only, because different authors performed experiments at the same conditions.

All data were analyzed prior to their use. Any data found to be inconsistent were not used for the parameter estimation and were not included in the standard deviation calculation.

When the same investigator reports more than one experimental point at the same conditions, we calculated the average value and used it as *m* in equation 4-1. In this way, no great weight is given to a single source.

For a given system, the *ASD* obtained for all the experimental data used is compared to the average absolute deviation (*AAD*) between the results calculated by the extended UNIQUAC model and the values reported by each reference.

$$AAD = \frac{\sum_{i=1}^{ndata} \left| m_{\text{experimental}} - m_{Extended\ UNIQUAC} \right|}{ndata} \tag{4-3}$$

These *AAD* values for each reference used in the present work are given in table 4-3 to table 4-19. The mean *AAD* (*MAAD*) for all the references dealing with each system used is given at the bottom of each table. In most cases the *AAD* for each data set is lower than the *ASD* so that the difference between experimental and calculated solubilities is within experimental accuracy.

In equation 4-3, *ndata* stands for the number of experimental data used from each reference.

Table 4-1 shows the values of the standard deviation for the different data sets at constant temperature and pressure for the system $SrSO_4$-H_2O. The calculated average standard deviation is also given in table 4-1.

Table 4-2 shows the values for the *ASD* for all the binary systems studied in this paper and for the ternary system $CaSO_4$-Na_2SO_4-H_2O. As mentioned previously, the *ASD* could not be calculated for the rest of the ternary and the quaternary systems.

Table 4-1
Experimental data used to calculate the *SD* for the system $SrSO_4$-H_2O

Number of data	***T* (°C)**	***P* (bar)**	***SD* (m)**
8	25	1	3.6E-05
2	30	1	5.7E-05
3	50	1	9.5E-05
2	75.5	1	1.1E-05
2	89.5	1	4.1E-06
2	100	1	5.0E-05
2	150.5	5	1.0E-04
2	200	15.6	2.8E-07
2	250	40	1.1E-06
		***ASD* (m):**	**4.1E-05**

Table 4-2
Calculated *ASD* values for different systems

System	***ASD* (m)**	
$BaSO_4$-H_2O	2.1E-06	
$BaCl_2$-H_2O	4.0E-02	
NaCl-H_2O	1.8E-01	
$SrSO_4$-H_2O	4.1E-05	
$SrCl_2$-H_2O	4.0E-02	
$CaSO_4$-H_2O	7.8E-04	
Na_2SO_4-$CaSO_4$-H_2O	1.8E-02	Na_2SO_4
	3.8E-04	$CaSO_4$

4.2 Systems Containing Barium

The results of the SLE-data correlation containing barium, performed in this work, are illustrated in tables 4-3 to 4-9 and figures 4-2 to 4-9. Experimental data are plotted along with calculated curves.

4.2.1 $BaSO_4$-H_2O System

The experimental and calculated phase diagrams for the system $BaSO_4$-H_2O at a constant pressure of 500 bar and a constant temperature of 200ºC are shown in figures 4-2 and 4-3, respectively. Barite solubility increases with temperature up to around 100-125ºC and starts decreasing for higher temperatures. Regarding pressure, a considerable increase from $8\cdot10^{-6}$ to $2.4\cdot10^{-5}$ mol $BaSO_4$ (kg H_2O)$^{-1}$ (m) is observed when the pressure is increased from 1 to 1000 bar. Of all the systems containing barite studied in the present work, only the $BaSO_4$-H_2O and $BaSO_4$-NaCl-H_2O systems have been studied at high pressures and temperatures, as they are the ones with scale deposition problems. The rest of the systems will be shown at atmospheric pressure and temperatures up to around 100ºC. The same applies to the other systems investigated in the present chapter; only $SrSO_4$-H_2O, $SrSO_4$-NaCl-H_2O, $CaSO_4$-H_2O and $CaSO_4$-NaCl-H_2O are considered relevant for scale formation and are studied at high temperature and pressure.

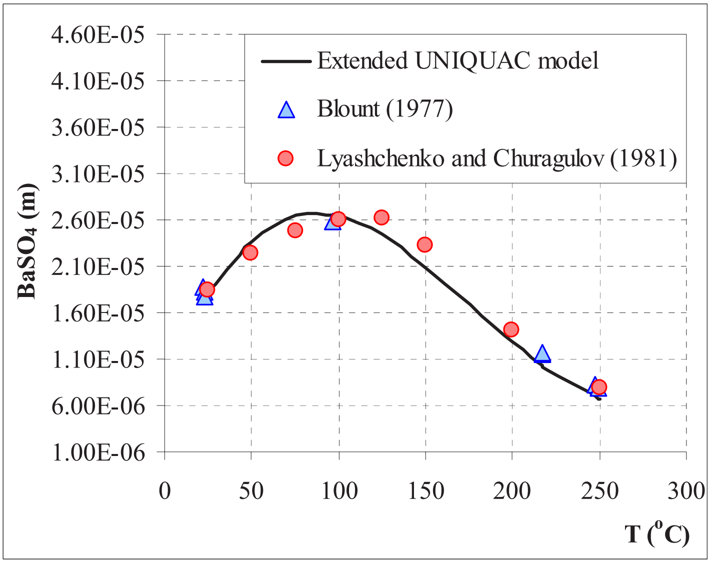

Figure 4-2. Experimental and calculated solid-liquid phase diagram for the $BaSO_4$-H_2O system at 500 bar

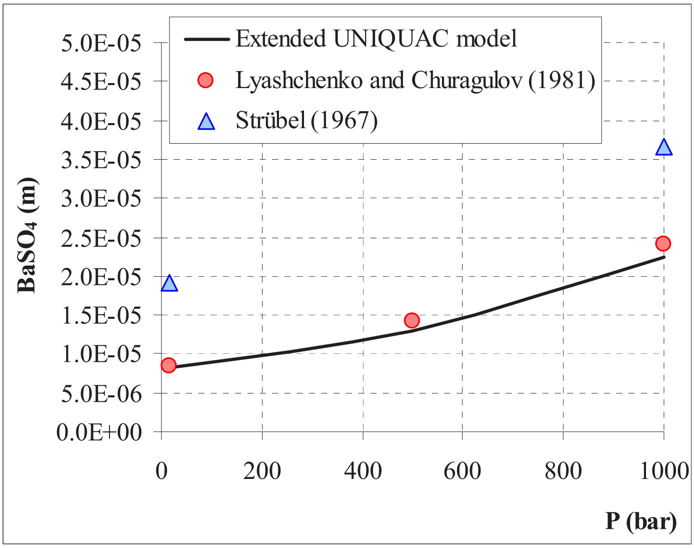

Figure 4-3. Experimental and calculated solid-liquid phase diagram for the $BaSO_4$-H_2O system at 200ºC

The representation by the extended UNIQUAC model of the solubility curves shown in figure 4-2 and figure 4-3 is very good, with a mean absolute deviation (*MAAD*) of $1.6 \cdot 10^{-6}$ m, well below the average experimental standard deviation (*ASD*: $2.1 \cdot 10^{-6}$ m). These values, together with a list of references for the experimental data used for parameter estimation, are presented in table 4-3. The total number of data found in the reference is given, together with the number of data chosen for parameter estimation in this work (in brackets).

Table 4-3
Experimental binary $BaSO_4$-H_2O SLE data sets used for parameter estimation

T (ºC)	*P* (bar)	Number of data	*AAD* (m)	Reference
25	1	1 (1)	1.8E-06	Trendafelov et al. (1994)
25	1	1 (1)	1.4E-06	Brower and Renault (1971)
25/95	1	6 (6)	5.5E-07	Templeton (1960)
23/279	36/1406	40 (32)	1.1E-06	Blount (1977)
25/300	1/1000	27 (27)	2.2E-06	Lyashchenko and Churagulov (1981)
99.8/600	4.8/2100	18 (0)		Strübel (1967)
			***MAAD* (m):**	**1.6E-06**

Strübel (1967) and Blount (1977) report data (11 and 8 points, respectively) at temperatures and pressures outside the range correlated in this work (up to 300ºC and 1000 bar).

The data of Strübel (1967) show very large deviations from model calculations and from other experimental data. Figure 4-3 shows the large disagreement when the data of Strübel

(1967) are compared to those of Lyashchenko and Churagulov (1981). The same disagreement is also found at other temperatures and pressures, when compared to other references from table 4-3. Moreover, in some of Strübel's (1967) measurements, a decrease in barite solubility is observed for increasing pressure. Strübel's (1967) data were not used for the evaluation of model parameters because of this apparent lack of reliability.

4.2.2 $BaCl_2$-H_2O System

The experimental data and the correlation results for the binary $BaCl_2$-H2O system are given in table 4-4 and plotted in figure 4-4. The *MAAD* between experimental and calculated solubilities is within experimental accuracy (*ASD* of 0.04 m).

Although the mean absolute deviation for this system is lower than the average experimental standard deviation, there are three references (Schreinemakers, 1911, Uspenskaya et al., 1955 and Moshinskii and Tikhomirova, 1973) for which the mean absolute deviation between calculated and experimental data is slightly higher than the average experimental standard deviation. Figure 4-4 shows that these three references seem to over- and under-estimate barium chloride solubility, when compared to the other ten references in table 4-4. This disagreement justifies the larger absolute deviation, although its value is low enough to keep these data sets.

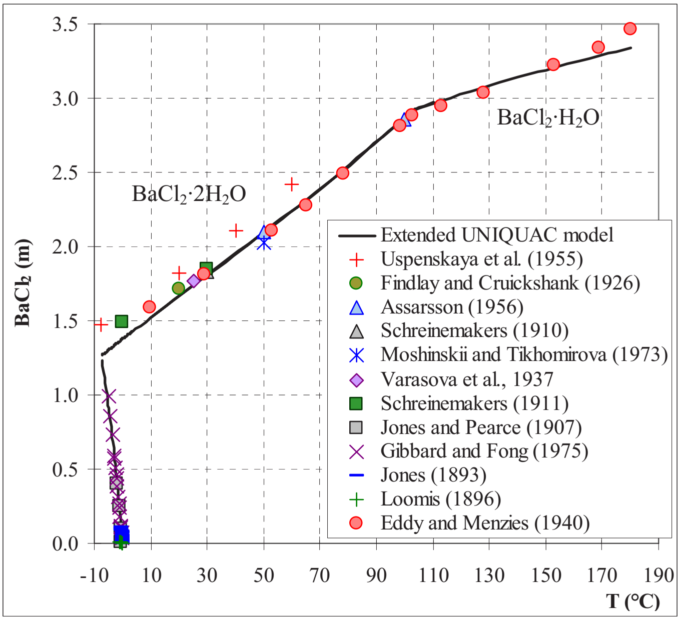

Figure 4-4. Experimental and calculated solid-liquid phase diagram for the $BaCl_2$-H_2O system at 1 bar.

Table 4-4
Experimental binary $BaCl_2$-H_2O SLE data sets used for parameter estimation

T (°C)	*P* (bar)	Number of data	*AAD* (m)	Reference
-7.6/60	1	4 (4)	1.2E-01	Uspenskaya et al. (1955)
-5/-0.1	1	17 (17)	1.3E-02	Gibbard and Fong (1975)
-1.9/-0.5	1	6 (6)	9.5E-03	Jones and Pearce (1907)
-0.9/0	1	5 (4)	1.1E-03	Loomis (1896)
-0.5/0	1	39 (39)	1.1E-02	Jones (1893)
0/30	1	2 (2)	7.8E-02	Schreinemakers (1911)
9.7/180	1/8.15	12 (12)	4.1E-02	Eddy and Menzies (1940)
20	1	1 (1)	4.0E-02	Findlay and Cruickshank (1926)
25	1	1 (1)	3.0E-02	Varasova et al., 1937
30	1	1 (1)	2.2E-02	Schreinemakers and de Baat (1909)
30	1	1 (1)	2.2E-02	Schreinemakers (1910)
50	1	1 (1)	6.9E-02	Moshinskii and Tikhomirova (1973)
50/100	1	2 (2)	4.9E-03	Assarsson (1956)
			***MAAD* (m):**	**2.2E-02**

4.2.3 Na_2SO_4-$BaSO_4$-H_2O System.

We found only one reference (Jiang, 1996) dealing with the ternary system Na_2SO_4-$BaSO_4$-H_2O. Lieser (1965) and Felmy et al. (1990) also studied the latter system at 20 and 25ºC, respectively, but unfortunately they reported their data only as plots. The accuracy of these measurements is questionable as the disagreement among the sources is large. The problem is aggravated by the fact that barite solubility in Na_2SO_4-H_2O solutions is considerably lower than in pure water, because of the common-ion effect. Measurement of such low concentrations (of the order of $10^{-7}/10^{-8}$ m) becomes very difficult and likely to include large errors. In his paper, Jiang (1996) made no comparison with other sources with the result that it is impossible to determine the reliability of such measurements. The aqueous solutions were determined by atomic absorption spectroscopy and Jiang (1996) claims that the error is between ± 0.05%. According to Vetter et al. (1983), this technique can lead to relative deviations that are much larger than the value reported by Jiang (1996).

The range of temperatures and pressures covered for this system and the number of experimental data are given in table 4-5. The average absolute deviation between calculated and experimental data is also shown. The average experimental standard deviation for that reference could not be calculated as different measurements at the same conditions (temperature, pressure and Na_2SO_4 concentration) were not available.

The representation of the extended UNIQUAC model for the ternary system $BaSO_4$-Na_2SO_4-H_2O at 20ºC and 1 bar is shown in figure 4-5.

Table 4-5
Experimental ternary $BaSO_4$-Na_2SO_4-H_2O SLE data sets used for parameter estimation

T (°C)	*P* (bar)	Number of data	*AAD*$_{BaSO4}$ (m)	Reference
0/80	1	60 (60)	5.0E-08	Jiang (1996)
			***MAAD* (m):**	**5.0E-08**

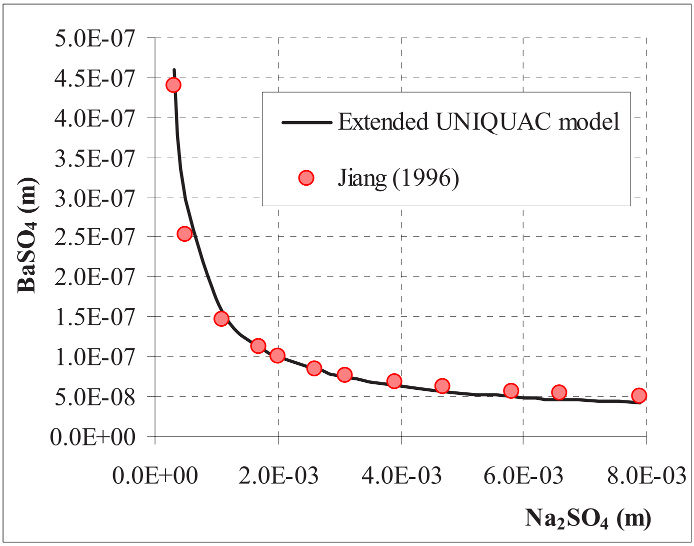

Figure 4-5. Experimental and calculated solid-liquid phase diagram for the $BaSO_4$-Na_2SO_4-H_2O system at 20°C and 1 bar.

4.2.4 $BaCl_2$-NaCl-H_2O System

The extended UNIQUAC model is also able to accurately represent the ternary system $BaCl_2$-NaCl-H_2O, presented in table 4-6 and figure 4-6. As mentioned previously, no experimental standard deviation could be calculated because of the lack of measurements carried out at the same experimental conditions.

Table 4-6
Experimental ternary $BaCl_2$-NaCl-H_2O SLE data sets used for parameter estimation

T (°C)	*P* (bar)	Number of data	*AAD*$_{BaCl2}$ (m)	Reference
-6.4/-0.2	1	21 (21)	5.3E-03	Gibbard and Fong (1975)
0/50	1	2 (2)	1.3E-01	Speranskaya (1954)
20	1	7 (7)	9.3E-02	Findlay and Cruickshank (1926)
30	1	10 (10)	8.3E-02	Schreinemakers and de Baat (1909)
			***MAAD* (m):**	**9.2E-02**

Speranskaya (1954) reports two measurements at 0 and 50ºC that deviate considerably from the model calculations. As no additional data for the ternary system are given at those conditions, it is not possible to compare these points with other measurements and determine their accuracy. The rest of the 38 points used are in close agreement with the extended UNIQUAC model and the system is satisfactorily represented by the model.

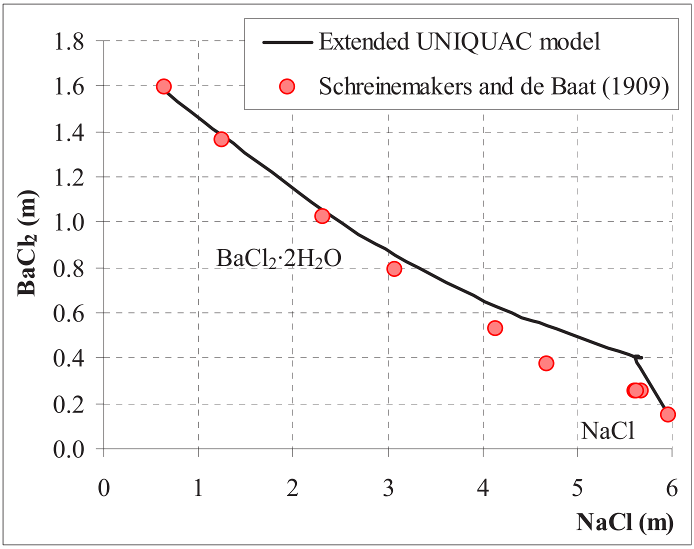

Figure 4-6. Experimental and calculated solid-liquid phase diagram for the $BaCl_2$-NaCl-H_2O system at 30ºC and 1 bar.

4.2.5 $BaSO_4$-NaCl-H_2O System

Table 4-7 presents an overview of the data used for evaluation of the model parameters for the system $BaSO_4$-NaCl-H_2O is given. The temperature and pressure range of each data set are listed, along with the average absolute deviation between calculated and experimental data for $BaSO_4$. The number of data points found and used from each set of data is also given in table 4-7. A more detailed review about the different experimental procedures employed in the different studies is given in Chapter 9.

Many of the data are shown to be inaccurate and most of them could not be tested for their reliability. It is clear, at certain conditions, the measurements are erroneous, as two sources report rather different values. Because of the lack of data at the same conditions it is impossible to determine which sources can be trusted. The extended UNIQUAC model is able, however, to accurately correlate experimental NaCl-$BaSO_4$-H_2O data, as shown in figures 4-7 and 4-8. The accuracy of the model is very good even for very high NaCl concentrations (up to 5 m NaCl), and also at high temperatures and pressures. Figure 4-8 shows the change in the solubility tendency with temperature depending on the NaCl concentration. For high ionic strengths, barite solubility increases constantly with temperature, while for low ionic strengths a maximum solubility is observed around 100-150ºC.

Table 4.7
Experimental quaternary NaCl-$BaSO_4$-H_2O SLE data sets used for parameter estimation

T (°C)	P (bar)	Number of data	AAD_{BaSO4} (m)	Reference
20/350	1/165	41 (40)	2.9E-05	Strübel (1967)
25/95	1	108 (108)	1.6E-05	Templeton (1960)
25	1	8 (8)	3.2E-05	Davis and Collins (1971)
80/120	1/414	34 (0)		Schulien (1987)
94/253	5/560	35 (35)	3.4E-05	Blount (1977)
95/340	1/165.4	84 (71)	2.2E-04	Uchameyshvili et al. (1966)
			***MAAD* (m):**	**7.5E-05**

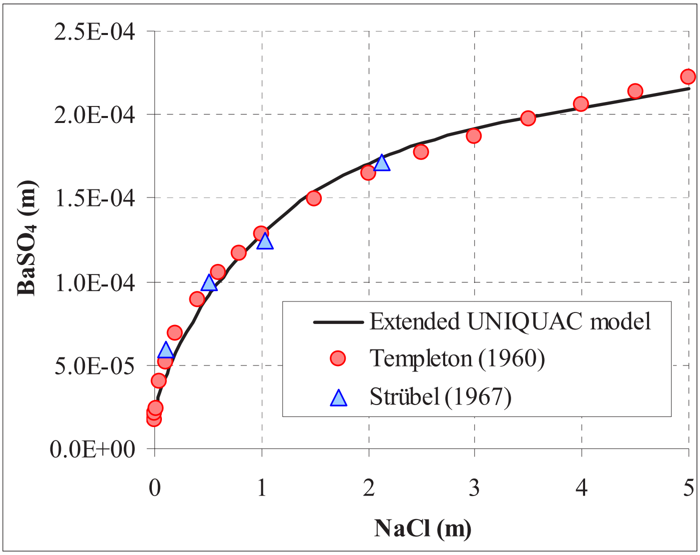

Figure 4-7 Experimental and calculated solid-liquid phase diagram for the $BaSO_4$-NaCl-H_2O system at 50ºC and 1 bar.

Uchameyshvili et al. (1966) and Strübel (1967) performed measurements outside the temperature range of interest in this work.

Uchameyshvili et al. (1966) data show a relatively large scatter at some conditions (i.e., barite solubilities at 0.25 m NaCl and 170°C varied from $8.66 \cdot 10^{-5}$ to $9.77 \cdot 10^{-5}$ m). When compared to Templeton (1960), the values reported by Uchameyshvili et al. (1966) are considerably lower, being the measurements by Templeton (1960) at 95°C comparable to the values given by Uchameyshvili et al. (1966) at 140°C. The latter investigators suggest such difference may be due to the different particle size employed (Uchameyshvili et al. (1966) used a single crystal while Templeton (1960) used finely crystalline powder).

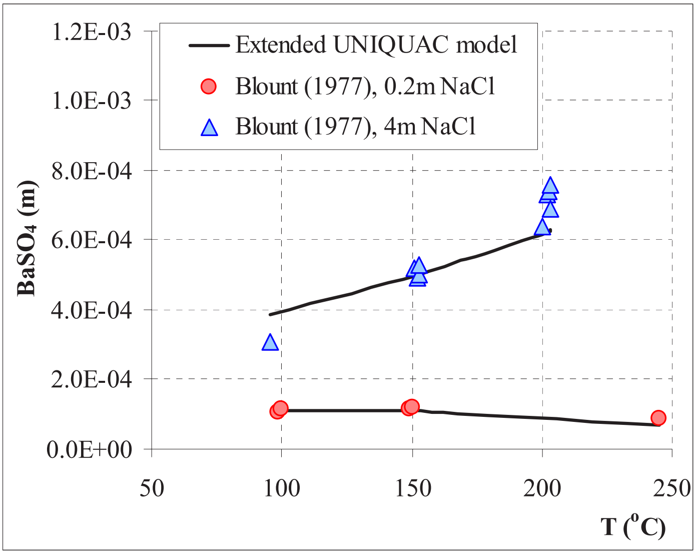

Figure 4-8 Experimental and calculated solid-liquid phase diagram for the $BaSO_4$-NaCl-H_2O system at 500 bar.

The data reported by Strübel (1967) at 90 and 100°C are consistent with those by Uchameyshvili et al. (1966) at 95°C, and also quite lower than the values by Templeton (1960). In general, the measurements performed by Strübel (1967) agree very well with the ones by Templeton (1960) for low temperatures (from 20 to 50°C). For higher temperatures, the disagreement is large, being more pronounced the larger the temperature is. Templeton (1960) shows a very large increase on barite solubility with increasing temperature from 65 to 95°C, while the influence of this temperature range is less pronounced (and practically negligible from 60 to 80°C) for the data reported by Strübel (1967). For example, similar solubility values are obtained by Templeton (1960) at 65°C and by Strübel (1967) at 80°C, under the same NaCl concentration.

At temperatures above 100°C and pressures equal to the saturation pressure of the solution, the data reported by Uchameyshvili et al. (1966) and Blount (1977) are in agreement in the region of overlap. Nevertheless, that agreement is lost for the high pressure (100 to 500 bar) range, where Blount (1977) reports low solubilities compared to Uchameyshvili et al. (1966) (the measurements by Uchameyshvili et al. (1966) at the saturation pressure of the solution are comparable to Blount's (1977) values at 500bar). As it happened for Uchameyshvili et al. (1966), a large scatter is also observed for Blount's (1977) data, especially at 150 and 200°C, where solubility values may vary from $6.4\cdot10^{-4}$ to $7.6\cdot10^{-4}$ m $BaSO_4$. Results obtained by Templeton (1960) and Strübel (1967) are considerably higher than those obtained by Blount (1977). The latter results show smoother variations with temperature, pressure and NaCl concentration. Blount (1977) calculated solubility values for barite in NaCl solutions at 25°C from the values of the solubility product and the activity coefficients from a modified Debye-Hückel equation. The results he obtained are below those reported by Templeton (1960) and Strübel (1967), and agree with the data reported by Puchelt (1967)[1]. Calculated thermodynamic quantities from Blount (1977) measurements closely agree with those calculated from thermal and solution density data.

Davis and Collins (1971) measurements are slightly lower than those by Templeton (1960) and Strübel's (1967) at 20, 25 and 30°C, but the general agreement is good.

According to Uchameyshvili et al. (1966), barite solubility increases steadily with increasing temperature for 2 m NaCl solutions, while it passes through a maximum for 0.25 m NaCl solutions, and it bends for 1 m NaCl solutions. The same monotically positive increase in barite solubility with increasing temperature was observed by Templeton (1960) for NaCl concentrations higher than 1 M, and by Blount (1977) for NaCl concentrations of 4 m. Contrary to this behaviour, Schulien (1987) reports a maximum in barite solubility between 100 and 120°C, independently of the NaCl content of the solution. The results given by Schulien (1987) are extremely low when compared to any other source in table 4.7. Moreover, the tendency followed by barite solubility with pressure seems to be wrong. No real changes are noticed in the solubility value when the pressure is increased from 1 to 414 atm. In some experiments, a slight reduction in barite solubility is observed when the pressure is increased to 414 bar, and a maximum is obtained at 200 bar.

Monnin (1999) developed a model for the solubility of barite in electrolyte solutions to 200°C and 1000 bar. The results predicted by his model at 80°C are in full agreement with Templeton's (1960) data, but that agreement is lost (10% RD) at 100°C when the results are compared to the experimental values determined by Strübel (1967) and Blount (1977) in the 1 to 3 M NaCl concentration range. Monnin's (1999) results are also systematically higher than Schulien's (1987) measurements at 80, 100, and 120°C and at 1, 200 and 400 bar.

---

[1] Puchelt (1967) reported his measurements only in plots, and therefore his values could not be used for parameter estimation. They were used, nevertheless, for comparison with other sources.

We can conclude there is a general disagreement among the different solubility measurements reported by the sources in table 4-7, especially at high temperatures and pressures. As a general tendency, it seems Templeton (1960) reports the highest values of solubility, followed by Uchameyshvili et al. (1966), Strübel (1967), and finally Blount (1977). Schulien's (1987) data are notably lower than the previous sources for any experimental condition.

4.2.6 $BaCl_2$-$SrCl_2$-Na_2SO_4 System

In order to estimate the interaction energy parameter between Ba^{2+} and Sr^{2+} the data by Qadirie (1990) were used. Qadirie (1990) performed solubility measurements in solutions containing $BaCl_2$, $SrCl_2$ and Na_2SO_4 at 20, 40 and 60°C and 1 atm. He analyzed both the concentration in the liquid phase and the composition of the solid phase, which was reported as a solid solution $(Ba^{2+}, Sr^{2+})SO_4^{2-}$. Nevertheless, the ratio $Ba^{2+}/(Ba^{2+} + Sr^{2+})$ in the solid solution was equal to 0.5 for most of the cases and could correspond to the formation of the double salt $BaSO_4{\cdot}SrSO_4$ instead of a solid solution. Thus, the system was modelled assuming the double salt $Ba{\cdot}Sr(SO_4)_2$ as the solid phase. Whenever the ratio $Ba^{2+}/(Ba^{2+} + Sr^{2+})$ was different from 0.5, two different solid phases were assumed to appear: the double salt $Ba{\cdot}Sr(SO_4)_2$ together with a pure salt $BaSO_4$ [for ratios $Ba^{2+}/(Ba^{2+} + Sr^{2+})$ higher than 0.5] or $SrSO_4$ [for ratios $Ba^{2+}/(Ba^{2+} + Sr^{2+})$ lower than 0.5]. The accuracy of the results obtained led us to conclude that the assumptions done are correct. Table 4-8 shows the average absolute deviation between the extended UNIQUAC model and the experimental data for the solubility of $BaCl_2$ and $SrCl_2$.

Table 4-8
Experimental $BaCl_2$-$SrCl_2$-Na_2SO_4-H_2O SLE data sets used for parameter estimation

T **(°C)**	***P*** **(bar)**	**Number of data**	***AAD*$_{Ba++}$ (m)**	***AAD*$_{Sr++}$ (m)**	**Reference**
20/60	1	112 (112)	2.8E-03	3.0E-03	Qadirie (1990)
		MAAD **(m):**	**2.8E-03**	**3.0E-03**	

4.2.7 Ba^{2+}-Mg^{2+} and Ba^{2+}-Ca^{2+} Interaction Energy Parameters

The binary energy interaction parameters for the pairs Ba^{2+}-Mg^{2+} and Ba^{2+}-Ca^{2+} were estimated on the basis of experimental SLE data for the ternary systems $BaCl_2$-MCl_2-H_2O, and the quaternary systems MCl_2-$BaSO_4$-H_2O and $Ca(NO_3)_2$-$BaCl_2$-H_2O, where M represents Ca and Mg. The sources employed, number of experimental data used and ranges of temperature and pressure covered are reported in table 4-9. The average absolute deviation between calculated and experimental data is given for Ba^{2+}.

Table 4-9
Experimental SLE data sets used for parameter estimation

T (°C)	P (bar)	Number of data	AAD_{Ba2+} (m)	Reference
25	1	8 (8)	8.0E-06	Davis and Collins (1971)[a]
25	1	12 (12)	8.9E-07	Neuman (1933) [a]
110/275	1/60	18 (18)	2.1E-04	Uchameyshvili et al. (1966)[a]
45/100	1	27 (27)	5.6E-02	Assarsson (1956)[b]
25	1	10 (10)	5.1E-05	Davis and Collins (1971)[c]
100/255	1/44	36 (36)	4.9E-04	Uchameyshvili et al. (1966)[c]
-17.5/60	1	97 (97)	7.3E-02	Uspenskaya et al. (1955)[d]
80/120	1	63 (63)	6.0E-02	Uspenskaya and Bergman (1955)[d]
25	1	7 (7)	2.5E-01	Varasova et al. (1937)[e]

[a] Quaternary $MgCl_2$-$BaSO_4$-H_2O system
[b] Ternary $MgCl_2$-$BaCl_2$-H_2O system
[c] Quaternary $CaCl_2$-$BaSO_4$-H_2O system
[d] Quaternary $Ca(NO_3)_2$-$BaCl_2$-H_2O system
[e] Ternary $CaCl_2$-$BaCl_2$-H_2O system

Puchelt (1967) measured barite solubility data in $MgCl_2$ and $CaCl_2$ solutions, but unfortunately he reported his measurements only in plots, and therefore his values could not be used for parameter estimation. They were used, nevertheless, for comparison with other sources. There is a very large discrepancy between the tendency followed by Puchelt (1967) and that given by Davis and Collins (1971) for the $CaCl_2$-$BaSO_4$-H_2O system. Davis and Collins (1971) obtained a maximum barite solubility ($7.8 \cdot 10^{-5}$ m) for $CaCl_2$ concentrations around 0.2 m, while Puchelt (1967) obtained the maximum solubility (around $2 \cdot 10^{-4}$ m) for a 1.8 m $CaCl_2$ solution. For the $MgCl_2$-$BaSO_4$-H_2O system, both Puchelt (1967) and Davis and Collins (1971) got a maximum in barite solubility for similar $MgCl_2$ concentrations (around 1.8 m), but the former investigator reports higher $BaSO_4$ values. For this system, there is a very good agreement between Neuman's (1933) and Davis and Collins' (1971) data in the region of overlap.

The data given by Uchameyshvili et al. (1966) for both $MgCl_2$-$BaSO_4$-H_2O and $CaCl_2$-$BaSO_4$-H_2O systems cannot be compared to the previous sources due to the different temperature and pressure ranges covered. Nonetheless, the tendency reported by Uchameyshvili et al. (1966) for barite solubility with increasing chloride concentration is much more pronounced than that shown by Puchelt (1967) and Davis and Collins (1971).

Figure 4-9 shows the calculations performed by the extended UNIQUAC model for the systems $CaCl_2$-$BaSO_4$-H_2O and $MgCl_2$-$BaSO_4$-H_2O. The model is able to fit experimental data fairly accurately, even at relatively high chloride concentrations. Further experimental data are needed to clarify barite behaviour in $CaCl_2$ and $MgCl_2$ solutions.

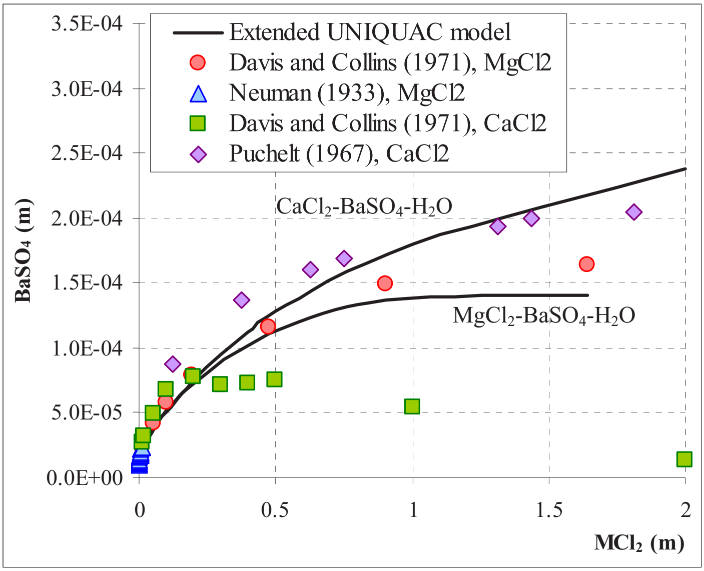

Figure 4-9. Experimental and calculated solid-liquid phase diagram for the $MgCl_2$-$BaSO_4$-H_2O and $CaCl_2$-$BaSO_4$-H_2O systems at 25ºC and 1 bar

The formation of anhydrite ($CaSO_4$) or gypsum ($CaSO_4 \cdot 2H_2O$) for high chloride concentrations in the $CaCl_2$-$SrSO_4$-H_2O system has been reported by Uchameyshvili et al. (1966) and Monnin (1999). For barite, $CaSO_4$ precipitation is less documented than in the previous system due to the lower barite solubility (one order of magnitude lower than that of celestite). Thus, the sulphate content is not high enough to allow gypsum to precipitate. Uchameyshvili et al. (1966) observed, nevertheless, the formation of $CaSO_4$ for temperatures higher than 230ºC. According to Monnin (1999), the anhydrite stability field is reached for solutions containing 0.165 m $CaCl_2$ at 210ºC, and 0.5 m $CaCl_2$ at 165ºC. When anhydrite precipitates from barite saturated solutions, the aqueous sulphate content decreases and the barium concentration increases. Even though anhydrite formation is reported by Uchameyshvili et al. (1966), their data do not follow that behaviour and are better modeled when equilibrium with only barite is considered (Monnin, 1999).

4.3 Systems Containing Strontium

4.3.1 $SrSO_4$-H_2O System

The experimental and calculated phase diagrams for the system $SrSO_4$-H_2O at a constant pressure of 200 bar and at constant temperatures of 25, 100 and 200°C are shown in figures 4-10 and 4-11, respectively. Both diagrams are simple, with only one solid phase ($SrSO_4$). The decrease of celestite solubility with increasing temperature from 25ºC is very large, dropping from $7.5\cdot10^{-4}$ m at 25°C to $6\cdot10^{-5}$ m at 250°C. The calculated solubility compares well with the experimental data, which are presented in table 4-10, together with the temperature and pressure range covered and the average absolute deviation between the extended UNIQUAC results and the experimental data. The value of the *MAAD* ($1.6\cdot10^{-5}$ m) is below the average experimental standard deviation of the data used for parameter estimation, which was found to be $4.1\cdot10^{-5}$ m.

Table 4-10
Experimental binary $SrSO_4$-H_2O SLE data sets used for parameter estimation

T **(°C)**	***P*** **(bar)**	**Number of data**	***AAD*** **(m)**	**Reference**
0/98	1	7 (0)		Wolfmann (1896)
2/35	1/1013	18 (0)		MacDonald and North (1974)
2.8/32.3	1	3 (3)	1.6E-05	Kohlrausch (1908)
5/95	1	11 (0)		Gallo (1935)
10.3/89.3	1	19 (19)	6.3E-06	Reardon and Armstrong (1987)
20	1	1 (0)		Lieser (1965)
20	1	1 (1)	2.7E-05	Belfiori (1940)
22/600	1/1990	28 (12)	1.6E-05	Strübel (1966)
24.4/250	1/600	72 (72)	1.7E-05	Howell et al. (1992)
25/125	1/2.3	4 (0)		Vetter et al. (1983)
25	1	1 (1)	4.5E-05	Müller (1960)
25	1	1 (1)	7.9E-07	Campbell and Nancollas (1969)
25	1	1 (0)		Selivanova and Zubova (1956)
25	1	2 (2)	1.9E-05	Culberson et al. (1978)
25	1	1 (1)	1.5E-05	Brower and Renault (1971)
25	1	1 (0)		Marden (1916)
30	1	1 (1)	5.7E-05	Campbell and Cook (1935)
85.5/154.4	5.6/211.5	10 (3)	2.4E-05	Jacques and Bourland (1983)
194/426	13.7/343	13 (0)		Booth and Bidwell (1950)
			MAAD **(m):**	**1.6E-05**

At 86°C, some of the measurements of celestite solubility reported by Jacques and Bourland (1983) decrease considerably with pressure (from $7\cdot10^{-4}$ m to $4.7\cdot10^{-4}$ m when pressure increases from 1 to 200 bar). Additionally, the data are very scattered, with solubility values ranging from $5.6.10^{-4}$ m to $8.3.10^{-4}$ m at 38°C and 100 bar. Nevertheless, some other data reported for the binary system (at 149.4°C and 80.7 bar, and at 154.4°C and 108.2 and 109.4 bar) do not show any irregularity and are close to other measurements at similar conditions reported by different authors. Only some of the solubility values given by Jacques and Bourland (1983) were therefore used in the present work.

Gallo (1935) reported celestite solubilities in pure water in clear disagreement with the general tendency followed by most of the references shown in table 4-10. The same lack of reliability is shown for the measurements done by Marden (1916), Lieser (1965), and Selivanova and Zubova (1956). These authors report higher solubilities than the rest of the data sets analyze, being possible that surface poisoning effects contributed to the enhancement of the solubility (Reardon and Armstrong, 1987). The presence of adsorbed substances (particularly phosphates) at the surface of strontium sulphate crystals markedly affects the critical supersaturation and the rates of spontaneous precipitation and dissolution of that mineral (Campbell and Nancollas, 1969).

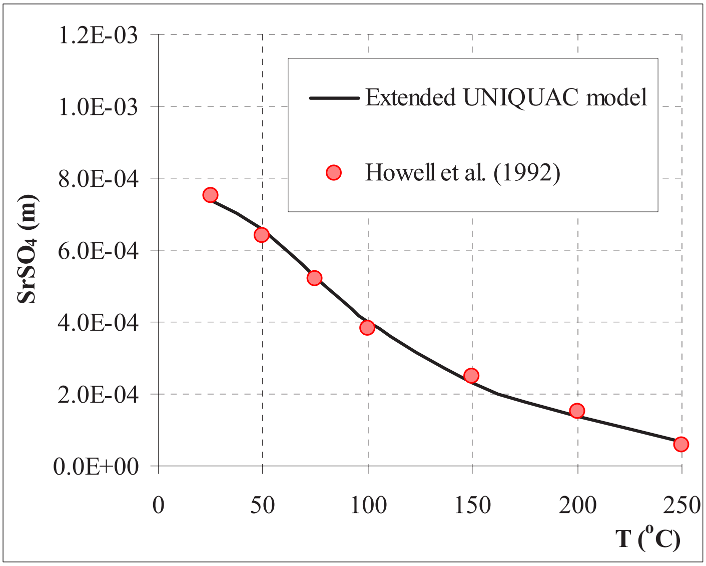

Figure 4-10. Experimental and calculated solid-liquid phase diagram for the $SrSO_4$-H_2O system at 200 bar.

The data of Wolfmann (1896) display, by far, the greatest discrepancies with respect to the other studies (as large as $6 \cdot 10^{-4}$ m). Furthermore, his data do not follow the expected trend of increasing solubility with pressure.

The only measurement from MacDonald and North (1974) that could be compared to other sources was the one at 2°C and 1 bar (the other experimental conditions were unique). The solubility reported at those conditions by MacDonald and North (1974) disagrees considerably with the values reported by the different authors in table 4-10 at similar conditions. Thus, this source was not considered reliable.

Vetter et al. (1983) performed measurements in pure water and in NaCl solutions at 25, 75, 95 and 125°C. They adopted a radioactive tracer technique using ^{90}Sr and some of the results were cross-checked using ^{35}S instead of ^{90}Sr. Both methods led to relative deviations as large as 30%.

The data of Booth and Bidwell (1950) are of relatively low precision as they deviate systematically from the majority of other studies.

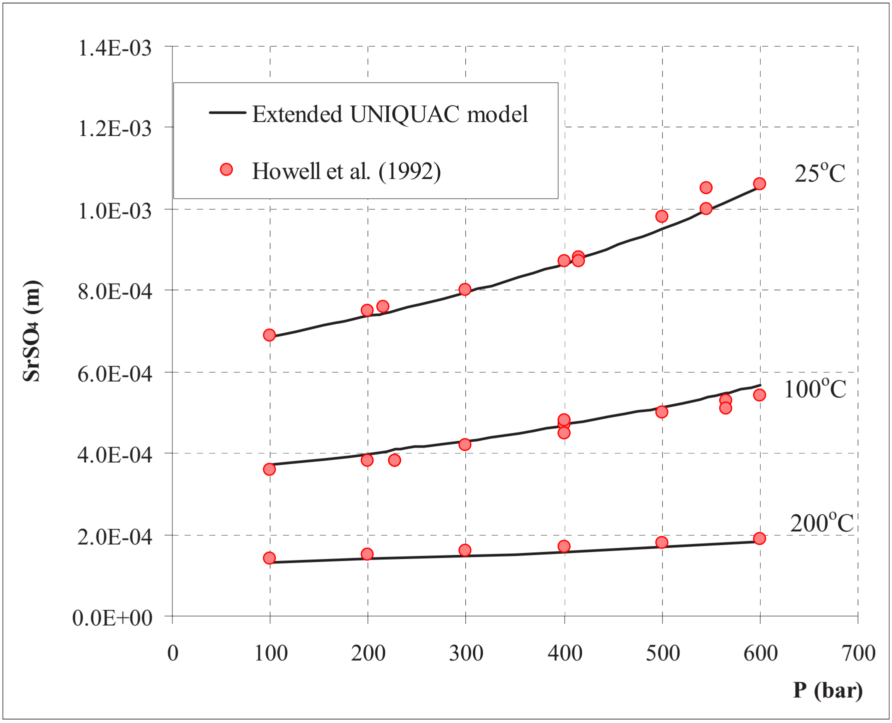

Figure 4-11. Experimental and calculated solid-liquid phase diagram for the $SrSO_4$-H_2O system at 25, 100 and 200 ºC.

4.3.2 $SrCl_2$-H_2O System

The binary phase diagram for the system $SrCl_2$-H_2O is shown in figure 4-12. The extended UNIQUAC model can represent the experimental data for this system with high accuracy and the agreement between the calculated and experimental eutectic point and peritectic points is good. The results for the $SrCl_2$ salt with reference to the experimental data are given in table 4-11. Due to the lack of experimental data at the same conditions, the calculated experimental *ASD* value is not very reliable. It is only based on the difference between the data reported by Assarsson (1953) and Moshinskii and Tikhomirova (1973) at 50ºC. The value for the mean average absolute deviation between experimental data and extended UNIQUAC calculations is low compared to the solubility values (*MAAD* of 0.1 m for solubilities in the range of 3 to 7 m).

Table 4-11
Experimental binary $SrCl_2$-H_2O SLE data sets used for parameter estimation

T (ºC)	*P* (bar)	Number of data	*AAD* (m)	Reference
-6/-0.05	1	10 (10)	6.5E-02	Jones and Pearce (1907)
18/114	1	18 (18)	1.1E-01	Assarsson (1953)
25	1	1 (1)	1.2E-01	Rard and Miller (1982)
50	1	1 (1)	2.8E-01	Moshinskii and Tikhomirova (1973)
			***MAAD* (m):**	**1.0E-01**

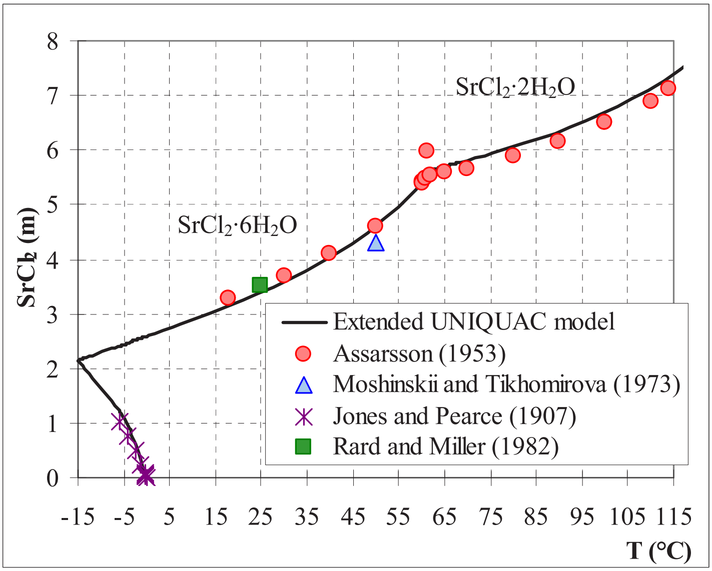

Figure 4-12. Experimental and calculated solid-liquid phase diagram for the $SrCl_2$-H_2O system at 1 bar.

4.3.3 $SrSO_4$-Na_2SO_4-H_2O and $SrCl_2$-NaCl-H_2O Systems

As mentioned previously for the case of barite, the average experimental standard deviation for the ternary systems $SrSO_4$-Na_2SO_4-H_2O and $SrCl_2$-NaCl-H_2O could not be calculated, because of the lack of experimental measurements at the same temperature, pressure and solution composition. The experimental standard deviation for the binary systems $SrSO_4$-

H_2O ($4.1\cdot10^{-5}$ m) and $SrCl_2$-H_2O ($4.0\cdot10^{-2}$ m) was therefore taken as reference. Note that, as mentioned previously, the *ASD* for the system $SrCl_2$-H_2O is only based on two experimental values.

Tables 4-12 and 4-13 show the data sets used for these two ternary systems and the average absolute deviation between calculated and experimental data. The *MAAD* is in both cases lower than the average experimental standard deviation for the binary systems, demonstrating the ability of the model to represent the systems.

Table 4-12
Experimental ternary $SrSO_4$-Na_2SO_4-H_2O SLE data sets used for parameter estimation

T (°C)	*P* (bar)	Number of data	*AAD*$_{SrSO4}$ (m)	Reference
0/25	1	8 (8)	2.7E-05	Lucchesi and Whitney (1962)
25	1	1 (1)	4.8E-05	Brower and Renault (1971)
			***MAAD* (m):**	**3.0E-05**

Table 4-13
Experimental ternary $SrCl_2$-NaCl-H_2O SLE data sets used for parameter estimation

T (°C)	*P* (bar)	Number of data	*AAD*$_{SrCl2}$ (m)	Reference
18/114	1	27 (27)	1.7E-01	Assarsson (1953)
			***MAAD* (m):**	**1.7E-01**

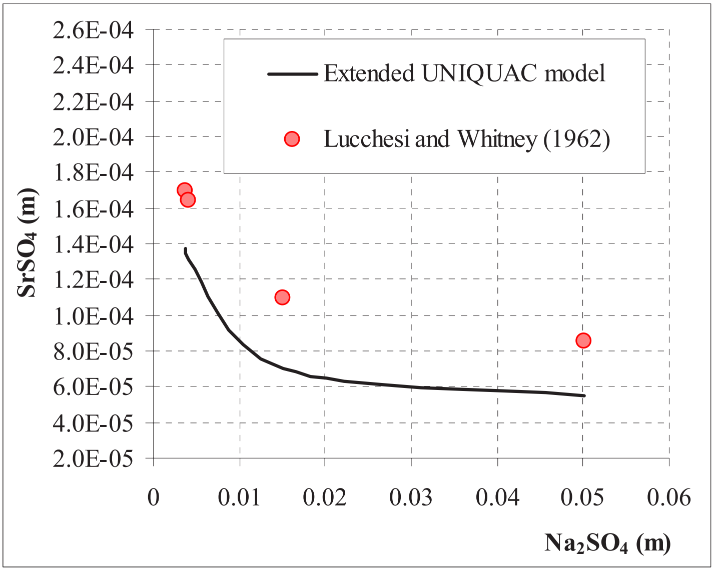

Figure 4-13. Experimental and calculated solid-liquid phase diagram for the $SrSO_4$-Na_2SO_4-H_2O system at -0.05°C and 1 bar.

Figure 4-13 shows the model calculations for the ternary system $SrSO_4$-Na_2SO_4-H_2O at -0.05°C and 1 bar. The calculated values are lower than the experimental ones, but the shape of the curve agrees with the experimental tendency. Moreover, the value for the *MAAD* between experimental and calculated data is lower than that for the binary system $SrSO_4$-H_2O, and the difference shown in figure 4-13 may be regarded as experimental inaccuracy (only one source was used for the ternary system, and therefore comparison to other sources was not possible).

Figure 4-14 shows the extended UNIQUAC calculations for the ternary system $SrCl_2$-NaCl-H_2O at 60°C and 1 bar. For low NaCl concentrations, the solid phases are $SrCl_2 \cdot 6H_2O$ and $SrCl_2 \cdot 2H_2O$, while NaCl appears for higher concentrations. The appearance and disappearance of these salts is well correlated by the model.

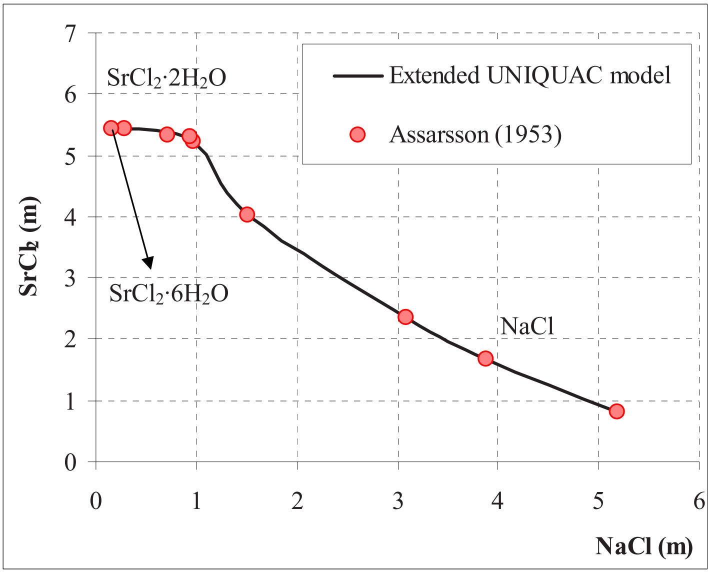

Figure 4-14. Experimental and calculated solid-liquid phase diagram for the $SrCl_2$-NaCl-H_2O system at 60°C and 1 bar.

4.3.4 $SrSO_4$-NaCl System

Table 4-14 shows the different data used for the system $SrSO_4$-NaCl-H_2O. The temperature and pressure ranges for each data set are listed, as well as the average absolute deviation between the calculated and experimental data. A more detailed explanation about the different experimental procedures used and possible sources of error is presented in Chapter 9.

As mentioned previously and shown in figure 4-1, there is a large disagreement among the different authors as regards experimental celestite solubility data in NaCl solutions. This disparity is aggravated at high temperature and pressure conditions. This variability may be related to the experimental difficulties associated to this mineral. According to Campbell and Cook (1935), supersaturated solutions of celestite are characterized by long term stability. Campbell and Nancollas (1969) aware of the propensity of this mineral for surface poisoning effects, while Enüstün and Turkevich (1960) assure the solubility of $SrSO_4$ depends on the particle size. Most of the studies on celestite solubility do not consider these experimental problems and so the available solubility data in the literature are sometimes unreliable and inaccurate.

Table 4-14
Experimental quaternary $SrSO_4$-NaCl-H_2O SLE data sets used for parameter estimation

T (^oC)	*P* (bar)	Number of data	AAD_{SrSO4} (m)	Reference
-0.05/25	1	10 (0)		Lucchesi and Whitney (1962)
9/20	1	2 (2)	1.3E-03	Gallo (1935)
10.3/40	1	36 (36)	1.8E-04	Reardon and Armstrong (1987)
20/60	1	26 (26)	5.4E-04	Qadirie (1990)
20/90	1	32 (32)	2.2E-04	Strübel (1966)
25	1	10 (10)	1.2E-04	Davis and Collins (1971)
25	1	5 (5)	3.3E-04	Brower and Renault (1971)
25	1	1 (1)	2.9E-04	Culberson et al. (1978)
25	1	8 (0)		Müller (1960)
25/253.5	1/600	436 (436)	4.4E-04	Howell et al. (1992)
25/125	1/2.3	24 (0)		Vetter et al. (1983)
80/120	1/414	49 (0)		Schulien (1987)
100/305	0.2/165	41 (41)	5.1E-04	Jacques and Bourland (1983)
			***MAAD* (m):**	**4.2E-04**

A relatively good agreement is found in figure 4-1 for low NaCl concentrations (up to less than 1m NaCl). From that concentration, there are two sources (Müller, 1960 and Lucchesi and Whitney, 1962) reporting measurements that disagree considerably with the main tendency. For the first reference, even the solubility curve shape is different. Müller (1960) measured solubility values at 25°C and 1 atm in different NaCl solutions from 0.4 to 5.1 m. His data show a much higher solubility value and do not show a reversal in the solubility behaviour between 2 and 5 m NaCl, as observed by the other sources performing measurements at the same conditions. These unreliable data may be the result of an inadequate analytical technique (titration) to determine very low Sr^{2+} concentrations

Celestite solubility decreases with increasing temperature from 25ºC (from 0 to 25ºC celestite solubility increases with increasing temperature). This tendency is not clearly followed by the data reported by Schulien (1987) at atmospheric pressure. Schulien (1987) concluded that additional measurements are required to determine whether that deviation from the probable trend is due to analytical errors or inhomogeneities in the solutions. Regarding the trend followed with pressure, Schulien (1987) data show some inconsistencies. For some temperatures and NaCl concentrations, the solubility increases continuously from 1 to 400 bar. For other conditions the effect of pressure is negligible, and in other cases the effect is reversed, and the highest solubilities are found for the lowest pressures. According to Schulien (1987), this inconsistency is due to the small changes in solubility values with pressure, which lie within the variability of the experimental technique. As mentioned for barite measurements, the results given by Schulien (1987) for $SrSO_4$ show a large scatter for some experimental conditions (e.g., at 80°C), and disagree with most of the sources given in table 4-14. Such disagreement may result as a consequence of the low time waited before performing analysis, and aggravated by the lack of agitation of the sample.

Howell et al. (1992) agrees with Strübel (1966), Davis and Collins (1971), Culberson et al. (1978) and Reardon and Armstrong (1987) in the regions of overlap, for low sodium chloride concentrations (up to around l.5 m NaCl). For higher concentrations, the agreement is not so good, and Howell et al. (1992) report lower solubility data than the other sources. Moreover, there are some inconsistencies for some of the measurements reported by Howell et al. (1992). At the highest temperatures reported (200 and 250°C) the trend followed by the data for increasing pressures is wrong, and the values reported at 600 bar are lower than at 500 bar, and in some cases even lower than values at 200 bar. Also, scatter in the experimental data is found for the high temperature ($T > 200°C$) and high sodium chloride concentrations (3 m and higher).

Vetter et al. (1983) report solubility values at 25ºC in relatively good agreement with many other sources. Nonetheless, that agreement is lost at higher temperatures, where Vetter et al. (1983) report very low values when compared to Strübel (1966), Jacques and Bourland (1983) or Howell et al. (1992). Also, the shape of the solubility curve reported by Vetter et al. (1983) at constant NaCl concentration differs from the ones followed by the rest of the sources. Vetter et al. (1893) used a radioactive tracer technique using ^{90}Sr to determine Sr^{2+} concentrations. In some measurements, they cross-checked the results by using ^{35}S as well. The two methods lead to solubility values differing as much as 30%.

Brower and Renault (1971) data agree with the majority of the sources reporting solubility data at 25°C and 1 atm when the NaCl concentration is lower than 1 m. For 1 m, the solubility reported by Brower and Renault (1971) is considerably larger than the values measured by Davis and Collins (1971), Vetter et al. (1983) and Howell et al. (1992). Finally, it seems that Davis and Collins (1971) report higher solubility values than Reardon and Armstrong (1987) for some similar conditions, while Strübel (1966) data are larger than Jacques and Bourland (1983) data, in the region of overlap. No further conclusions about the reliability of these sources can be taken due to the lack of additional information.

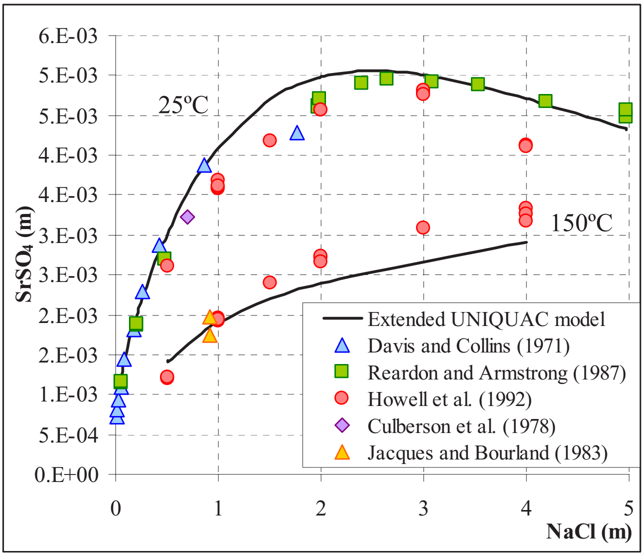

Figure 4-15. Experimental and calculated solid-liquid phase diagram for the $SrSO_4$-NaCl-H_2O system at 25ºC and 1 bar, and 150ºC and 5 bar.

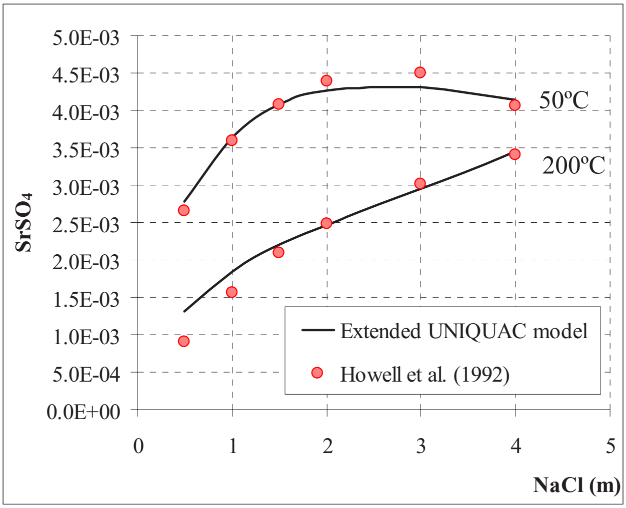

Figure 4-16. Experimental and calculated solid-liquid phase diagram for the $SrSO_4$-NaCl-H_2O system at 100 bar.

The experimental and calculated phase diagrams for the system $SrSO_4$-NaCl-H_2O at 25ºC and 1 bar, and at 150°C and the saturation pressure of the solution are shown in figure 4-15. The phase diagram at 50 and 200ºC and a constant pressure of 100 bar is shown in figure 4-16. The effect of NaCl concentration on celestite solubility depends on temperature. For low temperatures (0-75ºC), $SrSO_4$ solubility reaches a maximum for NaCl concentrations around 2-3 m, and then starts decreasing for higher concentrations. For high temperatures (100-300ºC), celestite solubility increases constantly with NaCl concentration.

4.3.5 Sr^{2+}-Mg^{2+} and Sr^{2+}-Ca^{2+} Interaction Energy Parameters

The value of the binary energy interaction parameters between Sr^{2+} and Mg^{2+} or Ca^{2+} was estimated on the basis of experimental SLE data for the ternary system MSO_4-$SrSO_4$-H_2O, and the quaternary systems MCl_2-$SrSO_4$-H_2O, where M stands for Ca and Mg. The sources found, the total number of data reported, and the temperature and pressure ranges covered by each source are presented in table 4-15. The average absolute deviation between calculated and experimental data is given for Sr^{2+}.

Celestite solubility increases with the $CaCl_2$ concentration and, at a certain chloride amount, the solid calcium sulphate stability field is reached (Monnin and Galinier, 1988). Then, gypsum or anhydrite will be the phases precipitating and controlling the sulphate content in the solution. According to Monnin (1999), gypsum forms at 25ºC in solutions containing more than 0.75 m $CaCl_2$. At 75ºC anhydrite is the stable solid calcium sulphate phase, and it will appear for $CaCl_2$ concentrations above 0.5 m. That value decreases to 0.24 and 0.06 m $CaCl_2$ when the temperature is raised to 95 and 125ºC, respectively. Analyzing the data reported by Brower and Renault (1971), Davis and Collins (1971), Culberson et al. (1978), and Vetter et al. (1983), it seems clear neither gypsum nor anhydrite did precipitate in any of the experiments reported, although their stability fields were reached.

Table 4-15
Experimental SLE data sets used for parameter estimation

T (ºC)	*P* (bar)	Number of data	AAD_{Sr2+} (m)	Reference
25	1	1	1.5E-04	Culberson et al. (1978)[a]
25	1	4	1.8E-03	Brower and Renault (1971)[a]
25	1	9	3.0E-04	Davis and Collins (1971)[a]
25/125	1	27	2.0E-04	Vetter et al. (1983)[a]
25	1	2	1.9E-04	Brower and Renault (1971)[b]
25	1	1	4.2E-04	Culberson et al. (1978)[c]
25	1	2	8.0E-04	Brower and Renault (1971)[c]
25	1	9	7.6E-04	Davis and Collins (1971)[c]
25-125	1	27	3.5E-04	Vetter et al. (1983)[c]
25	1	1	2.8E-04	Brower and Renault (1971)[d]

[a] Quaternary $MgCl_2$-$SrSO_4$-H_2O system
[b] Ternary $MgSO_4$-$SrSO_4$-H_2O system
[c] Quaternary $CaCl_2$-$SrSO_4$-H_2O system
[d] Ternary $CaSO_4$-$SrSO_4$-H_2O system

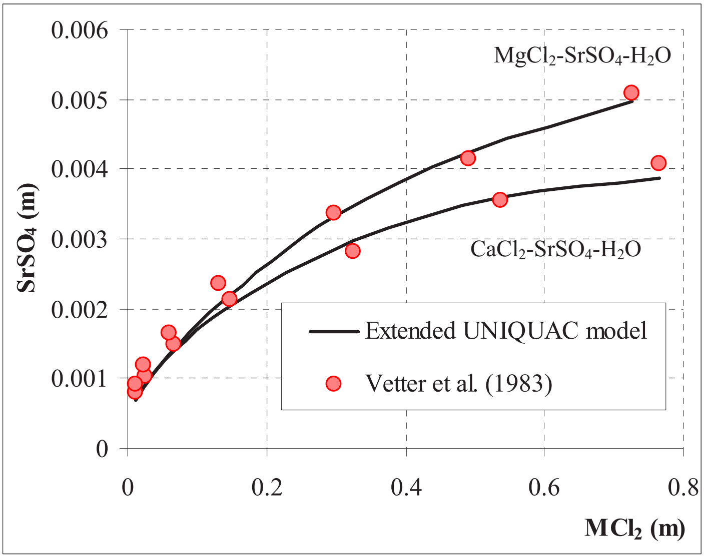

Figure 4-17. Experimental and calculated solid-liquid phase diagram for the $MgCl_2$-$SrSO_4$-H_2O and $CaCl_2$-$SrSO_4$-H_2O systems at 95ºC and 1 bar.

Figure 4-17 shows the calculations performed by the extended UNIQUAC model for the systems $CaCl_2$-$SrSO_4$-H_2O and $MgCl_2$-$SrSO_4$-H_2O. The representation of the model for the quaternary systems is very good. Figure 4-17 shows than an increasing chloride concentration results in a salting-in effect, increasing the solubility of celestite.

4.4 Systems Containing Calcium

4.4.1 $CaSO_4$-H_2O System

The *r* and *q* parameters for Ca^{2+} and the interaction parameters between Ca^{2+} and H_2O, Cl^- and SO_4^{2-} were determined from a large number of experimental solubility data of salts containing the mentioned ions. Therefore, only the interaction parameter between Ca^{2+} and Na^+ and the pressure parameters α and β need to be regressed in the present work from experimental SLE data.

Many studies on the solubility of anhydrite and gypsum in pure water are available in literature, although, at high temperatures and pressures, the number of experimental measurements decreases dramatically. The references used in this work for the binary $CaSO_4$-H_2O system, the temperature and pressure ranges covered, and the number of experimental data are given in table 4-16.

The experimental and calculated phase diagram for the system $CaSO_4$-H_2O at a constant pressure of 1000 bar is shown in figure 4-18. Extended UNIQUAC calculations are in very good agreement with the experimental data and the average absolute deviation between the model calculations and the experimental measurements is within experimental accuracy. A thorough analysis of the data was performed prior to the parameter estimation because the solubility data reported by numerous workers were not in agreement, perhaps because of the high instability of some of the forms of calcium sulphate. Solubility determinations by the usual isothermal method are rather difficult or may even be impossible (Zdanovskii and Spiridonov, 1967).

Table 4-16
Experimental binary $CaSO_4$-H_2O SLE data sets used for parameter estimation

T (°C)	*P* (bar)	Number of data	*AAD* (m)	Reference
0/80	1	5 (3)	1.8E-04	Kydynov and Druzhinin (1957)
0/92	1	9 (9)	4.7E-04	Posnjak (1938)
0/100	1	5 (2)	1.4E-04	Zdanovskii and Spiridonov (1967)
0.5/25	1	2 (2)	1.0E-04	Culberson et al. (1978)
14	1	1 (0)		D'Anselme (1903)
18	1	1 (0)		Kohlrausch and Rose (1893)

Table 4-16 (continuation)
Experimental binary $CaSO_4$-H_2O SLE data sets used for parameter estimation

T (°C)	*P* (bar)	Number of data	*AAD* (m)	Reference
18/218	1/22.1	6 (4)	1.6E-04	Melcher (1910)
20	1	1 (1)	5.1E-04	Kuznetsov (1946)
22/26	1	3 (3)	1.7E-04	Cameron and Seidell (1901)
25	1	1 (0)		Cameron and Bell (1907)
25	1	1 (1)	1.5E-04	Dietrich (1916)
25	1	1 (1)	1.9E-04	Kolosov (1958)
25	1	1 (1)	1.9E-04	Kolosov (1959)
25	1	2 (2)	1.5E-04	Rza-Zade and Rustamov (1963)
25	1	1 (1)	1.5E-04	Shternina and Frolova (1949)
25	1	1 (1)	1.8E-04	Seidell and Smith (1904)
25	1	1 (1)	1.9E-04	Jones (1939)
25	1	2 (0)		Kruchenko and Beremzhanov (1976)
25/26	1	2 (2)	4.1E-05	Rza-Zade and Rustamov (1961)
25/35	1	3 (2)	1.5E-04	Madgin and Swales (1956)
25/50	1	8 (5)	5.5E-04	Bock (1961)
25/75	1	4 (2)	1.4E-04	Hill and Wills (1938)
25/80	1	5 (0)		Taperova (1940)
25/100	1	6 (3)	2.8E-04	Hill and Yanick (1935)
26/82	1	2 (0)		Cameron (1901)
30/50	1/290	15 (10)	7.1E-03	Manikhin (1966)
35	1	1 (1)	1.3E-04	Lepeshkov and Fradkina (1959)
35	1	1 (1)	1.3E-04	Valyashko and Petrova (1952)
35	1	1 (1)	1.3E-04	Novikola (1957)
35	1	1 (1)	1.3E-04	Lepeshkov and Novikova (1958)
35/60	1	3 (2)	1.6E-04	Dobberstein (1991)
35/65	1	4 (3)	5.1E-04	Hill (1937)
40	1	1 (1)	1.4E-04	Barba et al. (1984)
40/100	1	4 (3)	2.1E-04	Hill (1934)
40/125	1	6 (2)	1.4E-04	Marshall et al. (1964)
50/83.5	3/1010	32 (2)	8.4E-04	Blount and Dickson (1973)
55	1	5 (0)		Bodaleva and Lepeshov (1956)
55	1	1 (1)	1.7E-03	Sveshnikova (1952)
73/202.5	118/1410	17 (8)	1.2E-03	Blount and Dickson (1969)
96/263	2/1010	54 (54)	7.9E-04	Dickson et al. (1963)
100/195	1/13.8	53 (53)	6.2E-04	Hall et al. (1926)
100/200	1/15.6	12 (8)	1.3E-04	Gardner and Glueckauf (1970)
100/220	1/23.2	13 (13)	1.0E-04	Partridge and White (1929)
100/300	1/1000	15 (15)	3.6E-04	Lyashchenko and Churagulov (1981)
110	1	1 (0)		Gromova (1960)
141/408	3.7/287.2	22 (13)	3.3E-04	Booth and Bidwell (1950)
			***MAAD* (m):**	**7.6E-04**

The phase diagram for the binary system $CaSO_4$-H_2O contains a peritectic point at about 45°C, where the stable solid phase changes from gypsum to anhydrite. At temperatures higher than 45°C, gypsum will therefore become a metastable phase and its dissolution will be suppressed by anhydrite crystallization, which is a more stable solid phase at those conditions. The same applies to anhydrite if the temperature is lower than 45°C, in which case gypsum will be the solid phase with the lowest solubility. Finally, a third, metastable solid phase, hemihydrate ($CaSO_4 \cdot 0.5H_2O$), may appear in the binary $CaSO_4$-H_2O system.

Many investigators measured both anhydrite and gypsum solubilities in pure water for temperature conditions where these solid phases are metastable and many other references also report $CaSO_4 \cdot 0.5H_2O$ as the solid phase, which is unstable at all temperatures. As we are only interested in the equilibrium phases at a given temperature and composition, all the experimental data concerning anhydrite below 40°C, gypsum above 45°C and the salt $CaSO_4 \cdot 0.5H_2O$ at any temperature were not used for parameter estimation. Both anhydrite and gypsum measurements in the temperature interval 40-45°C are used in the present work, because of the disagreement found in literature concerning the temperature of the peritectic point.

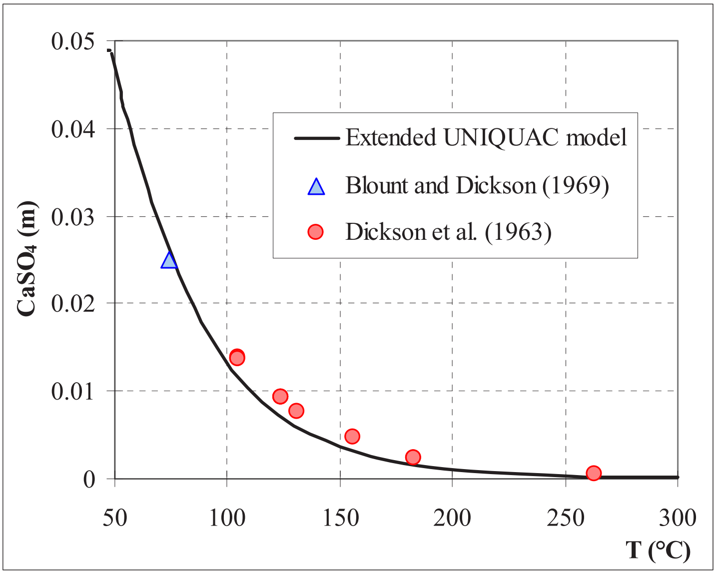

Figure 4-18. Experimental and calculated solid-liquid phase diagram for the $CaSO_4$-H_2O system at 1000 bar.

The sources reporting experimental measurements where a metastable phase is the solid phase are: Kohlrausch and Rose (1893), Melcher (1910), Hill (1934, 1937), Hill and Yanick

(1935), Hill and Wills (1938), Taperova (1940), Bodaleva and Lepeshov (1956), Madgin and Swales (1956), Bock (1961), Marshall et al. (1964), Manikhin (1966), Zdanovskii and Spiridonov (1967), Gardner and Glueckauf (1970), Blount and Dickson (1973), Kruchenko and Beremzhanov (1976) and Dobberstein (1991). Some of the references cited also report measurements in which the solid phase is stable. Such experimental data will be used unless they disagree with the tendency followed by the majority of the sources, which is the case for the stable phases reported by Taperova (1940), Bodaleva and Lepeshov (1956) and Kruchenko and Beremzhanov (1976).

When comparing the different available sources at atmospheric pressure, some measurements were found to be in disagreement with the tendency followed by the majority of the experimental data reported in table 4-16. Such data sets were not used for parameter estimation: Cameron (1901), D'Anselme (1903), Cameron and Bell (1907), and Gromova (1960).

The Kydynov and Druzhinin (1957) measurements at temperatures higher than 60°C seem to be inaccurate when compared to others.

Hall et al. (1926) report very scattered data at all the conditions analyzed. For example, the anhydrite solubility at 122°C and 2.11 bar varies from 0.0033 m to 0.005 m. Nevertheless, all data from this source were used because it was not possible to distinguish between the good and bad data.

4.4.2 $CaSO_4$-Na_2SO_4 System

The solubility diagram for the ternary system $CaSO_4$-Na_2SO_4-H_2O at 35°C and 1 bar is shown in figure 4-19, where the solid phase gypsum up to about 24 wt.% of Na_2SO_4; at this point the solid phase changes to glauberite ($Na_2SO_4 \cdot CaSO_4$) and thenardite (Na_2SO_4) when the Na_2SO_4 concentration increases to about 32 wt.%. The gypsum curve shows a maximum and a minimum, which is a shape that is well represented by the extended UNIQUAC model. Nevertheless, when the temperature increases the calculations performed by the model lose some accuracy, probably because of the difficulty encountered by any model in following curves with such large tendency changes. Table 4-17 shows the data sources used for the ternary system $CaSO_4$-Na_2SO_4-H_2O, together with the average absolute deviation between the model calculations and the experimental data. The mean absolute deviation *MAAD* is larger than the average experimental standard deviation *ASD*. The results are fairly accurate, considering that only one parameter was used (the rest had already been determined). A further study of such a system, with the possibility of modifying additional parameters, would very probably lead to much more accurate results.

Many of the solubility measurements performed by Hill and Wills (1938) correspond to metastable phases, and therefore where not used for parameter estimation. The same criterion is applied to the data reported by Cameron et al. (1907) and Kydynov and Druzhinin (1957).

Table 4-17
Experimental ternary $CaSO_4$-Na_2SO_4-H_2O SLE data sets used for parameter estimation

T (°C)	*P* (bar)	Number of data	AAD_{CaSO4} (m)	Reference
0/80	1	31 (15)	6.8E-03	Kydynov and Druzhinin (1957)
18	1	2 (2)	5.3E-03	Mecke (1935)
22	1	8 (8)	1.6E-03	Cameron and Seidell (1901)
25	1	1 (1)	2.9E-03	Nikolskaya and Moshkina (1958)
25	1	1 (0)		Cameron et al. (1907)
25	1	4 (2)	1.2E-03	Madgin and Swales (1956)
25	1	11 (11)	1.7E-03	Cameron and Breazeale (1904)
25	1	12 (12)	1.7E-03	Kolosov (1959)
25/75	1	144 (45)	3.8E-04	Hill and Wills (1938)
35/55	1	7 (5)	2.2E-03	Lepeshkov and Fradkina (1959)
40	1	11 (11)	7.0E-04	Barba et al. (1984)
110	1	13 (13)	6.2E-04	Gromova (1960)
			***MAAD* (m):**	**1.6E-03**

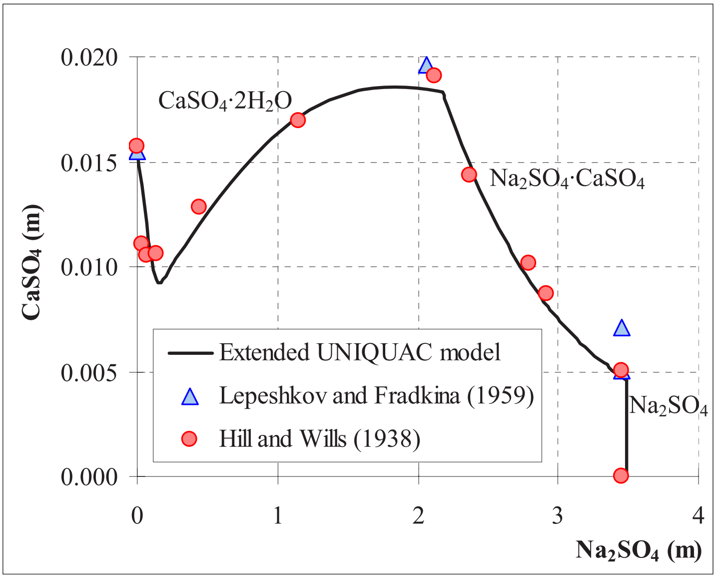

Figure 4-19. Experimental and calculated solid-liquid phase diagram for the $CaSO_4$-Na_2SO_4-H_2O system at 35ºC and 1 bar

4.4.3 $CaSO_4$-$CaCl_2$-H_2O and $CaSO_4$-NaCl-H_2O Systems

As mentioned before, the additional parameters required for the Na-Ca-SO_4-Cl-H_2O system were already known. The experimental data sets given in table 4-18 for the ternary system $CaSO_4$-$CaCl_2$-H_2O and in table 4-19 for the quaternary system $CaSO_4$-NaCl-H_2O were therefore not used for parameter estimation. The references dealing with these two systems, the conditions of temperature and pressure covered, and the number of experimental measurements are given in these two tables. The values of the *AAD* between experimental data and the extended UNIQUAC model are also presented.

Table 4-18
Experimental ternary $CaSO_4$-$CaCl_2$-H_2O SLE data sets used for parameter estimation

T **(°C)**	***P*** **(bar)**	**Number of data**	AAD_{CaSO4} **(m)**	**Reference**
0/55	1	17	3.0E-03	Sveshnikova (1949)
20	1	5	6.3E-04	Kuznetsov (1946)
25	1	13	6.3E-04	Rza-Zade and Rustamov (1963)
25	1	13	6.3E-04	Rza-Zade and Rustamov (1961)
25	1	1	6.4E-04	Perova (1957)
25	1	9	3.8E-04	Cameron and Seidell (1901)
55	1	11	2.0E-03	Sveshnikova (1952)
55	1	13	2.3E-03	Campbell and Marsh (1959)
110	1	8	7.1E-04	Gromova (1960)
			MAAD **(m):**	**1.5E-03**

Table 4-19
Experimental quaternary $CaSO_4$-NaCl-H_2O SLE data sets used for parameter estimation

T **(°C)**	***P*** **(bar)**	**Number of data**	AAD_{CaSO4} **(m)**	**Reference**
-21.2/-3	1	40	2.8E-01	Korolev (1937)
-4.5/-1.5	1	5	4.8E-01	Semenchenko and Zavada (1931)
14	1	17	1.7E-02	D'Anselme (1903)
15/82	1	55	1.7E-02	Cameron (1901)
18	1	2	4.0E-03	Mecke (1935)
19	1	9	1.8E-02	Foret (1943)
20	1	9	1.2E-02	Orlov (1902)
25	1	15	1.6E-02	Shternina and Frolova (1949)
25	1	26	1.4E-02	Rza-Zade and Rustamov (1963)
25	1	35	7.6E-03	Melnikova and Moshkina (1973)
25	1	16	8.7E-02	Cameron et al. (1907)
25/35	1	67	1.0E-02	Madgin and Swales (1956)
25/50	1	48	3.0E-02	Bock (1961)
40/200	1/15.5	134	2.1E-02	Marshall et al. (1964)
94/302	1/1063	77	1.1E-01	Blount and Dickson (1969)
100/200	1/15.4	19	9.2E-02	Il'inskii and German (1936)
110	1	7	1.5E-01	Gromova (1960)
			MAAD **(m):**	**5.8E-02**

Table 4-20
Thermodynamic properties (NIST, 1990) and related parameters

	$\Delta_r G_f^0$ (kJ mol^{-1})	$\Delta_r H_f^0$ (kJ mol^{-1})	C_{p1} (J mol^{-1}K^{-1})	C_{p2} (J mol^{-1}K^{-2})
Sr^{2+}	-559.48	-545.8	-1124.756[a]	3.450446[a]
$BaCl_2\cdot H_2O$	-1055.669	-1160.79	120	0
$BaCl_2\cdot 2H_2O$	−1296.32	−1460.13	161.96	0
$BaSO_4$	−1361.866[a]	−1467.929[a]	104.0038	0
$SrSO_4$	− 1341.538[a]	−1452.955[a]	100	0
$SrCl_2\cdot 2H_2O$	−1284.587[a]	−1456.694[a]	160.2	0
$SrCl_2\cdot 6H_2O$	−2240.92	−2623.8	320	0
$BaSO_4\cdot SrSO_4$	−2714.505[a]	−2954.863[a]	201.75	0
$CaSO_4$	−1321.8	−1436.132[a]	70.21[b]	0.009874[b]
$CaSO_4\cdot 2H_2O$	−1797.407[a]	−2026.294[a]	91.38[b]	0.318[b]
$Na_2SO_4\cdot CaSO_4$	−2594.808	−2816.396	140.25[b]	0.2907[b]
Na_2SO_4	-1270.16	-1387.08	128.2	0
$CaCl_2$	−748.1	−795.8	72.59	0
$CaCl_2\cdot 2H_2O$	−1253.87	−1402.9	153	0
$CaCl_2\cdot 4H_2O$	−1738.434	−2014.119	233	0
$CaCl_2\cdot 6H_2O$	−2219.378	−2607.658	313	0

[a] Values estimated from experimental SLE data.
[b] Values taken from Kelley, 1960.

4.5 References in Chapter 4

Archer, D.G., 1992. Thermodynamic properties of $NaCl+H_2O$ system II. Thermodynamic properties of NaCl (aq), $NaCl\cdot 2H_2O$ (c), and phase equilibria. J. Phys. Chem. Ref. Data 21, 793-829.

Arnorsson, E., 1989. Deposition of calcium carbonate minerals from geothermal waters. Theoretical considerations. Geothermics 18, 33-39.

Assarsson, G.O., 1953. Equilibria in aqueous systems containing Sr, K, Na and Cl. J. Phys. Chem. 57, 207-210.

Assarsson, G.O., 1956. Equilibria in the ternary system $MgCl_2$-$BaCl_2$-H_2O between 18 and 100°C. Phys. Chem. 60, 1436-1439.

Atkinson, G., Oklahoma, U., Raju, K., Aramco, S., Howell R.D., 1991. The thermodynamics of scale prediction. SPE 21021, 209-215.

Barba, D., Brandani, V., Di Giacomo, G., 1984. Solubility of calcium sulfate dihydrate in the system Na_2SO_4. J. Chem. Eng. Data 29, 42-45.

Belfiori, P., 1940. The effect of alkali nitrites on several difficulty soluble sulfates. Ann. Chim. Applicata 30, 233-237.

Blount, C.W., Dickson, F.W., 1969. The solubility of anhydrite ($CaSO_4$) in NaCl-H_2O from 100 to 450°C and 1 to 1000 bars. Geochimica et Cosmochimica Acta 33, 227-245.

Blount, C.W., Dickson, F.W., 1973. Gypsum-anhydrite equilibria in systems $CaSO_4$-H_2O and $CaSO_4$-NaCl-H_2O. American Mineralogist 58, 323-331.

Blount, C.W., 1977. Barite solubilities and thermodynamic quantities up to 300 °C and 1400 bars. American Mineralogist 62, 942-957.

Bock, E., 1961. On the solubility of anhydrous calcium sulphate and of gypsum in concentrated solutions of sodium chloride at 25°C. Can. J. Chem. 39, 1746-1751.

Bodaleva, N.V., Lepeshov, I.N., 1956. Investigation of phase equilibria in the system K_2SO_4-$MgSO_4$-$CaSO_4$-H_2O at 55°C. Zh. Neorgan. Khim. 1 (5), 995-1007.

Booth, H.S., Bidwell, R.M., 1950. Solubilities of salts in water at high temperatures. J. Amer. Chem. Soc. 72, 2567-2575.

Brower, E., Renault, J., 1971. Solubility and enthalpy of the barium strontium sulfate solid solution series. New Mexico State Bureau of Mines and Mineral Resources, Circular 116.

Cameron, F.K., 1901. Solubility of gypsum in aqueous solutions of sodium chloride. J. Phys. Chem. 5, 556-576.

Cameron, F.K., Seidell, A., 1901. Solubility of gypsum in aqueous solutions of certain electrolytes. J. Phys. Chem. 5, 643-655.

Cameron, F.K., Breazeale, J.F., 1904. Calcium sulphate in aqueous solutions of potassium and sodium sulphates. J. Phys. Chem. 8, 335-340.

Cameron, F., Bell, J., 1907. The action of water and aqueous solutions upon soil phosphates. U. S. Dept. Agr., Bull. 41.

Cameron, F.K., Bell, J.M., Robinson, W.O., 1907. The solubility of certain salts present in alkali soils. J. Phys. Chem. 11, 396-420.

Campbell, A.N., Cook, E.J.R., 1935. A study of precipitation from supersaturated solutions of strontium sulfate. J. Amer. Chem. Soc. 57, 387-390.

Campbell, J.A., Marsh, F.L., 1959. The system magnesium bromide, ammonium bromide, and water at 25^{o}C. J. Phys. Chem. 63, 316-317.

Campbell, J.R., Nancollas, G.H., 1969. The crystallization and dissolution of strontium sulfate in aqueous solution. J. Phys. Chem. 73, 1735-1740.

Culberson, C.H., Lathman, G., Bates, R.G., 1978. Solubilities and activity coefficients of calcium and strontium sulfate in synthetic seawater at 0.5^{o}C and 25^{o}C. J. Phys. Chem. 82, 2693-2699.

D'Anselme, A., 1903. Bull. Soc. Chim. 29 (3), 373.

Davis, J.W., Collins, A.G., 1971. Solubility of barium and strontium sulfates in strong electrolyte solutions. Environmental Science & Technology 5, 1039-1043.

Dickson, F.W., Blount, C.W., Tunell, G., 1963. Use of hydrothermal solution equipment to determine the solubility of anhydrite in water from 100^{o}C to 275^{o}C and from 1 bar to 1000 bars pressure. American Journal of Science 261, 61-78.

Dietrich, 1916. Kaminer Handbuch der Balneologie Vol.1, pp.205.

Dobberstein, K.U., 1991. Dichte und Viskositätsmessungen in ternäre Elektrolytlösungen. Dissertation, Martin-Luther-Universität Halle Wittenberg.

Dyer, S.J., Graham, G.M., 2002. The effect of temperature and pressure on oilfield scale formation. Journal of Petroleum Science and Engineering 35, 95-107.

Eddy, R.D., Menzies, A.W.C., 1940. The solubilities of certain inorganic compounds in ordinary water and in deuterium water J. Phys. Chem. 44, 207-235.

Enüstün, B.V., Turkevich, J., 1960. Solubility of fine particles of strontium sulfate. J. Amer. Chem. Soc. 82, 4502-4509.

Felmy, A.R., Rai, D., Amonette, J.E., 1990. The solubility of barite and celestite in sodium sulfate: evaluation of thermodynamic data. J. Sol. Chem. 19 (2), 175-185.

Findlay, A., Cruickshank, J., 1926. The reciprocal salt pair (Na, Ba)-(Cl, NO_3) in aqueous solution at 20^{o}C. J. Chem. Soc., 316-318.

Foret, J., 1943. Nonexistence of the paradox claimed to exist in the solubility of gypsum in aqueous solutions of NaCl. Compt. Rend. 217, 264-266.

Gallo, G., 1935. Equilibrium of strontium sulfate and water at various temperatures. Ann. Chim. Applicata 25, 628-631.

Gardner, A.W., Glueckauf, E., 1970. Thermodynamic data of the $CaSO_4$ solution process. Trans. Faraday Soc. 66, 1081-1086.

Gibbard, H.F., Fong, S.L., 1975. Freezing points and related properties of electrolyte solutions III. The systems NaCl-$CaCl_2$-H_2O and NaCl-$BaCl_2$-H_2O. J. Sol. Chem. 4, 863-872.

Gill, J.S., 1998. Silica scale control. Chemical Treatment, 41-45.

Graham, G.M., Mackay, E.J., 2003. A background to inorganic scaling-mechanisms, formation and control. 5th Intl. SPE Oilfield Scale Symposium. Aberdeen, UK.

Gromova, E.T., 1960. The solubility isotherm of the Na-Ca-Cl-SO_4-H_2O system at 110^{o}C. Russian Journal of Inorganic Chemistry 5, 1244-1247.

Hall, R.E., Robb, J.A., Coleman, C.E., (1926). The solubility of calcium sulfate at boiler-water temperatures. J. Am. Chem. Soc., 927-938.

Harvey, A.H., Perskin, A.P., Klein, S.A., 1996. NIST/ASME steam properties formulation for general and scientific use.

He, S., Morse, J.W., 1992. Prediction of halite, gypsum, and anhydrite solubility in natural brines under subsurface conditions. Computer & Geosciences 19, 1-22.

Hill, A.E., 1934. Ternary Systems XIX. Calcium sulfate, potassium sulfate and water. J. Am. Chem. Soc. 56, 1071-1078.

Hill, A.E. and Yanick, N.S., 1935. Ternary system. Calcium sulfate, ammonium sulfate and water. J. Am. Chem. Soc. 57, 645-651.

Hill, A.E., 1937. The transition temperature of gypsum to anhydrite. J. Am. Chem. Soc. 59, 2242-2244.

Hill, A.E., Wills, J. H., 1938. Ternary systems XXIV. Calcium sulfate, sodium sulfate and water. J. Am. Chem. Soc. 60, 1647-1655.

Howell, R.D., Raju, K., Atkinson, G., 1992. Thermodynamics of "Scale" mineral solubilities 4. $SrSO_4$. J. Chem. Eng. Data 37, 464-469.

Il'inskii, V.P., German, N.A., 1936. Tr. Vses. Nauch.-Issled. Inst. Gal.

Jacques, D.C., Bourland, B.I., 1983. A study of solubility of strontium sulphate. SPEJ, 292-300.

Jiang, C., 1996. Solubility and solubility constant of barium sulfate in aqueous sodium sulfate solutions between 0 and 80°C. J. Sol. Chem. 25 (1), 105-111.

Jones, H.C., 1893. Über die Bestimmung des Gefrierpunktes sehr verdünnter Salzlösungen. Z. Phys. Chem. 11, 529-551.

Jones, H.C., Pearce, J.N., 1907. Dissociation as measured by freezing point lowering and by conductivity-bearing on the hydrate theory. The approximate composition of the hydrates formed by a number of electrolytes. Am. Chem. J. 38, 683-743.

Jones, F.E., 1939. The quaternary system $CaO-Al_2O_3-CaSO_4-H_2O$ at 25°C. Trans. Faraday Soc. 35, 1484-1510.

Juranek, J., Skollova, Z., Harnova, J., 1987. MINEQUA-Part I. A program for computing the chemistry of calcium carbonate in mineralized and thermal waters. Geothermics 16, 263-270.

Kaasa, B., 1998. Prediction of pH, mineral precipitation and multiphase equilibria during oil recovery. Ph.D. thesis. Institutt for Uorganisk Kjemi. Norges Teknisk-Naturvitenskapelige Universitet, Trondheim, pp. 5-272.

Keevil, N. B., 1942. Vapor pressures of aqueous solutions at high-temperatures. J. Am. Chem. Soc. 64, 841-850.

Kelley, K.K., 1960. High-temperature heat-content, heat-capacity, and entropy data for the elements and inorganic compounds. Bulletin/Bureau of Mines 584, 1-211.

Kohlrausch, F., Rose, F., 1893. Die Löslichkeit einiger schwer löslicher Körper in Wasser, beurteilt aus der elektrischen Leitfähigkeit. Z. Physik. Chemie 12, 234-243.

Kohlrausch, F., 1908. Über gesättigte wässerige Lösungen schwerlöslicher Salze. II. Teil: Die gelösten Mengen mit ihrem Temperaturgang. Z. Physik. Chemie 64, 129-169.

Kolosov, A.S., 1958. Isotherm in the system MgSO4-CaSO4 at 25°C. Akad. Nauk SSSR 12, 29-38.

Kolosov, A.S., 1959. The system Na, Mg, Ca, SO_4, H_2O at 25°C. Izv. Sib. Otd. Akad. Nauk SSSR 3, 67-75.

Korolev, V.F., 1937. Akad. Nauk SSSR 15, 28.

Kruchenko, V.P., Beremzhanov, V.A., 1976. The solubilities of the salts in the calcium sulphate-hydrochloric acid-water system at 25°C. Russian Journal of Inorganic Chemistry 21, 152-153.

Krumgalz, B.S., Starinsky, A., Pitzer, K.S., 1999. Ion-interaction approach: pressure effect on the solubility of some minerals in submarine brines and seawater. Journal of Solution Chemistry 28 (6), 667-692.

Kuznetsov, A.M., 1946. On the solubility of $CaSO_4$ in the system $CaCl_2-HCl-H_2O$. Zh. Prikl. Khim. 19 (12), 1335-1339.

Kydynov, M., Druzhinin, I.G., 1957. The solubility of the system of the sulfates of calcium and sodium at 0, 20, 40, 60, and 80°C and the glauberite rocks of Tien-Shan. Izv. Akad. Nauk Kirg. SSSR 4, 89-117.

Lepeshkov, I.N., Novikova, L.V., 1958. Physico-chemical investigation of the system $K_2SO_4-MgSO_4-CaSO_4-H_2O$ at 35°C. Zh. Neorgan. Khim. 3 (10), 2395-2407.

Lepeshkov, I.N., Fradkina, Kh. B., 1959. Salt solubilities in the $CaSO_4-Na_2SO_4-NaCl-H_2O$ system at 35 and 55°C. Russian Journal of Inorganic Chemistry 4, 1297-1301.

Lieser, K.H., 1965. Radiochemische messung der löslichkeit von erdalkalisulfaten in wasser und in natriumsulfatlösungen. Z. Anorg. Allg. Chem. 335 (5-6), 225-231.

Loomis, E.H., 1896. Über den Gefrierpunkt verdünnter wässeriger Lösungen. Physical Review 3, 270-292.

Lown, D.A., Thirsk, H.R., Lord W.J., 1968. Effect of pressure on ionization equilibria in water at 25°C. Trans. Faraday Soc. 64, 2073-2080.

Lucchesi, P.J., Whitney, E.D., 1962. Solubility of strontium sulphate in water and aqueous solutions of hydrogen chloride, sodium chloride, sulphuric acid and sodium sulphate by the radiotracer method. J. Appl. Chem. 12, 277-279.

Lyashchenko, A.K., Churagulov, B.R., 1981. Influence of pressure on the temperature coefficients of the solubility of electrolytes in water. Russ. J. Inorg. Chem. 26, 642-644.

MacDonald, R.W., North, N.A., 1974. The effect of pressure on the solubility of $CaCO_3$, CaF_2 and $SrSO_4$ in water. Can. J. Chem. 52, 3181-3186.

Madgin, W.M., Swales, D.A., 1956. Solubilities in the system $CaSO_4-NaCl-H_2O$ at 25°C and 35°C. J. Appl. Chem. 6, 482-487.

Manikhin, V.I., 1966. Solubility of calcium sulfate under high pressures. Gidrokhim. Mater 41, 192-196.

Marden, J.W., 1916. Solubilities of the sulfates of barium, strontium, calcium and lead in ammonium acetate solutions at 25°C and a criticism of the presents methods for the separation of these substances by means of ammonium acetate solution. J. Amer. Chem. Soc. 38, 310-316.

Marshall, W.L., Slusher, R., Jones, E.V., 1964. Aqueous systems at high temperature XIV. J. Chem. Eng. Data 9, 187-191.

Mecke, P., 1935. Über die Löslichkeit von calciumsulfat und calciumhydroxyd. Zement 24 (48), 764-766.

Melcher, A.C., 1910. The solubility of silver chloride, barium sulphate, and calcium sulphate at high temperatures. J. Am. Chem. Soc. 32, 50-66.

Melnikova, Z.M., Moshkina, I.A., 1973. The solubility of anhydrite and gypsum in the system Na,Mg,Ca,Cl,SO_4-H_2O at 25°C. Ser. Khim. Nauk. 2, 18-26.

Millero, F.J., 1981. The effect of pressure on the solubility of minerals in water and seawater. Geochimica et Cosmochimica Acta 46, 11-22.

Monnin, C., Galinier, C., 1988. The solubility of celestite and barite in electrolyte solutions and natural waters at 25°C: A thermodynamic study. Chemical Geology 71, 283-296.

Monnin, C., 1999. A thermodynamic model for the solubility of barite and celestite in electrolyte solutions and seawater to 200ºC and to 1 kbar. Chemical Geology 153, 187-209.

Moshinskii, A. S., Tikhomirova, K. A., 1973. Equilibrium between zinc chloride and alkaline earth metal chlorides in an aqueous medium at 50°C. Russ. J. Inorg. Chem. 18, 431-433.

Møller, N., Greenberg, J.P., Weare, J.H., 1998. Computer modeling for geothermal systems: Predicting carbonate and silica scale formation, CO_2 breakout and H_2S exchange. Transport in Porous Media 33, 173-204.

Müller, G., 1960. Die Löslichkeit von Coelestin ($SrSO_4$) in wässerigen NaCl- und KCl-Lösungen. Neues Jahrb. Mineral. Mon., 237-239.

Neuman, E.W., 1933. Solubility relations of barium sulfate in aqueous solutions of strong electrolytes. J. Am. Chem. Soc. 55, 879-884.

Nikolskaya, Y.P., Moshkina, I.A., 1958. The Na, Ca, SO_4, HCO_3 - H_2O system at 25°C and 1 atm. CO_2 pressure. Zh. Neorgan. Khim. 3 (2), 498-500.

NIST Chemical Thermodynamics Database Version 1.1, 1990. U.S. Department of Commerce, National Institute of Standards and Technology, Gaithesburg MD 20899.

Novikola, L.V., 1957. Study of solubility in the equilibrium in the system $CaSO_4$-$MgSO_4$-H_2O at 35°C by the method of labelled atom. Zh. Neorgan. Khim. 2 (3), 662-668.

Orlov, N.A., 1902. Obshchest. Chast. Khim. 34, 951.

Partridge, E., White, A.H., 1929. The solubility of calcium sulfate from 0 to 200°C. J. Am. Chem. Soc. 51, 360-370.

Perova, A.P., 1957. Solubility isotherms in the aqueous magnesium chloride calcium sulfate system at 25 and 55°C. Sb. Tr. Voronezh. Otd. Vses. Khim. Obshch. im Mendeleva 1, 155-163.

Pitzer, K.S., 1991. Activity coefficients in electrolyte solutions, 2nd edition. CRC Press, Boca Raton, pp. 293-422.

Posnjak, E., 1938. The system $CaSO_4$-H_2O. American Journal of Science 35, 247-272.

Potapov, V.V., Kashpura, V.N., Alekseev, V.I., 2001. A study of the growth of deposits in geothermal power systems. Thermal Engineering 48 (5), 395-400.

Puchelt, H., 1967. Zur Geochemie des Bariums im exogenen Zyklus. Sitzungsberichte der Heidelberger Akademie der Wissenschaften, Heidelberg (Germany).

Qadirie, A.R., 1990. Experimente zum Fällungsverhalten im System Barium-Strontium-Sulfat und Vergleich mit natürlichen Ausfällungen. Diplomarbeit (Teil 2), Mathematisch-Naturwissenschaftlichen Fakultät der Christian-Albrechts-Universität zu Kiel.

Rard, J.A., Miller, D.G., 1982. Isopiestic determination of the osmotic and activity coefficients of aqueous CsCl, $SrCl_2$, and mixtures of NaCl and CsCl at 25°C. J. Chem. Eng. Data 27, 169-173.

Reardon, E.J., Armstrong, D.K., 1987. Celestite ($SrSO_4$(s)) solubility in water, seawater and NaCl solution. Geochimica et Cosmochimica Acta 51, 63-72.

Rza-Zade, P.F., Rustamov, P.G., 1961. Isotherms in the system $MgCl_2$-$CaCl_2$-$CaSO_4$-H2O at 25°C. Azerb. Khim. Zh. 4, 127-131.

Rza-Zade, P.F., Rustamov, P.G., 1963. Solubility isotherm in the system NaCl-$CaCl_2$-$CaSO_4$-H_2O at 25°C. Azerb. Khim. Zh. 1, 57-63.

Schreinemakers, F.A.H., de Baat, W.C., 1909. Gleichgewichte in quaternaren Systeme. Z. Physik. Chem. 65, 586-594.

Schreinemakers, F.A.H., 1910. Gleichgewicht in quaternären Systemen. Das System: Natriumoxyd - Baryumoxyd - Salzsäure und Wasser. Zeitschrift für Physikalische Chemie 68, 83-103.

Schreinemakers, F.A.H., 1911. Le point de transformation de sels doubles. Archives Néerlandaises des Sciences Exactes et Naturelles 15, 396-402.

Schroeder, W.C., Gabriel, A., Partridge, E.P., 1935. Solubility equilibria of sodium sulfate at temperatures of 150 to 350°C. I. Effect of sodium hydroxide and sodium chloride. J. Am. Chem. Soc. 57, 1539-1546.

Schulien, S., 1987. High-temperature/high-pressure solubility measurements in the systems $BaSO_4$-NaCl-H_2O and $SrSO_4$-NaCl-H_2O in connection with scale studies. SPE symposium (SPE 16264), San Antonio, Texas.

Seidell, A., Smith, J.G., 1904. The solubility of calcium sulphate in solutions of nitrates. J. Phys. Chem. 8, 493-499.

Selivanova, N.M., Zubova, G.A., 1956. Polarography and thermodynamics IV. Thermodynamic properties and solubility of strontium sulfate. Trudy Moskov. Khim.-Teknol. Inst. im. D.I. Mendeleeva, 38-46.

Semenchenko, V.K., Zavada, E.A.. 1931. Krioskopija vodnykh rastvorov smesej jelektrolitov. Zhurnal obshchei khimii 1, 1121-1931.

Shams El Din, A.M., Mohammed, R.A., 1989. The problem of alkaline scale formation from a study on Arabian Gulf water. Desalination 71, 313-324.

Shternina, E.B., Frolova, E.V., 1949. Akad. Nauk SSSR 17, 354.

Sorbie, K.S., Mackay, E.J., 2000. Mixing of injected, connate and aquifer brines in waterflooding and its relevance to oilfield scaling. Journal of Petroleum Science and Engineering 27, 85-106.

Speranskaya, E.I., 1954. Reactions of nitrates and chlorides of sodium and barium in melts and in aqueous solutions. Akad. Nauk. SSSR 24, 212-221.

Strübel, G., 1966. Die hydrothermale Löslichkeit von Cölestin im System $SrSO_4$-NaCl-H_2O. Neues Jahrb. Mineral. Mon., 99-107.

Strübel, V.G., 1967. Zur Kenntnis und genetischen Bedeutung des Systems $BaSO_4$-NaCl-H_2O. Neues Jahr. Miner. Monatsh., 223-234.

Sveshnikova, V.N., 1949. Solubility isotherms in the system $CaSO_4$-$CaCl_2$-H_2O at 25 and 55^oC and $CaSO_4$-KCl-H_2O at 25^oC. Izv. Sektora Fiz.-Khim. Anal. Akad. Nauk SSSR 17, 345-351.

Sveshnikova, V.N., 1952. Phase equilibria in the reciprocal system $CaSO_4$-KCl-H_2O at 55^oC. Otd. Khim. Nauk 1, 44-51.

Taperova, A.A., 1940. L'analyse physicochimique dans le domaine du traitement des phosphates par l'acide sulfurique. Zhurnal Prikladnoi Khimii 13 (5), 643-52.

Templeton, C.C., 1960. Solubility of barium sulfate in sodium chloride solutions from 25^o to 95^oC. Journal of Chemical and Engineering Data 5 (4), 515-516.

Thomsen, K., Rasmussen, P., Gani, R., 1996. Correlation and prediction of thermal properties and phase behaviour for a class of electrolyte systems. J. Chem. Eng. Science 51, 3675-3683.

Thomsen, K., Rasmussen, P., 1999. Modeling of vapor-liquid-solid equilibrium in gas-aqueous electrolyte systems. Chemical Engineering Science 54, 1787-1802.

Trendafelov, D., Balarew, C., Zlateva, I., Keremidtchieva, B., Gradinarov, S., 1994. Investigations of the $BaSO_4$ conversion to $BaCO_3$ in the quaternary reciprocal water-salt system $BaSO_4+K_2CO_3 = BaCO_3+K_2SO_4$. Comptes Rendus de l'Academie Bulgare des Science 47 (1), 47-50.

Uchameyshvili, N.Y., Malinin, S.D., Khitarov, N.I., 1966. Solubility of barite in concentrated chloride solutions of some metals at elevated temperatures in relation to problems of the genesis of barite deposits. Geochem. Int. 10, 951-963.

Uspenskaya, L.N., Bergman, A.G., 1955. Solubility in the reciprocal salt system Barium, Calcium, Nitrate, Chloride at 80, 100 and 120^oC. Zh. Obshch. Khim. 25, 1277-1284.

Uspenskaya, L.N., Glushkova, N.P., Bergman, A.G., 1955. Solubility in the reciprocal salt system Barium, Calcium, Nitrate, Chloride from the freezing point to 60^oC. Zh. Obshch. Khim. 25 (9), 1658-1673.

Valyashko, M.G., Petrova, V.M., 1952. Tr. Vses Nauch.-Issled. Inst. Galurgii 23, 162.

Varasova, E.N., Mischenko, K.P., Frost, O.I., 1937. Investigation of the thermodynamic properties of saturated water-salt systems (heat capacity and vapor pressure for the system $BaCl_2$-$CaCl_2$-H_2O at 25^oC. Zh. Obshch. Khim. 7, 1284-1291.

Vetter, O.J.G., Vandenbroeck, I., Nayberg, J., 1983. $SrSO_4$: the basic solubility data. Society of Petroleum Engineers, 271-281.

Wolfmann, I., 1896. Studium über die Löslichkeitsverhältnisse einiger Strontiumsalze. Besonders des Strontiumsulfates. Österr. Ungar. Z. Zuckerind. 25, 986-997.

Yousef, A.M., Elkanzi, E.M., Singh, H., 2001. Prediction of supercritical CO_2 solubility using the Krichevsky-Ilinskaya equation with v2 as an adjustable parameter. J. of Supercritical Fluids 20, 105-112.

Yuan, M., Todd, A.C., Sorbie, K.S., 1994. Sulfate scale precipitation arising from seawater injection: a prediction study. Marine and Petroleum Geology 11(1), 24-30.

Yuan, M.D., Anderson, M., Jamieson, E., 1997. Investigation and improvement of $BaSO_4$ scale inhibition tests. Society of Petroleum Engineers 37304, 765-768.

Zdanovskii, A.B., Spiridonov, F.P., 1967. Polytherm for the solubilities of various forms of $CaSO_4{\cdot}xH_2O$ in water between 0 and 100^oC. Zhurnal Prikladnoi Khimii 40, 1152-1154.

Zhang, Y., Shaw, H., Farquhar, R., Dawe, R., 2001. The kinetics of carbonate scaling-application for the prediction of downhole carbonate scaling. Journal of Petroleum Science and Engineering 29, 85-95.

Zhenhao, D., Møller, N., DeRocher, T., Weare, J.H., 1996. Prediction of boiling, scaling and formation conditions in geothermal reservoirs using computer programs. Geothermics 25 (6), 663-678.

5. Carbonate Scaling Minerals

This chapter is devoted to the calculation of the solubility of different carbonate minerals by means of the extended UNIQUAC model. It has been submitted with the title “Prediction of mineral scale formation in geothermal and oilfield operations using the extended UNIQUAC model. Part II. Carbonate scaling minerals” in Geothermics (authors: Ada Villafáfila García, Kaj Thomsen and Erling H. Stenby). In the following, it will be demonstrated that the extended UNIQUAC model is able to give a very good representation of the solid-liquid-vapour phase equilibria for carbonate systems, in the whole temperature, pressure and concentration range investigated. In most of the cases, the absolute deviation between extended UNIQUAC calculations and the experimental data is within experimental accuracy. Table 5-1 shows the values for the *ASD* calculated from the experimental data reported for the different systems studied in this paper.

Table 5-1
Calculated *ASD* values for different systems

System	***ASD* (m)**
CO_2-H_2O	4.1E-02
CO_2-NaCl-H_2O	2.2E-02
CO_2-Na_2SO_4-H_2O	2.7E-02
$CaCO_3$-CO_2-H_2O	1.3E-03
$BaCO_3$-CO_2-H_2O	2.3E-04
$SrCO_3$-CO_2-H_2O	
$MgCO_3$-CO_2-H_2O	1.8E-02

The surface area and volume parameters obtained from the present work together with the values required for other species obtained by Thomsen and Rasmussen (1999) are given in table 5-15. The binary energy interaction parameters for the extended UNIQUAC model are shown in table 5-16 and table 5-17. Finally, the two new pressure parameters added to the extended UNIQUAC model to account for the pressure dependency are given in table 5-18. The parameters obtained from the present work are marked in bold.

The values for the standard state Gibbs free energy, enthalpy and heat capacity for the different crystalline phases analyzed are taken (whenever it was available) from the NIST Chemical Thermodynamics Database (1990). Those values are also reported in table 5-19.

5.1 CO_2 Solubility

5.1.1 CO_2 Solubility in Pure Water

Most of the papers dealing with calcite ($CaCO_3$) solubility in CO_2-saturated water do not report the CO_2 concentration in the liquid, but only the $CaCO_3$ solubility and the partial pressure of CO_2. In order to be able to use those data, the amount of CO_2 in the solution at the experimental conditions is needed. Therefore, a program calculating CO_2 solubility in water as a function of temperature and pressure was developed. The extended UNIQUAC model was used to calculate activity coefficients in the liquid phase, while gas phase fugacities were calculated according to the Soave-Redlich-Kwong equation of state, using classical mixing rules.

It was assumed that the CO_2 solubility in $CaCO_3$ solutions is very close to the CO_2 solubility in pure water at the same conditions. This assumption is based on the fact that calcite solubility in water is so low that it will not influence the gas solubility significantly. This assumption is supported by table 5-2, where CO_2 solubility values in the $CaCO_3$-H_2O solutions reported by Malinin (1963) are compared to the values obtained from the program. The highest relative deviation is found to be 5.7%, and the average relative deviation is 3.1%. These values are low enough and demonstrate that the influence of calcite on CO_2 solubility in the liquid phase can be neglected without leading to large errors.

Diamond and Akinfiev (2003) reviewed 25 experimental studies on CO_2 solubility in pure water in the temperature range from -1.5 to 100°C, and pressures from 1 to 1000 bar. Different criteria were used to analyze the references, giving them a different weight factor depending on their reliability. All the points with the highest accuracy (according to Diamond and Akinfiev, 2003): Wiebe and Gaddy (1939, 1940), Bartholome and Friz (1956), Matous et al. (1969), Zawisza and Malesinska (1981), Müller et al. (1988), Bamberger et al. (2000), and Anderson (2002)) were used in this work for parameter estimation. Some of the points with very low accuracy (according to Diamond and Akinfiev, 2003) were rejected (Wroblewski (1883), Sander (1912), Hähnel (1920), Kritschewsky et al. (1935), Vilcu and Gainar (1967), Stewart and Munjal (1970), Teng et al. (1997), and Servio and Englezos (2001)).

Table 5-3 shows all the publications used for the system CO_2-H_2O, the ranges of temperature and pressure covered by them, the number of data points reported by each publication, the number of data points used in the present work (in brackets), and the average absolute deviation between our calculations and the experimental data. The calculated CO_2 solubilities in pure water compare well with the experimental data, with a mean absolute deviation of

$3.6 \cdot 10^{-2}$ m CO_2, while the average standard deviation for the experimental data is $4.1 \cdot 10^{-2}$ m CO_2.

Table 5-2
Calculated versus experimental CO_2 solubility in $CaCO_3$-H_2O solutions.

T	***P***	**CO_2 solubility in pure water (m)**		***RD***
(°C)	**(bar)**	**Malinin (1963)**	**Our model**	**(%)**
150	10.9	0.053	0.056	5.66
150	20.2	0.133	0.138	3.76
150	21.7	0.146	0.151	3.42
150	35.1	0.262	0.263	0.38
150	54.2	0.409	0.411	0.56
150	54.3	0.410	0.414	0.98
150	57.5	0.443	0.437	-1.35
150	59.2	0.457	0.450	-1.53
150	145.1	0.955	0.973	1.88
150	200.1	1.192	1.228	3.02
225	57.9	0.318	0.337	5.97
225	80.4	0.523	0.553	5.74
225	131.4	0.955	1.002	4.92
225	135.3	0.978	1.034	5.73
225	199.1	1.458	1.518	4.12
225	200.1	1.468	1.525	3.88
225	398.2	2.660	2.767	4.02
225	402.1	2.680	2.788	4.03

Table 5-3
Experimental CO_2-H_2O VLE data sets used for parameter estimation.

T **(°C)**	***P*** **(bar)**	**Number of data**	***AAD*** **(m)**	**Reference**
0/12.4	5/30.4	12 (0)		Wroblewski (1883)
0/15	5/45.6	14 (0)		Hähnel (1920)
0/25	0.1/1	19 (19)	5.3E-04	Morgan and Maass (1931)
0/25	1	3 (3)	1.7E-03	Kiss et al. (1937)
0/25	10/45	12 (0)		Stewart and Munjal (1970)
0/50	1.00E+00	18 (18)	6.0E-04	Harned and Davis (1943)
0/60	1/9	65 (65)	8.7E-03	Wasmund and Bultmann (1980)
0/100	1/96	95 (95)	2.8E-02	Zelvenskii (1937)
0.2/40	1.00E+00	3 (3)	7.2E-04	Markham and Kobe (1941a)
1/5	9/21	9 (9)	9.6E-03	Malegaonkar et al. (1997)
1/15	1/22	53 (53)	8.2E-03	Anderson (2002)
1/35	1.00E+00	8 (8)	1.1E-03	Murray and Riley (1971)
100/200	3/81	49 (49)	3.6E-02	Müller et al. (1988)
3.9/10	20/42	9 (0)		Servio and Englezos (2001)

Table 5-3 (continuation)
Experimental CO_2-H_2O VLE data sets used for parameter estimation.

T (°C)	*P* (bar)	Number of data	*AAD* (m)	Reference
5/20	64.4/295	24 (0)		Teng et al. (1997)
5/65	0.5/0.8	10 (10)	3.0E-04	Zheng et al. (1997)
10/30	1/20	15 (15)	1.6E-02	Bartholome and Friz (1956)
10/70	10/160	23 (0)	1.7E-02	Oleinik
11.5/40	0.1/0.9	24 (24)	1.2E-03	Novak et al. (1961)
12/40	50/506	42 (42)	1.0E-01	Wiebe and Gaddy (1940)
13.3/74.7	1	19 (19)	1.9E-03	Morrison and Billett (1952)
15/25	1.00E+00	2 (2)	1.2E-03	Geffcken (1904)
15/55	1	5 (5)	1.4E-03	Postigo et al. (1978)
15.6/93.3	6.9/202.7	16 (16)	2.8E-02	Gillespie and Wilson (1982)
20/30	4.8/29	40 (0)		Kritschewsky et al. (1935)
20/34	1	8 (8)	6.9E-04	Kunerth (1992)
20/35	25/76	20 (0)		Vilcu and Gainar (1967)
20/60	24/167	34 (0)		Sander (1912)
21.2/21.8	1	4 (4)	2.1E-03	Curry and Hazelton (1938)
22.8/25.5	1	6 (6)	3.9E-04	Van Slyke (1939)
25	1	1 (1)	3.8E-04	Markham and Kobe (1941b)
25	21.7/53.3	7 (7)	4.0E-02	Yang et al. (2000)
25/45	1.00E+00	4 (4)	1.0E-03	Yeh and Peterson (1964)
25/75	48	20 (20)	8.9E-03	Malinin and Savel'eva (1972)
25/150	48	10 (10)	1.5E-02	Malinin and Kurovskaya (1975)
30/80	9.3/39.3	13 (13)	8.8E-03	Matous et al. (1969)
33/213	8/5.8	7 (6)	2.0E-02	Cramer (1982)
40/120	1/92.6	39 (0)		Kiepe et al. (2002)
5.00E+01	10.6/58	7 (7)	2.2E-03	Rumpf et al. (1994)
50/80	40/141	29 (29)	1.1E-02	Bamberger et al. (2000)
50/100	25/709	29 (29)	6.6E-02	Wiebe and Gaddy (1939)
50/100	100/800	9 (0)		Shagiakhmetov and Tarzimanov (1981
50/200	1.5/54	33 (33)	9.2E-03	Zawisza and Malesinska (1981)
50/350	200/3500	108 (14)	1.4E-01	Tödheide and Franck (1963)
80/198	20.4/102	33 (33)	2.2E-02	Nighswander et al. (1989)
101/120	23.3/703	26 (26)	9.9E-02	Prutton and Savage (1945)
110/350	100/1500	121 (39)	2.2E-01	Takenouchi and Kennedy (1964)
114/348	5/162	36 (23)	6.0E-03	Ellis (1959b)
150/350	100/1400	39 (0)		Takenouchi and Kennedy (1965)
177/334	25/199	15 (6)	3.7E-02	Ellis and Golding (1963)
			***MAAD* (m):**	**3.6E-02**

The original papers of Oleinik (unknown year) and Shagiakhmetov and Tarzimanov (1981) were not found. The data were taken from Diamond and Akinfiev (2003), who also obtained these measurements quoted in references different from the original publications. Although the measurements reported by both sources compare well with the majority of the references analyzed, the lack of the original sources led us to discard the data for parameter estimation. The same criteria is followed for the CO_2 solubilities in pure water given by Takenouchi and Kennedy (1965). They measured the solubility of CO_2 in 6 and 20 wt% NaCl solutions, and they also included in their work data for the solubility of CO_2 in pure water. Nevertheless, it is not explained where the latter data were taken from.

Some of the references rejected by Diamond and Akinfiev (2003) were used in the present work for parameter estimation, as they are believed to be accurate enough, and the agreement among those sources and the ones considered reliable is rather good.

The weight factor given by Diamond and Akinfiev (2003) to the data reported by Gillespie and Wilson (1982) is 0.33. Diamond and Akinfiev (2003) claim that those points deviate systematically from the majority of other studies, but we think the deviation is small enough to consider the source reliable. Figure 5-1 shows all the CO_2-H_2O data used in the present work at 30°C and the correlation by the extended UNIQUAC model. The agreement between the data reported by the reference mentioned above and Wiebe and Gaddy (1940), Bartholome and Friz (1956) and Matous et al. (1969) is quite good even at high pressures. The same agreement is also found at other temperatures. The latter references were all given a weight factor of one, and therefore it was decided to use the measurements reported by Gillespie and Wilson (1982) for parameter estimation.

Only one out of the seven measurements performed by Cramer (1982) was analyzed by Diamond and Akinfiev (2003) (the other six points were out of the *T*/*P* range of interest in that source). Cramer's (1982) work was discarded by Diamond and Akinfiev (2003) due to its "deviation from the assumption of $\gamma_{CO2} \rightarrow 1$ at low solubility". Figure 5-1 compares the rejected point with the measurements performed by Bartholome and Friz (1956), which was given a weight factor of unity. It is clearly observed that both sources agree very well, and therefore the tendency followed by the activity coefficient in both cases should be the same. When comparing the other six points to reliable sources, a good agreement is found in most of the cases. The highest deviation is found at 146°C. This point was therefore not used for parameter estimation.

The solubilities reported by Yang et al. (2000) agree rather well with many other sources, and therefore it was decided to use those points for parameter estimation.

The solubility values measured by Zelvenskii (1937) agree remarkably well with the majority of other studies. Diamond and Akinfiev (2003) claim that at temperatures above 50°C the CO_2 activity coefficient does not tend to zero for low concentrations. But the values reported by Zelvenskii (1937) at temperatures higher than 50°C are remarkably close to those from

Wiebe and Gaddy (1940), and Müller et al. (1988), both sources with a weight factor of unity. Therefore, if the temperature and pressure conditions coincide, and the solubility values are so close, the value of the activity coefficient should be similar. If two of the sources are considered reliable, the third one should also be given credibility.

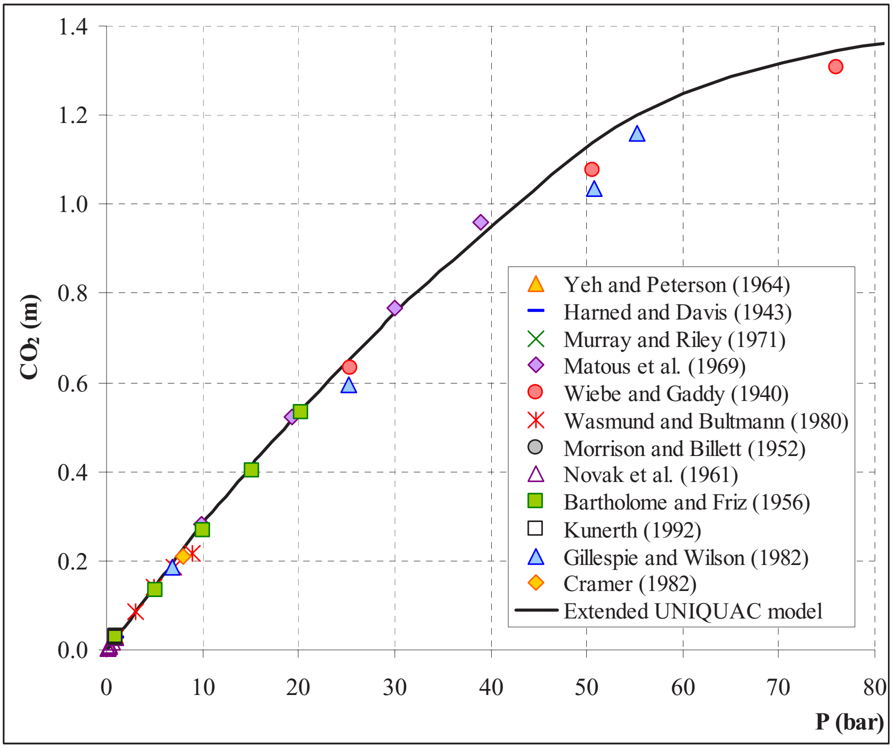

Figure 5-1. Experimental and calculated vapour-liquid phase diagram for the CO_2-H_2O system at 30°C

Finally, measurements performed by Malinin and Kurovskaya (1975) were also used for parameter estimation, as they agreed with most of the reliable sources.

Some sources report experimental data at temperatures and/or pressures out of the range of interest in the present work. That is the case of Ellis (1959b), Ellis and Golding (1963), Tödheide and Franck (1963) and Takenouchi and Kennedy (1964). The number of experiments performed by these authors under the conditions of interest in the present work is 23, 6, 14 and 39, respectively.

The other references given in table 5-3 and not analyzed by Diamond and Akinfiev (2003) were all used for parameter estimation, as they agreed very well with the trusted sources. Only the values reported by Kiepe et al. (2002) were discarded, as they deviate considerably from the main tendency, especially at pressures higher than 50 bar.

The calculated and experimental CO_2 solubility in pure water at 150°C is shown in figure 5-2, where the good agreement between the extended UNIQUAC model and the data is observed even at very large pressures. Only data up to 1000 bar were used for parameter estimation, but figure 5-2 shows that predictions performed by our model at larger pressures (up to 1500 bar) are very accurate. Carbon dioxide solubility increases considerably with pressure, changing from 0.028 m CO_2 at 7.7 bar to 2.8 m CO_2 at 1500 bar.

Figure 5-3 shows the solubility of carbon dioxide in water at a constant pressure of 100 bar. CO_2 solubility in water decreases very steeply with temperature from 25 to 100°C, while the influence of temperature becomes almost negligible in the temperature range from 100 to 200°C. For higher temperatures, the carbon dioxide solubility decreases again with increasing temperature. The shape of the experimental curve is very well represented by the extended UNIQUAC model. Table 5-3 shows the value of the mean average absolute deviation between the model calculations and the experimental data used in this work. This value, $3.6 \cdot 10^{-2}$ m CO_2, is lower than the experimental *ASD* ($4.1 \cdot 10^{-2}$ m CO_2), and therefore it can be concluded that the calculations and predictions for the CO_2-H_2O system are within experimental accuracy.

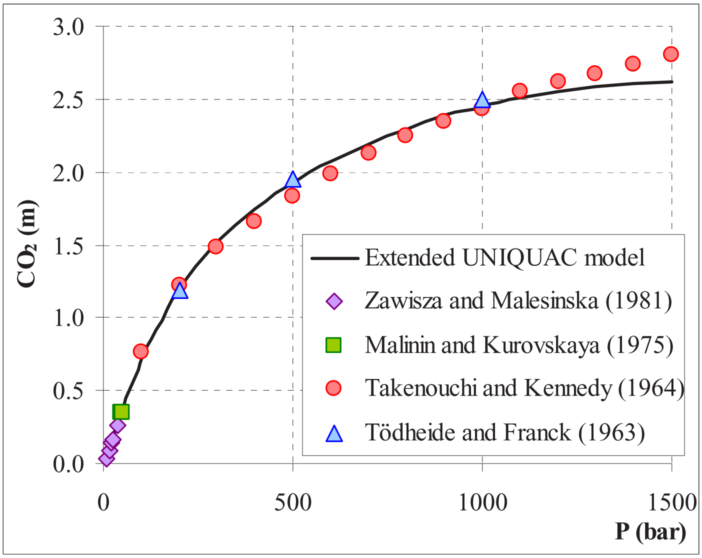

Figure 5-2. Experimental and calculated vapour-liquid phase diagram for the CO_2-H_2O system at 150°C

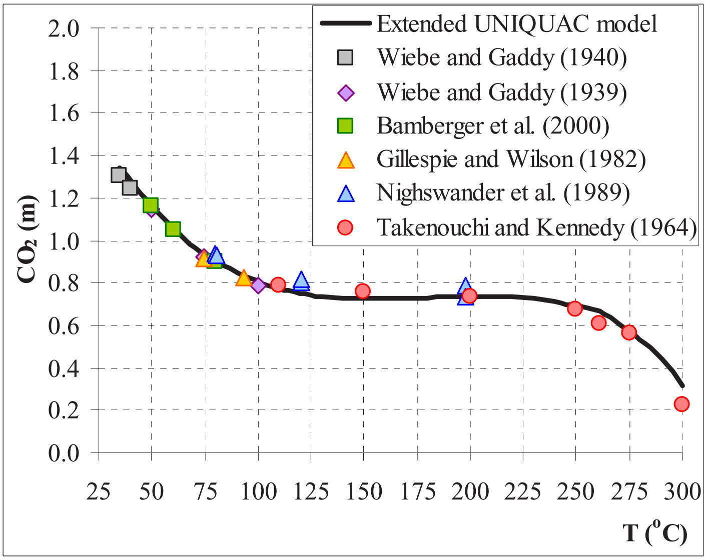

Figure 5-3. Experimental and calculated vapour-liquid phase diagram for the CO_2-H_2O system at 100 bar

5.1.2 CO_2 Solubility in Aqueous Solutions of NaCl and Na_2SO_4

In order to be able to apply our model to the calculation of vapour-liquid-solid equilibria in natural waters, the main constituents of such kind of waters have to be accounted for. For this reason, we found necessary to study and model the carbon dioxide solubility in different electrolyte solutions, such as solutions containing NaCl and Na_2SO_4. The interaction parameters between CO_2, HCO_3^-, CO_3^{2-} and Na^+, Cl^- and SO_4^{2-} have been previously determined by Thomsen and Rasmussen (1999) on the basis of VLE and SLE data. The temperature and pressure range covered by them is from 0 to 100°C and from 1 to 100 atm, respectively. Those ranges are not enough for the purposes of the present work. Extrapolation to higher temperatures and pressure did not give accurate results, and therefore parameter estimation was carried out on the basis of VLE data covering a wider range of both temperature and pressure.

The VLE behaviour in aqueous solutions may be quite different than in pure water. The thermodynamic properties of the solution can vary significantly as a consequence of the interactions between molecules and ionic species. Depending on the kind of salt, the gas solubility may be raised (salting-in effect) or decreased (salting-out effect). For carbon dioxide solubility in NaCl and Na_2SO_4 solutions, a large salting-out effect is noticed.

However, the general form and trend of the solubility curves is approximately the same as for the system CO_2-H_2O (Takenouchi and Kennedy, 1965).

5.1.2.1 CO_2 Solubility in NaCl Solutions

Table 5-4 shows the sources found in the literature reporting carbon dioxide solubility in sodium chloride solutions at different temperatures and pressures. The number of experimental determinations for each source and the number of data used in the present paper (in brackets) is also given there.

Table 5-4
Experimental CO_2-NaCl-H_2O VLE data sets used for parameter estimation.

T(°C)	*P*(atm)	Number of data	*AAD* (m)	Reference
0/50	1	90 (90)	9.7E-04	Harned and Davis (1943)
0/90	1	31 (0)		He and Morse (1993)
0.2/40	1	15 (15)	1.3E-03	Markham and Kobe (1941a)
15/35	1	27 (27)	1.3E-03	Yasunishi and Yoshida (1979)
20/35	1	16 (16)	1.7E-03	Vazquez et al. (1994)
25	1	8 (8)	1.5E-03	Onda et al. (1970)
25/150	48.9	27 (27)	2.5E-02	Malinin and Kurovskaya (1975)
25/75	48	13 (13)	4.3E-02	Malinin and Savel'eva (1972)
40/160.8	4.6/96.4	63 (63)	1.5E-02	Rumpf et al. (1994)
80/200.5	21.1/100.3	34 (0)		Nighswander et al. (1989)
172/334	25/213.6	59 (0)		Ellis and Golding (1963)
25	1	7 (7)	1.9E-03	Yasunishi et al. (1979)
250/450	100/1400	86 (30)	1.3E-01	Takenouchi and Kennedy (1965)
100/500	200/2500	178 (32)	1.2E-01	Naumov et al. (1974)
5/65	0.5/0.9	18 (0)		Zheng et al. (1997)
			***MAAD* (m):**	**3.1E-02**

Rumpf et al. (1994) developed a model using Pitzer's (1973) equations to predict CO_2 solubility in sodium chloride solutions based on their experimental determinations. The results obtained by them agree very well with Markham and Kobe (1941a), Malinin and Savel'eva (1972), and Yasunishi and Yoshida (1979). The average relative deviation for the total pressure between the model given by Rumpf et al. (1994) and the previous sources is 2.4%, 1.7% and 1.5%, respectively (values calculated by Rumpf et al., 1994). On the other hand, the dataset by Ellis and Golding (1963) disagrees with the model of Rumpf et al. (1994), with an average relative deviation of 5.7%. Therefore, it will not be used for parameter estimation. The data by Nighswander et al. (1989) agree only fairly with the model of Rumpf et al. (1994), and they also disagree with Takenouchi and Kennedy (1965). Both

Takenouchi and Kennedy (1965) and Nighswander et al. (1989) determined carbon dioxide solubility at 200°C and at comparable pressures, but at different NaCl concentrations of 1 and 0.17 m, respectively. Even though the salt concentrations are different, the measurements gave similar results for the CO_2 solubility, indicating that there is no salting-out effect. Thus, the data by Nighswander et al. (1989) were not used for parameter estimation.

The shape of the carbon dioxide solubility curve in NaCl solutions obtained from the data of He and Morse (1993) and Zheng et al. (1997) differs from the curves obtained by the different datasets shown in table 5-4. The decrease in carbon dioxide solubility as a consequence of increasing concentration is much flatter for the data of He and Morse (1993) and Zheng et al. (1997) than claimed by the rest of the sources employed. He and Morse (1993) compared the value for the second dissociation constant for CO_2 they obtained from their measurements to literature. A clear disagreement is found when compared to Thurmond and Millero (1982) and Patterson et al. (1982, 1984). Their pK values seem to agree with those by Harned and Bonner (1945). The data of He and Morse (1993) and Zheng et al. (1997) were therefore not used in the present work.

The effect of pressure on the carbon dioxide solubility in NaCl solutions reported by Naumov et al. (1974) does not agree with the data of Malinin and Kurovskaya's (1975). The first source reports solubility values at 100°C and 100 bar very close to the values given by Malinin and Kurovskaya (1975) at 100°C and 48 bar, covering a NaCl concentration range from 0.5 to 6 m. The latter source is in good agreement with Malinin and Savel'eva (1972), which was mentioned previously due to its agreement with many other sources in table 5-4. On the other hand, Naumov et al. (1974) agrees quite well with Takenouchi and Kennedy (1965), especially at high temperatures (250 and 300°C). At lower temperatures (150 and 200°C) the influence of NaCl concentration on CO_2 solubility reported by both sources is somehow different. The values given by Naumov et al. (1974) at 0.5 and 5 m are very close to those by Takenouchi and Kennedy (1965) at 1 and 4.3 m, respectively. After analyzing all these data sets it seems clear that a general disagreement is found among the different sources. Nevertheless, the regions of overlap of the different studies are rather narrow, and a clear conclusion about the reliability of the sources cannot be achieved. Therefore, it was decided to employ them all in the present work. Both Takenouchi and Kennedy (1965) and Naumov et al. (1974) performed measurements at higher temperatures and pressures than the range of interest in this work (56 and 146 measurements, respectively).

At 30 and 35°C and 1 atm total pressure, there is some scatter among the data reported by three sources: Harned and Davis (1943), Yasunishi and Yoshida (1979), and Vazquez et al.

(1994). Nevertheless, the differences are not so large and they can be regarded as reasonable experimental standard deviations.

The experimental and calculated phase diagram for the system CO_2-NaCl-H_2O at a constant temperature of 160°C and NaCl concentrations of 4 and 6 m is shown in figure 5-4. Carbon dioxide solubility increases with increasing pressure, while it decreases for increasing salt concentration.

Figure 5-5 shows experimental data in the pressure range from 60 to 70 bar, together with the model calculations, at both 4 and 6 m NaCl. The reason why data from a pressure range were used instead of isobaric data is the lack of isobaric data. Figure 5-5 includes calculations performed by the model at the experimental conditions (grey dots and triangles) together with the calculations at a constant pressure of 60 bar (lines). As already mentioned for figure 5-4, the salting-out effect can also be observed in figure 5-5. CO_2 solubility decreases considerably with increasing temperature, passing from 0.53 m at 40°C to 0.22 m at 160°C, for 4 m NaCl solutions.

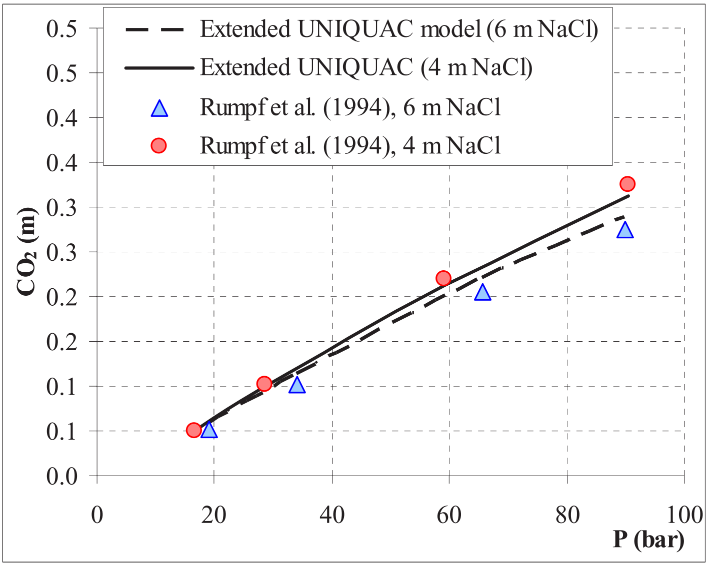

Figure 5-4. Experimental and calculated vapour-liquid phase diagram for the CO_2-NaCl-H_2O system at 160°C.

The representation by the extended UNIQUAC model of the solubility of carbon dioxide in NaCl solutions is very good, even for very concentrated solutions (close to the saturation of NaCl). The mean absolute deviation between the model calculations and the experimental points is $3.1\cdot10^{-2}$ m, while the average standard deviation for the experimental points is

$2.2\cdot10^{-2}$ m. The latter value is mainly based on data at atmospheric conditions, due to the lack of experimental measurements at the same NaCl concentration, temperature and pressure. If only data at pressures larger than 1 atm are considered in the calculation of *ASD*, the value is increased to $1.5\cdot10^{-1}$ m.

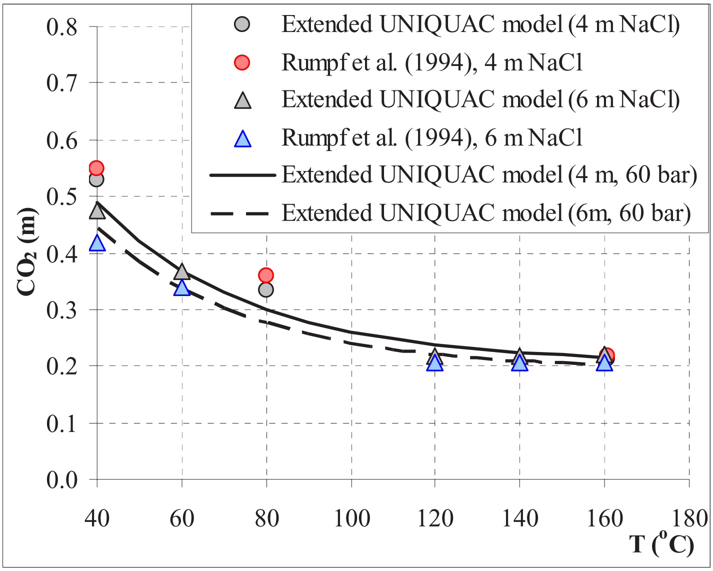

Figure 5-5. Experimental and calculated vapour-liquid phase diagram for the CO_2-NaCl-H_2O system at 60-70bar. Lines represent calculations at a constant pressure of 60 bar, while grey dots and triangles represent calculations at the experimental pressure (in the range from 60 to 70 bar), which are compared to the experimental data (red and blue dots and triangles).

Table 5-4 shows the *AAD* for each one of the CO_2-NaCl-H_2O sources employed in the present work. There, it can be seen that the value of *AAD* for all the sources at atmospheric pressure is lower than $2.2\cdot10^{-2}$ m. For some sources dealing with higher pressures (Malinin and Kurovskaya, 1975 and Rumpf et al., 1994) the value is lower or very close to $2.2\cdot10^{-2}$ m. Only for the investigations at high pressure conditions the average absolute deviation between the extended UNIQUAC calculations and the experimental data is larger than $2.2\cdot10^{-2}$ m (but always lower than 0.15 m). Therefore, it can be concluded that extended UNIQUAC calculations are within experimental accuracy, and the model is able to represent correctly the salting-out effect and the temperature and pressure dependence of the carbon dioxide solubility in NaCl solutions (from very dilute solutions to almost the saturation point).

5.1.2.2 CO_2 solubility in Na_2SO_4 solutions

Sodium sulphate also produces a relatively large salting-out effect for aqueous CO_2 solutions, reducing the gas solubility in the solution when compared to that in pure water.

Literature data on the solubility of carbon dioxide in aqueous solutions of sodium sulphate is scarce. Furthermore, most of the available data were measured at pressures around 1 atm and not very high temperatures. The sources found in literature reporting CO_2 solubility in Na_2SO_4 solutions are given in table 5-5. The range of temperature and pressure covered, and the number of measurements performed and used in this work (in brackets) for parameter estimation can also be found there.

Table 5-5
Experimental CO_2-Na_2SO_4-H_2O VLE data sets used for parameter estimation.

***T*(°C)**	***P*(atm)**	**Number of data**	***AAD* (m)**	**Reference**
0/90	0.3/1	24 (0)		He and Morse (1993)
15/35	1	26 (26)	1.3E-03	Yasunishi and Yoshida (1979)
25	1	3 (3)	3.7E-04	Onda et al. (1970)
25	1	5 (5)	7.9E-04	Yasunishi et al. (1979)
25/40	1	8 (8)	8.8E-04	Markham and Kobe (1941a)
40/160	4.2/93.8	102 (102)	7.0E-03	Rumpf and Maurer (1993)
50/75	1/200	26 (0)		Corti et al. (1990b)
			***MAAD* (m):**	**5.3E-03**

As observed for the CO_2 solubility in NaCl solutions, the shape of the carbon dioxide solubility curve in Na_2SO_4 solutions obtained from the data of He and Morse (1993) differs from the curves shown by the sources given in table 5-5. The decrease in carbon dioxide solubility as a consequence of increasing concentration is much flatter for He and Morse's (1993) data than claimed by the rest of the sources employed. Moreover, when He and Morse's (1993) data were compared to others at similar conditions, a disagreement for the former dataset was always found. Therefore, these data were not used for parameter estimation.

As done for NaCl solutions previously, Rumpf and Maurer (1993) also used Pitzer's (1973) equations to predict CO_2 solubility in sodium sulphate solutions based on their experimental determinations. The agreement between the model by Rumpf and Maurer (1993) and the datasets reported by Markham and Kobe (1941a) is very good, with an average relative deviation in the partial pressure of carbon dioxide of 2.6% (value calculated by Rumpf and Maurer, 1993). The agreement is also good when comparing to Onda et al. (1970), Yasunishi and Yoshida (1979) and Yasunishi et al. (1979). On the other hand, quite large deviations were obtained when comparing to Corti et al. (1990b), with an average relative deviation of 14.2%, and a maximum relative deviation as large as 37%. Thus, it was decided not to use the latter source in the present work.

The experimental and calculated phase diagrams for the system CO_2-Na_2SO_4-H_2O at a constant temperature of 140°C, and at pressures in the range of 80-90 bar are shown in figure 5-6 and figure 5-7, respectively. CO_2 solubility in Na_2SO_4 solutions behaves in a very similar way as in NaCl solutions. A salting-out effect is observed in both figures. Regarding temperature, carbon dioxide solubility decreases quite fast with increasing temperature in the range 0-100°C, while the slope of the curve is much flatter for higher temperatures. The solubility of CO_2 in 1 m Na_2SO_4 solution decreases from 0.6 m at 50°C to 0.4 m at 160°C.

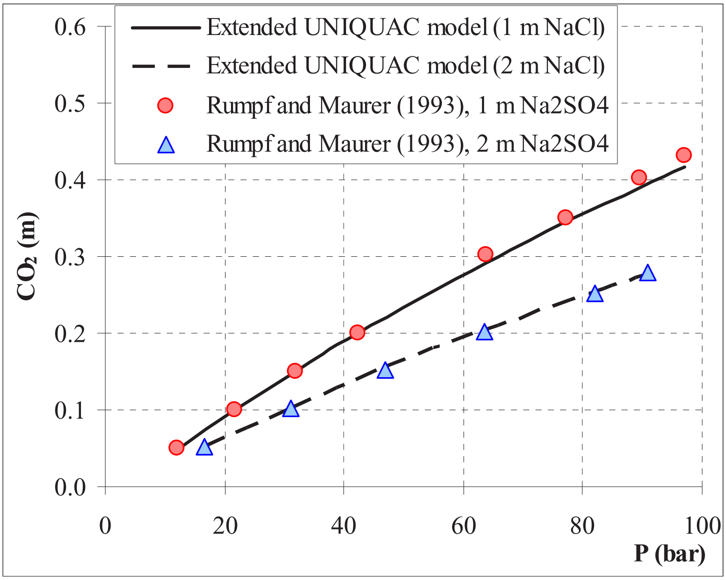

Figure 5-6. Experimental and calculated vapour-liquid phase diagram for the CO_2-Na_2SO_4-H_2O system at 140°C.

The calculated solubility compares very well with the experimental data presented in table 5-5. The value of *MAAD* ($5.3 \cdot 10^{-3}$ m) is well below the *ASD* ($2.7 \cdot 10^{-2}$ m). The latter value was calculated taking into account all the experimental points, and not only those coming from different sources, due to the lack of data at the same conditions.

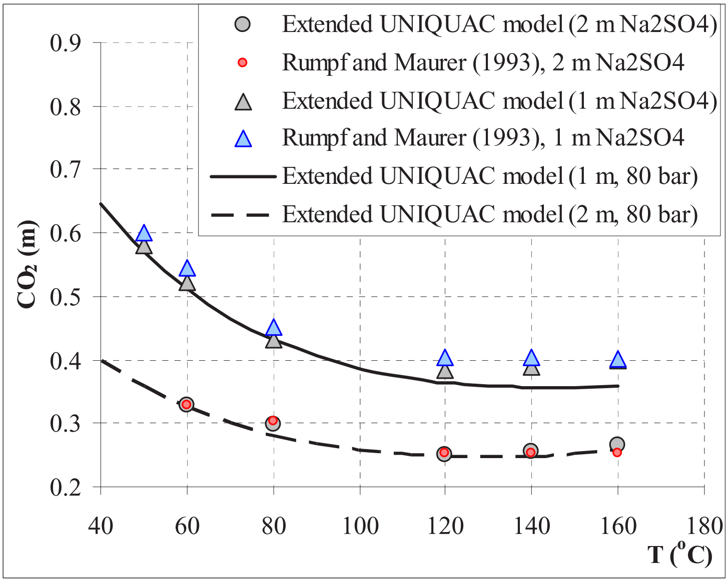

Figure 5-7. Experimental and calculated vapour-liquid phase diagram for the CO_2-Na_2SO_4-H_2O system at 80-90bar. Lines represent calculations at a constant pressure of 80 bar, grey dots and triangles represent calculations at the experimental pressure (in the range from 80 to 90 bar), which are compared to the experimental data (red and blue dots and triangles)

5.1.2.3 CO_2 Solubility in NaCl-Na_2SO_4 Solutions

Only one source (Yasunishi et al., 1979) studying the quaternary system CO_2-NaCl-Na_2SO_4-H_2O has been used for parameter estimation. Yasunishi et al. (1979) performed 15 measurements of carbon dioxide solubility in solutions of NaCl and Na_2SO_4 at 25°C and 1 atm. The results obtained for this quaternary systems are also very satisfactory, with a *MAAD* of $9.3 \cdot 10^{-4}$ m. Figure 5-8 shows experimental and calculated CO_2 solubilities in NaCl-Na_2SO_4 solutions as a function of the ionic strength of the solution, at 25°C and 1 atm.

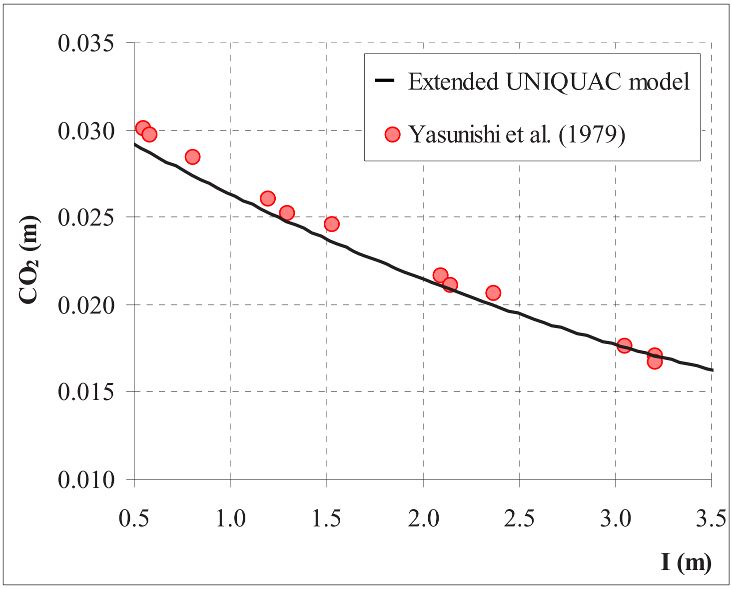

Figure 5-8. Experimental and calculated CO_2 solubility in $NaCl$-Na_2SO_4-H_2O solutions of ionic strength I, at 25°C and 1 bar.

5.2. $CaCO_3$-H_2O and $CaCO_3$-CO_2-H_2O systems

The solubility of calcite is highly influenced by the amount of carbonic acid present in the solution ($CaCO_3$ solubility increases with CO_2 concentration). In that sense, calcite solubility studies (and, in general, any carbonate mineral study) can be divided into different groups according to the amount of carbon dioxide employed. In most of the cases, pure CO_2 is bubbled into the solution, and therefore the amount of CO_2 in the liquid phase corresponds to the gas solubility in the calcite-water solution, at the experimental temperature and pressure. A second line of studies deals with calcite solubility in pure water, freed of CO_2. To achieve that purpose, all the CO_2 dissolved in the water is expelled previous to its use by vigorous boiling. Finally, some authors perform experiments adding a given amount of CO_2 which is kept constant, while the temperature and/or pressure are changed.

Table 5-6 shows the sources reporting calcite solubility in pure water, and in CO_2-H_2O solutions, together with the range of temperatures and pressures investigated, and the number of experimental points.

Kendall (1912), Kindyakov et al. (1958), Morey (1962), MacDonald and North (1974) and Lyashchenko and Churagulov (1981) used water freed of carbon dioxide in their experiments. Kendall (1912) performed several experiments under atmospheric conditions. In three of his measurements, the CO_2 was removed from the air by passing it through a column and washing the air. None of these sources was used for parameter estimation, as very large discrepancies are found among the different investigators, and the tendency followed for increasing temperatures varies from one source to another. According to the data reported by Kendall (1912), calcite solubility increases with temperature from 25 to 100°C. MacDonald and North (1974) reported data from 1 to 25°C where the temperature influence on the solubility is practically negligible, and in most of the cases the lowest value is obtained for the lowest temperature used. For Morey's (1962) data, the temperature influence on the solubility of calcite is negligible from 25 to 165°C, while decreasing solubilities were obtained for temperatures increasing from 165 to 350°C.

Table 5-6
Experimental $CaCO_3$-H_2O SLE and $CaCO_3$-CO_2-H_2O SLVE data sets used for parameter estimation.

T (°C)	*P* (bar)	Number of data	*AAD* (m)	Reference
0/55	1	2 (2)	8.4E-04	Yanat'eva (1955a)
0/102	1/101	98 (98)	1.6E-03	Miller (1952)
0.1/89.7	1	141 (133)	3.8E-04	Plummer and Busenberg (1982)
1/23	1	5 (0)		Wells (unknown year)
1/25	25.3/962.6	32 (0)		MacDonald and North (1974)
10/60	1	8 (4)	8.3E-05	Wolf et al. (1989)
10/70	1	30 (30)	1.1E-04	Weyl (1959)
11/14	1	10 (0)		Treadwell and Reuter (1898)
15/40	1	49 (49)	4.9E-04	Leather and Sen (1909)
16	1	7 (7)	5.3E-04	Johnston (1915)
16	1	12 (12)	4.4E-11	Schloesing (1872)
16	1/6	4 (4)	2.2E-04	Engel (1889)
25	1/24	13 (0)		Mitchell (1923)
25	1	9 (9)	9.3E-04	Frear and Johnston (1929)
25	1/1000	3 (0)		Lyashchenko and Churagulov (1981)
25/75	1	2 (0)		Kindyakov et al. (1958)
25/100	1	6 (2)	3.7E-03	Kendall (1912)
25/350	200	10 (0)		Morey (1962)
30/80	3.4/179	51 (51)	1.6E-03	Sippel and Glover (1964)
70	1	1 (1)	4.0E-04	Yanat'eva (1960)
75/200	5.5/68.2	260 (254)	4.9E-04	Segnit et al. (1962)
98/302	1.9/142.3	59 (59)	6.1E-04	Ellis (1959a)
100/300	2/150	34 (34)	4.9E-04	Ellis (1963)
150/225	10.9/402	18 (18)	3.3E-04	Malinin (1963)
197/300	20/1000	48 (0)		Sharp and Kennedy (1965)
			MAAD (m):	**7.4E-04**

The solubility value reported by Kindyakov et al. (1958) at 25°C is around five times larger than the average measurement given by the other sources at the same conditions. The disagreement could be due to the presence of a gas phase containing carbon dioxide, in equilibrium with the solution, and enhancing calcite solubility. Nevertheless, the amount of CO_2 employed in the measurements (if any) is not mentioned, and thus this source was not used for parameter estimation.

Engel (1889), Treadwell and Reuter (1898), Mitchell (1923), Miller (1952), Yanat'eva (1955a), Ellis (1959a), Yanat'eva (1960), Segnit et al. (1962), Ellis (1963) and Malinin (1963) used a gas phase over the solution formed by pure carbon dioxide (plus the water vapour corresponding to the experimental conditions).

Schloesing (1872), Leather and Sen (1910), Kendall (1912), Johnston (1915), Wells (1915a), Frear and Johnston (1929), Weyl (1959), Sippel and Glover (1964), Sharp and Kennedy (1965), Plummer and Busenberg (1982) and Wolf et al. (1989) measured calcite solubility in CO_2-H_2O solutions, where the amount of CO_2 was smaller than the one corresponding to the saturation value. Most of these studies used a gas phase over the solution formed by air, or mixtures of carbon dioxide and N_2 or air in different proportions.

At 25°C, the solubility values reported by Wolf et al. (1989) are considerably lower than the average value given by many other sources at the same conditions, and therefore these points are not included in the parameter estimation. Also, low solubility values for calcite are reported by Plummer and Busenberg (1982) at 10°C, when compared to the data by Schloesing (1872) at 16°C or the data by Frear and Johnston (1929) at 25°C, all of them using very similar CO_2 amounts in the liquid phase.

None of the measurements performed by Sharp and Kennedy (1965) has been used in the present study, because their scatter is extremely large. At 200°C and a free CO_2 content of 0.73 m, calcite solubility varies from $2.6 \cdot 10^{-3}$ to $6.7 \cdot 10^{-3}$ m. Moreover, many points also show a wrong solubility tendency with temperature.

The datasets by Treadwell and Reuter (1898) and Mitchell (1923) were not used for parameter estimation. The latter source does not show any influence of pressure on the solubility for pressures higher than 15 bar (and up to 25 bar). Treadwell and Reuter (1898) disagree considerably when compared to other sources at similar conditions. According to Leather and Sen (1910) and Johnston (1915), Treadwell and Reuter (1898) did not attain equilibrium, a fact resulting in a lack of constancy of the calculated solubility product.

Segnit et al. (1962) measurements show a very large scatter, especially at 100°C, where $CaCO_3$ solubility varies from $8.5 \cdot 10^{-3}$ to $11.2 \cdot 10^{-3}$ m. They state their results agree satisfactorily with Ellis (1959a), but disagree somewhat with those obtained by Miller (1952) at 75 and 100°C at pressures above 10 atm. Nevertheless, the disagreement among all these sources was not extreme and all of them were used to estimate the required parameters (with the exception of 4 points given by Segnit et al. (1962) showing the largest disagreement with the main tendency).

The experimental and calculated phase diagrams for the $CaCO_3$-CO_2-H_2O system at a constant temperature of 100°C and at a constant pressure of 40 bar are shown in figure 5-9 and figure 5-10, respectively. The gas phase over the solution employed for all the measurements reported in figures 5-9 and 5-10 was pure carbon dioxide saturated with water vapour. Therefore, the increase of calcite solubility with increasing pressure also manifests the higher solubility of that mineral for higher CO_2 concentrations. Regarding temperature, a very sharp decrease of calcite solubility is observed for increasing temperature.

The large scatter in the experimental data can be observed in figure 5-9. The experimental standard deviation was calculated from data coming from different sources. When more than one point is given by the same author at the same conditions, the average of the values reported is calculated and compared to the rest of the sources reporting data at the same temperature and pressure. Therefore, the scatter shown in figure 5-9 for the measurements of Segnit et al. (1962) is not included in the calculation of the standard deviation.

Even though in most of the cases the CO_2 content in the system was calculated instead of being experimental, the results obtained for the calcite solubility are very close to the experimental data. The mean absolute deviation between the calculations using extended UNIQUAC and the experimental measurements ($7.4 \cdot 10^{-4}$ m) is lower than the experimental standard deviation, which was calculated to be $1.3 \cdot 10^{-3}$ m. It is confirmed, therefore, that the model is also applicable to the system $CaCO_3$-CO_2-H_2O.

Some authors reported the CO_2 concentration in the liquid phase, as well as the calcite solubility: Ellis (1959a) and Malinin (1963). In both cases, the experimental values were used instead of our calculations (and in both cases the difference between the reported values and the ones calculated by our program was very small).

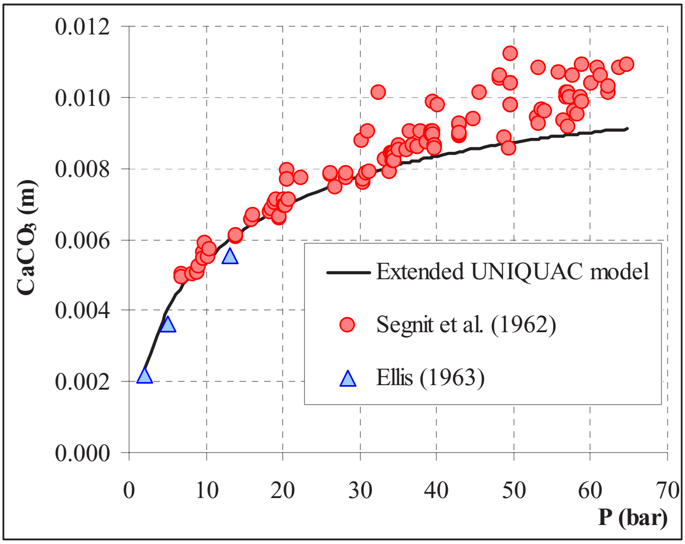

Figure 5-9. Experimental and calculated solid-liquid phase diagram for the $CaCO_3$-CO_2-H_2O system at 100°C. Gas phase formed by CO_2 (g) and H_2O (g).

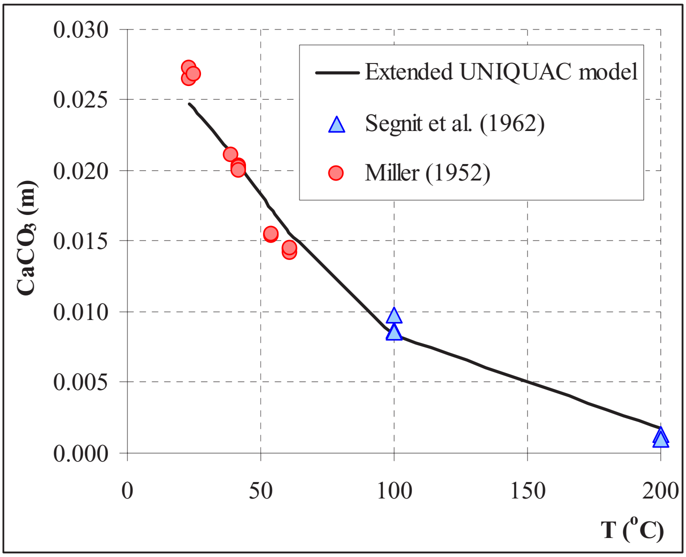

Figure 5-10. Experimental and calculated solid-liquid phase diagram for the $CaCO_3$-CO_2-H_2O system at 40 bar. Gas phase formed by CO_2 (g) and H_2O (g).

5.3 $BaCO_3$-H_2O and $BaCO_3$-CO_2-H_2O systems

Very few studies on the solubility of witherite ($BaCO_3$) in pure water and in pure water under various CO_2 partial pressures have been found in literature. Among them, only a couple report solubility values at temperatures higher than 25°C or pressures larger than atmospheric. The list of experimental data used for parameter estimation is presented in table 5-7. The total number of data found in each source is given, together with the number of data chosen for parameter estimation in this work (in brackets). Information about the ranges of temperature and pressure covered is also included.

The experiments performed by Kohlrausch and Rose (1893), McCoy and Smith (1911), Townley et al. (1937), and Trendafelov et al. (1994) used water freed of CO_2. The rest of the experimental data were determined under different CO_2 partial pressures. Malinin (1963) and Busenberg and Plummer (1986) used pure CO_2 saturated with water vapour as the gas phase. The latter authors also reported five experimental points where mixtures of N_2 and CO_2 in different proportions replaced the pure CO_2 in the gas phase. Schloesing (1872) used mixtures of air and CO_2 as the gas phase, with CO_2 partial pressures ranging from 0.0005 to 0.98 atm. From the latter references, only Malinin (1963) reported the amount of CO_2 contained in the liquid phase, while the rest of the sources only measured the partial pressure of CO_2. For such cases, we made similar assumptions to calculate the free carbon dioxide content in the solution as done previously for calcite: The CO_2 amount was calculated from the parameters estimated for the CO_2-H_2O system in the present work. In this case we assumed CO_2 solubility in witherite solutions is approximately equal to that in pure water. $BaCO_3$ is a sparingly soluble salt in water, and it is reasonable to believe it will not influence carbon dioxide solubility to a large extent. When comparing our calculations with the CO_2 contents reported by Malinin (1963) in $BaCO_3$-H_2O solutions (see table 5-8), the assumption made seems to be accurate.

Table 5-7
Experimental $BaCO_3$-H_2O and $BaCO_3$-CO_2-H_2O SLVE experimental data sets used for parameter estimation.

T(°C)	*P*(atm)	Number of data	*AAD* (m)	Reference
-2/90	1	150 (150)	9.5E-05	Busenberg and Plummer (1986)
16	1	12 (12)	7.5E-04	Schloesing (1872)
18	1	1 (1)	9.7E-06	Kohlrausch and Rose (1893)
25	1	1 (1)	4.7E-05	McCoy and Smith (1911)
25	1	2 (2)	4.2E-05	Trendafelov et al.(1994)
25/40	1	2 (0)		Townley et al. (1937)
100/225	17/107	15 (0)		Malinin (1963)
			***MAAD* (m):**	**1.4E-04**

A significant disagreement is observed among some of the data sources listed in table 5-7. The recalculated values for the equilibrium constant for different sources in table 5-7 vary over three orders of magnitude, and the temperature dependence of the equilibrium constant cannot be determined from these data (Busenberg and Plummer, 1986). For example, the value of -8.8 given by Townley et al. (1937) for $\log K_{BaCO_3}$ is too low when compared to many other sources dealing with the same system. On the other hand, the value of -5.5 reported by Benes and Selecká (1973) for $\log K_{BaCO_3}$ is too large compared to data from the sources shown in table 5-7.

Table 5-8
Calculated versus experimental CO_2 solubility in $BaCO_3$-H_2O solutions.

***T* (°C)**	***P* (bar)**	**CO_2 solubility in pure water (m)**		***RD* (%)**
		Malinin (1963)	**Our model**	
100	16.7	0.161	0.163	1.24
100	32.4	0.308	0.313	1.62
100	52.0	0.482	0.480	-0.41
150	14.8	0.087	0.091	4.60
150	19.5	0.127	0.132	3.94
150	27.2	0.193	0.198	2.59
150	35.5	0.264	0.266	0.76
150	53.3	0.405	0.406	0.25
150	55.4	0.421	0.422	0.24
150	83.7	0.625	0.621	-0.64
150	107.1	0.750	0.767	2.27
225	27.2	0.025	0.028	12.00
225	42.8	0.173	0.187	8.09
225	79.4	0.519	0.544	4.82
225	98.8	0.693	0.720	3.90

Most of Malinin's (1963) solubility data cannot be compared to other sources given in table 5-7, as he is the only author who used temperatures above 100°C. The value of the equilibrium constant for $BaCO_3$ calculated from Malinin's (1963) data at 100°C and various CO_2 pressures is about 0.5 log units smaller than the value calculated by Busenberg and Plummer (1986) (Busenberg and Plummer, 1986).

The equation reported by Busenberg and Plummer (1986) for the equilibrium constant of $BaCO_3$ agrees with many other sources (Schloesing, 1872, Holleman, 1893, McCoy and Smith, 1911, Millero et al., 1984). Their value at 25°C ($\log K_{BaCO_3} = -8.562$) is also very similar to the one reported by the NIST Chemical Thermodynamics Database (1990). This agreement, and the fact that Busenberg and Plummer (1986) report the most detailed study on witherite solubility, covering a wide range of temperatures, makes us take their work as the reference for the modelling of the system $BaCO_3$-CO_2-H_2O.

The heat capacity of witherite as a function of temperature was experimentally studied by Gurevich et al. (1999) at very low temperatures, -253.12 – 65.66°C. Busenberg and Plummer (1986) derived a relation to calculate the equilibrium constant as a function of temperature, in the temperature range -2 to 90°C. From this relation, a temperature dependent C_p value can be derived. There is, however, a change in the sign of C_p for temperatures larger than 100°C (which is above the temperature range analyzed by them). Extrapolation of that relation to temperatures above the interval studied (-2 to 90°C) is therefore not possible. For this reason, we chose to use the value reported by the NIST Chemical Thermodynamics Database (1990). As the temperature range covered is small enough, the heat capacity may be considered constant with temperature.

Table 5-7 shows the agreement between the experimental data and the extended UNIQUAC model calculation is excellent. The *MAAD* ($1.4 \cdot 10^{-4}$ m) is well below the *ASD* ($2.3 \cdot 10^{-4}$ m). Due to the lack of measurements performed at the same temperature, pressure and CO_2 partial pressure, the *ASD* was mainly calculated from the standard deviation found in the data by Busenberg and Plummer (1986).

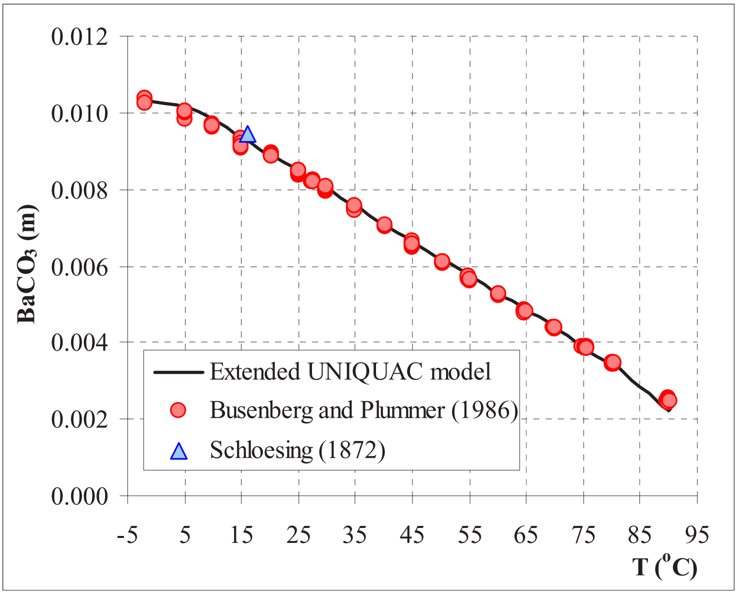

Figure 5-11. Experimental and calculated solid-liquid phase diagram for the $BaCO_3$-CO_2-H_2O system at atmospheric pressure. Gas phase formed by CO_2 (g) and H_2O (g).

The experimental and calculated SLE phase diagram for the system $BaCO_3$-CO_2-H_2O at constant atmospheric pressure is shown in figure 5-11. The gas phase is formed by CO_2 (g) and H_2O (g) (in amounts corresponding to the saturation pressure of the solution at the given temperature). As it can be observed from figure 5-11, witherite solubility decreases with increasing temperature in the range -2 to 90°C.

5.4 $SrCO_3$-H_2O and $SrCO_3$-CO_2-H_2O systems

According to Kapustinsky and Dezideryeva (1946), the research on the thermodynamics of strontium and its compounds is far from exhaustive. This lack of research is even more noticeable for the case of strontianite ($SrCO_3$). Large disagreements are found when comparing calorimetric data and calculations from the equilibrium constants, and the heat of reaction is calculated in most of the cases from quite old determinations. This problem is manifested in the heat of formation of strontianite from the elements given by two different studies carried out at practically the same time: Kelley and Anderson (1935) and Rossini and Bichowsky (1936). The values reported are -1168.2 and -1215 kJ/mol, respectively.

Table 5-9
Experimental $SrCO_3$-H_2O and $SrCO_3$-CO_2-H_2O SLVE experimental data sets used for parameter estimation.

T (°C)	*P* (atm)	Number of data	*AAD* (m)	Reference
2/91.2	1	60 (60)	5.7E-05	Busenberg et al. (1984)
5/25	1	4 (0)		Miles and Burton (1972)
18	1	1 (0)		Kohlrausch and Rose (1893)
18	1	1 (0)		Haehnel (1924)
25	1	1 (1)	9.9E-06	Kapustinsky and Dezideryeva (1946)
25	1	7 (0)		Wattenberg and Timmermann (1937)
25	1	1 (0)		McCoy and Smith (1911)
25/40	1	2 (2)	5.8E-06	Townley et al. (1937)
50/200	1/50	66 (0)		Helz and Holland (1965)
			MAAD **(m):**	**5.5E-05**

The few sources studying strontianite solubility in pure water and in CO_2-H_2O solutions are shown in table 5-9, together with the number of experimental data reported and the range of temperature and pressure covered. Kohlrausch and Rose (1893), McCoy and Smith (1911), Townley et al. (1937), and Kapustinsky and Dezideryeva (1946) performed experiments in CO_2-free water. Miles and Burton (1972) reported three solubility points in water previously freed of CO_2, and one value using a solution in equilibrium with air. Haehnel (1924), Helz and Holland (1965), and Busenberg et al. (1984) used pure CO_2 saturated with water vapour as the gas phase, while Wattenberg and Timmermann (1937) used CO_2-H_2O solutions with different carbon dioxide amounts.

None of the sources using CO_2-H_2O solutions measured the carbon dioxide concentration in the liquid phase. Therefore, it was calculated from our CO_2 parameters as explained previously for the case of calcite.

Wattenberg and Timmermann (1937) did not report the partial pressure for carbon dioxide, but instead they gave the solution pH, the concentration of carbonate ions and the value of the second dissociation constant for CO_2. From those values and the first dissociation constant it was possible to calculate the free CO_2 in the solution.

Some of the studies given in table 5-9 show discrepant results. McCoy and Smith (1911) performed nine measurements of strontianite solubility at 25°C and CO_2 partial pressures ranging from 0.05 to 1.1 atm. They did not report those data, but only the average solubility product (defined as the product of the concentrations of Ba^{2+} and CO_3^{2-} ions). The solubility value calculated from it differs considerably from the rest of the sources in table 5-9. Other sources that were not used for parameter estimation due to their disagreement when compared to other experiments at the same conditions are Kohlrausch and Rose (1893) and Haehnel(1924).

Helz and Holland (1965) used natural strontianite in their experiments containing as much as 5 mole percent $CaCO_3$. This impurity of the original solid phase may lead to erroneous solubility values. Their data show a high scatter and a poor reproducibility at the higher pressures, which probably results from experimental difficulties in the hydrothermal bomb method (Busenberg et al. 1984).

According to Busenberg et al. (1984), the experimental data by Miles and Burton (1972) in CO_2-free water show a much larger temperature dependency between 5 and 25°C than observed by them. That could indicate failure to achieve equilibrium at lower temperatures. This may be perfectly the case as the authors only ran the experiments for 6 hours. They used both radiometric and flame emission spectrophotometric methods to determine strontianite solubility. The results obtained from both methods agree very well. Nevertheless, their results in every case disagree with other sources and were not used for parameter estimation in the present work.

The data reported by Wattenberg and Timmermann (1937) could only be compared to those by Busenberg et al. (1984). A very large disagreement is observed, but the lack of additional data makes it difficult to determine the most reliable source. We chose to use Busenberg et al. (1984) because they report 60 solubility measurements covering a wide range of temperature (from 2 to 91.2°C), while Wattenberg and Timmermann (1937) only reported 7 experimental data at a constant temperature of 25°C. Apart from the wider temperature range of the solubility study performed by Busenberg et al. (1984), their results are also supported by the close agreement[1] with the calculations of Garrels et al. (1960) at 25°C in CO_2 saturated water, Townley et al. (1937) at 25 and 40°C, and Sonderegger et al. (1976) at 30, 40 and 50°C in CO_2 saturated water, although in the latter case, insufficient data were available to correct the equilibrium constants to Busenberg et al. (1984) aqueous model (Busenberg et al. 1984).

The values found in the NIST Chemical Thermodynamics Database (1990) for the standard state enthalpy and Gibbs free energy of $SrCO_3$ are very similar to the ones reported by Busenberg et al. (1984), and are the ones used in the present work. The value of the standard state heat capacity as a function of temperature was taken from Busenberg et al. (1984). Due to the relatively low number of experimental data (63) only the binary interaction parameter between Sr^{2+} and CO_2 was estimated, while the parameters Sr^{2+}-HCO_3^- and Sr^{2+}-CO_3^{2-} were fixed.

The experimental and calculated strontianite solubility in water saturated with CO_2 at different temperatures and 1 atm total pressure is shown in figure 5-12. It can be observed that our results agree exceptionally well with the experimental data. Values for the mean average absolute deviation between our calculations and the experimental data are shown in table 5-9. The *MAAD* for all the data used is as low as $5.5 \cdot 10^{-5}$ m $SrCO_3$. Such value cannot be compared to the *ASD* as the lack of experimental data at similar conditions makes it impossible to determine a reliable average experimental standard deviation. Nevertheless, the value of *MAAD* is very low, especially taking into account the solubility reported by Busenberg et al. (1984) is of the order of 10^{-3} m $SrCO_3$.

---

[1] The comparison is performed by Busenberg et al. (1984). They recalculate the equilibrium constants reported in different sources according to the model employed by them.

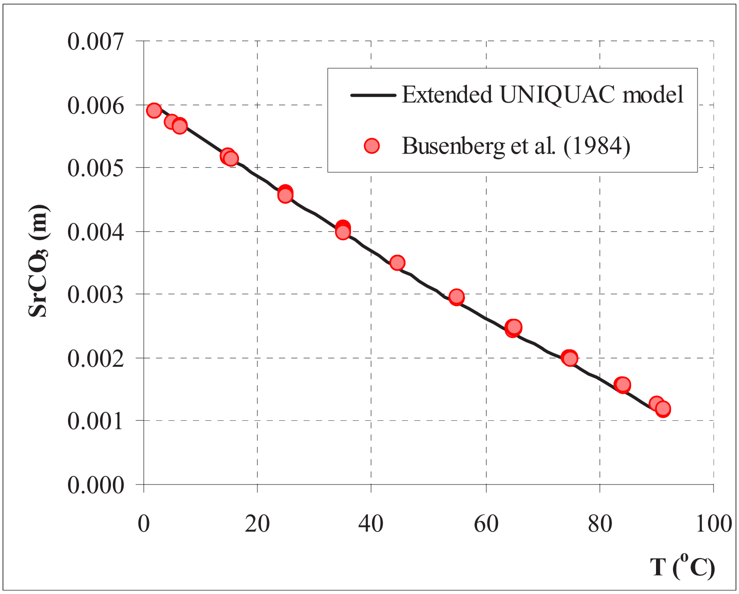

Figure 5-12. Experimental and calculated solid-liquid phase diagram for the $SrCO_3$-CO_2-H_2O system at atmospheric pressure. Gas phase formed by CO_2 (g) and H_2O (g).

5.5 $MgCO_3$-H_2O and $MgCO_3$-CO_2-H_2O

Magnesium is one of the common species found in natural waters. Therefore, the study of magnesium carbonate solubility in pure water and in CO_2-H_2O solutions is of great importance in the present work. Unfortunately, the system $MgCO_3$-CO_2-H_2O is characterized by tremendous experimental chaos. Dismaying discrepancies are found regarding solubility values, stable solid phases at given temperature and pressure conditions, chemical formulae for the different solids, values for the standard state Gibbs free energy, enthalpy and heat capacity, etc. Moreover, most of the data are very old, and recent studies on this system are very scarce. Cameron and Briggs (1901) assured "every investigator who has attempted to study magnesium carbonate in solution has experienced very great experimental difficulties". According to Christ and Hostetler (1970) "no carbonate mineral has proven more difficult to investigate experimentally than magnesite." Königsberger et al. (1999) assure the situation did not improve in the 30 years period which separates their work from Christ and Hostetler's (1970). More reliable experimental data on the $MgCO_3$-CO_2-H_2O system are obviously needed.

Before showing some of the results obtained by the extended UNIQUAC model for this system, a more detailed explanation about the different problems encountered when trying to model it will be addressed.

5.5.1 Chemical Formula for Hydromagnesite

The chemical formula for hydromagnesite is a source of disagreement among different investigators. In general, most of the published formulae for this mineral can be divided into two groups, although additional suggestions in disagreement with both of the main two tendencies are also available in the literature.

Baron and Favre (1958), Kazakov et al. (1959), Yanat'eva and Rassonskaya (1961), Morandi (1969), Riesen (1969), Raade (1970), Robie and Hemingway (1972, 1973), Sayles and Fyfe (1973), Dandurand and Schott (1977) and Königsberger et al. (1999) agree on the chemical formula $5MgO{\cdot}4CO_2{\cdot}5H_2O$. On the other hand, Moressée and Cesaro (1910), Palache et al. (1951), Carpenter (1963), Hostetler (1964) and Langmuir (1965a) support the formula $4MgO{\cdot}3CO_2{\cdot}4H_2O$.

Leitmeier (1915) studied the composition of the basic magnesium carbonate which forms in CO_2-saturated solutions at temperatures between 60 and 100°C. His 37 analyses correspond to the formula $4MgO{\cdot}3CO_2{\cdot}XH_2O$, where X is between 4 and 6. Therefore, his study was closer to the second group.

Takahashi (1927) used in his study the chemical formula $5MgO{\cdot}4CO_2{\cdot}7H_2O$ for hydromagnesite, very close to the first group, but with additional water molecules.

The disagreement on the hydromagnesite chemical formula may be due to the relative similarity in the mole proportions for the different alternatives, which makes it difficult to use chemical analysis alone to differentiate them (Davies and Bubela, 1973).

The consequence of the use of different hydromagnesite type phases of varying composition is a great variety of contradicting solubility data. The solubility behaviour of the different phases may be rather different. Königsberger et al. (1999) assure that the formula $5MgO{\cdot}4CO_2{\cdot}7H_2O$ has a relatively larger solubility than $4MgO{\cdot}3CO_2{\cdot}4H_2O$.

Hydromagnesite is the most problematic mineral in the $MgCO_3$-CO_2-H_2O system regarding its chemical formula, but some discrepancies are also found for other minerals. The accepted formula for lansfordite by the majority of the investigators is $MgCO_3{\cdot}5H_2O$. Nevertheless, completely different expressions, such as $4MgO{\cdot}3CO_2{\cdot}22H_2O$ (Moressée and Cesaro, 1910) can be found in the literature.

5.5.2 Stability

The solubility product for magnesite at 25°C varies according to the publication from $10^{-5.10}$ to $10^{-10.3}$ (Christ and Hostetler, 1970). These values correspond to a free energy of formation of magnesite, at 25°C, ranging from -1012.5 to -1042.2 kJ/mol. The consequence of such a large variation is completely different relative stabilities for the various minerals in the system $MgCO_3$-CO_2-H_2O. For example, if we accept as true the activity product of $10^{-5.1}$ given by Langmuir (1965a), the solid phases periclase (MgO), brucite ($Mg(OH)_2$), magnesite ($MgCO_3$), hydromagnesite, nesquehonite ($MgCO_3{\cdot}3H_2O$), and lansfordite ($MgCO_3{\cdot}5H_2O$) will all have stability fields at different values of temperature, carbon dioxide partial pressure and activity of water. On the other hand, if we consider as true the activity product of $10^{-8.1}$ reported by Rossini et al. (1961) and Robie and Waldbaum (1965), only magnesite and brucite will be stable phases at surface and near-surface conditions, while hydromagnesite, nesquehonite and lansfordite will be highly metastable.

Even though many different solubility diagrams for the system $MgCO_3$-CO_2-H_2O may be found in the literature, most of the investigations follow either Langmuir's (1965a) or Rossini's et al. (1961) approaches, whose stability relations as function of temperature and CO_2 pressure are given in figures 5-13 and 5-14, respectively. In the following section, we will try to compile the available information regarding both approaches, and the arguments given by the investigators in order to support their chosen stability diagrams.

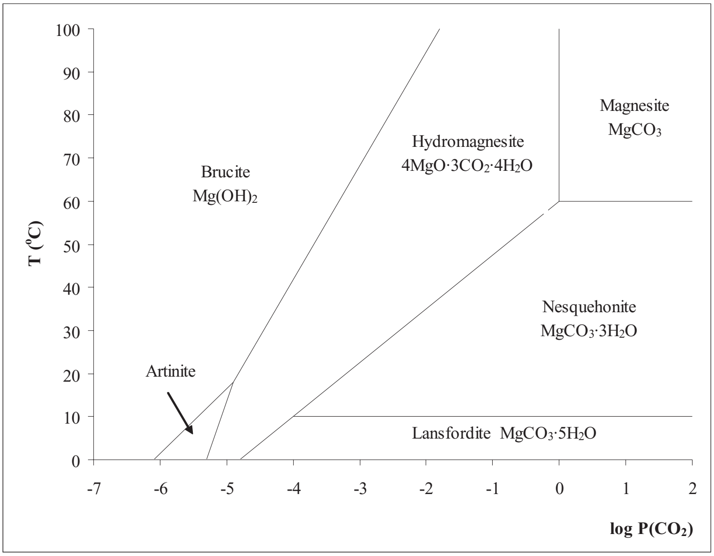

Figure 5-13. Solid-liquid phase diagram for the $MgCO_3$-CO_2-H_2O system according to Langmuir (1965a).

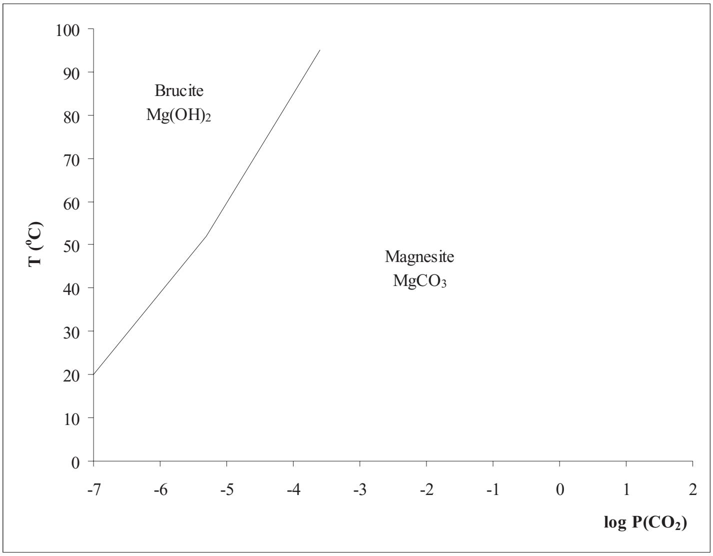

Figure 5-14. Solid-liquid phase diagram for the $MgCO_3$-CO_2-H_2O system according to Rossini et al. (1961).

5.5.2.1 Langmuir's (1965a) Approach

Langmuir (1965a) determined phase relationships based upon free energies of formation estimated from entropy. His first argument to support his study is the agreement with geological evidences. He assures the scarcity of magnesium carbonates under surface conditions may be well explained due to their great solubility (at 25°C and 1 atm, nesquehonite solubility is 24 times larger than calcite solubility). Solid phases that are considered metastable by Rossini's et al. (1961) approach are present in several locations. Both lansfordite and nesquehonite are found in caves and coal mines where temperatures are low and CO_2 pressures ten or more times greater than atmospheric. Nesquehonite has been found in Sounion, in the Lavrion mining district in Greece (Giester et al. 2000). Lansfordite appears in the hydromagnesite deposits of British Columbia (Langmuir, 1965a). Both nesquehonite and lansfordite are present in stalactites from an anthracite mine at Nesquehoning, USA (Genth, 1888, Genth and Penfield, 1890). The natural occurrences of these minerals have also been reported by Cesaro (1910), Poitevin (1924) and Fenoglio (1930, 1933, 1935, 1936). On the other hand, hydromagnesite occurrences have been listed by Palache et al. (1951) and by Alderman and Von der Borch (1961). The formation of magnesite is favoured at high ionic strength, high CO_2 pressure and high temperature (larger than 60°C). These conditions are easier to achieve in evaporate deposits, where magnesite is reported (Schaller and Henderson, 1932, Stewart, 1949). Also, this mineral is formed through the desiccation of hydromagnesite in warm or dry climates (Alderman and Von der Borch, 1961, Graf et al., 1961, Kinsman, 1964).

According to Langmuir (1965a), the synthesis of magnesite in aqueous solutions has only been achieved at temperatures above 50°C (Pfaff, 1894, D'Ans and Gloss, 1938, Schloemer, 1952, Baron and Favre, 1958, Kazakov et al., 1959). Many times, as in the case of Pfaff (1894), such synthesis is carried out in high ionic strength solutions to favour it. Christ and Hostetler (1970) suggested that the ion Mg^{2+} has a highly hydrated nature, and hence it is relatively unreactive. Therefore, saline conditions (for which the activity of water will be lowered) should favour magnesite crystallization. However, in natural environments at surface temperatures, both nesquehonite and hydromagnesite will precipitate directly from solution, whereas it has not yet been definitively established that magnesite can form in this way (Hostetler, 1964). Even some investigators rejecting Langmuir's (1965a) solubility diagram assure that magnesite is found generally associated with hyper saline environments (Sayles and Fyfe, 1973).

In his paper, Langmuir (1965a) also lists the reasons why he thinks the stability relations given by Rossini et al. (1961) are inaccurate. The Gibbs free energy value reported by Rossini et al. (1961) was largely based on a thermal decomposition study by Marc and Simek (1913). The latter authors based their calculations on a reaction which was not determined reversibly. The same technique was also used by other authors but the agreement among them is not good, and there is no agreement either when comparing the results to other different methods.

The value reported by Rossini et al. (1961) is also supported by Harker and Tuttle (1955) and Stout and Robie (1963), but Langmuir (1965a) assures the experimental evidence is suspect in both studies because the possibility of complexing between magnesium ion and carbonate and bicarbonate has not been taken into account.

Christ and Hostetler (1970) also rejected Langmuir's (1965a) approach after performing solubility measurements at 90°C over different periods of time. The longest period of time was 163 days, but it is not clear whether or not the equilibrium was attained. From the data reported it can be seen that the pH is still not constant, and neither is the Mg^{2+} concentration (which changes from 0.160 after 140 days to 0.174 m after 163 days). Christ and Hostetler (1970) assure equilibrium was almost achieved after 4, 8 and 20 days (depending on the sample).

The Gibbs free energy value for magnesite reported by Rossini et al. (1961) is very similar to that of calcite given by Langmuir (1964), with activity products for those minerals of $10^{-8.4}$

and $10^{-8.1}$, respectively. Therefore, it would be expected a similar behaviour for both salts, but this is not the case. Magnesite is not formed in the oceans where $a_{Mg^{2+}} \cdot a_{CO_3^{2-}} \approx 10^{-7.1}$ and $a_{Ca^{2+}} \cdot a_{CO_3^{2-}} \approx 10^{-7.9}$, although calcite forms easily under these conditions (Garrels and Thompson, 1962). Another large difference in the behaviour of both minerals is related to their hydrates. The hydrates of magnesium carbonate are formed in water below 100°C at CO_2 pressures around 1 atm. On the other hand, the calcium carbonate does not form hydrates under the same conditions (Langmuir, 1964). Langmuir (1965a) rejects the kinetic argument in order to explain the disagreement between Rossini's et al. (1961) solubility diagram and geological evidences. According to him, kinetic arguments should not be valid unless a reliable free energy value is determined, which does not seem to be the case.

Langmuir's (1965a) stability relations are accepted by many investigators, as Schott and Dandurand (1975), and Dandurand and Schott (1977), who established their diagram on the basis of enthalpy of formation. They recalculated the values correcting with more recent and precise free enthalpies of formation and entropies of oxides and ions in the solution, and included the variation of the entropy with temperature. According to the values obtained, magnesite, nesquehonite, lansfordite, hydromagnesite, artinite and brucite all have stability fields.

Leitmeier (1915) studied magnesium carbonate solubility in pure water, and concluded lansfordite is the stable solid phase below 10°C, nesquehonite is the stable phase in the temperature range from 10 to 55-65°C, and hydromagnesite is obtained for higher temperatures. The same stability relations are found in solubility studies in the $MgCO_3$-CO_2-H_2O system performed by Dell and Weller (1959), Kazakov et al. (1959) and Yanat'eva and Rassonskaya (1961).

Ponizovskii et al. (1960) obtained lansfordite as solid phase in their solubility measurements at 0°C and CO_2 pressures varying from 2 to 10 atm.

Ming and Franklin (1985) synthesized both lansfordite and nesquehonite from CO_2-saturated $Mg(HCO_3)_2$ solutions by degassing with air. They concluded lansfordite is unstable when exposed to the atmosphere at temperatures larger than 10°C.

López Gómez (1975) assures brucite is the solid phase in equilibrium with the $MgCO_3$-CO_2-H_2O solution up to a carbon dioxide pressure of $3.85 \cdot 10^{-4}$ atm. For higher CO_2 partial pressures, the stable phase at 25°C is nesquehonite.

Several investigators reported magnesite solubility (Engel, 1889, Leitmeier, 1915, Wells, 1915b, Bär, 1932, Leick, 1932, Halla and Ritter, 1935, Yanat'eva, 1954, 1955a, 1955b, 1957a, 1957b, Garrels et al., 1960, Morey, 1962, Stout and Robie, 1963, Halla and Van

Tassel, 1964, Christ and Hostetler, 1970, Levchenko et al., 1970, Kittrick and Peyrea, 1986). Most of them used natural magnesite as the starting solid phase, instead of a pure solid, and attained equilibrium only from undersaturation. There is a general discordance among these data, which could be explained as a consequence of the different impurities encountered in natural rocks. Also, the disagreement could suggest that equilibrium is not reached in some studies. This is the case of Wells (1915b), who measured concentrations over different periods of time, up to 60 days. It is obvious from those results that equilibrium was not attained, as a constant solubility value was not obtained. He compared his results to waters containing a high amount of magnesium and total carbonate, and concluded "either the waters are all supersaturated with respect to magnesite, or else the solubility found for magnesite had not yet reached its maximum value". The same behaviour is observed in the experiments performed by Leick (1932). He obtained two different solid phases according to the time waited before the analysis. For the shorter periods, he did not report the formula of the solid, although we believe it is magnesite as he used this mineral as starting material, and the time was in all the cases shorter than 5 hours. For longer periods of time (from 16 to 48 hours) he reported a solid phase which did not contain any CO_2 (brucite). From those results, it seems clear that magnesite is only obtained at the beginning, when the equilibrium is not attained, and a change to brucite is obtained afterwards. In the present work, only the data measured after the longest period of time will be used.

In general, it is not very clear in the literature whether artinite becomes a stable phase, but in case it does, the field of stability should be at low temperatures, and between the fields of brucite and hydromagnesite. Baron and Wyart (1958) considered this mineral stable at lower temperatures than nesquehonite. Kazakov et al. (1959) found both artinite and brucite at 20°C. Palache et al. (1951) found artinite deposits associated with hydromagnesite and brucite. The chemical formula used for this mineral by Palache et al.(1951), Langmuir (1965a), Robie and Hemingway (1972, 1973) and Königsberger et al. (1999) is $Mg_2(OH)_2CO_3 \cdot 3H_2O$.

Langmuir's (1965a) approach is also supported by the study performed by Chase (1998). The value reported by Chase (1998) is the one reported in the NIST Standard Reference Database Number 69.

5.5.2.2 Rossini's et al. (1961) Approach

Rossini's et al. (1961) determination of the Gibbs free energy for magnesite is in very good agreement with the corresponding value determined by Robie and Waldbaum (1965).

According to these values, the only stable phases in the temperature range from 0 to 100°C are brucite (at low CO_2 pressures) and magnesite. Many investigators follow the stability relations derived from Rossini's et al. (1961) approach (Stout and Robie, 1963, Hostetler, 1964, Robie, 1965, Christ and Hostetler, 1970, Sayles and Fyfe, 1973, Kittrick and Peyrea, 1986, Robie and Hemingway, 1995, Königsberger et al., 1999, Giles, 2001). Nevertheless, the agreement on the Gibbs free energy value among all these sources is not always good. There is also a large disagreement with respect to the values of the free enthalpy of formation of magnesite found in literature. These enthalpy values are based on the determinations of solubility at room temperature performed by Leick (1932), Halla and Ritter (1935), Yanat'eva (1955b), Morey (1962), and Halla and Van Tassel (1964); or are derived from calorimetric studies by Robie and Waldbaum (1965) and Robie and Hemingway (1973), confirmed by the solubility measurements at 90°C performed by Christ and Hostetler (1970).

Königsberger et al. (1999) modelled the system Na_2CO_3-$MgCO_3$-$CaCO_3$-H_2O at low temperatures, and derived a value for the Gibbs free energy for magnesite which was very close to the one reported by Rossini's et al. (1961) and Robie and Waldbaum (1965). Nevertheless, when these values are compared to the ones listed by Christ and Hostetler (1970) and Kittrick and Peyrea (1986), it is observed the latter are 2.5 and 4.5 kJ mol^{-1} more positive, respectively, than Königsberger's et al. (1999) value.

Giles (2001) assures magnesite is the only stable phase in a magnesium carbonate solution, from the eutectic point up to 25°C, and in the CO_2 pressure range from $1 \cdot 10^{-4}$ to 1 atm. According to her, the stability order is magnesite > hydromagnesite > nesquehonite (for temperatures above 8.5°C) or lansfordite (for temperature lower than 8.5°C). Giles's (2001) conclusions are in accordance with the calorimetric study on hydromagnesite by Robie and Hemingway (1972, 1973). These investigators concluded hydromagnesite is the stable phase, and not nesquehonite. This idea is also supported by additional studies (D'Ans and Gloss, 1938, Latimer, 1952, Garrels et al., 1960) that assure nesquehonite is an unstable phase. The explanation they give to the fact that nesquehonite appears at certain conditions for large periods of time is that the transformation from nesquehonite to hydromagnesite may become kinetically possible only at high temperatures. According to Davies and Bubela (1973), hydromagnesite is more common in nature than nesquehonite, even though natural conditions of temperature would favour the precipitation of nesquehonite. They concluded nesquehonite transforms into hydromagnesite through an intermediate hydrate. Königsberger et al. (1999) also support the reasoning of nesquehonite being an unstable phase. They used a Gibbs free energy for this mineral 1 kJ mol^{-1} lower than the value reported by Robie and Hemingway (1972, 1973), and managed to reproduce very well hydromagnesite solubility in CO_2-H_2O

and in 3 m $NaClO_4$ and $KHCO_3$ solutions. Their model does not predict that nesquehonite becomes more stable than hydromagnesite at 1 atm CO_2 pressure.

According to Christ and Hostetler (1970), the natural occurrence of magnesite is much more common than nesquehonite or hydromagnesite. They claim that in the hydromagnesite deposits of the Kamloops, Atlin, and Cariboo districts of British Columbia, magnesite is forming at the expense of hydromagnesite.

Additional data on magnesium carbonate stability and solubility are obviously needed, in order to throw some light into the rather complex matrix created for this system. The use of different techniques and newer approaches (note that most of the studies are around 30-40 years old) could help to develop a clearer idea about the real stability relations and the solubility behaviour at different conditions of temperature, pressure and CO_2 concentration. It is also important to mention that any condition introducing a possible source of error must be avoided. In that sense, natural minerals should not be used to perform experiments. Such minerals will always contain different amounts and kinds of impurities, which will obviously influence the solubility behaviour to some extent. It seems clear analyzing the sources mentioned before that the time required to attain equilibrium in the $MgCO_3$-CO_2-H_2O system is very large. Therefore, experimental conditions favouring a shorter time should be encouraged (small particle size, agitation, etc.).

In the present work we have chosen to follow Langmuir's (1965a) stability relations, even though there is no clear evidence that this choice is more reliable. We do think the arguments given by Langmuir (1965a) and his followers are somehow stronger than Rossini's et al. (1961). Moreover, the value given by the NIST Chemical Thermodynamics Database (1990) for the Gibbs free energy for magnesite is very close to Langmuir's (1965a). This is the same source of standard thermodynamic data that was used for all other components in this work. Even if the approach by Rossini et al. (1961) is the correct one, it seems clear that kinetic impediments control the deposition/dissolution of magnesite. Thus, in the context of scale formation in oil and geothermal wells, it is more convenient to model the solubility of the different minerals likely to precipitate on the inner walls of pipes and equipment within a reasonable period of time.

The NIST Chemical Thermodynamics Database (1990) did not report any value for the Gibbs free energy of lansfordite, nesquehonite, and brucite. Starting guesses for those values were calculated from the value reported for magnesite and for water as:

$$G_f^0(MgCO_3 \cdot nH_2O) \cong G_f^0(MgCO_3) + nG_f^0(H_2O) \qquad \textbf{(5-1)}$$

These values were later fitted to experimental data. The same procedure was also used for the calculation of the standard state enthalpy and heat capacity.

Contrary to the assumptions made for other carbonate minerals, the effect of magnesium carbonate on CO_2 solubility cannot be neglected. The solubility of nesquehonite is rather large when compared to carbonates such as calcite, strontianite or witherite. Therefore, in order to determine the interaction parameters between Mg^{2+} and $CO_2/HCO_3^{2-}/CO_3^{2-}$ we were limited to the use of those sources reporting both the salt solubility and the CO_2 concentration in the liquid phase. The references used, together with the ranges of temperature and pressure covered, and the number of experimental determinations carried out and used in the present work (in brackets), are given in table 5-10. Table 5-11 shows additional studies on the $MgCO_3$-CO_2-H_2O system, where the amount of CO_2 in the liquid phase is unknown.

Only a few sources dealing with lansfordite solubility were found in literature: Beckurts (1881), Merkel (1924), Ponizovskii and Vladimirova (1959), Ponizovskii et al. (1960), Yanat'eva and Rassonskaya (1961) and Corti et al. (1990a). All these sources used pure CO_2 saturated with water vapour as the gas phase.

Table 5-10
Experimental $MgCO_3$-H_2O and $MgCO_3$-CO_2-H_2O SLVE experimental data sets used for parameter estimation (CO_2 concentration in the liquid phase reported).

T(°C)	*P*(atm)	Number of data	*AAD* (m)	Reference
0	1	1 (1)	1.2E-04	Gothe (1915)
0/80	6/64	20 (0)		López Gómez (1975)
12.1/16	1	17 (0)		Treadwell and Reuter (1898)
12.5	1/6	8 (0)		Seyler and Lloyd (1917)
20	1	12 (0)		Wells (1915b)
20/39	1	27 (27)	2.9E-03	Leather and Sen (1914)
20/158		45 (0)		Corti et al. (1990a)
25	1	23 (23)	6.0E-03	Wattenberg and Timmermann (1937)
25	6/21	6 (6)	1.3E-02	Mitchell (1923)
25/290	200	12 (0)		Morey (1962)
35/200	0.06/15.4	10 (8)	1.9E-05	Travers and Nouvel (1929)
100	1	4 (1)	4.1E-06	Leick (1932)
			***MAAD* (m):**	**4.2E-03**

Brucite solubility in pure water, freed of carbon dioxide, was determined by Gothe (1915), Travers and Nouvel (1929), Leick (1932) and Morey (1962). Brucite solubility in CO_2-H_2O solutions was measured by Kline (1929) and Corti el al. (1990a.). The former used mixtures of air and carbon dioxide, in different proportions, as the gas phase. The latter author used pure CO_2 in the gas phase, previously saturated with $MgCO_3$ solution. To obtain low carbon dioxide pressures (required for the stability of brucite) vacuum was used.

Table 5-11
Experimental $MgCO_3$-CO_2-H_2O SLVE experimental data sets where the CO_2 concentration in the liquid phase is unknown.

T(°C)	*P*(atm)	Number of data	Reference
0	4	1	Ponizovskii and Vladimirova (1959)
0	4/10	4	Ponizovskii et al. (1960)
0/55	1	2	Yanat'eva (1955a)
0/55	1	3	Yanat'eva (1957a)
0/60	2/56	15	Haehnel (1924)
0/90	1	18	Yanat'eva and Rassonskaya (1961)
3.5/50	1/9	26	Engel (1889)
5	1/6	6	Merkel (1924)
10/40	1/5	7	Beckurts (1881)
17	1	1	Bär (1932)
20	1	1	Leitmeier (1915)
21	1	1	Halla and Van Tassel (1964)
25	1	23	Kline (1929)
25	1	6	Kittrick and Peyrea (1986)
25	1	1	Yanat'eva (1957b)
25	1	2	Yanat'eva (1955b)
25	1	1	Levchenko et al. (1970)
25	1	1	Yanat'eva (1954)
25	1	1	Halla and Ritter (1935)
25	1	1	Garrels et al. (1960)
25	1	1	Stout and Robie (1963)
90	1	48	Christ and Hostetler (1970)

Nesquehonite solubility in CO_2-H_2O solutions was determined by Beckurts (1881), Engel (1889), Treadwell and Reuter (1898), Leather and Sen (1914), Wells (1915b), Seyler and Lloyd (1917), Mitchell (1923), Haehnel (1924), Kline (1929), Bär (1932), Wattenberg and Timmermann (1937), Yanat'eva and Rassonskaya (1961), López Gómez (1975) and Corti et al. (1990a). Most of these sources used pure CO_2 saturated with water vapour in the gas phase. Leather and Sen (1914) and Wells (1915b) used air, while Treadwell and Reuter (1898), Kline (1929) and Wattenberg and Timmermann (1937) used mixtures of air and CO_2, containing different amounts of the latter gas.

Hydromagnesite solubility determinations under a pure CO_2 gas phase were carried out by Engel (1889), Yanat'eva and Rassonskaya (1961) and Corti et al. (1990a).

Literature on experimental determination of magnesite solubility in water and in CO_2-H_2O solutions is mentioned in a previous paragraph of this chapter. Most of the sources cited employed carbon dioxide saturated with water vapour in the gas phase. Christ and Hostetler (1970) also used mixtures of CO_2 and N_2 (same procedure as followed by Levchenko et al., 1970), while Kittrick and Peyrea (1986) employed air. According to Langmuir (1965a), magnesite should not be stable for the majority of the experimental conditions employed by the sources studying the solubility of this mineral. Only experiments at temperatures above 60°C and 1 atm carbon dioxide pressure may be concordant with the stability relations followed here.

Some of the sources mentioned in table 5-10 did not explicitly report the solid phase obtained in their equilibrium measurements (Beckurts, 1881, Treadwell and Reuter, 1898, Leather and Sen, 1914 and Merkel, 1924). In those cases we assumed the solid phase is the stable one at the experimental temperature and CO_2 pressure.

Many of the data in table 5-10 were not used in the present work for parameter estimation as they included some kind of error: The reported solid phase at the experimental conditions is not stable according to Langmuir (1965a); the data disagree with the majority of the sources; etc.

Nesquehonite solubility in CO_2-H_2O solutions increases with the total CO_2 amount. Such behaviour is followed by all the sources given in table 5-10, but for Treadwell and Reuter (1898), where for some solubility measurements at the highest carbon dioxide concentrations, constant nesquehonite solubility is observed for increasing CO_2 amounts. As mentioned before for calcite, Treadwell and Reuter’s (1898) experiments were conducted under imperfect conditions, and supersaturation is to be expected (Leather and Sen, 1914).

Travers and Nouvel (1929) determined brucite solubility in pure water. Two out of the ten measurements performed contained a very low amount of $Mg(OH)_2$ which could not be determined by the analytical technique used. As a consequence, they reported zero as the solubility value. Those two points were therefore not used in the present work.

Morey (1962) determined $MgCO_3$ solubility in water freed of CO_2 at 200 atm total pressure. After X-ray study, he concluded magnesite was the stable solid phase from 25 to 150°C, and this mineral was completely changed to brucite for temperatures higher than 150°C (and up to 290°C). He also found some sepiolite crystals ($Mg_4Si_6O_{15}(OH)_2 \cdot 6H_2O$), which must appear due to the use of natural rock containing impurities. For some temperatures, Morey (1962) obtained mixtures of magnesite and brucite, and he claimed that magnesite would have been completely replaced by brucite if he had waited longer. Thus, maybe his data are affected by the fact that equilibrium was not attained, and magnesite did not have enough time to convert into brucite. This could explain the appearance of magnesite when the only stable phase in the absence of carbon dioxide in the solution is brucite.

As mentioned previously, it is believed that the measurements reported by Wells (1915b) do not correspond to equilibrium, and thus they were not used in the present work. Moreover, he measured the solubility of both magnesite and nesquehonite in water at the same conditions (20°C and 1 atm). Following Langmuir's (1965a) approach, the first phase should not be stable at those conditions.

Seyler and Lloyd (1917) concluded "crystallized magnesium carbonate has no definite solubility in pure water. It decomposes into basic carbonates and magnesium hydrogen carbonate, whilst a certain amount of carbonate is also dissolved". Under the same experimental conditions, they obtained different $MgCO_3$ concentrations depending on the ratio of water to solid employed. When equilibrium is attained, a unique solubility value should be obtained independently of the initial amounts of solid and solvent used. Therefore, Seyler and Lloyd's (1917) data were not used in the present work.

Corti et al. (1990a) report neither the partial pressure of carbon dioxide nor the total pressure used in the experiments. After analyzing the experimental procedure employed, it is clear they performed experiments with different CO_2 quantities, which are sometimes achieved by removing carbon dioxide from the gas phase applying vacuum. But the vacuum pressure is unknown, and therefore the data could not be used.

Wattenberg and Timmermann (1937) did not report the amount of carbon dioxide contained in the liquid phase, but they gave the values of the solution pH and the bicarbonate concentration. From those values, together with the equilibrium constant, the amount of CO_2 was calculated following the same procedure as in the case of $SrCO_3$, where the same source is also used.

López Gómez (1975) presented in his paper several plots for the solubility in the ternary system MgO-CO_2-H_2O at various temperatures and carbon dioxide pressures. He also reports the CO_2 solubility in saturated $MgCO_3$ solutions at 25°C. He mentions he used data from different investigators to draw the solubility curves, but it is not clear which data are his and which are from other sources. He did not analyze the solid phase in equilibrium with the solution at the experimental conditions. When data from this source are compared to others (mainly to Mitchell (1923) at pressures larger than 1 atm, and to available sources in table 5-10 at 25°C and atmospheric pressure) it is clear the solubility of both the salt and carbon dioxide is very much overestimated in that paper.

The experimental and calculated $MgCO_3$ solubility as a function of the CO_2 concentration in the solution at 39°C and 1 atm total pressure is shown in figure 5-15. As expected from Langmuir's (1965a) phase diagram at 39°C, only one solid phase, nesquehonite, is formed in the whole range of CO_2 concentration presented. Nesquehonite solubility increases with the amount of carbon dioxide, from 0.015 m $MgCO_3\cdot3H_2O$ at 0.007 m total CO_2 to 0.08 m $MgCO_3\cdot3H_2O$ at 0.17 m total CO_2. The calculated solubility compares very well with the experimental data. Due to the lack of data at the same conditions, it was impossible to calculate a reliable value for the average experimental standard deviation for nesquehonite. To get at least an idea about the order of magnitude of *ASD*, a determination was done considering the only two experimental points at very similar conditions (25°C, 0.52 m total CO_2, and 13.2 atm total pressure; and 25°C, 0.54m total CO_2 and 16.2 atm total pressure, respectively). The obtained *ASD* is $1.8\cdot10^{-2}$ m $MgCO_3\cdot3H_2O$. When such value is compared to the *MAAD* between our model calculations and the experimental data ($4.2\cdot10^{-3}$ m) it is clear extended UNIQUAC calculations are remarkably good.

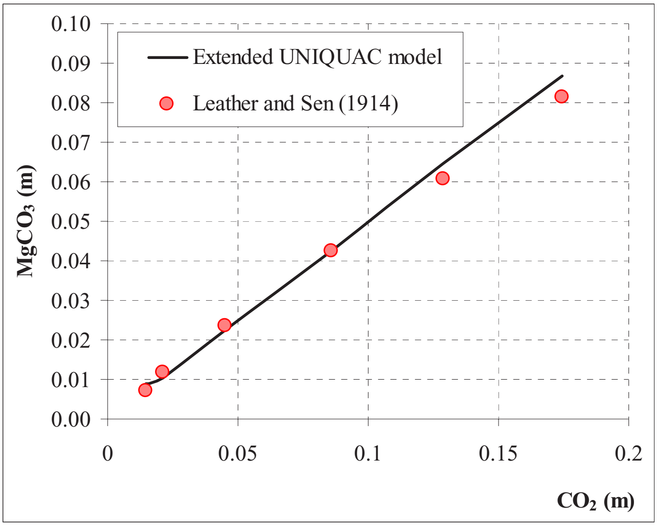

Figure 5-15. Experimental and calculated $MgCO_3$ solubility as a function of the CO_2 concentration in solution, at 39°C and 1 atm total pressure. Gas phase formed by CO_2 (g) and H_2O (g).

For the case of brucite, the same problem was encountered when trying to calculate the *ASD*. If we follow the same procedure as before and use the only two experiments carried out at similar conditions (100°C, $7.2\cdot10^{-5}$ m CO_2, and 1 atm; and 100°C, $7.5\cdot10^{-5}$ m CO_2, and 1 atm, respectively) the value obtained for the *ASD* is $4.3\cdot10^{-6}$ m $Mg(OH)_2$. For this salt, extended UNIQUAC calculations are less accurate than for nesquehonite, and the *MAAD* between the model and the data is $1.7\cdot10^{-5}$ m $Mg(OH)_2$.

The binary phase diagram for the system $MgCO_3$-H_2O covering a temperature range from 100 to 158°C, at the saturation pressure, is shown in figure 5-16. The only solid phase encountered at those conditions is brucite, its solubility decreases with increasing pressure.

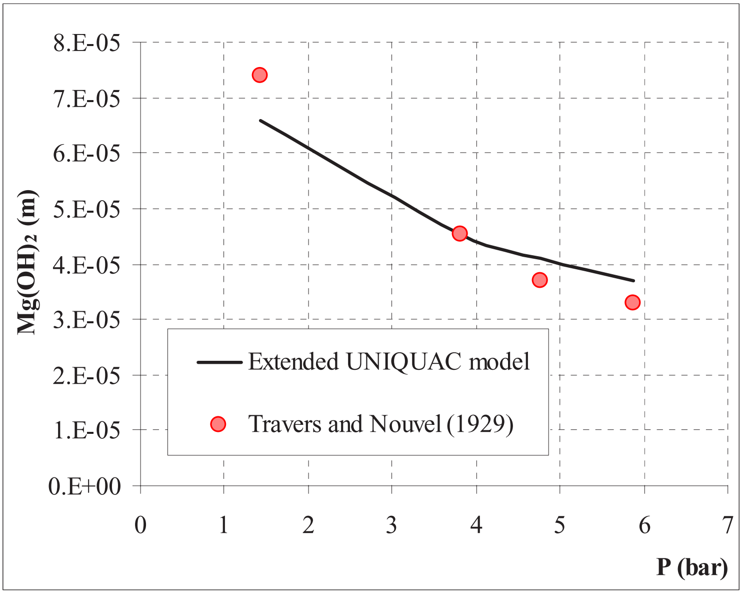

Figure 5-16. Experimental and calculated solid-liquid phase diagram for the binary $MgCO_3$-H_2O system at the saturation pressure.

Once the parameters required for the system $MgCO_3$-CO_2-H_2O were obtained on the basis of the VLSE experimental data reported in table 5-10, they can be used to perform some calculations for the data sets where the amount of carbon dioxide in the liquid phase is unknown (data reported in table 5-11). The solubility of CO_2 in the $MgCO_3$ solution at the experimental temperature and carbon dioxide pressure can be calculated by means of the new parameters. Once the amount of carbon dioxide is estimated, the experimental points could be added to the original VSLE database and refit the parameters based on a larger experimental study. Nevertheless, such improvement of the experimental $MgCO_3$-CO_2-H_2O database and of the parameters was not possible, as the experimental determinations reported in table 5-11 are also characterized by a tremendous lack of agreement. Many of them do not follow the stability field followed by Langmuir (1965a) and report magnesite as the only stable phase at temperatures and CO_2 pressures where lansfordite or nesquehonite should form and be stable. That is the case for all the data reported by Leitmeier (1915), Bär (1932), Halla and Ritter (1935), Yanat'eva (1954, 1955a, 1955b, 1957a, 1957b), Garrels et al. (1960), Stout and Robie

(1963), Halla and Van Tassel (1964), Christ and Hostetler (1970), Levchenko et al. (1970), Kittrick and Peyrea (1986). Several authors agree on the fact that Kline's (1929) work is not precise (Kazakov et al., 1959, Langmuir, 1965a, Harvie et al., 1984). The greatest shortness of his work is the extremely low aging period, which varied between 3 and 5 days. Therefore, it is very unlikely that the solutions Kline (1929) measured had achieved equilibrium. According to Kazakov et al. (1959), this could well explain some of the incongruences found in Kline's (1929) work, as the formation of different solid phases under very similar conditions. Harvie et al. (1984) tried to fit Kline's (1929) results, but they did not succeed, even though different attempts were done, including complexes such as $MgHCO_3^+$. They realized in order to explain those data, it was needed to assume that enormous changes in the interactions occur over a very small concentration range. Kline (1929) was not congruent either when he determined the solubility product of nesquehonite based on a graphic extrapolation to infinite dilution, even though solubility measurements of that mineral cannot be extended below an ionic strength about 0.05 due to the formation of brucite (Langmuir, 1965a).

The aging time measured by Engel (1889) (9 hours) is extremely low for the system considered and it is very unlikely that equilibrium was reached. In his paper he shows the amounts of HCl employed in the titration of different solutions at the same temperature and carbon dioxide pressure, according to the starting solid phase (magnesite or nesquehonite). The amounts of acid employed are completely different, proving that equilibrium was not attained, at least for one of the solutions.

Some of the solid phases reported by Yanat'eva and Rassonskaya (1961) are not stable at the given conditions, according to Langmuir's (1965a) stability diagram.

Haehnel (1924) obtained the same solubility value for nesquehonite at 18°C and CO_2 pressures changing from 18 to 56 atm, which makes his determinations rather suspect. In the experimental procedure followed, samples were taken at atmospheric pressure and analyzed afterwards. Decreasing the carbon dioxide partial pressure from a few atmospheres (up to 56 atm) to room conditions will very likely result in erroneous solubility determinations, as part of the CO_2 will evaporate from the liquid phase.

Large discrepancies are found between the data reported by Beckurts (1881) and Merkel (1924). None of these datasets were taken from the original sources, but from Haehnel (1924), who did not mention the solid phase obtained. Thus, the differences could be due to different solids being involved in the equilibrium. When Beckurts' (1881) data at 20°C are compared to those by Mitchell (1923) at 25°C, the agreement seems good. The experimental

CO_2 pressure is larger for Mitchell (1923), but the tendencies followed by both sources are in good agreement. An additional problem of both sources is the choice of units to characterize the system. The solubility is expressed as weight percent of $MgCO_3$ (the same unit as used by Ponizovskii and Vladimirova, 1959). As the total amount of CO_2 is unknown, the exact composition of the solution is unknown. Therefore, calculations could only be approximate, assuming the percentage is referring only to the amount of water and salt, and excluding the CO_2 (aq). Due to the lack of the original sources, the antiquity of the data, and the imprecision of at least one of the two datasets mentioned, those sources were not used for parameter estimation in the present work.

5.6 $MgCO_3$-$CaCO_3$-CO_2-H_2O System

The binary interaction parameter for the interaction between Ca^{2+} and Mg^{2+} has already been fitted to ternary data containing both calcium and magnesium together with chloride or nitrate. Thus, the analysis of dolomite ($CaCO_3 \cdot MgCO_3$) studies and the system $CaCO_3$-$MgCO_3$-CO_2-H_2O is not necessary for the purpose of parameter estimation. Nonetheless, due to the complexity found for the ternary system $MgCO_3$-CO_2-H_2O, it was considered relevant to study this system in detail.

Similar to the magnesium carbonate system, the system $CaCO_3$-$MgCO_3$-CO_2-H_2O is also characterized by large experimental discrepancies regarding solubility values, stability relations, and values for the standard state Gibbs free energy and enthalpy. The experimental difficulties mentioned before for the $MgCO_3$-CO_2-H_2O system are also found in the present case. Dolomite has not been successfully obtained in laboratory near room conditions because of an extremely slow kinetics (apparently, it requires geological times to precipitate this solid). Dolomite is present in many ancient sediments, while it does not appear in modern marine sediments (Kazakov et al., 1959). The only way to overcome this problem is to increase the velocity of the reaction enormously. This objective can be attained by increasing the concentration of CO_2 in the solution by increasing the pressure. In fact, dolomite has been successfully crystallized under hydrothermal conditions in different solutions (Graf and Goldsmith, 1955, Rosenberg and Holland, 1964, Rosenberg et al., 1967, Sureau, 1974). Due to the impossibility to precipitate dolomite, the equilibrium at atmospheric conditions cannot be checked from supersaturation, and only undersaturation experiments have been carried out. All data thus contain the uncertainty whether or not equilibrium has been reached during the experiments. According to Hsu (1963), published values for the activity product of dolomite at 25°C and 1 atm vary from 10^{-17} to 10^{-20}. Such disagreement may be caused by different reasons. In the first place, as mentioned before, true thermodynamic equilibrium may not have been established for most of the available data. The use of natural dolomite in many of the experiments will also introduce an additional source of diversity in the results, as a consequence of the influence of the different impurities found together with $CaCO_3 \cdot MgCO_3$. The use of pure commercial solid is therefore encouraged, although the synthesis of dolomite in laboratory is not easy.

One of the consequences of the disagreement found in literature for the systems $MgCO_3$-CO_2-H_2O and $CaCO_3$-$MgCO_3$-CO_2-H_2O is reflected in the calculated values for the standard state enthalpy of formation of dolomite. Two different approaches have been used to determine this value: calorimetric studies (Stout and Robie, 1963, Navrotsky and Capobianco, 1987), and determinations from solubility measurements (Yanat'eva, 1955b, Halla, 1958, Kramer, 1959, Garrels et al., 1960, Halla et al., 1962, Stout and Robie, 1963, Langmuir, 1965b, Dandurand and Schott, 1977, Robie and Hemingway, 1995, Königsberger et al., 1999). The values obtained differ from -2144.34 kJ mol^{-1} given by Dandurand and Schott (1977) to -2175.26 kJ mol^{-1} determined by Garrels et al. (1960).

Stout and Robie (1963) determined the standard state heat capacity and entropy of dolomite by calorimetric methods. They also calculated standard state enthalpies and Gibbs free energies from a thermodynamic analysis of dolomite decomposition data by Graf and Goldsmith (1955), and from solubility data of dolomite, magnesite and calcite in aqueous solutions saturated with CO_2 at 1 atm pressure (Yanat'eva, 1954). The values obtained for the enthalpy change for the reaction

$$CaCO_3 + MgCO_3 \Leftrightarrow CaCO_3 \cdot MgCO_3 \qquad \textbf{(5-2)}$$

at 25°C by the two analysis methods employed are very similar (-12.30 and -12.84 kJ mol^{-1}, respectively). These values compare relatively well with the one given by Navrotsky and Capobianco (1987). They determined the enthalpy of formation of dolomite by solution calorimetry at 85°C, obtaining an enthalpy change for reaction 5-2 of -11.48 kJ mol^{-1}. However, when they calculated the enthalpy of formation from data given by Robie et al. (1978), they obtained a rather different value (-3.76 kJ mol^{-1}). Such value is closer to the calculations performed by Halla (1958) from solubility measurements at the two triple points (dolomite and calcite/magnesite in equilibrium with the saturated solution). Halla (1958) obtained a value of -3.97 kJ mol^{-1} when using the data reported by him (Halla, 1936), while this value changed to -5.27 kJ mol^{-1} for the data reported by Yanat'eva (1955b).

Königsberger et al. (1999) calculated the Gibbs free energy of formation (-2172 kJ mol^{-1}) and the enthalpy of formation (-2334.8 kJ mol^{-1}) of dolomite from the solubility data of dolomite in 3 m $NaClO_4$ solutions at 25°C given by Riesen (1969). These values are consistent with those calculated by Stout and Robie (1963), resulting in enthalpy and Gibbs free energy changes for reaction 5-2 of -12.9 and -11.3 kJ mol^{-1}, respectively.

Robie and Hemingway (1995) used considerably more positive values for the enthalpy and Gibbs free energy of formation of dolomite (-2324.5 and -2161.3 kJ mol^{-1}, respectively). These values agree with the ones published in NIST Chemical Thermodynamics Database (1990): -2326.3 and -2163.4 kJ mol^{-1}, respectively. Also, Langmuir (1965b) suggested the use of -2160 kJ mol^{-1} as the value for the Gibbs free energy of dolomite.

Dandurand and Schott (1977) reported very positive values for both the standard state Gibbs free energy and enthalpy of dolomite. They determined the former value (-2144.34 kJ mol^{-1}) from Baron's (1960) experiments on dolomite synthesis. If experimental data by Graf and Goldsmith (1956) are used instead, the value is -2147.06 kJ mol^{-1}.

Tables 5-12 and 5-13 show a summary of the different Gibbs free energies and enthalpies of formation of dolomite found in literature.

Table 5-12

Values for enthalpy and Gibbs free energy of formation of dolomite found in literature.

Reference	Solubility Data	$\Delta_f H^0$ (kJ mol^{-1})	$\Delta_f G^0$(kJ mol^{-1})
Dandurand and Schott (1977)	Baron (1960)		-2144.3
Dandurand and Schott (1977)	Graf and Goldsmith (1956)		-2147.1
Langmuir (1965b)			-2160.0
Kramer (1959)	Kramer (1959)		-2161.0
Robie and Hemingway (1995)		-2324.5	-2161.3
NIST (1990)		-2326.3	-2163.4
Königsberger et al. (1999)	Riesen (1969)	-2334.8	-2172.0
Garrels et al. (1960)			-2175.3

Table 5-13

Values for the change of standard state enthalpy and Gibbs free energy of reaction 5-2 found in literature.

Reference	Data	$\Delta_r H^0$ (kJ mol^{-1})	$\Delta_r G^0$ (kJ mol^{-1})
Stout and Robie (1963)	Graf and Goldsmith (1955)	-12.30	-11.30
Stout and Robie (1963)	Yanat'eva (1954)	-12.84	
Halla (1959)	Halla (1936)	-3.97	-2.97
Halla (1959)	Yanat'eva (1955)	-5.27	-4.26
Navrotsky (1987)	calorimetry	-11.48	
Navrotsky (1987)	Robie et al. (1978)	-3.76	

The diversity of standard state Gibbs free energy and enthalpy values shown in table 5-12, together with the diversity also found for the system $MgCO_3$-CO_2-H_2O, results in completely different solubility diagrams for the system $CaCO_3$-$MgCO_3$-CO_2-H_2O (Bär, 1932, Halla and Ritter, 1935, Yanat'eva, 1949, 1952, 1955b, 1957a, Baron and Favre, 1958, Kazakov et al., 1959, Berg and Borisova, 1960a, Garrels et al., 1960, Yanat'eva and Rassonskaya, 1961, Yanat'eva et al., 1961, Lippmann, 1980). Little knowledge is available about the dolomitization process and the intermediate phases presented in it. Many authors (Rosenberg and Holland, 1964, Berner, 1967, Bischoff, 1968, Katz, 1971, Plummer and Mackenzie, 1974) support that the solid phase precipitating in the $CaCO_3$-$MgCO_3$-CO_2-H_2O system and the time required to achieve equilibrium is determined by the activity ratio between calcium and magnesium in the solution.

Yanat'eva (1949, 1952, 1955b, 1957a) obtained calcite, dolomite and magnesite as the solid phases in equilibrium with the solution at 0, 25, 55 and 70°C, and CO_2 pressures of 0.0012 and 1 atm. The appearance of one or another salt (or the triple points) depends on the amounts of Mg^{2+} and Ca^{2+} in the solution. This approach is also followed by Bär (1932) at 17°C, by Halla and Ritter (1935) at 25-40°C, by Lippmann (1980) at 25°C, and by Garrels et al. (1960) at 25°C, all the studies at 1 atm of CO_2 pressure. For the latter investigators, hydromagnesite becomes a stable phase with respect to magnesite and dolomite only at very low carbon dioxide pressures, much lower than the earth surface conditions. Kramer (1959) and Garrels et al. (1960) claim that dolomite is stable in sea water at 25°C. Dolomite even forms when calcite is present in sea water since a smaller carbonate ion concentration is required for dolomite saturation, when comparing to calcite. The reason why calcite is observed instead of dolomite in recent marine sediments is due to the slow rate at which dolomite is formed.

On the other hand, Yanat'eva and Rassonskaya (1961) and Yanat'eva et al. (1961) obtained as solid phases calcium carbonate and the hydrated magnesium carbonates $4MgCO_3 \cdot Mg(OH)_2 \cdot 4H_2O$, $MgCO_3 \cdot 3H_2O$ and $MgCO_3 \cdot 5H_2O$, depending on the temperature. A very similar result is obtained by Baron and Favre (1958) at a partial CO_2 pressure of 0.001 atm. The solid phases in equilibrium with the solution are calcite and nesquehonite at 25 and 40°C, aragonite, nesquehonite and hydromagnesite at 70°C, and aragonite and hydromagnesite at 100°C.

Yanat'eva and Rassonskaya (1961) used a mixture of aragonite and nesquehonite as starting solids for the study of the quaternary system $CaCO_3$-$MgCO_3$-CO_2-H_2O. They obtained isotherms with two branches, corresponding to the crystallization of the pure salts ($CaCO_3$ and $MgCO_3 \cdot 5H_2O$ at 0°C, $CaCO_3$ and $MgCO_3 \cdot 3H_2O$ at 20 and 40°C, and $CaCO_3$ and $4MgCO_3 \cdot Mg(OH)_2 \cdot 4H_2O$ at 55, 70 and 90°C). Nevertheless, the isotherms obtained at 0°C were depending on the order of mixing of the initial salts. When nesquehonite was introduced all at once, the eutectic solutions contained 330.4 mmoles $Mg(HCO_3)_2$ and 0.55 mmoles $Ca(HCO_3)_2$ per kg of solution. Those quantities increased to 396 mmoles of $Mg(HCO_3)_2$ and 2.76 mmoles of $Ca(HCO_3)_2$ per kg of solution when nesquehonite was introduced in two or three portions at 4-5 minutes intervals. The solid phases obtained in both cases were also different. In the first case aragonite and nesquehonite were found, while in the second case the trihydrate was substituted by lansfordite. The explanation of the different solubility behaviour under equal temperature and CO_2 pressure conditions must be explained as metastable equilibrium, at least for one of the two solutions.

Berg and Borisova (1960a, 1960b) tried to avoid the problem reported by Yanat'eva and Rassonskaya (1961) and placed the initial solid phases (calcite and magnesite) simultaneously in the reaction vessel. After equilibrium, the common crystallization point was obtained. They also performed one experiment where magnesite was substituted by nesquehonite, obtaining rather different amounts of calcium and magnesium carbonates in the solution, and obtaining in that case calcite and nesquehonite as solid phases. Such behaviour manifests, again, that equilibrium was not attained.

According to Bär (1932), Halla and Ritter (1935) and Yanat'eva (1949, 1952, 1955b, 1957a), the points obtained by Berg and Borisova (1960a, 1960b), Yanat'eva and Rassonskaya (1961) and Yanat'eva et al. (1961) fall within the region representing supersaturation with respect to dolomite. Therefore, the absence of dolomite indicates a condition of metastable equilibrium. Such condition, however, proved very persistent and no notable changes were observed during a year, even when some dolomite was introduced in the reaction vessel.

Kazakov et al. (1959) slowly mixed solutions of calcium and magnesium bicarbonate while aerating with atmospheric air. In all the experiments performed covering temperatures from 20 to 60°C, the bottom phases were either calcite and nesquehonite or calcite and hydromagnesite, depending on the CO_2 concentration in the solution. However, at 150°C, and using a much higher CO_2 pressure than in the previous measurements, the phase precipitating from solution was dolomite. Kazakov et al. (1959) concluded dolomite is not formed in open systems where the partial pressure of carbon dioxide is similar to that of normal atmospheric air, but it is easily developed in a closed system at an elevated partial pressure of CO_2. Unfortunately, Kazakov et al. (1959) did not report either the total pressure or the partial pressure of carbon dioxide for their experiments in closed systems.

Other investigators support the coexistence of dolomite and magnesium calcites ($Ca_xMg_{(1-x)}CO_3$) as stable solid phases for the system $CaCO_3$-$MgCO_3$-CO_2-H_2O. Graf and Goldsmith (1955) investigated the transformation of metastable magnesian calcites into dolomite at temperatures above 500°C. Lower temperatures were not included in the study due to the extremely slow process. They concluded that magnesium calcite of 15 mol% $MgCO_3$ and dolomite are the stable phases in the $MgCO_3$-$CaCO_3$-CO_2-H_2O system at 700°C. Bertram et al. (1991) focused on the solubility of magnesian calcites at low temperatures. They concluded at 50°C dolomite and calcite low in magnesium are the stable phases, a fact that is also observed petrographically. The higher the temperature, the more enriched in magnesium the calcite stable phase. Due to the lack of experimental data the composition of stable magnesian calcites is not known.

In order to be consistent with the approach chosen to explain the stability relations in the $MgCO_3$-CO_2-H_2O system, the values given by the NIST Chemical Thermodynamics Database (1990) for both the Gibbs free energy and enthalpy of formation of dolomite are chosen in the present work. Also, the standard state heat capacity is reported by the NIST Chemical Thermodynamics Database (1990). These values agree with Langmuir (1965b), whose phase diagrams for the magnesium and calcium carbonate are followed in this work.

Table 5-14 shows all the publications found for the system $CaCO_3$-$MgCO_3$-CO_2-H_2O, the ranges of temperature and pressure covered by them and the number of data points reported by each publication. Only a few sources (some of the measurements by Leather and Sen, 1914, Mitchell, 1923 and Kazakov et al., 1959) reported the amount of CO_2 contained in the $CaCO_3$-$MgCO_3$ solution.

Table 5-14
Experimental $MgCO_3$-$CaCO_3$-CO_2-H_2O SLE experimental data sets.

T(°C)	*P*(atm)	Number of data	Reference
0/55	1	6	Yanat'eva (1955b)
0/90	1	41	Yanat'eva and Rassonskaya (1961)
17	1	2	Bär (1932)
20/150	1/15	12	Kazakov et al. (1959)
22	1	2	Dandurand and Schott (1977)
22/31	1	141	Hsu (1963)
25	1	3	Yanat'eva (1957a)
25	1/16	7	Mitchell (1923)
25	1	4	Yanat'eva (1952)
25	1	2	Berg and Borisova (1960a)
25	1	2	Berg and Borisova (1960b)
25/38.8	1	13	Halla and Ritter (1935)
25/340	200	11	Morey (1962)
30/33	1	40	Leather and Sen (1914)
70	1	3	Yanat'eva (1960)
100	1	4	Leick (1932)

Additional sources dealing with the system $CaCO_3$-$MgCO_3$-CO_2-H_2O but not reported in table 5-14 are Yanat'eva 1955a, 1957b, Yanat'eva and Danilova, 1956, Yanat'eva et al., 1961. They are not included in table 5-14 as the data presented in those papers refer to data that were published previously by the same authors.

Most of the references used CO_2 saturated with water vapour in the gas phase (Mitchell, 1923, Bär, 1932, Halla and Ritter, 1935, Yanat'eva, 1952, 1955b, 1960, Berg and Borisova 1960a, 1960b, Yanat'eva and Rassonskaya, 1961). Some investigators employed air instead (Kazakov et al., 1959, Dandurand and Schott, 1977) or mixtures of CO_2 and air in different proportions (Leather and Sen, 1914, Mitchell, 1923). Finally, some of the experiments are performed using water freed of CO_2 and with no gas phase over the solution (Leick, 1932, Morey, 1962).

A deep analysis to the data presented in table 5-14 will be done in the next paragraphs, as many of the sources are considered unreliable.

Mitchell (1923) performed three measurements in solutions containing both calcite and nesquehonite, using pure CO_2 in the gas phase. For the lowest pressure, the solid phase could not be successfully determined, while dolomite was obtained in the other two measurements. He also performed three additional measurements using natural calcite from Algeria, and mixtures of air and CO_2 in the gas phase covering partial pressures of carbon dioxide from 0.25 to 1 atm. He concluded the solutions were supersaturated with respect to dolomite due to an extremely low rate of precipitation.

Leather and Sen (1914) tried to attain equilibrium in the $CaCO_3$-$MgCO_3$-CO_2-H_2O system following two different directions: By precipitation of dolomite from supersaturated solutions of calcium and magnesium bicarbonate, and by dissolution of natural dolomite. For the first data set, the authors claim that the amount of magnesium carbonate in solution is much larger than expected. This fact could be explained as a supersaturated solution due to the low time allowed for equilibration (seven days). Due to this short time, Leather and Sen (1914) state “it is improbable that in any of the experiments a state of equilibrium had set in”. In the second data set, a larger time of contact between the different phases was allowed (up to 250 days) for three of the experiments, although the rest of the measurements were performed after 8 to 13 days. This time is too short for equilibrium to be attained. In addition to that, the dolomite employed contained some impurities as iron oxide, insoluble silicates and sand, and Leather and Sen (1914) did not use any device to keep a constant temperature during the experiments. They confined the experimental setup in a room whose temperature was constant within ± 1°C. Nevertheless, a more precise control of temperature is recommended. Some of the experiments were carried out adding a second solid phase (nesquehonite or calcite) to the solution to analyze its influence on the solubility behaviour. After plotting the data it can be clearly concluded that true equilibrium was not attained.

Morey (1962) used natural dolomite from Maryland. From 25 to 209°C the X-ray analysis of the solid phase shows it to be dolomite, while from 209 to 304°C the solid phase changes to calcite and brucite. As the water employed in the experiments was previously freed of CO_2, and there was no gas phase over the solution, brucite should be the solid phase encountered in all the experiments according to Langmuir (1965a).

Hsu (1963) determined the solubility and solubility product of dolomite based on shallow ground-water samples from an aquifer in central Florida formed by dolomitic limestone. The main constituents of these waters are calcium, magnesium and bicarbonate, although different amounts of additional constituents are also present. The author assumed the waters had reached equilibrium with respect to dolomite as a consequence of the large contact period between the waters and the rocks (the rate of ground water flow is very slow). Moreover, the ratio between magnesium and calcium concentrations was kept rather constant, suggesting the attainment of calcite-dolomite-solution equilibrium. Nevertheless, the solubility may be influenced by the rest of the species in solution. The amount of total dissolved solids in some cases cannot be neglected (values up to 3560 ppm). Another source of error is the inconstancy of temperature, which varies from 22 to 31°C during the measurements. The author reports the amount of bicarbonate in solution and the pH, but he claims those values "are usually quite inaccurate because of the tendency of bicarbonate in solution to equilibrate with the atmospheric CO_2".

Many of the sources reported in table 5-14 follow stability relations that are in disagreement with the approach followed in the present paper. This is the case of Bär (1932), Halla and Ritter (1935) and Yanat'eva (1952, 1955b, 1957a, 1960).

5.7 Parameters

Table 5-15

Extended UNIQUAC *r* and *q* parameters, fitted to experimental data

	r	*q*
H_2O	0.92	1.40
CO_2 (aq)	**0.75**	**2.45**
Na^+	1.40	1.20
H^+	0.14	$0.1\cdot10^{-15}$
Ba^{2+}	**15.67**	**14.48**
Ca^{2+}	3.87	1.48
Sr^{2+}	**7.14**	**12.89**
Mg^{2+}	5.41	2.54
OH^-	9.40	8.88
Cl^-	10.39	10.20
SO_4^{2-}	12.79	12.44
CO_3^{2-}	10.83	10.77
HCO_3^-	8.08	8.68

Table 5-16

$u_{ik}^0 = u_{ki}^0$ parameters for calculating extended UNIQUAC interaction energy parameters ($u_{ik} = u_{ik}^0 + u_{ik}^t(T - 298.15)$)

	H_2O	CO_2 (aq)	H^+	Na^+	Ca^{2+}	Ba^{2+}	Sr^{2+}	Mg^{2+}	OH^-	Cl^-	SO_4^{2-}	CO_3^{2-}	HCO_3^-
H_2O	0												
CO_2 (aq)	**8.838254**	**302.248**											
H^+	1×10^4	**10^{10}**	0										
Na^+	733.2863	**172.392**	10^{10}	0									
Ca^{2+}	496.3523	**2839.83**	10^{10}	**-100**	**0**								
Ba^{2+}	**-0.37858**	**2500**	**10^{10}**	**779.06**	**2989.759**	**0**							
Sr^{2+}	**543.1096**	**-100.74**	**10^{10}**	**-103.9**	**-402.783**	**2500**	**0**						
Mg^{2+}	-2.04282	**-581.18**	10^{10}	-70.96	155.2324	**628.5288**	**-400.581**	0					
OH^-	600.4952	**2500**	10^{10}	1398.1	164.6378	**2500**	**2500**	**736.423**	1562.9				
Cl^-	1523.393	**1613.01**	10^{10}	1443.2	1805.59	**1403.17**	**1895.877**	2049	1895.5	2214.8			
SO_4^{2-}	752.8792	**1942.4**	10^{10}	845.14	1258.103	**2500**	**2500**	1407.21	1225.7	2036.1	1265.83		
CO_3^{2-}	361.3877	**2500**	10^{10}	547.95	**-769.706**	**2500**	**2500**	**100**	1588	2724.9	1216.76	1458.344	
HCO_3^-	577.0502	**526.305**	10^{10}	1101.9	**2881.408**	**2500**	**2500**	**100**	2500	1736.6	990.48	800.0081	771.038

Table 5-17

$u_{ik}^t = u_{ki}^t$ parameters for calculating extended UNIQUAC interaction energy parameters ($u_{ik} = u_{ik}^0 + u_{ik}^t(T - 298.15)$)

	H_2O	CO_2 (aq)	H^+	Na^+	Ca^{2+}	Ba^{2+}	Sr^{2+}	Mg^{2+}	OH^-	Cl^-	SO_4^{2-}	CO_3^{2-}	HCO_3^-
H_2O	0												
CO_2 (aq)	**0.86293**	**0.35871**											
H^+	0	0	0										
Na^+	0.48719	**-0.4363**	0	0									
Ca^{2+}	-8.0654	**10.876**	0	**-4.656**	**0**								
Ba^{2+}	**0.58244**	**0**	**0**	**2.338**	**72.084**	**0**							
Sr^{2+}	**1.2742**	**0**	**0**	**-0.62**	**-4.2533**	**0**	**0**						
Mg^{2+}	-3.5542	**-2.855**	0	1.3394	5.1921	**0**	**-1.437**	0					
OH^-	8.5455	**0**	0	20.278	3.6084	**0**	**0**	**0**	5.6169				
Cl^-	14.631	**15.015**	0	15.635	11.14	**14.89**	**15.689**	12.132	13.628	14.436			
SO_4^{2-}	9.4905	**4.7896**	0	11.681	50.446	**0**	**10**	2.2791	8.5902	12.407	8.3194		
CO_3^{2-}	3.3516	**0**	0	3.782	**-22.727**	**0**	**0**	**1**	2.7496	5.7267	7.0067	-1.3448	
HCO_3^-	-0.38795	**-3.7342**	0	1.829	**35.213**	**0**	**0**	**1**	0	14.035	6.9646	1.7241	-0.0198

Table 5-18

α and β parameters for calculating the solubility product pressure dependency

	α	β
$BaSO_4$	**1.636629×10^{-3}**	**3.333826×10^{-7}**
$SrSO_4$	**1.035686×10^{-3}**	**7.153236×10^{-7}**
$CaSO_4$	**2.328718×10^{-3}**	**-8.421355×10^{-7}**
$CaSO_4\times2H_2O$	**1.078224×10^{-3}**	**3.078141×10^{-7}**
NaCl	**9.927134×10^{-5}**	**-1.358719×10^{-8}**
$CaCO_3$	**-3.916945×10^{-3}**	**-2.092925×10^{-5}**

Table 5-19

Thermodynamic properties and related parameters. Bold numbers are taken from the NIST Chemical Thermodynamics Database (1990). The rest of the values were fitted to experimental data.

	$\Delta_r G_f^0$ (kJ mol^{-1})	$\Delta_r H_f^0$ (kJ mol^{-1})	C_{p1} (J mol^{-1}K^{-1})	C_{p2} (J mol^{-1}K^{-2})	C_{p3} (J mol^{-1}K^{-2})
CO_2 (aq)	**-385.98**	**-413.8**	**243**	**0**	**0**
$CaCO_3$	-1129.057	-1208.726	**81.88**	**0**	**0**
$Mg(OH)_2$	-833.51	-921.1407	**77.03**	**0**	**0**
Na_2SO_4	**-1270.16**	**-1387.08**	**128.2**	**0**	**0**
NaCl	-384.1258	-411.9584	45.13074	0	0
$MgCO_3$	**-1012.1**	**-1095.8**	**75.52**	**0**	**0**
$MgCO_3{\cdot}3H_2O$	-1723.487	-1953.29	301.4968	0	0
$MgCO_3{\cdot}5H_2O$	-2197.745	-2524.95	367.367	0	0
$3MgCO_3{\cdot}Mg(OH)_2{\cdot}3H_2O$	-4602.818	-5069.43	478.6986	0	0
$BaCO_3$	-1136.054	-1222.907	85.5	0	0
$SrCO_3$	-1139.745	-1227.633	1259.146863	-2.827237	-21149.44
$CaCO_3{\cdot}MgCO_3$	**-2140.89**	**-2302.72**	**157.4**	**0**	**0**

5.8 References in Chapter 5

Alderman, A.R., Von der Borch, C.C., 1961. Occurrence of magnesite-dolomite sediments in South Australia. Nature 192, 861.

Anderson, G.K., 2002. Solubility of carbon dioxide in water under incipient clathrate formation conditions. J. Chem. Eng. Data 47, 219-222.

Arnorsson, E., 1989. Deposition of calcium carbonate minerals from geothermal waters. Theoretical considerations. Geothermics 18, 33-39.

Bamberger, A., Sieder, G., Maurer, G., 2000. High pressure (vapor-liquid) equilibrium in binary mixtures of (carbon dioxide + water or acetic acid) at temperatures from 313 to 353 K. Journal of Supercritical Fluids 17 (2), 97-110.

Baron, G., Favre, J., 1958. The present state of research directed to the synthesis of dolomite. Inst. Français Pétrole Rev. et Ann. Combustible Liquides 13, 1067-1085.

Baron, G., Wyart, J., 1958. Sur le role des facteurs physicochimiques dans la synthese hydrothermale de la giobertite CO_3Mg a partir des solutions de bicarbonate de magnésium. Acad. Sci. Comptes Rendís 247, 485-487.

Baron, G., 1960. Sur la synthese de la dolomite application au phenomene de dolomitisation. Revue de L' Institut Français du Pétrole 15, 3-68.

Bartholome, E., Friz, H., 1956. Solubility of carbon dioxide in water at high pressures. Chem. Ing. Tech. 28, 706-708.

Beckurts, H., 1881. Beiträge zur kenntniss der carbonate des magnesiums. Arch. Pharm. 18, 429-443.

Benes, P., Selecká, H., 1973. Ion pair formation and solubility of barium carbonate in aqueous solutions. Radiochem. Radioanal. Lett. 13, 339-348.

Berg, L.G., Borisova, L.A., 1960a. Solubility isotherms of the ternary systems Mg^{2+}, $Ca^{2+}//CO_3^{2-}$, H_2O, Na^+, $Ca^{2+}//CO_3^{2-}$, H_2O and Na^+, $Mg^{2+}//CO_3^{2-}$, H_2O at 25°C and PCO_2 = 1 atmosphere. Russian Journal of Inorganic Chemistry 5, 618-620.

Berg L.G., Borisova L.A., 1960b. Metastable equilibria in the quaternary reciprocal system Mg^{2+}, $Ca^{2+}// CO_3^{2-}$, SO_4^{2-}, H_2O at 25°C and PCO_2=1 atmosphere. Russian Journal of Inorganic Chemistry 5, 620-622.

Berner, R.A., 1967. Comparative dissolution characteristics of carbonate minerals in the presence and absence of aqueous magnesium ion. American Journal of Science 265, 45-70.

Bertram, M.A., Mackenzie, F.T., Bishop, F.C., Bischoff, W., 1991. Influence of temperature on the stability of magnesian calcite. American Mineralogist 76, 1889-1896.

Bischoff, J.L., 1968. Kinetics of calcite nucleation: magnesium ion inhibition and ionic strength catalysis. J. Geophys. Res. 73, 3315-3322.

Busenberg, E., Plummer, L.N., Parker, V.B., 1984. The solubility of strontianite ($SrCO_3$) in CO_2-H_2O solutions between 2 and 91°C, the association constants of $SrHCO_3^+$(aq) and $SrCO_3^0$(aq) between 5 and 80°C, and an evaluation of the thermodynamic properties of Sr^{2+}(aq) and $SrCO_3$(cr) at 25°C and 1 atm total pressure. Geochimica et Cosmochimica Acta 48, 2021-2035.

Busenberg, E., Plummer, L.N., 1986. The solubility of $BaCO_3$(cr) (witherite) in CO_2-H_2O solutions between 0 and 90°C, evaluation of the association constants of $BaHCO_3^+$(aq) and $BaCO_3^0$(aq) between 5 and 80°C, and a preliminary evaluation of the thermodynamic properties of Ba^{++}(aq). Geochimica et Cosmochimica Acta 50, 2225-2233.

Bär, O., 1932. Beitrag zum thema dolomitentstehung. Zentralblatt für mineralogie und paläontologie, 46-62.

Cameron, F.K., Briggs, L.J., 1901. Equilibrium between carbonates and bicarbonates in aqueous solution. The Journal of Physical Chemistry 5, 537-555.

Carpenter, A.B., 1963. Mineralogy of the system CaO-MgO-CO_2-H_2O at Crestmore, California. PhD Dissertation, Harvard University, USA.

Cesaro, G., 1910. Crystalline form and composition of hydrated carbonate magnesite. Bull. Cl. Acad. R. Belg. 4, 234-235.

Chase, M.W., 1998. NIST-JANAF Thermochemical Tables, 4th edition, J. Phys. Chem. Ref. Data, Monograph 9, 1-1951.

Christ C.L., Hostetler P.B., 1970. Studies in the system MgO-SiO_2-CO_2-H_2O (II): The activity product constant of magnesite. American Journal of Science 268, 439-453.

Corti, H.R., de Pablo, J.J., Prausnitz, J.M., 1990a. Phase equilibria for aqueous systems containing salts and carbon dioxide. Application of Pitzer's theory for electrolyte solutions. J. Phys. Chem. 94, 7876-7880.

Corti, H.R., Krenzer, M.E., de Pablo, J.J., Prausnitz, J.M., 1990b. Effect of a dissolved gas on the solubility of an electrolyte in aqueous solution. Ind. Eng. Chem. Res. 29, 1043-1050.

Cramer, S.D., 1982. The solubility of methane, carbon dioxide, and oxygen in brines from 0° to 300°C. US Bureau of Mines Report of Investigations, vol. 8706, pp.1-17.

Curry, J., Hazelton, C.L., 1938. The solubility of carbon dioxide in deuterium oxide at 25°C. J. Am. Chem. Soc. 60, 2771-2773.

Dandurand J.L., Schott J., 1977. Stabilite de la magnesite et de la dolomite; interpretation des resultats de mise en solution et de synthese par thermodiffusion. Bull. Soc. Fr. Mineral. Cristallogr. 100, 94-99.

D'Ans, J., Gloss, G., 1938. Über das $MgCO_3{\cdot}3H_2O$, über basische Carbonate, neue Doppelverbindungen des Magnesiumcarbonats und über basische Magnesiumsulfate. Kali 32, 155-158.

Davies, P.J., Bubela, R., 1973. The transformation of nesquehonite into hydromagnesite. Chem. Geol. 12, 289-300.

Dell, R.M., Weller, S.W., 1959. The thermal decomposition of nesquehonite, $MgCO_3{\cdot}3H_2O$, and magnesium ammonium carbonate $MgCO_3(NH_4)_2CO_3{\cdot}4H_2O$. Trans. Faraday Soc. 55, 2203-2220.

Diamond, L.W., Akinfiev, N.N., 2003. Solubility of CO_2 in water from -1.5 to 100°C and from 0.1 to 100 MPa: evaluation of literature data and thermodynamic modeling. Fluid Phase Equilibria 208 (1-2), 265-290.

Dyer, S.J., Graham, G.M., 2002. The effect of temperature and pressure on oilfield scale formation. Journal of Petroleum Science and Engineering 35, 95-107.

Ellis, A.J., 1959a. The solubility of calcite in carbon dioxide solutions. American Journal of Science 257, 354-365.

Ellis, A.J., 1959b. The solubility of carbon dioxide in water at high temperatures. American Journal of Science 257, 217-234.

Ellis, A.J., 1963. The solubility of calcite in sodium chloride solutions at high temperatures. American Journal of Science 261, 259-267.

Ellis A.J., Golding R.M., 1963. The solubility of CO_2 above 100°C in water and in NaCl solutions. American Journal of Science 261, 47-60.

Engel, M., 1889. Sur la solubilité des sels en présence des acides, des bases et de sels. Ann. Chim. Phys. 17, 349-369.

Fenoglio, M.1930. The presence of nesquehonite in the Viu serpentine of the Lanzo Valley. Atti R. Accad. Lincei, Cl. Sci. Fis. Mat. Nat., Rend. 11, 310-316.

Fenoglio, M., 1933. Lansfordite from the mine at Cogne in the Aosta Valley. Period. Mineral. 4, 433-462.

Fenoglio, M., 1935. Research on nesquehonite from the mine at Cogne in the Aosta Valley. Period. Mineral. 6, 1-17.

Fenoglio, M., 1936. Natural hydrated neutral and basic magnesium carbonates. Atti R. Accad. Lincei, Cl. Sci. Fis. Mat. Nat., Rend. 24, 219-222.

Frear, G.L., Johnston, J., 1929. Solubility of calcium carbonate in certain aqueous solutions. Journal of American Chem. Society 51, 2082-2093.

Garrels, R.M., Thompson, M.E., Siever, R., 1960. Stability of some carbonates at 25°C and one atmosphere total pressure. American Journal of Science 258, 402-418.

Garrels, R.M., Thompson, M.E., 1962. A chemical model for sea water at 25°C and one atmosphere total pressure. American Journal of Science 260, 57-66.

Geffcken, G., 1904. Beiträge zur Kenntnis der Löslichkeitsbeeinflussung. Z. Physik. Chem. 49, 257-302.

Genth, F.A., 1888. Lansfordite, a new mineral. Z. Krystallogr. Mineral. 14, 255-256.

Genth, F.A., Penfield, S.L., 1890. On lansfordite, nesquehonite, and a phseudomorph by nesquehonite on lansfordite. Z. Krytallogr. Mineral. 17, 561.

Giester, G., Lengauer, C.L., Rieck, B., 2000. The crystal structure of nesquehonite, $MgCO_3{\cdot}3H_2O$, from Lavrion, Greece. Mineral and Petrology 70, 153-163.

Giles, M., 2001. Carbonates mineral solubility at low temperatures in the Na-K-Mg-Ca-H-Cl-SO_4-OH-HCO_3-CO_3-CO_2-H_2O system. Geochimica et Cosmochimica Acta 65(12), 1883-1896.

Gill, J.S., 1998. Silica scale control. Chemical Treatment, 41-45.

Gillespie, P.C., Wilson, G.M., 1982. Gas Processor Association, Tulsa, Research Report RR48 (cited in Diamond and Akinfiev (2003)).

Gothe, E., 1915. Solubility of calcium carbonate and magnesium carbonate in water free from carbon dioxide, with a consideration of the s2. Chem. Ztg. 39, 305-307.

Graf, D.L., Goldsmith, J.R., 1955. Dolomite-magnesian calcite relations at elevated temperatures and CO_2 pressures. Geochimica et Cosmochimica Acta 7, 109-128.

Graf, D.L., Goldsmith, J.R., 1956. Some hydrothermal syntheses of dolomite and protodolomite. J. Geol. 64, 173-186.

Graf, D.L., Eardley, A.J., Shimp, N.F., 1961. A preliminary report on magnesium carbonate formation in Glacial Lake Bonneville. Jour. Geology 69, 219-223.

Graham, G.M., Mackay, E.J., 2003. A background to inorganic scaling-mechanisms, formation and control. 5th Intl. SPE Oilfield Scale Symposium. Aberdeen, UK.

Gurevich, V.M., Gavrichev, K.S., Gorbunov, V.E., Danilova, T.V., Golushina, L.N., Khodakovskii, I.L., 1999. Low-temperature heat capacity of witherite $BaCO_3$(c).

Geochemistry International 39(10), 1007-1014.

Haehnel, O., 1924. Über die Löslichkeit det Carbonate des Strontiums, des Bariums and der Schwermetalle in Wasser unter hohen Kohlendioxyddrucken sowie über die Eigenschaften solcher Lösungen. J. Prakt. Chem. 108, 187-193.

Halla, F., Ritter, F., 1935. Eine Methode zur Bestimmung der Änderung der freien Energie bei Reaktionen des Typus A(s) + B(s) = AB(s) und ihre Anwendung auf das Dolomitproblem. Zeitschr. Phys. Chem. 175A, 63-82.

Halla, F., 1936. Mitteilungen der Wiener mineralogischen Gesellschaft. Tschermaks Mineral. Petrog. Mitt. 101, 275-278.

Halla, F., 1958. Thermodynamics of dolomite formation. I. A revision. Zeitschrift fuer Physikalische Chemie 17, 368-374.

Halla, F., Chilingar, G.V., Bissel, H.J., 1962. Thermodynamic studies on dolomite formation and their geologic implications: An interim report. Sedimentology 1, 296-303.

Halla, F., Van Tassel, R. 1964. Löslichkeitsanomalien beim Magnesit. Redes Rundschau 1, 42-43.

Harker, R.I., Tuttle, O.F., 1955. Studies in the system CaO-MgO-CO_2. Part 1. The thermal dissociation of calcite, dolomite and magnesite. American Journal of Science 235, 209-224.

Harned, H.S., Davis, R., 1943. The ionization constant of carbonic acid in water and the solubility of CO_2. J. Am. Chem. Soc. 65, 2030-2037.

Harned H.S., Bonner F.T., 1945. The first ionization of carbonic acid in aqueous solutions of sodium chloride. J. Am. Chem. Soc. 67, 1026-1031.

He S., Morse J.W., 1993. The carbonic acid system and calcite solubility in aqueous Na-K-Ca-Mg-Cl-SO_4 solutions from 0 to 90°C. Geochimica et Cosmochimica Acta 57, 3533-3554.

Harvie C.E., Möller N., Weare J.H., 1984. The prediction of mineral solubilities in natural waters: The Na-K-Mg-Ca-H-Cl-SO_4-OH-HCO_3-CO_3-CO_2-H_2O system to high temperatures and pressures. Geochimica et Cosmochimica Acta 48, 723-751.

Helz, G.R., Holland, H.D., 1965. The solubility and geologic occurrence of strontianite. Geochimica et Cosmochimica Acta 20, 1303-1315.

Holleman, A.F., 1893. Bestimmungen der Löslichkeit sogenannter Unlöslicher salze. Z. Phys. Chem. 12, 125-139.

Hostetler, P.B., 1964. The degree of saturation of magnesium and calcium carbonate minerals in natural waters. I.A.S.H. Comm. Subterranean Waters 64, 34-39.

Hsu, K.J., 1963. Solubility of dolomite and composition of Florida ground waters. Journal of Hydrology 1, 288-310.

Hähnel, O., 1920. Centr. Min. Geol. 25, 25-32 (cited in Diamond and Akinfiev (2003)).

Johnston, J., 1915. The solubility-product constant of calcium and magnesium carbonates. Jour. Am. Chem. Soc. 37, 2001-2020.

Juranek, J., Skollova, Z., Harnova, J., 1987. MINEQUA-Part I. A program for computing the chemistry of calcium carbonate in mineralized and thermal waters. Geothermics 16, 263-270.

Kapustinsky, A.F., Dezideryeva, L.P., 1946. The thermodynamics of strontium. Trans. Faraday Soc. 42, 69-77.

Katz, A., 1971. Zoned dolomite crystals. J. Geol. 79, 38-51.

Kazakov, A.V., Tikhomirova, M.M., Plotnikova, V.I., 1959. The system of carbonate equilibria. Internat. Geol. Rev. 1(10), 1-39.

Kelley and Anderson, 1935. U.S. Bureau of Mines. Bull. 384 (cited in Kapustinsky and Dezideryeva, 1946).

Kendall, J., 1912. The solubility of calcium carbonate in water. Philos. Mag. Ser. 23(6), 958-976.

Kiepe, J., Horstmann, S., Fischer, K., Gmehling, J., 2002. Experimental determination and prediction of gas solubility data for CO_2 + H_2O mixtures containing NaCl or KCl at temperatures between 313 and 393 K and pressures up to 10 MPa. Industrial & Engineering Chemistry Research 41(17), 4393-4398.

Kindyakov, P.S., Khokhlova, A.V., Lapchinskaya, L.L., 1958. Solubility in the reciprocal system lithium carbonate-calcium hydrate-water. Tr. Mosk. Inst. Tonkoi Khim. Tekhnol. 7, 32-44.

Kinsman, D.J.J., 1964. Recent carbonate sedimentation near Abu Dhabi, Trucial Coast, Persian Gulf. PhD dissertation, Imperial College, London.

Kiss, A.V., Lajtai, I., Thury, G., 1937. Über die Löslichkeit von Gasen in Wasser-Nichtelektrolytgemischen. Z. anorg. allg. Chemie 233, 346-352.

Kittrick, J.A., Peyrea, F.J., 1986. Determination of the gibbs free energy of formation of magnesite by solubility methods. Soil Sci. Soc. Am. J. 50, 243-247.

Kline, W.D., 1929. Solubility of magnesium carbonate in water and CO_2. J. Am. Chem. Soc. 51, 2093-2097.

Kohlrausch, F., Rose, F.F., 1893. Die Löslichkeit einiger schwer Löslicher Körper im Wasser, beurteilt aus der elektrischen Leitungsfähigkeit der Lösungen. Z. Physik. Chemie 12, 234-243.

Kritschewsky, I.R., Shaworonkoff, N.M., Aepelbaum, V.A., 1935. Gemeinsame Löslichkeit der Gase in Flüssigkeiten unter Druck. Zeit. Phys. Chem. A 175, 232-238.

Kunerth, W., 1992. Solubility of CO_2 and N_2O in certain solvents. Phys. Rev. 2, 512-524.

Königsberger, E., Königsberger, L-C., Gamsjäger, H., 1999. Low-temperature thermodynamic model for the system Na_2CO_3-$MgCO_3$-$CaCO_3$-H_2O. Geochimica et Cosmochimica Acta 63(19/20), 3105-3119.

Langmuir, D., 1964. Stability of carbonates in the system CaO-MgO-CO_2-H_2O. PhD dissertation, Harvard University.

Langmuir, D., 1965a. Stability of carbonates in the system MgO-CO_2-H_2O. Journal of Geology 73, 730-750.

Langmuir, D., 1965b.Stability of carbonates in the system CaO-MgO-CO_2-H_2O. Journal of Geology 73(5), 730-754.

Latimer, W.M., 1952. The oxidation states of the elements and their potentials in aqueous solutions. 2nd ed. Englewood Cliffs. N.J., Prentice Hall.

Leather, J.W., Sen, J.N., 1910. The system water, calcium carbonate, carbonic acid. Memoirs of the Department of Agriculture in India 1, 117-131.

Leather, J.W., Sen, J.N., 1914. The systems: (a) water, magnesium carbonate and carbonic acid, (b) water, calcium carbonate, magnesium carbonate and carbonic acid. Memoirs Dept. Agric. India Chem. Series 3(8), 205-221.

Leick, J., 1932. The solubilities of calcium carbonate and of magnesium carbonate in water that is free from carbonic acid. Zeitschrift für Analytische Chemie 87, 415-422.

Leitmeier, H., 1915. Zur kenntnis der carbonate II. Neues Jahrb. Mineralog., Abt. B, 655-700.

Levchenko,V.M., Minkin, M.B., Dukhina, T.P., 1970. Magnesium carbonate solubility. Pochvovedenie 8, 144-148.

Li, Y.H., Crane, S.D., Coleman, J. R., 1995. Novel approach to predict the co-precipitation of $BaSO_4$ and $SrSO_4$. SPE 29489, 447-461.

Lippmann, F., 1980. Phase diagrams depicting aqueous solubility of binary mineral systems. Neues Jahrb. Mineralog. Abh. 139, 1-25.

López Gómez, P., 1975. El sistema ternario MgO-CO_2-H_2O. Ion Revista Española de Química Aplicada 35, 417-430.

Lyashchenko, A. K., Churagulov, B. R., 1981. Influence of pressure on the temperature coefficients of the solubility of electrolytes in water. Russ. J. Inorg. Chem. 26, 642-644.

MacDonald, R.W., North, N.A., 1974. The effect of pressure on the solubility of $CaCO_3$, CaF_2 and $SrSO_4$ in water. Can. J. Chem. 52, 3181-3186.

Malegaonkar, M.B., Dholabhai, P.D., Bishnoi, P.R., 1997. Kinetics of carbon dioxide and methane hydrate formation. The Canadian Journal of Chemical Engineering 75, 1090-1099.

Malinin, S.D., 1963. An experimental investigation of the solubility of calcite and witherite under hydrothermal conditions. Geokhimiia 650-667, 631-645.

Malinin, S. D., Savel'eva, N. I., 1972. Carbon dioxide solubility in sodium chloride and calcium chloride solutions at temperatures of 25, 50, and 75.deg. and elevated carbon dioxide pressure. Geokhimiya, 643-653.

Malinin, S. D., Kurovskaya, N. A., 1975. Carbon dioxide solubility in solutions of chlorides at elevated temperatures and carbon dioxide pressure. Geokhimiya, 547-550.

Marck, R., Simek, A., 1913. Über die thermische dissoziation des magnesiumkarbonats. Zeitschr. Anorg. Chem 82, 17-49.

Markham, A.E., Kobe, K.A., 1941a. The solubility of carbon dioxide and nitrous oxide in aqueous salt solutions. J. Am. Chem. Soc. 63, 449-454.

Markham, A.E., Kobe, K.A., 1941b. The solubility of carbon dioxide in aqueous H_2SO_4, $HClO_4$. J. Am. Chem. Soc. 63, 1165-1166.

Matous, J., Sobr, J., Novak, J.P., Pick J., 1969. Solubility of carbon dioxide in water at pressures up to 40 atm. Collection Czechoslav. Chem. Commun. 34, 3982-3985.

McCoy, H.N., Smith, H.J., 1911. Equilibrium between alkali-earth carbonates, carbon dioxide and water. J. Am. Chem. Soc. 33, 468-476.

Merkel, 1924. Wagners Jahresbericht der Chemie 13, 213.

Miles, D.L., Burton, J.D., 1972. The solubility of strontium carbonate in water. Journal of the Chemical Society, Dalton Transactions, 1691-1692.

Miller, J.P., 1952. A Portion of the system calcium carbonate-carbon dioxide-water, with geological implications. Am. J. of Science 250, 161-203.

Millero, F.J., Milne, P.J., Thurmond, V.L., 1984. The solubility of calcite, strontianite, and witherite in NaCl solutions at 25°C. Geochimica et Cosmochimica Acta 48, 1141-1143.

Ming, D.W., Franklin, W.T., 1985. Synthesis and characterization of lansfordite and nesquehonite. Soil Science Society of American Journal 49, 1303-1308.

Mitchell, A.E., 1923. Studies on the dolomite system. Part II. J. Chem. Soc. 123, 1887-1904.

Morandi, M., 1969. La dissociazione termica dell'Idromagnesite e della Nesquehonite. Mineral. Petrogr. Acta 15, 93-108.

Moressée, M., Cesaro, G., 1910. Forme cristalline et composition du carbonate magnésique hydraté préparé par M. Moressée. Sa relation avec la Lansfordite. Bull. Acad. Roy. Belg., 234-265.

Morey, G.W., 1962. The action of water on calcite, magnesite, and dolomite. American Mineralogist 47, 1456-1460.

Morgan, O.M., Maass, O., 1931. An investigation of the equilibria existing in gas-water systems forming electrolytes. Canadian journal of research 5, 162-199.

Morrison, T.J., Billett, F., 1952. The salting-out of non-electrolytes. Part I. The effect of ionic size, ionic charge, and temperature. Journal of Chemical Society, 3814-3822.

Murray, C.N., Riley, J.P., 1971. The solubility of gases in distilled water and sea water IV. Carbon dioxide. Deep-Sea Research 18, 533-541.

Müller, G., Bender, E., Maurer,G., 1988. The vapor-liquid equilibrium of the ternary system ammonia-carbon dioxide-water for high water concentrations at 373-473 K. Ber. Bunsenges. Phys. Chem. 92, 148-160.

Naumov, V.B., Khakimov, A.K., Khodakovskii, I.L., 1974. Solubility of carbon dioxide in concentrated chloride solutions at high temperatures and pressures. Geokhimiya 1, 45-55.

Navrotsky, A., Capobianco, C., 1987. Enthalpies of formation of dolomite and of magnesian calcites. American Mineralogist 27, 782-787.

Nighswander, J.A., Kalogerakis, N., Mehrota, A.K., 1989. Solubilities of carbon dioxide in water and 1 wt% NaCl. J. Chem. Eng. Data 34, 355-360.

NIST Chemical Thermodynamics Database Version 1.1, 1990. U.S. Department of Commerce, National Institute of Standards and Technology, Gaithesburg MD 20899.

NIST Standard Reference Database Number 69, 2003. NIST Chemistry Book (http://webbook.nist.gov/chemistry/).

Novak, J., Fried, V., Pick, J., 1961. Löslichkeit des Kohlendioyds in Wasser bei verschiedenen Drücken und Temperaturen. Collect. Czech. Chem. Commun. 26, 2266-2270.

Oleinik, P.M. Neftepromyslovoe Delo 8, p.7 (cited in Diamond and Akinfiev (2003)).

Onda K., Sada E., Kobayashi T., Kito S., Ito K., 1970. Salting out-parameters of gas solubility in aqueous salt solutions. Journal of Chemical Engineering of Japan 3, 18-24.

Palache, C., Berman, H., Frondel, C., 1951. The system of mineralogy, vol. 2, 7th edition, New York, John Wiley and Sons.

Patterson, C.S., Slocum, G.H., Busey, R.H., Mesmer, R.E., 1982. Carbonate equilibria in hydrothermal systems: First ionization of carbonic acid in NaCl media to 300°C. Geochimica et Cosmochimica Acta 46, 1653-1663.

Patterson C.S., Busey R.H., Mesmer R.E., 1984. Second ionization of carbonic acid in NaCl media to 250°C. J. Solution Chemistry 13, 647-661.

Pfaff, F.W., 1894. Beiträge zur Erklärung über die Entstehung des Magnesits und Dolomits. Neues Jahrb. Mineralog, 485-507.

Pitzer, K.S., 1973. Thermodynamics of electrolytes I. Theoretical basis and general equations. J. Phys. Chem. 77, 268-277.

Plummer, L.N., Busenberg, E., 1982. The solubilities of calcite, aragonite and varetite in CO_2-H_2O solutions between 0 and 90°C, and an evaluation of the aqueous model for the system $CaCO_3$-CO_2-H_2O. Geochimica et Cosmochimica Acta 46, 1011-1040.

Plummer, L.N., Mackenzie, F.T., 1974. Predicting mineral solubility from rate data: application to the dissolution of magnesian calcites. American Journal of Science 274, 61-83.

Poitevin, E., 1924. A new occurrence of landsfordite from Atlin, BC. Am. Mineral. 9, 225-228.

Ponizovskii, A.M., Vladimirova, N.M., 1959. Solubility of the system Na, Mg, Cl, HCO_3 - H_2O. Dokl. Akad. Nauk. SSSR 126(1), 345-346.

Ponizovskii, A.M., Vladimirova, N.M., Gordon-Yanovskii, F.A., 1960. The solubility relation in the system Na, Mg-Cl, HCO_3-H_2O at 0°C with carbon dioxide at 4 and 10 kg/cm^2. Russ. J. Inorg. Chem. 5, 1250-1252.

Postigo, M.A., Pedrosa, G., Katz, M., 1978. Nuevo método experimental para la determinación de solubilidad de gases en líquidos. Anales Asoc. Quim. Argentina 66, 25-30.

Potatov, V.V., Kashpura, V.N., Alekseev, V.I., 2001. A study of the growth of deposits in geothermal power systems. Thermal Engineering 48 (5), 395-400.

Prutton, C.F., Savage, R.L., 1945. The solubility of carbon dioxide in calcium chloride-water solutions at 75, 100, 120°C and high pressures. J. Am. Chem. Soc. 67, 1550-1154.

Raade, G., 1970. Dypingite, a new hydrous basic carbonate of magnesium from Norway. Am. Min. 55, 1457-1465.

Riesen, W.F., 1969. Thermodynamische Untersuchungen am quaternären System Ca^{2+}-Mg^{2+}-CO_2-H_2O. PhD thesis. Universität Bern.

Robie, R.A., 1965. Heat and free energy of formation of herzenbergite, troilite, magnesite, and rhodochrosite calculated from equilibrium data. U.S. Geol. Survey 525, 65-72.

Robie, R.A., Hemingway, B.S., 1972. The heat capacities at low-temperatures and entropies at 298.15 K of nesquehonite, $MgCO_3{\cdot}3H_2O$, and hydromagnesite, $5MgO{\cdot}4CO_2{\cdot}5H_2O$. Am. Mineral. 57, 1768-1781.

Robie, R.A., Hemingway, B.S., 1973. The enthalpies of formation of nesquehonite, $MgCO_3{\cdot}3H_2O$, and hydromagnesite, $5MgO{\cdot}4CO_2{\cdot}5H_2O$. J. Res. U.S. Geol. Survey 1, 543-547.

Robie, R.A., Hemingway, B.S., Fisher, J.R., 1978. Thermodynamic properties of minerals and related substances at 298.15 K and 1 bar (10^5 Pascals) pressure and at higher temperatures. USGS Bull. 1452, U.S. Government Printing Office, Washington, D.C., pp. 456.

Robie, R.A., Hemingway, B.S., 1995. Thermodynamic properties of minerals and related substances at 298.15K and 1 Bar (10^5 Pascals) pressure and at higher temperatures. U.S. Geol. Survey Bull. 2131.

Robie, R.A., Waldbaum, D.R., 1965. Thermodynamic properties of minerals at high temperature and one atmosphere pressure. U.S. Geol. Survey Bull., 1-256.

Rossini and Bichowsky, 1936. Thermochemistry (cited in Kapustinsky and Dezideryeva, 1946).

Rossini, F.D., Wagman, D.D., Evans, W.H., Levine, S., Jaffe, I., 1961. Selected values of chemical thermodynamic properties. Part I. Tables: U.S. Natl. Bur. Standard Circ. 500.

Rosenberg, P.E., Holland, H.D., 1964. Calcite-Dolomite-Magnesite stability relations in solutions at elevated temperatures. Science 145(1), 700-701.

Rosenberg, P.E., Burt, D.M., Holland, H.D., 1967. Calcite-dolomite-magnesite stability relations in solutions: the effect of ion strength. Geochimica et Cosmochimica Acta 31, 391-396.

Rumpf B., Maurer G., 1993. An experimental and theoretical investigation on the solubility of carbon dioxide in aqueous solutions of strong electrolytes. Ber. Bunsenges. Phys. Chem. 97(1), 85-97.

Rumpf, B., Nicolaisen, H., Öcal, C., Maurer, G., 1994. Solubility of carbon dioxide in aqueous solutions of sodium chloride: experimental results and correlation. J. Solution Chemistry 23, 431-448.

Sander, W., 1912. Über die Löslichkeit der Kohlensäure in Wasser und einigen andern Lösungsmitteln unter höhern Drüken. Z. physik. Chem. 78, 513-549.

Sayles, F.L., Fyfe, W.S., 1973. The crystallization of magnesite from aqueous solution. Geochimica et Cosmochimica Acta 37, 87-99.

Schaller, W.T., Henderson, E.P., 1932. Mineralogy and drill cores from the potash field of New Mexico and Texas. U.S. Geol. Survey Bull. 833, pp. 124.

Schloemer, H., 1952. Hydrothermal studies in the system $CaO-MgO-CO_2-H_2O$. Neues Jahrb. Mineral. Monatshefte, 129-135.

Schloesing. 1872. Compt. Rend. 74, 1552-1556.

Schott, J., Dandurand, J.L., 1975. Stability of natural carbonates. New values for the free energies of formation of phases in the $MgO-CO_2-H_2O$ and $CaO-MgO-CO_2-H_2O$ systems. C.R. Hebd. Seances Acad. Sci., Ser. C 280 (1). 1247-1250.

Segnit, E.R., Holland, H.D., Biscardi, C. J., 1962. The solubility of calcite in aqueous solutions - I. Geochimica et Cosmochimica Acta 26, 1301-1331.

Servio, P., Englezos, P., 2001. Effect of temperature and pressure on the solubility of carbon dioxide in water in the presence of gas hydrate. Fluid Phase Equilibria 190, 127-134.

Seyler, C.A., Lloyd, P.V., 1917. Studies of the carbonates. Part III. Lithium, calcium, and magnesium carbonates. Journal of Chemical Society 111, 994-1001.

Shagiakhmetov, R.A., Tarzimanov, A.A., 1981.Deposited document SPSTL200khp-D81-1982 (cited in Diamond and Akinfiev (2003)).

Shams El Din, A.M., Mohammed, R.A., 1989. The problem of alkaline scale formation from a study on Arabian Gulf water. Desalination 71, 313-324.

Sharp, W.E., Kennedy, G.C., 1965. The system $CaO-CO_2-H_2O$ in the two phase region calcite + aqueous solution. J. Geol. 60, 391-403.

Sippel, R.F., Glover, E.D., 1964. The solution alteration of carbonate rocks. The effects of temperature and pressure. Geochimica et Cosmochimica Acta 28, 1401-1417.

Soave, G., 1972. Equilibrium constants from a modified Redlich-Kwong equation of state. Chem. Eng. Sci. 27, 1197-1203.

Sonderegger, J.L., Brower, K.R., LeFebre, V.G.A., 1976. A preliminary investigation of strontianite dissolution kinetics. Amer. J. Sci. 276, 997-1022.

Sorbie, K.S., Mackay, E.J., 2000. Mixing of injected, connate and aquifer brines in waterflooding and its relevance to oilfield scaling. Journal of Petroleum Science and Engineering 27, 85-106.

Stewart, F.H., 1949. The petrology of the evaporates of the Eskdale No. 2 boring east Yorkshire, pt. I. The lower evaporate bed. Mineralog. Mag. (London) 28 (206), 621-675.

Stewart, P.B., Munjal, P., 1970. Solubility of carbon dioxide in pure water, synthetic sea water, and synthetic sea water concentrates at -5° to 25°C and 10 to 45 atm pressure. Journal of Chemical and Engineering Data 15, 67-71.

Sureau, J.F., 1974. Étude expérimentale de la dolomitisation de la calcite. Bull. Soc. Fr. Minéral. Cristallogr. 97, 300-312.

Takahashi, G., 1927. Investigation on the synthesis of potassium carbonate by Mr. Engel. Bull. Imp. Hyg. Lab. (Tokyo) 29, 165-262.

Takenouchi, S., Kennedy, G.C., 1964. The binary system H_2O-CO_2 at high temperatures and pressures. American Journal of Science 262, 1055-1074.

Takenouchi, S., Kennedy, G.C., 1965. The solubility of carbon dioxide in NaCl solutions at high temperatures and pressures. American Journal of Science 263, 445-454.

Teng, H., Yamasaki, M., Chun, K., Lee, H., 1997. Solubility of liquid CO_2 in water at 2 temperatures from 278K to 293K and pressures from 6.44 Pa to 29.49 MPa and densities of the corresponding aqueous solutions. J. Chem. Thermodyn. 29, 1301-1310.

Thomsen, K., Rasmussen, P., 1999. Modeling of vapor-liquid-solid equilibrium in gas-aqueous electrolyte systems. Chemical Engineering Science 54, 1787-1802.

Thurmond, V.L., Millero, J.F., 1982. Ionization of carbonic acid in sodium chloride solutions at 25°C. J. Soln. Chem. 11, 447-456.

Townley, R.W., Whitney, W.B., Felsing, W.A., 1937. The solubilities of barium and strontium carbonates in aqueous solutions of some alkali chlorides. J. Amer. Chem. Soc. 59, 631-633.

Travers, A., Nouvel, 1929. Sur la solubilité de $Mg(OH)_2$ aux temperatures élevés. Compt. Rend. Hebd. 188, 499-501.

Treadwell, F.P., Reuter, M., 1898. Über die Löslichkeit der Bikarbonate des Calciums und Magnesiums. Zeitschrift fur Anorganische Chemie 17, 171-204.

Trendafelov, D., Balarew, C., Zlateva, I., Keremidtchieva, B., Gradinarov, S., 1994. Investigations of the $BaSO_4$ conversion to $BaCO_3$ in the quaternary reciprocal water-salt system $BaSO_4 + K_2CO_3 = BaCO_3 + K_2SO_4$. Comptes Rendus de l'Academie Bulgare des Sciences 47 (1), 47-50.

Tödheide, K., Franck, E.U., 1963. Das Zweiphasengebiet und die kritische Kurve im System Kohlendioxid-Wasser bis zu drucken von 3500 bar. Z. Phys. Chem. 37, 387-401.

Van Slyke, D.D., 1939. Determination of solubilities of gases in liquids with use of the Van Slyke-Neill manometric apparatus for both saturation and analysis. J. Biol. Chem. 130, 545-554.

Vazquez, G., Chenlo, F., Pereira, G., Peaguda, J., 1994. Carbon dioxide solubility in aqueous solutions of sodium chloride, copper (II) sulfate, potassium iodide and sodium bromide. Anales de Química 90(5-6), 324-328.

Vilcu, R., Gainar, I., 1967. Löslichkeit der gase unter druck in flüssigkeiten. I. Das system kohlendioxid-wasser. Rev. Roum. Chim. 12(2), 181-189.

Wat, R.M.S., Sorbie, K.S., Todd, A.C., Chen, P., Jiang, P., 1992. Kinetics of $BaSO_4$ crystal growth and effect in formation damage. SPE 23814, 429-437.

Wasmund, R., Bultmann, H., 1980. Einfluss des Saccharosegehalts auf die CO_2-Absorption wässriger Lösungen. Zuckerind. 105, 1085-1087.

Wattenberg, V.H., Timmermann, E., 1937. Die Löslichkeit von Magnesiumkarbonat und Strontiumkarbonat in Seewasser. Kieler Meeresforschungen 2(1), 81-94.

Wells, R.C., 1915a. The solubility of calcite in water in contact with the atmosphere, and its variation with temperature. J. Washington Academy of Sciences 5, 617-622.

Wells, R.C., 1915b. Solubility of magnesium carbonate in natural water. Journal of American Chemical Society 37, 1704-1707.

Weyl, P.K., 1959. The change in solubility of calcium carbonate with temperature and carbon dioxide content. Geochimica et Cosmochimica Acta 17, 214-225.

Wiebe, R., Gaddy, V.L., 1939. The solubility in water of carbon dioxide at 50, 75 and 100°C, at pressures to 700 atmosferes. J. Am. Chem. Soc. 61, 313-318.

Wiebe, R., Gaddy, V.L., 1940. The solubility of carbon dioxide in water at various temperatures from 12 to 40°C and at pressures to 500 atm. J. Am. Chem. Soc. 62, 815-817.

Wolf, M., Breitkopf, O., Puk, R., 1989. Solubility of calcite in different electrolytes at temperatures between 10 and 60°C and at CO_2 partial pressures of about 1kPa. Chemical Geology 76, 291-301.

Wroblewski, S.V., 1883. Ann. Phys. Chem.18, 290-308 (cited in Diamond and Akinfiev (2003)).

Yanat'eva O.K., 1949. Solubility in the system Ca, Mg / CO_3, SO_4-H_2O. Doklady Akademiia Nauk SSSR, 479-481.

Yanat'eva O.K., 1952. Solubility of dolomite in water salt solutions. Akad. Nauk SSSR 20, 252-286.

Yanat’eva, O.K., 1954. Solubility in the system $CaCO_3$-$MgCO_3$-H_2O at different temperatures and pressures of CO_2. Doklady Akad. Nauk. SSSR 96, 777-779.

Yanat'eva, O.K., 1955a. Solubility isotherms at 0 and 55°C for the system Ca, Mg||CO_3, SO_4-H_2O. Akad.Nauk SSSR 26, 266-269.

Yanat'eva, O.K., 1955b. Solubility in the system $CaCO_3$-$MgCO_3$-H_2O at different temperatures. Zhurnal Neorganicheskoi Khimii 1, 1473-1476.

Yanat'eva O.K., Danilova E.P., 1956. Application of the solubility diagram of the system $CaCO_3$-$MgCO_3$-H_2O for the characterization of certain carbonate rocks. Zhurnal Prikladnoi Khimii 29, 1152-1159.

Yanat'eva, O.K., 1957a. Solubility polytherms of the system ($CaCO_3$ + $MgSO_4$ || $CaSO_4$ + $MgCO_3$)-H_2O. Doklady-Akademii Nauk SSSR 112, 1056-1058.

Yanat'eva, O.K., 1957b. Solubility of the System Ca,Mg-CO_3, SO_4-H_2O at 25°C and PCO_2 of 0.0012atm. Zh. Neorgan. Khim. 2(9), 2183-2187.

Yanat'eva, O.K., 1960. The 70°C solubility isotherm of the Ca-Mg-CO_3-SO_4-H_2O system. Russian Journal of Inorganic Chemistry 5, 1247-1250.

Yanat'eva, O.K., Rassonskaya, I.S., 1961. Metastable equilibria and solid phases in the $CaCO_3$-$MgCO_3$-H_2O system. Russian Journal of Inorganic Chemistry 6, 730-733.

Yanat'eva, O.K., Rapoport, G.S., Rassonskaya, I.S., Ustinova, M.B., 1961. Physicochemical studies of calcium and magnesium carbonates applicable to the production of Sovelite. Zhurnal Prikladnoi Khimii 34, 2347-2350.

Yang, S.O., Yang, I.M., Kim, Y.S., Lee, C.S., 2000. Measurement and prediction of phase equilibria for water + CO_2 in hydrate forming conditions. Fluid Phase Equilibria 175, 75-89.

Yasunishi A., Tsuji M., Sada E., 1979. Solubility of CO_2 in aqueous mixed salt solutions. Advances in Chemistry Series 177, 189-203.

Yasunishi A., Yoshida F., 1979. Solubility of carbon dioxide in aqueous electrolyte solutions. Journal of Chemical and Engineering Data 24, 11-14.

Yeh, S.-Y., Peterson R.E., 1964. Solubility of carbon dioxide, krypton, and xenon in aqueous solutions. Journal of Pharmaceutical Sciences 53, 822-824.

Yuan, M., Todd, A.C., Sorbie, K.S., 1994. Sulfate scale precipitation arising from seawater injection: a prediction study. Marine and Petroleum Geology 11(1), 24-30.

Yuan, M.D., Anderson, M., Jamieson, E., 1997. Investigation and improvement of $BaSO_4$ scale inhibition tests. Society of Petroleum Engineers 37304, 765-768.

Zawisza, A., Malesinska, B., 1981. Solubility of carbon dioxide in liquid water. J. Chem. Eng. Data 26, 388-391.

Zelvenskii, Y.D., 1937. The solubility of carbon dioxide under pressure. Jour. Chem. Industry 14, 1250-1257.

Zheng, D-Q., Tain-Min, G., Knapp, H., 1997. Experimental and modeling studies on the solubility of CO_2, $CHClF_2$, CHF_3, $C_2H_2F_4$ and $C_2H_4F_2$ in water and aqueous NaCl solutions under low pressures. Fluid Phase Equilibria 129, 197-209.

6. Sodium Chloride

This chapter will analyze the performance of extended UNIQUAC for the system NaCl-H_2O at high pressure. This work has been submitted for publication as part of the paper titled "Prediction of mineral scale formation in geothermal and oilfield operations using the extended UNIQUAC model. Part II. Carbonate scaling minerals" in Geothermics (authors: Ada Villafáfila García, Kaj Thomsen and Erling H. Stenby).

6.1 NaCl-H_2O System

The volume and surface area parameters for Na^+ and Cl^-, together with all the binary interaction parameters required for the binary system NaCl-H_2O were reported in a previous paper (Thomsen and Rasmussen, 1999). Only the pressure parameters α and β for NaCl need therefore to be estimated on the basis of SLE data at high pressures. Values for these parameters are given in tables 5-15 to 5-18 in Chapter 5. The values for the standard state Gibbs free energy, enthalpy, and heat capacity for NaCl are reported in table 5-19.

The few studies found on the solubility of sodium chloride in pure water at pressures larger than the atmospheric pressure are reported in table 6-1. The experimental conditions and the number of measurements carried out and used in the present work (in brackets) are also given.

Table 6-1
Experimental NaCl-H_2O SLE data sets used for parameter estimation.

T (°C)	*P* (bar)	Number of data	*AAD* (m)	Reference
0/30	1/40	14 (14)	2.2E-02	Moeller (1862)
24	1/1500	10 (8)	6.6E-03	Cohen et al. (1911)
25	1/735.5	7 (7)	1.3E-02	Sill (1916)
30	1/1911	14 (6)	7.2E-03	Adams and Hall (1931)
75/300	1/57.5	9 (9)	5.1E-01	Liu and Lindsay (1972)
101.9/168.3	1/5.3	2 (2)	1.1E-01	Eddy and Menzies (1940)
150/350	3.5/137.7	8 (7)	4.4E-01	Schroeder et al.(1935)
183/646.2	7.3/405.8	18 (0)		Keevil (1942)
			***MAAD* (m)**:	**1.6E-01**

Cohen et al. (1911) withdrew samples for analysis after reducing the experimental pressure, a procedure which can lead to solid deposition and can cause erroneous measurements. Sill (1916) realized this problem and developed a new pressure bomb to avoid it. The agreement between both sources is very good, which seems to prove the results from Cohen et al. (1911) were not affected by solid deposition prior to solubility analysis.

Liu and Lindsay (1972) compared their results with those by Keevil (1942) and Seidell[1] (1965), and assured the agreement among the different sources is very good. They chose for comparison a plot of the solubility expressed as log(molality) versus temperature. When the plot units are changed to molality instead, it can be clearly observed that there is a large disagreement between Keevil (1942) and Liu and Lindsay (1972), with solubility differences as large as 1.75 m NaCl around 250°C. Keevil (1942) also disagrees with the data by Schroeder et al. (1935), and it can be concluded that Keevil's (1942) solubility measurements are considerably lower than the main tendency followed by the other sources reported in table 6-1. Keevil (1942) determined the vapour pressure of sodium chloride solutions at high temperatures. According to him, the experimental method used afforded an approximate measure of the solubility, useful in confirming the solubility curves at high temperatures. But it may be possible that the accuracy is not high enough to use those solubility data for parameter estimation.

Schroeder et al. (1935) reported both experimental temperature and NaCl solubility, but they did not mention the experimental pressure (which was the saturation pressure of the solution). In order to use these data, the total pressure was calculated from:

$$P = a_w P_w^{sat} \tag{6-1}$$

where P_w^{sat} is the saturation pressure for pure water at temperature T. The water activity was calculated according to the NaCl model presented by Archer (1992). The saturation pressure of water was calculated by the NIST/ASME steam properties formulation for general and scientific use (Harvey et al., 1996).

Some sources (Cohen et al., 1911, Adams and Hall, 1931 and Schroeder et al., 1935) determined sodium chloride solubility in pure water at temperatures or pressures above the range of interest in the present paper. That explains why the number of points used for parameter estimation is in many cases lower than the number of points reported.

The results obtained for the system NaCl-H_2O at high pressure can be divided into two different groups: up to 150°C, and from 150 to 300°C. For the first data set, the results obtained are very satisfactory, with a mean average absolute deviation between extended UNIQUAC calculations and the experimental data ($1.5 \cdot 10^{-3}$ m) lower than the average

---

[1] Seidell (1965) did not perform any experiment himself, but compiled data from Cohen et al. (1911), Sill (1916), and Adams and Hall (1931).

experimental standard deviation ($7.6 \cdot 10^{-3}$ m). Therefore, we can conclude that the calculations for the temperature range 0-150°C are within experimental accuracy.

Figure 6-1, the solubility diagram for the binary NaCl-H_2O system at 30°C, shows such good accuracy. Even though only experimental data up to 1000 bar were used for parameter estimation (higher pressures are difficult to find in geothermal and oil wells), figure 6-1 shows data up to 2000 bar. The prediction done by the extended UNIQUAC model for so large pressures is very good. Therefore, it can be concluded that although the parameters are estimated from data up to 1000 bar, the range of applicability is not limited to that pressure. The predictions performed by the extended UNIQUAC model in the pressure range from 1000 to around 2000 bar are within the experimental accuracy. The mean average absolute deviation between our calculations and the experimental data (8 points reported by Adams and Hall, 1931; and 2 points reported by Cohen et al., 1911) is $2.2 \cdot 10^{-3}$ m NaCl, well below the *ASD* of $7.6 \cdot 10^{-3}$ m.

Figure 6-1 also shows that the influence of pressure on sodium chloride solubility is not strong, as it only increases from 6.17 m NaCl at 1 bar to 6.45 m NaCl at 2000 bar. About 16 gram of salt will therefore precipitate from each kilo of water saturated with NaCl at 2000 bar if the pressure is reduced to atmospheric pressure.

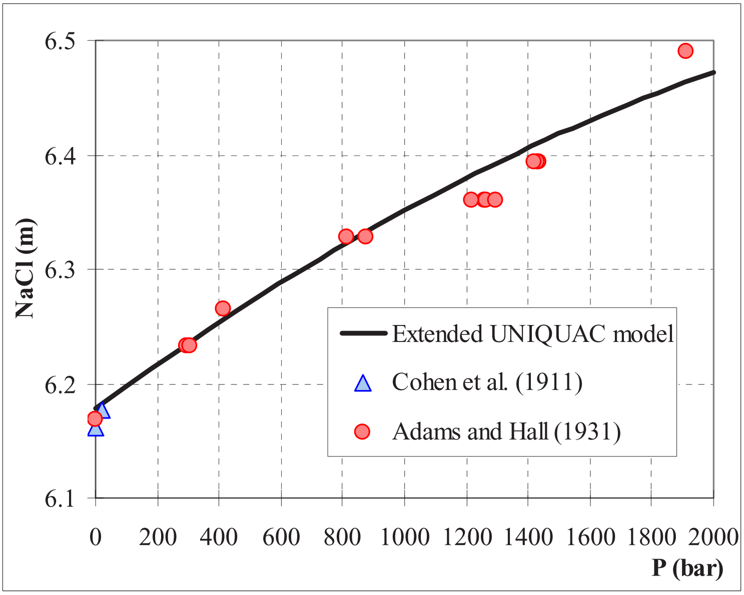

Figure 6-1. Experimental and calculated solid-liquid phase diagram for the NaCl-H_2O system at 30°C

The good agreement between the model and the experimental data from the first data set is not found for the second data set, which covers the temperature range from 150 to 300°C. The *MAAD* between the extended UNIQUAC calculations and the experimental data at high temperatures is $5.3 \cdot 10^{-1}$ m, which is larger than the *ASD*. There are only three sources covering that range of temperatures (Schroeder et al., 1935, Eddy and Menzies, 1940 and Liu and Lindsay, 1972). Schroeder et al. (1935) and Liu and Lindsay (1972) report solubility values quite close at similar T and P conditions. The latter investigators did not measure the solubility experimentally. Instead, they used an indirect method to obtain, from vapour pressure data, values for both the osmotic coefficient and concentration of saturated solutions. Liu and Lindsay (1972) claim that their method gives considerable precision. The lack of additional information on the system at high temperatures makes it difficult to determine the reliability of both datasets.

The *AAD* for each one of the sources used for the NaCl-H_2O system is shown in table 6-1. The *ASD* found for the experimental data at pressures higher than 1 atm is $7.6 \cdot 10^{-2}$ m NaCl, while the *ASD* for data at atmospheric pressure was calculated to be $5.3 \cdot 10^{-2}$ m. According to the International Critical Tables (1928), the solubility of sodium chloride in water is estimated experimentally with an accuracy of 0.2% ($3.4 \cdot 10^{-2}$ m) below 55°C and 1 atm, and of 0.5% ($8.6 \cdot 10^{-2}$ m) in the range 60 to 110°C. Above this temperature the accuracy is unknown (Eddy and Menzies, 1940). It is likely that the standard deviation at pressures higher than 1 atm is larger than those values, as the experimental conditions imply a higher difficulty. For all the sources in table 6-1 the *AAD* is lower than the *ASD*, except for Schroeder et al. (1935), Eddy and Menzies (1940) and Liu and Lindsay (1972), which happen to be the sources reporting experimental data at the highest temperatures.

The results obtained by the extended UNIQUAC model at atmospheric pressure and temperatures up to 110°C, and the sources at those conditions, are not mentioned here due to space considerations. Nevertheless, all the calculations performed at atmospheric pressure are within experimental accuracy. The mean average absolute deviation between extended UNIQUAC calculations and the experimental data for all the sources employing atmospheric pressures is $4.6 \cdot 10^{-2}$ m NaCl, while the average standard deviation for those experimental data is higher ($5.3 \cdot 10^{-2}$ m).

6.2 References in Chapter 6

Adams, L.H., Hall, R.E., 1931. The influence of pressure on the solubility of sodium chloride in water. A new method for the measurement of the solubilities of electrolytes under pressure. Journal of the Washington Academy of Sciences 21(9), 183-194.

Archer, D.G., 1992. Thermodynamic properties of NaCl+H_2O system II. Thermodynamic properties of NaCl (aq), NaCl·2H_2O (c), and phase equilibria. J. Phys. Chem. Ref. Data 21, 793-829.

Cohen, E., Inouye, K., Euwem, C., 1911. Piezochemische studien VII. Z. Physik. Chem. 75, 257-304.

Eddy, R.D., Menzies, A.W.C., 1940. The solubilities of certain inorganic compounds in ordinary water and in deuterium water. J. Phys. Chem. 44, 207-235.

Harvey, A.H., Perskin, A.P., Klein, S.A., 1996. NIST/ASME steam properties formulation for general and scientific use.

International Critical Tables, 1928. Vol. 3. McGraw-Hill Book Co., New York, pp.369.

Keevil, N.B., 1942. Vapor pressures of aqueous solutions at high-temperatures. J. Am. Chem. Soc. 64, 841-850.

Liu, C-T., Lindsay, W.T., 1972. Thermodynamics of sodium chloride solutions at high temperatures. Journal of Solution Chemistry 1(1), 45-69.

Moeller, 1862. Ueber den Einflufs der Drucke auf die Löslichkeit einiger Salze. Annals of Physics 117, 386-416.

Schroeder, W.C., Gabriel, A., Partridge, E.P., 1935. Solubility equilibria of sodium sulfate at temperatures of 150 to 350°C. I. Effect of sodium hydroxide and sodium chloride. Journal of the American Chemical Society 57, 1539-1546.

Seidell, A., 1965. Solubilities of inorganic and metal-organic compounds. Am. Chem. Soc., 4th ed., vol. 2, pp. 959.

Sill, H., 1916. The influence of pressure on solubility. Journ. Am. Chem. Soc. 38, 2632-2643.

Thomsen, K., Rasmussen, P., 1999. Modeling of vapor-liquid-solid equilibrium in gas-aqueous electrolyte systems. Chemical Engineering Science 54, 1787-1802.

7. Prediction of Scaling Minerals Solubilities in Natural Waters: Validation of the Model

The ability of the model to simulate within experimental accuracy the solubility behaviour of scaling minerals in binary, ternary and quaternary systems, from -20 to 300ºC, and up to 1000 bar, has been demonstrated in Chapters 4 to 6. In this chapter, the model will be validated by comparing our predictions to independent real natural waters data that were not used during the parameterization process. The brine compositions and observed scale occurrences were collected from published data (Mitchell et al., 1980, Jacques and Bourland, 1983, Yuan and Todd, 1991, Yuan et al., 1993).

The solid-liquid, vapour-liquid and speciation equilibria calculations explained in Chapter 3 have been implemented into SPECS (Separation and Phase Equilibrium Calculations). The program has been developed at IVC-SEP and is provided with a friendly user interface which allows the user to perform a great variety of tasks, including several equations of states and excess models, and a wide database of 100 components (http://www.ivc-sep.kt.dtu.dk/research/specs.htm). For electrolyte systems, the user can select up to 8 different ions among the species H_2O, $CO_2(aq)$, Na^+, K^+, Mg^{2+}, Ca^{2+}, NH_4^+, Ba^{2+}, H^+, Cu^{2+}, Ni^{2+}, Sr^{2+}, Fe^{2+}, Zn^{2+}, Mn^{2+}, Co^{2+}, Cl^-, SO_4^{2-}, NO_3^-, OH^-, CO_3^{2-}, HCO_3^-, SO_3^-, HSO_3^-, and $S_2O_5^{2-}$. Two different tasks are available: Calculation of binary, ternary and quaternary phase diagrams at constant pressure, and scale predictions for a given composition, temperature and pressure. In the latter case, the output file reports the solubility indices of the different salts forming the feed stream, and the precipitating minerals at equilibrium. The maximum amount of solid phase(s) precipitating is also reported. As a scaling prediction model, SPECS is useful to determine whether scale may occur at certain locations within the reservoir, and the maximum amount of precipitation to be expected. The model cannot directly predict the scaling rate, but it may be also useful in that sense as it determines the degree of supersaturation. SPECS determines the solid phase(s) precipitating at thermodynamic equilibrium. Whether that(those) phase(s) precipitate in reality or not is also determined by many other factors as kinetics. Therefore, it may be possible that any other salts which is supersaturated in the feed stream precipitates instead of that found at thermodynamic equilibrium.

7.1 Validation of the Model

Jacques and Bourland (1983) predicted celestite scaling tendency in three brines from the same field using an empirical equation developed from their own solubility measurements. Yuan and Todd (1991) also tested the scaling tendency in those waters using the model they developed for barium, strontium, and calcium sulphates based on Pitzer's framework. The results obtained by Jacques and Bourland (1983) and Yuan and Todd (1991), together with the results obtained by us, are reported in table 7-1. The chemical analyses of the waters and field observations regarding scale are also reported in table 7-1. In order to keep electrical neutrality in the solution, the amounts of Cl^- reported by Jacques and Bourland (1983) were slightly increased to 85910.7, 76517.9 and 84308.4 $mg \cdot L^{-1}$ for brines A, B and C, respectively. It was assumed that the density of the brines was comparable to that of water at the same temperature and pressure. Brine A corresponds to a well that had borderline $SrSO_4$ scaling tendency. Brine B was from a well that had $SrSO_4$ scale when untreated with scale inhibitor. Brine C came from a well without scaling problems. SI stands for solubility index, which is the activity product divided by the solubility product.

Table 7-1
$SrSO_4$ scale formation prediction

($mg \cdot L^{-1}$)	**A[1]**	**B[2]**	**C[3]**
Sr	560	565	550
Na	43817	39292	44275
Ca	7930	6977	6967
Mg	1422	1270	1215
Cl	85555	76148	83957
SO_4	210	540	100
HCO_3	232	311	360
T (ºF)	230	230	230
P (psig)	2500	2500	2500
SI ($SrSO_4$)			
Jacques and Bourland (1983)	1.01	2.38	0.43
Yuan and Todd (1991)	1.04	1.70	0.72
SPECS	1.39	3.72	0.68
Field Observation			
	Borderline	Scale	No scale

[1] A corresponds to a well that had borderline SrSO4 scaling tendency.

[2] Brine B was from a well that had SrSO4 scale when untreated with scale inhibitor.

[3] Brine C came from a well without scaling problems.

The agreement between our results and those reported by Jacques and Bourland (1983), and Yuan and Todd (1991), is good. In the three cases, the solubility index for celestite is above one for brines A and B, and below one for brine C, predicting scaling problems in wells A and B, but not in C. Our predicted solubility indices are the largest ones for brines A and B. Neither Jacques and Bourland (1983) nor Yuan and Todd (1991) included in their models the possibility of precipitation of any other mineral but $CaSO_4$, $SrSO_4$ and $BaSO_4$ (Jacques and Bourland (1983) did not even consider the possibility of co-precipitation of different sulphate minerals, but focused only on $SrSO_4$). This fact may explain the different solubility indices obtained in table 7-1. SPECS also predicts precipitation of $CaCO_3$ for the three brines.

The composition of the formation water of one of the major oilfields in the North Sea (Forties oilfield) and of the North sea injection water is reported in table 7-2. The sulphate scaling tendency in the mixed injection and formation water was predicted by SPECS at different temperatures and pressures, and the results obtained by our model have been compared to predictions performed by Mitchell et al. (1980), Yuan and Todd (1991), and Yuan et al. (1993) for the same waters. Figures 7-1 to 7-4 illustrate the predicted results by SPECS. In all the cases, the largest saturation index is obtained for barite, and the lowest one for gypsum or anhydrite. Thus, barite is the most likely mineral to precipitate, unless kinetic impediments avoid it. At all temperature and pressure conditions, mixtures of injection and formation water containing from 0 to 100% seawater were undersaturated with respect to both anhydrite and gypsum. For mixtures ranging from 20 to 80% seawater, the model predicts barite and celestite precipitation, but for 20% seawater at 25ºC and 300 bar, where the saturation index for $SrSO_4$ is 0.9873. The amounts of solid precipitating are also indicated in figures 7-1 to 7-4. Note that the mixing ration at which maximum mineral precipitation is obtained does not correspond to the maximum supersaturation. For example, at 25ºC and 1 bar, the largest predicted amount of $BaSO_4$ precipitation (350 $mg \cdot L^{-1}$) is obtained at 20% seawater, while the largest supersaturation (SI equal to 1200) corresponds to 60% seawater.

The agreement between our results and those reported by Mitchell et al. (1980), Yuan and Todd (1991), and Yuan et al. (1993) is very good. The same minerals are predicted to precipitate, and the maximum calculated amounts of precipitated $SrSO_4$ and $BaSO_4$ are very close. Yuan and Todd's (1991) results are presented in figures 4A to 5D in their paper, and in figures 1 and 2 in Yuan el al's. (1993) paper. According to Yuan and Todd (1991), these predictions are confirmed by field observation and have been reported by Mitchell et al. (1980), Hughes and Whittingham (1982), and Tanner and Whittingham (1986).

It can be observed in figures 7-1 to 7-4 that barite is more likely to form at 25ºC than at 100ºC, and its precipitation is also favoured at low pressures. On the other hand, celestite is more likely to precipitate at 100ºC than at 25ºC, and its precipitation is also favoured at low pressures. Regarding the ratio between injected and seawater, the largest solubility indices for both salts are found around 60% seawater, while the maximum amount of precipitation is found at different mixture ratios depending on temperature and pressure.

Table 7-2
Composition of Forties and North Sea water

Ions ($mg \cdot L^{-1}$)	Forties water	North Sea water
Na	30200	11000
K	430	340
Mg	480	1320
Ca	3110	403
Ba	250	0
Sr	660	0
Cl	53000	19800
SO_4	0	2480
HCO_3	360	135

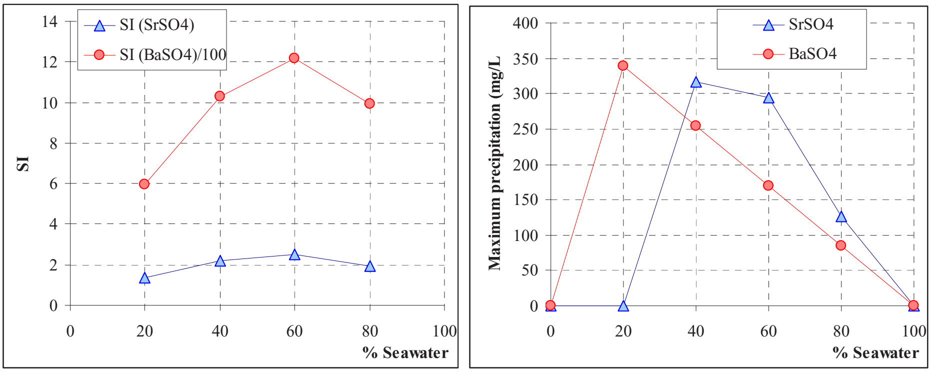

Figure 7-1. SPECS predictions for mixtures of North Sea and Forties water at 25°C and 1 bar

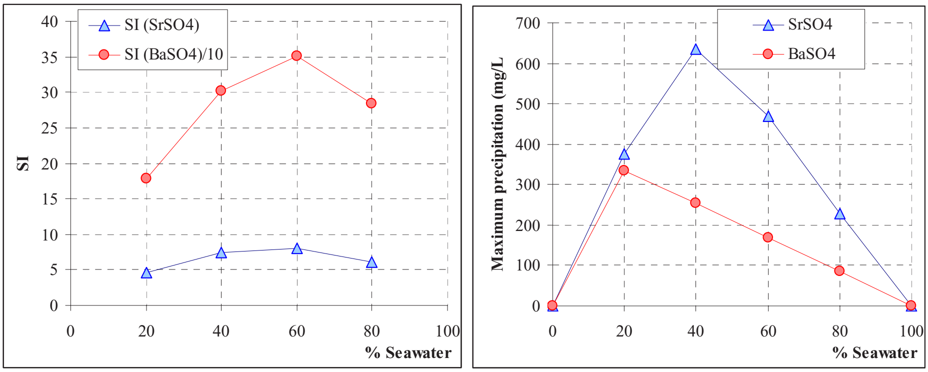

Figure 7-2. SPECS predictions for mixtures of North Sea and Forties water at 100°C and 1 bar

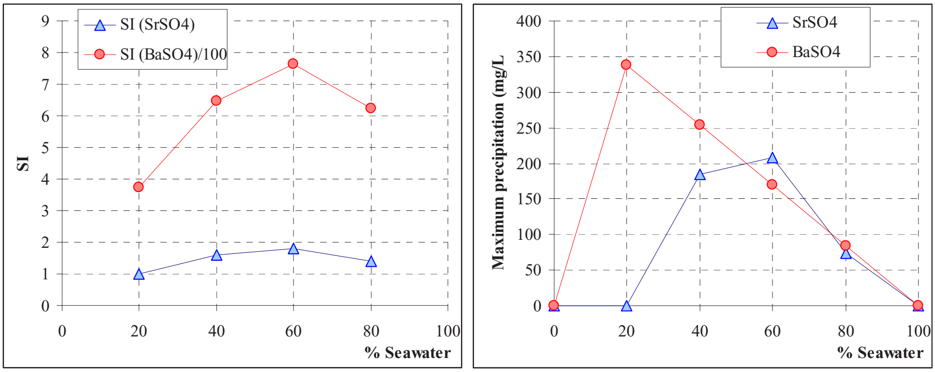

Figure 7-3. SPECS predictions for mixtures of North Sea and Forties water at 25°C and 300 bar

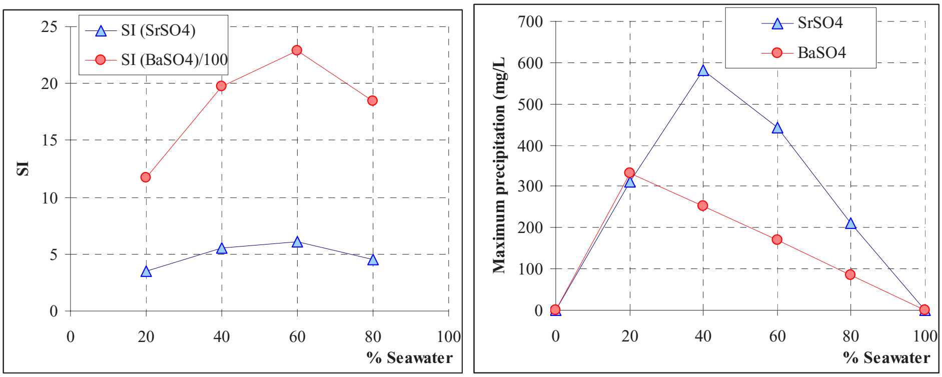

Figure 7-4. SPECS predictions for mixtures of North Sea and Forties water at 100°C and 300 bar

Graham et al. (2003) studied scaling problems in the Kittiwake field, located in the central North Sea. The reservoir is characterized by high salinities and calcium concentrations, and relatively large temperatures (around 130ºC) downhole. The composition of the field and the sea water is reported in table 7-3.

As the field matured, the water cut increased over 80% and scaling problems started to be severe. The formation of anhydrite scale downhole has been reported by Graham et al. (2003). Predictions were performed by SPECS, obtaining saturation indices above 1 for anhydrite when the seawater to formation water ratio was over 70%, while the solution was found to be undersaturated for lower ratios. Thus, our predictions are in agreement with field observations. Celestite and barite precipitation is also predicted, agreeing with Graham et al's. (2003) calculations. The maximum amount of precipitation for the different sulphates against the seawater-formation water ratio is given in figure 7-5. The amounts of maximum precipitation for both $BaSO_4$ and $SrSO_4$ predicted by SPECS are in remarkably good agreement with Graham et al.'s (2003) predictions. Regarding anhydrite, the latter investigators report higher amounts of mineral precipitating, and predict $CaSO_4$ scale formation for lower ratios than 70% seawater. Nonetheless, Kittiwake field has been in production since the 1980s, and severe anhydrite scale formation has only become important for the mature field, when the water cut increased over 80%.

Table 7-3

Composition of Kittiwake formation water and central North Sea water

Ions ($mg·L^{-1}$)	Kittiwake formation water	Sea water
Na	56000	10890
Ca	14500	428
K	4350	460
Mg	10600	1368
Ba	24	0
Sr	265	0
SO4	0	2960
Cl	147097	19773

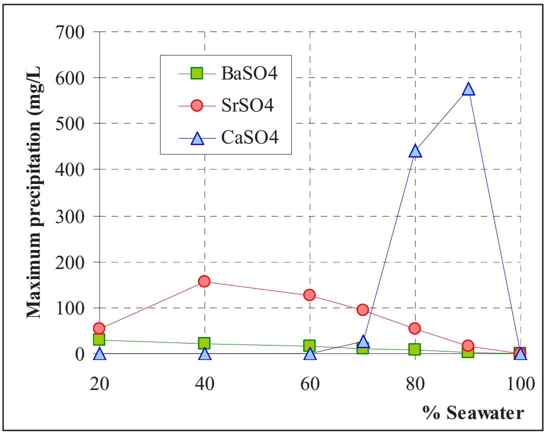

Figure 7-5. SPECS predictions for mixtures of North Sea and Kittiwake formation water at 130°C and 68 bar

7.2 References in Chapter 7

Graham, G.M., Frigo, D.M., Poynton, N., 2003. Calcium sulphate (anhydrite) scale control in a mature asset-the Kittiwake and Fulmar reservoirs. SPE 80386, 1-11.
Hughes, C.T., Whittingham, K.P., 1982. The selection of scale inhibitors for Forties field. SPE European Petroleum Conference, London.
Jacques, D.C., Bourland, B.I., 1983. A study of solubility of strontium sulphate. SPEJ, 292-300.
Mitchell, R.W., Grist, D.M., Boyle, M.J., 1980. Chemical treatments associated with North Sea projects. JPT, 904-912.
Tanner, R.N., Whittingham, K.P., 1986. Scale control during waterflooding operations: A field appraisal of inhibitor requirement and performance. SPE 14127.
Yuan, M.D., Todd, A.C., 1991. Prediction of sulfate scaling tendency in oilfield operations. Society of Petroleum Engineers, 237-250.
Yuan, M.D., Todd, A.C., Sorbie, K.S., 1993. Sulphate scale precipitation arising from seawater injection: a prediction study. Marine and Petroleum Geology 11 (1), 24-30.

8. Experimental Determination of Solubilities

In the process of designing and selecting the most appropriate setup and/or analytical technique to determine experimentally the solubility of sparingly soluble salts ($BaSO_4$ and $SrSO_4$ in particular) in water and NaCl solutions at high temperature and pressure, different alternatives were studied. All those alternatives (synthetic fluid inclusions technique, electrochemical technique, quartz crystal microbalances, and conductivity measurements), together with their physical base, potentials, advantages and disadvantages for the present purpose, will be presented in this chapter.

Results for conductivity measurements can be found in Appendix II.

8.1 General Overview

There is a large variety of methods to determine the solubility of solids in liquids, depending on the characteristics of the system analyzed and the range of temperature, pressure and concentration to be covered. According to Hefter and Tomkins (2003), they can be divided into direct or indirect methods. In the latter case, the solubility product is the quantity determined experimentally instead of the solid solubility, which can be calculated afterwards from the previous value.

Direct methods can also be divided in two subgroups (Hefter and Tomkins, 2003): Analytical methods (the solubility is determined by chemical analysis of the liquid and solids in equilibrium) and synthetic methods (the solubility is determined via the variation of a property of a solution of known initial concentration when changing temperature, pressure or composition).

The experimental procedure followed in analytical methods consists of preparing the sample and agitating it at constant temperature and pressure until equilibrium is reached. At this point the solid is separated from the liquid and the latter is analyzed in order to determine the solubility. It is important to keep a constant temperature and pressure during the separation process, otherwise some precipitation or dilution may take place and contaminate the results. The solid phase should also be analyzed (chemical analysis, X-ray, infrared spectra) after proper drying, to assure it did not undergo any modification during the experiment. Many different devices can be used to follow this procedure, but they are all formed by three main parts:

- Vessel containing the test solution placed inside a device to keep constant temperature (oven, jacket, thermostatic bath, etc.) and a constant pressure.

- Agitation device (magnetic stirrer, rotator, vibrator, oscillator, etc.).
- Sampling device connected to a separation device (a filter generally, although centrifugation or decantation can also be employed).

An alternative to the agitation device to provide a good contact between the liquid and solid phases is the use of a column containing the solid phase, through which the liquid is percolated.

In order to obtain reliable data the experimental difficulties of the particular system to study must be carefully reviewed and solved. In general, the following points must be taken into account before starting any solubility measurement:

- The starting solid material should not contain any impurities, to avoid contamination of the results, especially for sparingly soluble salts.
- The solid should be characterized with respect to its composition and structure. It is also convenient to reanalyze the solid after the experiment in order to check it did not undergo any modification.
- Special care must be taken when using reagents that can experience denaturalization due to hygroscopocity, oxidation, etc.
- The time required to achieve equilibrium must be determined prior to the measurements to make sure supersaturation or undersaturation is avoided, and that no metastable phases are present. Whenever possible, the equilibrium should be approached from different directions. If this is not an option, the solubility constant calculated from different initial conditions can be used to test the equilibrium.
- It is also important to take into account possible interactions between the test solution and the recipients used for storage or the atmosphere.
- If separation of the solid and liquid phases is required, it must be performed under the experimental temperature and pressure.

There is no general method or equipment to determine solubilities of water-salt systems at high temperatures and pressures. For each system the setup has to be designed according to the temperature and pressure ranges covered, and the characteristics of the particular system. The systems of interest in the present work are sparingly soluble compounds, which are generally characterized by a slow kinetics. Therefore, analytical methods are preferred against synthetic methods. Due to the large temperatures, pressures and salt concentrations to be covered, an adequate material standing those conditions and resistant to corrosion must be employed. A ceramic material avoids corrosion problems, but introduces experimental error to the measurements due to its porosity. Nevertheless, Plevachuk and Sklyarchuk (2000) used a ceramic cell with a special design to minimize loss of solution through the pores in the experimental determination of solubilities. Some authors (Jacques, D.C., Bourland, 1983, Howell et al., 1992) performing experiments at high temperature, pressure and salt concentration report corrosion of 316 stainless steel after short periods of use. Alternative materials found in the literature are Boron nitride (Sokolovskii et al., 1995), 316 stainless steel covered with a silver layer (Strübel, 1966), Teflon-lined 318 stainless steel (Schulien, 1987), Hastelloy C (Jacques and Bourland, 1983), Titanium alloy (Howell et al., 1992), platinum liner in a stainless steel vessel (Jensen, 1996), Haynes satellite number 25 (Sharp and Kennedy, 1965). Working under nitrogen atmosphere also helps to reduce corrosion problems.

The low solubility of both $BaSO_4$ and $SrSO_4$ in pure water and in NaCl solutions requires an analytical technique with very low detection limits. Different analytical procedures have been employed to analyze both barium and strontium contents: chemical, colorimetric, atomic absorption spectrometry, radioactive tracer methods, atomic emission, liquid scintillation counting, X-ray fluorescence, isotope dilution mass spectrometry (Bender et al., 1972). In some cases, gravimetric methods are also employed, although they are not recommended for so low solubility values.

8.2 Synthetic Fluid Inclusion Technique

The synthetic fluid inclusion technique (SFIT) is a relatively new experimental procedure which allows the measurement of pressure-volume-temperature-composition (PVTX) properties of aqueous solutions in a wide range of temperature, pressure, and composition. The SFIT is based on the analysis of lab-generated fluid inclusions (microsamples of fluid entrapped as imperfections within crystals (Sterner and Bodnar, 1984)). This method is especially useful to study high salinity fluids at elevated temperature and pressure, because it avoids the problems of corrosion and sampling which appear in conventional techniques (Schmidt and Bodnar, 2000).

The SFIT has been established as a proven method for the determination of phase equilibria and volumetric properties in aqueous fluid systems containing salt and volatiles. PVTX properties in the system $NaCl\text{-}CO_2\text{-}H_2O$ at elevated temperatures and pressures were determined by Schmidt et al. (1995), and Schmidt and Bodnar (2000). Synthetic fluid inclusions have also been used with success to determine solid-liquid equilibrium and volumetric and critical properties in the $NaCl\text{-}H_2O$ system by Sourirajan and Kennedy (1962), Sterner and Bodnar (1984), and Bodnar (1995); and in the $KCl\text{-}H_2O$ system by Bodnar and Sterner (1985).

8.2.1 Experimental Procedure

The SFIT is based on the isolation of samples in quartz (SiO_2) at the desired experimental *T* and *P*, for a posterior study under a microscope. The first step is the preparation of the quartz cylinders (around 2-3 cm long and 4 mm diameter) used to isolate the sample. The cylinders are heated to around 350^{o}C. Then, they are removed from the oven and immersed in cold, distilled water, causing the cracking of the quartz due to the instantaneous temperature drop. The water remaining in the fractures is dried using a vacuum oven at 110^{o}C. After this, the cores can be stored in vacuum desiccators until the experiments are carried out (Bodnar, 1995). This procedure has proven to create a large number of closely spaced fractures without leading to the core disintegration (Sterner and Bodnar, 1984).

The second step is to trap part of the solution of known composition in the fissures of the quartz core. To do so, one quartz cylinder is introduced into a platinum capsule together with the solution of interest. The system is heated and pressurized to experimental conditions using an oven and a high pressure autoclave. Part of the solution will enter the fractures in the quartz. Due to dissolution and reprecipitation processes, the fractures will partially heal, and small amounts of solution become isolated (fluid inclusions). According to Bodnar and Sterner (1985), the density and composition of the fluid trapped is representative of the bulk fluid present in the capsule, and no change is experienced during quenching to ambient conditions.

The third step is to analyze the fluid inclusions to determine the PVTX properties of interest once the sample is cooled to room conditions. The quartz cores are cut into disks 0.25-0.5 mm thick, and polished on both sizes before being examined under a microscope provided with a heating/cooling stage (Bodnar, 1995). At room temperature, the inclusions generally contain two or more phases, although they are originally trapped in a single, homogeneous fluid phase at the *T*/*P* formation conditions. These multiple phases appear as a consequence of phase changes during cooling. A heating/cooling stage coupled to the microscope is used to determine the temperatures at which the different phases disappear, providing the information needed to determine PVTX properties of aqueous solutions.

8.2.2 Application of SFIT to Solubility Measurements

To determine solubility values, synthetic fluid inclusions of different known concentrations are trapped following the procedure explained before. If the solution is supersaturated at room conditions, the inclusion will contain an additional solid phase. The temperature of dissolution of such a phase is measured, and a relationship between solubility and temperature, at a given pressure, can be obtained.

8.2.3 Drawbacks of the SFIT

The use of SFIT implies certain assumptions (Vityk and Bodnar, 1998):

- The inclusion traps a single, homogeneous phase.
- Nothing is added or lost from the inclusion after it is trapped.
- No reactions take place within the fluid inclusion between the time of trapping it and analyzing it.
- The inclusion volume remains constant.

According to Vityk and Bodnar (1998), not all these assumptions are always certain. Even though Sterner and Bodnar (1984) performed a great variety of experiments concluding that inclusions trap representative samples of the parent solutions, other workers (Barnes et al., 1969) have reported that they may not.

Another disadvantage of SFIT is the slow fracture healing rates. Schmidt and Bodnar (2000) run experiments during about eight weeks for temperatures of 300^{o}C.

Special care must also be taken regarding the inclusion's size. If the fluid inclusions are too small (2 to 3 μm) the phase changes are often very difficult to observe. On the other hand, for large inclusions (larger than about 10 μm) high internal pressures during heating for homogenization are generated. Such pressures result in a stretch or decrepitate of the quartz core. The maximum internal pressure an inclusion in quartz can stand without stretching or crackling decreases for increasing inclusion size.

The main disadvantage of this technique for the present purpose is the saturation of the solutions with silica. Therefore, the experiments would determine barite solubility in the $BaSO_4$-SiO_2-NaCl-H_2O system, which is not the aim of the present work. Maybe, this problem could be solved trying to find a material which allows the formation of fluid inclusions but does not interfere with the system being investigated.

8.3 Electrochemical Technique

An electrochemical-based technique to investigate deposition of different scaling minerals on metallic surfaces has been presented by Morizot et al. (1999), Neville et al. (1999), Neville and Morizot (2000), and Morizot and Neville (2001). The results obtained (for $CaCO_3$ by Neville et al., 1998 and Morizot et al., 1999; for both $CaCO_3$ and $BaSO_4$ by Morizot and Neville, 2001 and Morizot et al., 2002; and for $CaCO_3$, $MgCO_3$ and $Mg(OH)_2$

by Neville and Morizot, 2002) show this method to be a promising tool for studying nucleation and growth of mineral scale at solid surface, as well as inhibitor performance. It could also be used as a method for online monitoring of scale formation down the well. The technique is also a good tool to find out the relationship between the scale formation precipitated from the bulk solution and the one formed at a solid surface. According to Hasson (1996), field experience shows that inhibition does not follow the same behaviour as predicted in the laboratory test from bulk solution precipitation rates.

The oxygen reduction reaction (reaction 8-1) on a rotating disk electrode (RDE) surface can be followed and related to the extent of surface scale.

$$O_2 + 2H_2O + 4e^- \rightarrow 4(OH)^- \qquad \textbf{(8-1)}$$

We believe the same principle could also be used to measure solubility of sparingly soluble minerals at different temperatures and pressures.

8.3.1 Background

The technique is based on the change observed in the rate of reaction 8-1 at a RDE surface under potentiostatic control when scale starts forming on it. The schematic of the technique is presented in figure 8-1. At the beginning, the diffusing oxygen reaches the whole electrode surface area (A_i). Once scale has deposited, the surface available to the oxygen is reduced (A_f), and thus the extent of reaction 8-1.

The mass transport of oxygen by diffusion under varying hydrodynamic conditions to the surface of the electrode is analyzed by using the transport equations developed by Levich (1942), Adams (1969), and Filinovsky and Pleskov (1976). A rotating disk electrode is chosen because the mass transport to its surface is well defined and uniformly distributed along the whole surface, and can be varied by changing the rotational speed.

For a reaction under mass control (as it is the case for equation 8-1) at a constant potential, the limiting current (i_L, mA) can be related to the RDE rotational speed (ω, rad·s^{-1}) via equation 8-2

$$i_L = 0.62nFAC^b D^{2/3} \nu^{-1/6} \omega^{1/2} \qquad \textbf{(8-2)}$$

where n is the number of electrons involved in electrode reaction, F is the Faraday's constant (96487 C equiv^{-1}), A is the electrode area in cm^2, C^b is the bulk concentration of electroactive species in mol dm^{-3}, D is the diffusion coefficient of the electroactive species in cm^2 s^{-1}, and ν is the kinematic viscosity in cm^2 s^{-1}. For reaction 8-1, the electroactive species is oxygen.

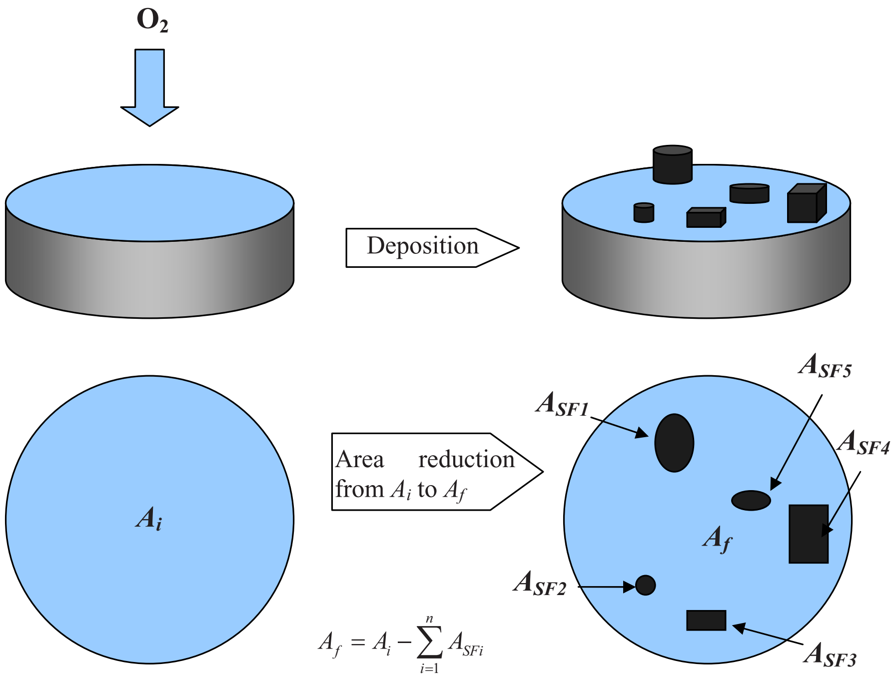

Figure 8-1. Schematic representation of active surface area before and after scale deposition (A_{SF} stands for area of solid formation).

For a constant rotation speed, equation 8-2 shows that the limiting current remains constant unless there is a change in the electrode surface area. Therefore, a decrease in i_L will correspond to scale formation on the surface. Equation 8-2 is used to calculate the difference in active surface area before and after scale formation has taken place.

This method has been validated by using image analysis. The surface coverage determined by this technique and that determined by image analysis are in good agreement, increasing the accuracy for highly covered surfaces (Neville et al., 1998).

8.3.2 Experimental Procedure

The experimental procedure consists of three main steps:

- Analysis of the i_L vs. $\omega^{1/2}$ behaviour for a clean electrode to determine the initial active surface area.
- Immersion of the electrode in a supersaturated solution of the species of interest and waiting for the scale to form on the surface.
- Final analysis to determine the extent of scale formation on the surface.

The different slope of the plots i_L vs. $\omega^{1/2}$ during the initial and final analysis is a consequence of the decrease in the active surface area as a result of solid deposition, as all the other variables in equation 8-2 are kept constant. Comparison of the two data sets will indicate the percentage of electrode surface covered by solid:

$$\%\ \text{covered} = \frac{m_1 - m_2}{m_1} \cdot 100 \tag{8-3}$$

where m_1 is the gradient i_L vs. $\omega^{1/2}$ for the clean electrolyte, and m_2 is the same gradient for the scaled electrolyte.

Two separate apparatus are required to carry out the three steps. The setup to generate scale formation on the electrode surface is shown in figure 8-2 (a), while the experimental setup for the electrochemical analysis is shown in figure 8-2 (b). The latter is a three-electrode electrochemical cell. The working electrode is the RDE, while the reference electrode is a saturated calomel electrode (SCE). A platinum electrode is used as the inert auxiliary electrode (Neville et al., 1999). The RDE speed is measured via a tachometer.

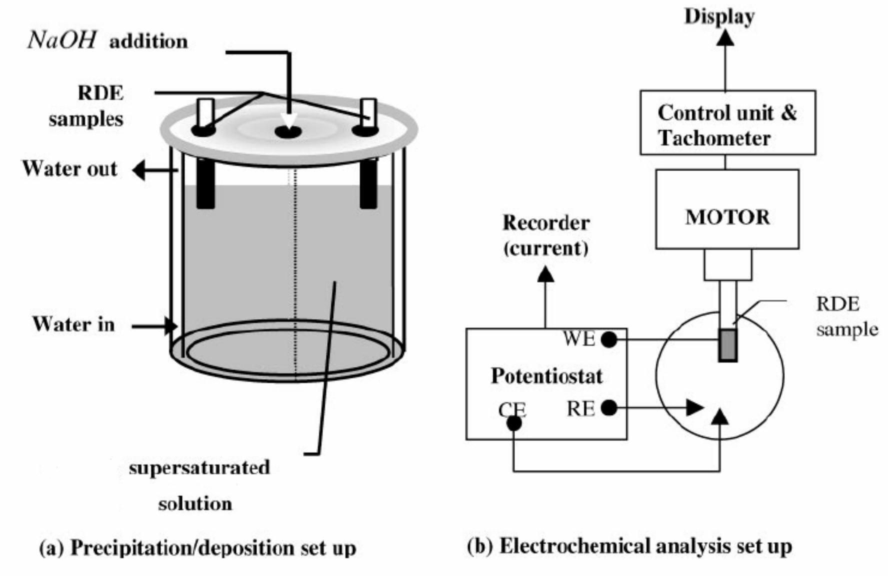

Figure 8-2. Experimental setup for (a) precipitation and deposition of salt and (b) electrochemical analysis (Neville and Morizot, 2000).

The performance of different inhibitors can be easily studied using this new technique. The response to the addition of a given quantity of inhibitor to the supersaturated solution in contrast to the inhibited solution can be analyzed in the same way as explained previously.

8.3.3 Application to Solubility Measurements

The principle used to develop the new technique presented above could be used to perform solubility measurements. The appearance of the first particle of solid on the electrode can be followed by measuring the current i_L. According to equation 8-2, for a constant temperature, pressure and angular velocity, the limiting current has a constant value unless the electrode area changes as a consequence of solid formation. Such change in the current value can be used to determine the solubility.

The kinematic viscosity and the diffusion coefficient depend on both temperature and pressure. Therefore, both the electrochemical cell and the precipitation/deposition setup should be maintained at the same T and P conditions. In order to avoid dissolution of the scale when analyzing the current, a solution at equilibrium with respect to the precipitating solid, and with the same NaCl concentration as the precipitation setup, should be used as analysis solution.

An alternative procedure could be based on using the same device both for the electrochemical analysis and the precipitation process. A solution of known composition of the species of interest in a known concentration of NaCl is employed as analysis solution. The temperature is increased to the desired value, and pressure is increased to a value higher to the pressure corresponding to the solubility point. In that way, an undersaturated solution is the starting point for the experiment. Pressure is decreased slowly and the current is recorded, until a decrease in the current is observed. That point corresponds to the first solid deposited on the electrode, and indicates the pressure at which the original solution reaches solid-liquid equilibrium. The same procedure can be followed for different temperatures and NaCl concentrations covering the required ranges of temperature and composition. If we want to attain equilibrium from a supersaturated solution, the pressure will be slowly increased instead of decreased, until a current change is observed. However, if the attainment of equilibrium is slow, this procedure can be time consuming.

8.3.4 Drawbacks of the Electrochemical Method

The development of the electrochemical approach follows some assumptions that may not always be true, and therefore, could affect the final results:

- The solid deposited on the electrode surface does not allow oxygen transport through the crystal lattice, and therefore the electrochemical reaction only takes place on the free surface.

- The corrosion reaction of the substrate with the electrolyte does not influence the results.
- Deposits do not re-dissolve once they have been formed.
- The rate of oxygen reduction is constant, and the diffusion coefficient of oxygen to the active sites is constant for bare and scaled electrolytes.

The deposited solid may have a complex shape, with parts not completely in contact with the surface (i.e., ellipsoidal). The oxygen reduction reaction could take place on those "cavities" formed by the solid, at a lower rate than on the free surface, but this possibility has not been accounted for by this technique.

The method assumes the surface is equally accessible for oxygen reduction. Nevertheless, the deposition of crystals will induce local turbulence effect, which will enhance the supply of oxygen near the solids.

Neville et al. (1999) noticed that the relationship i_L vs. $\omega^{1/2}$ showed a small degree of non linearity when scale had deposited on the electrode's surface. Even though a good linear correlation coefficient was obtained (0.99), this behaviour indicates that the non uniform layer created on the electrode is generating some instability. The problem may be important when having many scale layers.

When studying the applicability of the electrochemical technique to solubility measurements, several inconvenient points were found:

- All the studies performed using the electrochemical technique were performed at room temperature and atmospheric pressure (Neville and Morizot (2000) performed some measurements at 80°C and 1 atm). Accuracy and feasibility of the technique at high temperature and pressure has not been addressed.
- The kinematic viscosity and the diffusion coefficient depend on pressure, and even though the dependence is not very strong, changing its value may lead to different limiting currents for the same surface area.
- After every change in the pressure conditions, it is required to wait the time needed to attain equilibrium for the particular system being analyzed. Therefore, for slow reactions, this procedure is not appropriate.
- If two different devices are employed (one for the electrochemical analysis and another one for the precipitation process), the electrode should be transferred from one to another at a constant temperature and pressure to avoid experimental errors.

8.4 Quartz Crystal Microbalances

Quartz crystal resonators are widely used nowadays for physical, chemical and biochemical sensing. This device is sensitive to mass changes at its surface, being called quartz crystal microbalance (QCM). It is a microgravimetric technique capable of measuring as small as ng order of mass changes on the surface of the crystal (Iitaka et al., 1997). This accuracy is reduced when the fluid in contact with the quartz is a liquid.

8.4.1 Background

8.4.1.1 Piezoelectricity

Quartz crystal microbalances are based on the phenomenon of piezoelectricity, which is a coupling between a material's mechanical and electrical behaviours. When a mechanical stress is applied on a piezoelectric material, an electrical charge appears on its surface. This phenomenon is called piezoelectricity. Piezoelectric materials also display a converse piezoelectric effect: When an electrical charge is applied, the material deforms mechanically.

Many crystalline materials exhibit piezoelectric behaviour, but only a few materials exhibit the phenomenon strongly enough to use them in applications taking advantage of piezoelectricity. Quartz, Rochelle salt, lead titanate zirconate ceramics, barium titanate and polyvinylidene fluoride are found among these materials.

A quartz crystal sensor will be formed by the quartz disc with electrodes on both sides. The thickness of the disk has to be very small in order to have a high sensitivity (Ferrari et al., 2000). The quartz crystal resonator is sensitive to mass changes at its surface. Therefore, it can be used as a quartz crystal microbalance to measure changes of a known mass of salt placed on the crystal, due to dissolution in a liquid media. Salt precipitation on the crystal surface from a supersaturated solution can also be studied by means of the QCM.

8.4.1.2 Frequency Response

There are different factors affecting the frequency response of a piezoelectric quartz crystal (Guigard et al., 2001):

- Mass located on the crystal surface
- Pressure
- Temperature
- Properties of the fluid surrounding the crystal (density and viscosity)

- Mounting effects

Considering all the effects mentioned above, the measured frequency (F) of a quartz crystal can be expressed as:

$$F = F_0 + \Delta F_m + \Delta F_P + \Delta F_T + \Delta F_f \qquad \textbf{(8-4)}$$

where F_0 is the crystal's inherent frequency, ΔF_m is the frequency change due to mass placed on the crystal, ΔF_P is the frequency change due to the pressure, ΔF_T is the frequency change due to the temperature, and ΔF_f is the frequency change due to changes in the density and viscosity of the surrounding fluid. The mounting effects, or external stresses, are kept constant if handling of the crystal is avoided through the experiment (Guigard et al., 2001).

8.4.1.2.1 Mass Effects

Several equations can be found in the literature relating the frequency change of a crystal immersed in a gaseous phase as a consequence of the mass placed on its surface (ΔF_m). The first relationship was proposed by Sauerbrey (1959):

$$\Delta F_m = -\frac{2F_0^2}{N \cdot A\sqrt{\rho_q c_q}}\Delta m \qquad \textbf{(8-5)}$$

where ρ_q is the crystal density, c_q the crystal stiffness, Δm the change of mass located on the crystal, N the harmonic and A the crystal area.

According to equation 8-5, the mass sensitivity of the crystal is not dependent on the kind of deposited material. It only depends on crystal's properties (density, stiffness, area and inherent frequency). Therefore, calibration is not required. Nevertheless, Sauerbrey (1959) assumed the mass placed on the quartz could be assimilated to an increase in the effective thickness of the quartz resonator. The film added was assumed to have the same density and acoustic properties as quartz. Those assumptions reduce the range of applicability of equation 8-5 to small mass loads and ratios of $\Delta F/F_0$ lower than 2% (Hayward et al., 1998).

The use of quartz crystal microbalances in liquids is more complicated than in gaseous media. In this case the frequency shift is due to two contributions: The mass load and the effect caused by changes in the liquid properties. Kanazawa and Gordon (1985) studied the changes in the quartz crystal frequency when it was immersed in a viscous medium, and developed an equation accounting for such changes.

$$\Delta F = \frac{-F_0^{3/2}}{N}\sqrt{\frac{\rho\mu}{\rho_q c_q \pi}} \tag{8-6}$$

where ρ and μ are the density and viscosity of the bulk fluid, respectively.

Combining equations 8-5 and 8-6:

$$\Delta F_{Total} = -\frac{2F_0^2}{N\sqrt{\rho_q c_q}}\left(\frac{\Delta m}{A} + \sqrt{\frac{\rho\mu}{4\pi F_0}}\right) \tag{8-7}$$

8.4.1.2.2 Temperature and Pressure Effects

In order to quantify the pressure and temperature effect on the frequency shift of the quartz crystal, initial experiments could be performed using a clean crystal. When the frequency has stabilized for the unload crystal, the pressure can be increased keeping a constant temperature. The frequency shift measured is a consequence of the pressure effect exerted on the crystal and the changes in density and viscosity of the liquid, and thus the frequency measured is

$$F = F_0 + \Delta F_P + \Delta F_f \tag{8-8}$$

ΔF_f can be quantified using equation 8-6 once the viscosity and density of the liquid are known. The process can be repeated until all the pressures of interest have been covered, and all the values for ΔF_P have been calculated. The same procedure can be followed to study the frequency shift due to temperature. In this case the frequency is given by

$$F = F_0 + \Delta F_T + \Delta F_f \tag{8-9}$$

Again, the different values of ΔF_f for the range of temperatures of interest can be calculated from equation 8-6.

In case the term ΔF_f cannot be calculated accurately at the large temperatures and pressures of interest (up to 300°C and 700 bar) a different approach can be followed. The effects of pressure, temperature and changes in liquid density and viscosity can be grouped in a single term ΔF_{TPf}, so that the measured frequency at each temperature and pressure pair is

$$F = F_0 + \Delta F_{TPf} \tag{8-10}$$

The advantage of such procedure is a lower experimental error:

- The experimental errors introduced by the density and viscosity calculations and/or measurements are avoided.

- The addition of the experimental errors implied in the separate measurements of the temperature and pressure effects is avoided. Instead, a lonely measurement is done reducing the total error.

Another advantage of using the term ΔF_{TPf} is that it would include any other possible effect taking place in the system and not accounted for in a proper way when using equations 8-8 and 8-9 (e.g., the effect of the mass of water adsorbed to the crystal surface).

The disadvantage of the procedure is the need to perform experiments for each temperature and pressure pair of interest. In this case, for each temperature the whole range of pressures has to be covered, and vice versa, increasing considerably the number of experiments to perform.

Both procedures could be followed for a set of T and P points in order to know if the experimental error for the first approach is considerably larger that when using the second approach. Depending on the results, the most appropriate procedure can be chosen.

A very tight control of the temperature is needed through the experiment to obtain reliable results and a stable frequency. The resonant frequency is a sensitive function of temperature, and small temperature fluctuations can swamp the typical frequency shifts involved with the mass variations. When working with gases, the intrinsic temperature dependence of the QCM is negligible near room temperature (around 1-3 Hz $^{o}C^{-1}$). When the crystals are immersed in liquid, much larger changes in frequency with temperature are observed. Ferrari et al. (2000) carried out experiments on several uncoated sensors having a value for F of 7 MHz, and obtained a thermal sensitivity (dF/dT) around -470 Hz $^{o}C^{-1}$, which corresponded to -67 ppm $^{o}C^{-1}$. Another effect which needs to be accounted for is the importance of the temperature history of the crystal. It is often observed that the frequency versus temperature curve obtained going from T_1 to T_2 does not coincide with the curve obtained going from T_2 to T_1.

8.4.2 Experimental Procedure

Preliminary studies to the solubility experiments are required in order to characterize the frequency response of the clean quartz crystal against changes in both temperature and pressure (and the consequent changes in fluid properties). The quartz crystal will be placed inside the pressure vessel in contact with the liquid medium. Temperature and pressure will be then increased to the desired values. When the frequency has stabilized, the value of ΔF_{PTf} will be calculated according to equation 8-10. The procedure will be repeated for the whole range of temperatures and pressures of interest. When the liquid is different from distilled water, all the range of concentrations to be used in the solubility experiments has to be analyzed. It would be convenient to use an equal volume of water or solution to determine ΔF_{PTf}, in case this factor could influence the results. Nevertheless, this influence could also be studied by performing experiments using different volumes of water/solution under the same temperature and pressure conditions.

Once the value of ΔF_{PTf} is known for all the conditions to be studied, the solubility measurements can start. Two different approaches could be used:

- Precipitation of salt on the QCM from a supersaturated solution
- Dissolution of the solid salt deposited on the QCM

The first approach was used by Abdel-Aal et al. (2001) to study the adhesion mechanism of $CaCO_3$ scale at 25°C. Eun. et al. (1999) studied the growth of cadmium selenite and barium sulphate crystals on a QCM from supersaturated solutions. Guigard et al. (2001) measured the solubility of two copper salts in supercritical CO_2 using the dissolution approach.

The disadvantage of the precipitation approach is the possibility of solid formation on the vessel walls, which will not be accounted for by the QCM. Anyhow, this problem could also appear when following the dissolution method, due to a continuous process of dissolution and reprecipitation, although it is thought to happen in a lower extent.

The main drawback of the dissolution approach is the necessity of placing the solid salt on the crystal surface. The equations developed to relate frequency shifts and mass changes assumed the mass on the crystal to be a thin layer with constant properties. Bond et al. (1997) solved this problem by adhering the microcrystals ($[(C_4H_9)_4N][Ce(CO)_5I]$) to the electrode by smearing the electrode surface with a cotton swab containing the powdered material. They transferred masses between 3 and 6 μg by this procedure. Nonetheless, those values are too low even for the lowest soluble salts of our interest. Guigard (2001) generated a layer on the crystal by allowing the solvent to evaporate. They dissolved the salt in water and placed a known volume of that solution on the crystal using a syringe. Afterwards, the solvent is allowed to evaporate. The mass of salt placed on the crystal can be calculated using two different methods. The first one implies the knowledge of the volume and concentration of the solution placed on the crystal. The second method is based on the frequencies measured before and after the crystal loading, and on the use of equation 8-5. Guigard et al. (2001) reported an average deviation of 28% for the masses of bis(thenoyltrifluoroacetonato)copper(II) measured using these two methods. They explain the difference as experimental errors introduced due to remaining mass on the syringe tip, volume delivered, concentration and solvent residue on the crystal. They believe the mass calculated from Sauerbrey's (1959) equation is more accurate than that from volume and density.

For slightly soluble salts (as $BaSO_4$ and $SrSO_4$), the homogeneous deposition of powdered solid salt directly on the crystal surface would be the easiest way to proceed. In order to assure the method is reliable, the equations presented before could be tested by performing different experiments where the mass loaded is known. If the equations are found to give inaccurate results, a calibration could solve the problem.

Once the salt is deposited on the crystal, the temperature and pressure conditions are increased to the desired value. To do so, an oven and a pressure vessel connected to a pump can be used. When the equilibrium has been reached and the frequency has stabilized, F is measured. This procedure is repeated for the different T and P conditions to be analyzed.

The setup to determine solubility of sparingly soluble salts in a liquid phase at high temperature and pressure, by means of the QCM technique, is represented in figure 8-3. To avoid breakage of the QCM, a very tight and fast-acting pressure control system is required. Otherwise, the differential pressure between the liquid and gaseous phases could easily cause the crystal breakage. To get good sensitivity, the crystal's thickness is less than 1 mm, and therefore the differential pressure it can stand is very low. The same setup could also be used replacing the air by a liquid phase, but it would imply a considerable decrease in the sensitivity of the QCM.

Apart from the assumptions done in the development of equations 8-4 to 8-10 and the difficulties to place the solid salt homogeneously on the crystal surface, the main disadvantage of this method is the large cost and complexity of the design. For these reasons, it was discharged for the present purpose, although it is believed to have a high potential for the determination of solubility of sparingly soluble salts, avoiding at the same time the problems found in such cases to come across a reliable analytical technique.

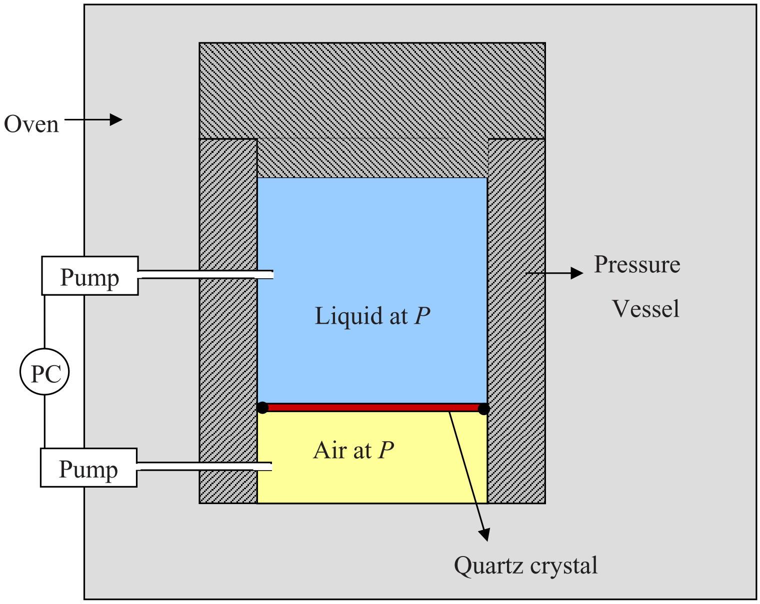

Figure 8-3 Experimental QCM setup

8.5 Conductivity Measurements

Conductivity of a solution is a measurement of its ability to carry an electrical current. The electrical conductivity increases with the amount of solids dissolved, and therefore, it has been widely used to determine salt concentrations in water. To measure conductivity, a constant voltage is applied across two electrodes separated by a constant distance. The electrical current transported through the solution depends on the number and type of ions dissolved in it.

The conductivity technique has previously been used at high pressures and temperatures to study asphaltenes precipitation (Fotland, 1996). The liquid-liquid coexistence curve on the phase diagram of the Pb-Ga system was determined on the basis of electroconductivity measurements by Sokolovskii et al. (1995). Plevachuk and Sklyarchuk (2000) developed an experimental technique for electrical conductivity measurements in a wide temperature range (up to 1730°C) under high pressures (up to 500 bar).

8.5.1 Background

There are many different methods to determine solubility of solids in liquids. One way to perform such measurement is by the so-called synthetic methods, where no chemical analysis is required. A sample of known initial composition is prepared. One of the equilibrium parameters (*E*, being temperature, pressure or composition; or any function of *E*) is then modified and one of the system properties (*P*) is followed. When there is a phase change, a break will appear in the plot *P* vs. *E* (or *f(E)*). This principle may be used to measure the solubility of salts in water.

8.5.2 Experimental Procedure

Even though synthetic methods are not recommended for sparingly soluble salts, as they are usually characterized by slow kinetics, conductivity experiments were performed for $SrSO_4$-H_2O systems in order to study the real feasibility of this technique for our purposes. Celestite ($SrSO_4$) was chosen over barite due to the extremely low conductivity values for the latter salt. In order to simplify the experimental setup, and as the main purpose was to verify the validity of the method for our needs, the experiments were performed at room temperature and pressure. The electrical conductivity of celestite-water solutions was followed (*P*) when changing the composition (*E*). The concentration of salt in the solvent was continuously decreased by adding a constant flow rate of distilled water, by means of an ISCO pump. The conductivity was measured by a conductivity meter (Lutron CD-4303). If experiments had to be carried out at high constant pressures, a bellow connected to a pump could be located inside a pressure vessel containing the solution. The pump introducing water to the system would work in a constant flow mode, while the pump connected to the bellow would supply a constant pressure. Operating in this way, water is constantly introduced into the vessel, which will maintain a constant pressure due to the volume compensation of the bellow.

A supersaturated solution at room temperature and pressure was prepared, by adding a known amount of pure commercial powder $SrSO_4$ in a known volume of distilled water. The solution was stirred with a magnetic stirrer, and the conductivity was constantly measured at the same time as a very low water flux is added to the vessel containing the solution. The experimental setup is shown in figure 8-4.

When a new volume of water is added to the solution, part of the excess solid will dissolve, keeping a constant conductivity value. This procedure will go on until the last particles of solid are dissolved. From that moment, a new addition of water to the solution will cause a dilution process, and therefore the conductivity will experience a decrease. Therefore, the break in the plot conductivity vs. solution volume will indicate when dilution starts to take place. The solubility value at the experimental conditions can be calculated from the initial weight of salt and the initial volume of water, together with the volume of water added until the break point appears.

The results from the different conductivity experiments carried out are presented in Appendix II. The conclusion drawn from those results is the lack of validity of this experimental procedure to determine celestite solubility in pure water. The slow kinetics of the system (equilibrium was attained only after at least 20 hours) makes any synthetic technique inappropriate to obtain reliable solubility measurements in a reasonable time.

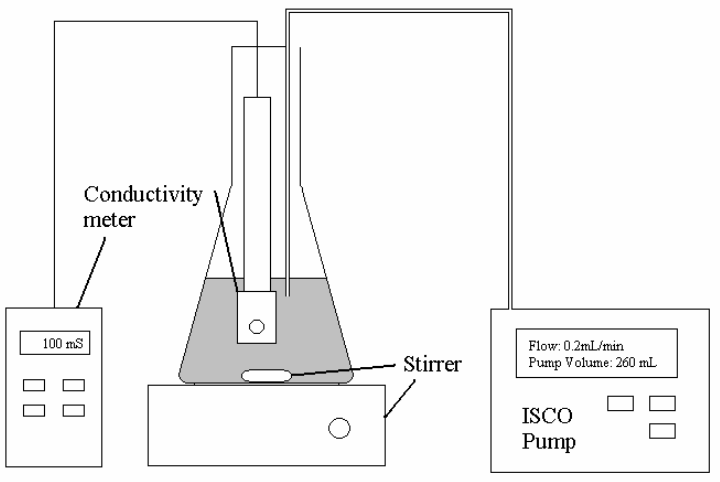

Figure 8-4 Experimental conductivity setup

8. 6 References in Chapter 8

Abdel-Aal, N., Satoh, K., Sawada, K., 2001. Study of adhesion mechanism of calcareous scaling by using quartz crystal microbalance technique. Analytical Sciences 17, 825-828.

Adams, R.N., 1969. Electrochemistry at solid electrodes, Dekker, 1969

Barnes, H.L., Lusk, J., Potter, R.W., 1969. Composition of fluid inclusions. Proceedings of COFFI (ed. E. Roedder) 2, 13.

Bender, M., Snead, T., Chan, L.H., Bacon, M.P., Edmond, M., 1972. Barium intercalibration at Geosecs I and III. Earth and Planetary Science Letters 16, 81-83.

Bodnar, R.J., Sterner, S.M., 1985. Synthetic fluid inclusions in natural quartz. II. Application to PVT studies. Geochimica et Cosmochimica Acta 49, 1855-1859.

Bodnar, R., 1995. Experimental determination of the PVTX properties of aqueous solutions at elevated temperatures and pressures using synthetic fluid inclusions: H_2O-NaCl as an example. Pure & Applied Chemistry 67 (6), 873-880.

Bond, A.M., Colton, R., Mahon, P.J., Tan, W.T., 1997. Tetrabutylammonium cation expulsion versus perchlorate electrolyte anion uptake in the electrochemical oxidation of microcrystal of $[(C_4H_9)_4N][Ce(CO)_5I]$ mechanically attached to a gold electrode: A voltammetric and quartz crystal microbalance study. J. Solid State Electrochem. 1, 53-61.

Borngräber, R., Schröder, J., Lucklum, R., Hauptmann, P., 2002. Is an oscillator-based measurement adequate in a liquid environment?. IEEE Transactions on Ultrasonics, Ferroelectrics, and Frequency Control 49 (9), 1254-1259.

Eun, H., Umezawa, Y., 1999. Quartz crystal microbalance for selenite sensing based on growth of cadmium selenite crystals immobilized on a monolayer of phosporylated 11-mercapo-1-undecanol. Microkim. Acta 131, 177-185.

Ferrari, V., Marioli, D., Taroni, A., Ranucci, E., 2000. Multisensor array of mass microbalances for chemical detection based on resonant piezo-layers of screen-printed PZT. Sensors and Actuators 68, 81-87.

Filinovsky, V., Pleskov, Y., 1976. Rotating disk and ring electrodes in investigations of surface phenomena at the metal-electrode surface. Progress in Surface and Membrane Science, Vol. 10. Cadenhead, D.A., Danielli, J. (Eds.), Academic Press, London.

Fotland, P., 1996. Precipitation of asphaltenes at high pressures; experimental technique and results. Fuel science and technology int'l. 14 (1&2), 313-325.

Guigard, S.E., Hayward, G.L., Zytner, R.G., Stiver, W.H., 2001. Measurement of solubilities in supercritical fluids using a piezoelectric quartz crystal. Fluid Phase Equilibria 187-188, 233-246.

Hasson, D., 1996. Influence of the flow system on the inhibitory action of $CaCO_3$ scale prevention additives. Desalination 108, 67-80.

Hayward, G.L., Thompson, M., 1997. A transverse shear model of a piezoelectric chemical sensor. Journal of Applied Physics 83 (4), 2194-2201.

Hefter, G.T., Tomkins, R.P.T., 2003. The experimental determination of solubilities. John Wiley & Sons, vol. 6, West Sussex, England.

Howell, R.D., Raju, K., Atkinson, G., 1992. Thermodynamics of "Scale" mineral solubilities 4. $SrSO_4$. J. Chem. Eng. Data 37, 464-469.

Iitaka, K., Tani, Y., Umezawa, Y., 1997. Orthophosphonate ion-sensors based on a quartz crystal microbalance coated with insoluble orthophospate salts. Alalytica Chimica Acta 338, 77-87.

Jacques, D.C.; Bourland, B.I., 1983. A study of solubility of strontium sulphate. SPEJ 292-300.

Jensen, J.P., 1996. Phase equilibria for aqueous electrolyte systems at high temperature and pressure. Ph.D. Thesis, Department of Chemical Engineering, Technical University of Denmark.

Kanazawa, K.K., Gordon, J.G., 1985. Anal. Chim. Acta 175, 99.

Levich, B.G., 1942. Acta Physicochimica URSS 17, 257

Morizot, A.P., Neville, A., Hodgkiess, T., 1999. Studies of the deposition of $CaCO_3$ on a stainless steel surface by a novel electrochemical technique. Journal of Crystal Growth 198/199, 738-743.

Morizot, A.P., Neville, A., 2001. Using an electrochemical approach for monitoring kinetics of $CaCO_3$ and $BaSO_4$ scale formation and inhibition on metal surfaces. Society of Petroleum Engineers, 220-223.

Morizot, A.P., Neville, A., Taylor, J.D., 2002. An assessment of the formation of electrodeposited scales using scanning electron and atomic force microscopy. Journal of Crystal Growth 237-239, 2160-2165.

Neville, A., Morizot, A.P., 2002. Calcareous scales formed by cathodic protection – an assessment of characteristics and kinetics. Journal of Crystal Growth 243, 490-502.

Neville, A., Morizot, A.P., 2000. A combined bulk chemistry/electrochemical approach to study the precipitation, deposition and inhibition of $CaCO_3$. Chemical Engineering Science 55, 4737-4743.

Neville, A., Hodgkiess, T., Morizot, A.P., 1999. Electrochemical assessment of calcium carbonate deposition using a rotating disc electrode (RDE). Journal of Applied Electrochemistry 29, 455-462.

Plevachuk, Y.; Sklyarchuk, V., 2000. Electrophysical measurements for strongly aggressive liquid semiconductors. Meas. Sci. Technol. 11, 1-4.

Sauerbrey, G. 1959. Use of quartz vibrator for weighing thin layers and as a micro-balance. Zeitschrift für Physik 155 (2), 206-222.

Schmidt, C., Bodnar, R.J., 2000. Synthetic fluid inclusions: XVI. PVTX properties in the system H_2O-NaCl-CO_2 at elevated temperatures, pressures, and salinities. Geochimica et Cosmochimica Acta 64 (22), 3853-3869.

Schulien, S., 1987. High-temperature/high-pressure solubility measurements in the systems $BaSO_4$-NaCl-H_2O and $SrSO_4$-NaCl-H_2O in connection with scale studies. SPE symposium (SPE 16264), San Antonio, Texas.

Sharp, W.E., Kennedy, G.C., 1965. The system CaO-CO_2-H_2O in the two phase region calcite + aqueous solution. J. Geol. 60, 391-403.

Sokolovskii, B.; Plevachuk, Y.; Didoukh, V., 1995. Electroconductivity and liquid-liquid equilibrium in the Pb-Ga system. Phys. Stat. Sol. (a) 148, 123-128.

Sourirajan, S., Kennedy, G. C., 1962. The system H_2O-NaCl at elevated temperatures and pressures. American J. Sci. 260, 115-141.

Sterner, S.M., Bodnar, R.J., 1984. Synthetic fluid inclusions in natural quartz I. Compositional types synthesized and applications to experimental geochemistry. Geochimica et Cosmochimica Acta 48, 2659-2668.

Strübel, G., 1966. Die hydrothermale Löslichkeit von Cölestin in System $SrSO_4$-NaCl-H_2O. Neues Jahrb. Mineral. Mon., 99-107.

Vityk, M.O., Bodnar, R.J., 1998. Statistical microthermometry of synthetic fluid inclusions in quartz during decompression reequilibration. Contrib Mineral Petrol 132, 149-162.

9. BaSO$_4$ Solubility in NaCl at High Temperature and Pressure

A study of the solubility of barite (BaSO$_4$) in sodium chloride solutions from very diluted to highly concentrated solutions, under hydrothermal conditions, was undertaken in connection with research on the scale formation problem found in many industrial processes. The deposition of barium sulphate as scale from highly concentrated brines found in oil and geothermal wells is a common problem (Templeton, 1960). The thermodynamic models used to predict mineral solubility in natural waters must be based on a relatively large amount of accurate experimental data of the scale forming phases at the different conditions of temperature, pressure and composition found in real life. Some of the available data on the solubility of barium sulphate in sodium chloride are inconsistent, and most of the published data only cover a narrow range of low temperature (around 25^{o}C) and NaCl concentration, and are measured at atmospheric pressure. The use of such data can lead to weak models and inaccurate predictions. The few sources dealing with high temperature and pressure cannot be cross-checked due to the different experimental conditions. Therefore, a larger databank is necessary to understand and predict the causes of precipitation and dissolution of barite in nature.

An experimental setup has been developed in order to measure the solubility of barite and/or celestite (SrSO$_4$) in aqueous solutions of sodium chloride (NaCl) at high temperatures (up to 250^{o}C), high pressures (up to 700 bar), and high ionic strengths (from very diluted NaCl solutions up to the saturation point). The setup is shown in figures aIII-3 and aIII-4 in Appendix III.

9.1 Previous Studies of BaSO$_4$ Solubility in NaCl Solutions

The solubility of barium sulphate in sodium chloride solutions has been previously studied by Templeton (1960), Uchameyshvili et al. (1966), Strübel (1967), Davis and Collins (1971), Blount (1977), and Schulien (1987). Nevertheless, published data on the solubility of barite at temperatures above 25^{o}C and pressures larger than 1 atm are scarce. The ranges of temperature, pressure and NaCl concentration covered by the different investigators are given in table 9-1.

The experimental procedure followed by the majority of the sources determining barite solubility in NaCl solutions can be divided into four main steps:

- Preparation of the starting solid by precipitation. In some cases natural barite or commercial crystalline powder is employed, and this step may be avoided.

- Placement of a solution containing excess of $BaSO_4$ in a device keeping constant temperature and pressure. This step may include agitation of the sample during the equilibration period. In some studies, only one of the variables is kept constant (e.g., pressure), while the other (e.g., temperature) is changed slowly.
- Sampling of the solution after equilibrium is reached.
- Analysis of the Ba^{2+} concentration.

The main differences among the procedures used by the different investigators are found in the choice of analytical technique, device to heat, pressurize and agitate the samples, etc. A summary of the experimental procedure followed by each investigator is reported in table 9-2.

Table 9.1
Experimental measurements of $BaSO_4$ solubility in NaCl solutions

T (^oC)	*P*(bar)	NaCl (m)	Number of data	Reference
20/350	1/165	0.1-2	41	Strübel (1967)
25/95	1	0.1-5	108	Templeton (1960)
25	1	0.01-2	8	Davis and Collins (1971)
80/120	1/414	0.1-2	34	Schulien (1987)
94/253	5/560	0.2-4	35	Blount (1977)
95/340	1/165.4	0.25-2	84	Uchameyshvili et al. (1966)

Table 9-2
Experimental procedures used to determine $BaSO_4$ solubility in NaCl solutions

Reference	Agitation	Initial solid	Pressurizing	Filter	Dilution
Templeton (1960)	Stirrer	Precipitated $BaSO_4$	No	Millipore hypodermic syringe filter	Yes
Uchameyshvili et al. (1966)	Rocking	Natural barite	No	No	No
Strübel (1967)		Natural barite		No	No
Davis and Collins (1971)	Shaking	Precipitated $BaSO_4$	No	Double Watman no. 42 filter paper	No
Blount (1977)	Rocking	Precipitated $BaSO_4$	Pressure vessel (±3 bar)		Some
Schulien (1987)	No	Commercial powder $BaSO_4$	2 pressure vessels	0.5 µm Millipore filter	Yes

Reference	Time (h)	Heating	Analysis	P medium
Templeton (1960)	24-48	Water bath (± 0.05^{o}C)	Ba: spectrographic method (±5%) S: microreduction-colorimetric method (±0.3 mgL^{-1})	
Uchameyshvili et al. (1966)	48-72	Electrical resistance furnace	Syngle crystal weight-loss method	
Strübel (1967)	10-2500[a]		Single crystal weight-loss method X-ray fluorescence	
Davis and Collins (1971)	72	Heat lamp (±1^{o}C)	Liquid scintillation counting (±20%)	
Blount (1977)	48-288	Muffle furnace (±1.5%)	Ion exchange resin + X-ray fluorescence (±5%[b])	Water
Schulien (1987)	4-48	Environmental chamber	Atomic absorption spectrometry (±3%)	Nitrogen (g)

[a] 10 h were waited for the experiments at 600ºC, while 2500 h were waited when the experimental temperature was 150ºC.
[b] for high NaCl concentrations (4 m) the uncertainty is larger (around 7%)

9.1.1 Starting Material

In the majority of studies the solid employed was either natural barite (Uchameyshvili et al., 1966, Strübel, 1967) or precipitated barium sulphate (Templeton, 1960, Davis and Collins, 1971, Blount, 1977), which may lead in both cases to experimental errors. Only Schulien (1987) used commercial crystalline $BaSO_4$ powder.

Natural barite contains different amounts of other species which will affect the barium concentration in the solution. According to Blount (1977), natural barites may contain mineral inclusions which will dissolve increasing the ionic strength and modifying barite solubility.

Precipitated $BaSO_4$ can also lead to erroneous solubility measurements resulting from poor solid crystallinity or occluded reactants. According to Balarew (1925), $BaSO_4$ precipitates contain up to as much as 1% of occluded $BaCl_2$. Templeton (1960) used commercial $BaCl_2$ and Na_2SO_4 to obtain barite with a 0.026% excess of soluble sulphate.

9.1.2 Analytical Techniques

A wide variety of analytical procedures were used by different investigators to determine the solubility of barium sulphate. Templeton (1960) analyzed the barium content by a spectrographic method (Grabowski and Unice, 1958) resulting in a precision of 5% for barium concentrations larger than 3 mg L^{-1}. Total sulphur was determined by a microreduction-colorimetric method (Johnson and Nishita, 1952), allowing a precision of 0.3 mg L^{-1} in the concentration range from 1 to 45 mg L^{-1}. All the measurements were carried out both from supersaturation and undersaturation, to assure equilibrium was attained.

The single-crystal weight-loss method was employed by Uchameyshvili et al. (1966) and Strübel (1967). The latter also analyzed the total barium content by X-ray fluorescence. Due to the low solubility of $BaSO_4$ in water (of the order of 10^{-5} m) and in NaCl solutions (of the order of 10^{-4} m) the weight-loss method is not recommended. Uchameyshvili et al. (1966) used a very accurate (0.01 mg) microanalytical balance, but they also employed considerably large quantities of natural barite crystals (from 2 to 7 g) and low volumes of solution (40 mL), which may lead to large errors by the weight-loss method.

Davis and Collins (1971) measured the sulphate concentration of a radioisotope-tagged (^{35}S) solution of precipitated $BaSO_4$ by liquid scintillation counting, resulting in efficiency around 20%. Total barium was also analyzed by emission spectroscopy, but the precision obtained for concentrations of 1 mg L^{-1} and lower was not satisfying. When the data of the barium ion and the sulphate ion are given separately, it can be clearly observed the disagreement between both experimental techniques is very high.

Blount (1977) determined the amount of barium by X-ray fluorescence after taking up the barium contained in the experimental solution by means of a chelating ion-exchange resin. To avoid interferences, high ionic strength solutions were diluted 1:10. The accuracy of the method is reported to be better than ± 5%. Nevertheless, the uncertainty of barium analysis for 4 m NaCl solutions is quite large (around ± 7%). When having high ionic strength media the recovery of barium by the resin may be interfered by other cations, sodium in this case.

Finally, Schulien (1987) analyzed the barium content in the sample by atomic absorption spectroscopy, reporting an accuracy of ± 3%.

9.1.3 Dilution

Some of the previous analyses (at atmospheric pressure and room temperature) are performed directly on the experimental samples, without previous dilution. The solubility of barite decreases with decreasing pressure and may also decrease with decreasing temperature. Therefore, dilution is a requirement in most of the cases to avoid precipitation when both temperature and pressure are decreased from the experimental values to room conditions. Otherwise, erroneous low solubility values are very likely to be measured as a result of precipitation.

From the sources shown in table 9-1, only Templeton (1960) and Schulien (1987) diluted their samples with barium free-NaCl solution of the same concentration as in the experiment, prior to the change of the experimental conditions and the analysis. Templeton (1960) only diluted the samples for the determination of barium, while sulphate determinations were made on the undiluted samples.

Blount (1977) only diluted high ionic strength samples to avoid interferences during the ion exchange process to recover barium. The limit value chosen by Blount (1977) to decide whether dilution was required or not is not mentioned in his publication. Therefore, it is not possible to determine the data that may be affected by precipitation before analysis.

It is unlikely that Uchameyshvili et al. (1966) and Strübel (1967) data are affected by this experimental error as the weight-loss method is employed.

Davis and Collins (1971) only performed measurements at 25°C and 1 atm, thus their data are also safe from this experimental error.

9.1.4 Agitation

Agitation of the sample is provided by means of a stirrer (Templeton, 1960), a shaker (Davis and Collins, 1971), or by rocking the setup (Uchameyshvili et al., 1966, Blount, 1977). Schulien (1987) did not use any kind of mixing mechanism in the sample solution.

9.1.5 Time Required to Attain Equilibrium

The time waited for the different investigators before performing the analysis varies from 4 hours (Schulien, 1987) to 2500 hours (Strübel, 1967). Even though Schulien (1987) usually waited 24 hours prior analysis, he assures the results did not vary after 4 hours.

9.1.6 Temperature

Different devices were employed to increase and keep a constant temperature. Templeton (1960) used a water bath thermostat controlled to within ± 0.05^{o}C. Uchameyshvili et al. (1966) introduced the vessel containing the solution into and electrical resistance furnace and measured the temperature by means of a Chromel-Kopel thermocouple accurate to ± 1-3^{o}C. Similar ovens to heat up the solution were also used by Blount (1977) and Schulien (1987). A heat lamp was employed to slightly increase the temperature above the stabilized room temperature (25 ± 1^{o}C) for Davis and Collins (1971) measurements.

9.1.7 Pressure

There are only two sources in table 9-1 performing experiments at pressures larger than 1 atm or the saturation pressure of the solution (Blount, 1977 and Schulien, 1987). Blount (1977) uses a pressure vessel formed by an inner cell containing the sample and surrounded by an outer space. Water is pumped to or out from the space in order to control the pressure. Schulien (1987) employed a high pressure autoclave vessel and nitrogen gas as pressure medium.

9.1.8 Filtration

The filtration procedure followed by some of the sources shown in table 9-1 (Templeton, 1960, Blount, 1977) is inaccurate, as the samples were filtered at atmospheric conditions. Large changes in temperature and pressure will then be experienced by the solution while it is being filtered, which could lead to solid deposition in the sampling tube or in the filter. Part of those deposits could also be re-dissolved when taking out new samples.

Templeton (1960) withdrew the samples through a Millipore hypodermic syringe filter. Davis and Collins (1971) used a double Watman number 42 filter paper. Blount (1977) withdrew samples by opening a valve located at the other end of a pipe connected to the sample cell. Schulien (1987) filtrated at the experimental conditions by using a 0.5 μm Millipore filter connecting two pressure vessels.

As mentioned in Chapter 4, many of the data are shown to be inaccurate and most of them could not be tested for their reliability. It is clear, at certain conditions, the existence of erroneous measurements, as two sources report rather different values. Nevertheless, due to the lack of data at the same conditions it is not possible to conclude which sources are reliable.

Even though the procedure followed by Schulien (1987) seems to be the most reliable experimentally (commercial powder $BaSO_4$ used as starting solid, filtration under experimental conditions, dilution prior analysis to avoid precipitation), his results strongly disagree with the other sources shown in table 9-1. The main shortcoming of Schulien's (1987) work is the short time awaited to assure equilibrium (he assures 4 hours were enough). Moreover, no agitation device is employed, and thus, it is very unlikely that his solutions were at equilibrium. This fact could explain the much lower values reported by Schulien (1987) when compared to other sources in table 9-1.

Some of the measurements performed by Blount (1977) may be affected by precipitation of $BaSO_4$ during filtration or prior analysis, which could explain the low values obtained.

Uchameyshvili et al. (1966) and Strübel (1967) data may contain some inaccuracies as a consequence of the use of natural barite and the single crystal weight-loss method to analyze the solubility.

9.2 Previous Studies of $SrSO_4$ Solubility in NaCl Solutions

As mentioned in a previous chapter, there is a large disparity in the reported solubility values for celestite in sodium chloride solutions. This inconsistency is aggravated at high temperature and pressure conditions. Table 9-3 shows the ranges of temperature, pressure and NaCl concentration covered by different investigators reporting $SrSO_4$ solubility in NaCl-H_2O.

The experimental procedure followed by the majority of the sources determining celestite solubility in NaCl solutions can be divided in the same four main steps reported previously for barite. Culberson et al. (1978) employed a different approach using a 1 cm internal diameter column packed with solid $SrSO_4$ through which the NaCl solution is passed various times. To prevent channelling, the solid was inverted several times and allowed to resettle before each measurement.

A summary of the experimental procedure followed by each investigator is reported in table 9-4.

Table 9-3

Experimental measurements of $SrSO_4$ solubility in NaCl solutions

T (°C)	*P* (bar)	NaCl (m)	Number of data	Reference
-0.05/25	1	0.004-0.05	10	Lucchesi and Whitney (1962)
10.3/40	1	0.05-5.6	36	Reardon and Armstrong (1987)
20/90	1	0.1-2.6	32	Strübel (1966)
25	1	0.01-2	10	Davis and Collins (1971)
25	1	0.5	5	Brower and Renault (1971)
25	1	0.73	1	Culberson et al. (1978)
25	1	0.4-5.1	8	Müller (1960)
25/253.5	1/600	0.5-5	436	Howell et al. (1992)
25/125	1/2.3	0.2-5.7	24	Vetter et al. (1983)
80/120	1/414	0.1-2	49	Schulien (1987)
100/305	0.2/165	0.2-3.7	41	Jacques and Bourland (1983)

Table 9-4

Experimental procedures used to determine $SrSO_4$ solubility in NaCl solutions

Reference	Agitation	Initial solid	Pressurizing	Filter	Dilution
Lucchesi and Whitney (1962)	Rods	Precipitated $SrSO_4$	No	No	No
Reardon and Armstrong (1987)	Rods	Precipitated $SrSO_4$	No	No	No
Strübel (1966)		Natural celestite	No		
Davis and Collins (1971)	Shaking	Precipitated $SrSO_4$	No	Double Whatman no. 42 filter paper	No
Brower and Renault (1971)	Rods	Precipitated $SrSO_4$	No	No	No
Culberson et al. (1978)	No	Precipitated $SrSO_4$	No	No	No
Müller (1960)		Precipitated $SrSO_4$			
Howell et al. (1992)	No	Precipitated $SrSO_4$	High pressure pump	Coarse (40-60μm) fritted glass filter	Yes
Vetter et al. (1983)	Shaking	Precipitated $SrSO_4$	No	No	No
Schulien (1987)	No	Commercial powder $SrSO_4$	2 pressure vessels	0.5 μm Millipore filter	Yes
Jacques and Bourland (1983)	Rods	Precipitated $SrSO_4$	2 pressure vessels	Yes	Yes

Reference	Time (h)	Heating	Analysis	P medium
Lucchesi and Whitney (1962)		Thermostat (±0.005°C)/Ice-water bath	Liquid scintillation counting (±1%)	
Reardon and Armstrong (1987)		Water bath	Atomic absorption spectrometry (±1%) Ion chromatography for sulphates (±5%)	
Strübel (1966)	35-340	Oven		
Davis and Collins (1971)	72	Heat lamp (±1°C)	Liquid scintillation counting (±20%)	
Brower and Renault (1971)			Atomic absorption spectrometry (±10%)	
Culberson et al. (1978)		Water jacket + controller (±0.05°C)	Atomic absorption spectrometry	
Müller (1960)	48		Titration	
Howell et al. (1992)	24	Oven + T controller (±1°C)	Atomic absorption spectrometry	
Vetter et al. (1983)	72-168	Heat box	Liquid scintillation counting (90Sr, 32S)	
Schulien (1987)	4-48	Environmental chamber	Atomic absorption spectrometry (±1%)	Nitrogen (g)
Jacques and Bourland (1983)	72	Oven + T controller (±0.1°C)	Atomic absorption spectrometry	Nitrogen (g)

9.2.1 Starting Material

The majority of the studies of celestite solubility used $SrSO_4$ synthesized by reaction of a sulphate salt, usually Na_2SO_4, and a strontium salt, usually $SrCl_2$ (Lucchesi and Whitney, 1962, Brower and Renault, 1971, Davis and Collins 1971, Culberson et al., 1978, Jacques and Bourland, 1983, Vetter et al., 1983, Howell et al. 1992). Reardon and Armstrong (1987) obtained celestite by titrating a 0.003 m H_2SO_4 solution with a $Sr(OH)_2$ solution to a pH of 5.7, which, according to these investigators, ensures a purer solid than the one obtained with $SrCl_2$ and Na_2SO_4. They also performed tests to assure their starting material was not affected by surface poisoning effects before the solubility experiments were conducted. Müller (1960) precipitated celestite from commercial solutions of $SrCl_2$ and H_2SO_4. Natural mineral from Girgenti, Bristol and Gembeck containing 0.09% CaO and barium traces was employed by Strübel (1966). The latter investigator also used precipitated $SrSO_4$ in some of his measurements. Only Schulien (1987) used commercial crystalline $SrSO_4$ in his solubility determinations. As mentioned previously for the case of barite, the use of either natural minerals of precipitated strontium sulphate may lead to experimental errors. Therefore, the use of crystalline commercial powder is preferred.

9.2.2 Analytical Techniques

Mainly, two analytical techniques were used to determine strontium concentrations in the samples: Liquid scintillation counting (LSC) and atomic absorption spectrometry (AAS). Lucchesi and Whitney (1962), Davis and Collins (1971) and Vetter et al. (1983) used LSC, resulting in efficiencies between 1% (Lucchesi and Whitney, 1962) and 20% (Davis and Collins, 1971). AAS was used by Brower and Renault (1971), Culberson et al. (1978), Jacques and Bourland (1983), Reardon and Armstrong (1987), Schulien (1987) and Howell et al. (1992), resulting in efficiencies between 1% (Reardon and Armstrong, 1987, Schulien, 1987) and 10% (Brower and Renault, 1971). Müller (1960) determined the Sr^{2+} concentration by titration, a method which is not recommended for the low solubility values being analyzed. Reardon and Armstrong (1987) also determined sulphate concentrations on selected samples by ion chromatography, obtaining larger analytical uncertainties (± 5%) than when using AAS. Vetter et al. (1983) used two different tagged isotopes (^{90}Sr and ^{32}S) for cross-checking of the results. In some case, their deviations were as large as 30 %.

Two sources (Lucchesi and Whitney, 1962 and Reardon and Armstrong, 1987) performed analysis on the final solid phase. Lucchesi and Whitney (1962) used X-ray powder diffraction photographs on the solid, concluding it was pure strontium sulphate. Reardon and Armstrong (1987) analyzed the sodium content of the final solid, in order to prove that substantial substitution of Cl^- for SO_4^{2-} and Na^+ for Sr^{2+} did not occur in the solid phase.

9.2.3 Dilution

To avoid precipitation of strontium sulphate when pressure is decreased from the experimental value to atmospheric pressure, the samples were diluted with water (Howell et al., 1992) or NaCl solution (Schulien, 1987, Jacques and Bourland, 1983). All other sources shown in table 9-3 performed experiments at atmospheric pressure, and therefore dilution is not required (celestite solubility has a maximum around 25ºC).

9.2.4 Agitation

Agitation of the sample is provided by means of a shaker (Davis and Collins, 1971 and Vetter et al., 1983), or a roller/rod (Lucchesi and Whitney, 1962, Brower and Renault, 1971, Jacques and Bourland, 1983, Reardon and Armstrong, 1987). Culberson et al. (1978), Schulien (1987) and Howell et al. (1992) did not use any kind of mixing mechanism in the sample solution.

9.2.5 Time Required to Attain Equilibrium

The equilibration time waited for the different investigators before sampling varies from 4 hours (Schulien, 1987) to 340 hours (Strübel, 1966). As in the case of barite, Schulien (1987) carried out experiments in time intervals from 4 to 72 hours, concluding that the results did not vary after 4 hours, when equilibrium had been attained. Brower and Renault (1971) monitored the conductivity of the $SrSO_4$-H_2O system as a function of time to verify the attainment of equilibrium. According to them, equilibrium is reached in less than one minute by dissolution, but may be much slower by precipitation. Reardon and Armstrong (1987) approached the equilibrium from both super and undersaturation, increasing or decreasing progressively the temperature. This procedure was also followed by Lucchesi and Whitney (1962) for some of their measurements. Davis and Collins (1971) prepared all samples in duplicate to assure equilibrium.

9.2.6 Temperature

Davis and Collins (1971) used a heat lamp to slightly increase the temperature above a stabilized room at 25 ± 1°C. An oven was used by Strübel (1966), Jacques and Bourland

(1983), Schulien (1987) and Howell et al. (1992), to increase the temperature up to 90, 305, 120 and 253°C, respectively. Some of the ovens were equipped with temperature controllers to keep the temperature as constant as possible (± 0.1°C for Jacques and Bourland, 1983, and ± 1°C for Howell et al., 1992). Reardon and Armstrong (1987) employed a water bath. Vetter et al. (1983) performed some measurements at room temperature, where no heating device or temperature controller was used. For the high temperature solubility determinations (up to 125°C), the solution was place inside a thermally insulated constant temperature heat box. Culberson et al. (1978) kept a constant temperature throughout the column by means of a water jacket and a proportional temperature controller to within ± 0.05°C. Lucchesi and Whitney (1962) used a thermostat regulated at 25 ± 0.005°C for their solubility determinations at this temperature, while an ice-water bath was used for the measurements at -0.05°C.

9.2.7 Pressure

Only a few sources (Jacques and Bourland, 1983, Schulien, 1987, Howell et al., 1992) performed experiments at pressures larger than 1 atm or the saturation pressure of the solution. Howell et al. (1992) employed a pressure vessel connected to a high pressure pump. Jacques and Bourland (1983), and Schulien (1987) used two pressure vessels (one containing the solution and the other to filtrate under experimental conditions) and employed nitrogen as pressurizing medium. At the high temperature and pressure conditions measured, nitrogen solubility may be relatively high both in water and in NaCl solutions, and may have some influence on the results obtained. According to Sun et al. (2001), the solubility of nitrogen in water at 150°C and 400 bar (conditions measured by Schulien, 1987) is 0.1386 m, while this value decreases to 0.0638 m at the same conditions for a 4 m NaCl solution.

9.2.8 Filtration

After equilibrium is obtained, separation of the liquid and solid phases under conditions as close as possible to those of the test is required. Howell et al. (1992) prevented the pass of solid particles into the sample using a coarse (40-60 µm) fritted glass filter mounted inside the reaction vessel. The size of the filter pore selected by Howell et al. (1992) is 10 times larger than in the rest of the literature on $SrSO_4$ solubility in water and in NaCl solutions. Jacques and Bourland (1983) devised a two pressure vessel system where $SrSO_4$ was dissolved to the saturation point in one vessel and then filtered under experimental conditions to the second vessel. A very similar procedure formed also by two pressure vessels connected through a filter was used by Schulien (1987). The filter membrane used was a Millipore Fluoropore filter of 0.5 µm pore size. Davis and Collins (1971) used a double Whatman number 42 filter paper. The rest of the sources shown in table 9-3 do not report to have filtrated the samples. Vetter et al. (1983) did not use a filter, but allowed the solution to settle for some time, usually 24 hours.

9.3 Our Experimental Method

An excess of crystalline powder $BaSO_4$ was added to NaCl solutions, and the mixtures were heated up and pressurized. After agitating for the time required to attain equilibrium, the solution was filtrated under the experimental conditions and the samples were stored for analysis by inductively coupled mass spectrometry (ICP-MS).

9.3.1 Materials

Extra pure (97.5-100 %) finely powdered commercial barium sulphate (222515000 from Acros Organics) was used in the experiments. All water used was distilled water. Commercial sodium chloride (207790010 from Acros Organics) of 99.5 % purity was used. Due to the highly hygroscopic characteristics of sodium chloride, the powder was dried at $100^{o}C$ in an oven during 16 hours prior to its use and always placed inside a desiccator.

9.3.2 Experimental Device

The experimental device designed and built to carry out experimental determinations of $BaSO_4$ and $SrSO_4$ solubility in the systems $NaCl\text{-}BaSO_4\text{-}H_2O$ and $NaCl\text{-}SrSO_4\text{-}H_2O$ is shown in Figure 9-1.

The system is mainly formed by two high pressure vessels in series with two pumps, connected through a filter and placed inside an oven.

The pressure vessels (TOC3-20-HC276/Piston from High Pressure Equipment Company (HIP), http://www.highpressure.com) are tubular piston reactors made of Hastelloy C 276. This material is chosen in order to avoid corrosion problems found for 316 stainless steel (Jacques and Bourland, 1983, Howell et al., 1992). Each vessel is formed by a 20” long cylindrical body of ¾” internal diameter (ID) and 1½” outside diameter (OD), and two caps provided with Kelrez o-rings. The volume of the pressure vessels is selected according to DTU’s safety regulations (pressure-volume ratio limited to 200 bar L^{-1} for high pressure equipment). The vessels can stand up to 300°C and 10000 psi. Figure 9-2 shows the cross section of a pressure vessel and a cap.

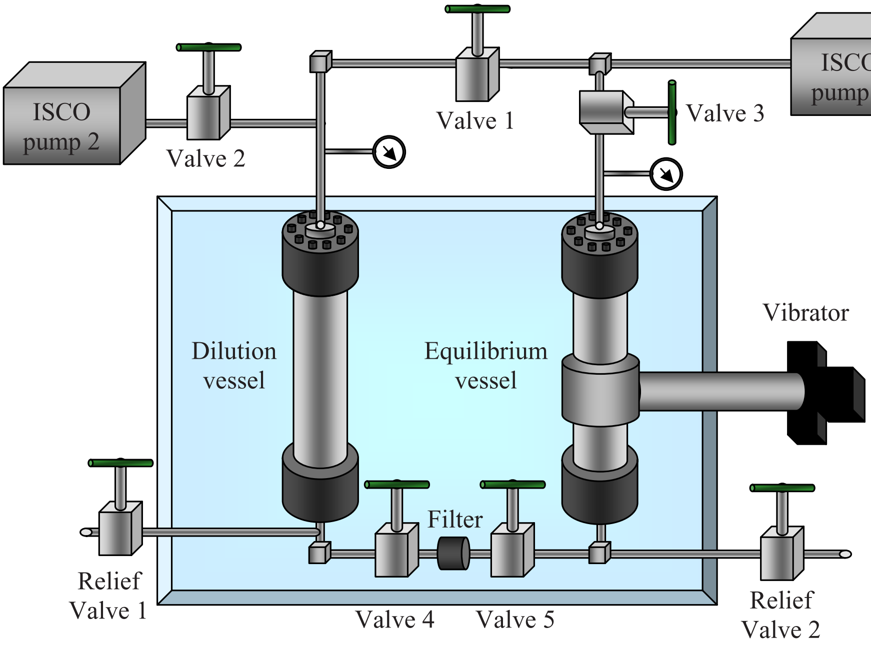

Figure 9-1. Experimental setup for the high pressure/high temperature solubility measurements

The line filter (10-51AF4-5HC276 from HIP) is formed by four sintered stainless steel filter discs of 0.5 µm pore size inserted in a body made of Hastelloy C 276, material also used for the end covers. It can stand up to 10000 psi.

The oven (UT6420 from Heraeus) has a total volume of 375L, whit a chamber size 554 mm width, 1319 mm long and 522 mm depth. The oven is provided with a Digicon electronic temperature controller and digital display of the set point and the real temperature value. It allows excellent temperature uniformity (2%). The uncertainty in the temperature measured by the oven is ± 0.5°C.

The pumping system (ISCO pump 1 and ISCO pump 2 in figure 9-1) consists of a pressure/flow rate controller and a piston-driven pump module (D Series Syringe Pumps 100DX from ISCO). The cylinders, pistons and caps are made of Nitronic 50, and the seals are manufactured of graphite-impregnated Teflon. The ISCO pumps can work in two different modes: constant flow and constant pressure. The pump is also supplied with two valves that can be handled to reverse the flow direction. In that way, each pump can either drive water to the pressure vessel or remove water from the pressure vessel. The uncertainty in the pressure measured by the ISCO pump is ± 0.05 bar. The maximum pressure is 10000 psi, while the flow can vary from $1\cdot10^{-5}$ mL min^{-1} to 50 mL min^{-1}. The pump capacity is 103 mL. Additional readings (accuracy of 100 psi) of the pressure can be done in the two pressure gauges (4.5PG10 from HIP) placed in the line with each pressure vessel.

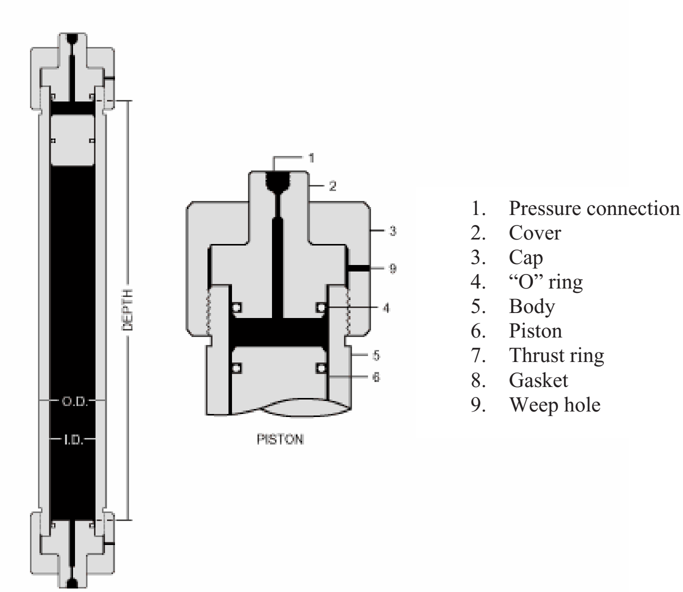

1. Pressure connection
2. Cover
3. Cap
4. “O” ring
5. Body
6. Piston
7. Thrust ring
8. Gasket
9. Weep hole

Figure 9-2. Cross-section of piston high pressure vessel and cap

The two valves located inside the oven (valves 4 and 5 in figure 9-1) are high temperature valves (30-11HF4-HT from HIP), standing up to 538°C and 30000 psi. The body is manufactured from high tensile type 316 stainless steel with grafoil packing. They are provided with an extension to remove the stuffing box away from the hot area of the valve, and allowing placing the handle outside the oven for an easier operation of the equipment.

The valves placed outside the oven (valves 1 and 2 in figure 9-1; 30-11HF4 from HIP) work at room temperature and therefore do not need special features as the previous ones. The valve body is made of high tensile type 316 stainless steel and hardened 17-4PH stainless steel for the lower section stems. The packing includes 90 durometer Buna-nitrile O-ring. They can stand up to 30000 psi.

The safety valves (Safety Head LPSH2-1/4A from BuTech Pressure Systems) are fitted with a rupture disc with a nominal burst pressure of 10000 psi (relief valves 1 and 2 in figure 9-1). Both the safety heads and the rupture discs are manufactured in 316 stainless steel.

All the additional components of the experimental device schematized in figure 9-1 (tubing, adapters, couplings, tees, etc.) were manufactured in 316 stainless steel. The tubing OD is ¼”.

To provide agitation a pneumatic turbine-vibrator (NCT 10 from Copenhagen Vibrator Products ApS) is connected to the equilibrium vessel.

9.3.3 Experimental Procedure

Sufficient excess of powder barite was added to a NaCl solution of the desired concentration. After vigorous agitation, this sample was used to fill the equilibrium vessel. The dilution vessel was filled with a known amount of distilled water[1]. The tubing connecting both ISCO pumps with the vessels, and the tubing connecting both vessels and the filter is filled with water by pumping liquid from the ISCO pumps. This operation will assure an exact value of the filtrated volume, which could be erroneous if air is present in any of the mentioned pipes. The vessels are then transferred to the preheated oven chamber and properly screwed in both ends. Placing the vessels and the filtration system inside an oven will keep a constant temperature distribution.

Valves 4 and 5 (see figure 9-1) are closed to assure no sample is passing from one vessel to another. The whole system is pressurized to the desired pressure by using ISCO pump 1 in a constant pressure mode and keeping valves 1 and 3 open. To provide mixing of the solution in the equilibrium vessel a vibrator was used. After allowing the sample to attain equilibrium the solution is filtered at the experimental temperature and pressure by driving liquid from the equilibrium vessel to the dilution vessel through a 0.5 µm pore size filter. This operation requires the use of two ISCO pumps: ISCO pump 1 will work in the constant pressure mode, while ISCO pump 2 will work in the constant flow mode. Operating in this way, ISCO pump 1 will maintain a constant pressure by a positive displacement of the piston in the equilibrium vessel, while ISCO pump 2 will move the piston in the dilution vessel upwards, allowing the filtrated solution to be hold in the dilution vessel. To avoid water to bypass from one pump to the other, valve 1 must be closed during the filtration. A schematic diagram of the filtration procedure is shown in figure 9-3.

Once the desired volume of sample has been filtered, the pressure is decreased to 1 atm and the system cooled down to room temperature before taking the sample out and storing it for a later analysis. Precipitation as a consequence of the changes in both temperature and

---

[1] NaCl solution substitutes distilled water in the filtration reactor when dilution with the available volume of water is not enough to avoid barite precipitation when decreasing the experimental temperature and pressure to room conditions.

pressure is avoided due to the dilution process taking place in the dilution vessel. Previous calculations determine the maximum filtration volume allowed to assure precipitation will not take place when the experimental conditions are changed to atmospheric pressure and room temperature.

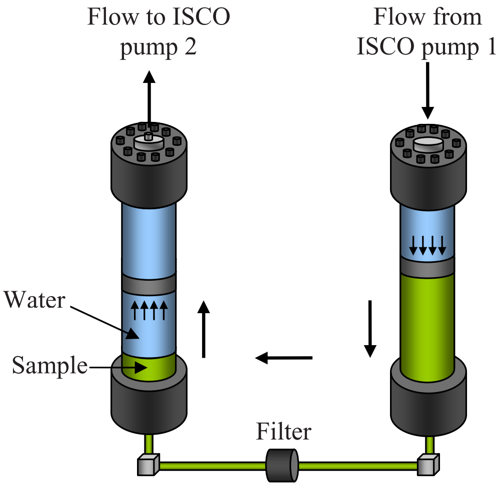

Figure 9-3. Filtration process

9.3.4 Experimental Uncertainties

The temperature was measured within ± 0.5°C, and the uncertainty of the experimental pressure was ± 0.05 bar.

The uncertainty associated with weighing starting materials (NaCl) during sample preparation is ± 0.05 mg. The volume of NaCl sample prepared was always 1 L, and thus the largest error, corresponding to the lowest NaCl concentration employed (0.1 M) is ± $8.6 \cdot 10^{-4}$ %.

The uncertainty related to the weight of the distilled water used to fill in the dilution vessel is ± 0.5 mg. That uncertainty is translated into absolute deviation values for barite concentration within the range 10^{-11} to 10^{-10} m. The highest deviation found for all the measurements performed is $2.72 \cdot 10^{-10}$ m $BaSO_4$ (± $3.1 \cdot 10^{-4}$ %), a value low enough to be neglected. For NaCl solubility determinations, the absolute deviation is found within the range $4.7 \cdot 10^{-5}$ to $6.6 \cdot 10^{-5}$ M (molarity).

The uncertainty associated to the filtration volume is ± 0.005 mL, which results in absolute deviations for the concentration of $BaSO_4$ of the order of 10^{-8} m. The highest absolute deviation found is $8.54 \cdot 10^{-8}$ m $BaSO_4$, a value that can be neglected if we take into account the measured concentrations are of the order of 10^{-5} m. For NaCl solubility determinations, the absolute deviation is found within the range $1\cdot10^{-3}$ to $2.3\cdot10^{-3}$ M.

The standard deviations and variation coefficients associated to the ICP-MS determinations are given in tables aIII-1 to aIII-3 in Appendix III.

9.4 Analytical Technique: Inductively Coupled Plasma Mass Spectrometry

The determination of barite solubility is a rather complex task due to the difficulty of finding a reliable analytical technique able to measure accurately so low concentrations. Any colorimetric/gravimetric/titration technique, or any technique involving the measurement of masses and/or volumes must be rejected, as it will very likely imply large experimental errors. Barite solubility in water is of the order of 10^{-5} m, while barite solubility in NaCl solutions is of the order of 10^{-4} m. Moreover, in order to avoid precipitation when the experimental temperature and pressure are brought to atmospheric conditions, high dilution rates are required. Thus, the final concentrations to be measured may be well below 1 ppm (and therefore, the detection limit of the analytical technique should be at least 10 times lower).

Vetter et al. (1983) studied the accuracy of atomic absorption (AA), atomic emission (AE) and liquid scintillation counting (LSC) in the determination of $SrSO_4$ concentrations. They prepared solutions of known amounts of Sr^{2+} in distilled water and in solutions of NaCl, $MgCl_2$ and $CaCl_2$, and analyzed them by AA, AE and LSC. They concluded that AE is consistently inaccurate and, thus, unreliable. The same conclusion is supported by Davis and Collins (1971) when studying $BaSO_4$ solubility.

According to Vetter et al. (1983), the AA method gave systematically low values of strontium concentration, with a relative deviation with respect to their standards as high as 16%. This value is expected to be even larger for barite due to its lower solubility. Rollemberg and Curtius (1982) used flameless atomic absorption to determine barium in natural waters, after separating it from the interfering ions by ion-exchange chromatography. The relative deviation was over 10% for most of the measurements, and reached 20% for 100 ppm samples, even though the detection limit of the device used was 9 ppm. Roe and Froelich (1984) determined barium with a precision about ± 13% by graphite furnace atomic absorption, with a detection limit of 0.6 ppm.

Vetter et al. (1983) state high accuracy can be obtained in $SrSO_4$ determinations by LSC. Nevertheless, Davis and Collins (1971) measured the sulphate concentration of a radioisotope-tagged (^{35}S) solution of precipitated BaSO$_4$ by LSC, resulting in a low reproducibility (± 20%)

All the problems found in the literature for AA and AE, together with the capabilities found at DTU, made us choose ICP-MS to determine our BaSO$_4$ concentrations.

9.4.1 Introduction

Inductively coupled plasma mass spectrometry (ICP-MS) is widely used for trace (ppb-ppm) and ultra-trace (ppq-ppb) elemental analysis. ICP-MS has become the most prominent MS technique due to its extremely low detection limits (see figure 9-4) for the majority of the elements and its multi-element capability (Stuewer and Jakubowski, 1998). Since 1983, when the technique was made commercially available, ICP-MS devices have been used worldwide in many different application areas such as environmental, geochemical, medical, nutritional, nuclear, chemical, metallurgical, etc. ICP-MS has clear advantages when compared to other spectroscopic techniques (flame atomic absorption, inductively coupled plasma optical emission spectrometry, emission atomic absorption): It can be used for multi elemental analysis of solid, liquid and vapour samples; it is fast (it can determine all the elements in about six minutes); it has lower detection limits (see figure 9-4) and a larger linear interval than any other spectroscopic technique; and it can be used for isotopic analysis.

Figure 9-4 shows the detection limits achievable by a quadrupole-based ICP-MS device.

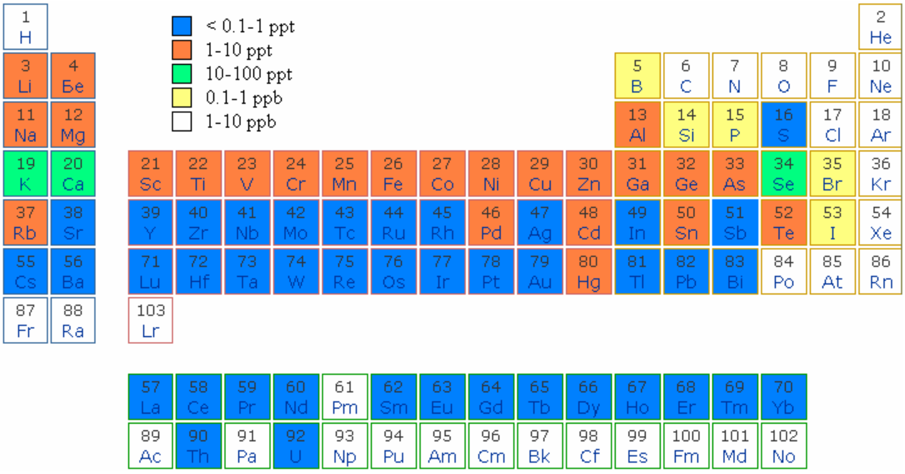

Figure 9-4. Approximate detection limits achievable by ICP-MS

9.4.2 Principles of Operation

There is a wide range of commercial ICP-MS systems with different capabilities, strengths and limitations. Nevertheless, most of them are formed by nebulizer, spray chamber, plasma torch, MS interface, ion lenses, mass separation device and ion detector. The schematic diagram of a typical ICP-MS instrument is shown in figure 9-5. The sample, which is generally a liquid, is pumped into a nebulizer where aerosol is generated. The finest droplets are selected by means of a spray chamber, and transported into the plasma, where the sample follows different processes as it travels: vaporization, atomization and ionization. Most of the ions generated are positively charged due to the removal of one electron from the outer shell of the atom by the energy (heat) applied from a plasma discharge. The ions are then transported into the mass separation device passing through an interface which allows a gradual change of pressure from atmospheric conditions to the vacuum required by the mass spectrometer. The current of ions is focused by different ion lenses and transformed into an electrical signal in the ion detector after proper separation in the mass spectrometer.

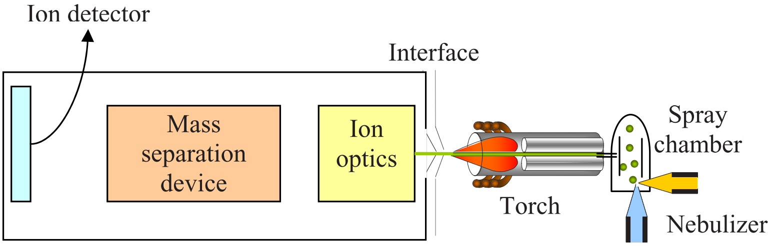

Figure 9-5. Schematic of and ICP-MS system

9.4.2.1. Sample Introduction

The sample containing the analyte of interest may be introduced in the torch as a gas or as aerosol of fine droplets or solid particles. The fine aerosol generation is achieved by a nebulizer followed of a spray chamber for droplet selection. In the nebulizer, the liquid sample is broken up into fine aerosol. Figure 9-6 shows a pneumatic nebulizer, where the mechanical force of a gas flow (generally argon) is used to generate a droplet dispersion of the analyte solution (Thomas, 2001). Alternative pneumatic nebulizer designs are available in the market to fulfil different requirements (e.g., high TDS or small sample volume).

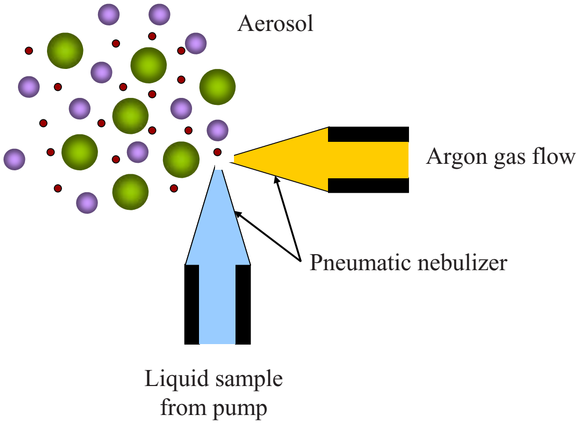

Figure 9-6. Pneumatic cross-flow nebulizer

Once the aerosol is formed in the nebulizer, the finest droplets (smaller than 8 μm in diameter, representing 1-2% of the total aerosol) are selected by a spray chamber. The most common spray chamber is the so-called double-pass or Scott chamber. The aerosol enters through a central tube and runs through the whole length of the chamber. The largest droplets fall due to gravity forces and will be removed through a drain tube, while the finest droplets pass to the space between the central tube and the outer wall and are transported to the torch.

9.4.2.2 Torch and Plasma

The system to generate the plasma is formed by a torch and a copper coil supplied by a radio frequency (RF) power (typically 750-1500 W). The RF passing through the coil will generate an intense electromagnetic field. Then, a high voltage spark from a Tesla coil causes some electrons of the flowing argon to be removed from their atoms. The electrons are accelerated by the magnetic field and crash against new argon atoms stripping off more electrons. The chain reaction will continue and will transform the gas into atoms, ions and electrons forming a high temperature plasma discharge (around 10000 K), which is maintained by the continuous RF supply.

The sample aerosol is driven at a very high velocity to the plasma, creating a hole or channel in the centre of the plasma. Then, the sample undergoes different physical changes as it travels through the different temperature zones of the plasma. These changes can be seen in more detail in figure 9-7. The first step is desolvation of the droplet, which becomes a solid microparticulate. Then the solid is vaporized and passes into a gaseous form, and afterwards atomization takes place. The ground-state atoms will collide with argon electrons and will be transformed into positive ions.

Argon is the most common gas used to sustain the ICP. It has a high first ionization energy (16 eV), and therefore it is very convenient to ionize most of the elements of the periodic table, with ionization energies in most of the cases below 10 eV (corresponding to > 50 % ionization). At the same time, it also has a very high second ionization energy (27 eV), resulting in a very low population of Ar^{+2} ions. Nevertheless, different gases may be used for plasma generation, and it has been noticed that mixtures of argon and N_2, Xe, or H_2 may substantially reduce certain polyatomic ions (Jarvis et al., 1992).

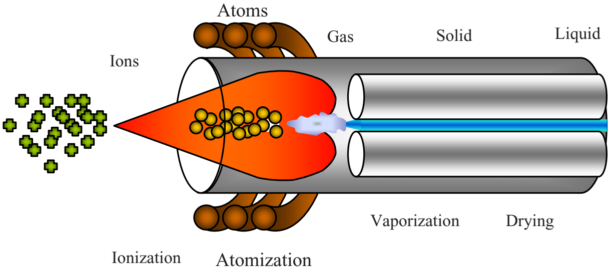

Figure 9-7. Physical changes experienced by the sample through the torch

9.4.2.3 Interface Region

Once the positively charged ions are generated in the plasma, they are conducted to the mass spectrometer, which works at high vacuum (10^{-4}-10^{-6} torr). As the plasma is generated under atmospheric pressure, a middle step is required in order to efficiently transport the ions keeping electrical integrity. This is the purpose of the interface region. It is formed by two metallic cones (sampler cone and skimmer) with very small orifices in the centre, and maintained at a vacuum of about 1 Torr.

9.4.2.4 Ion Focusing System

After the ions leave the skimmer, they must reach the mass separation device. Ion lenses placed between the skimmer cone and the mass spectrometer (ion optics) are used to focus and transmit the ion beam. The ion optics consists of a group of metallic plates, barrels or cylinders associated to different voltages. Their purpose is to focus the ions and to reject particulates, neutral species and photons from reaching the mass analyzer and detector.

In many devices a grounded metal disc is placed right after the skimmer in order to stop particulates, neutral species and photons, while the ions are able to move around it and go on their way to the mass analyzer. Another option to get rid off undesired species is to place the mass analyzer below or above the central stream axis, so only the desired focused ions are in the same axis as the analyzer (see figure 9-8).

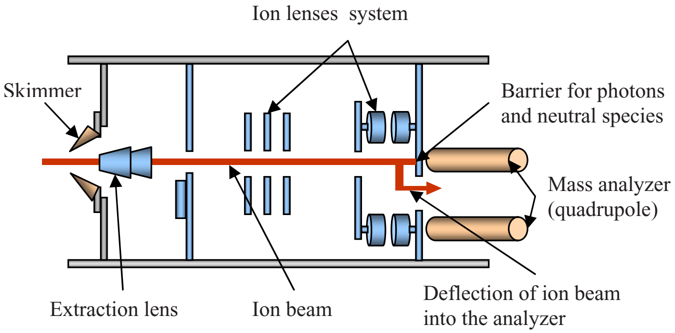

Figure 9-8. Ion lenses diagram

9.4.2.5 The Mass Analyzer

After the ions emerge from the ion optics, they pass to the mass separation device and are separated according to their mass to charge ratio. Its objective is to allow analytes of a given mass to charge ratio to pass through the separation device and enter the detector, while the non-analyte, interfering and matrix ions are filtered.

The most used mass analyzer is the so-called quadrupole. It is formed by four metal rods or metal surfaces forming a squared cross section. A diagram of this configuration is shown in figure 9-9. A direct current (DC) is applied on one pair of opposite rods, while a radio frequency field (RF) is applied to the other pair. If the current values are selected properly, only ions of a given mass to charge ratio will have a stable path through the rods and will emerge at the end of it (red ion in figure 9-9). The rest of the ions will strike the rods and be nebulized, or will pass through the rods space. In any case, those ions will be lost and will not reach the detector. Then, the scanning process is repeated for a different analyte with a different mass to charge ratio, and the process goes on until all the analytes of interest have been scanned.

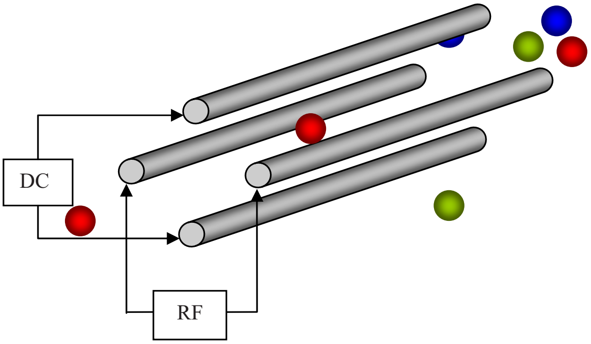

Figure 9-9. Quadrupole mass spectrometer

9.4.2.6. Ion Detector

After the desired mass to charge ratios to analyze have been separated in the previous step, the ions must be counted and transformed into an electrical signal in order to be able to determine the element concentration. The channeltron electron multiplier is an open glass cone coated with a semiconductor material, having the capability of generating electrons from a hitting ion. The upper part of the cone is biased to a negative potential of around -3kV, while the back part of the device near the collector is kept at ground. Therefore, the resistance of the coating varies with the position. When a positive ion leaves the mass analyzer it is attracted to the negative potential at the mouth of the channeltron and hits this surface. As a consequence, one or more secondary electrons form, and they move down the tube due to the potential gradient. In their way down the tube, these secondary electrons strike new areas of the coating surface, and more secondary electrons are emitted. The process is repeated many times and the result is a discrete pulse formed by many millions of electrons (10^8) (Jarvis et al., 1992). This pulse is conducted to a pre-amplifier where it is detected, and to a digital discriminator and counting circuit, where the pulses above a certain amplitude are counted.

9.4.3. Interferences in ICP-MS

The interferences in ICP-MS can be divided into spectroscopic interferences and non-spectroscopic interferences, or matrix effects. The first type of interferences may be also divided in four different subgroups: isobaric overlap, polyatomic ions, refractory oxide ions and doubly charged ions. The matrix effects can also be divided into two subgroups:

Suppression and enhancement effects, and physical effects caused by high total dissolved solids.

9.4.3.1 Isobaric Overlap

The isobaric overlap is found when the sample to analyze contains two elements which have isotopes of the same mass to charge ratio. Actually, the mass to charge ratio of those isotopes may differ, but in a very small quantity which cannot be resolved by the quadrupole mass analyzer. The use of a high resolution mass analyzer may solve this problem and discriminate between very small differences in mass to charge ratios.

This kind of interference is only found for mass to charge ratios above 36, and they increase for low masses, while are not frequent for high masses. There are overlaps with the plasma gas (generally Ar) and the impurities it contains (Xe, Kr). The most abundant isotope of argon is ^{40}Ar (99.6%), making the determination of either ^{40}Ca (96.9%) or ^{40}K (0.01%) impossible.

Isobaric overlaps can be avoided by choosing another isotope of the element free of interferences. If this is not a possibility (there is no isotopes free of interferences or the natural abundance is too low) mathematical corrections using another isotope (free of interferences) of the interfering element may be applied. For example, the determination of ^{204}Pb in the presence of Hg will be interfered by ^{204}Hg. A correction based on the isotope ^{201}Hg, which is free of interferences, may solve the problem:

$$^{204}Pb = \text{Total signal} - {}^{201}Hg \cdot (6.7/13.8) \quad \textbf{(9-1)}$$

where 6.7 and 13.8 are the natural abundances in weight percentage of ^{204}Hg and ^{201}Hg, respectively.

9.4.3.2 Polyatomic Ions

Polyatomic ions result from the combination of two or more atomic species (e.g., NOH^+, Ar_2H^+). They are the most important type of interference, although in practical analysis there are relatively few serious interference effects if care is taken in the sample preparation process. They are generally formed by the combination of argon, hydrogen and oxygen (the most abundant species in the plasma) among them or with any other element present in the sample (e.g., $^{40}Ar^{40}Ar$, $^{40}Ar^{16}O$, $^{40}Ar^{1}H$). Polyatomic ion peaks are only significant up to a mass to charge ratio around 82.

The amount of polyatomic ions depends on many factors, being the most important ones the geometry of the extraction system, operating parameters for plasma and nebulizer systems, and the characteristics of the sample.

For this type of interference mathematical corrections are not a reliable solution as polyatomic ion peaks may be relatively large compared to the analyte contribution. Therefore, whenever possible, the selection of another isotope not interfered by polyatomic ions is preferred, even though the natural abundance of such isotope is low.

Many of the polyatomic ion interferences contain oxygen and/or hydrogen originated from the dissociation of vapour water from the solution. To reduce such interferences it is necessary to reduce the population of both oxygen and hydrogen ions. This may be achieved by decreasing the temperature in the spray chamber with a cooling system.

9.4.3.3 Refractory Oxides

Refractory oxides result from the incomplete dissociation of the sample matrix or from a recombination of ions in the plasma tale. The consequence is refractory oxides of the type MO^+, MO_2^+ or MO_3^+, interfering 16, 32 and 48, respectively, mass units above the M^+ peak. For the majority of elements the ratio MO^+/M^+ is lower than 1.5%, while the ratio MO_2^+/M^+ is lower than 0.002%. Generally, the appearance of refractory oxides is determined by the monoxide bond strength of the element, being the formation of MO^+ favoured for the highest oxide bond strength.

The percentage of refractory oxides can be minimized by optimizing the radio frequency power (higher power will break more oxides) and the nebulization flow (determines the location in the axis at which dissociation of the molecules is complete).

9.4.3.4 Doubly Charged Ions

The big majority of ions generated in the plasma are of type M^+, although doubly charged ions may also be formed. The presence of M^{2+} will be determined by the second ionization energy of that element and by the operation conditions of the plasma. Only elements with a second ionization energy lower than the first ionization energy of the plasma gas (16 eV in the case of Ar) will generate M^{2+} ions. These elements are alkaline earths, rare earths, and some transition metals. The nebulizer flow can also influence on the amount of doubly charged ions. If the flow is too low, the plasma temperature will increase resulting in a larger amount of M^{2+}. Generally, the amount of doubly charge ions is lower than 1 %.

The consequence of the appearance of M^{++} ions is the decrease in the M^+ signal, and the possibility of isobaric overlaps in m/2. When alternative isotopes cannot be used, some corrections will be needed in order to minimize these interferences.

9.4.3.5 Physical Effects Caused by High Dissolved Solids

The use of ICP-MS is limited to samples containing small amounts of dissolved solids. Solutions with a TDS content above 500 mg L^{-1} cause a considerable signal drift over short periods of time. Moreover, the nebulizer and sampling cones are easily blocked by the solids due to their small orifices. For these reasons, samples containing more than 0.2 % of TDS are not recommended for ICP-MS analysis under continuous flow. Working with transient signals the amounts of solids can be increased up to 2-3 %.

The signal drift experienced at the beginning as a consequence of solid deposition on the cones can be reduced if a similar solution is employed for 20 minutes previous to the analysis. Operating in that way the signal will be more stable and some corrections may be applied to reduce this effect. The signal drift can be corrected by using internal standards.

9.4.3.6 Suppression and Enhancement Effects

Suppression and enhancement effects result from a high concentration of easily ionized elements in the sample. The causes generating them are not very clear, although many investigators think they appear due to changes in the flux and composition of the ion beam. Such changes appear as a consequence of space charge effects around the skimmer area. The final result is suppression (generally) or enhancement of the signal, being the effects more pronounced for light elements than for heavy ones.

Non spectroscopic interferences are difficult to quantify and to control. A previous scan of the sample is recommended in order to have a closer knowledge of the sample and to find out possible interferences. Some possibilities to decrease their effects are:

- Dilution of the sample to decrease the TDS below 0.2 % (or 2% when working with transient signal)
- Internal standards with similar mass and ionization energy to that of the analyte in order to control the signal drift
- Instrumental optimization
- Standard addition calibration techniques
- Separation of the analyte from the matrix (ion exchange separation, co-precipitation)

9.5 Results

9.5.1 Time Required to Achieve Equilibrium

The first set of experiments performed was devoted to estimate the time required to achieve equilibrium for the $BaSO_4$-NaCl-H_2O system at the slowest conditions (lowest temperature, pressure and NaCl concentration to be measured: 50ºC, 100 bar and 0.1 m). Once this time is determined, experiments covering the temperature range 50-250ºC, the pressure range 100-600 bar, and the concentration range 0.1-6 m NaCl can be carried out.

To determine the equilibrium time, 17 experiments in 0.1 m NaCl solutions were carried out at 50ºC and 100 bar, keeping those conditions constant for different periods of time. In order to check the reproducibility of the results, some of the experiments were repeated up to 3 times. The final samples were analyzed by ICP-MS, and the ICP-MS results were corrected for the dilution process in order to get the real concentration of $BaSO_4$ in the original sample. Eight different standards of 50, 100, 150, 200, 500, 1000, 1500 and 2000 ppb of barium in pure water were used for calibration, together with a blank solution containing no barium. Those standards covered the whole concentration range to be measured. The calibration curves are shown in figure aIII-1 in Appendix III. Four isotopes of barium (^{135}Ba, ^{136}Ba, ^{137}Ba and ^{138}Ba) were followed, the final results being the average of all of them. Each measurement was repeated five times. The results are given in table aIII-1 in Appendix III. In order to cross-check the ICP-MS results, a commercial standard containing 100 ppb of barium along with other components is used.

The results obtained for the first set of experiments are given in figure 9-10. In order to study the influence of the agitation process in the final time required to achieve equilibrium, two different sets of experiments were performed: Using vibration during the whole experimental run (blue triangles), and using a combination of vibration for a time reported in figure 9-10, plus 16 h (red circles) or 44 h (green square) without any kind of agitation. The measurements performed by Templeton (1960) and Strübel (1967) at 50ºC, 0.1 m NaCl and 1 atm are included for comparison.

Figure 9-10 does not show the expected increasing barium concentration with time for low time values, and a plateau from a certain time corresponding to equilibrium. Therefore, it is not possible to determine the equilibrium time from these results. Moreover, the concentration measured for the 100 ppb Ba^{2+} commercial standard is 219.6 ppb, and thus corresponding to a residual deviation of 119.6%. No clear explanation has been found for this extreme inaccuracy, since the device was calibrated for the whole range of concentrations measured, and the calibration curves show a nice linearity with R^2

coefficients above 0.999 in all the cases. The large errors could be related to the different matrix used in our samples (around 0.1 % NaCl) and in the commercial standard. Nevertheless, this is not a very likely explanation, since both matrices are simple, and a tuning of the ICP-MS device is performed prior to the measurements, using a standard containing different elements covering the whole range of masses. Therefore, the setup should be prepared to measure accurately any component, independently of its mass to charge ratio and the matrix (provided that its salinity is below 2-3 %).

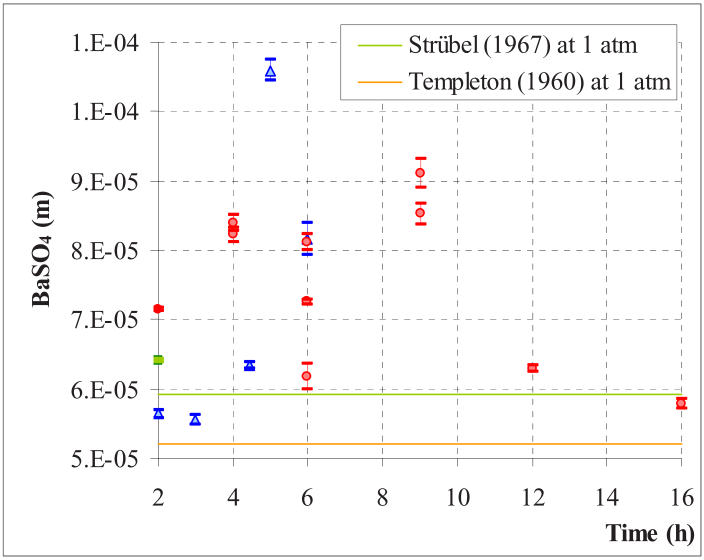

Figure 9-10. Barium concentrations after different running times. Red circles represent experiments where the sample was vibrated for X hours, and kept at constant *T* and *P* for another 16 hours. Blue triangles represent experiments where the sample was vibrated for X hours and filtrated directly afterwards. Green squares represent experiments where the sample was vibrated for X hours, and kept at constant *T* and *P* for another 44 hours.

Due to the unreliable results obtained in figure 9-10, some of the previous ICP-MS measurements were repeated. In order to resemble the experimental samples, the new standards (400, 800 and 1200 ppb of Ba^{2+}) were prepared in 0.1% NaCl instead of pure water, and the blank was a 0.1% NaCl solution. Calibration curves for the different isotopes are shown in figure aIII-2 in appendix III. Three additional standards of 100, 500 and 1000 ppb of Ba^{2+} in 0.1% NaCl were prepared to cross-check the results, together with the commercial standard (100 ppb) used previously. The new measurements are reported in table a3-II in Appendix III. Figure 9-11 compares the new results (DTU_2) with the previous ones (DTU_1).

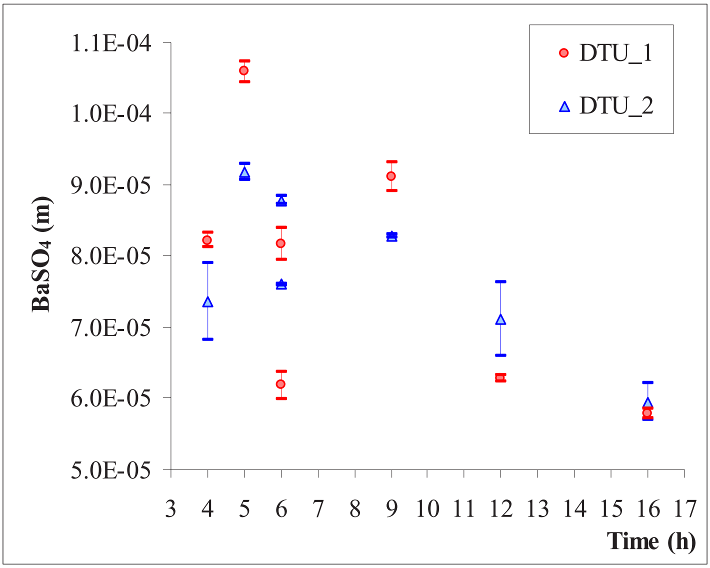

Figure 9-11. Barium concentration from ICP-MS measurements for different running times. DTU_1 refers to the first measurements (reported in table aIII-1 in Appendix III), while DTU_2 refers to the second ICP-MS measurements on the same samples (reported in table aIII-2 in Appendix III).

It is clear from figure 9.11 that the analytical technique used is not reliable, and the results are affected by a random error. Only for one of the samples measured (16 h), the values obtained from both analysis agree. The rest of the points are characterized by extreme deviations. Moreover, the measured values for the 4 different standards used as tests evidence the inaccuracy of the measurements. Table 9-5 shows the real and measured values for those standards, together with the %*RD*, always above 27%, and reaching up to 90%.

Table 9-5
Real and measured standard's concentrations by ICP-MS

Real concentration (ppb)	Measured concentration (ppb)	% RD
100	162.5	**62.5**
500	659.7	**31.9**
1000	1277.8	**27.8**
100	190.3	**90.3**

After measurements failed twice in the ICP-MS device located at the Chemistry department of DTU, and with no clear explanation about the causes of the failure, it was decided to use an alternative ICP-MS device to clarify whether the equipment was the source of the error. All the 17 samples were sent to a certified laboratory (Steins Laboratorium A/S) to be measured by ICP-MS. Among the samples, 4 standards of 500, 1000, 1500, 2000 and 2500 ppb Ba^{2+} in 0.1 % NaCl were included to cross-check the results. The values reported by the laboratory for the samples and standards are given in table aIII-3 in Appendix III. Figure 9-12 compares the new laboratory results with measurements performed at DTU. Again, the same inaccuracy and extreme deviations between the different data is observed. The highest deviation is found for the measurements after 12 hours, where the concentration ranges from $6.3 \cdot 10^{-5}$ m to $1.5 \cdot 10^{-4}$ m.

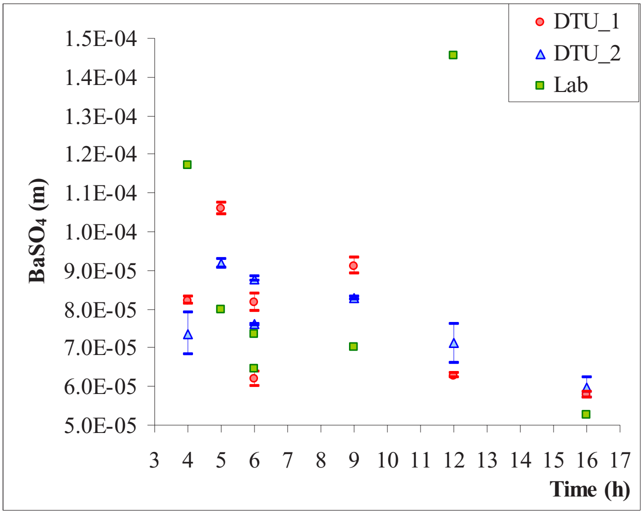

Figure 9-12. Comparison of different ICP-MS measurements

The results reported by the laboratory for the prepared test-standards are given in table 9-6. Those result evidence the lack of reliability of the analytical technique for our particular case, since the lowest residual deviation is around 20%, while the highest *RD* value is above 100%. The laboratory assures to have used two NIST certified reference solutions to check the measurements, obtaining good results (also reported in table 9-6). We cannot find an explanation to this behaviour, unless the different matrix in samples and reference solutions plays an important role in the different values obtained. It is addressed that high salinity solutions involve problems and signal drifts in ICP-MS measurements, but that should not be the case for dilute concentrations (the NaCl content in our samples ranges from 0.05 to 0.1 %).

The experimental conditions, filtration volumes and dilution masses used in experiments 1 to 17, together with the calculated $BaSO_4$ concentration from the ICP-MS measurements is reported in tables aIII-4 and aIII-5 in Appendix III.

Table 9-6
Real and measured standard's concentrations by ICP-MS by Stein Laboratorium A/S

Real c (ppb)	Measured c (μg L^{-1})	Measured c (ppb)	% RD
500	1100	1097	**119.5**
1000	1600	1596	**59.6**
1500	2000	1995	**33.0**
2000	2400	2394	**19.7**
2500	3700	3691	**47.7**
148.0[a]	144.5	144.5	**-2.4**
544.2[b]	522.4	522.4	**-4.0**

[a] NIST 1640 certified reference solution
[b] NIST 1643 certified reference solution

In a final attempt to obtain reliable results, the technique of inductively coupled plasma optical emission (ICP-OES) was tested. Five different samples (reported in table 9-7) were analyzed. In order to determine the reproducibility of the technique, numbers 1 and 2 correspond to the same sample (experiment 13 in table aIII-1 in Appendix III). Numbers 3 and 4 are standards containing 500 and 1500 ppb Ba^{2+} in 0.1% NaCl. To tackle the possible influence of the NaCl matrix, a standard of the same concentration as number 4 (1500 ppb) but using pure water instead was also examined. Unfortunately, the results show again a large disparity between the measured and actual concentrations. The outcome for standards 4 and 5 is rather close, and evidences that matrix effects are not the explanation to the inaccurate results. Moreover, the concentrations for 1 and 2 should be equal, since both correspond to the same sample, but contrary to that, they differ with almost 200 ppb. Such discrepancy shows that the technique is not reliable for our purpose, regardless of the matrix.

Table 9-7
ICP-OES measurements

Number	Real c (ppb)	Measured c (ppb)
1		1770
2		2010
3	500	1050
4	1500	2040
5	1500	1960

New measurements were not performed due to the lack of time and capabilities. Internal standards could have been used to examine the influence of the matrix on the final results, although this is not believed to be the problem. Matrix effects should affect in the same manner number 1 and 2 in table 9-7, but this is not the case. Therefore, an alternative source of error must account for such disparity.

After the unfruitful results obtained for barite solutions, our experimental setup was tested with NaCl solutions in order to demonstrate it is capable of determining the solubility of salts at high temperatures and pressures.

9.5.2 Validation of the Setup

The experimental procedure and setup were validated by measuring sodium chloride solubility at high temperature and pressure. A salt with a high solubility in water was chosen in order to avoid the analytical problems found for barite. The NaCl concentration was determined by titration with $AgNO_3$.

The first step in the validation of the setup was determining the time required to reach equilibrium for the binary $NaCl-H_2O$ system. For this purpose, different experiments at 30ºC and 1 atm were performed, for different running times. Figure 9-13 shows the NaCl concentration behaviour against the experimental time, along with some experimental data available in the literature for comparison.

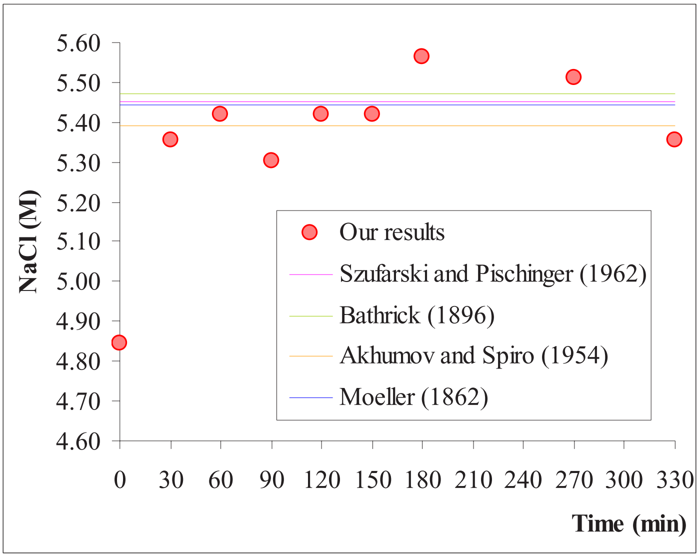

Figure 9-13. Determination of the equilibrium time for the system $NaCl-H_2O$ at 30ºC and 1 atm with agitation (vibration). M refers to molarity.

Figure 9-13 shows a steep increase in NaCl concentration for the low time values, while it reaches a plateau for times above around 30 minutes. When comparing our results to those published by Moeller (1862), Bathrick (1896), Akhumov and Spiro (1954) and Szufarski and Pischinger (1962) at the same experimental conditions, a general agreement is observed. Therefore, it can be concluded that the system NaCl-H_2O at 30ºC and 1 atm reaches equilibrium after 60 minutes of vibration. This time is expected to be lower when temperature is raised.

If no agitation is used, the NaCl concentration increases much slowly with time, as observed in figure 9-14. In this case, more than seven hours are required to guarantee equilibrium.

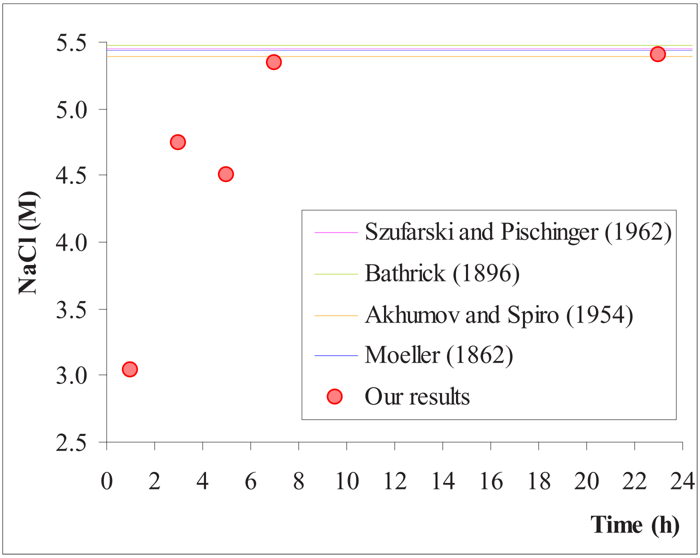

Figure 9-14. Determination of the equilibrium time for the system NaCl-H_2O at 30ºC and 1atm when no agitation is used. M refers to molarity.

To make sure all our experimental values correspond to equilibrium conditions, vibration was used for a minimum of two hours for each determination.

The next step in the validation of the setup was comparing our results with available literature data. Measurements of sodium chloride solubility at high pressure are not very abundant. A more detailed explanation about the experimental conditions and number of measurements found in the literature on the solubility of sodium chloride in pure water at pressures larger than the atmospheric pressure is reported in table 6-1 in Chapter 6. Three sources (Cohen et al., 1911, Sill, 1916, and Adams and Hall, 1931) report NaCl solubility data at high pressure and temperatures in the range 24 to 30ºC which are in close agreement with each other. Thus, we performed different experiments at 30ºC and different pressures in order to compare our results to the available data. The experimental conditions and calculated solubilities are reported in table aIII-8 in Appendix III. Figure 9-15 shows the values for the NaCl solubility in pure water at 30ºC and pressures ranging from 1 to 400 atm obtained from our experimental measurements, along with experimental data available in the literature and calculations by the extended UNIQUAC model. All the sources show a close agreement among them, and also with our new values and the model calculations. Therefore, it is proven our setup is capable of replicating available published data.

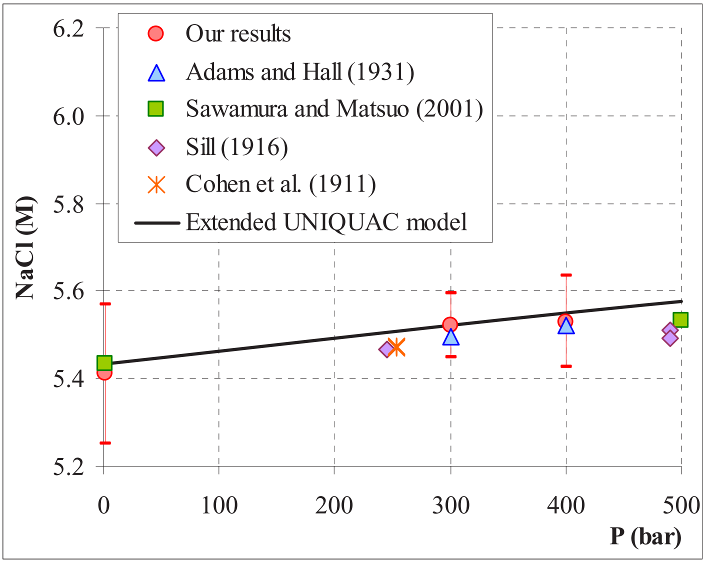

Figure 9-15. NaCl solubility (in molarity) in pure water at 30ºC

The reproducibility of the results was studied at 100ºC and different pressures, especially at 500 bar. The experimental conditions were chosen in order to demonstrate results are reproduced not only at low temperature and pressure, but also at more complex experimental conditions. Figure 9-16 shows the determination of sodium chloride solubility in pure water at 100ºC and different pressures. Extended UNIQUAC calculations are also reported. No data at 100ºC or similar and pressures larger than 1 atm were found in the literature, and therefore only one point at atmospheric pressure is given. The point corresponds to the average solubility value out of 22 sources found in the literature. The experimental conditions used, titration volumes and calculated results are reported in table aIII-9 in Appendix III.

The reproducibility of experiments at 100 and 300 bar is very good, with a variation coefficient (*CV*, equation aIII-1 in Appendix III) as low as 0.21 and 0.83 %, respectively. This accuracy is not so high at 500 bar, where the variation coefficient increases to 4.84 %. Nonetheless, the value is low enough to demonstrate experiments can be reproduced, and the experimental setup can be used to accurately determine salt solubility at high temperature and pressure. The agreement of our experimental solubilities with extended UNIQUAC calculations is also remarkably good.

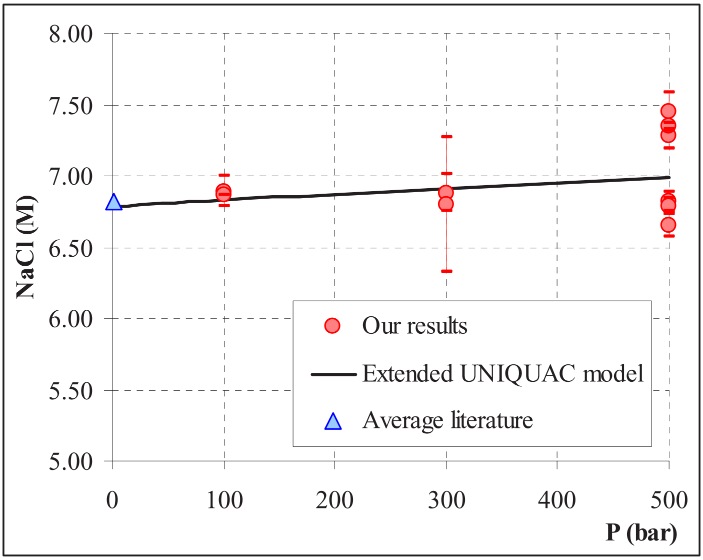

Figure 9-16. NaCl solubility (in molarity) in pure water at 100ºC

After analyzing the results shown in figures 9-15 and 9-16 it seems clear the experimental setup developed is capable of determining salt solubility at high temperature and pressure. The problems encountered when studying barite are therefore related to inaccuracies in the analytical technique.

9.6 References in Chapter 9

Adams, L.H., Hall, R.E., 1931. The influence of pressure on the solubility of sodium chloride in water. A new method for the measurement of the solubilities of electrolytes under pressure. Journal of the Washington Academy of Sciences 21(9), 183-194.

Akhumov, E.I., and Spiro, N.S., 1954. Rastvorimost' khloridov v soljanoj kislote. Zhurnal Prikladnoj Khimii 11 (27), 1163-1169.

Balarew, D. 1925. Löslichkeit und korngrösse. 1. Z. Anorg. Allg. Chem. 145, 122-126.

Bathrick, H. A., 1896. Precipitation of salts. J. Phys. Chem. 1, 157-169.

Blount, C.W., 1977. Barite solubilities and thermodynamic quantities up to 300 ºC and 1400 bars. American Mineralogist 62, 942-957.

Brower, E., Renault, J., 1971. Solubility and enthalpy of the barium strontium sulphate solid solution series. New Mexico State Bureau of Mines and Mineral Resources, Circular 116.

Cohen, E., Inouye, K., Euwem, C., 1911. Piezochemische studien. VII.. Z. Physik. Chem. 75, 257-304.

Culberson, C.H., Lathman, G., Bates, R.G., 1978. Solubilities and activity coefficients of calcium and strontium sulfate in synthetic seawater at 0.5ºC and 25ºC. J. Phys. Chem. 82, 2693-2699.

Davis, J.W., Collins, A.G., 1971. Solubility of barium and strontium sulfates in strong electrolyte solutions. Environmental Science & Technology 5, 1039-1043.

Grabowski, R.J., Unice, R.C., 1958. Quantitative spectrochemical determination of barium and strontium. Analytical Chemistry 30, 1374-1379.

Howell, R.D., Raju, K., Atkinson, G., 1992. Thermodynamics of "Scale" mineral solubilities 4. $SrSO_4$. J. Chem. Eng. Data 37, 464-469.

Jacques, D.C.; Bourland, B.I., 1983. A study of solubility of strontium sulphate. SPEJ 292-300.

Jarvis, K.E., Gray, A.L., Houk, R.S., 1992. Handbook of Inductively Coupled Plasma Mass Spectrometry. Blackie & Sons Ltd., Suffolk, Great Britain.

Johnson, C.M., Nishita, H. 1952. Analytical Chemistry 24, 736.

Lucchesi, P.J., Whitney, E.D., 1962. Solubility of strontium sulphate in water and aqueous solutions of hydrogen chloride, sodium chloride, sulphuric acid and sodium sulphate by the radiotracer method. J. Appl. Chem. 12, 277-279.

Moeller, K., 1862. Ueber den Einflufs des Drucks auf die Löslichkeit einiger Salze. Annals of Physics 117, 386-417.

Müller, G., 1960. Die Löslichkeit von Coelestin ($SrSO_4$) in wässerigen NaCl- und KCl-lösungen. Neues Jahrb. Mineral. Mon., 237-239.

Reardon, E.J., Armstrong, D.K., 1987. Celestite ($SrSO_4$(s)) solubility in water, seawater and NaCl solution. Geochimica et Cosmochimica Acta 51, 63-72.

Roe, K.K., Froelich, P.N., 1984. Determination of barium in seawater by direct injection graphite furnace atomic absorption spectrometry. Anal. Chem. 56, 2724-2726.

Rollemberg, M.C.E., Curtius, A.J., 1982. Flameless atomic absorption determination of barium in natural waters using the technique of standard additions. Mikrochimica Acta 2, 441-447.

Sawamura, S., Matsuo, H., 2001. Solubility of several organic and inorganic compounds at high pressure. Koatsuryoku no Kagaku to Gijutsu 11(2), 129-136.

Schulien, S., 1987. High-temperature/high-pressure solubility measurements in the systems $BaSO_4$-NaCl-H_2O and $SrSO_4$-NaCl-H_2O in connection with scale studies. SPE symposium (SPE 16264), San Antonio, Texas.

Sill, H., 1916. The influence of pressure on solubility. Journ. Am. Chem. Soc. 38, 2632-2643.

Strübel, G., 1966. Die hydrothermale Löslichkeit von Cölestin in System $SrSO_4$-NaCl-H_2O. Neues Jahrb. Mineral. Mon., 99-107.

Strübel, V.G., 1967. Zur Kenntnis und genetischen Bedeutung des Systems $BaSO_4$-NaCl-H_2O. Neues Jahr. Miner. Monatsh., 223-234.

Stuewer, D., Jakubowski, N., 1998. Elemental analysis by inductively coupled plasma mass spectrometry with sector field instruments: A progress report. Journal of Mass Spectrometry 33, 579-590.

Sun, R., Hu, W., Duan, Z., 2001. Prediction of nitrogen solubility in pure water and aqueous NaCl solutions up to high temperature, pressure, and ionic strength. Journal of Solution Chemistry 30(6), 561-573.

Szufarski Z., Pischinger E., 1962. Badania rozpuszczalnosci weglanu, siarczanu i chlorku sodowego. Przemysl Chemiczny 41, 695-698.

Templeton, C.C., 1960. Solubility of barium sulfate in sodium chloride solutions from 25^o to 95^oC. Journal of Chemical and Engineering Data 5 (4), 515-516.

Thomas, R., 2001. A beginner’s guide to ICP-MS. Part II. The sample-introduction system. Spectroscopy 16 (5), 56-60.

Uchameyshvili, N.Y., Malinin, S.D., Khitarov, N.I., 1966. Solubility of barite in concentrated chloride solutions of some metals at elevated temperatures in relation to problems of the genesis of barite deposits. Geochem. Int. 10, 951-963.

Vetter, O.J.G., Vandenbroeck, I., Nayberg, J., 1983. $SrSO_4$: the basic solubility data. Society of Petroleum Engineers, 271-281.

10. Conclusions

The solubility of sparingly soluble salts found in natural waters has been studied in connection to the problem of scale formation found in geothermal and oilfield operations.

The extended UNIQUAC model presented by Thomsen and Rasmussen (1999) has been chosen to calculate aqueous phase activity coefficients, while the Soave-Redlich-Kwong equation of state is used to calculate fugacities in the gas phase. The model has been improved by the addition of two parameters in order to account for the pressure dependency of solubility. The extended UNIQUAC model has been chosen over other alternatives due to its excellent relationship between accuracy and simplicity. It only requires two parameters per species, plus two parameters per species pair, while the temperature dependency is accounted for in the model equations. The figures presented through this thesis show that the extended UNIQUAC model is capable of giving accurate results even at very high temperatures and pressures. Most of the data used for the parameter estimation could be reproduced by the model within the experimental accuracy.

More than 7000 SLE measurements have been collected, covering a wide range of temperature (up to 300°C), pressure (up to 1000 bar) and concentrations up to saturation. All these data have been analyzed prior to their use, and those found to be unreliable have not been used for parameter estimation. Unknown parameters for the species CO_2(aq), H^+, Na^+, Ba^{2+}, Sr^{2+}, Ca^{2+}, Mg^{2+}, Cl^-, OH^-, SO_4^{2-}, CO_3^{2-} and HCO_3^-, and for their interactions, have been estimated on the basis of those SLE data.

The extended UNIQUAC model with the new parameters has been used to calculate vapour-liquid, solid-liquid, and speciation equilibria in systems found to form scale in geothermal and oilfield operations. The scaling minerals $CaSO_4$, $CaSO_4{\cdot}2H_2O$, $SrSO_4$, $BaSO_4$, $CaCO_3$, $BaCO_3$, $SrCO_3$, $MgCO_3$, $MgCO_3{\cdot}3H_2O$, $MgCO_3{\cdot}5H_2O$, $Mg(OH)_2$, and $3MgCO_3{\cdot}Mg(OH)_2{\cdot}3H_2O$ have been studied.

The validity of the model has been demonstrated by performing solubility calculations for different scaling minerals in natural waters. The model has been implemented in the computer program SPECS developed at IVC-SEP. This program has been employed to determine solubility indices of complex electrolyte solutions of high ionic strength up to high temperatures and pressures. The match of our results with field observations, and the agreement with other sources, makes us confident about the reliability of the extended UNIQUAC model.

The simplicity of the model, together with the good performance obtained for all the systems investigated, make our model an appropriate choice as a tool to study scale formation. As the model only contains binary interaction parameters, it can be applied to any multicomponent system for which the binary parameters are known.

The experimental part of the Ph.D. project was intended to complete the gaps found in the literature reporting barite solubility in NaCl solutions. In this context, alternative experimental procedures have been addressed and evaluated. An experimental setup to determine salt solubility at high temperature (up to 300ºC) and pressure (up to 10000 psi) has been designed and built. The setup has been validated performing measurements of sodium chloride solubility in pure water at 30 and 100ºC, and different pressures. Experiments have also been carried out for $BaSO_4$-NaCl-H_2O solutions at 50ºC and 100 bar, in order to determine the time required by that system to attain equilibrium. Problems with the analytical techniques employed (ICP-MS and ICP-OES) have resulted in unreliable data and in the impossibility to further study the system $BaSO_4$-NaCl-H_2O.

References in Chapter 10

Thomsen, K., Rasmussen, P., 1999. Modeling of vapor-liquid-solid equilibrium in gas-aqueous electrolyte systems. Chemical Engineering Science 54, 1787-1802.

Appendix I: Helgeson's and Bromley's Models

In this section, I will briefly present the thermodynamic models developed by Helgeson (Helgeson, 1967, 1969, Helgeson and Kirkham, 1974a, b, 1976; Helgeson et al., 1978, 1981, Shock and Helgeson, 1988, Johnson et al., 1992) and Bromley (1973). Both models were studied at the very beginning of this Ph.D. project in order to address their applicability to calculate and predict the solubility behaviour of scaling minerals in multicomponent solutions at high temperature and pressure.

Helgeson Model

Helgeson calculated successfully thermodynamic and transport properties of aqueous species at temperatures up to 1000°C and pressures up to 5 kbar. A detailed description of the equations developed can be found in Shock and Helgeson (1988).

Standard States

- Minerals and pure liquids: Unit activity of the pure component at all pressures and temperatures.
- Gases: Unit fugacity of the hypothetical ideal gas at 1 bar and any temperature.
- Aqueous species other than water: Unit activity of the species in a hypothetical 1 molal solution referenced to infinite dilution at any pressure and temperature.

Gibbs Free Energy

The standard state Gibbs free energy ($\Delta G^0_{P,T}$) of minerals, gases, and aqueous species at T and P can be calculated from the standard state Gibbs free energy of formation ($\Delta_f G^0$) of the species from its elements in their stable phase at the reference pressure (P_0) and temperature (T_0), and a term accounting for the differences in the standard state Gibbs free energy of the species that arise from changes in pressure and temperature ($G^0_{P,T} - G^0_{P_0,T_0}$):

$$\Delta G^0_{P,T} = \Delta_f G^0 + (G^0_{P,T} - G^0_{P_0,T_0}) \qquad \textbf{(aI-1)}$$

For the *j-th* aqueous solute species, the second term on the right hand side of equation aI-1 can be calculated as (Tanger and Helgeson, 1988)

$$
\begin{aligned}
&G^0_{j,P,T} - G^0_{j,P_0,T_0} = -S^0_{j,P_0,T_0}(T-T_0) - c_{1,j}\left(T\ln\left(\frac{T}{T_0}\right) - T + T_0\right) + a_{1,j}(P-P_0) \\
&+ a_{2,j}\ln\left(\frac{\Psi+P}{\Psi+P_0}\right) - c_{2,j}\left(\left(\left(\frac{1}{T-\Theta}\right) - \left(\frac{1}{T_0-\Theta}\right)\right)\left(\frac{\Theta-T}{\Theta}\right) - \left(\frac{T}{\Theta^2}\right)\ln\left(\frac{T_0(T-\Theta)}{T(T_0-\Theta)}\right)\right) \\
&+ \left(\frac{1}{T-\Theta}\right)\left(a_{3,j}(P-P_0) + a_{4,j}\ln\left(\frac{\Psi+P}{\Psi+P_0}\right)\right) \\
&+ w_j(Z+1) + w_{j,P_0,T_0}(Z_{P_0,T_0}+1) + w_{P_0,T_0}Y_{P_0,T_0}(T-T_0)
\end{aligned}
\tag{aI-2}
$$

where Ψ and Θ are constants equal to 2600 bar and 228 K, respectively, S^0 is the standard state entropy, Z and Y are solvent Born functions (dependent on both pressure and temperature), $a_{i,j}$ and $c_{i,j}$ are P/T independent adjustable regression parameters unique to the *j-th* aqueous solute species, and w is the Born coefficient.

For a mineral or gas, equation aI-2 is transformed into

$$
\begin{aligned}
&G^0_{j,P,T} - G^0_{j,P_0,T_0} = -S^0_{j,P_0,T_0}(T-T_0) + \sum_{i=1}^{1+\Phi T} a_i\left[T_{i+1} - T_i - T_{i+1}\ln\left(\frac{T_{i+1}}{T_i}\right)\right] + \\
&+ \sum_{i=1}^{1+\Phi T}\left\{\frac{(-c_i - b_i T_{i+1} T_i^2)(T_{i+1}-T_i)^2}{2T_{i+1}T_i^2}\right\} \\
&+ V^0_{P_0,T}(P-P_0) - \sum_{i=1}^{\Phi P}\int_{Pti,T}^{P}\Delta V^0_{ti}\,dP - \sum_{i=1}^{\Phi T}\frac{\Delta H^0_{ti}}{T_{ti}}(T-T_{ti})
\end{aligned}
\tag{aI-3}
$$

where Φ_P (0 for gases) denotes the number of phase transitions from (P_0, T) to (P, T). $P_{ti,T}$ represents the pressure of the *i-th* phase transition at T, where $P_0 < P_{ti,T} < P$. Φ_T (0 for gases) is the number of phase transitions from (P_0, T_0) to (P_0, T), being $T_1 = T_0$ and $T_{i>1} = min(T, T_{ti-1,P0})$. a_i, b_i, and c_i correspond to adjustable regression coefficients that are unique to the specified mineral or gas from T_i to T_{i+1}. V^0 and H^0 are the standard molal volume and standard state enthalpy.

For any reaction among *i'* minerals and gases (excluding water), *j'* aqueous solute species, and water:

$$
\Delta_r G^0_{P,T} = \sum_{i=1}^{i'} v_i \Delta G^0_{i,P,T} + \sum_{j=1}^{j'} v_j \Delta G^0_{j,P,T} + v_{H_2O}\Delta G^0_{H_2O,P,T}
\tag{aI-4}
$$

and

$$
\ln K_{P,T} = \frac{-\Delta_r G^0_{P,T}}{RT}
\tag{aI-5}
$$

where v_i, v_j, and v_{H_2O} refer to the stoichiometric reaction coefficients of the subscripted species, R is the universal gas constant, and $K_{T,P}$ the equilibrium constant at T and P.

Activity Coefficients

Activity coefficients for cation *i*, anion *l* and neutral species *n* can be calculated as

$$\log\gamma_i = -\frac{A\, z_i^2 \bar{I}^{1/2}}{\Lambda} + \Gamma_\gamma + w_i^{abs}\sum_k b_k y_k \bar{I} + \sum_l \frac{b_{il}\bar{y}_l \bar{I}}{\psi_l} \qquad \textbf{(aI-6)}$$

$$\log\gamma_l = -\frac{A\, z_l^2 \bar{I}^{1/2}}{\Lambda} + \Gamma_\gamma + w_l^{abs}\sum_k b_k y_k \bar{I} + \sum_i \frac{b_{il}\bar{y}_i \bar{I}}{\psi_i} \qquad \textbf{(aI-7)}$$

$$\log\gamma_n = \Gamma_\gamma + w_n\sum_k b_k y_k \bar{I} + \sum_i \frac{b_{ni}\bar{y}_i \bar{I}}{\psi_i} + \sum_l \frac{b_{nl}\bar{y}_l \bar{I}}{\psi_l} \qquad \textbf{(aI-8)}$$

where A is the Debye-Hückel parameter, z is the ionic charge, $\bar{I}$ is the effective ionic strength, and b_{il}, b_{ni}, and b_{nl} are the short-range interaction parameters. Γ_γ is a mole fraction/molality conversion factor:

$$\Gamma_\gamma = -\log(1 + 0.0180153m') \qquad \textbf{(aI-9)}$$

m' is the sum of molalities of all solute species.

The activity coefficient for the *k-th* component consisting of the *i-th* and *l-th* ions is

$$\log\gamma_{\pm,k} = -\frac{A\,|z_i z_l|\bar{I}^{1/2}}{\Lambda} + \Gamma_\gamma + \frac{w_k}{\nu_k}\sum_k b_k y_k \bar{I} + \frac{\nu_{i,k}}{\nu_k}\sum_l \frac{b_{il}\bar{y}_l \bar{I}}{\psi_l} + \frac{\nu_{l,k}}{\nu_k}\sum_i \frac{b_{il}\bar{y}_i \bar{I}}{\psi_i} \qquad \textbf{(aI-10)}$$

where

$$\Lambda = 1 + \mathring{a}_k b \bar{I}^{1/2} \qquad \textbf{(aI-11)}$$

$$\psi_i = \frac{Z_i^2}{2} \qquad \textbf{(aI-12)}$$

$$\psi_k = \frac{\sum_i \nu_{i,k} Z_i^2}{2} = \sum_i \nu_{i,k}\psi_i \qquad \textbf{(aI-13)}$$

$$b_k = \frac{w_k}{\psi_k}\cdot 10^{-11} \qquad \textbf{(aI-14)}$$

$$y_i = \frac{\psi_i m_{t,i}}{I} = \frac{\psi_i \sum_k \nu_{i,k} m_k}{I} \qquad \textbf{(aI-15)}$$

$$y_k = \frac{\psi_k m_k}{I} \qquad \textbf{(aI-16)}$$

$\bar{y}_i$ is defined in the same way as y_i, but using $\bar{I}$ instead of I. Equations aI-12 and aI-15 can be applied to cations and anions. b is the Debye-Hückel B parameter, and $\mathring{a}_k$ is an ion size parameter for the electrolyte.

The equations summarized above permit calculation of activity coefficients in mixed as well as single electrolytes at 25°C and 1 bar. Complex equations depending on T, P, T_0, P_0, a_i, Θ, *Ψ, w, Y,* and c_i, among other variables, are used to calculate the short-range interaction parameters at any other temperature and pressure.

Calculations Performed

Most of the work performed by Helgeson is focused on binary systems. He did not report any result for ternary or higher order systems in the papers reviewed (Helgeson and Kirkham, 1974a, b, 1976, Shock and Helgeson, 1988, Helgeson et al., 1981, Pokrovskii et al., 1997a, b, Sverjensky et al., 1997). Some work was performed trying to reproduce some of those binary results, but the agreement between experimental and calculated data was not good. Figures aI-1 and aI-2 show the calculations for the binary systems NaCl-H_2O and NaOH-H_2O. DH-Helgeson refers to the first term of equation aI-10, while Helgeson refers to the addition of all the terms in equation aI-10.

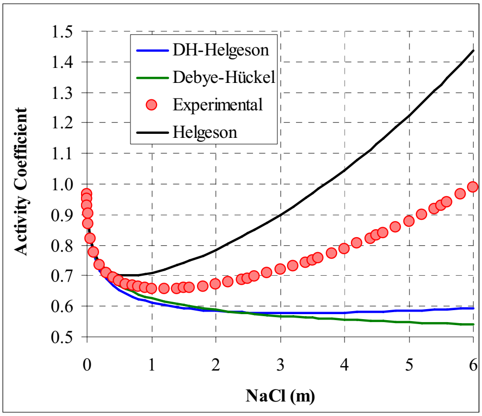

Figure aI-1. Mean activity coefficient for the system NaCl-H_2O at 25°C and 1 bar.

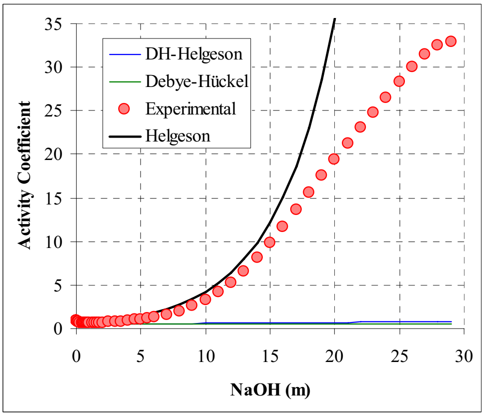

Figure aI-2. Mean activity coefficient for the system NaOH-H_2O at 25°C and 1 bar.

Apart from the impossibility to reproduce Helgeson's results, the final number of parameters required to implement Helgeson's approach is rather large. Such number increases considerably when the temperature and pressure are different from 25ºC and 1 bar. Many of the required parameters were not available for most of the scaling minerals of interest in the present work. Therefore, the use of Helgeson's framework for the purpose of the present Ph.D. is not a recommendable choice, and it does not report any advantage when compared to extended UNIQUAC.

Bromley's Model

The great achievement of the model proposed by Bromley is the use of just one interaction parameter for each salt. Many of those parameters are reported in literature (Zemaitis et al., 1986, Borge et al., 1996, Belaustegi et al., 1998, Raposo et al., 1998).

Chaiko et al. (1988) assure that Bromley's method often works well for both single and multicomponent electrolyte solutions at ionic strengths lower than 6 m. Zhaoyue et al. (1995) compared Bromley's model with Pitzer's model for binary systems at temperatures in the range 15-25°C, and 1 bar. In general, Pitzer's method performs better, but in some systems the agreement between Bromley's estimations and experimental data was very close. Nonetheless, in many other systems Bromley's model can lead to significant over or under estimation.

The molal activity coefficient of ion *i* in a multicomponent solution at 25°C can be expressed as (Zemaitis et al., 1986).

$$\ln \gamma_i = -\frac{A z_i^2 I^{½}}{1 + I^{½}} + F_i \qquad \textbf{(aI-17)}$$

where A is the Debye-Hückel constant, I the ionic strength, and z_i the charge of ion i. F_i is a summation of interaction parameters. The first term on the right hand side of equation aI-17 is the Debye-Hückel activity coefficient, used in a mol fraction scale, while the second term is given in a molal scale. Therefore, there is some incongruence related to the units chosen for equation aI-17.

$$F_i = \sum_l \dot{B}_{il} z_{il}^2 m_l \qquad \textbf{(aI-18)}$$

$$F_l = \sum_i \dot{B}_{il} z_{il}^2 m_i \qquad \textbf{(aI-19)}$$

where subscript *i* denotes cation and *l* anion

$$z_{il} = \frac{z_i + z_l}{2} \qquad \textbf{(aI-20)}$$

The terms $\dot{B}$ are calculated as

$$\dot{B}_{il} = \frac{(0.06 + 0.6B_{il})|z_i z_l|}{\left(1 + \frac{1.5}{|z_i z_l|} I\right)^2} + B_{il} \qquad \textbf{(aI-21)}$$

B_{il} is a parameter accounting for ion-ion interactions.

The equations presented above do not take into account interactions between two ions with the same charge, or any higher order interactions.

For molecular species *n*, Setschénow equation is used:

$$\ln \gamma_n = \ln\left(\frac{m_n^0}{m_n}\right) = k m_s \qquad \textbf{(aI-22)}$$

where m_n^0 is the solubility of the gas in pure water, m_n the solubility of the gas in the multicomponent solution, *k* the salting out parameter, and m_s the molality of the salt in the solution.

The water activity for a single electrolyte solution can be calculated from the osmotic coefficient as

$$\ln a_w^0 = -\frac{M_s \nu m}{1000} \Phi \qquad \textbf{(aI-23)}$$

where M_s is the molecular weight of the solvent, *m* represents the electrolyte molality, and *v* is the number of ions the electrolyte dissociates into. To calculate the water activity of a multicomponent solution it is necessary to apply equation aI-23 to each electrolyte present in the mixture. Once these values are obtained, the method suggested by Meissner and Kusik can be used (Zemaitis et al., 1986):

$$\log(a_w)_{mix} = \sum_i \sum_l W_{il} \log(a_w^0)_{il} + r \qquad \textbf{(aI-24)}$$

where $(a_w^0)_{il}$ is the hypothetical pure solution water activity for electrolyte *il*. Further information about the calculation of W_{il} and *r* can be found in Zemaitis et al. (1988).

The temperature dependence of the activity coefficient presented by Bromley is accounted by two terms: The Debye-Hückel *A* parameter, and the *B* parameter. Bromley presented two alternative equations to correlate the effect of temperature on *B*, including four additional parameters

$$B = B_1 \ln\frac{T - 243}{T} + \frac{B_2}{T} + B_3 + B_4 \ln T \qquad \textbf{(aI-25)}$$

$$B = \frac{B_1}{T - 230} + \frac{B_2}{T} + B_3 + B_4 \ln T \qquad \textbf{(aI-26)}$$

It is believed the use of Bromley's model is not adequate for multicomponent solutions, since it employs the concept "molality of the electrolyte" in equation aI-23 to calculate water activity. That term can lead to confussion and different results depending on the interpretation given to the system and the electrolytes considered to be formed (i.e., a system formed by K^+, Na^+, Cl^- and SO_4^- can be regarded as a mixture of NaCl and K_2SO_4; or Na_2SO_4 and KCl; or NaCl, K_2SO_4, and KCl, etc). Table aI-1 shows different result which can be obtained using the concept of "molality of the electrolyte" for a multicomponent solution formed by $CaCl_2$, $CaSO_4$, NaCl, and Na_2SO_4, even though the total concentrations of the species are constant (4 m Ca^{2+}, 2 m Na^+, 3 m Cl^-, and 3.5 m SO_4^-).

Table aI-1
Different "molality of the electrolyte" results for a common-ion solution

	Solution 1		**Solution 2**	
	Cation (m)	**Anion (m)**	**Cation (m)**	**Anion (m)**
$CaCl_2$	1	2	0.75	1.5
$CaSO_4$	3	3	3.25	3.25
NaCl	1	1	1.5	1.5
Na_2SO_4	1	0.5	0.5	0.25

References in Appendix I

Belaustegi, Y., Olazabal, M. A., Madariaga, J. M., 1999. Development of a Modified Bromley's Methodology for the estimation of ionic media effects on solution equilibria. Part 4. The chemical model of Fe(III) with the halide ligands in aqueous solution at 25ºC Fluid Phase Equilibria 155, 21-31.

Borge, G., Castaño, R., Carril, M. P., Corbillón, M. S., Madariaga, J. M., 1996. Development of a Modified Bromley's Methodology (MBM) for the estimation of ionic media effects on solution equilibria Part 1. Calculation of the interaction parameters in the molar and molal scales at 25ºC Fluid Phase Equilibria, 121, 85-98.

Bromley, L.A., 1973. Thermodynamic properties of strong electrolytes in aqueous solutions. AIChE Journal 19, 313-320.

Chaiko, D.J., Fredrickson, D.R., Reichley-Yinger, L., Vandegrift, G.F., 1988. Separation Science and Technology 23, 1435-1451.

Helgeson, H.C., 1967. Thermodynamics of complex dissociation in aqueous solutions at elevated temperatures. J. Phys. Chem. 71, 3121-3136.

Helgeson, H.C., 1969. Thermodynamics of hydrothermal systems at elevated temperatures and pressures. Amer. J. Sci. 267, 729-804.

Helgeson, H.C., 1970. Calculation of mass transfer in geochemical process involving aqueous solutions. Geochimica et Cosmochimica Acta 34, 569-592.

Helgeson, H.C., Kirkham, D.H., 1974 a. Theoretical prediction of the thermodynamic behaviour I. American Journal of Science 274, 1089-1198.

Helgeson, H.C., Kirkham, D., 1974 b. Theoretical prediction of the thermodynamic behaviour of aqueous electrolytes at high pressures and temperatures: II. Debye-Hückel parameters for activity coefficients and relative partial molal properties. Amer. J. Sci. 274, 1199-1261.

Helgeson, H.C., Kirkham, D.H., 1976. Theoretical prediction of the thermodynamic behaviour III American Journal of Science 276, 97-240.

Helgeson, H.C., Delany, J.M., Nesbitt, H., Wayne; B., Dennis, K., 1978. Summary and critique of the thermodynamic properties of rock-forming minerals. Pp 229

Helgeson H.C., Kirkham D.H., Flowers G.C., 1981. Theoretical prediction of the thermodynamic behaviour IV. American Journal of Science 281, 1249-1516.

Johnson, J.W., Oelkers, E.H., Helgeson, H.C., 1992. SUPCRT92: A software package for calculating the standard molal thermodynamic properties of minerals, gases, aqueous species, and reactions from 1 to 5000 bar and 0 to 1000ºC. Computers and Geosciences 18, 899-947.

Pokrovskii, V.A., Helgeson, H.C., 1997a. Thermodynamic Properties of Aqueous Species and the Solubilities of Minerals at High Pressures and Temperatures: The System Al_2O_3-H_2O-KOH. Chemical Geology 137, 221-242.

Pokrovskii, V.A., Helgeson, H.C., 1997b. Geochimica et Cosmochimica Acta 61, 2175-2183.

Raposo, J. C., Sanz, J., Borge, G., Olazábal, M. A., Madariaga, J. M., 1998. Fluid Phase Equilibria 155, 1-19.

Shock, E.L., Helgeson, H.C., 1988. Calculation of the thermodynamic and transport properties. Geochimica et Cosmochimica Acta 52, 2009-2036.

Sverjensky, D.A., Shock, E.L., Helgeson, H.C., 1997. Geochimica et Cosmochimica Acta 61, 1359-1412.

Tanger, J. C., Helgeson, H. C., 1988. American Journal of Science, 288, 19-98.

Zhaoyue, M., Seinfeld, J.H., Saxena, P., Kim, Y.P., 1995. Aerosol Science and Technology 23, 131-154.

Zemaitis, J. F. Jr., Clark, D. M., Rafal, M., Scrivner, N. C., 1986. Handbook of aqueous electrolyte thermodynamics, design institute for physical property data, New York.

Appendix II: Conductivity Measurements

In this Appendix, complementary data and results for the conductivity measurements performed for $SrSO_4$-H_2O solutions and presented in Chapter 8 are included.

The amount of initial salt and distilled water used in the preparation of the starting celestite ($SrSO_4$) solutions for the different conductivity measurements are reported in table aII-1. The added water flow rate can also be seen there.

Table aII-1
Experimental conditions

Experiment	$SrSO_4$ (g)	$V_{initial}$ (mL)	*rate* (mL·min^{-1})
1	0.0711	500	0.2
2	0.0718	500	0.2
3	0.0787	500	0.2

Figure aII-1 and aII-2 show the results obtained for experiment 1. A relatively flat zone corresponding to a total solution volume around 510-530 mL is observed. From that point, the conductivity decreases continuously. This could be interpreted as the result of a dilution process. Nevertheless, the first measurements in figure aII-1 show an unexpected positive slope. The increasing conductivity with volume must be explained as a dissolution process, consequence of the lack of equilibrium in the original sample. This behaviour manifests the unsuitability of synthetic methods for our purposes as the time to attain equilibrium is too long.

To be completely sure the lack of equilibrium in the original sample was responsible of the positive slope in figure aII-1, a new experiment (experiment 2) was performed. In experiment 2, additional volumes of water were only added once the initial sample was at equilibrium (constant value of conductivity over the time). Stirring was used to accelerate the equilibrium, which was only observed after 20 hours. The results for experiment 2 are shown in figure aII-3.

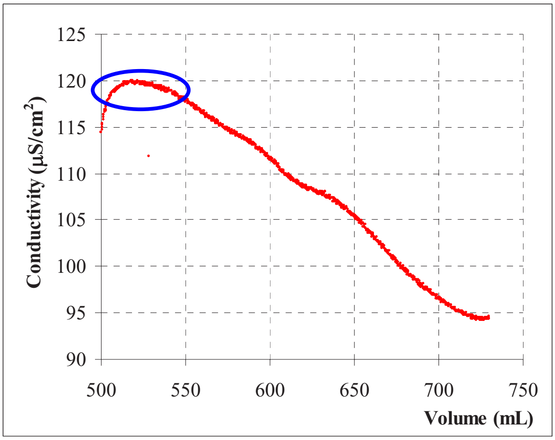

Figure aII-1. Results for experiment 1

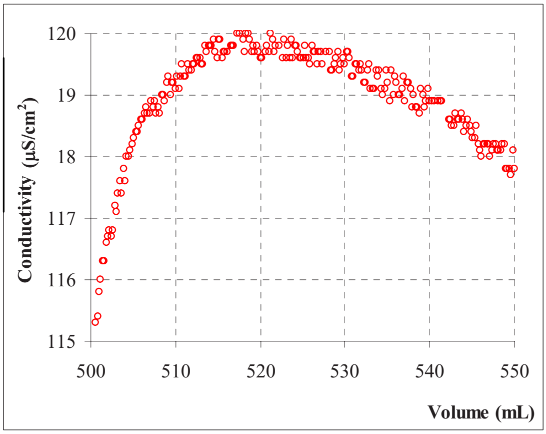

Figure aII-2. Results for experiment 1: amplified section of figure aII-1

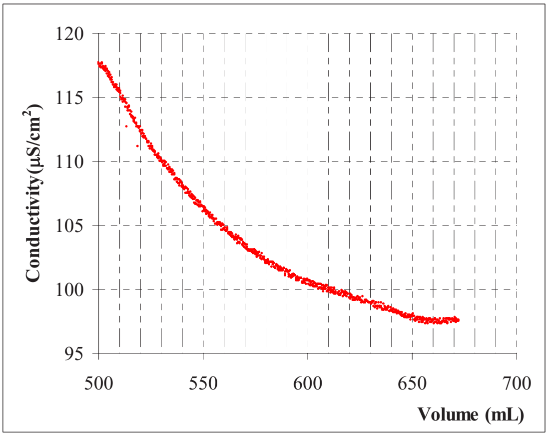

Figure aII-3. Results for experiment 2

Comparing figures aII-1 and aII-3, it is clear the initial increase in conductivity observed in experiment 1 is consequence of a dissolution process.

In figure aII-3, a continuous decrease in conductivity is observed. This can only be explained as a dilution process, meaning that either the original sample was undersaturated (very unlikely) or that the equilibrium is not reached for any of the measurements. The excess of $SrSO_4$ placed in the original sample was calculated according to literature data on the solubility of celestite in pure water. To verify whether undersaturation was the responsible cause of the shape of figure aII-3, a solution containing a rather larger amount of salt in the same initial volume of distilled water was prepared (experiment 3). The new solution was clearly saturated, and some solid particles could be observed at the bottom of the vessel after equilibrium was reached (constant conductivity after stirring the solution for several hours). The results for experiment 3 are shown in figure aII-4.

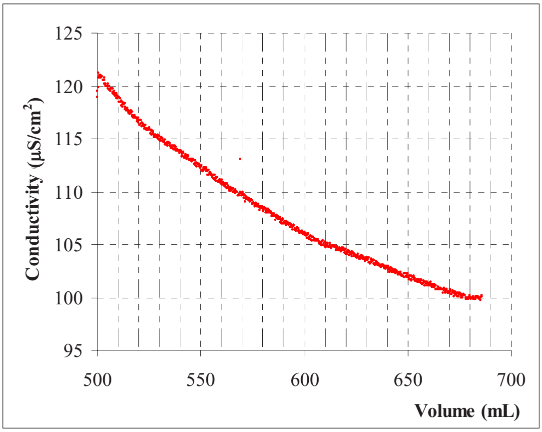

Figure aII.4. Results for experiment 3

Figure aII-4 proves the conductivity continuously decreases when adding more solvent, even though solid phase is present in the vessel. Therefore, this behaviour must be a consequence of kinetic impediments for the $SrSO_4$-H_2O system. It is reported by many authors that alkaline earth metal sulphates have slow dissolution kinetics. Thus, after adding an amount of water, even though such amount is very low, dissolution of solid particles takes several hours and the solution is not allowed to reach equilibrium before the next addition. So, the dilution effect is much faster than the dissolution process, and the former effect is the only one observable in the measurements performed.

References in Appendix II

Bock, J., Bestgen, H., Elschner, S., Preisler, E., 1993. Large shaped parts of melt cast BSCCO for applications in electrical engineering. IEEE Transactions of Applied Superconductivity 3 (1), 1659-1662.

Appendix III: BaSO$_4$ Solubility in NaCl at High Temperature and Pressure

Appendix III is a complement to Chapter 8 on the solubility of BaSO$_4$ in sodium chloride solutions at high temperatures and pressures. The experimental conditions used, volumes of solution filtrated, ICP-MS results, and BaSO$_4$ concentrations are given in tables aIII-1 to aIII-5. Results concerning the system NaCl-H$_2$O are reported in tables aIII-6 to aIII-9.

The calibration curves used for the ICP-MS measurements for samples 1 to 17 are shown in figure aIII-1. The results from the ICP-MS analysis performed at the Chemistry department of DTU for experiments 1 to 17 are reported in table aIII-1. *SD* stands for standard deviation, and *CV* is the variation coefficient:

$$CV = \frac{SD}{Mean} \cdot 100 \qquad \textbf{(aIII-1)}$$

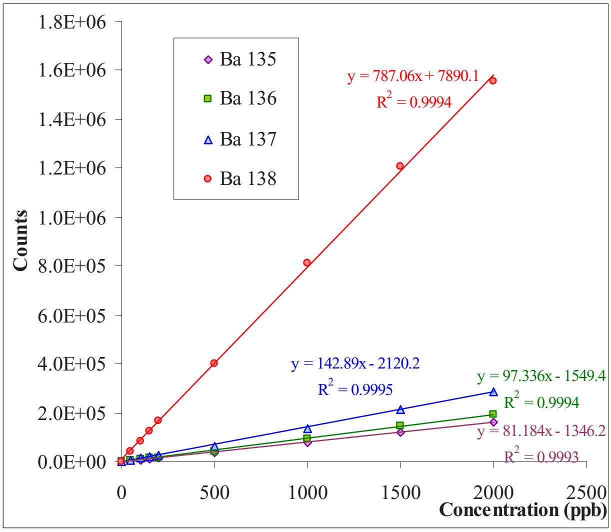

Figure aIII-1. Calibration curves for ICP-MS measurements for experiments 1 to 17

Table aIII-1
ICP-MS results for experiments 1 to 17

Exp.	^{135}Ba (ppb)	^{136}Ba (ppb)	^{137}Ba (ppb)	^{138}Ba (ppb)	Mean (ppb)	*SD* (ppb)	*CV* (%)
1	1543.44	1561.01	1550.65	1565.50	**1555.15**	9.98	0.64
2	2072.65	2074.04	2074.08	2021.59	**2060.59**	26.01	1.26
3	1775.02	1789.19	1783.58	1768.95	**1779.18**	8.97	0.50
4	1751.30	1759.40	1754.89	1748.29	**1753.47**	4.79	0.27
5	1353.23	1362.34	1357.52	1386.52	**1364.90**	14.88	1.09
6	1571.53	1574.12	1571.86	1586.50	**1576.00**	7.10	0.45
7	1374.91	1381.44	1381.86	1408.09	**1386.58**	14.69	1.06
8	2009.18	2018.96	2007.12	1957.34	**1998.15**	27.69	1.39
9	2110.26	2118.51	2104.78	2041.09	**2093.66**	35.49	1.70
10	1545.27	1539.47	1545.25	1567.64	**1549.41**	12.46	0.80
11	1412.89	1421.26	1421.17	1451.07	**1426.60**	16.78	1.18
12	2047.93	2041.17	2035.25	1992.80	**2029.29**	24.87	1.23
13	797.32	803.49	802.25	849.12	**813.05**	24.20	2.98
14	746.89	750.06	752.38	799.20	**762.13**	24.81	3.26
15	993.11	995.63	1000.68	1053.01	**1010.61**	28.44	2.81
16	1124.15	1124.57	1129.97	1176.33	**1138.76**	25.19	2.21
17	1289.64	1289.39	1293.20	1327.15	**1299.85**	18.29	1.41
100[a]	218.636677	218.535794	217.793408	223.234442	**219.55**	2.48	1.13

[a] Test-Standard containing 100 ppb Ba^{2+}

The calibration curves used for the second ICP-MS measurements for samples 10 to 17 are shown in figure aIII-2. The results from the second ICP-MS analysis performed at the Chemistry department of DTU for experiments 10 to 17 are reported in table aIII-2.

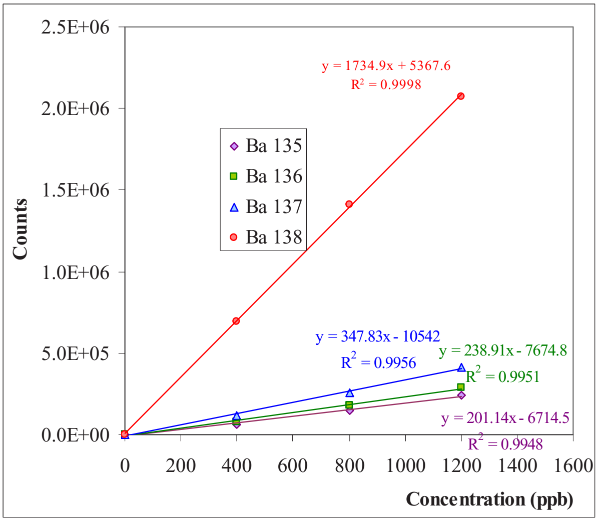

Figure aIII-2. Calibration curves for second ICP-MS measurements for experiments 10 to 17

Table aIII-2
Second ICP-MS results for experiments 10 to 17

Exp.	^{135}Ba (ppb)	^{136}Ba (ppb)	^{137}Ba (ppb)	^{138}Ba (ppb)	Mean (ppb)	*SD* (ppb)	*CV* (%)
10	1825.62	1817.95	1802.62	1564.02	1752.55	126.05	7.19
11	1507.72	1507.30	1486.31	1373.16	1468.62	64.42	4.39
12	1895.46	1886.21	1864.30	1618.33	1816.08	132.48	7.29
13	997.13	1000.65	999.37	1000.36	999.38	1.60	0.16
14	856.36	857.56	852.97	880.85	861.94	12.76	1.48
16	1087.37	1091.83	1089.58	1076.24	1086.26	6.92	0.64
16	1038.46	1035.54	1034.72	1031.45	1035.04	2.88	0.28
17	1137.17	1134.62	1127.53	1107.70	1126.75	13.34	1.18
100[a]	162.53	162.88	162.20	162.23	162.46	0.32	0.20
500[b]	646.86	651.46	650.38	690.01	659.68	20.32	3.08
1000[c]	1291.24	1298.00	1291.62	1230.42	1277.82	31.75	2.48
100_2[d]	188.83	188.82	189.57	194.02	190.31	2.50	1.31

[a] Standard containing 100 ppb of Ba^{2+} in 0.1% NaCl solution
[b] Standard containing 500 ppb of Ba^{2+} in 0.1% NaCl solution
[c] Standard containing 1000 ppb of Ba^{2+} in 0.1% NaCl solution
[d] Commercial standard containing 100 ppb of Ba^{2+}.

Table aIII-3
Laboratory ICP-MS results for experiments 1 to 17 and test-standards

Exp.	Ba (μg L^{-1})	*CV* (%)
1	1700	1.6
2	1400	1.6
3	1300	1.6
4	1300	1.6
5	1200	1.6
6	1300	1.6
7	1400	1.6
8	1200	1.6
10	3600	1.6
11	1300	1.6
12	2900	1.6
13	850	1.6
14	720	1.6
16	910	1.6
16	880	1.6
17	980	1.6
500[a]	1100	1.6
1000[a]	1600	1.6
1500[a]	2000	1.6
2000[a]	2400	1.6
2500[a]	3700	1.6

[a] Standards in 0.1 % NaCl. Their Ba^{2+} concentration corresponds to the value given in table aIII-3.

The sample volumes filtrated in the experiments, the mass of water placed in the dilution vessel and the final barite concentration calculated from the ICP-MS results is reported in table aIII-4 for experiments 1 to 8, and in table aIII-5 for experiments 10 to 18.

Table aIII-4
Experimental variables and calculated concentrations for experiments 1 to 9

Exp.	Time (h)	$V_{filtrated}$ (mL)	Dilution mass (g)	$ICP\text{-}MS_{DTU1}$ (ppb)	$BaSO_{4,DTU1}$ (m)	$ICP\text{-}MS_{Lab}$ ($\mu g\ L^{-1}$)	$BaSO_{4,Lab}$ (m)
1	4	74.18	30.03	1555.15	6.34E-05	1700	6.92E-05
2	4[a]	74.43	30.11	2060.59	8.39E-05	1400	5.69E-05
3	6[a]	74.32	30.07	1779.18	7.25E-05	1300	5.29E-05
4	2[a]	74.81	30.20	1753.47	7.14E-05	1300	5.28E-05
5	3	74.81	30.22	1364.90	5.55E-05	1200	4.87E-05
6	2[b]	74.41	30.13	1576.00	6.41E-05	1300	5.28E-05
7	2	74.16	30.09	1386.58	5.64E-05	1400	5.68E-05
8	6[a]	74.67	30.23	1998.15	8.11E-05	1200	4.86E-05
9	9[a]	75.98	30.47	2093.66	8.52E-05	3600	1.46E-04

Table aIII-5
Experimental variables and calculated concentrations for experiments 10 to 18

Exp.	Time (h)	$V_{filtrated}$ (mL)	Dilution mass (g)	$ICP\text{-}MS_{DTU1}$ (ppb)	$BaSO_{4,DTU1}$ (m)	$ICP\text{-}MS_{DTU2}$ (ppb)	$BaSO_{4,DTU2}$ (m)	$ICP\text{-}MS_{Lab}$ ($\mu g\ L^{-1}$)	$BaSO_{4,Lab}$ (m)
10	12[a]	74.88	30.30	1549.41	6.29E-05	1752.55	7.1096E-05	3600	1.46E-04
11	16[a]	74.72	30.28	1426.60	5.78E-05	1468.62	5.9539E-05	1300	5.26E-05
12	4[a]	74.93	30.34	2029.29	8.22E-05	1816.08	7.3582E-05	2900	1.17E-04
13	6[a]	89.90	22.12	813.05	6.18E-05	999.38	7.5961E-05	850	6.45E-05
14	6	102.05	23.04	762.13	5.96E-05	861.94	6.7399E-05	720	5.62E-05
15	6	106.01	23.01	1010.61	8.17E-05	1086.26	8.7837E-05	910	7.34E-05
16	9[a]	105.15	23.06	1138.76	9.11E-05	1035.04	8.2812E-05	880	7.02E-05
17	5	104.57	22.77	1299.85	1.06E-04	1126.76	9.1815E-05	980	7.97E-05
18	7	105.19	23.02			986.61	7.9207E-05	780	6.25E-05

[a] Apart form the agitation time reported in table aIII-5, the solution was kept at constant temperature and pressure with no agitation for another 16 h.

[b] Apart form the agitation time reported in table aIII-5, the solution was kept at constant temperature and pressure with no agitation for another 44 h.

Table aIII-6 reports the NaCl concentration found in samples that have been agitated for different periods of time. The experimental samples were diluted with distilled water (the dilution rate is reported in the third column of table aIII-6), and the concentration of NaCl (C_{NaCl}) was determined by titration with $AgNO_3$ 0.1 M:

$$C_{NaCl} = \frac{C_{AgNO_3} \cdot V_{AgNO_3}}{V'_{NaCl}} \qquad \textbf{(aIII-2)}$$

where V_{AgNO_3} is the volume of $AgNO_3$ used in the titration, and V'_{NaCl} is the volume of the undiluted NaCl sample (i.e., if the dilution rate is 5:250, $V'_{NaCl} = 5V_{NaCl}/250$).

Table aIII-6

Determination of the time required to attain equilibrium for the system NaCl-H_2O at 30ºC and 1 atm using agitation (vibration)

Exp.	Time (min)	Dilution NaCl:H_2O	V_{AgNO3_1} (mL)	V_{AgNO3_2} (mL)	V_{NaCl} (mL)	NaCl (M)	*SD* (M)
NaCl_1	0	5:250	1.9	1.9	2	4.85	0.00
NaCl_2	15	5:250	2.2	2.2	2	5.61	0.00
NaCl_3	30	5:250	2.1	2.1	2	5.36	0.00
NaCl_4	60	4:250	1.7	1.7	2	5.42	0.00
NaCl_5	90	1:100	2.6	2.6	5	5.30	0.00
NaCl_6	120	2:500	0.4	0.45	2	5.42	0.45
NaCl_7	150	8:500	1.6	1.8	2	5.42	0.45
NaCl_8	270	5:250	5.4	5.3	5	5.51	0.07
NaCl_9	330	5:250	5.2	5.2	5	5.36	0.00

Table aIII-7

Determination of the time required to attain equilibrium for the system NaCl-H_2O at 30ºC and 1 atm without using agitation

Exp.	Time (h)	Dilution NaCl:H_2O	V_{AgNO3} (mL)	C_{AgNO3} (M)	V_{NaCl} (mL)	NaCl (M)
NaCl_10	1	10:100	91.2	0.05	15	3.04
NaCl_11	3	5:250	9.5	0.1	10	4.75
NaCl_12	5	5:250	9.0	0.1	10	4.50
NaCl_13	7	5:250	10.7	0.1	10	5.35
NaCl_14	23	5:250	5.4	0.1	5	5.40

Table aIII-8

NaCl solubility in pure water at 30ºC

Exp.	P (bar)	$V_{filtrated}$ (mL)	Dilution mass (g)	Dilution NaCl:H_2O	V_{AgNO3_1} (mL)	V_{AgNO3_2} (mL)	V_{AgNO3_3} (mL)	V_{NaCl} (mL)	NaCl (M)	*SD* (M)
NaCl_15	100	36.23	86.885	10:100	2.7	2.6	2.6	2	6.60	0.14
NaCl_16	300	45.05	60.035	10:100	4.4	4.4	4.3	2.5	5.52	0.07
NaCl_17	300	50.17	75.249	20:200	3.25	3.3	3.3	2	5.38	0.05
NaCl_18	400	45.14	75.487	10:100	3.0	3.1	3.1	2	5.53	0.10
NaCl_19	400	45.16	75.744	10:100	3.2	3.2	3.3	2	5.84	0.10
NaCl_20	400	41.03	75.113	10:100	2.9	3.0	2.9	2	5.80	0.11

Table aIII-9

NaCl solubility in pure water at 100ºC

Exp.	P (bar)	$V_{filtrated}$ (mL)	Dilution mass (g)	Dilution NaCl:H_2O	V_{AgNO3_1} (mL)	V_{AgNO3_2} (mL)	V_{AgNO3_3} (mL)	V_{NaCl} (mL)	NaCl (M)	*SD* (M)
NaCl_21	100	44.78	71.82	10:100	3.4	3.5	3.5	2	6.89	0.11
NaCl_23	100	40.49	74.92	5:100	1.9	1.9	1.9	2.5	6.87	0.00
NaCl_24	300	45.17	65.72	10:100	5.5	5.5	5.7	3	6.88	0.13
NaCl_25	300	41.24	75.72	5:100	0.7	0.8	0.8	1	6.80	0.47
NaCl_26	500	36.78	74.02	5:100	1.5	1.55	1.5	2	7.45	0.13
NaCl_27	500	42.08	75.45	5:100	2.35	2.3	2.3	3	6.65	0.08
NaCl_28	500	45.12	74.48	10:100	8.65	8.45	8.55	5	6.82	0.07
NaCl_29	500	45.18	74.42	10:100	9.05	9.1	9.3	5	7.28	0.09
NaCl_30	500	45.19	73.40	10:100	9.3	9.35	9.3	5	7.35	0.02
NaCl_31	500	36.47	74.20	10:100	3.45	3.4	3.4	2.5	6.79	0.05

Figure aIII-3. Experimental setup

Figure aIII-4. Experimental Setup II

Ada Villafáfila García

Measurement and Modeling of Scaling Minerals

ISBN: 87-91435-30-7